europhysics
conference
abstracts

24th European Physical Society Conference on

Controlled Fusion and Plasma Physics

Berchtesgaden, 9th-13th June 1997

Editors: M. Schittenhelm, R. Bartiromo and F. Wagner

Contributed Papers, Part IV

Published by: The European Physical Society

Series Editor: Prof. R. Pick, Paris

Managing Editor: G. Thomas, Geneva

Volume 21A
Part IV

24th European Physical Society Conference on

Controlled Fusion and Plasma Physics

Kongresshaus Berchtesgaden, Germany

9 - 13 June 1997

Editors: M. Schittenhelm, R. Bartiromo and F. Wagner

europhysics
conference
abstracts

24th European Physical Society Conference on

Controlled Fusion and Plasma Physics

Berchtesgaden, 9th-13th June 1997

Editors: M. Schittenhelm, R. Bartiromo and F. Wagner

Contributed Papers, Part IV

Published by: The European Physical Society

Series Editor: Prof. R. Pick, Paris

Managing Editor: G. Thomas, Geneva

Volume 21A
Part IV

EUROPHYSICS CONFERENCE ABSTRACTS is published
by the European Physical Society, ©1997

The Proceedings may be purchased from Max-Planck-Institut für Plasmaphysik, Boltzmannstrasse 2, 85748 Garching, Germany.

Preface

The 24th European Physical Society Conference on Controlled Fusion and Plasma Physics, under the auspices of the Plasma Physics Division of the European Physical Society, was hosted by the Max-Planck-Institut für Plasmaphysik Garching, Germany. Following the guidelines of the Board of the EPS Plasma Physics Division, the 1997 Conference included topics from the areas of: Tokamaks; Stellarators; Alternative Magnetic Confinement Schemes; Magnetic Confinement Theory and Modelling; Plasma Edge Physics; Plasma Heating; Current Drive and Profile Control; Diagnostics; Basic Collisionless Plasma Physics; Highly Compressed and Non Stationary Plasmas.

The scientific programme and paper selection were the responsibility of the International Programme Committee appointed by the Board of the EPS Plasma Physics Division. The Programme Committee selected 523 contributed papers (out of 651 submitted abstracts) for presentation as posters in four sessions at the meeting. Guideline for the composition of the poster session was to display the various contributions of larger teams in one session and to place teams of similar goals and interests into different sessions.

As in the past, the Proceedings are printed after the meeting, giving authors the opportunity to present their latest results in four-page papers. According to EPS Plasma Physics Division regulations, the Conference Proceedings contain the four-page papers of all those contributions for which at least one author was a registered participant at the Conference. All submitted papers satisfy this condition. 51 papers were not presented at the Conference and not submitted to the Scientific Secretary though they had originally been accepted by the Programme Committee. This caused some problems in the organisation of the poster sessions. As only in a few cases the cancellation had technical reasons, it is strongly recommended for future conferences that along with the submission of an abstract a guarantee has to be provided that an accepted paper will be presented

The four volumes of the proceedings will be mailed to all registered participants of the Conference. The papers of the 8 Review Lectures and 20 Topical Lectures will be published in a Special Issue of the journal 'Plasma Physics and Controlled Fusion', which will also be mailed to all registered participants.

M. Schittenhelm, R. Bartiromo and F. Wagner

July 1997

Programme Committee

R. Bartiromo	IGI del CNR, Italy - Chairman
E. Ascasibar	CIEMAT, Madrid, Spain
D. Gresillon	LPMI/EP, Palaiseau, France
R.D. Hazeltine	Texas University, USA
F. Hofmann	CRPP/EPFL, Lausanne, Switzerland
A. Litvak	IAP, Nizhny Novgorod, Russia
L. Stenflo	Umea University, Sweden
F. Sluijter	Eindhoven University, Netherlands
D.F.H. Start	JET Joint Undertaking, Abingdon, U. Kingdom
U. Samm	Forschungszentrum Jülich, Germany
F. Serra	Universidad Technica, Lisboa, Portugal
T. Todd	UKAEA Fusion, Abingdon, United Kingdom
F. Wagner	IPP, Garching, Germany
R. Weynants	ERM, Brussels, Belgium

Local Organising Committee

F. Wagner	Chairman
G. Zankl	Vice Chairman
M. Schittenhelm	Scientific Secretary
A. Eggeling (Ms).....	Conference Secretary
T. Geist	
H. Jahreiss	Finance Officer
Ch. Stahlberg (Ms)	
K.-H. Steuer	

Acknowledgements

The Conference Organisers gratefully acknowledge financial support from the following:

Accel Instruments GmbH
Bayerische Vereinsbank AG
Cray Research GmbH
BESTEC GmbH
European Commission
Kurdirektion Berchtesgaden
Oxford Instruments
Spinner GmbH
Max-Planck-Institut für Plasmaphysik

Contents of
Europhysics Conference Abstracts
Volume 21A (Part I - Part IV)

Index of Contributed Papers

Contributed Papers

Contents of Part I (Poster Session 1)

Contents of Part II (Poster Session 2)

Contents of Part III (Poster Session 3)

Contents of Part IV (Poster Session 4)

H-mode confinement on ASDEX Upgrade

Edge Profile Investigations Close to the Density Limit of Various Plasma Regimes in ASDEX Upgrade

V Mertens, H S Bosch, M Kaufmann, M Maraschek, J Neuhauser, H Salzmann, J Schweinzer, W Suttrop, ASDEX Upgrade Team

Max-Planck-Institut für Plasmaphysik, EURATOM Association, 85748 Garching, Fed. Rep. of Germany

Introduction :

The highest achievable density in a tokamak is restricted by an upper boundary called the density limit (DL). In the Ohmic- and L-mode the discharges disrupt when their densities reach this limit. In the H-mode, however, the limit is characterized by a smooth back-transition into the L-mode. Empirically, the density limit is quite successfully described even on machines of different sizes by the Greenwald limit $\bar{n}_e^{GW} = \kappa < j >$ (κ is the plasma elongation and $< j >$ the area averaged plasma current density) [1]. It is originally developed for L-mode discharges with only intrinsic impurities without additional impurity injection. A pronounced feature is its heating power P_{heat} independency. Since the ITER concept aspires an operation density slightly above this limit ($\approx 1.3\ \bar{n}_e^{GW}$), one needs reliable scenarios to overcome it without deterioration of the energy confinement time. The H-mode is, therefore, the preferred operation mode. Additionally, the divertor has to be protected against thermic overload as can be caused e.g. by strong ELMs. One possibility is here the addition of impurities which radiate in the edge and remove the power poloidally uniformely as much as possible. Moreover, this methode aids the development of divertor detachment. Since both the H- and L-mode density limit is commonly believed to be an edge physics effect, we focus our studies on the boundary. The L-mode density limit is quite well understood as a thermal instability limit (Marfe) and increases moderately with heating power [2]. The physics of the H-mode density limit, which is found to be nearly independent of heating power [2], is on the other hand still not completely unraveled. One explanation recently proposed by FW Perkins [3] connects it with the reach of the ballooning limit, i.e. critical pressure gradients, in the edge. Another attempt is discussed by K Borrass [4] who correlates the limit in both the L- and H-mode with the achievement of full divertor detachement.

This paper deals mainly with the comparison of edge parameter characteristics of conventional gas-puff refuelled H- and L-mode discharges with and without auxiliary impurity seeding. Especially, the density and pressure behaviour will be discussed.

Discharge Parameters and Diagnostics :

Our investigations concentrate on lower single null discharges (R = 1.65 m, a = 0.5 m, $\kappa \sim 1.6$) in deuterium with plasma currents of 0.8 MA (low $\overline{Z}_{eff}$) and 1.0 MA (high $\overline{Z}_{eff}$) applying up to 10 MW NBI heating power. The corresponding safety factors q_{95} vary between 3 and 4. The line averaged electron density $\overline{n}_e$ ranges between $0.8 \cdot 10^{20} m^{-3}$ and $1.2 \cdot 10^{20} m^{-3}$. Highly radiative mantle discharges are performed by injecting mostly Neon gas into the main chaimber.

The edge densities and temperatures mainly presented are measured by a Li-beam diagnostics, measuring the local density slightly below the outside midplane and the

Thomson scattering diagnostics measuring n_e and T_e vertically in the outer lower plasma zone.

Experimental Observations :
The H-mode is generally accessible when the power flowing across the separatrix into the boundary $P_{sep} = P_{heat} - P_{rad}^{bulk}$ exceeds a certain limit depending on density and toroidal magnetic field $P_{sep}^{L \to H} = c \cdot \overline{n}_e B_t$ where the constant c depends mainly on ion species and ion ∇B drift direction [5]. Closely above the threshold the H-mode is characterized by high frequency type-III ELM's ($\partial \nu_{ELM} / \partial P_{sep} < 0$). Deeper in the H-mode the ELM activity changes to low frequency type-I ELMs ($\partial \nu_{ELM} / \partial P_{sep} > 0$) [6].

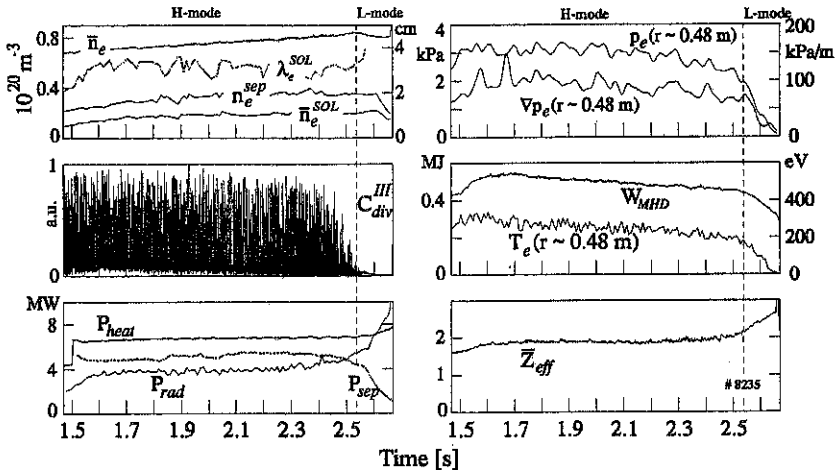

Figure 1: *This is an example of a discharge which is successively driven by strong deuterium puffing into H- and L-mode density limit. The vertical dashed lines indicate the H→L-mode back-transition, i.e. the non-disruptive H-mode density limit.*

We start with a typical example to reach the density limit in both the H- and L-mode via intense deuterium puffing (see Fig. 1). Since the heating power is well above the threshold the first phase exhibits type-I ELMs. In parallel, strong gas-puffing leads to a smooth increase of $\overline{n}_e$. The attached divertor regime at low and medium densities alters to detached phases in between ELM's as seen by the drop in the baseline of the C_{div}^{III} signal from 2.3 s. During the ELM's, however, the divertor still reattaches. From about 2.48 s the ELM's exhibit type-III character and the related power flux to the divertor is strongly suppressed. When the power into the edge or the edge temperature falls below a certain value, which coincides with detachment also during type-III ELMs, the discharge falls back into the L-mode (here at $\approx$ 2.54 s). The correlated densities are associated with the H-mode density limit [2]. The fraction of totally radiated power to heating power varies between 60-70 % and $\overline{Z}_{eff}$ remains below about 2. After the transition in the L-mode the divertor reattaches sometimes depending on the edge parameters. If the endeavours

to increase $\overline{n}_e$ continue, an X-point Marfe develops, grows into the bulk plasma and the discharge disrupts (L-mode density limit) [2]. Applying additional impurity injection, this H/L-mode–disruption sequence is qualitatively very similar, but $\overline{Z}_{eff}$ and radiation fraction is significantly higher with 3-4 and 80-100 %, respectively, and the density profiles are much steeper. The electron temperature profiles, however, are quite insensitive to the regime and depend mainly only on the safety factor.

Focussing on the edge and mostly on the low $\overline{Z}_{eff}$ cases, the local separatrix densities n_e^{sep} are found to rise stronger than the line averaged densities up to the phase where the divertor starts to detach. At the H- and L-mode DL the separatrix density behaves like $n_e^{sep} \propto \overline{n}_e{}^2$ reflecting the strong broadening of the density profile towards high densities. In parallel, the density decay length λ_e^{SOL} and the line averaged density in the scrape-off layer (SOL) $\overline{n}_e^{SOL}$ increase in the early $\overline{n}_e$ ramp, but saturate close to the H→L-mode back-transition. This satiation effect is clearly seen if one studies $\overline{n}_e^{SOL}$ and λ_e^{SOL} as function of the neutral particle flux densities. Separatrix densities and $\overline{n}_e^{SOL}$ and λ_e^{SOL} of both H- and L-mode show a common linear relationship (see Fig. 2). Typical SOL density decay length are 3-5 cm. Impurity seeded discharges exhibit in the bulk as well as in the SOL (see Fig. 2 b) noticeably more peeked profile shapes. Furthermore, the electron pressure and its gradients ∇p_e increase with P_{heat}, respectively P_{sep}. The gradients close to the edge in type-I ELM phases are found to be nearly constant, $\nabla p_e(0.46m \lesssim r \lesssim 0.50m) \approx$ const. At higher density in type-III ELM phases the pressure as well as ∇p_e is clearly reduced and the pressure profiles tend to flatten towards the separatrix $\nabla p_e(r \sim 0.49m) < \nabla p_e(r \sim 0.47m)$, see Fig. 3. Further edge data not restricted to density limit discharges are presented at this conference by W Suttrop [7] and J Schweinzer [8].

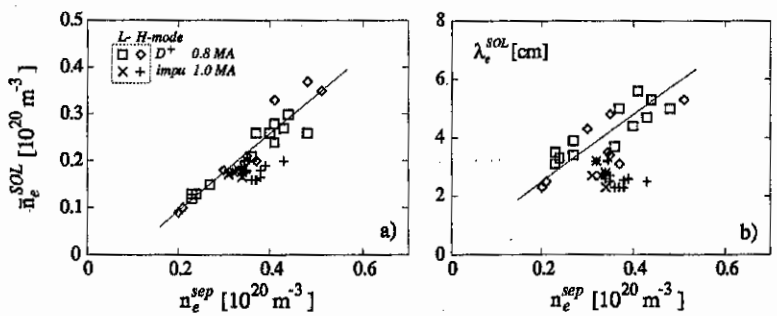

Figure 2: *Relation between the separatrix density and the SOL density and decay length at the density limit in different regimes.*

There exists another small operational window to reach line averaged densities in the vicinity of the Greenwald limit without external gas-puffing. Slightly above the L→H-threshold at low power fluxes the type-I ELM frequency can be so small that the good H-mode confinement leads to an increase of $\overline{n}_e$ up to the Greenwald limit. In our case frequencies below 100 Hz are necessary. Owing to the missing gas-puff and the correlated low recycling level the confinement is despite high $\overline{n}_e$ not degraded. The achieved $\overline{n}_e$ are even

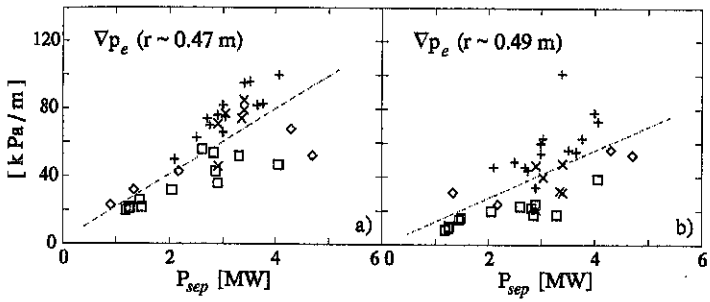

Figure 3: *Measured electron pressure gradients in the edge at the density limit in different regimes. The critical gradient for ballooning modes is ≈ 110 kPa/m and ≈ 170 kPa/m for 0.8 MA and 1 MA discharges, respectively.*

slightly higher than those produced with strong deuterium puffing. Edge densities and detachment behaviour are, however, clearly representative for low recycling discharges.

Summary :
In ASDEX Upgrade absolute densities in the range of the ITER operation point have been established with pure gas-puffing. In the H-mode the density limit is preceeded by divertor detachment in between type-I ELMs and successively a transition to type-III ELM phase with clear detachment. The edge densities and related scale lengths in both H- and L-mode show common behaviour and saturation with developing detachment. The saturation can partly be attributed to the reduction of the penetration depth of neutral particles in the SOL [9]. The pressure gradients are reduced during the approach to the density limit and do clearly not reach the critical pressure gradients for ballooning modes. Additionally, the measured pressure gradients do not seem to scale like $\nabla p_{crit} \propto I_p^2$ as the ballooning mode scaling suggests. The H-mode confinement is, in addition, noticeably reduced close to the H-mode density limit [2].

It is unprobable that the operational window connected with low ELM frequencies for achievement of high bulk densities can be used in ITER, since it is very restricted in heating power and the divertor heat load is not mitigated by detachment. In general, the edge data show a stronger correlation of the DL with divertor detachment than with the reach of critical pressure gradients.

References :
[1] M Greenwald et al, Nuclear Fusion **28**, 1988, 2199
[2] V Mertens et al, IAEA, 1996, Montreal, IAEA-F1-CN-64/A4-4
[3] FW Perkins et al, IAEA, 1996, Montreal, IAEA-CN-64/FP-24
[4] K Borrass et al, Nucl. Fus., **37**, 523 (1997)
[5] F Ryter et al, Physica Scripta, **51**, 1995, 643
[6] H. Zohm, Plasma Phys. Control. Fusion **38**, 105 (1996)
[7] W Suttrop et al, this conference
[8] J Schweinzer et al, this conference
[9] J Stober et al, Controlled Fusion and Plasma Physics (Proc. 23rd Europ. Conf. Kiev 1996) **20C** III 1023

Investigations of tungsten in the central plasma of ASDEX Upgrade

K. Asmussen, R. Neu, R. Dux, W. Engelhardt, K. Fournier[1], J.C. Fuchs, K. Krieger, J. Rice[2], V. Rohde, D. Schlögl, M. Sokoll, A. Thoma, and the ASDEX Upgrade Team

Max-Planck-Institut für Plasmaphysik, EURATOM-Association, Garching, Germany
[1] Lawrence Livermore National Laboratory, Livermore, Ca., USA
[2] Plasma Fusion Center, Massachusetts Institute of Technology, Cambridge, Ma., USA

The tungsten concentration c_W in the main plasma of ASDEX Upgrade was determined by observation of the quasicontinuum structure of W in the 5 nm region. The calibrated intensity of this structure was used to monitor the tungsten inventory in the main plasma. Tungsten concentrations as low as 10^{-6} were detected by means of spectroscopic observations in the VUV-region. In 85% of all investigated discharges c_W were found to be below $2 \cdot 10^{-5}$. Correlation studies were performed to investigate the dependence of c_W on plasma parameters.

Identification of tungsten and determination of c_W

The tungsten divertor experiment at ASDEX Upgrade [1] offered the possibility to test tungsten as a plasma facing component under fusion relevant divertor conditions. Of major interest was the resulting concentration c_W in the main plasma and the dependence of c_W on other plasma parameters. In preliminary studies tungsten was injected into the plasma by means of laser ablation. The temporal development of the total radiation measured by a bolometer camera system allowed to subtract the background radiation and to obtain the total tungsten radiation. A comparison of the measured radiation $P_{W,meas}$ with calculated radiation losses $p_{W,calc}$ [2] yields $c_W = P_{W,meas}/(p_{W,calc} \cdot n_e^2)$. In a fusion experiment with a continuous source of tungsten like the W divertor at ASDEX Upgrade it is not possible to subtract the background radiation of the plasma to get the weak tungsten radiation. Therefore a spectroscopic method was used to detect tungsten and to determine its concentration in the main plasma. The observation of the plasma was performed by means of a grazing incidence spectrometer with a time resolution of up to 5 ms and a spectral range 4 nm – 30 nm. Additionally a Bragg-crystal-spectrometer was used to investigate the x-ray-region at about 0.7 nm. In these wavelength regions single lines of Br- to Ni-like ions could be observed[3], which occur only in additionally heated plasmas because of the high ionization energies. The usually dominating spectral structure in both ohmic, L- and H-mode discharges, however, was the tungsten quasicontinuum at about 5 nm, which is emitted by W-ions in the neighborhood of Ag-like tungsten (W^{27+})[4]. Therefore this structure was used to monitor W and to determine c_W. In order to get a quantitative information a regression with several sample spectra was done to simulate the measured grazing incidence spectra. The method is demonstrated in fig. 1, which shows in

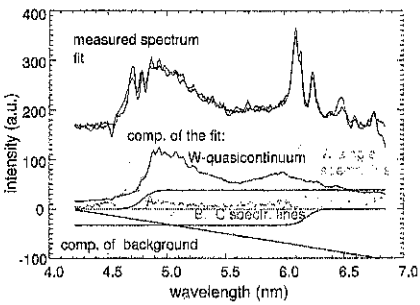

Fig. 1: Determination of the tungsten inventory in the main plasma by a fit of the VUV spectrum at about 5 nm. The calibration of the intensity ($I_{qc} \rightarrow c_W$) was done by comparision with the total tungsten radiation after W laser ablation.

the upper half the input spectrum together with the fit result and in the lower half the sample spectra (background, B-, C-, O-lines, W quasic., and W single lines). The intensity I_{qc} of the quasicontinuum was calibrated by means of c_W determined from the total radiation losses in W laser ablation discharges. The obtained concentration is valid for the plasma shell with $T_e \approx 1$ keV. The thickness of the emitting shell decreases in discharges with high central T_e, because it is shifted to the plasma edge. Therefore a correction factor has to be applied, which is in the range of 0.5–2. The concentration determined by this spectroscopic method in W laser ablation discharges agrees within 50% with the concentration determined with the help of the bolometer camera system for discharges with W-LBO.

Correlation studies

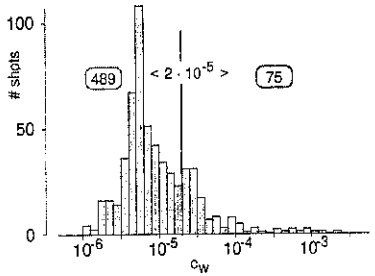

Fig. 2: About 85% of the observed discharges show c_w below $2 \cdot 10^{-5}$.

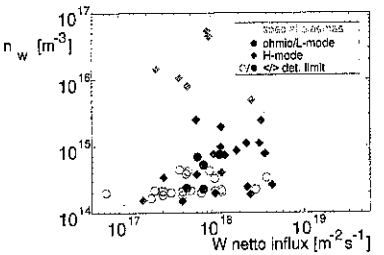

Fig. 3: Weak dependence of the central W density on the W influx from the divertor plates (special plasmas are shaded grey)

Fig.2 shows the distribution of discharges as a function of maximum c_W of the discharge. About 85% of all investigated plasmas show tungsten concentrations below $2 \cdot 10^{-5}$ (75% below $1 \cdot 10^{-5}$). c_W almost never reached values which influenced the chosen discharge program. Only in a very few discharges with special parameters (co-injection, low voltage of the neutral beam heating, improved confinement regimes after switch off of NBI beams) c_W was higher and the radiation was sometimes strong enough to cause hollow T_e-profiles. Several plasma parameters, e.g. plasma current, toroidal field, n_e, etc., were investigated with respect to their influence on c_W. The lack of clear dependences indicates that the transport of tungsten is influenced by parameters which were not considered in the global analysis (cf. [5]). Especially the dependence of the W density $n_W = c_W \cdot n_e$ on the tungsten influx caused by erosion of the divertor plates is obscured by the transport history which the tungsten ions have already experienced on their way into the main plasma. This is elucidated in fig. 3, where n_W is shown as a function of the net tungsten influx from the divertor plates $\Gamma_{W,div}$, which is calculated from the intensity of the dominating WI line at 400.9 nm (the redeposition of the sputtered W is considered)[6]. Although there is an increase of n_W with increasing $\Gamma_{W,div}$ the spread of the data points is rather broad.

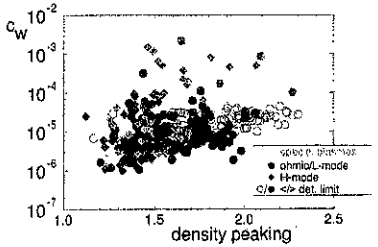

Fig. 4: Correlation between the density peaking and c_W.

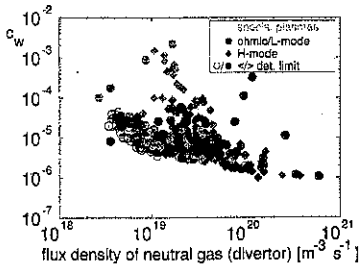

Fig. 5: c_W as a function of the influx of neutrals in the divertor region.

A somewhat clearer dependence was found on the density peaking and on the neutral flux density in the divertor region in case of H-mode discharges. Fig. 4 and fig. 5 show the correlation graphs for these two parameters. In the case of ohmic and L-mode discharges the weak dependence is caused by the detection limit of the spectroscopic observation. For H-mode discharges c_W increases with the density peaking (which could be a result of neoclassical effects) and decreases with increasing neutral flux density. The later effect is demonstrated in fig. 8 which shows the time traces for several plasma parameters for #7923. At about 3 s the flux density of the neutral increases and at the same time c_W decreases below the detection limit.

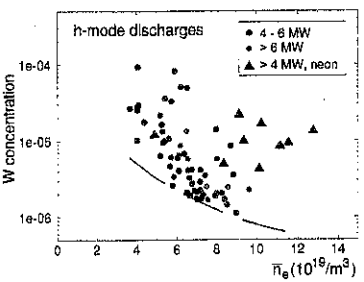

Fig. 6: Comparision of c_W as a function of n_e for different H-mode plasmas.

The influence of the density on c_W is demonstrated in fig. 6. The dashed line marks again the detection limit of the spectroscopic method. The decrease of c_W with density is more pronounced for plasmas with lower heating power (grey/black circles). In CDH-mode-discharges, however, there seems to be no decrease with the density. This effect can be explained by the density peaking of the n_e-profile, which is usually observed in those plasmas.

An example of a discharge with very good confinement is given in fig. 7. The H-factor (ITER89P) in this discharge was above two. After the start of the neutral beam heating (5 MW) the tungsten reaches very rapidly the T_e = 1 keV shell of the plasma, which is located at $\rho_{pol} \approx 0.8$ (W_{qc} -signal). The transport of tungsten to the plasma center, however, is very low. This can be seen from the temporal behaviour of the intensity of the isolated W lines (W_{sl} -signal, see fig. 1), which reaches its maximum 200 ms after the start of the NBI. Although energy confinement is good for these conditions, the maximum concentration remains below $2 \cdot 10^{-5}$ and no accumulation occurs.

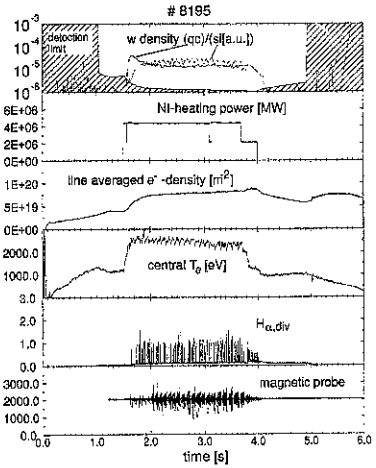

Fig. 7: Example of a discharge with high H-factor ($H_{ITER89P} > 2$) (# 8195).

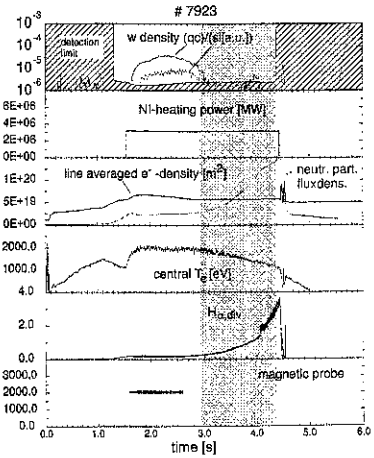

Fig. 8: Variation of c_W with the neutral flux density).

Summary and Outlook

The concentration c_W of tungsten in ASDEX Upgrade discharges in the plasma shell with $T_e \approx 1$ keV was determined from the intensity of the quasicontinuum structure of W at about 5 nm. The intensity I_{qc} of this structure was calibrated by comparison with the intensity I_{qc} during W laser injection experiments and theoretical radiation losses. In 85% of all discharges (ohmic, L- and H-mode) c_W was below $2 \cdot 10^{-5}$. The dependence of c_W on the W influx from the divertor plates was found to be very weak. This indicates a dominant role of the edge and main plasma transport. The remaining discharges with higher W concentrations could be identified as special scenarios (Co-injection, low NBI-voltage, high triangularity, improved confinement after reduction of NBI-power, and density peaking in H-mode plasmas). A reduction of c_W could be achieved with increasing plasma edge density.

The tungsten transport into and in the main plasma will be investigated by means of calculations with the transport code STRAHL [4]. Necessary W profiles will be obtained by means of the lines of the Br- to Ni-like tungsten ions in the plasma center and and the quasi-continuum at the plasma boundary. The influence of the divertor retention on the central W concentration will be investigated with a $W(CO)_6$-Probe, which is able to inject W both in the divertor region and in the boundary region (mid plane) of ASDEX Upgrade.

References

[1] R. Neu et al., *Plasma Phys. Contr. Fusion*, 38 (1996) A165
[2] D. E. Post et al.,*Atomic Data and Nuclear Data Tables*, 20:397–439, 1977
[3] R. Neu et al., submitted to *Journal of Phys. B*
[4] J. Sugar et al., *J. Opt. Soc. Am. B*, 10:1321,1993
[5] R. Dux et al., this conference
[6] A. Thoma et al., this conference

Ion Dynamics Observed by High Resolution Spectroscopy in the ASDEX Upgrade Divertor I and II

J. Gafert, D. Coster*, C. Dorn*, B. Napiontek*, U. Schumacher,
NBI-Team* and ASDEX Upgrade-Team*

Institut für Plasmaforschung, Universität Stuttgart, Pfaffenwaldring 31
D-70569 Stuttgart, Germany

* MPI für Plasmaphysik, EURATOM Association, D-85748 Garching, Germany

1 Introduction

For the optimum control of plasma power, fuel gas, impurities, and helium ash in future fusion reactors it is necessary to study divertor physics in present-day fusion experiments carefully. These studies have to combine detailed modelling with experimental investigations of the spatial and temporal distributions of density, species composition, temperatures and flow velocities of ions. High resolution spectroscopy in the ASDEX Upgrade divertor I was demonstrated to be a suitable technique to obtain experimental information on the spatial and temporal behavior of the dynamics of atoms and ions, i. e. on their temperatures and flow velocities. Combining poloidal lines of sight ($\perp \vec{B}$) with toroidal ones directed along and opposite to the magnetic field lines the atom and ion dynamics in the area between the outer divertor tiles and the X-point as well as in parts of the inner divertor were studied using high resolution spectroscopy [1]. The highly resolved emission spectra are not only determined by the Zeeman splitting, but also by Doppler broadening and Doppler shift, from which the temperatures and flow velocities can be deduced, respectively. By this means the dependencies of ion dynamics on different discharge conditions of ASDEX Upgrade were analyzed [2].

2 Experimental Results on Ion Dynamics in the ASDEX Upgrade Divertor I

Making use of a 2D-CCD camera and a Fastie-Ebert spectrometer with Echelle grating, highly resolved emission spectra of atoms and ions emitting along up to 74 lines of sight (perpendicular, parallel and antiparallel to the magnetic field) were recorded. The characteristic features of these measurements are:

- The HeI line — as a means for probing neutrals not coupled to the magnetic field lines — does not show a significant Doppler shift in ASDEX Upgrade discharges with an attached highly recycling divertor plasma. Hence, the corresponding velocity distribution is isotropic with respect to the poloidal and toroidal lines of sight and, therefore, no preferential flow of neutral helium parallel or perpendicular to the magnetic field lines is observed.
- The emission spectra of all impurity ions show pronounced Doppler shifts due to their coupling to the magnetic field lines. The flow velocities are directed towards the target plates in the outer as well as in the inner divertor.

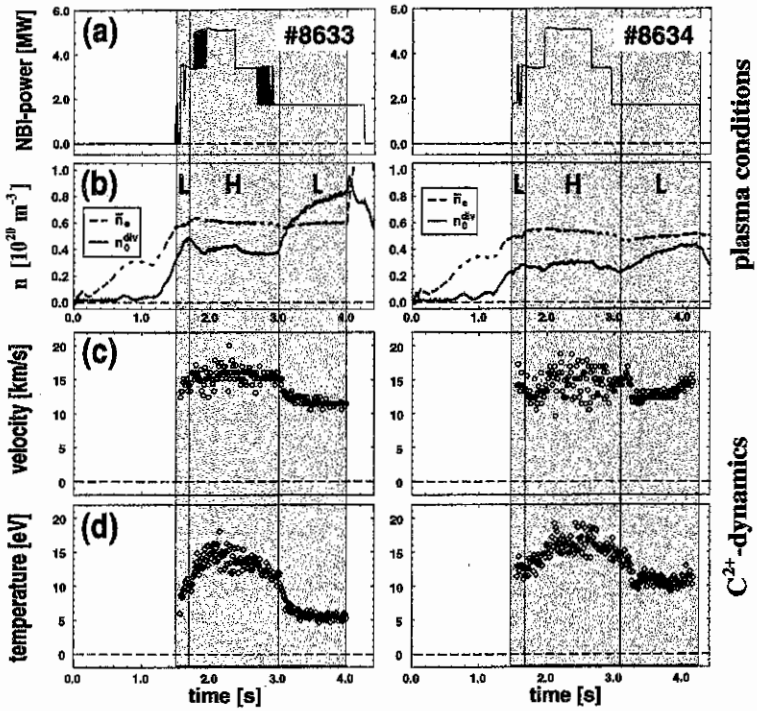

Figure 1: *Dependencies of C^{2+}-ion dynamics on L- and H-mode as deduced from highly resolved CIII-spectra ($\lambda \approx 465$ nm). Toroidal magnetic field B_t = -2.5 T. Plasma current I_p = 1.0 MA. (a) Neutral beam injection power, (b) neutral divertor density (full line) and line averaged midplane electron density (dashed line), (c) C^{2+}-flow velocities towards the outer divertor plates and (d) the C^{2+}-temperatures as a function of time.*

- Due to the matrix-like arrangement of the lines of sight it was possible to determine ion speeds in the outer and in the inner divertor: C^{2+}-ions flow with the same speed ($\approx$ 11 km/s) in the inner divertor ($\approx$ 200 mm above the plates) as in the outer divertor ($\approx$ (50–100) mm above the plates).
- Comparing L- and H-mode phases significant differences are observed in the ion dynamics that are illustrated in Fig. 1 for two ASDEX Upgrade hydrogen discharges. Using different NBI powers (Fig. 1a) and gas blow scenarios well defined L-H-transitions could be performed with the midplane electron density ($\overline{n}_e$) staying nearly constant in time and the density in the divertor (n_0^{div}, Fig. 1b) increasing in the L-mode. The parameters obtained from numerical fits to the CIII spectra ($\lambda \approx 465$ nm) are plotted in Fig. 1c and d. In both discharges the flow velocities of the C^{2+}-ions (Fig. 1c) show only small variations between 10 km/s and 13 km/s in the L-mode, while they increase up

to 20 km/s in the H-mode with the scatter being caused by the integration over ELMs. A similar behavior is seen for the temperature of the C^{2+}-ions (Fig. 1d): The values during the L-mode phases are clearly lower than in the H-mode and remain nearly constant. In the H-mode, however, the C^{2+}-ions are — most probably due to the ELMs — heated up to about 20 eV. Concerning the L-modes of the two discharges, the C^{2+}-temperature for #8634 ($\approx$ 10 eV) is about a factor of 2 larger than that for #8633 ($\approx$ 5 eV). The reason is the approximately doubled density in the divertor (Fig. 1b) that leads to the observed reduction of the temperature by roughly a factor of 2.

- The large range of the data in the H-mode is a consequence of the ELMs that can not be resolved completely due to the integration time (1 ms) of the 2D-CCD camera. Nevertheless, by a more detailed correlation analysis of states of constant plasma conditions, a reduction of the C^{2+}-velocity with increasing CIII-intensity is found. If an ELM causes the amount of carbon to rise, then the reduced velocity — averaged along a toroidal line of sight — can be considered as experimental evidence for the backflow of ions from the divertor plates.
- the experimental results referring to the L-mode phases of these and other discharges were compared to the results of B2-EIRENE code calculations [3] for similar conditions in the L-mode. Although these simulations were not especially adapted to the corresponding ASDEX Upgrade discharges, the C^{2+}-velocity from B2-EIRENE is only 50 % too high, and the ranges for the ion temperature overlap nearly completely.

3 ASDEX Upgrade Divertor II: Changes, Improvements and Goals

As described before, the lines of sight in divertor I were arranged in a way to cover both the outer and a part of the inner divertor area. Although this setup was advantageous in many respects, it has a disadvantage resulting from the chord integration that complicates the interpretation of the measured data. For the toroidal lines of sight, the intensity contributing to a spectrum is collected from two regions (in the outer divertor) with different distances from the target plates. This leads to a limitation of the spatial resolution and is probably the main reason why the expected differences during and between ELMs did not yet show up as clearly as desired. Therefore, for the changed geometry of the ASDEX Upgrade Divertor II, the toroidal lines of sight were designed on the basis of B2-EIRENE calculations and optimized to run mainly through one emission region only. The projections of 12 of these new chords into a poloidal plane are plotted in Fig. 2 together with the calculated magnetic flux surfaces. The lines of sight — especially those in the outer divertor — are to yield flow velocities and temperatures of several ions with a sufficient spatial resolution now. As in divertor I, there are again some lines of sight viewing — through the X-point — into the inner divertor, from which information should be obtainable on the velocities there.

In addition, 105 new poloidal lines of sight were installed which are illustrated in Fig. 3. In the outer and in the inner divertor area, there are mainly two observation systems,

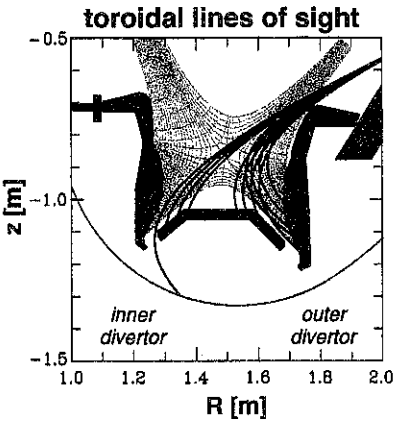

Figure 2: *A subset of 12 toroidal lines of sight in the ASDEX Upgrade Divertor II projected into a poloidal plane; the outer and inner divertor area are covered to allow for spatially resolved velocity measurements*

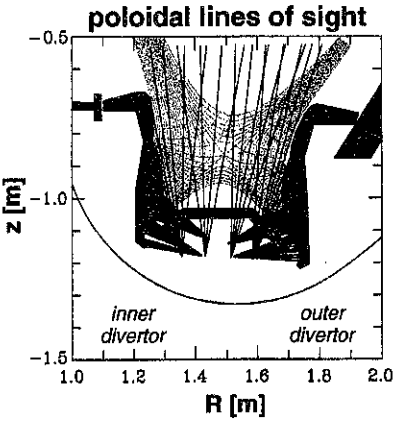

Figure 3: *Poloidal lines of sight in the ASDEX Upgrade Divertor II. The area in front of the target plates can be probed with high spatial resolution; the X-point region is covered by chords viewing in z-direction.*

each consisting of about 20 lines of sight. One set of chords points directly onto the strike-point tiles, while the other one is oriented upwards (in z-direction) and probes the region between the baffle and the core plasma. There are several improvements in connection with this new setup: First, spatial emission profiles can be obtained in the outer and inner divertor range, thereby determining the location of atom- and ion-emission experimentally with high accuracy. Second, the ion temperatures can now be measured separately in front of the outer and the inner target plates. Third, 5 valves have been installed in this area to blow several diagnostic gases into the divertor. By comparing the spectra of poloidally identical lines of sight in sectors with and without valves, the topic of chemical erosion can be addressed.

Finally, we note that not only all the lines of sight in the divertor, but also chords viewing the main plasma can be combined with the spectrometers of different resolution available. Using this enhanced set of spectroscopic diagnostics, important subjects of divertor physics will be investigated in more detail. These are, e. g., the ion dynamics on the timescale of the ELMs, the question of flow reversal, the in-out asymmetry of the ion temperatures or the nature of impurity production.

References

[1] Gafert, J., et al., Europhys. Conf. Abstr. **20C**, Part III, 1015–1019 (1996).

[2] Gafert, J., et al., Plasma Phys. Control. Fusion, submitted.

[3] Schneider, R., et al., J. Nucl. Mater. **196–198** 810 (1992).

Low-Z-Impurity Transport Coefficients at ASDEX Upgrade

S de Peña Hempel, R Dux, A Kallenbach, H Meister, ASDEX Upgrade Team
MPI für Plasmaphysik, EURATOM Association, D-85748 Garching, Germany

Introduction

Impurity transport studies were conducted in ASDEX Upgrade by injecting short puffs of *He* or *Ne* gas during an otherwise steady-state phase of a discharge. Charge exchange recombination spectroscopy (CXRS) measurements were used to monitor the temporal evolution of the radial impurity profiles subsequent to these puffs. Following the temporal evolution of the profiles the diffusion coefficient D and the convective velocity v were determined. The radial profiles and parametric dependences of the particle transport coefficients are analysed in different confinement regimes. Furthermore the dynamic behaviour of the transport during sawtooth-free discharge periods and ELMs is studied and compared with model predictions.

Determination of local transport coefficients

Spatially and temporally resolved impurity densities in the core plasma of the ASDEX Upgrade tokamak are obtained in neutral beam heated discharges from CXRS measurements with a set of 14 viewing lines of sight. The transport coefficients are determined by first inferring the particle flux Γ from the measured temporal evolution of the impurity density profile by inverting the continuity equation in the source free region. The assumption of zero sources is only accurate inward of the region of ionization at the plasma edge ($\rho_{\mathrm{pol}} < 0.8$ for *Ne* and $\rho_{\mathrm{pol}} < 0.95$ for *He*). The impurity fluxes are described by the extended Fick's Ansätz $\Gamma(r,t) = -D(r)\nabla n(r,t) + v(r)n(r,t)$ which assumes the particle flux to be made up of a diffusive flux and an unspecified convective flow which incorporates any additional terms not dependent on the density gradient. Thus, the normalized flux $\frac{\Gamma}{n}$ at a particular minor radius is an offset linear function of the density scale length $\frac{\partial n}{n}$, consistent with expectations for a trace impurity and time-independent transport coefficients. From such a curve the diffusion coefficient is determined by the absolute value of the slope of the linear regression to the data and the convective velocity by the y-intercept. To overcome the instrumental noise in the experimental data, which gives the main contribution to the uncertainty in the determination of the transport coefficients, smooth functions are used to fit the temporal evolution and radial profile.

Dependences and scaling laws for the impurity transport coefficients

Empirical scaling laws for the particle transport coefficients were determined by extending the previously described flux analysis to 74 different neutral-beam-heated L-, H- and CDH-mode discharges covering the parameter range: $1.89 < B_{\mathrm{tor}}[T] < 2.69$, $1.99 < P_{\mathrm{tot}}[MW] < 9.13$, $4.49 < \bar{n}_e[10^{19}\frac{1}{m^3}] < 11.75$ und $1.15 < m_{\mathrm{eff}}[amu] < 1.90$. The variation range in the plasma current was too narrow to examine any dependence on this parameter and so the evaluation of the scaling was restricted to discharges with $I_p = 1\,MA$. In addition the effect of possible collinearities with the magnetic field could be eluded. Furthermore, only *He* and *Ne* pulses during otherwise steady-state phases of a discharge were analysed. This was accomplished by allowing a maximal excursion of 10% in the time evolution of the line-integrated electron density, neutral injection heating power and energy confinement time.

In the plasma core region a nonlinear regression of the diffusion coefficient yields

$$D(\rho_{\mathrm{pol}} = 0.2) = 0.293 \cdot B_{\mathrm{tor}}^{-0.183\pm0.082} \cdot P_{\mathrm{tot}}^{0.473\pm0.026} \cdot m_{\mathrm{eff}}^{-0.666\pm0.047} \qquad (1)$$

irrespective of the discharge confinement mode. Within the uncertainties in the determination of this scaling no significant dependence on the injected impurity species or the electron density is found. In addition, the diffusion coefficients are determined to vary roughly as the square root of the total heating power. They exhibit a marked dependence on the background plasma species and decrease with the toroidal magnetic field. Figure 1a) demonstrates the good reproduction of the measured diffusion coefficients by the scaling law of equation 1.

In the outer plasma region the inferred parameter dependencies show the same tendencies as found for the plasma core. However the errors of the exponents in this region are comparable to the exponents themselves and are therefore of no sufficient quality to determine the dependences exactly. Individual regressions for the different confinement regimes lead to similar results. In good agreement with the results of gas puff or gas modulation experiments in other machines, the diffusion coefficient for stationary plasma conditions is one or two orders of magnitude larger than the prediction of the neoclassical transport theory over the complete radial range and has a hollow radial profile.

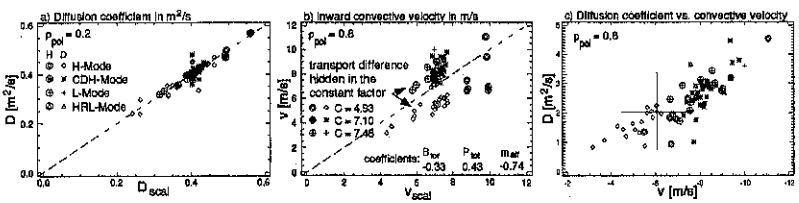

Figure 1: *a: Measured central diffusion coefficient versus the prediction of the scaling law of equation 1. b: Measured pinch velocity versus scaling law at the plasma edge. c: Inward pinch velocity versus diffusion coefficient at* $\rho_{\mathrm{pol}} = 0.8$.

The inward convective velocity on the contrary only exceeds the neoclassical value at radii larger than $\rho_{\mathrm{pol}} \sim 0.6$, where it shows a strong correlation with the diffusion coefficient (fig.1c), suggesting that a common mechanism gives rise to both transport coefficients. For $\rho_{\mathrm{pol}} \geq 0.6$ the scaling of both transport coefficients exhibits similar dependences as have been put forward for the diffusion coefficient in the core region (tabular in fig.1c), however, there is a marked influence of the confinement regime on the impurity transport behaviour. This cannot be explained by any parameter dependence and is hidden in the constant scaling factor. Due to its large relative error no parameter dependences could be inferred for the pinch velocity in the central plasma.

A comparison of the impurity transport coefficient with published results for the electron transport [1,2] points out a good agreement in the absolute magnitude and radial profile shape of the coefficients as well as a clear parallelism concerning the analyzed parametric dependencies. Further on a satisfactory correlation with the scaling laws for the energy and the angular momentum confinement time [3] is found.

Instationary accumulation phenomena in sawtooth-free discharge periods

The impurity transport coefficients in the previous paragraph were determined in saw-

toothing discharges and represent sawtooth averaged values. For instationary accumulation phenomena during sawtooth-free discharge periods the impurity transport in the plasma center shows a different behaviour. The suppression of sawteeth observed in some radiating boundary CDH-mode discharges is accompanied by the development of density peaking [4] and a slightly enhanced energy confinement. Simultaneous measurement and evaluation of the carbon and neon CXR-spectra in addition with Z_{eff}-profile measurements from the deconvolution of the line integrated bremsstrahlung background radiation shows that although these phases exhibit a central accumulation of neon and a strong peaking of the soft x-ray and Z_{eff}-profiles the carbon density profile evolution remains unchanged.

The transport analysis in these sawtooth-free discharge periods leads to a diffusion coefficient that reduces to neoclassical values for poloidal fluxes smaller than $\rho_{\text{pol}} \sim \sqrt{2}\rho_{\text{pol}}^{\text{inv}} \approx 0.65$. For larger radii the diffusivity is not affected by the sawtooth collapse. This is consistent with the picture that the sawteeth induce a strong convective particle flow inside and outside the q=1-surface. Otherwise, the measured pinch velocity is not significantly altered by this process.

A self consistent modelling of the impurity transport and radiation with the radial impurity transport code STRAHL from the given electron and impurity densities [5] shows that for discharges without sawteeth the central ($\rho_{\text{pol}} < 0.6$) transport can be described by neoclassical terms. This modelling, however, predicts also a small but not observed peaking of the carbon density. Such an inconsistency may be due to the neglected friction between the impurity species.

Dynamic transport behaviour during type I ELM's

Due to the limitations of the detection system regarding its minimal exposure and readout time, the dynamic ELM-behaviour has to be investigated by a special mapping procedure to fasten the effective temporal resolution of the CCD system. This is achieved by analysing steady state discharge periods and considering each ELM as the consequence of the repetition of the same event. Using the maxima of the characteristic H_α-signal as the indicator for each ELM a time base can be constructed, which allows the projection of the density evolution measured in such a phase (up to 200 ELM's) onto one unique event. To obtain the real temporal behaviour of the density over an ELM the mapped signal is deconvolved with the CCD-exposure function. The study of the edge transport behaviour is restricted to helium, because the described analysis is only accurate inward of the ionisation region of the observed impurity.

The ELM's are described by an enhancement of the particle diffusion coefficient from $D \approx 1\,\frac{m^2}{s}$ up to $D_{\text{max}} \approx 6\,\frac{m^2}{s}$ in combination with an outward directed convective flow with a pinch velocity in the order of $+15\,\frac{m}{s}$ (fig.2b). However, the contributing of each term to the total particle flow is ambiguous. The rise of the transport coefficients is localized in a $\sim 10\,cm$ wide layer inside the separatrix. The given error bars include the statistical uncertainity in the evaluation of the transport coefficients from the Γ_Z^{norm}–$\partial n_Z^{\text{norm}}$–plots. The density relaxation after the ELM collapse (dashed lines) is found to be well described by the same set of transport coefficients as derived from gas puff experiments (dotted lines). The pronounced decrease of v in the region outside $\rho_{\text{pol}} = 0.95$ is possibly due to not neglegible source terms in the continuity equation. The *He*-transport coefficients derived for this region should therefore be treated with care.

The transport coefficients are compared with measurements of the effective electron diffusion coefficient and heat conductivity (fig.2c). The time evolution, the absolute magnitude and the localization of the different measurements is found to be in good qualitative and

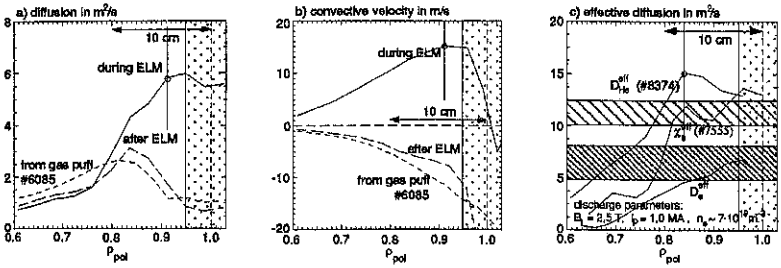

Figure 2: *Measured diffusion coefficient a) and pinch velocity b) for an ELM. c) shows a comparison of the effective He-diffusivity with values for the electron diffusion coefficient and heat conductivity.*

quantitative agreement ($D_{He}^{\text{eff}} \approx D_e^{\text{eff}} \approx \chi_e^{\text{eff}}$), suggesting that a strong link exists between thermal, electron and impurity transport during ELMs. The driving mechanism should therefore be of convective and ambipolar nature.

The predictions of model calculations based entirely on parallel particle fluxes along stochastic magnetic fields during magnetic ELM precursor activity correspond quite well to the experimental data of COMPASS-D [6] and ASDEX Upgrade [7]. The magnetic perturbation is assumed to be created by helical perturbation current filaments which are modelled to match the phase and amplitude of the ELM precursor signal measured by the Mirnov diagnostic. Subsequent field line tracing shows an ergodization between island chains and in a radial transport enhancement due to parallel particle motion along the radially excursing field lines. However the achieved good quantitative agreement between model and measurement has to be treated with care because the calculated heat conductivity is based on the transport formula of Rechester-Rosenbluth [8] which describes a conductive and non ambipolar process. This is inconsistent with the experimental results, which exhibit almost equal thermal and particle transport rates. Nevertheless, an extension of the former model including nonlinear bunching of the electrons [9] shows that the edge electron heat flux can be convective and ambipolar constrained and described by a Rechester-Rosenbluth diffusivity, but with the slow ion thermal velocity as the streaming factor $\chi_\perp^{\text{T}} = v_i \frac{\langle(\partial r)^2\rangle}{(\partial l)} \left(\frac{\omega}{k v_i}\right)^2$. The determination of the fluctuation phase velocity $u = \frac{\omega}{k}$ will be possible with the new extended magnetic coil arrangement at ASDEX Upgrade and a quantitative comparison of the modelling results to the experiment is expected.

References

[1] J O'Rourke *et al.*, Plasma Physics And Controlled Fusion 35:585–594, 1993
[2] J-L Lachambre *et al.*, Plasma Physics And Controlled Fusion 38:1943–1966, 1996
[3] H Meister, Diploma Thesis, Universität Augsburg, 1996
[4] A Kallenbach *et al.*, Plasma Physics And Controlled Fusion 38:2097–2112, 1996
[5] R Dux *et al.*, Proc. of the 23rd EPS, Kiev, I: 25–28, 1996
[6] R Buttery *et al.*, Proc. of the 22nd EPS, Bournemouth, III: 273-276, 1995
[7] H Reimerdes, IPP Report 1/300, 1996
[8] A B Rechester and M N Rosenbluth, Physical Review Letters (40)1:38–41,1978
[9] P W Terry *et al.*, Phys.Plasmas, 3(5):1999–2005,1996

Modelling of Impurity Transport and Radiation for ASDEX Upgrade Discharges

R. Dux, K. Asmussen, R. Neu, S. de Peña-Hempel, V. Rohde,
A. Thoma, and the ASDEX Upgrade-team
MPI für Plasmaphysik, EURATOM Association, Garching, Germany

Introduction

During the tungsten divertor experiment at ASDEX Upgrade the global tungsten concentrations in the main plasma c_W showed only a weak correlation with the WI-fluxes in the divertor. This implies a strong dependence of the particle confinement time of tungsten on the plasma parameters. A decrease of c_W with rising plasma density and heating power and particular discharge scenarios with the tendency for tungsten accumulation could be identified [1]. In this paper a strong decrease of the tungsten confinement on the impurity concentration of light impurities is demonstrated. Neo-classical transport in the edge of the confined plasma might explain this dependence and has been investigated using the radial impurity transport code STRAHL.

Dependence of tungsten transport on carbon concentration

To asses the effect of light impurities on tungsten transport in the main plasma a type-I ELM'y H-mode discharge with a strongly varying carbon concentration has been investigated. The parameters for this deuterium discharge #8503 are $P_{NI} = 7.5MW$, $B_t = 2.5T$, $I_p = 1MA$, $q_{95} = 4$ and $n_e \approx 8 \cdot 10^{19} m^{-3}$.

Fig.1 shows the temporal behaviour of the tungsten flux in the divertor and at the mid-plane, and of the carbon and tungsten densities in the plasma bulk.

The density of fully ionized carbon in the main plasma was determined from charge exchange spectroscopy on 16 line-of-sights covering the whole plasma cross section. The neutral tungsten influx at the outer divertor plate was measured with a poloidally scanning visible spectrometer [2] and the data points are the maximum values for every scan over the outer target. The particle flux was calculated from the photon flux using S/XB-values from laboratory measurements [2]. The time trace in fig.1 represents the net influx by subtracting the calculated part of prompt redeposited particles [2]. The net influx amounts to $\approx 10\%$ of the total influx. At the mid-plane the tungsten flux has been measured as a function of time using a rotatable deposition probe. The probe was located in the open field line region between two limiters. The tungsten density at a poloidal flux label of $\rho_{pol} \approx 0.75$ was determined from the intensity of the quasi continuum at $\lambda = 5nm$

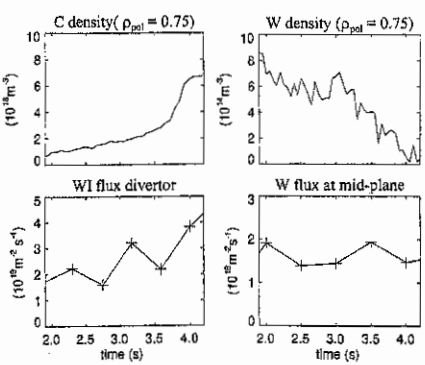

Figure 1: Time traces of carbon and tungsten densities in the plasma bulk and tungsten flux densities for discharge # 8503. The rising carbon density leads to an increased influx of W in the divertor. However, the W density in the main plasma strongly decreases.

(due to transitions of ions with charge around $Z = 28$) which was measured by a grazing incidence spectrometer on a central line-of-sight.

Towards the end of the NI-heated phase of the discharge CCD-camera observations show a bright glow from parts of the ICRH-antennas and the deposition probe leading to a strongly rising carbon density in the plasma. The rising carbon density is accompanied by an increase of the WI influx by a factor of ≈ 2 as expected from the dominance of impurity impact on the sputtering of tungsten [2]. During this phase the tungsten flux onto the probe at the mid-plane remains constant. The most prominent effect is seen from the time trace of the W density in the plasma bulk. It shows a strong decrease and falls below the detection limit at $t = 4.0s$. The line averaged electron density increases by 15% and the average temperature decreases by 15% during the shown time interval, while the radiated power fraction changes from 40% to 50%. For $t < 3.75s$ type-I ELM's are observed which change to compound ELM's for later times.

Calculation of tungsten transport due to impurity-impurity friction

The calculations were performed with the impurity transport code STRAHL using the measured electron density and temperature profiles. Various experimental and calculated profiles for the time $t = 3.6s$ are given in fig. 2. Electron density profiles result from defolded interferometric measurements using lithium beam measurements for the density profile at the plasma edge. Electron temperature was measured with ECE diagnostics and around the separatrix with Thomson scattering. The anomalous diffusion coefficient in fig.2 (equal for C and W) was taken from an analysis of impurity density evolution after gas puffing of helium and neon in similar H-mode discharges [3]. It represents a time averaged value including the effects of sawtooth crashes and ELM's on the impurity transport. In a first step the drift velocity for carbon v^C was determined from the measured density profiles of C^{6+} for the time interval $t = 2.0 - 3.6s$. The profile shape is almost unchanged in this phase and the density change is slow enough to evaluate the drift velocity from the slope of the density profile in the source free region ($\rho_{pol} < 0.85$). Outside that region v^C was simply kept constant at the value of $\rho_{pol} = 0.85$. The resulting drift velocity is directed inward over the whole plasma cross section being in accordance with the gas puffing results mentioned above [3]. The value of v^C for $\rho_{pol} > 0.85$ can not be checked with the measurement of C^{6+}-densities. However, there must be an inward drift to cause no contradiction between the calculated carbon density profile and the measured electron density for the time ($t > 4.0s$) with a very high carbon concentration. The drift velocity was taken to be constant for the whole time interval and the experimentally unknown carbon influx was adapted to fit the observed carbon densities.

In a second step it was checked whether neo-classical transport might explain the strong decrease of the tungsten density in the plasma bulk. The total collision frequency of W is strongly influenced by the collisions of tungsten with carbon (W-C) being a factor of ≈ 4 more frequent than collisions with deuterium (W-D) for the depicted time $t = 3.6s$ in fig.2. The plot of the collisionality ν^* times the inverse aspect ratio $\epsilon^{3/2}$ shows that tungsten is in the Pfirsch-Schlüter regime for all radii. Carbon is in the plateau regime for $\rho_{pol} < 0.75$ and in the Pfirsch-Schlüter regime outside, and deuterium is in the banana regime for most of the plasma cross-section and in the plateau regime for $\rho_{pol} > 0.9$. Thus, the neo-classical transport parameters of tungsten D^W and v^W are dominated by the Pfirsch-Schlüter terms. These terms were calculated from the formulas of Wenzel and Sigmar [4] where the deuterium density n_D was calculated from the electron density

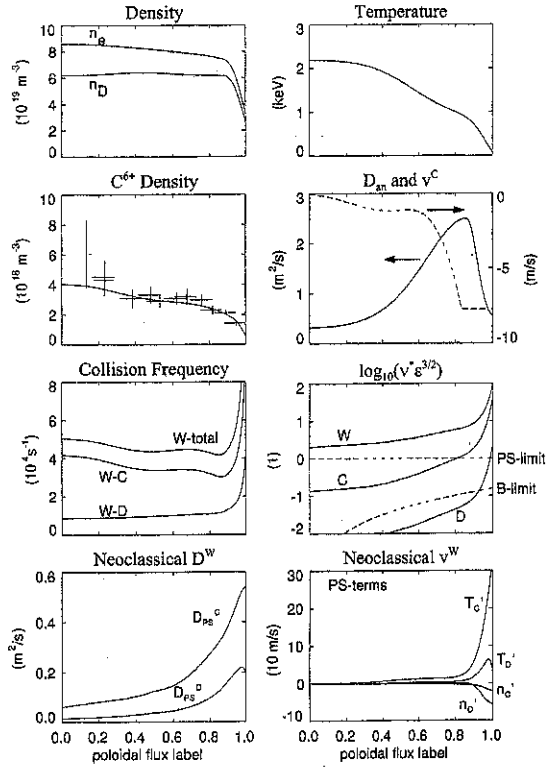

Figure 2: Various profiles for discharge #8503 at t=3.6 s versus the poloidal flux label.

considering the dilution due to carbon. The temperature for all species was assumed to be equal. The diffusion coefficient of tungsten due to collisions with carbon is given by $D_{PS}^{C} = D_{PS}^{D}\alpha_C\sqrt{m_C/m_D}$ where D_{PS}^{D} is the diffusion coefficient due to collisions with deuterium and $\alpha_C = n_C Z_C^2/n_D$ is the impurity strength of carbon. The drift velocity of tungsten is the sum of the density gradient terms v_n^X and the temperature gradient terms v_T^X:

$$v_n^X = D_{PS}^X Z_W K_X \frac{n_X'}{n_X}$$

$$v_T^X = D_{PS}^X Z_W H_X \frac{T_X'}{T_X}$$

with $X = C$ or $X = D$. The dimensionless factors K_X and H_X are for deuterium $K_D \approx 1$ and $H_D \approx -0.5$ leading to an inward drift for the density-gradient term and an outward drift for the temperature-gradient term. For carbon these factors are $K_C \approx 1/Z_C$ and $H_C \approx H_D$. For typical density and temperature profiles the outward drift due to the temperature-gradient of carbon dominates all other terms for sufficiently high impurity

strengths α_C. In these calculations tungsten could be treated in the trace limit and the dilution due to W could be neglected.

Two transport calculations for tungsten were performed: one with $D^W = D_{an} + D_{neo}$ and $v^W = v_{neo}$ and another one with $D^W = D_{an}$ and $v^W = v^C$. The influx was taken from the divertor net WI flux density and an estimated area of $0.5m^2$. The penetration of tungsten into the confined region is determined by the ionisation length, the parallel loss time and the transport parameters in the SOL. The parameter set in both cases was adapted to yield a penetration probability of $\approx 4\%$ in both cases being in accordance with investigations of the tungsten flux pattern [5]. When taking the carbon transport parameters the calculated tungsten density at $\rho_{pol} = 0.75$ (dotted line in fig.3) is too high by about an order of magnitude and the time dependence simply reflects the increasing influx. The neo-classical calculation shows the observed decrease, however, the absolute values can only be fitted when multiplying the neo-classical drift by a factor of 0.3. For a constant separatrix density of tungsten the density at $\rho_{pol} = 0.75$ is determined by the integral of v/D from the separatrix to $\rho_{pol} = 0.75$. In fig.3 the average diffusion coefficient and drift in this radius interval is given as a function of time. Even for low carbon strengths α_C the tungsten distribution is hollow. The lowest graph in fig.3 gives the calculated ratio of the W density at $\rho = 0.75$ to the density at $\rho = 1$ as a function of the carbon impurity strength.

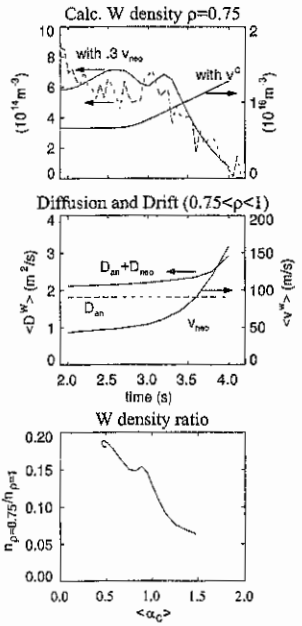

Fig. 3: Experimental and calculated W-densities for #8503 using two sets of transport parameters.

Conclusion

It has been shown by these calculations that the influence of carbon on the tungsten transport can qualitatively be described by neo-classical effects. C and W have oppositely directed drift velocities in the radial range $\rho_{pol} > 0.75$ and the tungsten profiles are hollow for the whole investigated parameter range. The outward drift resulting from the friction with medium-Z impurities is beneficial for the use of high-Z plasma facing components. However, the experimental uncertainties of densities, temperatures and carbon strength in this range and the rough estimate of the tungsten influx do not allow a quantitative check of the neo-classical transport coefficients.

References

[1] K. Asmussen, R. Neu *et al.*, this conference.
[2] A. Thoma *et al.*, submitted to PPCF.
[3] S. de Pena Hempel *et al.* , this conference.
[4] K. W. Wenzel and D. J. Sigmar, Nucl. Fusion **30**, 1117 (1990).
[5] K. Krieger *et al.*, this conference.

Spectroscopic Measurements of the Tungsten Erosion in the ASDEX Upgrade Divertor

A. Thoma, K. Asmussen, R. Dux , K. Krieger, A. Herrmann, B. Napiontek, R. Neu, J. Steinbrink, M. Weinlich, U. Wenzel, ASDEX Upgrade Team
Max-Planck-Institut für Plasmaphysik, IPP-EURATOM Association,
D–85748 Garching and D-10117 Berlin, Germany

Introduction

An important design issue for future fusion devices is the surface material of the divertor target plates. Besides the proper mechanic and thermodynamic qualities the lifetime of the target plates should be high [1, 2]. The released impurities should affect the main plasma as little as possible. In todays devices low-Z materials are used to keep the radiated power in the main plasma low. On the other hand high-Z materials like tungsten are expected to exhibit a much lower net erosion due to the low sputtering yield. An effective prompt redeposition in the local magnetic field [3, 4] helps to keep the impurity content low. The disadvantage of high-Z materials is the high radiation power in the core plasma [5].

Experiments

A tungsten divertor was mounted in ASDEX Upgrade to investigate its behavior under reactor relevant conditions [6]. The tungsten coated tiles [7] covered more than 90% of the strike point zone in the divertor. The line of sight of the boundary layer spectrometer (BLS) at ASDEX Upgrade was swept over the target plates during the discharges and visible as well as VUV spectra were recorded. The tungsten erosion was measured by observing a WI spectral emission line at 400.9 nm, which had a typical intensity of $\approx 10^{-2}$ $Wm^{-2}sr^{-1}$. The S/XB value was used to compute the influx of neutral tungsten atoms via $\Gamma_{part} = S/XB \times \Gamma_{photon}$. S/XB was derived from a separate laboratory experiment for the temperature range 2...18 eV. To obtain values above 20 eV an oven was inserted in the ASDEX Upgrade divertor to sublime $W(CO)_6$ at the strikepoint position. Comparing the emission intensities of WI and OII yields the S/XB ratio.

The particle flux to the target plate is derived from thermographic measurements and from flush mounted Langmuir probes in the divertor. The presented data were measured in plasma discharges with divertor electron temperatures in the range from 2 to 60 eV and power loads to the target plates ranging from 2×10^4 to 6×10^6 Wm^{-2}.

Results and Discussion

Figure 1 shows typical timetraces during an ohmically heated plasma discharge. In the beginning (1-1.5s) the flux to the target plates is low but a high plasma temperature (T_e=60 eV) leads to high sputtering values. Later on, the increasing particle flux compensates partly the drop in the electron temperature (T_e=20 eV). The resulting spatial resolved erosion pattern is plotted in figure 2. One can see a rapid drop of the tungsten erosion at the edge of the tungsten tiles. There is no large radial migration of the released tungsten atoms. The tungsten emission is peaked at the maximum of the deuterium flux and at the maximum of the electron temperature. The radial resolved net erosion,

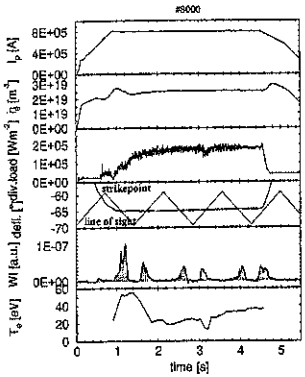

Fig. 1: Typical time traces for an ohmic plasma discharge. The rows show the plasma current (I_p), the line averaged electron density ($\bar{n}_e$) in the midplane, the power load on the target plates, the strikepoint and the observation position, the WI emission intensity and the electron temperature (T_e) close to the strikepoint. As the strikepoint is intersected during the spatial scan tungsten erosion is detected.

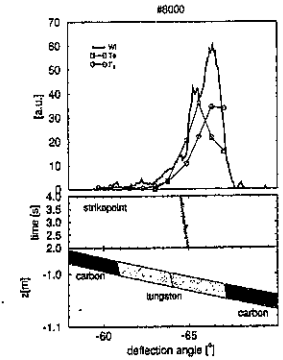

Fig. 2: Spatial profiles of the WI intensity, the electron temperature (T_e) and the particle flux (Γ_D) at the outer target plate. The tungsten emission is radially located at the tungsten tiles. The double peaked emission profile can be explained as a result of the convoluted effects of the electron temperature and the deuterium flux.

determined by probe measurements, also reflects the radial flux pattern [8].

Increasing the power load onto the target plates by raising the additional heating power to 7.5 MW neutral beam injection increases the WI emission by one order of magnitude. The tungsten erosion drops immediately as the particle flux to the target plates is reduced and shows no measurable dependency on the target surface temperature.

During a density limit discharge the divertor electron temperature decreases from 60 eV to below 2 eV. The tungsten influx drops below the detection limit as the density is raised. To quantify the tungsten erosion, a variety of plasma discharges with very different parameters was analyzed. The measured tungsten influx at the strikepoint position was normalized to the deuterium/hydrogen flux. The result is presented in figure 3. About 60% of the shown measurements are H-Mode discharges. The lines in figure 3 represent the results from TRIM sputtering simulations, based on ion beam measurements and taking into account the energy and angular distribution of an isotropic Maxwellian distribution accelerated in the sheath potential [9, 8]. Comparison of the modelled data for a pure deuterium plasma with the experimental results exhibits a significantly higher erosion of tungsten than for pure deuterium sputtering. Simulations are also done for plasmas with 1% C^{+3} or 1% C^{+4}. The higher mass of carbon leads to a higher sputtering yield. The carbon ions also gain an additional impact energy in the range of $E_{C^{+z},acc} \approx Z \cdot 3kT_e$ in the sheath potential of $\approx 3kT_e$. The simulations containing the carbon contribution are in much better agreement with the experimental data. In summary the experimental results can be modelled by a divertor plasma with about 0.5% charged light impurities

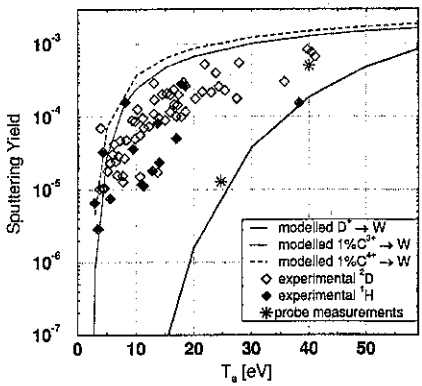

Fig. 3: The symbols show the measured sputtering yield of tungsten. The lines represent results from calculations assuming different carbon impurity charge states and the expected sputtering yield for pure deuterium sputtering [8]. There are also two points of net erosion from probe measurements overlayed in this graph [8], from which the prompt redeposition fraction of tungsten can be evaluated.

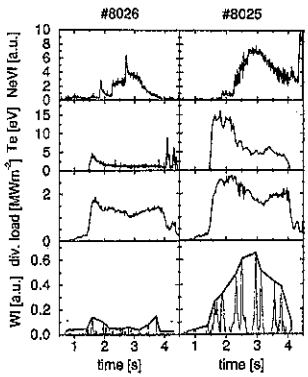

Fig. 4: 1 MA attached ELMy H-mode plasma discharges with Neon puffs. #8026 represents a typical discharge with a low electron temperature in the divertor. The tungsten influx is below the detection limit. In discharge #8025 the divertor electron temperature remains above 5 eV during the neon puff and the time dependence of the tungsten influx correlates clearly with the time dependence of the $NeVI$ in the core plasma.

which leads to the conclusion that the sputtering of tungsten is clearly dominated by the plasma impurities. A similar increase of the sputtering yield by impurities was found for molybdenum during argon puffing [10].

Additional impurities

The injection of additional impurities can also reduce the electron temperature by an increased radiative loss. In ASDEX Upgrade neon is typically used for cooling of the boundary plasma. Figure 4 shows as an example the measurements of two different attached discharges with neon puffs in the main chamber of AUG. The $NeVI$ signal in the midplane gives an estimate of the time dependence of the neon concentration.

One discharge (#8026) shows a low divertor electron temperature, in the other one (#8025) the neon gas puff did not lower the electron temperature below 5 eV. In the cold divertor plasma of discharge #8026 the additional neon concentration lowers the tungsten influx below the detection limit. In discharge #8025 the influx follows clearly the time dependence of the $NeVI$ emission. The tungsten erosion increases with the additional neon despite of the temperature and divertor power load drop, which is caused by the neon injection. The increased erosion is caused by the additional neon. These observations are consistent with the rapid drop of the sputtering yield of tungsten impacted by Ne^{+3}, which reaches a value of 2×10^{-1} for plasma temperatures above 20 eV and decreases to less than 10^{-4} below 4 eV [3]. In discharges with divertor plasma temperatures below 2 eV, like the CDH-mode, no tungsten erosion could be measured.

Redeposition

As neutral tungsten atoms are released from the surface they will be ionized by the divertor plasma and can be redeposited by the gyromotion in the magnetic field. The fraction of the ionization length to the effective gyration radius determines the fraction of prompt redeposited tungsten atoms within the first gyration [3]. Additionally to the spectroscopically measured yield for the tungsten erosion, figure 3 shows results for the net erosion, determined by measuring the tungsten loss of probes [8]. The difference in these quantities can be interpreted as prompt redeposition. For the high temperature point at 40eV (n_e=7×10^{18}m^{-3}) the net erosion is about 50 % of the initially eroded tungsten. The prompt redeposition at lower temperatures (T_e=25eV,n_e=1×10^{20}m^{-3}) is at least 95%. The difference in the redeposition can be explained by the different electron densities of both discharges. The measured values can be compared with the expected values as shown in figure 5.

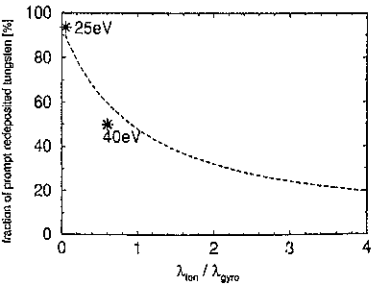

Fig. 5: Comparison of the measured (*) and predicted (- -) redeposition of tungsten [3].

Summary

The tungsten erosion in the ASDEX Upgrade divertor has been measured by observing the *WI* emission at 400.9 *nm*. Taking into account the *S/XB* value the influx is calculated for various plasma conditions. The resulting sputtering yield is in the range of 10^{-4} for most divertor plasma conditions. The erosion of tungsten in ASDEX Upgrade is dominated by the intrinsic plasma impurities like carbon. Adding impurities without cooling the boundary plasma increases the sputtering yield due to the additional impact energy, gained by the particle in the sheath potential. In general the cooling of the divertor plasma reduces the tungsten erosion remarkably. It is experimentally verified that an efficient redeposition can be achieved at high electron densities in the divertor plasma.

References

[1] PACHER, H. et al., St. Raphaël, France, 1996, to be published in J. Nucl. Mater.
[2] JANESCHITZ, G. et al., J. Nucl. Mater. **220-222** (1995) 73.
[3] NAUJOKS, D. et al., Nucl. Fusion **36** (1996) 671.
[4] ROTH, J. et al., J. Nucl. Mater. **220–222** (1995) 231.
[5] POST, D. et al., At. Data Nucl. Data Tables **20** (1977) 397.
[6] NEU, R. et al., Plasma Phys. Controlled Fusion **38** (1996) A165.
[7] GARCÍA-ROSALES, C. et al., accepted for publ. in Nucl. Fusion Technology .
[8] KRIEGER, K. et al., St. Raphaël, France, 1996, J. Nucl. Mater., in press.
[9] NAUJOKS, D. et al., J. Nucl. Mater. **230** (1996) 93.
[10] KURZ, C. et al., J. Nucl. Mater. **220-222** (1995) 963.

Line and Recombination Emission in the ASDEX Upgrade Divertor at High Density

B. Napiontek, U. Wenzel*, K. Behringer, D. Coster, J. Gafert, R. Schneider, A. Thoma, M. Weinlich and ASDEX Upgrade-Team
Max-Planck-Institut für Plasmaphysik, EURATOM Association, Garching and *Berlin

Introduction

The most promising divertor regime for ITER is the detached, high density divertor with its high radiation losses. Therefore we focus the spectroscopic investigations on this state to understand the emission properties, the behavior of the intrinsic impurity sources and the plasma parameters.
The radiation of carbon and deuterium was investigated by means of a scanning VUV spectrometer. The spatial distributions of the resonance line emission of carbon and deuterium were integrated to obtain the total radiation power losses. A small temperature dependent correction to get the total carbon radiation in the divertor was also included. The density dependence of the radiated power was measured in a density ramp with 3.5 MW heating power.
Detached divertor plasmas are characterized by strong hydrogen radiation which can be used for plasma diagnostics. By these means spectroscopical measurements of electron temperature and density in ASDEX Upgrade were carried out which are comparable to the recent experiments at Alcator C-Mod [1]. We will discuss the properties of cold, dense divertor plasmas and describe a method for T_e and n_e measurements which shall be compared with results of plasma modelling using the codes B2-EIRENE.
Despite the very low temperature in front of the plate carbon emission is high in the detached divertor. Therefore, we have studied the CD band in the visible to estimate the carbon influx via chemical erosion.

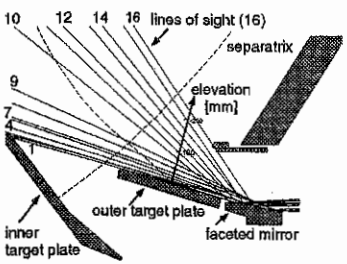

Figure 1: *Arrangement of the 16 poloidal sightlines of the divertor spectrometer. Another set of 30 sightlines views the plasma parallel to the outer target plate.*

Experiment

Experimental investigations were carried out with two spectroscopic systems. The divertor spectrometer (s. fig. 1) observed the plasma along several sightlines in the poloidal cross-section. There are 30 sightlines viewing the plasma parallel to the outer target plate in a distance of $1 \ldots 90\,mm$, another set of 16 sightlines is arranged fan-like. The collected light was fed via optical fibers to a Czerny-Turner or a Fastie-Ebert (Echelle grating) spectrometer with low and high spectral resolution, respectively. Several lines of sight were detected simultaneously by means of a fast CCD camera.

The boundary layer spectrometer (s. fig. 2) scanned the whole poloidal cross-section. In this way the inner and outer target plate could be observed. The light was analyzed by two spectrometers in the VUV and visible spectral range.

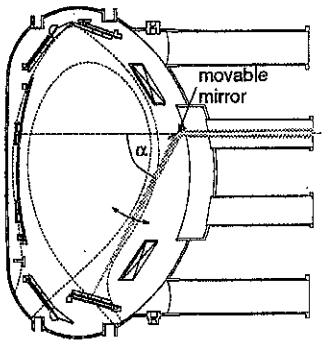

Figure 2: *Schematic view of the boundary layer spectrometer. A movable mirror allows scanning of the whole poloidal cross-section.*

Results: Power losses during a density ramp

The divertor radiation was investigated in an L-mode discharge with $3.5\,MW$ heating power. By means of gas puffing, the line-averaged density in the midplane increased from $4.5 \cdot 10^{19} m^{-3}$ to $6.5 \cdot 10^{19} m^{-3}$. The ion saturation current of Langmuir probes in the target plates first increased, but then dropped by a factor of 4 at $3.1\,s$ due to detachment. Spectroscopically, power losses were obtained by summing over the resonance lines of carbon and deuterium in the VUV spectral range. In Fig. 3 the results are compared to the bolometer measurements. The power losses rise with increasing midplane density. The ratio of the carbon to deuterium emission changes from 1:1 to 2:1 during the ramp. Main radiator is the CIII ion. The spectroscopically measured values lie 30% below the bolometer values, possibly caused by other impurities (O, F, Cl, B).

The highest radiated power is observed in the detached divertor despite the very low temperature of about $1\,eV$ (s. next section), i.e. there is no drastic reduction of the carbon source. The high intensity of the CD band emission even at detachment suggests the process of chemical erosion. From the measured band intensity the methane influx can be calculated. On the other hand, the methane influx can be calculated using the ion flux to the target plates measured by Langmuir probes and the yield for chemical erosion. In Fig. 4 we compare both methods. The absolute values agree well in the attached phase. During detachment the influx calculated from the measured ion flux deviated significantly from the spectroscopic measurements. This is probably due to chemical erosion caused by the flux of atoms onto the target plates.

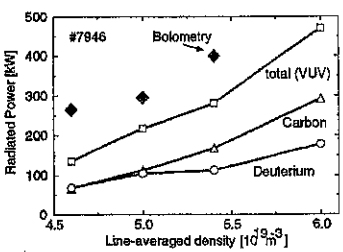

Figure 3: *Power radiated in the outer divertor as a function of the midplane density: carbon, deuterium and sum of both, compared with total losses measured by bolometers.*

Results: Recombining plasma

At maximum radiation the divertor is already detached. As indicated by the location of the emission zones of CIII and CIV the thermal front position is close to the X-point and the major part of the divertor is cold.

Under these conditions we observed the Balmer and Paschen continuum radiation and line radiation of the Balmer series up to transitions from level $n = 14$. When the plasma detaches there is a drop in electron temperature and an increase in electron density and therefore strongly increased rates for radiative and three-body recombination (s. [2]). This leads to a strong increase in hydrogen radiation. Fig. 5 compares two spectra at different times in an L-mode density limit discharge similar to the one discussed above. The ratio of Balmer to Paschen continuum radiation provides a sensitive method to measure the electron temperature. During the detachment the electron temperature decreased to $0.8 \ldots 1.4\,eV$ in the whole divertor. The electron density was determined from the absolutely calibrated Balmer continuum emission giving maximum values of $1 \cdot 10^{21} m^{-3}$. From the spectrum shown in Fig. 5 $1.1 \cdot 10^{20}\,m^{-3}$ was determined which is about a factor of 2 higher than the midplane density.

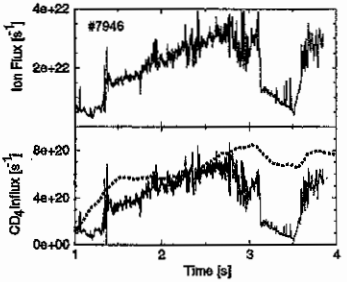

Figure 4: *Comparison of the methane influx measured spectroscopically (dotted line) and calculated from the ion flux to the target plate measured by Langmuir probes which is given separately in the upper graph.*

In order to investigate the optical thickness of the divertor plasma we measured simultaneously L_β and H_α with the boundary layer spectrometer. At moderate divertor densities the ratio of H_α to L_β intensities starts to increase with density indicating the effect of optical thickness. At higher densities and regarding L_α the effect must be even more pronounced. Thus in the region of high density plasmas, where the observed continuum radiation is preferentially emitted, recombination into the ground state via excited states is reduced. Therefore we expect that net recombination occurs in the outer zone of the divertor plasma and possibly near the target due to enhanced recombination rates by molecule encounters.

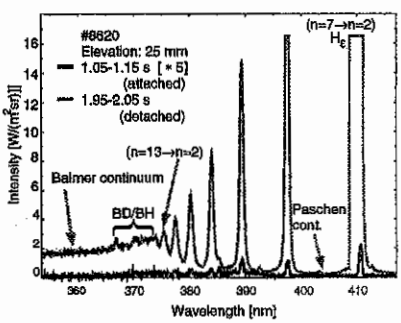

Figure 5: *Spectra around the Balmer series limit measured with the divertor spectrometer. The midplane density rises from* $4.1 \cdot 10^{19} m^{-3}$ *(at* $1.1\,s$*) to* $6.7 \cdot 10^{19} m^{-3}$ *(at* $2.0\,s$*) leading to fully detachment. The marked regions of continuum radiation are used for temperature determination.*

The arrays of lines of sight of the divertor spectrometer allow measurements of spatial T_e and n_e profiles. Spatial resolution is possible in the direction perpendicular to the target plates whereas along the line of sight the emission is integrated (s. Fig. 1). Due to dependence of the emissivity on n_e^2 the region with the highest density dominates the intensity. The temperature measurements represent the region with the highest temperature along the line of sight because of the steep dependence of the Balmer to Paschen

continuum ratio for $T_e \leq 2\,eV$. Therefore we get upper limits for T_e and n_e along the line of sight. This is illustrated in Fig. 6 which shows results of the modelling of the fully detached divertor plasma using B2-EIRENE [3] compared with the experiment.

Near the outer target plate (within about $10\,mm$) the modelled *mean* temperatures decrease due to the lower temperatures in the outer divertor. The spectroscopic temperature measurements are dominated by the inner divertor. Thus the measured spatial profiles can only be interpreted as profiles of mean values of T_e and n_e in the emission zone of the outer divertor at greater distances to the target plate. Therefore qualitative differences between the modelled mean parameters and the measurements (s. Fig. 6) especially for T_e near the target are to be expected. The agreement at greater distances to the target plates and for the electron density is quite good. We will overcome the problem of integrating along the outer and inner divertor in the new divertor configuration of ASDEX Upgrade where both parts of the divertor will be observed separately.

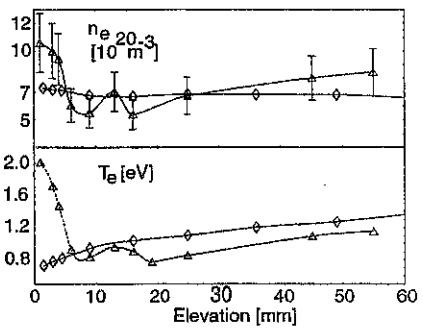

Figure 6: *Modelling* ($\diamond$) *and measurements* ($\triangle$, #8620 *at* 2.7 *s) of* T_e *and* n_e *profiles. The rise of measured electron temperature near the target plate is due to the effect of the inner divertor on line integrated intensity.*

Summary

Fully detached divertor plasmas in ASDEX Upgrade are characterized by low temperatures $T_e < 2\,eV$, high density $n_e \lesssim 1 \cdot 10^{21} m^{-3}$ and radiative and three-body recombination in the divertor volume. Despite the low electron temperature, carbon influx is very high caused by chemical erosion. The detached outer divertor reaches about $0.5\,MW$ radiated power due to both the high influx and the high electron density. Main radiators are deuterium and CIII.

The ratio of Balmer to Paschen continuum radiation provides a sensitive method for temperature measurements, however, the line integrated values are strongly weighted by the highest temperatures along sightline. Spatial profiles of electron density and temperature are in good agreement with first results of modelling recombining divertor plasmas in ASDEX Upgrade with B2-EIRENE.

References

[1] LUMMA, D. TERRY, J. L., and LIPSCHULTZ, B., PFC/JA-96-33, MIT, 1996
[2] BORRAS, K., et al., this conference, P4.019
[3] COSTER, D., et al., this conference, P4.013

Energy deposition at the divertor plates during elmy H-mode and poloidal and toroidal distribution of heat load on the wall inASDEX Upgrade

A. Herrmann, P. Franzen, W. Herrmann, C.F. Fuchs, M. Weinlich, ASDEX Upgrade team, NI-team, ICRH-team

Max-Planck-Institut für Plasmaphysik, EURATOM Association, Garching and Greifswald; Germany

Introduction

A crucial problem of future nuclear fusion reactors is the power handling. The operation of the next step tokamak ITER demands the handling of about 300 MW α-particle power crossing the separatrix. An additional difficulty arises from the envisaged H-mode operation, because this confinement regime is accompanied by edge localized modes (ELMs) which cause short lasting high power pulses across the separatrix which may be intolerably high. The energy transport due to ELMs and it's dependence on local and global plasma parameters has been carefully investigated in the ASDEX Upgrade tokamak. Additionally, the poloidal and toroidal distribution of the heat load of the inner walls of ASDEX Upgrade was measured time integrated by cooling water calorimetry.

Energy deposition to the divertor plates during elmy H-mode

One topic of this paper is the energy deposition onto the inner and outer divertor of ASDEX Upgrade during elmy H-mode phases as measured by thermography [1]. The time resolution of the thermography system is 260 μs/line and the spatial (radial) resolution is 2.7 mm/pixel and 3.2 mm/pixel for the outer and inner Divertor plates, respectively.

In a first step, the frequency behaviour of the power deposition to the inner plate was characterized by continuous wavelet analysis [2]. It was found, that there are qualitatively two classes for the frequency behaviour of type-I ELMs - periodic and aperiodic. For periodic ELMs the frequency is constant if the discharge conditions are unchanged. Aperiodic ELMs show a variation of the ELM frequency by a factor of up to two, though the global discharge conditions are kept constant.

Both types of ELM-behaviour are under investigation in this paper but the energy deposition to the inner and outer plate as well as the ELM-frequency are time averaged over about 20 ELM periods. The deposited energy is the sum of the deposition to the inner and outer plate, whereas the ratio inner to outer plate is about 3.

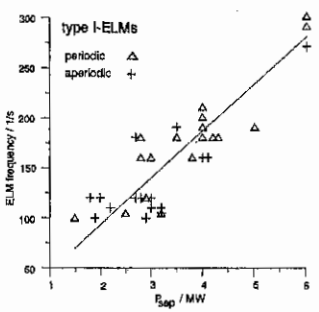

Fig. 1: The ELM frequency increase with the heating power.

Figure 1 shows the increase of the ELM-frequency with the power crossing the separatrix, P_{Sep}, as it is typical for type-I ELMs. A linear fit through the origin gives: $f_{ELM}(Hz) \sim 50 \times P_{Sep}(MW)$.

The energy deposited per ELM varies between 2 and 10 kJ/ELM and shows a tendency to increase with P_{Sep}. The energy loss in the midplane calculated from the electron temperature and the density profile measured in the midplane by Thomson scattering and Lithium beam, respectively, is about a factor of two higher (10–20 kJ/ELM) [3].

The fraction of power transported by an

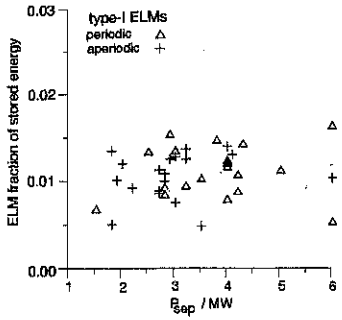

Fig. 2: The fraction of stored energy deposited per ELM to the target plates is between 1-2%

ELM, $\frac{\Delta W^{target}_{ELM} \cdot f_{ELM}}{P_{sep}}$, is in the order of 30%. This value is independent of P_{scp} and comparable to values of other tokamaks [4]. The same statement holds for the fraction of stored energy, $\frac{\Delta W^{target}_{ELM}}{W_{plasma}}$ which is in the order of 1–2 %, as shown in figure 2. The data under consideration are taken from low radiating discharges with $P_{sep} = (0.5 \pm 0.1) \times P_{in}$. From this and from the fact, that the fraction of transported power as well as the fraction of stored energy is constant follows that the ELM frequency is inverse proportional to the energy confinement time.

The constant ratio of the stored energy deposited per ELM to the target plates and the fact, that the temperature profiles are self-similar for a wide range of parameters [5], which is found from ECE measurements, implies that the energy extraction depth is independent of the heating power and depends only from the density profile. There is no significant difference in energy deposition for periodic and aperiodic ELMs.

Consequences for ITER. The value for the fraction of stored energy, which is comparable for ASDEX and JET [4], can be used to estimate the ELM effects on the divertor for ITER conditions. Assuming a heating power of P_{in} = 300 MW, and an energy confinement time of τ_e = 6 s the stored energy is W = 1.8 GW and the energy loss per ELM transported to the divertor, ΔW = 0.02–0.04 GW.

The deposition area is calculated from the major radius and a power decay length scaling derived for ASDEX Upgrade H-mode discharges [6], $\lambda_p^{target}(mm) = 6.36 \times 10^{-3} P_{sep}^{0.52} q_{95}^{0.7}$. With $\lambda_p^{target}(150MW, 3) \simeq 0.3m$ and $R_0 = 8.14m$ the deposition area is: $A_{dep} \simeq 30m^2$. Using this value the energy density at the target plate per ELM becomes, $w = (0.7 - 1.2)\frac{MWs}{m^2}$.

The uncertainty in this estimation is the contribution of the ITER geometry. While the fraction of stored energy is found to be constant for different tokamaks at about the same value, the decay length scaling is limited to ASDEX Upgrade data. If the major radius is a hidden parameter, the scaling should be modified to: $\lambda_p^{target}(mm) = \left(\frac{R_0^{ITER}}{R_0^{AUG}}\right)^{\alpha} \lambda_p^{target,AUG}$, with $\frac{R_0^{ITER}}{R_0^{AUG}} = \frac{8.14}{1.65} = 4.93$, resulting in $w = (4.93)^{-\alpha}(0.7 - 1.2)\frac{MWs}{m^2}$. If e.g. the power decay length scales with P_{sep}/R_0, α becomes -0.52 and w increases by a factor of 2.3.

Wether or the high energy density can be tolerated depends on the caused temperature increase, which is given by: $\Delta T = \frac{w}{\sqrt{\Delta t}} \frac{2}{\sqrt{\pi}} \frac{1}{\sqrt{\kappa \rho c_p}}$. With a heat conduction of, $\kappa = 1.2\frac{W}{cmK}$, and a product of density and specific heat of, $\rho c_p = 3.6\frac{Ws}{cm^3 K}$, which are typical for CFC-material envisaged for ITER divertor plates, the maximum temperature becomes: $\Delta T(K) = 58 \times \frac{w\left(\frac{MWs}{m^2}\right)}{\sqrt{\Delta t(s)}}$. The resulting temperature increase for a temporal ELM-width of Δt=1 ms, and α=0 is: $\Delta T = (1300 \div 2200)K$

This values are at the limit but depend on some uncertain values as α, and the ELM duration which may change the value for the temperature increase. If elmy H-mode is an operation scenario for ITER further on, the decay length scaling found on ASDEX Upgrade should be checked at other tokamaks.

Poloidal and toroidal distribution of heat load

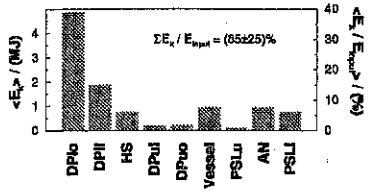

Fig. 3: Mean poloidal distribution of heat load in ASDEX Upgrade for normal operation conditions — single null neutral beam heated low radiative elmy H-mode discharges without disruptions. The acronyms are explained in the text.

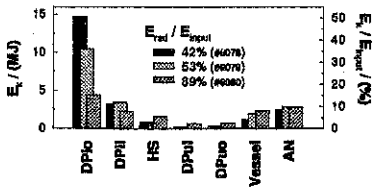

Fig. 4: Poloidal distribution of heat load in ASDEX Upgrade in dependence on the radiated energy fraction for three discharges with otherwise equal plasma parameters. At the time of these discharges, the heat load on both PSL was measured not yet. The acronyms are explained in the text.

Cooling water calorimetry. The cooling water calorimetry system at ASDEX Upgrade (CWC) measures the heat load on the inner wall tiles (and the vacuum vessel) poloidally and toroidally resolved, from the integrated temperature difference of inlet and return water temperature and the water flow rate. For each of the main component (lower outer (DPlo), lower inner (DPli), upper inner (DPui), and upper outer (DPuo) divertor plates and the inner heat shield (HS), respectively) a measuring device for each torus sector is installed. With the additionally measuring devices at the lower and upper stabilizing loops (PSLl, PSLu), ICRH antennas (AN) and the vacuum vessel, CWC covers more than 90% of the ASDEX Upgrade inner wall. The fraction of the energy measured by CWC to the total input energy - which should be unit - amounts to (85±25)%. The large scatter is due to radiation and charge exchange losses through ports which are not covered by CWC.

Poloidal distribution. Figure 3 shows the mean poloidal distribution of the heat load for discharges with normal operation conditions, i.e. single null neutral beam heated elmy H-mode discharges without disruptions and radiated energy fractions below 68 %. In this case, the lower outer divertor plates receive between 30 % and 40 % of the total input power, resulting in heat loads of up to 1 MJ per sector for discharges with 10 MW additional heating power. For the normal conditions, the inner divertor tiles receive about 15 % of the input energy. Between 5 % and 10 % of the input energy is deposited on the inner heat shield, the vacuum vessel, lower PSL and the ICRH antennas, whereas the heat load on the upper divertor and PSL is negligible. The heat load on the outer divertor tiles can be reduced by radiation in the plasma mantle by a factor of about 3 (fig. 4), with only a minor reduction of the heat load on the inner divertor tiles. Due to the increased radiation, the heat loads on the other inner wall components also increase, but this increase cannot account for the decrease of the divertor heat load due to loss channels not covered by CWC. The heat load on the outer divertor tiles is also reduced for L-mode and/or disruptive discharges, and discharges with the ion ∇B drift towards the upper divertor plates.

Toroidal distribution. Figure 5. shows as an example the mean toroidal distribution of the heat load on the outer divertor tiles. As can be seen, the distribution is asymmetric, the maximum values exceed the mean value by more than 15 %; however, the position of the maxima depends on the discharge conditions, especially on the direction of the ion ∇B drift. For the case of normal operation, i.e. $I_p > 0$ and $B_t < 0$, the direction of the ion ∇B drift is towards the lower divertor plates, and the maximum heat loads are on the tiles in sectors 10 to 13, whereas in the case of the ion ∇B drift towards the upper divertor plates, i.e. $I_p > 0$ and $B_t > 0$, the maximum heat loads are on the tiles in sectors 2 to 4. Apparently, the distribution exhibits a dominant n = 1 structure with a smaller n = 2 distribution. The depen-

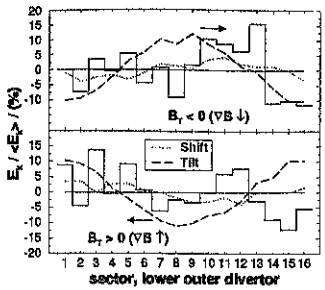

Fig. 5: Toroidal distribution of heat load in ASDEX Upgrade for normal operation conditions (see figure 3). The dashed and dotted lines show results of field line calculations (see text). The arrow denotes the direction of the shift of the maximum due to transport perpendicular to the field lines.

dence of the heat load distribution on the ion ∇B drift, and not on the sign of the magnetic field, is confirmed by discharges with counter NI injection (i.e. $I_p < 0$), where in the case of $B_t > 0$ the same distribution as in the case of $I_p > 0$ and $B_t < 0$ shows up. The measured asymmetry in the heat load distribution on the lower outer divertor plates is consistent with other toroidal asymmetries observed in ASDEX Upgrade. After the start of neutral injection, where the separatrix position was not much changed, a colored ring was observed at the outer divertor plates. The center of this ring was shifted against the geometrical axis in direction of sector 13. Similar observations were made by Langmuir probes in sectors 4 and 13: the separatrix positions differ by about 10 mm, also indicating a shift towards sector 13. Furthermore, all locked modes lock also in sector 13, as observed by the Mirnov coils. All these observations indicate that the magnetic axis of the magnetic field coils is somewhat misaligned to the geometrical axis of the vacuum vessel. In order to get some hints on the nature of the misalignment, we performed field line calculations, assuming that the radial transport in the midplane is symmetric and that the heat load on the targets is proportional to the field line density, for two scenarios with a n = 1 distortion: (a) a shift of the geometric axis of 5 mm towards sector 13, and (b) tilting the geometric axis in such a way that also a shift of 5 mm at the outer target plates results. Both scenarios reproduce the shift of the separatrix position very well; they also reproduce rather the heat load maximum position (see figure 5) as well as the dependence on the ion ∇B drift direction, if one considers the shift of the maximum heat load due to transport perpendicular to the field lines. However, only scenario (b) - which is technically the more improbable - also reproduces the amount of the maximum heat load enhancement. Hence, the observed toroidal asymmetries cannot be explained solely by geometrical effects, but other distortions play a role also, so perhaps a distortion of the magnetic field in the midplane by a not complete compensation of the iron yokes and the magnets of the neutral beam injection box located in sector 13. As a consequence for the ITER design, small distortions and misalignment of the magnetic structure can enhance the heat load on some special locations of the divertor by 10 % to 20 %, neglecting geometrical effects.

References

[1] A. Herrmann, W. Junker, K. Günther et al., Plasma Phys. Control. Fusion 37 (1995) 17
[2] V. Dose, G. Venus, H. Zohm, Phys. Plasmas 4(1997) 323
[3] H. Reimerdes, IPP-Report 1/300, p.57
[4] J. Lingertat, 4th European Fusion Physics Workshop, Stockholm, 11-13 December 1996
[5] W. Suttrop, Joint U.S.-European Transport Task Force Workshop, Madison WI, April 23-26, 1997
[6] A. Herrmann, M. Laux, O. Kardaun et al., 23rd EPS conference on Contr. Fusion and Plasma Phys. II d039 (1996)

Tungsten erosion and migration in ASDEX Upgrade

K. Krieger, H. Maier, V. Rohde, K. Asmussen, M. Balden, D. Coster,
J. Roth, R. Schneider, A. Thoma and ASDEX Upgrade Team
Max-Planck-Institut für Plasmaphysik, EURATOM-IPP Association
Garching und Berlin, Germany

1 INTRODUCTION

Tungsten erosion was investigated by observation of spectral lines in the main plasma and the divertor [1, 2] and by measuring material erosion on probes exposed to the divertor plasma [3]. Tungsten migration was investigated by measuring the tungsten deposition with midplane and divertor collector probes and by ion beam analysis of a complete poloidal set of plasma facing vessel components removed after the experimental campaign. The Monte-Carlo impurity transport code DIVIMP was employed for the interpretation of the measured data.

2 TUNGSTEN EROSION

Net tungsten erosion in the divertor was determined by exposing graphite probes covered with a thin (1–100nm) W-marker stripe oriented in radial direction and measuring the thickness of the marker before and after exposure by Rutherford backscattering analysis [3]. Further, the flux of eroded tungsten atoms was determined by spectroscopic observation of the respective line emission at 400.9 nm. For the interpretation of the results, both the particle flux to the target plates and the energy of the incident ions is required. Direct measurements of these quantities were provided by a set of flush mounted Langmuir probes.

As expected, significant tungsten erosion was only observed in operating regimes with high divertor temperatures like low density Ohmic discharges and H-mode discharges with ELMs [3, 2]. Figure 1c shows results of a divertor probe exposure in a series of such low-density Ohmic discharges. The marker erosion pattern is clearly correlated with the spatial distribution of the WI spectral line emission (Fig. 1b). The Langmuir probe results for T_e at the target plates (Fig. 1a) show that the energy of the deuterium ions is below the sputtering threshold energy of tungsten. Therefore, the observed erosion must be attributed to sputtering by low-Z impurities, in particular carbon and boron. Using sputtering yields for carbon impacting on tungsten from laboratory ion beam experiments and assuming a carbon concentration of 1% good agreement with the measured erosion fluxes can be achieved [2]. Further one observes that the erosion yields derived from the spectroscopically determined tungsten flux are generally higher than the net erosion obtained from the marker measurements. The discrepancy is attributed to redeposition of tungsten atoms from the plasma and to the effect of prompt local redeposition of W^+ ions, which occurs because of the small ratio of ionization length to gyro orbit radius of W^+ [4].

For a quantitative interpretation of the experimental results, the Monte Carlo impurity transport code DIVIMP was used to simulate the tungsten erosion and transport processes. For the discharge series described above, a two-dimensional background plasma model in the poloidal plane was created by a B2/EIRENE code simulation. In the given background plasma DIVIMP calculates the trajectories of an ensemble of tungsten atoms. The tungsten source was assumed to be due to sputtering by a 1% fraction of C^{3+} ions with an impact energy of $2T_i+3ZT_e$ (Z=3). Effects of prompt local redeposition, however, have not been included yet. The sputtered atoms move along straight lines until they become ionized. Their trajectories as ions are determined by friction, electrical and temperature gradient forces

along the magnetic field, and by anomalous diffusion across the magnetic field. The code follows the ions until they finally become redeposited again at a vessel component. Apart from the spatial distribution of erosion and deposition on plasma facing surfaces, it is also possible to calculate spectral line intensities along given spectrometer viewing chords.

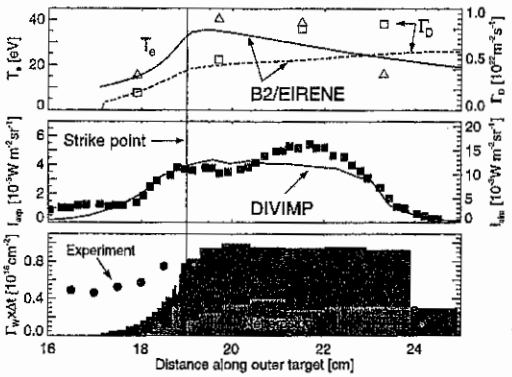

Figure 1 *a) Ion flux and electron temperature along the outer target plate for a series of low density ($\bar{n}_e = 2.5 \times 10^{19}$m^{-3}) Ohmic discharges with 18.7s divertor plasma operation. The dots represent Langmuir probe measurements while the lines denote results of the respective B2/EIRENE plasma model. b) WI spectral line emission above the outer target plate. The dots represent results from the Boundary Layer Spectrometer and the solid line the result of a DIVIMP simulation. c) Radial profile of tungsten marker erosion along the outer target plate surface. The dots denote the measured tungsten marker erosion.*

The solid lines in Fig. 1a represent the electron temperature and the deuterium flux at the outer target plate as calculated in B2/EIRENE. Model and experimental results agree well within the experimental error of the Langmuir probe measurements. The spatial distribution of the WI line emission calculated for the viewing chords of the ASDEX Upgrade boundary layer spectrometer shown in Fig. 1b also agrees very well with the experimental data, whereas the absolute value of the simulation is approximately 3 times larger, which reflects the uncertainties in the ionization and emission rate coefficients of tungsten. Outside the separatrix, the measured net erosion is higher than the calculated net erosion but still below the calculated total erosion. The reason for the discrepancy are graphite tiles adjacent to the target probe which lead to a decreased tungsten flux to the probe and correspondingly to a higher net erosion.

Inside the strike point position one observes significant erosion in contrast to the code results. This reflects that the probe measurements represent time integrals, while the spectroscopic results and the code simulations represent a single time slice in the stationary plasma phase. During plasma startup, the rather hot scrape-off layer sweeps across the target plate in outward direction to it's final stationary position leading to the observed erosion in the area from 16–19cm.

3 TUNGSTEN DIVERTOR RETENTION

For divertor retention, i.e. the capability of a divertor configuration to keep impurities from escaping to the upstream scrape-off layer (SOL) region and to the confined plasma, there is no unique definition in literature. In the following we use the ratio of the tungsten density

in the midplane SOL to the tungsten density at the target plates to characterize the retention capability. We determine the retention directly from measurements in the edge plasma and at the target plates. The often used method of correlation analysis of target erosion flux and central tungsten concentration suffers from large uncertainties about the cross field transport in the confined plasma [1]. Unfortunately, it is not possible to determine the tungsten density in the edge region directly. Instead, the tungsten flux in the midplane SOL was measured by deposition probes exposed in the shadow of the ICRH antenna limiters. The tungsten deposition corresponds to the radial flux of tungsten into the shadowed region. Assuming a simple model of purely diffusive radial transport, it is possible to extrapolate the measured tungsten deposition flux from the shadowed region towards the SOL. The target flux was derived from the WI line emission as described in section 2.

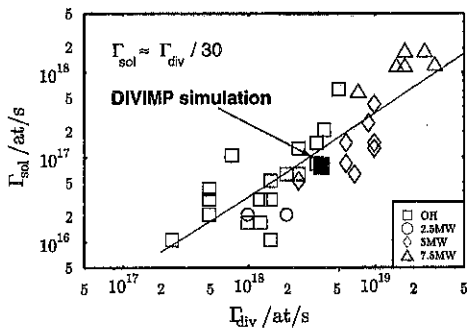

Figure 2 *Correlation of the tungsten flux at the midplane scrape-off layer derived from deposition measurements to the tungsten erosion flux measured spectroscopically at the outer target plate.*

As shown in Fig. 2 the midplane tungsten flux turned out to be proportional to the target erosion flux independent of the discharge conditions with an approximate ratio of 1/30 between mid plane and divertor. This yields a first estimate of the divertor retention capability for tungsten. For a more detailed analyis, the target and SOL tungsten density was determined by DIVIMP code simulations with the code results validated by the measured fluxes. From this analysis one obtains for the low density Ohmic discharges described above a divertor retention factor of $\simeq 0.01$. A fraction of 0.002 of the eroded tungsten atoms actually penetrates the confined plasma resulting in a core contamination of $\lesssim 2 \times 10^{-5}$ in good agreement with the measured central W-concentration.

With the successful demonstration of DIVIMP as a tool for the interpretation of the tungsten experimental results, further studies will concentrate on the properties of tungsten in reactor relevant discharge scenarios.

4 TUNGSTEN REDEPOSITION

The long term migration of tungsten eroded at the divertor target plates was investigated by measuring the amount of deposited tungsten on a complete poloidal set of plasma facing surface components removed after the experimental campaign. The samples were analyzed by Particle Induced X-ray Emission (PIXE) using a 1.5MeV Proton beam and the amount of deposited tungsten was derived from the intensity of the tungsten L_β doublet line at 9.68/9.96 keV.

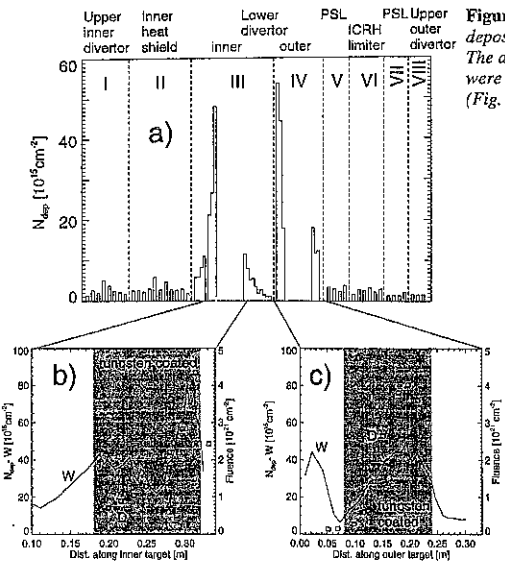

Figure 3 *a) Poloidal distribution of tungsten deposition on plasma facing vessel components. The data in the tungsten coated target area were obtained from graphite thermography tiles (Fig. 3b - inner target, 3c - outer target).*

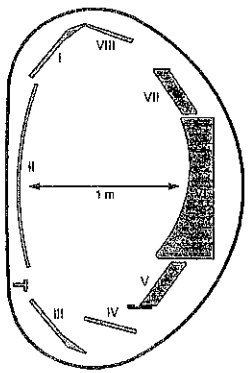

Fig. 3a shows the tungsten surface density along a poloidal set of plasma facing vessel components. All surfaces in the main chamber exhibit a roughly constant tungsten contamination, which is several times lower than the respective values for copper and iron. Comparison with results of the previous experimental campaigns yields an upper limit of $10^{15}/cm^2$ W-atoms deposited within $\simeq$ 3000 s plasma discharge time. On the other hand, in the lower divertor, we find up to one order of magnitude higher contamination level with the peak value near the average strike point location on the deposition dominated inner target plate (Fig. 3b) and a less pronounced broader maximum in the strike point region of the erosion dominated outer target plate. Both of these features coincide very well with the average particle flux in these areas [5]. However, a high level of tungsten deposition extends onto the graphite tiles adjacent to the W-coated area, which cannot be accounted for by changes of the strike point position alone.

REFERENCES

[1] ASMUSSEN, K. et al., Investigations of tungsten in the central plasma of asdex upgrade, P4.002, this conference, 1997.

[2] THOMA, A. et al., Spectroscopic measurements of the tungsten erosion in the ASDEX Upgrade divertor, submitted to PPCF.

[3] KRIEGER, K. et al., Study of gross and net erosion in the ASDEX Upgrade divertor, J. of Nucl. Mat., in press.

[4] NAUJOKS, D. et al., Nucl. Fusion **36** (1996) 671.

[5] FRANZEN, P. et al., Hydrogen isotope inventories in the asdex upgrade tungsten divertor tiles, P4.011, this conference, 1997.

Helium Exhaust and Transport in ASDEX Upgrade

H.-S. Bosch, D. Coster, R. Dux, G. Haas, A. Kallenbach, S. de Peña Hempel, K. Lackner, J. Neuhauser, R. Schneider and the ASDEX Upgrade Team
Max-Planck-Institut für Plasmaphysik, EURATOM Association, D-85748 Garching

1. Introduction

One of the important requirements for steady state operation of a fusion reactor is sufficient exhaust of the fusion-produced helium from the core plasma. This, however, involves two separate but linked processes, namely radial transport on closed flux surfaces in the core plasma and scrape-off layer (sol) transport into the divertor, including high divertor retention to optimize the pumping efficieny by increasing the helium density in front of the pump duct.

2. Core helium transport

The global helium exhaust time in ASDEX Upgrade has been shown to decrease strongly with increasing divertor neutral gas density[1], and this is attributed to improved divertor retention due to neutrals recirculating from the divertor chamber. Figure 1 compares the helium transport coefficients as deduced from CXRS-measurements for two CDH-mode discharges (with neon cooling and detached divertor plasma) with different values of the neutral gas flux density (as a measure of the neutral density) in the divertor chamber. In the discharge with the higher neutral flux density (#6131, $\phi_0 = 5.4 \times 10^{22}$ m^{-2}s^{-1}), the global helium confinement time, normalised to the energy confinement time ($\rho^*_{He} = \tau^*_{He}/\tau_E$) is 25 % smaller than in the discharge with lower neutral gas flux density (#6136, $\phi_0 = 4.0 \times 10^{22}$ m^{-2}s^{-1}), namely 6.4 compared with 8.4.

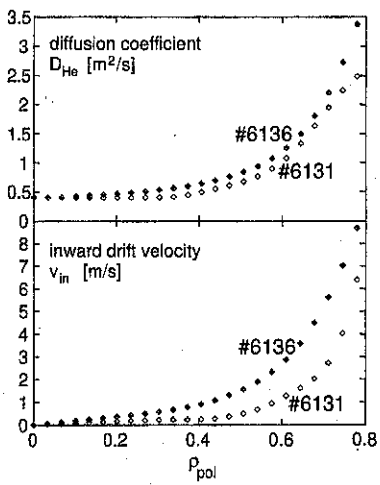

Figure 1: Helium transport coefficients for two CDH-mode discharges with different divertor neutral flux densities.

The core transport coefficients, however, are practically identical, as shown in figure 1, as the slightly higher D_{He} in #6136 is in principle offset by the v_{in} also being larger. The quantitative similiarity of core transport in these discharges was shown with the STRAHL code, including a simple scrape-off layer and divertor model [2]. To reproduce the experimentally measured decay times of the helium density, different sol and pumping time constants have to be used for both discharges, expressing the better sol transport in #6131, when using the transport coefficients from figure 1 for the core. Using these core coefficients, and identical time constants for sol and divertor, both discharges show identical helium decay times. This proves that the improvement in helium exhaust is solely determined by the physics in the scrape-off layer and divertor.

3. Scrape-off layer transport and divertor retention

It has been shown previously in ASDEX Upgrade, that the improvement in divertor compression with increased neutral gas density in the divertor chamber is due to this gas density, or the corresponding particle flux out of the divertor onto the divertor leg (internal recirculation), and not due to the externally fed deuterium flux in the main chamber [3]. That means, it is not the particle flux in the scrape-off layer that flushes the impurities into the divertor, but the internally recirculating fluxes in the lower part of the scrape-off layer, namely below the divertor baffle ring which is installed in ASDEX Upgrade at about the height of the X-point.

This physics picture was confirmed by 2d-modelling of the scrape-off layer and divertor plasma with the SOLPS-code package [1,4]. Not only do these simulations show the behaviour seen in experiment, namely the divertor compression increasing with divertor neutral flux density, and the compression of neon being higher than that of helium, but they also show that in higher density plasmas the helium (and neon) neutrals from the divertor plate are quickly ionised, and in ASDEX Upgrade they are transported radially by an almost "diffusive" process towards the outer edge of the scrape-off layer and into the divertor chamber. In this outer edge the impurity compression is determined by the deuterium flux towards the target plate, which is built up by the neutrals streaming towards the divertor plasma, as was shown with the modelling [1].

These results which have been observed in CDH-mode plasmas [3], are different from similiar experiments in DIII-D H-mode plasmas [5], where an improvement in divertor compression was found with increasing net particle throughput in the scrape-off layer. The influence of ELMs has been discussed as a possible reason for the difference, and figure 2 shows the results of experiments in ASDEX Upgrade with type-I ELM H-mode plasmas (I_p = 1 MA, B_t = 2.5 T, P_{NBI} = 5 MW). For a fixed divertor neutral flux density $\phi_{0,div}$, the pumping speed was varied (by closing valves to the turbomolecular pumps on a shot to shot basis), and the external gas flux was varied accordingly to keep $\phi_{0,div}$ constant (feedback-controlled).

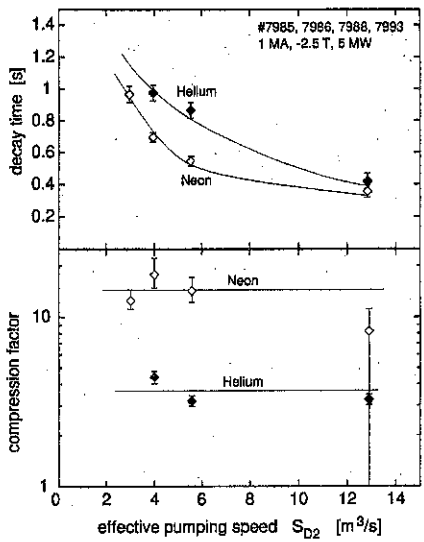

Figure 2: Exhaust rates (top) and compression factors (bottom) for He and Ne as a function of the pumping speed. The external deuterium flux into the main chamber was varied to keep the divertor neutral flux density in all discharges constant. While the exhaust rates decrease with increasing pumping speed, and net particle throughput, the divertor compression is independent of these two correlated parameters.

These experiments again show, that in ASDEX Upgrade the internal recirculation of

neutrals from the divertor region is responsible for the divertor compression of neon and helium. This is understandable from the above mentioned 2d modelling which shows that this internal flux in the region below the X-point is much stronger than the net particle influx, and therefore one can expect it to be the leading force. It also shows, however, that the geometry of the ASDEX Upgrade divertor plays an important role. The baffle ring is located about 14 cm above the outer divertor plate, i.e. the length of the divertor leg where the neutrals can again be ionised and where they can enhance the plasma flow, is rather large, and covers the whole region below the X-point.

In DIII-D the baffle ring is very close to the divertor plate, and the particle fluxes into the divertor chamber as well as the reflux of neutrals are strongly reduced. Therefore the scrape-off layer transport of impurities as discussed above for ASDEX Upgrade will not work, and the smaller effect of friction driven flow might become the leading force. This has to be confirmed by 2d modelling, but could easily explain the differences between the two experiments.

As discussed above, the divertor geometry in ASDEX Upgrade plays an important role for divertor compression of impurities. This also becomes evident when the magnetic configuration is varied, as seen in figure 3. Very similiar plasmas have been performed with different plasma shape. The separatrix of the standard equilibrium with a low triangularity is shown as solid line in figure 3, the separatrix of the medium triangularity plasma as a dotted line. These higher triangularity plasmas show generally better energy and particle confinement, but the two discharges shown here are almost identical in global parameters, as shown in figure 4. The separatrix density and the average sol density in #8197 are only slightly smaller than in #7492, as it is the case for the main chamber neutral gas flux density $\phi_{0,midplane}$. Also the plasma parameters at the target plates are similiar, but there is a large change in the divertor neutral flux density $\phi_{o,div}$, and in the deuterium compression $C=\phi_{o,div}/\phi_{0,midplane}$. Modelling of short Ne puffs in both discharges with STRAHL [6] shows that the Ne-compression in #8197 is almost negligible, and the reduction compared with #7492 is much larger than expected for the lower $\phi_{0,div}$ [7]. The shift of the X-point to smaller radii opens a gap between the scrape-off layer and the baffle ring, and thereby destroys the compression of deuterium as well as of the impurities.

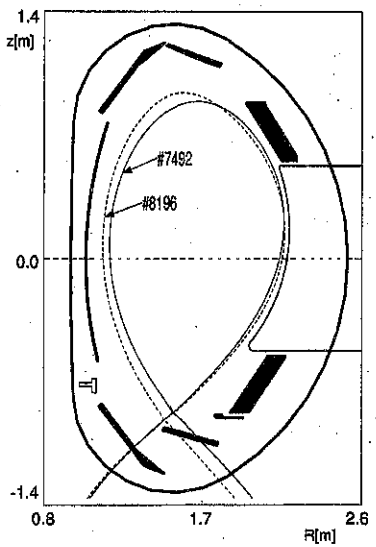

Figure 3: Magnetic configurations for the standard case in ASDEX Upgrade (#7492, solid line) and a higher triangularity plasma (#8196, dotted line).

4. Conclusions

It has been shown that exhaust of noble gas impurities (helium as well as neon) in ASDEX Upgrade is determined by transport in the sol and by the divertor compression. This can be influenced by the neutral gas in the rather open divertor chamber (in divertor I). Variations of the magnetic configuration, where the X-point is shifted to smaller radii and the region between sol and baffle ring is opened, deteriorate strongly the divertor compression of neon as well as of deuterium.

From B2-EIRENE modelling of the divertor compression of helium and neon, it is clear that the geometry of divertor I played an important role for this mechanism, where internally recirculating deuterium fluxes determine the divertor compression.

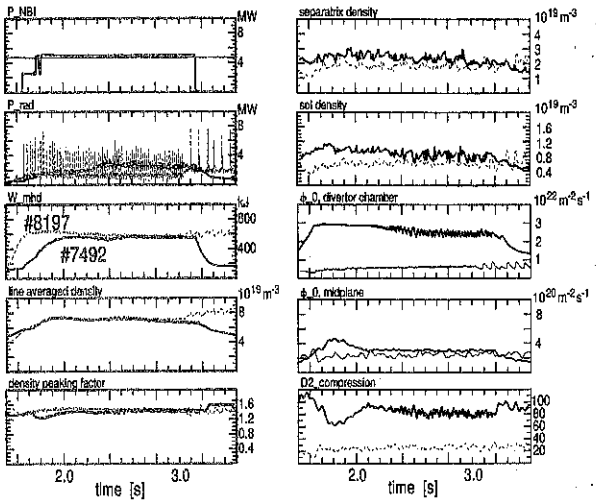

Figure 3: Plasma parameters for the discharges shown in figure 3 .

Therefore differences in He transport are expected for the modified divertor II of ASDEX Upgrade which will start operation soon. The new divertor will have vertical target plates which are LYRA-shaped to distribute the heat fluxes more homogeneously. Additionally, the private flux region is equipped with a dome-shaped baffle to prevent large influxes of neutrals to the main plasma through the X-point and to increase the neutral density in the divertor chamber for a given plasma flow towards the divertor. 2d-modelling of this divertor geometry predicts a better He compression compared with divertor I, mainly due to the vertical orientation of the target plates.

References

[1] Bosch, H.-S., Particle exhaust in radiative divertor experiments, Jour. Nucl. Mat., in press.

[2] Dux, R. et al., Plasma Phys. Controlled Fusion **38** (1996) 989.

[3] Bosch, H.-S. et al., Phys. Rev. Lett. **76** (1996) 2499.

[4] Coster, D. P. et al., B2-Eirene modelling of ASDEX Upgrade, Jour. Nucl. Mat., in press.

[5] Schaffer, M. et al., Direct measurement of divertor neon enrichment in DIII-D, Jour. Nucl. Mat., in press.

[6] Kallenbach, A. et al., this conference.

[7] Bosch, H.-S. et al., Particle exhaust studies in ASDEX Upgrade, submitted to PPCF.

HYDROGEN ISOTOPE INVENTORIES IN THE ASDEX UPGRADE TUNGSTEN COATED DIVERTOR TILES

P. Franzen, H. Maier, D. Schleußner, R. Behrisch, M. Balden, and The ASDEX Upgrade Team
Max-Planck-Institut für Plasmaphysik, EURATOM Association, Germany;
POB 1533, D-85740 Garching, Germany

ABSTRACT. The total hydrogen isotope inventories in the tungsten coated divertor tiles of ASDEX Upgrade were measured by thermal desorption spectroscopy and — in the near surface region — by nuclear reaction analysis. The highest amounts of deuterium ($\lesssim 5\times10^{22}$ D/m^2) are measured in the inner divertor region outside the separatrix due to the formation of a C:H layer on the tungsten by co-deposition of deuterium with carbon. The inventories in the outer divertor — where erosion dominates — are generally smaller by an order of magnitude.

1. INTRODUCTION

Apart from graphite and beryllium, the high-Z material tungsten is considered as plasma facing material for ITER. In order to provide an experimental data base for the ITER divertor, tungsten coated graphite tiles have been installed as divertor target plates in the tokamak ASDEX Upgrade for the experimental period December 1995 to July 1996 [1].

In order to obtain a measure and to improve the understanding of hydrogen retention in tungsten under reactor-like conditions, the total hydrogen isotope inventories of the tungsten divertor tiles of ASDEX Upgrade were measured with Thermal Desorption Spectroscopy (TDS). The near-surface deuterium inventory was measured by Nuclear Reaction Analysis (NRA).

2. EXPERIMENT

The tungsten coated carbon tiles had been installed in the ASDEX Upgrade divertor at the separatrix intersection areas (figure 1). They consist of a 500 μm thick plasma sprayed tungsten layer on a graphite substrate. In order to avoid hot spots at the edges, the tiles were tilted in toroidal direction. Hence, a part of each tile is shadowed from the plasma by the edge of the adjacent tile, and receives much less plasma flux than the non-shadowed part of the tile. In the following, we will denote the former region as 'shadow region', whereas the region with the full plasma impact will be denoted as 'plasma region'.

About 800 discharges were performed in the tungsten experimental period. Out of these,

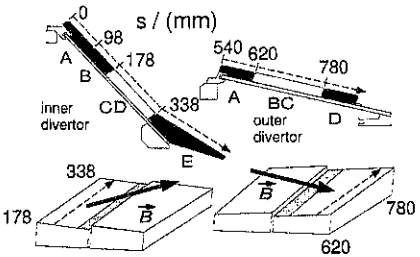

FIG. 1. *Position of the tungsten coated graphite tiles (CD and BC, respectively) in the ASDEX Upgrade divertor. The tiles are tilted in toroidal direction, resulting in regions shadowed from the plasma by the edge of the adjacent tile. The arrows denote the directions of the magnetic field lines. The other graphite tiles had no tungsten coating.*

about 480 discharges had been heated additionally by neutral injection. Initially, the heat load on the tungsten tiles was limited to 7 MW/m^2 in order to avoid damage, but during the experiments also discharges with full auxiliary heating power of 10 MW were performed, resulting in heat loads of more than 10 MW/m^2 [1]. Mostly, the discharges had deuterium as filling gas, and, in case of neutral injection, as well as injected atoms. Hydrogen as filling gas was used mainly in the middle of the experimental period and for the last 10 discharges. In the case of deuterium filling, hydrogen (H) is still present in the discharge. Typical values are 10% to 20%, while in the case of neutral injection with H^0, the H background amounts to about 60% [2]. From these figures and the number of different discharges, a mean H/D ratio in the plasma core of about 0.5 can be estimated.

Thermal Desorption Spectroscopy. The experimental setup used in this work for the TDS experiments is described in ref. [3]. The samples, having a diameter of about 12 mm and a thickness of about 3 mm, are cut out of the tungsten coated tiles and are heated by electron bombardment from the rear side up to 2100 K in a ultra high vacuum chamber. The desorbed gases are monitored by means of a calibrated quadrupole mass spectrometer (QMS) by the increase of the respective partial pressures at corresponding masses during the heating of the sample. The total hydrogen isotope inventories are obtained by adding up the respective atoms in all released hydrogen containing molecules (e.g. HD, D_2 and CD_4 for deuterium).

TDS spectra of hydrogen implanted in graphite show a broad peak in the range of 900 K to 1200 K, indicating the strong C-H bonds with energies of 2 eV to 4 eV [4]. TDS spectra of hydrogen desorbed from tungsten after implantation at room temperature reveal a two peak structure [5, 6]; a first peak at about 500 K to 600 K is attributed to intrinsic traps with concentrations of the order of $\lesssim$0.01 traps/W-atom and binding energies of about 0.5 eV. The second peak at about 700 K to 800 K occurs only after implantation with energies sufficient to produce displacement damage ($\geq$180 eV for D); hence, this peak is due to trapping at the damage sites with concentrations in the range of 0.1 to 0.2 traps/W-atom and trapping energies of about 1.5 eV. During implantation — in contrast to graphite — the solute amount of hydrogen in tungsten is of the same order as the trapped one; this solute amount is released after the implantation and can be seen in TDS spectra by an immediate rise of the released flux after the onset of the temperature ramp, when TDS is started shortly after the end of implantation. In the case of the ASDEX Upgrade samples, we can expect, that the solute amount of hydrogen in the tungsten was totally released during the storage of the samples (several months). The hydrogen isotope ions impinging the divertor plates have energies of the order of 100 eV, resulting in a mean range of less than 10 nm [5]. Hence, damage in the tungsten divertor tiles is not produced by the impinging deuterium ions, but due to the impact of multiple charged impurity ions (mainly carbon) from the plasma [1].

Surface Analysis. Thick deposited carbon containing layers on the tungsten surface were detected by means of 2 MeV H^+ Rutherford backscattering for all samples from the inner divertor. The thickness of these layers was estimated to be several μm, without large poloidal variations. In contrast, erosion dominates in the outer divertor: these samples hardly show any carbon deposition at all. The actual surface composition (mainly boron, carbon, oxygen, and tungsten) was determined by X-ray photoelectron spectroscopy (XPS). The largest amounts of boron (40%) and oxygen (20%) were detected in the plasma region of the inner divertor. However, even for the erosion dominated outer divertor samples, boron and oxygen are still present at the very surface.

Before performing TDS, the near-surface deuterium inventory was measured by NRA using the 790 keV ^{3}He(d,α)p reaction, resulting in an analyzing range of 0.5 μm (for pure tungsten) to 2 μm (for an amorphous co-deposited hydrocarbon layer). Hence, the analyzing depth depends on the not well known surface composition of the respective sample, leading to a relatively high uncertainty of the NRA results. Due to the larger surface roughness of the plasma-sprayed tungsten coatings, no deuterium depth profiles can be obtained. If deuterium containing layers with thicknesses exceeding the analyzing range are involved, NRA can only establish a lower limit for the results to be expected from TDS.

3. Results and Discussion

As in the case of the samples from the previously installed graphite divertor [2], the release of hydrogen isotopes from the tungsten coated tiles during TDS is dominated by H. The amounts are in the range of about (5-8)$\times 10^{22}$ H/m^2 for all samples. The by far largest part of this H can be attributed to the water uptake both on the tungsten front surface as well as on the graphite back surface during the storage of the samples in air [2]. Hence, we will restrict the following discussion on deuterium.

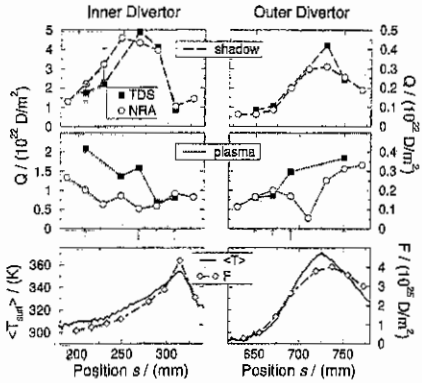

FIG. 2. *Distribution of the total D inventories (Q), measured by NRA and TDS, at the shadowed and the plasma regions of the tungsten coated tiles, respectively. Also shown are the distributions of mean surface temperature (<T_{surf}>), and the total incident D fluence (F). Note the different scales for the deuterium inventory plots.*

Deuterium Inventories. Figure 2 shows the deuterium inventories for the different regions of the inner and outer divertor as measured by TDS and NRA. Also shown are the distributions of the mean surface temperature during the discharges with auxiliary heating by neutral injection and the incoming fluence of deuterium, as measured by thermography and Langmuir probes, respectively. The latter distributions show corresponding maxima at about 310 mm and 725 mm, roughly indicating the mean position of the separatrix during the tungsten experimental period.

The highest deuterium inventories (about 5×10^{22} D/m^2) are measured in the shadowed region of the inner divertor outside the separatrix. At the position of the separatrix, the inventory shows a minimum, although the amount of deposited carbon shows only minor poloidal variations. The inventories of the outer divertor samples are generally smaller than the inner divertor inventories by a factor of 10; here the total inventories, measured by TDS, show a maximum at the separatrix position, whereas the inventories in the near surface region, measured by NRA, show a minimum at the separatrix. From this we can conclude, that deuterium retention in the case of the ASDEX Upgrade tungsten divertor tiles in the inner divertor is governed by co-deposition of deuterium with carbon ions from the plasma, whereas implantation governs the retention in the outer divertor. Co-deposition was also found outside the separatrix in the graphite tiles of the inner divertor [2]. The co-deposited layers of the inner divertor tiles are depleted at the separatrix position as well as in the plasma region due to the increased temperature. Furthermore, the deuterium inventories in the co-deposited layers are of the same order of magnitude as those in the graphite divertor tiles ($\lesssim2\times10^{23}$ D/m^2 [2]), taking into account the shorter exposure time of the tungsten coated tiles (about 700 compared to about 2000 discharges).

The total inventory in the tungsten coated divertor samples differs from the near surface inventory by only a factor of less than 2, except for the separatrix region of the outer divertor. This is in contrast to the graphite divertor samples, where the total inventory exceeds the near surface inventory by a factor of up to 100 indicating diffusion of large amounts of hydrogen out of the co-deposited/implanted layer into the graphite bulk to depths of some 100 μm [2]. This indicates, that diffusion out of the co-deposited layer into the underlying tungsten layer (inner divertor) is hindered by the tungsten/carbon interface. The fact, that the total inventories in the separatrix region of the outer divertor exceed the near-surface inventories, indicates that deuterium diffuses into the bulk of tungsten with ranges of some few μm (hence exceeding the implantation range by more than a factor of 1000), as it is assumed in models describing the behaviour of hydrogen in tungsten [5]. The combination of high fluxes and high temperatures at the outer separatrix region depletes the near surface region, but also results in a large amount of deuterium which can diffuse into the tungsten bulk and in the underlying graphite substrate (see below).

TDS Spectra of Deuterium. Figure 3 shows some examples of TDS spectra of the tungsten coated divertor samples. For the different regions in the inner and outer divertor, (at least) four different peaks can be distin-

guished and attributed to different deuterium retention mechanisms: (1) a small peak (shoulder) at about 500 K, as in the case of the outer divertor samples, due to trapping at intrinsic trapping sites in the tungsten layer; (2) a broader peak at about 900 K in the case of the samples from the outer divertor, due to trapping at ion induced damage sites in the tungsten layer; (3) at broad and large peak at 1000 K to 1100 K in the case of the samples from the inner divertor, due to C-H bonds in the co-deposited a:C-H layer — in agreement with the peak temperature of the D_2 release from the graphite divertor samples [2]; and (4) a sharp peak at about 1400 K in the case of the samples from the outer divertor, which might be due to trapping of deuterium in the underlying graphite substrate after diffusion through the tungsten layer. The latter retention mechanism is pronounced in the case of the samples from the separatrix region (s = 690 mm, 748 mm), where due to high temperatures and fluxes a relatively large amount of deuterium can diffuse through the tungsten layer. Generally, the peak positions are shifted to higher temperatures compared to laboratory results, indicating the diffusion of some deuterium out of deep regions of the samples.

4. Summary

The total hydrogen isotope inventories of the tungsten coated divertor tiles of ASDEX Upgrade — consisting of a 500 μm thick plasma sprayed tungsten layer on a graphite substrate — were measured with quantitative TDS. The near surface deuterium inventory (≈ 1 μm) was measured by nuclear reaction analysis (NRA) using the 790 keV ^{3}He(d,α)p reaction.

The total hydrogen isotope inventory measured 'in' the tungsten divertor tiles of ASDEX Upgrade is dominated in the case of the inner divertor by the build-up of thick co-deposited C-H layers (several μm) onto the tungsten surface outside the separatrix. The inventories in these co-deposited layers are of the same order of magnitude as the total hydrogen inventory measured in the previously installed graphite tiles. Increased temperatures, as in the separatrix region, deplete the co-deposited layer,

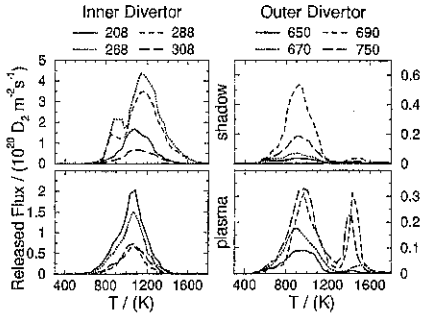

FIG. 3. *Released fluxes of D_2 during the heating of the samples for the shadowed and plasma regions of inner and outer divertor tiles. Heating ramps are of the order of 10 K/s. The legend numbers denote the sample positions, as indicated by the arrows in figure 2.*

reducing the deuterium inventory by a factor of 5. Diffusion of hydrogen out of the co-deposited C-H layer into the underlying tungsten layer is hindered by the tungsten/carbon interface. The inventories in the outer divertor samples are generally smaller by a factor of 10 than the inner divertor inventories; here the retention is governed by implantation and diffusion out of the implantation zone into the tungsten bulk. In the case of high fluences and high temperatures (separatrix), some hydrogen seems to diffuse into the graphite substrate.

Co-deposition with carbon from the plasma is the by far most effective hydrogen isotope retention mechanism for the tungsten coated divertor tiles installed in ASDEX Upgrade. This also will be the case in future fusion devices, as long as carbon is the main plasma impurity.

[1] R. Neu et al., Plasma Physics and Controlled Fusion **38** (1996) A165.

[2] P. Franzen et al., 1997, submitted to Nuclear Fusion.

[3] D. Schleußner et al., 1996, submitted to J. Vac. Sci. Technol.

[4] J. Sawicki, et al., J. Nucl. Mater. **162-164** (1989) 1019.

[5] P. Franzen et al., in *Proceedings of the 12th International Conference of Plasma Surface Interaction*, St. Raphaël, France, 1996, J. Nucl. Mat., in press.

[6] A. Haasz and J. Davis, ditto.

TRANSPORT ANALYSIS OF THE EDGE PLASMA IN H MODE DISCHARGES OF ASDEX UPGRADE

G. Becker, J. Stober, O. Gehre, H. Murmann, H. Salzmann,
J. Schweinzer, K.-H. Steuer, W. Suttrop, ASDEX Upgrade Team

Max-Planck Institut für Plasmaphysik,
Euratom-IPP Association, Garching
Germany

ABSTRACT. Profiles of the electron heat diffusivity χ_e and the ratio v_{in}/D in the steep gradient zone and in the core of high-density H-mode discharges are determined by transport analysis using a special version of the 1.5-D BALDUR code. It is found that the reduction of χ_e is strongest near the inner boundary of the steep gradient zone where it reaches a factor of 4. The v_{in}/D profile significantly rises at the edge which causes the steep density decline measured. No degradation of energy transport in the bulk plasma is seen when the density limit is approached.

Introduction

The energy and particle transport in the edge region of two high density H-mode discharges of ASDEX Upgrade is explored. In addition, the bulk transport is analysed and compared with the results from the periphery. Such investigations are feasible now, because the electron temperature and density profiles in the steep gradient zone have been measured with sufficient spatial resolution. Long-term objectives of this study are to develop more comprehensive scaling relations for transport coefficients and to improve the modeling of the steep gradient zone. It is planned to apply these results in simulations of current tokamaks and reactor grade devices like ITER.

Transport Model

The simulations are carried out with a special version of the 1.5-D BALDUR transport code [1,2,3] which also includes a scrape-off layer (SOL) modeling. In the confinement zone, empirical electron and ion heat diffusivities $\chi_e = \chi_i = \chi$, a diffusion coefficient $D = 0.6\ \chi_e$ and an inward drift velocity $v_{in} = C_v 2xD/(\rho_w x_s^2)$ are used [3]. A new scaling law for the effective heat diffusivity χ in high-density ELMy H-mode plasmas is applied [4]. It is compatible with the ITERH92-P ELMy H-mode scaling of the thermal energy confinement time [5] and has been validated against three JET and three DIII-D discharges from the ITER Profile Database, covering a wide parameter range, and against ASDEX Upgrade discharges. The coordinate x is the effective radius of a flux surface ρ normalized to the effective radius of the wall contour ρ_w and $x_s = \rho_s/\rho_w$ denotes the separatrix. In the calculations the separatrix is located at $x_s = 0.89$. The dimensionless factor C_v provides a measure of the peakedness of density profiles.

The radiative loss due to carbon is calculated by an impurity radiation model that solves rate equations for all ionization stages and takes into account an impurity

transport with the anomalous coefficients D_I = D and $v_{in,I} = v_{in}$. In the SOL, the deuteron flow along the magnetic field is computed with a Mach number M_D whose value is chosen such that the neutral density at the separatrix matches the value determined from low energy neutral flux spectra [6]. The cross-field transport coefficients in the SOL are set $\chi_e = \chi_i = 1.5\ m^2 s^{-1}$ and D = $0.9\ m^2 s^{-1}$, so that the measured temperature and density fall-off lengths are obtained.

The time evolution of the line averaged density in the discharge is prescribed in the calculations. A density feedback is applied which controls the influx of deuterium atoms. The neutral sources and the neutral density and temperature profiles are computed by a Monte Carlo code. Detailed transport analyses are feasible in the steep gradient zone, because the calculations are carried out on a non-equidistant grid with good spatial resolution.

Results and Discussion

The first H-mode discharge analysed is No. 7978 with $\bar{n}_e = 7.6{\times}10^{19}\ m^{-3}$, I_p = 1.2 MA, B_t = 2.5 T and P_{NI} = 5.0 MW ($D^0 \rightarrow D^+$). The influence of the Type I ELMs is taken into account in a time-averaged manner. Transport analysis is carried out under quasi-stationary conditions, so that only profiles of the v_{in}/D ratio can be determined in the interior plasma and in the steep gradient zone. The corresponding χ_e profiles are inferred from electron temperature measurements. In the calculations, the influx rate of carbon is adjusted such that the experimental Z_{eff} value of 1.7 is reached. Both the measured and the computed Z_{eff} profiles are flat. The radiative loss from closed flux surfaces is required for correctly computing the conductive heat flux and the electron temperature at the separatrix which is used to fix the separatrix position with the help of the measured temperature profile. At the nominal separatrix position, one measures $T_e = 190\ eV$ which significantly exceeds the computed separatrix temperature of 84 eV. The measured and calculated temperatures are found to coincide if the separatrix is shifted outward by 1 cm in the midplane.

The main results obtained at 3 s are given in Figs 1 to 4. Figure 1 shows the profiles of the electron density measured by DCN interferometry and Li-beam diagnostic (dashed curve), of the computed electron and deuteron density (solid curves) and of the corresponding v_{in}/D ratio required. Obviously, the flat electron density profile in the core is well modeled by the small v_{in}/D values resulting from the v_{in} scaling with $C_v = 0.2$. By contrast, the steep density decline measured in the edge zone is incompatible with the v_{in}/D ratios (dotted line) predicted by the v_{in} scaling. A good modeling is only achieved by the strongly rising v_{in}/D profile given. The electron temperature profile measured by ECE diagnostic (crosses) and Thomson scattering (squares), the calculated electron and ion temperature profile and the χ_e profile are plotted in Fig. 2. As can be seen, the scaling law for χ accurately predicts the electron temperature profile in the interior plasma. Moreover, the computed total energy agrees with the experimental W_{MHD} value of 656 kJ.

These results are consistent with the $H_{ITER89P}$ value of 1.6. Note that a very high temperature pedestal occurs in the steep gradient zone where χ_e is significantly reduced. Results from detailed transport analyses in the edge region are presented in Figs 3 and 4. The coordinate r is the minor half-axis of a flux surface and $r_s = 50$ cm denotes the separatrix position in the midplane. In Fig. 3, the measured (dashed curve) and computed electron density profiles are depicted. Extremely high v_{in}/D values, already given in Fig. 1, are found. A special treatment is necessary in the zone $r_s - 6cm \leq r \leq r_s$ in the midplane (corresponding to $0.76 \leq x \leq x_s$). Analysis of the experimental temperature profile $T_e(r)$ (see Fig. 4) showed that a detailed evaluation of $\chi_e(r)$ has to be carried out in the steep gradient zone of width $\Delta = 4$ cm, i.e. in the range $r_s - \Delta \leq r \leq r_s$ (corresponding to $0.80 \leq x \leq x_s$). The reduction of χ_e required is found to be space dependent. It is strongest near the inner boundary of this zone (see also Fig. 2), where it reaches a factor of 4. The heat diffusivities are evaluated with an accuracy of about ± 20 %. Note that the electron heat diffusivity is still anomalous, because the neoclassical χ_e values are two orders of magnitude smaller. We conclude that turbulence is reduced but not totally suppressed.

The second H mode discharge studied is No. 7649 with $\bar{n}_e = 8.5 \times 10^{19}\ m^{-3}$, $I_p = 1.0$ MA, $B_t = 2.5$ T and $P_{NI} = 5.0$ MW ($D^0 \rightarrow D^+$). It was selected because it is close to the density limit. The measured density profile is flatter than in the first shot and is well modeled in the bulk by the v_{in} scaling with $C_v = 0$. In the edge zone, the v_{in}/D profile is found to rise strongly as with the first shot. The measured electron temperature profile in the core and the energy content are well predicted by the scaling law for χ. It is emphasized that the energy transport is not degraded when the density limit is approached. This behaviour is indicative of a hard density limit. The factor $H_{ITER89P}$ is slightly reduced to 1.4 because of a lower temperature pedestal. This is found to result from a decline of Δ to about 2 cm which is observed in ASDEX Upgrade discharges with higher line averaged densities.

References

[1] Bateman, G., Princeton Plasma Phys. Lab., NJ, personal communication, 1993.

[2] Singer, C.E., et al., Comput. Phys. Commun. **49** (1988) 275.

[3] Becker, G., Nucl. Fusion **35** (1995) 39.

[4] Becker, G., Nucl. Fusion **36** (1996) 527.

[5] Kardaun, O., et al., in Plasma Physics and Controlled Nuclear Fusion Research 1992 (Proc. 14th Int. Conf. Würzburg, 1992), Vol.3, IAEA, Vienna (1993) 251.

[6] Stober, J., et al., Europhysics Conference Abstracts, Vol. 20 C, Part III (1996) 1023.

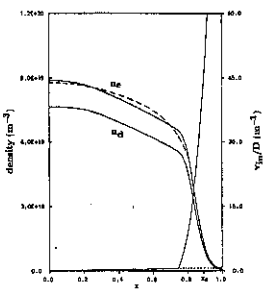

Fig.1. Profiles of electron density n_e measured by DCN interferometry and Li-beam diagnostic (dashed curve) and computed (solid curve), computed deuteron density n_d and corresponding v_{in}/D ratio. The normalized effective radius is denoted by x.

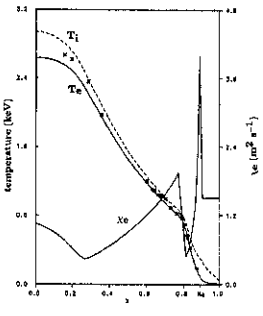

Fig.2. Profiles of electron temperature T_e measured by ECE diagnostic (crosses) and Thomson scattering (squares) and computed (solid curve), computed ion temperature T_i and electron heat diffusivity χ_e.

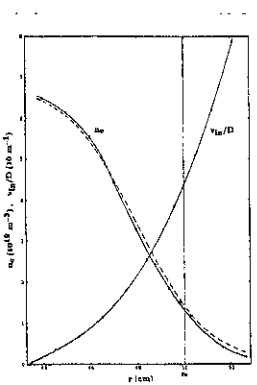

Fig.3. Profiles of measured (dashed curve) and computed (solid curve with dots) electron density and v_{in}/D ratio in the edge zone. The minor half-axis of a flux surface is denoted by r.

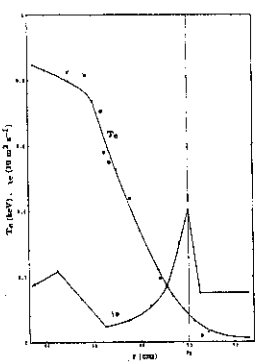

Fig.4. Profiles of measured (crosses and squares) and computed electron temperature and χ_e in the edge zone.

Evolution modelling of ASDEX Upgrade shots with B2-EIRENE.

D.P. Coster, H. Kastelewicz, R. Schneider and the ASDEX Upgrade Team.
Max-Planck-Institut für Plasmaphysik, D-85748 Garching, EURATOM Association, Germany

1 Introduction

We have used the coupled plasma multi-fluid[1, 2], Monte-Carlo neutrals[3] code, B2-Eirene[4, 5] to explore the density limit in ASDEX Upgrade. A two pronged approach has been taken. The first, relying on the observation by Borrass[6, 7] that the density limit is associated with the onset of volume recombination, used a feedback loop to add or remove particles by varying the target recycling coefficient to achieve a specified value of volume recombination. The second more closely follows the experimental procedure in a density ramp of puffing in gas and following the time evolution of the plasma.

2 Volume recombination feedback

This approach is based on the observation by Borrass[6, 7] that the density limit is associated with the onset of volume recombination. With this assumption we define the density limit density as the separatrix density when volume recombination accounts for about half the total recombination flux. We ran B2-Eirene with a feedback loop that varied the target recycling coefficient to achieve a specified volume recombination rate. This was done for a range of input powers, and for pure hydrogen (H) as well as hydrogen combined with carbon (H+C). Hydrogen rather than deuterium was used to match the choice in a particular set of experimental shots where it was chosen so that high power L-mode shots could be achieved (the lower L→H threshold of D would have meant that we would have had to deal with a transition out of H-mode as well as the density limit). Borrass argued that the critical parameter was the net input power, P_{net} (input power less the power radiated by impurities), rather than the input power, P_{in}, or the power crossing the separatrix, P_{sep}. The carbon runs allowed us to distinguish between these cases. By plotting the density limit density as a function of P_{in}, P_{sep} and P_{net} Borrass' result was confirmed — P_{net} gave the clearest ordering of the data. Figure 1 shows the plot for P_{net}, together with experimental results for H and D, as well as the density limit found using the density ramp scenario described in the next section.

The code results seemed to indicate a power dependence for the density limit density at low P_{net}, but a saturation at higher P_{net}. The data were further analysed by fitting simple power laws to the H and D experimental data, and to the volume recombination feedback data (with the highest power point exluded because of the density limit saturation). The experimental data showed an approximately square root dependence, with the code results demonstrating a somewhat weaker dependence (approximately cube root). This might be influenced by the choice of transport law, which was to have constant transport coefficients.

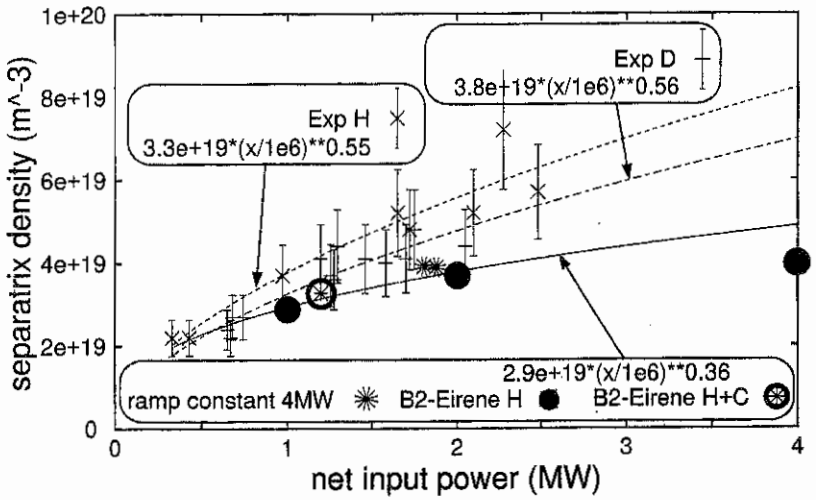

Figure 1: *Midplane separatrix density at the density limit versus net input power for the experiment (both H and D), and the results from the simulation, for the H and H+C feedback calculations, and for the density ramp case. Simple power laws were fitted to the experimental data (separately for H and D), and to the feedback code results (excluding the highest power point as there seemed to be a saturation in the density limit at higher input powers). The code shows a somewhat weaker power dependence.*

3 Density ramp simulation

Here we tried to more closely model the experimental scenario. B2-Eirene was used in the time-dependent mode to model the plasma together with a gas puff. To compress timescales so that the computation was feasible, the gas-puff rate was considerably higher than that used in the experiment, and this was partially compensated by using an artificial time enhancement for the Monte-Carlo treatment of the neutrals, as well as by puffing in the divertor region (despite this, about 2 months of cpu time on a high end work station was used). Four different transport laws were used: **constant** transport coefficients, **Bohm**-like, transport coefficients that were globally scaled by **1/n** measured in the midplane, and **flux-scaled** transport coefficients (with constant values in flux space resulting in higher real space numbers on the inboard side).

With the exception of the flux-scaled transport case (whose transport coefficients placed the starting plasma in a regime close to detachment at the beginning), these runs matched the experimental runs qualitatively, and in some cases gave good quantitative matches as well. The constant, Bohm and 1/n runs all showed detachment starting on the inner divertor leg, followed at a later time by the outer divertor leg detaching, and then the appearance of a MARFE. During the entire period a steady rise in fractional contribution

of volume recombination to total recombination was seen. The experiment showed the same development with respect to the bolometer, and, in a different but similar shot, showed the increase in volume recombination.

Experimental results for the H-α diagnostic viewing the inboard divertor are compared to the constant transport case simulation in figure 2. The constant, Bohm, and 1/n cases were all similar, with the flux-scaled case showing a shift in the maximum in the later stages to the left. The bolometer reconstructions were also compared: the Bohm and 1/n cases showed the most stable positioning of the MARFE, though the constant transport case could not be eliminated as a candidate. On this basis it is not yet possible to reject one of these transport laws.[1]

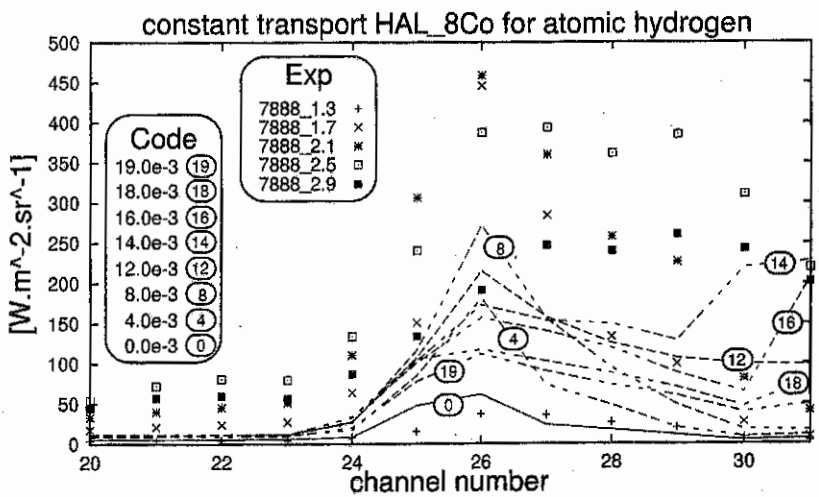

Figure 2: *Comparison of the H-α signals for the constant transport case with the experiment. Both show a rise and then a fall with time in the vicinity of channel 26, and a broadening at later times to the right. There is a systematic discrepancy for the lower numbered channels which might be related to recycling from the inner heat shield.*

4 Ongoing code developments

The introduction of the new LYRA divertor configuration on ASDEX Upgrade[8] has demanded modifications in the current SOLPS package so that the new baffle structures can be properly treated. Some calculations were done with a narrower grid that does

[1]The constant transport density ramp simulation (which was started first) has proved to be useful as results from it have been used in other work presented at this conference (Napiontek *et al.*, Gafert *et al.*, Verbeek *et al.*, Krieger *et al.*).

not treat recycling at the top of the baffle, but this grid is probably not sufficient when exploring detachment and the flattening of profiles that occurs close to detachment. We have just started calculations with a new, broader grid.

We are also in the process of upgrading from the current SOLPS4.0 to SOLPS5.0 by replacing the version of B2 that has been in use by a newer version of B2.5 from Braams[9]. We also hope to replace the current version of Eirene with a version capable of treating neutral-neutral collisions. In the coming months we plan to move from a staggered mesh treatment of the parallel momentum equation to a cell-centered version, and then to implement 1d addressing so that mesh refinement can then be introduced. In work done with Braams, the coding for drift terms has already been introduced into the new B2.5, but remains to be debugged.

5 Conclusions

These modelling results seem to confirm the analytic work of Borrass[6] that the net input power rather than the total input power or the power crossing the separatrix is the correct ordering parameter in examining the density limit. We seem to see a power dependence for the density limit for low powers, but a saturation at higher powers.

We have demonstrated that we can model the time evolution of the plasma by following the experimental procedure of having a gas puff. One problem that still remains is the long computation times that are required — efforts have started to parallelize B2 and Eirene.

On the basis of the density ramp scenario, 1/n- and Bohm- are favoured over constant-transport law scenarios, though the latter cannot be ruled out.

References

[1] B. J. Braams, *Computational Studies in Tokamak Equilibrium and Transport*, PhD thesis, Rijksuniversiteit, Utrecht, Nederland., 1986.

[2] B. J. Braams, Technical Report 68, Next European Torus, 1987.

[3] D. Reiter et al., J. Nucl. Mater. 220–222 (1995) 987; PSI 94 Mito.

[4] R. Schneider, D. Reiter, H. P. Zehrfeld, B. Braams, M. Baelmans, et al., J. Nucl. Mater. 196–198 (1992) 810.

[5] D. Reiter, J. Nucl. Mater. 196-198 (1992) 80.

[6] K. Borrass, R. Farengo, and G. Vlases, Nuclear Fusion 36 (1996) 1389.

[7] K. Borrass, R. Schneider, and R. Farengo, Nuclear Fusion 37 (1997) 523.

[8] H.-S. Bosch, D. Coster, S. Deschka, W. Engelhardt, C. Garcia-Rosales, et al., Technical Report IPP 1/281, Max-Planck-Institut für Plasmaphysik, 85748 Garching bei München, 1994.

[9] B. J. Braams, Contributions to Plasma Physics 36 (1996) 276.

2-D PIC Simulation of Hot Spot Formation on Target Plates and of Current Flow to Flat Langmuir Probes

K. Reinmüller, A. Bergmann
MPI für Plasmaphysik, IPP-EURATOM Association, D-85748 Garching, Germany

Introduction

In toroidal magnetic fusion devices, such as tokamaks or stellarators, there can be high local power fluxes to limiters or divertor target plates, which lead to high wall temperatures. The observed formation of hot spots and arcs[1] indicates an instability of the plasma-wall transition layer. This effect is studied by 2-D collisional particle simulations of the plasma in front of a thermally emitting wall. Also, the current flow to flat Langmuir probes in divertor target plates is studied by 2-D particle simulations. Langmuir probes flush-mounted into the divertor plates are an important diagnostic in tokamaks with a high power flux into the divertor.

The Particle-in-Cell code

A particle simulation code[2] with full resolution of the gyro motion (variables x, y, v_x, v_y, v_z) is employed for the calculations on a massively parallel computer. The particle motion is calculated in the self-consistent electric field and a homogeneous magnetic field. The Poisson equation is solved on a rectangular grid, and linear interpolation is used for charge deposition and interpolation of the electric field. The simulation area (Fig. 1) is bounded by two walls, and is periodic along the walls. One wall is emitting thermal electrons with an emission coefficient (Richardson law) depending on the wall temperature, which is calculated by solving the 2-d heat conduction equation for the wall with a fixed low temperature at the back side. Coulomb collisions are included by a Monte Carlo solution of the Fokker-Planck equation in each grid cell[3].

Development of hot spots on a target plate and their stability

A part of a plasma-facing wall is in thermal equilibrium when the deposited energy flux of plasma particles hitting the wall is equal to the energy loss of the wall due to heat conduction, thermal radiation, electron emission and sublimation. Electron emission reduces the potential difference between the plasma and the wall; this leads to a higher

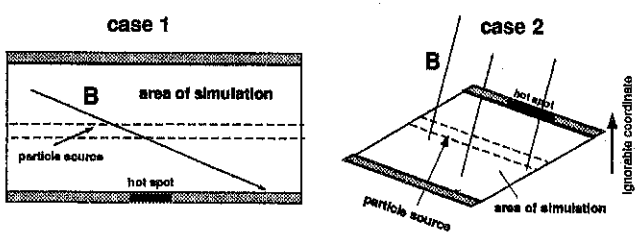

Figure 1: *Numerical grids for the PIC simulations*

electron flux onto the wall, and more energy is deposited there. Under certain conditions, depending on the plasma temperature and density as well as the wall properties, two stable thermal equilibria exist[4]: one with a low wall temperature, little thermal electron emission and a small energy flux onto the wall; the other one with a high wall temperature, strong emission and a high energy flux. This implies that regions with different wall temperature can exist at the same time (e.g. 'hot spots').

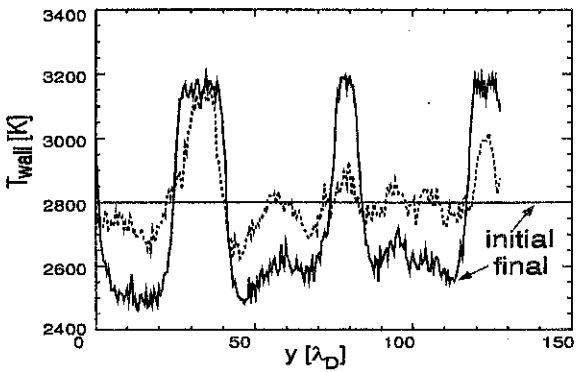

Figure 2: *Spontaneous development of hot spots: evolution of the wall temperature*

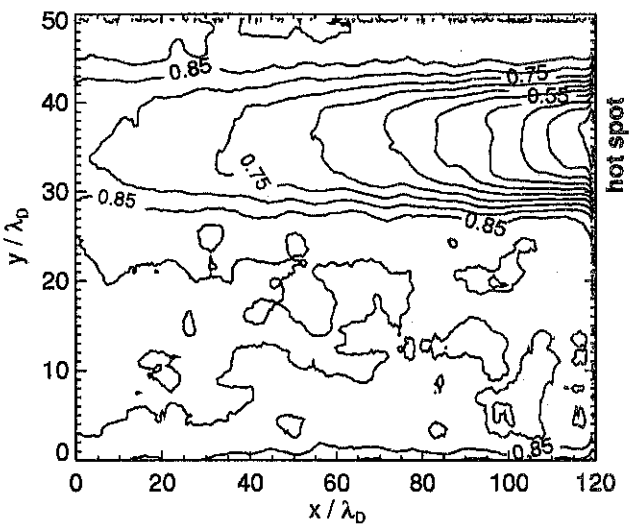

Figure 3: *Contour lines of the electron temperature in front of a hot spot normalized by the source temperature of the PIC simulation. The ion gyro radius is* $17\lambda_D$.

Starting from a wall with homogeneus temperature, we observe in our PIC simulations the development of such spots under the influence of random fluctuations (due to finite number of particles) (Fig. 2), unless the heat conductivity in the wall is too high. These spots are stable with a characteristic size within a small range. The plasma in front of a hot spot is cooler than the plasma in front of the surrounding cold wall because the emitted thermal electrons have a low temperature compared to the plasma temperature (Fig. 3). Hence, heat flows from the surrounding plasma into the region in front of the spot, resulting in additional heating of the hot spot. On the other hand, heat conduction inside the wall leads to a cooling of the hot spot.
In a different kind of simulations, where a part of the wall is initially at a higher temperature, but has the same properties as the rest of the wall, induced hot spots are formed if the heated part of the wall exceeds a minimum size, about the ion gyro radius. These spots then grow or shrink towards the characteristic size. If the mean free path length is of order of the ion gyro radius, a large induced spot is split up into two smaller spots. However, stable hot spots do not exist, if the collisionality of the plasma is very high.

Influence of an oblique magnetic field on the hot spots

If an oblique magnetic field $\vec{B}$ is applied, the spots start to move without changing their form. If the magnetic field has a component perpendicular to the simulation plane and another normal to the wall (case 2 in Fig. 1), the hot spots move in the $\vec{E} \times \vec{B}$ direction (Fig. 4 a), where $\vec{E}$ is the electric field in the sheath. In front of the hot spot, the electric field is reversed so that the emitted cold electrons drift in the opposite direction.
If the magnetic field is in the simulation plane (case 1), the hot spots move parallel to

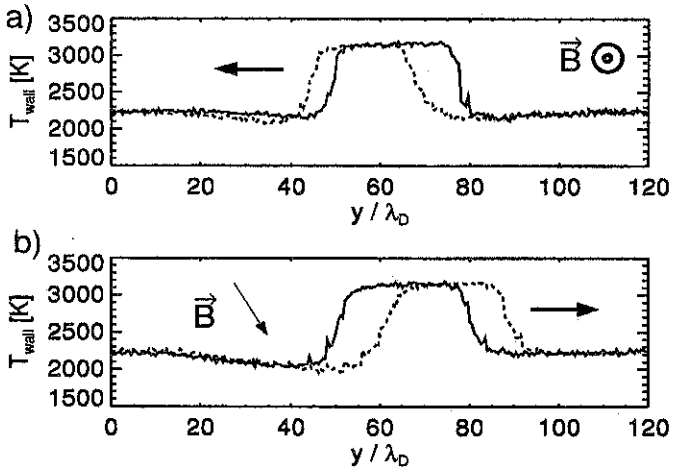

Figure 4: *Hot spot in an oblique magnetic field: (a) Motion in $\vec{E} \times \vec{B}$ direction, (b) Motion parallel to the wall (and perpendicular to $\vec{E} \times \vec{B}$ drift).*

the wall towards the side with the larger angle between $\vec{B}$ and the wall surface (Fig. 4 b), due to the different motion of the electrons and the ions. Owing to their large gyro radius, ions are focussed onto the right hand side of the hot spot. Hot electrons coming from the plasma, being bound to the fieldlines, travel along $\vec{B}$ towards the wall, while those emitted by the wall mostly have a parallel velocity component directed away from the wall. Hence, more cold electrons hit the left side of the hot spot, whereas more hot electrons hit the other side. These effects lead to a cooling of the left spot side, and a heating of the wall at the right hand side, and a movement of the spot towards the right results.

Current flow to flat Langmuir probes in a divertor plate

The current flow to flat Langmuir probes in a divertor plate which is intersected by a strong magnetic field at a small angle α, was studied by 2-D particle simulations with realistic values of probe size, gyro radius ρ, and angle of incidence α (read 'probe' for 'hot spot' in Fig. 1). The main results are (the details will be presented elsewhere): (i) Extending previous work[2], a new scaling of the ion current non-saturation with the angle of incidence was obtained, which is valid for probes of realistic size and for angles down to 1.5 degree; it can explain the measurements with such probes. (ii) The $\vec{E} \times \vec{B}$ drift in front of a negatively biased probe shifts the ion flux to the probe so that the additional current due to the lateral sheath growth is concentrated on one side. The electron flux to a positively biased probe is reduced by the $\vec{E} \times \vec{B}$ drift. This reduction is considerable for probe sizes below a poloidal gyro radius, $\rho / \sin \alpha$. (iii) The collisionless current flow across the magnetic field back to the wall adjacent to the probe was studied with simulations in which the current flow into the bulk plasma was suppressed. In these simulations, a current of order ion saturation current is drawn by only a part of the probe of a width of about a poloidal gyro radius. In case of grazing incidence, the current returns to the wall behind the probe (viewed along the field line).

Summary

Two-dimensional collisional particle simulations of the plasma in front of a thermally emitting wall have been performed. Fluctuations of the plasma parameters can lead to a stable state where different wall regions have different temperatures, Thus stable hot spots of a characteristic size can evolve. However, a very high collisionality prevents the formation of these spots. An oblique magnetic field causes the hot spots to move in $\vec{E} \times \vec{B}$ direction, as well as parallel to the wall. Also, the current flow to flat Langmuir probes in divertor plates was studied by 2-D particle simulations.

References

[1] B. Jüttner et al., Contrib. Plasma Phys. **34**, 472 (1994)
[2] A. Bergmann, Phys. Plasma **1**, 3598 (1994)
[3] R. Chodura, Europhys. Conf. Abstr. **10D**, 97 (1986)
[4] M. Z. Tokar, Nucl. Fusion **32**, 15 (1992)

Impurity Concentration as a Critical Parameter in a Diverted Scrape-off Layer

M. Laux *, A. Herrmann **, V. Rohde **, U. Wenzel *

Max-Planck-Institut für Plasmaphysik, EURATOM Association
**Garching, Boltzmannstr. 2, D-85748, Germany
*Bereich Plasmadiagnostik, D-10117 Berlin, Germany

Introduction

Essentially different central densities in a Tokamak discharge force different states of the divertor (e.g. [1],[2],[3]). At low densities the divertor plasma is attached and the impurity radiation is produced close to the plates. With rising density the divertor cools down and the radiation level increases until the radiation front retracts from the plate [9] leaving the immediate neighbourhood of the plate free of radiative losses. This development is accompanied by some reduction of the power flowing to the plate (e.g. [10]) usually called partial (energy) detachment [2]. If the density is increased further, this detachment develops until almost no power reaches the divertor plate (complete detachment). Whereas some experiments show a smooth transition through a chain of quasi-stationary states others are reported to exhibit a discontinuous jumping of the radiation front pointing to a bifurcation.

Simple 1D models ([4],[5],[6]) have identified the strong temperature dependences of both the parallel heat conduction and the radiation rate function of the impurities as essential ingredients to describe the divertor behaviour.

In this paper a very simple 1D model for the parallel electron heat conduction including a realistic radiation function and the sheath condition at the plate is applied to half of a SOL (midplane to one plate). The general aim is a better physical understanding demonstrated by convincing answers to questions like "What is the significance of using realistic radiative losses ?", "Can we relate common processes (e.g. partial detachment, retraction of the radiation zone) to specific properties of the model ?", or "What is the control parameter for the dynamics of the radiation zone?".

Furthermore, an analytical solution provides a fully transparent and retracable "benchmark" for more sophisticated 1D numerical models ([7],[8])

The Model

The model (fig. 1) is restricted to the 1D electron heat conduction parallel to the magnetic field lines with a strongly temperature dependent conduction coefficient

$$q(x) = -\kappa_0 T(x)^{5/2} \frac{dT(x)}{dx} \quad .$$

Power losses are assumed to be due to radiation from intrinsic impurities distributed along the whole parallel length

$$\frac{dq(x)}{dx} = -n_z(x)\, n(x)\, S[T(x)] \quad .$$

A prescribed temperature at the midplane, T(x=0) = T_m, is used as one boundary condition. The source of power is assumed to be localized at the same location and, therefore, introduced as the second boundary condition: q(x=0) = q_m.
The dependence of the radiation on local plasma parameters is described by modelling essential features (S_c and T_c) of the realistic radiation rate function (e.g. [11]) for Carbon in the SOL (fig. 2)

$$S(T) = S_c \frac{\theta(T - T_c)}{\sqrt{T/T_c}} \quad .$$

For simplicity it is assumed, that the impurity density n_z is proportional to the density of the background plasma and the impurity concentration does not depend on the length coordinate: $n_z(x) = c_z\, n(x)$. Furthermore, the electron pressure is taken to be constant allover SOL and divertor: $n(x)\, T(x) = p(x) = p_m$. To replace the pressure at midplane p_m, the reverse of the dimensionless Knudsen-number Kn is introduced $p_m = (\lambda_0/L_\parallel)\, T_m^3\, 1/Kn_m$ which is known to vary over almost three orders of magnitude during experimental density ramps.

The Solution

The problem can be solved analytically to obtain the dependence of the local energy flux density on the local temperature

$$q(T) = q_m \sqrt{\frac{max(T, T_c) - T_0}{T_m - T_0}}$$

with T_0 = T(q=0) = $T_m - T_c^7/(2\alpha T_m^6)$, and the inverted parallel temperature profile

$$x(T) = L_\parallel \sqrt{\frac{T_m - T_0}{\beta\, T_c}} \left\{ F[max(T, T_c)] + \theta(T_c - T) \frac{2}{7} \frac{1 - (T/T_c)^{7/2}}{\sqrt{1 - T_0/T_c}} \right\}$$

where

$$F(\xi) := [\, (8T_m^2 + 10T_mT_0 + 15T_0^2)\sqrt{T_m(T_m - T_0)} - (8\xi^2 + 10\xi T_0 + 15T_0^2)\sqrt{\xi(\xi - T_0)}\,] \,/\, (24T_c^3) + \frac{5}{8}\left(\frac{T_0}{T_c}\right)^3 (\ln \frac{\sqrt{T_m} + \sqrt{T_m - T_0}}{\sqrt{T_c}} - \ln \frac{\sqrt{\xi} + \sqrt{\xi - T_0}}{\sqrt{T_c}}) \quad .$$

α and β are coefficients depending on $1/Kn_m$ and q_m.
At the divertor plate a sheath develops that requires a matching condition $q(T_d) = q_d$ for the heat flux. The letter is determined by $q_d = \delta \sqrt{T_d}$. This sheath condition applied to q(T) establishes a relation between T_d and T_m for given $1/Kn_m$ and q_m. Postulating $T = T_d$ at the divertor plate, i.e. $x(T_d) = L_\parallel$, determines the adequate midplane temperature T_m for given q_m and $1/Kn_m$. Unfortunately, the inverse profile x(T) cannot be inverted analytically, so this last step has to be done numerically.

Results and Conclusions

For rising $1/Kn_m$ the divertor plasma cools down as expected and the temperature T_d at the plate falls (fig. 3). This process is accompanied by a rising radiative loss and, consequently, a reduction of the power flowing to the divertor plate. If T_d falls below the critical temperature T_c for the onset of the radiative losses the described model exhibits a retraction of the zone of maximum radiation away from the plate (figs. 4,5). In this range of $1/Kn_m$ the decrease of T_d can be rather dramatic. The retraction was found to have bifurcation character (development of a cusp) with respect to a critical impurity concentration c^* (about 4% for Carbon) as the control parameter (fig.3). For impurity concentrations below the critical value a smooth retraction takes place, whereas for higher concentrations the radiation front jumps upstream, showing a typical hysteresis for the re-attraction phase. The retraction of the radiation zone causes a decrease of the radiating volume (or length in a 1D model) that counteracts the strong rise of the losses and, consequently, decelerates the previously fast reduction of the power flux to the divertor plate. The related bend in $q_d(1/Kn_m)$ is usually interpreted as the stagnation of the divertor in a partially detached state (fig. 6). The model thus predicts an intimate relation between the retraction of the radiation zone and the partial (energy) detachment.

Additional Remark: Applied to the full SOL (from inner to outer plate), with an asymmetrically localized power source, the simple model leads to a qualitatively different branching of the power between the inner and outer parts of the SOL for impurity concentrations below or above the bifurcation value. This behaviour offers a new interpretation of the changes of the asymmetry of power deposition onto inner and outer plates, a crutial feature of a diverted tokamak discharge. If, for example, discharges with one orientation of the toroidal magnetic field show systematically a higher impurity concentration compared with discharges having the other orientation, the ratio of power fractions into the inner and outer divertor branch is qualitatively different. It should be pointed out that this model does not include any transport term having a direct dependence on the magnetic field direction.

References

[1] V.Mertens et al, Plasma Phys.Contr.Fusion 36 (1994) 1307
[2] T.W.Petrie et al, Nucl. Fusion 37 (1997) 321
[3] C.S.Pitcher et al, J.Nucl.Mat. 220-222 (1995) 213
[4] L.L.Lengyel, IPP preprint 1/191 (1981)
[5] P. Harbour, Contr.Plasma Phys. 28 (1988) 417
[6] H.Capes et al, Phys.Fluids B4 (1992) 1287
[7] P.Bachmann et al, this conference
[8] Yu.Igitkhanov et al, 22nd EPS Conf.Contr.Fus.Plasma Phys. Bournemouth 1995, IV-317
[9] U.Wenzel et al : "Spatial Radiation Profiles in the ASDEX Upgrade Divertor for Attached and Detached Plasmas", 12th PSI, St. Raphael, May 1996,
[10] A.Herrmann et al, 23rd EPS Conf.Contr.Fus.Plasma Phys., Kiev 1996, d039
[11] S.L.Allen et al, J. Nucl. Mat. 196-198 (1992) 804

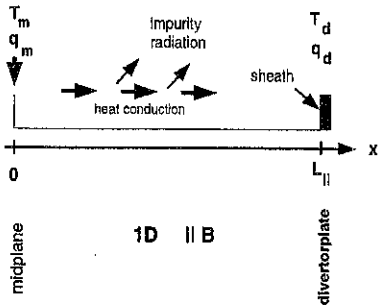

fig.1 the model (schematic drawing)

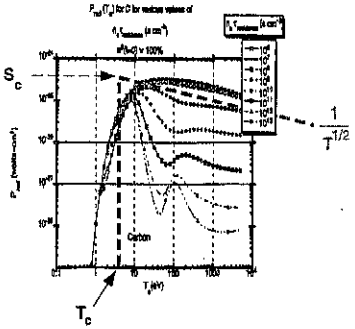

fig.2 the radiation function for C from [11] and the approximation used in the model

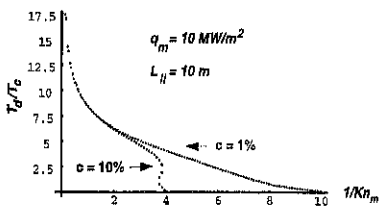

fig.3 divertor temperature versus reversed Knudsen number for different C concentrations

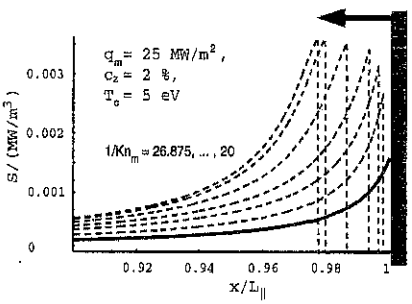

fig.4 retraction of the radiation front for rising $1/Kn_m$

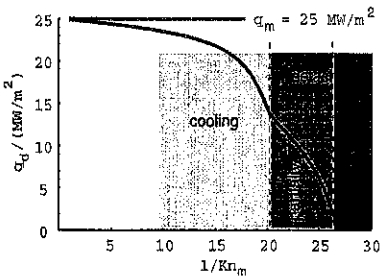

fig.6 power density at the plate versus reversed Knudsen number

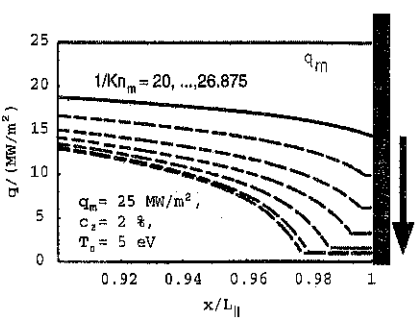

fig.5 profiles of the energy flux density for different reversed Knudsen numbers

Relation between Neutral Gas Flux Density and Parameters of the Scrape-Off Layer

J. Schweinzer, W. Sandmann, G. Haas, J. Neuhauser, H. Murmann, H. Salzmann,
ASDEX Upgrade- and NBI-Teams
Max-Planck-Institut für Plasmaphysik, EURATOM Association, D-85748 Garching

INTRODUCTION

Asdex Upgrade (AUG) diagnostic data has been compiled in a SAS-formated database which includes beside various global discharge parameters local ones of the plasma edge, the scrape-off layer (SOL) and the divertor. Especially measurements of T_e and n_e profiles with high spatially resolution have been recently included, which permit now a detailed statistical analyses of the inter-relation of various edge parameters and their relation to global ones.

Radial $n_e(r)$ profiles in the SOL (Scrape-Off-Layer) are measured routinely by means of a lithium beam probe. For a limited number of discharges the position of the Thomson scattering system was optimised for measurements (T_e) in the plasma edge. All T_e measurements presented here originate from these measurements.

The relation between the neutral gas flux density Γ_0 in the divertor measured by ionisation gauges and the midplane averaged SOL density ($n_e^{SOL} = 1/L^{SOL} \cdot \int n_e(r)dr$) will be discussed in chapt. 1

One major concern of investigations dealing with the plasma edge and the SOL is the radial position of the last closed flux surface (separatrix). In general the separatrix position at AUG is magnetically determined within an uncertainty of ± 5 mm. By assuming classical parallel heat conduction between midplane and divertor and with an estimate of the radial power flow across the separatrix, a midplane separatrix temperature can be predicted [1]. Within this assumptions a procedure to test the quality of the magnetically defined separatrix position will be described in chapt. 2.

By this means we investigate dependencies between edge parameters. Especially an T_e^{sep}, n_e^{sep} - diagram including all AUG discharge regimes helps to recognise the available operational space.

DIVERTOR NEUTRAL GAS FLUX DENSITY and n_e^{SOL}

The relation between neutral gas flux density Γ_0 in the divertor and midplane density profile parameters like n_e^{sep}, λ_{ne} and n_e^{SOL} seems to be of rather general nature [2]. Especially n_e^{sep} and n_e^{SOL} increase in a power law regression analysis with $\Gamma_0^{0.5}$ However, systematic deviations from this general behaviour are found.

In clean high density H-mode discharges near the H->L back-transition a considerable weaker increase of n_e^{sep} with $\Gamma_0^{0.2}$ has been observed [3], whereas n_e^{SOL} obeyed the general relation ($n_e^{SOL} \propto \Gamma_0^{0.5} q_{95}^{0.4}$, q_{95} ... safety factor). In these discharges the line averaged density saturated and could not be raised by gas puff which lead only to increased Γ_0, and n_e^{SOL} and most unwanted to a degratation of confinement [4].

In discharges with additional impurity puffs (Ne or N_2) the situation is quiet different (cf. fig. 1). In cases with considerable impurity puff no dependency of n_e^{SOL} with Γ_0 is observed. In addition, n_e^{SOL} values are within a rather small range of 1.8 - 2.2 • 10^{19} m^{-3} for nitrogen (I_p = 1MA, P_{heat}=7MW, $\Gamma_{nitrogen}$ = 6.0 - 12 • 10^{21} atoms/s) as well as for neon puffed cases (I_p = 0.8MA,1MA, P_{heat}=5-8MW, Γ_{neon} feedback controlled). These discharges are compared with two discharges (I_p = 0.8MA, P_{heat}=2.5,7.5MW) without additional impurity puff in fig.1. and one with only moderate N_2 puff (4.0 • 10^{21} atoms/s). All of them obey the general relation found for the high recycling regime. Towards lower n_e^{SOL} and Γ_0 values the high recycling regime is left which is indicated by the deviation of measured points from the straight line in fig. 1. In the low recycling regime a linear dependency of n_e^{sep} and n_e^{SOL} with Γ_0 has been found [2]. This transition region depends on the applied heating power and occurs in ohmic cases therefore at much lower Γ_0 values [2].

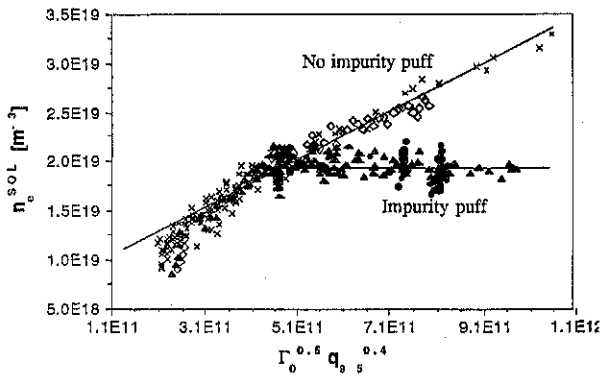

Fig. 1: Line averaged SOL density n_e^{SOL} vs. the result of a regression analysis (cf. text and [2]) for Deuterium discharges with and without additional impurity puffing. (X...D_2 only, ◇...moderate N_2 puff, ▲...N_2 puff, ■...Ne puff, lines to guide the eye.)

It is well known that puffing of impurities which preferentially radiate in the plasma edge and SOL help to reach the detached plasma regime. One might speculate that in the detached regime Γ_0 and n_e^{SOL} and thus also n_e^{sep} become completely decoupled and the SOL density becomes even independent at least in a first approximation from global discharge parameters.
In contradiction to the case of clean high density H-mode discharges the line averaged density in impurity puffed discharges (H-mode or CDH-mode) is stronger influenced by Γ_0.

SEPARATRIX POSITION TESTED by SOL MODEL

A 1.5D - model predicts a temperature at the separatrix (T_e^{mod}) and an exponential fall-off length λ_{Te} for the temperature profile in the SOL [1]. By combination of this two results the following formula for the separatrix temperature T_e^{mod} can be derived,

$$T_e^{mod}[eV] = \alpha \cdot \left[\frac{P_{SOL}[W]\, q_{95}^2}{\lambda_{T_e}[cm]} \right]^{2/7} \qquad (1)$$

where P_{SOL} denotes the power crossing the separatrix. The parameter α involves geometric factors like the plasma surface at separatrix radius and an averaged connection length between midplane and the divertor plates and can be determined by a linear regression fit. Such a fit (R^2=0.93) applied to a set of discharges covering almost the complete operational space of AUG, delivers $\alpha = 0.5$, where we used for P_{SOL} approximately $P_{heat} - P_{rad}$.

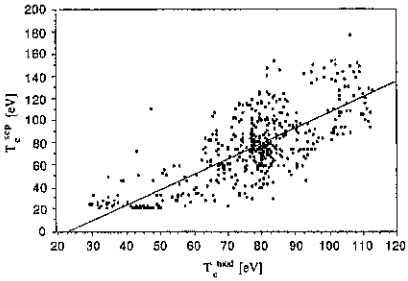

Fig. 2a: Measured separatrix temperature T_e^{sep} vs. T_e^{mod}, predicted by equ. 1.

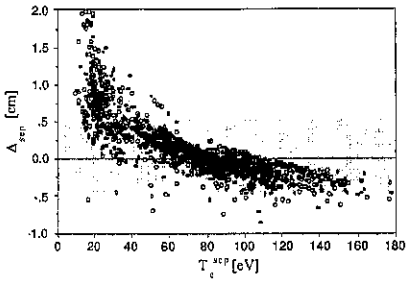

Fig. 2b: Shift in separatrix position to achieve $T_e^{sep} = T_e^{mod}$ (cf. text).

T_e^{mod} values cover a range from 30 - 115 eV, whereas measured T_e^{sep} values occur between 20 and 180 eV (cf. fig. 2a). Assuming the difference in both T_e values is due to an inaccurate magnetically defined separatrix position a shift Δ_{sep} of the latter can be estimated by $\Delta_{sep} = \lambda_{Te} \cdot [\ln(T_e^{mod}) - \ln(T_e^{sep})]$. Most of all Δ_{sep} values lie within ±5mm (cf. grey area in fig. 2b) in the high temperature range (T_e > 60 eV, cf. fig. 2b), which corresponds to the error in the magnetic separatrix position.

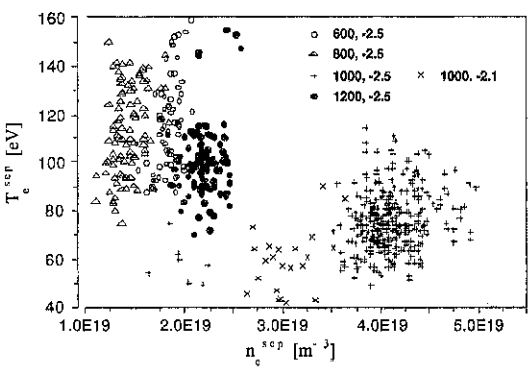

Fig. 3a: Measured T_e^{sep} vs. measured n_e^{sep} for H-Mode discharges (4.7 < P_{heat} < 5.3 MW, B_T=-2.1,-2.5 T, Ip=0.6-1.2MA).

For lower temperatures, however, shifts up to 1.5cm would be necessary to identify the T_e^{mod} value in the measured T_e-profile. This systematic increase of an inside shift of the separatrix position for lower T_e indicates the limit of applicability of the assumed model. In this low temperature region radiation zones above the target plates reduce the effective length along power has to be conducted which is not represented in the present model. Therefore, as long as Δ_{sep} is not in contradiction with the magnetic separatrix position the model can be used to correct the separatrix position. In the following only data is presented where magnetic and model derived separatrix are within ±5mm. The derived shifts Δ_{sep} can also be used to correct other separatrix parameters as e.g. measured n_e^{sep} data by $n_e^{cor} = n_e^{sep} \cdot \exp[\Delta_{sep} / \lambda_{ne}]$. Because λ_{ne} is considerable bigger than λ_{Te} this correction leads only to changes of less than 10%.

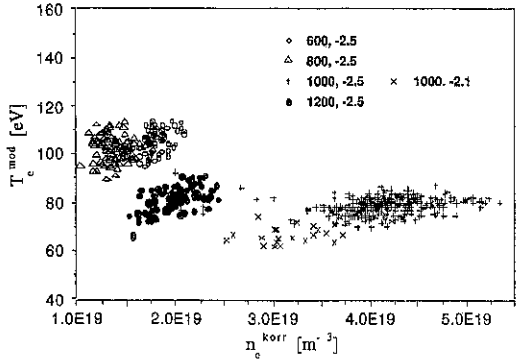

Fig. 3b: T_e^{mod} vs. n_e^{cor}, corrected for separatrix position, same discharges as in fig. 3a

In Fig. 3 a,b we compare original T_e, n_e (fig. 3a) data with "separatrix corrected" ones (fig. 3b) for a set of H-mode discharges where P_{heat} was restricted to values between 4.7 and 5.3 MW and primarily safety factor $q \propto B_T/I_P$ and density are varied. The dominant effect of the correction process is to reduce the scatter in the data. General trends, e.g. the q-dependence of T_e values recognised already in the original data are emphasised by the separatrix correction.

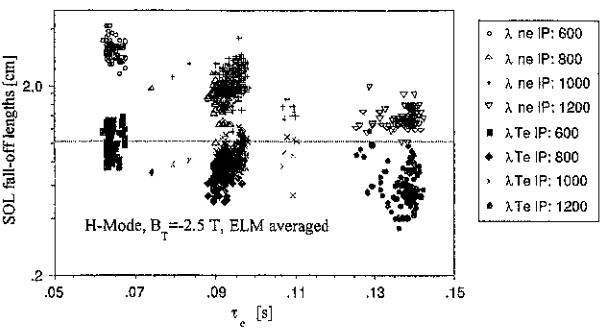

Fig. 4: SOL fall-off-lengths for temperature and density. H-Mode dataset with B_T=-2.5T, P_{heat}=4.7-5.3 MW. and variation in q (Plasma current IP in kA)

Fall-off-lengths of temperature λ_{Te} and density λ_{ne} (3-4 times larger as λ_{Te}) can be ordered by plasma current I_P or safety factor q (no B_T variation) and energy confinement time Thus even parameters outside closed flux surfaces seem to be connected to the global confinement behaviour of a discharge.

CONCLUSIONS

In clean H-mode discharges confinement deteriorates with increasing Γ_0 [4]. In addition n_e^{SOL} increases with Γ_0 and T_e^{sep} shows only a weak dependence on n_e^{sep}. Thus, the screening effect for neutrals in the SOL will increase and the density of neutrals on closed flux surfaces will even decrease when Γ_0 is raised [3], leading besides changes in confinement also to a limit of particle fuelling by gas puff. Therefore higher Γ_0 can hardly be the direct physical reason for the degradation of H-mode confinement. However, raising Γ_0 certainly changes the boundary conditions for the edge plasma where the H-mode barrier is located. Therefore Γ_0 must be correlated with key parameters for H-mode confinement (e.g. p_e or ∇p_e or fall-off-lengths λ_{Te}, λ_{ne}) which have to be identified by future analysis.

REFERENCES

[1] M. Keilhacker et al. Phys. Scr. T2/2, 443-453, 1982
[2] J. Schweinzer et al., contr. p. to 23nd EPS Conf. on Contr. Fusion & Plasma Phys., 1996
[3] V. Mertens et al., 1997, accepted for publication in Nucl. Fus.
[4] F. Ryter et al., IAEA-CN-64/AP1-5, Montreal, 1996

Bolometric measurements in the ASDEX Upgrade divertor

J.C. Fuchs, K.F. Mast, G. Haas, ASDEX Upgrade Team,
Max-Planck-Institut für Plasmaphysik, EURATOM-Association,
D-85748 Garching, Germany

1 Introduction

The radiation distribution in the ASDEX Upgrade divertor has been investigated by bolometric measurements. Eight lines of sight of a horizontal pinhole camera through the X-point and four lines of sight of collimators over each target plate are used to measure the radiation from the divertor and X-point region with a time resolution of up to 1 ms. These new divertor bolometers allow to determine the radiation distribution from the divertor region with a high spatial resolution and thus together with the other 72 bolometer lines of sight of ASDEX Upgrade they provide the possibility to perform a much improved tomographic reconstruction of the radiation distribution in a poloidal cross section of the plasma of both the bulk plasma and the divertor region.

Since bolometric measurements may be affected by the cooling effect of the neutral gas pressure, the influence of this neutral gas pressure on the measured line integrals has been studied in laboratory experiments.

2 Bolometric diagnostic at ASDEX Upgrade

In the ASDEX Upgrade tokamak radiation losses are recorded by 88 bolometers placed in six pinhole cameras and two collimators which are mounted around one poloidal cross section of the plasma inside the vacuum vessel (Fig. 1). The bolometers are miniaturized, low noise metal resistor bolometers [1] which are excited by a 50kHz sine wave and effectively suppress thermal drift and electromagnetic interferences. Radiation from the X-point and divertor region is observed with an 'horizontal' camera with 8 channels and a spatial resolution of about 6cm and two collimators with 4 channels over each target plate. Radiation from the main plasma is measured by four 'horizontal' cameras with together 48 channels and spatial resolutions between 3cm and 10cm and a vertical camera with 24 channels.

In order to obtain the distribution of the local radiation emissivity in a poloidal cross section of the plasma, the measured line integrals must be unfolded. This is done with the 'Anisotropic Diffusion Model Tomography' algorithm, which is based on the fact that the variation of the radiation emissivity along magnetic field lines is much smaller than perpendicular to them. This behaviour is described by an anisotropic diffusion model with different values of the diffusion coefficients $D_{\parallel}$, $D_{\perp}$ along and perpendicular to the magnetic field lines. [2]

3 Radiation distribution in the ASDEX Upgrade divertor

The measurements of the new X-point and divertor bolometers have been used to reconstruct the radiation distribution from both the divertor region and the main plasma for different types of plasma discharges.

3.1 CDH mode discharges

Fig. 1 shows the radiation distribution in a poloidal cross section for the transition from the H to the CDH mode [3]. During a shot with 1MA plasma current and 7.5MW neutral

injection neon has been puffed in order to achieve a detached divertor and a radiative boundary. The amount of the puffed neon was controlled such that the total radiated power was 80% of the input power. Fig. 1a shows the radiation distribution during the H mode before neon injection. The main radiation is located directly in front of the both divertor target plates. About 30% of the input power is radiated in the divertor, ca. 20% over the outer plate and 10% over the inner plate (the radiation over the inner plates is mainly due to ELMs, over which the bolometers generally integrate in time). Fig. 1b shows the radiation distribution during the neon puffing (CDH mode). A clear radiation boundary has been developed and the maximum of the radiation now is located above the X-point inside the closed flux surfaces. The radiation over each target plate has decreased to less than 5% of the input power.

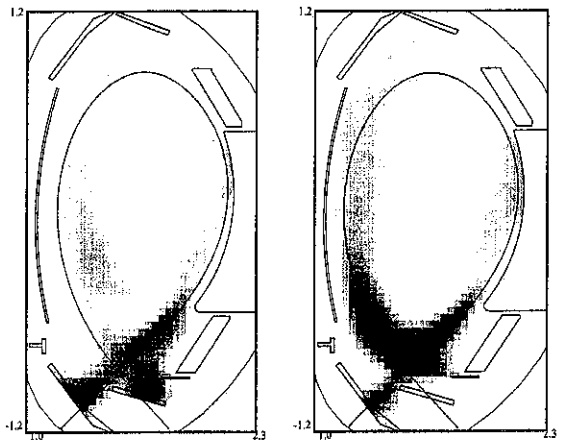

Figure 1: *Development of the radiation distribution during the transition from H mode (left) to CDH mode (right)*

3.2 Density limit shots

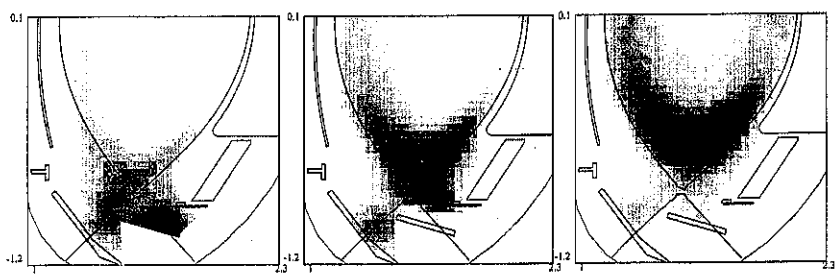

Figure 2: *Evolution of a marfe during an ohmically heated density limit shot: a) medium density, no marfe; b) increasing density, marfe starts to develop onto closed flux surfaces; c) density limit almost reached, marfe fully developed*

Fig. 2 shows the development of a marfe during an ohmically heated density limit shot. At a medium density (Fig. 2a) the maximum of the radiation is located over the outer target plate, ca. 30% of the total radiated power is radiated in the divertor region. With increasing density the radiation over the plate decreases and the maximum of the

radiation shifts upwards onto closed flux surfaces (Fig. 2b). Finally, the marfe on closed flux surfaces is fully developed and moves further upward (Fig. 2c). Now only less than 10% of the total radiated power comes from the divertor.

In density limit and density ramp shots with additional heating by neutral injection, the development of the radiation profiles is slightly different to the ohmically heated plasmas: Fig. 3 shows two radiation profiles from a density ramp shot with 800kA plasma current and 2.5MW neutral injection. The line averaged electron density has been varied up to $6.5 \cdot 10^{19}\mathrm{m}^{-3}$ and down again [4]. Fig. 3a shows the radiation profile in an early state at a medium density, where the maximum of the radiation is again located in front of the outer target plate. At the maximum density however (Fig. 3b) the maximum of the radiation has shifted upward, but no marfe on closed flux surfaces has been developed yet. With decreasing density, this behaviour is reversible and the maximum of radiation shifts down again over the outer target plate.

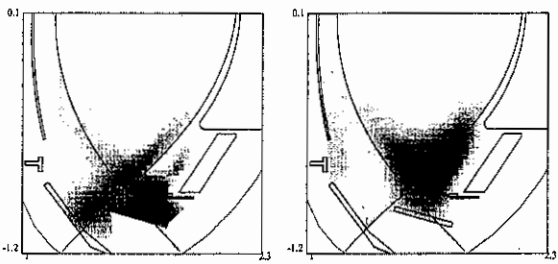

Figure 3: *Radiation profiles during a density ramp with neutral beam injection: a) medium density, radiation located at outer target; b) maximum density, radiation maximum shifted upward, but not onto closed flux surfaces*

In additionally heated density limit shots one finds that the marfe on closed flux surfaces develops only very late before the density limit is reached and does not stay on closed flux surfaces as long as in ohmically heated density limit discharges.

At low and medium densities, up to 80% of the total radiated power may be radiated from the divertor, with a clear maximum over the outer target plate (for L mode discharges). With increasing density, the radiation from the divertor region decreases to about 10% of the total radiated power (Fig. 4).

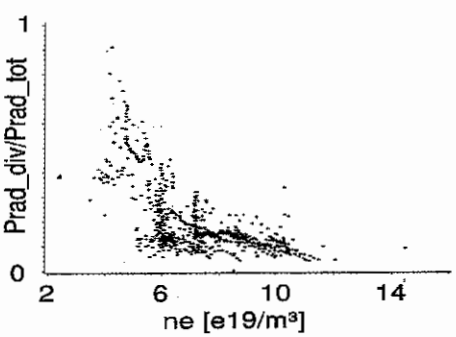

Figure 4: *Fraction of the power radiated from the divertor to the total radiated power as a function of the line averaged electron density n_e during L mode for several discharges with neutral beam injection*

4 Influence of the neutral gas pressure

Divertor radiation losses are favourably measured with bolometer cameras which are mounted inside the divertor chamber, close to the plasma. Such a positioning allows the

observation of the total divertor plasma volume and minimizes the plasma screening of charge exchange neutrals. But bolometric radiation measurements in the divertor may considerably be falsified at high neutral gas pressure which usually arises during high density, high power plasma discharges. Two effects of the neutral gas on the bolometer can be distinguished. Either the bolometer sensitivity and the bolometer bridge offset voltage varies with the gas pressure. In Fig. 5a the pressure dependence of the sensitivity

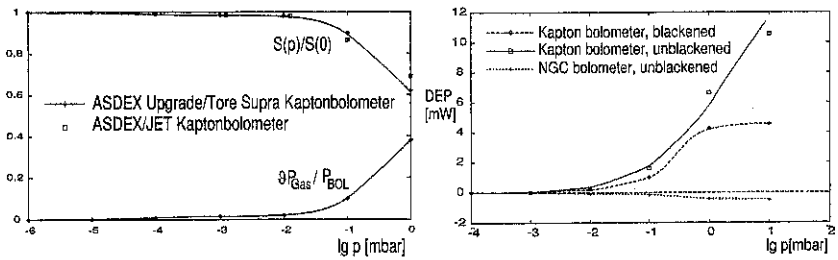

Figure 5: *Pressure dependence a) of the normalized bolometer sensitivity $S(p)/S(0)$ and the fraction of the gas cooling power $\vartheta P_{gas}(P)$ to the absorbed radiation power P_{BOL} in air; b) of the drift equivalence power DEP=offset voltage/S for various bolometer types in air*

of two types of Kapton bolometers in air as working gas is represented. This decrease of the sensitivity is common to most types of bolometers and is caused by heat conduction via the surrounding gas from the absorber to the housing of the bolometer corresponding to a reduction of the bolometer cooling time constant τ. More critically the offset voltage of the bolometer bridge varies with the gas pressure like a Pirani pressure gauge. Small differences in the parameters of related measuring and reference bolometers, mainly of the cooling time constants, result in substantial offset voltages at higher gas pressures (Fig. 5b). The offset can be positive or negative and depends in a complicated manner from the asymmetries of the bolometer detector and from the gas species. Kapton bolometers additionally show a sharp positive rise of their offset with higher gas pressures ($> 10^{-2}$mbar) which could be attributed to a strain gauge effect.

A much improved behaviour (Fig. 5b) was found for a newly developed high impedance MICA bolometer array with optimized ventilation (Neutral Gas Compensated Bolometer) which is mounted in the new Divertor II of ASDEX Upgrade.

Neutral gas pressures up to $5 \cdot 10^{-2}$mbar were measured in the divertor I of ASDEX Upgrade. The relevant offset voltages of the divertor I bolometers were compensated numerically in the tomographic reconstructions shown above, using measurements of an ionization pressure gauge [5] which was installed nearby.

References

[1]K.F. Mast, J.C. Vallet, C. Andelfinger et al., Rev. Sci. Instrum. **63**(3) (1991),744ff
[2]J.C. Fuchs, K.F. Mast, A. Hermann, K. Lackner et al., Contrib. 21st EPS (1994), 1308ff
[3]A. Kallenbach et al.,Nucl. Fusion **35**(1995), 1231ff
[4]B. Napiontek, U. Wenzel et al., this conference
[5]G. Haas et al., J. Nucl. Mater. **121**(1984), 151ff

Erosion of the main chamber walls of Tokamaks by CX-neutrals

H.Verbeek, J.Stober, D.P.Coster, and R.Schneider

Max-Planck Institut für Plasmaphysik, EURATOM Association,
D-85740 Garching, Germany

Introduction

Investigations on wall erosion have been widely concentrated on the divertors of plasma machines. However, the erosion in the main chamber and the transition region needs still to be considered, because of the limited lifetime of the wall and impurity influxes to the plasma.[1] The aim of this paper is to assess the parameters and conditions which influence the erosion of the walls.

The CX-spectra

At ASDEX Upgrade the CX fluxes and energy distributions have routinely been measured in the energy range of 20 to 1000 eV by the Low Energy Neutral particle Analyzer (LENA)[2] at one particular location at the outside wall. Its line of sight and that of an H_α monitor is horizontally, slightly above the midplane. The CX intensities and the shapes of the corresponding energy distributions, which can be characterized by the total fluxes and the mean energies (E_{mean}) depend largely on the discharge conditions. For constant heating power E_{mean} decreases when n_e is raised while the flux increases [3],[4]. As an example the CX-spectra in a NI heated Deuterium discharge at different n_e are shown in Fig.1. For discharges with auxiliary heating the flux increases usually with the heating power but E_{mean} shows no simple dependence. The CX intensity is roughly proportional to the local neutral gas density, which depends on the nearby recycling sources and external gas puffs, while E_{mean} depends on the edge plasma parameters.

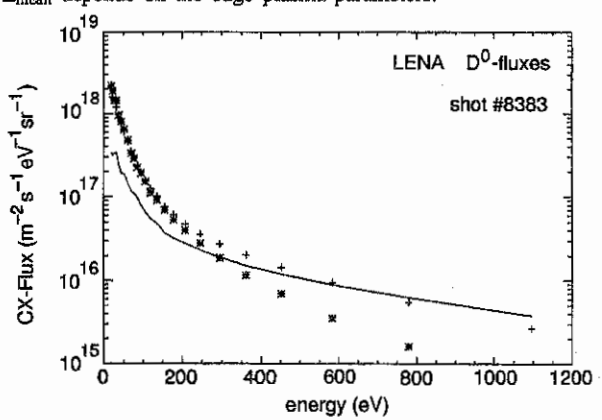

Figure 1 *shot #8383 with density ramp-up:*
(——) $n_e=7.0\times10^{19}m^{-3}$
(+++) $n_e=8.4\times10^{19}m^{-3}$
(***) $n_e=9.7\times10^{19}m^{-3}$
Gas D_2, P_{NI}=7.9 MW,

For the determination of the CX wall-erosion at the location of the LENA the measured CX spectra have to be multiplied by the energy dependent sputtering yields Y(E). However, the spectra have to be extended to lower energies (down to 1 eV) in the case of Carbon walls, where chemical sputtering is important, and to higher energies if walls of other materials are considered (the maximum of the sputtering yield for D on W e.g. is at 5 keV).The latter is possible from the measurements of the high energy CX-diagnostic, whose spectra overlap

nicely with those of LENA. The extension to lower energies is based on polynomial fits to the experimental data. For one particular shot (#7649, D_2 with I_p=1 MA, P_{NI}=5.2 MW, n_e=9×10^{19} m^{-3}),the procedure has been checked with flux simulations obtained from the T_i determination by EIRENE simulation [5], assuming an exponential decay of T_i in the SOL.

LENA measures the CX flux in a line of sight almost perpendicular to the separatrix. The wall is, however, seen by particles from the whole half space. Therefore the angular distribution of the CX neutrals has to be known. For shot #7649 (s.above) the spectra for lines of sight at angels 20, 40, 60, and 80 deg to the normal were calculated from the Eirene simulation. From these the angle integrated spectrum was determined. This had a very similar shape as compared to the LENA-spectrum. Therefore this could be taken into account merely by a factor.

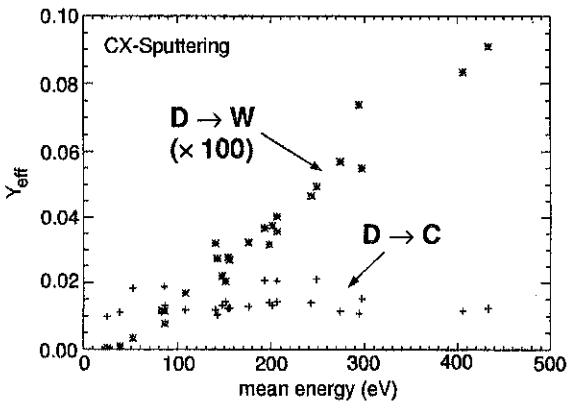

Figure 2 *Effective erosion yields Y_{eff} of C (+++) and W (***) ×100 for 26 randomly chosen ASDEX Upgrade shots*

Sputtering

For the erosion of Carbon walls the formula of Roth and G.-Rosales [6] was applied. This includes temperature and flux dependences. For the consideration of other possible wall materials also W, Be, SiC, TiC and WC were investigated. The corresponding sputtering yields were calculated by the Bohdansky formula and the data of Eckstein et al.[7]. The effective sputtering yields Y_{eff} were determined by multiplying the CX-spectra with the corresponding Y(E) , integration over all energies and normalization to the total CX-fluxes.

For a randomly taken number of shots with and without NI and a wide range of densities Y_{eff} was determined. It turns out that Y_{eff} rises monotonicly with E_{mean}. As an example Y_{eff} for W and C at 300K are shown in Fig.2. No points were omitted, and thus Fig.2 seems to be fairly universal. For the considered shots Y_{eff} for W increases by a factor of 50, while for C it varies only by a factor of 2 and for Be by a factor of 2.5. Y_{eff} for the other materials increases likewise with E_{mean}. This is due to the fact that the sputtering yield for W has a threshold energy for D of 178 eV while it is 26.2 eV for Be and of 1 eV for C because of the chemical effects. For the metals the dependence of Y(E) form the angle of incidence[7] could be taken into account using the above mentioned calculated spectra for different angles. This enhanced Y_{eff} by a factor of 2 for W and Be, but it is questionable, whether this applies since the walls have not at all atomically flat surfaces.

Toroidal and poloidal effects

Though LENA is located at a place where no strong neutral gas sources are nearby it is

difficult to estimate the wall erosion and the impurity influx to the entire machine from one local measurement since the CX fluxes vary strongly toroidally and poloidally.

Toroidal variations are mainly due to the differences in local neutral gas sources, recycling at protruding parts and external gas puffs. For ASDEX-Upgrade these variations have not be determined quantitativly so far.

To account for the poloidal effects the CX energy-distributions were modelled by B2-EIRENE calculations [8]. These give a selfconsistent calculation of the plasma taking into account the full geometry of ASDEX-Upgrade. Here we discuss the particular shot #7888 (H_2 with P_{NI} = 5MW with ramped-up density) at the 2 timepoints when the seperatrix-density n_e^{sep} is =3.2 and = 5.2 $\times 10^{19}$ m^{-3}. At the 1st timepoint the plasma was attached, at the 2nd fully detached. To achieve a good match between the simulation and the CX- and H_α measurements the T_i profile and the neutral sources in the main chamber had to be adjusted.

The necessary reduction of T_i in the outer SOL indicates that the diffusion coefficients used for modelling are not adequate for this outer layer, possibly due to flute mode driven anomalous transport [9]. The neutral source strength in the main chamber along the outer contour had to be shifted from the outside to the inside to keep the correct value of the experimental H_α intensity and to match the measured CX intensities. (B2-Eirene uses local recycling along the outer contour but in reality it is concentrated at the inner heatshield.) Since the main chamber source strength is only 1/100 of the divertor source this does not disturb significantly the self-consistency.

For the Monte Carlo calculation grid (the outermost contourline of which is shown in Fig. 3A) 216 lines of sight perpendicular to the outer SOL-contour were constructed and the associated CX-spectra were calculated as a first step. At the LENA location they agree fairly with the experimental CX spectra. The CX-flux distributions along the poloidal circumference are very different for the 2 cases, and in both vary the fluxes poloidally by up to 3 orders of magnitude and E_{mean} by a factor of 50.

From the spectra the total erosion yields Y_{tot} were calculated for different wall materials. The resulting Y_{tot} along the SOL-contourline are shown in Figs. 3B and 3C for carbon (at 300K) and tungsten walls for the 2 timepoints. Y_{tot} for W is multiplied by 430 because the tolerable concentration of an impurity considering radiation and dilution is for W ca. 1/430 than that for C [10]. It should be noted, that just above the divertor, the present choice of the lines of sight perpendicular to the contour is not sufficient to account for angular effects in this region. Neutral atom fluxes at the target plates are mainly due to dissociation of desorbed molecules which are not included in the CX spectra.

Conclusions

CX-sputtering in the main chamber occurs at different places for C or W walls for both low and high density. W sputtering is most severe in the main chamber while it is low in the transition region because E_{mean} is sufficiently high only in the main chamber. The minimum at the top of the machine for all materials is due to the low neutral gas density there. This is important for a proper material choice in future machines.

The W-flux is much lower at 2.45 s than at 1.75 s due to an increased density in the cold SOL which absorbs the hot neutrals coming from the central plasma, thereby reducing E_{mean}. C sputtering is increased almost everywhere since the chemical sputtering does not depend strongly on T_e but on the integral neutral flux (except target plates, where T_e is too low in the detached case). Considering plasma impurities it can be concluded that W would be a favorite wall material in the detached case, whereas C would be favorable in the low

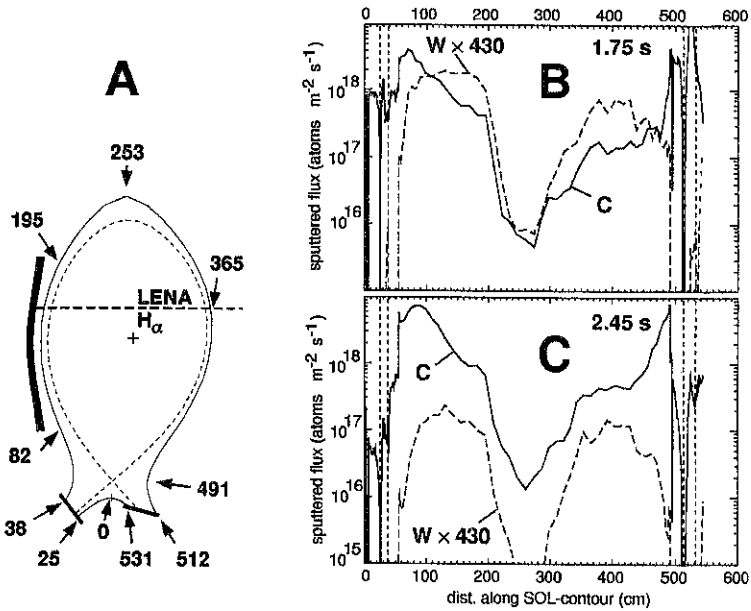

Figure 3 **A:** *The outermost contour and separatrix of the grid for the B2-EIRENE calculation. Divertor plates and inner heat shield are indicated. The distance along the contour is given in cm.* **B:** *Sputtered flux of C and W (dashed ×430) for #7888 along the SOL-contour at 1.75s (low density) and* **C:** *at 2.45s (high density,detached) . The vertical dotted lines in* **B, C** *indicate the position of the divertor plates.*

density case assuming that sputtered C and W atoms have the same probability to penetrate the plasma . Differences of the penetration behaviour for W and C are still under investigation. A favorable effect for W is the higher rate of prompt redeposition, which is estimated to be roughly 50 % (C < 10 %)[11].

Bibliography

[1] Mayer, M., Behrisch, R., Andrew, P., and Peacock, A., J.Nucl.Mat. **Proc.PSI 96** (1997).

[2] Verbeek, H., J.Phys. E: Sci.Instrum. **19** (1986) 964.

[3] Verbeek, H. and the ASDEX team, J.Nucl.Mat. **145-147** (1987) 523.

[4] Verbeek, H., Dose, V., Fu, J.-K., and the ASDEX team, J.Nucl.Mat. **162-164** (1989) 557.

[5] Stober, J. et al., Europhys.Conf.Abstr. **20C III** (1996) 1023.

[6] Roth, J. and Garcia-Rosales, C., Nucl.Fusion **36** (1996) 1647.

[7] Eckstein, W., Garcia-Rosales, C., Roth, J., and Ottenberger, W., IPP Report **9/82** (1993).

[8] Coster, D. P. et al., J.Nucl.Mat. **Proc.PSI 96** (1997).

[9] Bosch, H. S. et al., J.Nucl.Mat. **220-222** (1995) 558.

[10]Bohdansky, J., Roth, J., and Vernickel, H., in *Proc. 10thSOFT 1978*, pages 801-807, 1979.

[11]Naujoks, D. et al., Nucl.Fusion **36** (1996) 671.

NUMERICAL STUDY OF THE IMPACT OF DIVERTOR CLOSURE ON DETACHMENT

K. Borrass, D. Coster, R. Schneider

Max-Plank-Institut für Plasmaphysik, Euratom Association, Garching, Germany

Abstract: The impact of divertor closure on detachment is studied with the B2-EIRENE code package. Main focus is the observation that detachment seems to occur at unexpectedly low core densities in closed divertors. JET MARK-I and II horizontal plate configurations are adopted as study points. Effects of the observed magnitude are reproduced. While the increase of $i-n$ interactivity, expected for closed configurations, is found in the simulations, the main impact on the upstream density required for detachment is due to volume recombination which is significantly enhanced as a consequence of plate inclination and divertor chamber shape.

1. INTRODUCTION

Closed divertors have gained particular interest, owing to their potential to produce easier access to the detached regime and to reduce main chamber sputtering. In the JET MARK-II divertor, which was designed along this line of thinking, low power L-mode discharges show an onset of detachment (rollover of J_{sat}) and complete detachment at significantly lower core densities than in the less closed MARK-I divertor [1]. Since it has become obvious that complete detachment coincides with the achievement of the density limit [2], this raises concerns for ITER, where the required operation density seems to be in conflict with the Greenwald limit [3].

In this paper the impact of divertor geometry on detachment, particularly on the required upstream density n_S, is studied by simulating density ramp-up scenarios for two configurations with different divertor closure. Though the paper does not aim at detailed modelling, we adopt the MARK-I and II configurations as study points, in order to provide additional relevance of the results by producing qualitative and broad quantitative agreement with actual JET discharges.

The majority of mechanisms that determine the upstream density n_S are well described by a simple 2-P expression for n_S ($\chi_\perp, D_\perp = const$) [4, 5, 6]

$$n_S \propto \frac{P_{heat}^{5/7}(1-f_{rad}^{tot})^{5/7}(q_\psi R)^{1/14}}{(1-f_{rad}^{div})^{1/14}} \left[\frac{1-f_E}{f_P} \frac{T_D^{1/2}}{\frac{\xi}{1-f_{rec}} + \gamma T_D} \right]^{9/14} \qquad (1)$$

where T_D ($T_e = T_i$) is the divertor temperature, f_{rad}^{tot} the total radiative fraction, f_{rad}^{div} the fraction of P_{SOL} that is radiated, f_P the pressure drop along B, f_E the fraction of power into the recycling region that is lost due to $i-n$ interactions (and possibly volume recombination) and f_{rec} the ratio of the total recombination and ionization rates.

In JET the reduction of n_S is observed in discharges with virtually identical f_{rad}^{tot}, excluding different total radiative fractions as a possible cause. Eq. (1) also indicates that a change in the split between core and SOL radiation should have little impact. This suggests that the main cause for the observed difference is due to gas target physics as described by f_P, f_E and f_{rec}. These coefficients are directly relating to loss channels in, respectively, the momentum, energy and particle balances of a gas target. Since they can be easily determined from code output they provide a convenient frame to relate the differences between the two configurations to basic gas target processes.

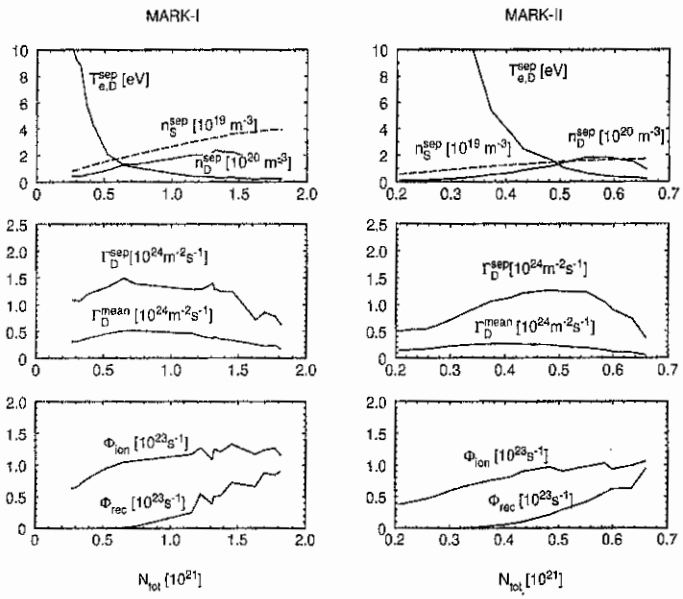

FIG. 1. *N_{tot} traces, where N_{tot} is the total number of ions, for a variety of inboard SOL quantities. n_D^{sep} and $T_{e,D}^{sep}$ are, respectively, the separatrix plasma density and electron temperature at the plate. Subscript S denotes upstream quantities. Γ_D^{sep} and Γ_D^{mean} are the separatrix and mean parallel particle flux densities at the plate. Φ_{ion} and Φ_{rec} are the total inboard ionization and recombination rates.*

The effect of f_{rec} in Eq. (1) is to increase the energy cost for ionization per ion hitting the plate through the additional internal recycling channel. Volume recombination also contributes to the energy and momentum losses in the gas target (f_P, f_E), but its impact is negligible as compared with that of $i-n$ interactions in the regime under consideration.

2. DESCRIPTION OF COMPUTATIONAL SET-UP

A detailed numerical study of detachment in a MARK-I horizontal plate configuration has been reported in Ref. [6]. To isolate the configurational aspects we adopt for MARK-II an identical set-up, except for the magnetic configuration (a so called standard fat, low triangularity configuration in this case) and the divertor geometry. Since our main interest is in gas target physics, we confine ourselves to a pure deuterium case, in order to avoid the complication of varying impurity radiative fractions. An input power of 1.8 MW is adopted, corresponding roughly to the net input power of a typical ohmic discharge. The incoming power is evenly distributed between electrons and ions. The simulation includes, in addition to the SOL region, part of the bulk plasma, defined by some interior flux surface. We simulate a typical density ramp-up scenario by performing a sequence of B2-EIRENE runs to steady state, successively increasing the particle content N_{tot} with otherwise constant input parameters. (Since different core fractions are covered in the simulations of MARK-I and II, the N_{tot} values are not directly comparable.)

3. SUMMARY OF RESULTS AND DISCUSSION

We start the discussion with Fig. 1, where a number of quantities are plotted versus N_{tot} for the two configurations under consideration. By comparing the corresponding curves one observes: (i) The values of n_S at $T_{e,D}^{sep} \simeq 5$eV, i.e., when $i-n$ collisions start to

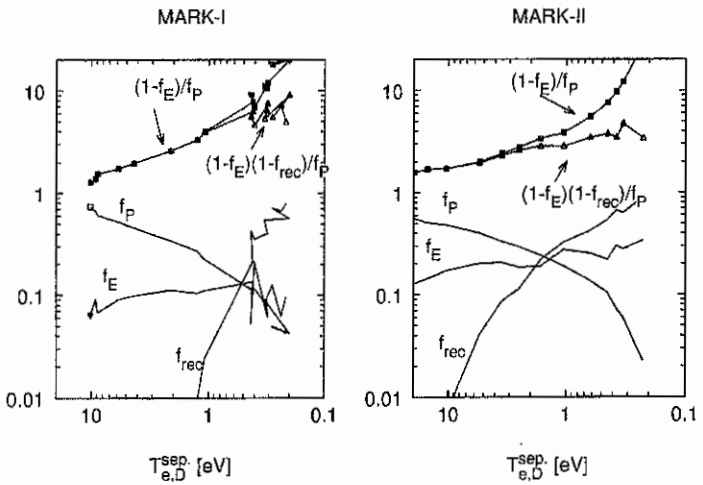

FIG. 2. f_P, f_E and f_{rec} versus $T^{sep}_{e,D}$. *According to Eq. (1)* $(1-f_E)/f_P$ *measures the effect of* $i-n$ *interactions, while* $(1-f_E)(1-f_{rec})/f_P$, *in addition, takes into account the impact of volume recombination.*

become effective, are equal in both cases, while n_S is systematically lower by an amount consistent with experimental findings in MARK-II at lower T_D values. (ii) In both cases the rollover of Γ_D^{mean} coincides with the onset of volume recombination. (iii) In the MARK-II case volume recombination starts at much higher divertor separatrix temperatures ($\simeq$ 5eV instead of $\simeq$ 1eV) and consequently rollover occurs at lower upstream density.

The situation is further clarified when discussed in terms of Eq. (1). In Fig. 2 the parameters f_P, f_E and f_{rec} as well as the combinations $(1-f_E)/f_P$ and $(1-f_{rec})(1-f_E)/f_P$ which describe the effects of $i-n$ interactions alone and the combined effect of $i-n$ interactions and volume recombination, respectively, are plotted versus $T^{sep}_{e,D}$. $T^{sep}_{e,D}$ is a better label than N_{tot} since it is more directly related to the elementary processes that determine f_P, f_E and f_{rec}. While f_P is not much affected by closure, f_E almost doubles in Mark-II. However, f_E remains too small to affect $(1-f_E)/f_P$. We thus conclude that, though closure enhances the effects of $i-n$ interaction, this is not the main cause for the decrease of n_S. On the other hand $(1-f_E)(1-f_{rec})/f_P$ is considerably lower in Mark-II and the decrease of n_S resulting from Eq. (1) agrees with the numerical results (see Fig. 1). This is entirely due to the considerably larger f_{rec}.

The increase of volume recombination and its onset at unexpectedly high separatrix electron temperatures in MARK-II ($\simeq$ 5eV) were the most surprising result of this study. The underlying mechanism can be understood with the help of Fig. 3. Fig. 3 illustrates a "thought experiment" where we start with a plate in position AO and plasma conditions where volume recombination just starts. (Since volume recombination depends much more strongly on temperature than density, this always occurs in off-separatrix regions.) If the target plate is moved into position BO, the plasma conditions upstream to the old target position are basically unchanged [2], while T_e drops drops towards the new plate position. Thus a cold, dense plasma region is formed which favours strong

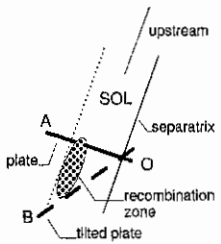

FIG. 3. *Schematic illustration of the impact of the plate inclination on volume recombination.*

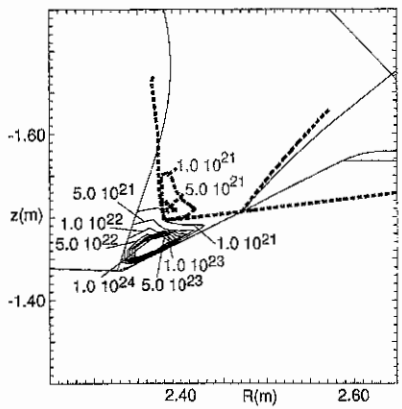

FIG. 4. *B2-EIRENE contour plot of the volume recombination rate in the divertor regions of MARK-I (solid lines) and MARK-II (dotted lines) at* $T_{e,D}^{sep} \simeq 1.5eV$. *The two graphs are merged into one such that the separatrix strike points coincide. Significant volume recombination occurs in MARK-II in areas which are cut-off by target plate and divertor chamber in MARK-I.*

volume recombination. This picture is supported by 2-D results as is demonstrated by Fig. 4, where for both configurations the recombination rate is plotted at $T_{e,D}^{sep} \simeq 1.5$, characteristic of the onset of volume recombination in MARK-I (see Fig. 1).

An immediate consequence of the proposed picture would be an atypical start of detachment in off-separatrix regions and a strong increase of D_α light from the inboard divertor corner. Both effects are seen in experiment [7].

In MARK-II the drop of n_S relative to MARK-I is found to be similar in horizontal and vertical plate discharges. It is not obvious whether the explanation proposed here for the horizontal plate configuration applies for vertical targets as well. This aspect will be addressed in a separate study.

Acknowledgement: The authors gratefully acknowledge discussions with R. Monk, A. Loarte and G. Vlases as well as the support by A. Loarte and E. Springmann in providing the JET configurations.

[1] VLASES, G.,et al., 16th IAEA Fusion Energy Conf. Montreal, 1996, paper IAEA/CN/64/A4-1
[2] BORRASS, K., SCHNEIDER, R., FARENGO, R., Nuclear Fusion. **37** (1997) 523
[3] JANESCHITZ, G., et al., Plasma Phys. Control. Fusion **37** (1995) A19-A35.
[4] BORRASS, K., JANESCHITZ, G., Nucl. Fusion **34** (1994) 1203.
[5] BORRASS, K., FARENGO, R., VLASES, G., Nuclear Fusion **36** (1996) 1389.
[6] BORRASS, K., COSTER, D., REITER, D., SCHNEIDER, R., Study of Recombining Gas Targets, to be published in J. Nucl. Mater (Proc. 12th Int. Conf. on Plasma Surface Interactions in Controlled Fus. Devices, PSI, St. Raphael, 1996).
[7] MONK, R.D. et al, The Effect of Divertor Closure on Detachment in JET, this conference.

Influence of Plasma Edge Pressure Gradient Limits on H-mode Confinement in ASDEX Upgrade

W. Suttrop, M. Kaufmann, O. Kardaun, K. Lackner, F. Ryter,
H. Salzmann, J. Schweinzer, J. Stober, ASDEX Upgrade team,
Max-Planck-Institut für Plasmaphysik, EURATOM Association, D-85748 Garching

Abstract

Stiffness of core temperature profiles in H-modes of ASDEX Upgrade links global confinement to the edge pressure gradient in cases where the density profile remains unchanged. This is the case particularly in low radiation discharges with hot plasma edge, where electron density profiles are flat almost out to the plasma boundary. As a consequence, confinement scalings for discharges near and below the ideal ballooning limit differ. In particular, the favourable density dependence predicted by the ITER ELMy H-mode scalings is lost in type I ELMy H-mode. Density profiles show significant variation, e.g. spontaneous peaking during Completely Detached H-modes (CDH-modes), which may allow to combine good confinement with low edge temperatures and favourable type III ELMs.

Introduction

From core transport models involving critical gradients (e.g. [1]) one expects that above a certain heating power, core temperature profiles will become stiff, i.e. increased heat flux results merely in faint augmentation of grad T. As a consequence, boundary conditions at the plasma edge can determine the stored kinetic energy. In particular, any upper temperature or pressure limit at the plasma edge, e.g. the ideal ballooning limit, potentially defines a fundamental performance limit.

In a related paper [2], regime boundaries in edge parameter space (T_e^b, n_e^b) as identified on the ASDEX Upgrade tokamak (ideal ballooning limit, H-mode threshold, type III ELM boundary and density limit) are discussed. Here we concentrate on the effect of proximity to the ideal ballooning limit at the edge to global confinement scalings. We consider a data set of 798 time intervals in 131 H-mode discharges in deuterium performed during 1996 on ASDEX Upgrade with single-null divertor configuration and ion grad-B drift towards X point. Parameters are plasma current $I_p = 0.6 \ldots 1.2$ MA, toroidal field $B_t = 1.5 \ldots 3$ T, line averaged density $\overline{n}_e = 2.3 \times 10^{19} \ldots 1.3 \times 10^{20}$ m^{-3}, and neutral deuterium beam heating power $P_{\mathrm{NBI}} = 2.5 \ldots 10$ MW.

Relation between edge and core confinement

On ASDEX Upgrade, stiffness of electron and ion temperature profiles is generally observed during neutral beam heated H-modes ($P_{heat} > 2.5$ MW). Fig. 1 a) shows that central T_e (taken at $\rho_p \approx 0.15$) and edge T_e (at $r = a - 2$ cm, both values measured by Thomson scattering) are nearly proportional for a variety of discharges near the ideal ballooning limit at the edge. A wide range of plasma parameters, particularly of $\overline{n_e}$, is covered by the data set (see above). The normalized electron pressure gradient $\alpha_e = 2\mu_0 R q_{95}^2 / B_t^2 \; p'_e$ during type I ELMy was found to be $\alpha_e = 1.6 \pm 20\%$ for the discharges in the data set. Also, type III ELMs can be obtained at the ideal ballooning limit in case of high edge density, if $T_e(r = a - 2$ cm) remains below 300 eV. Those cases adhere to the same edge-core relation. However, during L-mode and type III ELMy H-mode below the ballooning

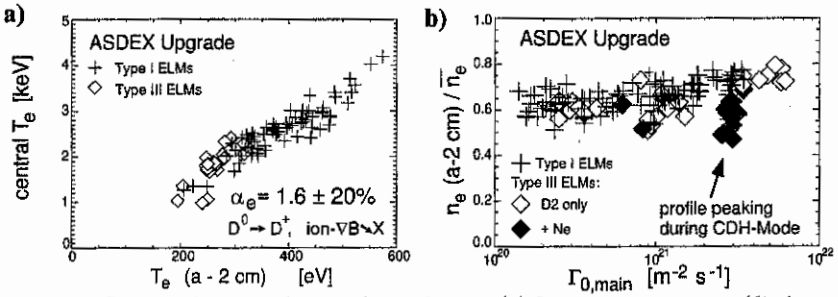

Figure 1: *Relation between plasma edge and core: (a) Electron temperature (discharges near the ideal ballooning limit at the edge), (b) relation between average and edge electron density for different levels of neutral gas flux.*

limit this relation between edge and core temperature breaks down, even at high P_{heat} (e.g. at high H-mode power threshold).

Density profiles in general do not show robust self-similarity. However, during type I ELMy H-mode the scrape-off layer and the plasma edge are hot ($T_e(r = a - 2\text{ cm}) \geq 300$ eV) and the combination of low neutrals penetration depth and low beam fuelling in ASDEX Upgrade produces flat density profiles almost out to the separatrix. Fig 1 b) shows that the electron density n_e at $r = a - 2$ cm amounts to approximately $0.6 \times \overline{n_e}$ (line averaged density) over a wide range of neutral flux in the main chamber, a good shielding of the scrape-off layer and the plasma edge within 2 cm from the separatrix. Hence, self-similarity exists here. In contrast, neon puffed (CDH-mode [3]) discharges, show peaking of the central density attributed to an anomalous inward drift [4].

As a consequence of density and temperature profile similarity, one expects a relation between edge pressure and stored energy. Furthermore, as the edge radial gradient lengths are not varying much during H-mode, a relation between edge pressure gradient and core confinement is observed for cases near the ballooning limit (Fig. 2).

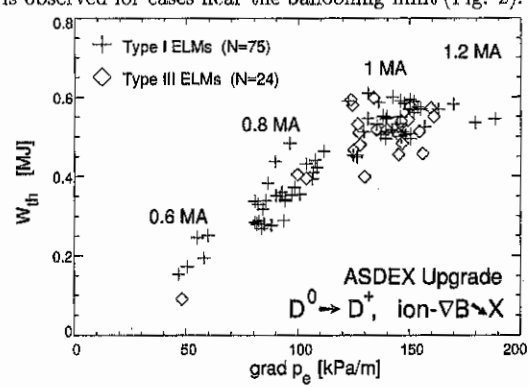

Figure 2: *Relation between thermal stored energy W_{th} and edge electron pressure gradient p'_e for discharges near the ideal ballooning limit at the edge (type I and type III ELMy H-mode).*

Stiffness of temperature profiles

Stiffness of core temperature profiles is usually very robust and not restricted to type I ELMy H-mode. An example is shown in Fig. 3, where in between two type I-ELMy H-mode phases, controlled neon gas puff has been used to radiate $\approx 85\%$ of the input power at the edge. Complete Detached H-mode (CDH-mode) has been achieved. During the CDH-phase, central density peaking (Fig. 3 b) is observed. The NBI power is kept constant. The core temperature profile (T_e profiles are shown in Fig. 3 c) remains almost unchanged despite the strong density perturbation, resulting in an increase in stored energy even above the level during the initial type I ELMy phase. During the CDH phase, there is a two-fold departure from the edge-core relation described above for type I ELMy H-mode: The edge temperature drops due to forced impurity radiation, and at the same time confinement improves when the peaking of the density profile builds up.

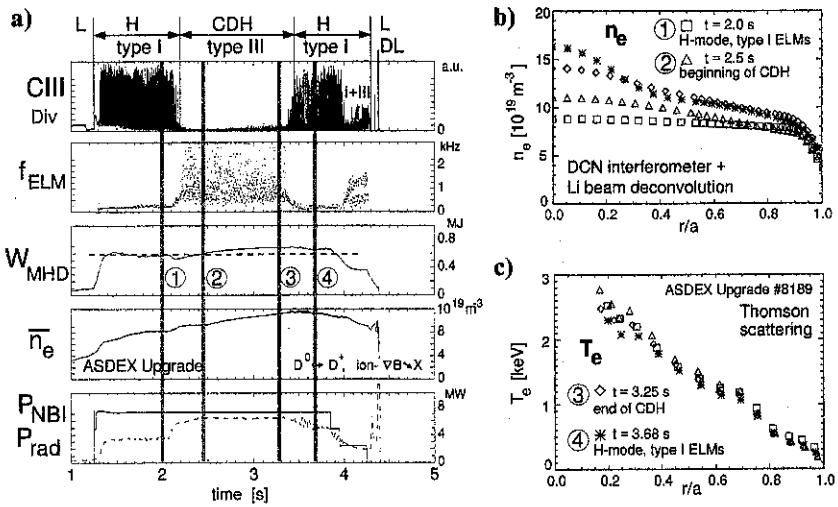

Figure 3: *Confinement improvement during a long CDH-phase (a) associated with central peaking of the density profile (b). The core electron temperature profile is stiff against the density change (c).*

Confinement at and below the ideal ballooning limit at the edge

Proportionality between stored energy and edge pressure gradient at the ballooning limit would imply that global confinement acquires the scaling of p'. This can be investigated by separate regression of p'_e and thermal stored energy W_{th} during type I ELMy H-mode (i.e. near the ideal ballooning limit) with respect to I_p, $\overline{n_e}$, B_t and P_{heat} (Fig. 4). The relations, found by ordinary least squares, are $p'_e(\text{edge}) = 158 \times 10^5 B_t^{-0.34\pm0.07} P_{\text{heat}}^{0.20\pm0.03} \overline{n}_e^{-0.09\pm0.06} I_p^{1.9\pm0.13}$ (kPa/m) and $W_{\text{th}} = 0.296 B_t^{-0.18\pm0.07} P_{\text{heat}}^{0.40\pm0.03}\, \overline{n}_e^{-0.02\pm0.06} I_p^{1.38\pm0.12}$ (MJ). The units of I_p, $\overline{n_e}$, B_t and P_{heat} are MA, 10^{19} m^{-3}, T, and MW, respectively. Note that both p'_e(edge) and W_{th} do not depend on $\overline{n}_e$, in contrast to the favourable density dependence predicted e.g. by ITERH-92P(y) [5]. The I_p dependence of W_{th} is somewhat larger than in ITERH-92P(y) and also than for type III ELMy H-modes below the ideal ballooning

limit in ASDEX Upgrade. However, it is smaller than that of p'_e. The latter effect, together with the retained P_{heat} dependence, appears as scatter of data points in Fig. 2 and indicates that p'(edge) may not be exactly the critical variable for confinement. It is speculated in [6] that the pressure or temperature at the edge pedestal top assumes this role. However, the edge pedestal width in ASDEX Upgrade shows little systematic variation, so that pressure gradient and pedestal pressure are almost proportional.

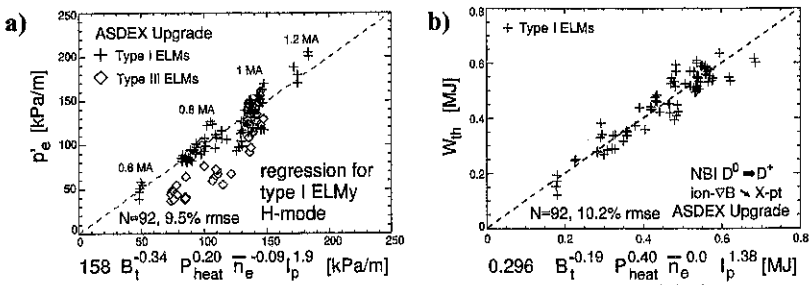

Figure 4: *Separate regression for type I ELMy H-mode discharges of (a) electron pressure gradient and (b) thermal stored energy.*

Analysis of type III ELMy discharges below the ideal ballooning limit yields a weaker scaling with I_p and more favourable B_t and n_e dependences while their confinement is below that of type I ELMy H-mode (with the exception of cases with strong density peaking) for the parameter range of ASDEX Upgrade encountered so far. Both scalings (near and far from the ballooning limit) match at high edge densities where, during type III ELMy H-modes, p'(edge) approaches the ideal ballooning limit.

Conclusion

A correlation between edge pressure gradient near the ideal ballooning limit and core confinement is found on ASDEX Upgrade which is based on robust temperature profile stiffness and flat density profiles during type I ELMy H-mode. A "near ballooning" confinement scaling results, which lacks the favourable density dependence of the ITER ELMy H-mode scalings but shows a somewhat stronger I_p dependence. A combination of good confinement and a sufficiently cold plasma edge, as to obtain divertor-compatible type III ELMs, seems possible by manipulation of the density profile. One successful scheme demonstrated on ASDEX Upgrade is the Completely Detached H-mode [3]. Another possibility would be central fuelling by deep pellet injection, where high fuelling efficiency can be achieved by injection from the high-field side [7].

References

[1] Kotschenreuther M *et al.* 1995 *Phys. Plasmas* **2** 2381
[2] Suttrop W *et al.* submitted to *Plasma Physics and Controlled Fusion*
[3] Gruber O *et al.* 1995 *Phys. Rev. Lett.* **74** 4217
[4] Becker G 1996 *Nuclear Fusion* **36** 1751
[5] H-mode Database Working Group 1992 Proc. 14th Int. Conf. IAEA Würzburg, Vol.3, p.251
[6] Janeschitz G *et al.* 1997 this conference
[7] Lang P *et al.* 1997 this conference

Particle transport determined from modulated gas puff

A.G. Peeters, H. Salzmann, O. Gehre, F. Ryter, W. Suttrop, B. Brüsehaber, and the ASDEX Upgrade team

Max Planck Institut für Plasmaphysik, Euratom-IPP Association
Boltzmannstrasse 2, 85748 Garching, Germany

The paper discusses the particle transport which is determined through modulated gas puff experiments in ASDEX Upgrade. The Thomson scattering data is used for the analysis, and a so called forward method is used to determine the transport coefficients.

Because the modulated ECRH experiments do not show any density modulations the equation that describes the density evolution is assumed independent of the temperature. The density (n) evolution is assumed to be given by the linear equation

$$\frac{\partial n}{\partial t} = \frac{1}{r}\frac{\partial}{\partial r}\left[rD(r)\frac{\partial n}{\partial r} + rV(r)n\right] + S(r,t) \qquad r(\psi) = \frac{1}{\pi}\sqrt{\frac{\mathcal{V}(\psi)}{2R_m}}, \tag{1}$$

where $S = S(r,t)$ is the particle source, and $D(r)$ ($V(r)$) is the diffusion (convection) coefficient. The transport operator is written in cylindrical coordinates with r being the effective radius of the flux surface labeled by the poloidal flux ψ, R_m is the major radius of the magnetic axis, and $\mathcal{V}$ is the volume enclosed by the surfaces on which the poloidal flux is ψ.

Method of analysis

A so called forward method is used to determine the transport coefficients. In this method the transport equation is solved for certain values of the transport coefficients. Using a non-linear fitting algorithm the transport coefficients are adapted until the solution of the transport equation (1) fits best to the measurements. If radial profiles of the coefficients are to be found, this procedure is an under-determined problem. Therefore, one has to limit the number of possible solutions. It is preferable to find the smoothest profile of the coefficients that is allowed by the measurements. Such a solution can be found by regularization.

The code that performs the analysis solves the transport equations in the region where $S(r,t) \approx 0$, for a given set of frequencies, mostly the modulation frequency only. The diffusion (D) and pinch (V) coefficient are given on a grid of the radial coordinate, r_i $i = 1 \rightarrow N$. The transport equation is then solved and the solution n_c is determined at the radial points (r_j $j = 1 \rightarrow M$) where the density is measured by Thomson scattering. The nonlinear fit procedure then minimizes the following function

$$F(D(r_i), V(r_i)) = \mathcal{R} + \frac{1}{2}\chi^2, \tag{2}$$

where

$$\mathcal{R} = \alpha \frac{\sum_{i=1}^{N} (\partial D_i/\partial r)^2}{\sum_{i=1}^{N} D_i^2} + \alpha \frac{\sum_{i=1}^{N} (\partial V_i/\partial r)^2}{\sum_{i=1}^{N} V_i^2} \tag{3}$$

and

$$\chi^2 = \sum_{j=1}^{M} \left(\frac{\Re n_e(r_j) - \Re n(r_j)}{\sigma_j} \right)^2 + \left(\frac{\Im n_e(r_j) - \Im n(r_j)}{\sigma_j} \right)^2 . \tag{4}$$

Here, n is the measured density profile, σ is the standard deviation of the measurement, and $\Re$ ($\Im$) denotes the real (imaginary) part of the Fourier amplitude. Minimizing the last term in equation (2) yields the normal least square fit to the data. Minimizing the first term yields a solution for which the gradients of the coefficients are minimized, i.e. a smooth function. The coefficient α is chosen such that the obtained fit lies within the error bars of the measurements. In this way a fit to the data is found which is both acceptable and has the most smooth radial profiles of the diffusion and pinch coefficients.

Results

As an example two shots will be discussed, one (#8005) in which the working gas is Deuterium and one (#8618) in which the working gas is Hydrogen. The gas puff is modulated with a frequency of 5 Hz. The plasma parameters of the two shots are similar, and are given in table 1.

Table 1. Plasma parameters of the analyzed shots

shot	gas	I_p	B_t	n 10^{19} m^{-3}	T_e keV
8005	D_2	1 MA	-2.5 T	4.6	1.4
8618	H_2	1 MA	-2.5 T	5.1	1.1

The diffusion coefficient and pinch velocity for the Deuterium case obtained from the 5 Hz component is shown in Fig. 1 together with the obtained fits to the data. The results for the Hydrogen case are shown in Fig. 2. The error bars on the diffusion and pinch are estimated using different sets of data points. These error bars only show how the uncertainty in the measurement influences the determination of the transport coefficients within this method. Of course non-smooth profiles of the coefficients can be constructed for which the solution fits just as well to the data. In this sense the error bars are arbitrarily large.

The diffusion coefficient increases towards the plasma edge. A large inward pinch is found at the edge. The transport coefficients for the case with Hydrogen are higher compared with the Deuterium case. These results agree with those previously found on ASDEX [1].

The question whether the obtained transport coefficients from the modulation also explain the steady state profiles is investigated by simultaneously fitting the Fourier

amplitude of the modulation frequency and the steady state profile. The agreement for the Deuterium case is reasonable (it must be noted that V in this case is not accurately determined from the 5Hz component, see Fig. 1), whereas no good fit is obtained in the Hydrogen case.

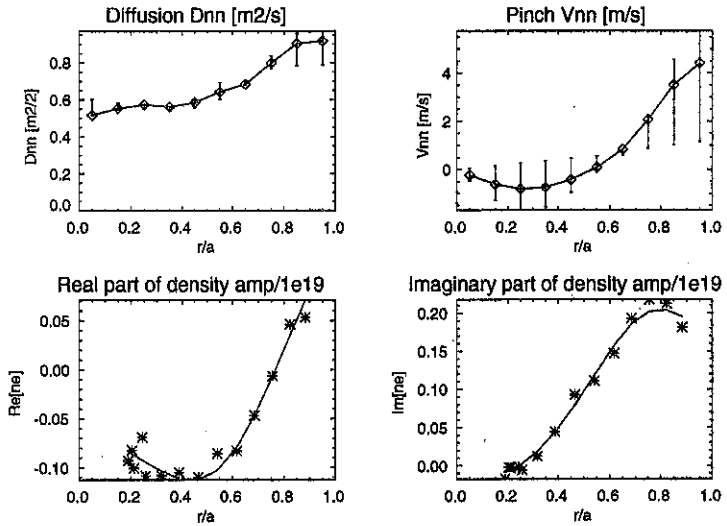

Fig. 1. Obtained results for the Deuterium case

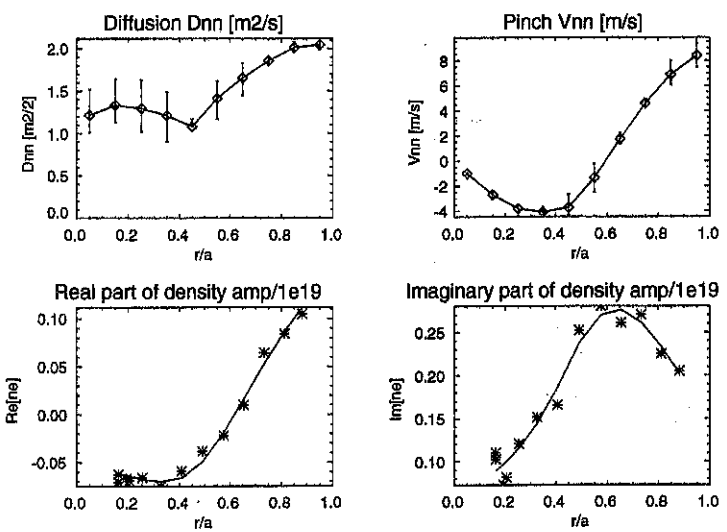

Fig. 2. Obtained results for the Hydrogen case

Temperature perturbation during modulated gas puff

During the modulated gas puff experiments a large temperature perturbation is observed, which increases in amplitude towards the plasma centre. This in contrast to the density perturbation which decreases in amplitude. This temperature perturbation nevertheless can be explained largely from the convective terms in the linearized energy balance

$$\frac{3}{2}n\frac{\partial \tilde{T}}{\partial t} = \nabla n D_{\mathrm{TT}} \nabla \tilde{T} - \frac{5}{2}\tilde{\Gamma}\nabla T_0 - T_0 \nabla \tilde{\Gamma} - \frac{3}{2}T_0 \tilde{S} + \tilde{Q}_{\mathrm{heat}}, \qquad (5)$$

where the tilde denotes the perturbation and the index zero the unperturbed quantity. In Eq. (5) T is the temperature, Γ the particle flux, and Q_{heat} is the external heating (in this case Ohmic heating). With the particle transport determined the measured temperature can be fitted with Eq. (5), in which one new unknown appears, the heat diffusion coefficient D_{TT}. A reasonable fit can be obtained as shown in Fig. 3. The heat diffusion coefficient, however, is larger that the ones obtained in modulated ECRH experiments, which indicates that other terms in the transport equation might play a role. In future experiments modulated gas puff and modulated ECRH experiments will be combined to determine the coupling more accurately.

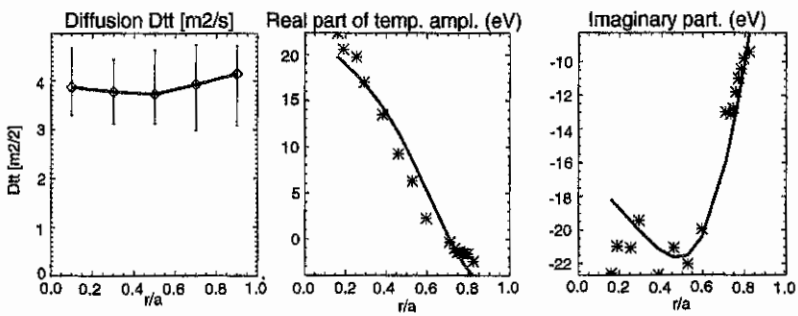

Fig. 3. Results of the fit to the temperature perturbation (Deuterium case).

Conclusion

The transport coefficients can be determined accurately from Thomson scattering using the forward method. This method has the advantage that no processing of the data is necessary, which would lead to additional sources of errors. The most smooth profile of the coefficients obtained by the method allows for a study of the radial dependence.

References

[1] K.W. Gentle, O. Gehre, K. Krieger, Nucl. Fusion **32**, 217 (1992).

Radiative Cooling and Improved Confinement in ASDEX Upgrade

A. Kallenbach, R. Dux, A. Bard, S. de Peña Hempel, J. C. Fuchs, A. Gude, H. Salzmann, J. Schweinzer, M. Weinlich and the ASDEX Upgrade Team
MPI für Plasmaphysik, EURATOM Association, D-85748 Garching, Germany

Introduction

The typical experimental domain of radiatively cooled scenarios is characterized by strong gas puffing and cold divertor conditions. While almost complete power removal by radiation could be demonstrated on ASDEX Upgrade with neon cooling [1], only moderate energy confinement improvement above the L-mode level ($H^{ITER89p} \approx 1.6$) is obtained. On the other hand, very good confinement ($H^{ITER89p} > 2$) can be achieved with very low neutral flux levels in the main chamber which is synonymous for a low SOL electron density. In this case, the confinement improvement is attributed to an edge barrier, leading to a pressure pedestal. But, divertor electron temperatures are high for these conditions. In this paper, such a discharge with edge pedestal and neon radiative cooling is compared with the standard cold divertor, type-III ELMy CDH-scenario, where confinement gain is attributed to core density profile peaking. The radiative efficiency $P_z = \delta P_{rad}/\delta Z_{eff}$ turns out to be degraded for the hot divertor conditions. The origin of this degradation is investigated by impurity transport modelling.

Radiative cooling for hot divertor conditions

Fig. 1 shows time traces of a discharge (#8197) with slightly increased triangularity and plasma volume and a low SOL electron density (see Table 1). A short neon puff at t=3 s leads to a moderate increase of the core radiation and a weak reduction of the target power load. The ELM frequency is reduced from 60 Hz to 14 Hz, resulting in high peak target power loads after the neon puff. While the generally lower ELM frequency is attributed to the higher triangularity, it can not be distinguished whether the improved confinement is caused by the plasma shaping directly or by the low neutral flux level / SOL electron density. The long ELM events which can be seen in Fig. 1 after the neon puff consist of short bursts of individual ELMs: The quiescent H* phases are terminated by a type-I ELM which is succeeded by 2-4 type III ELMs within 10 milliseconds. The sawtooth

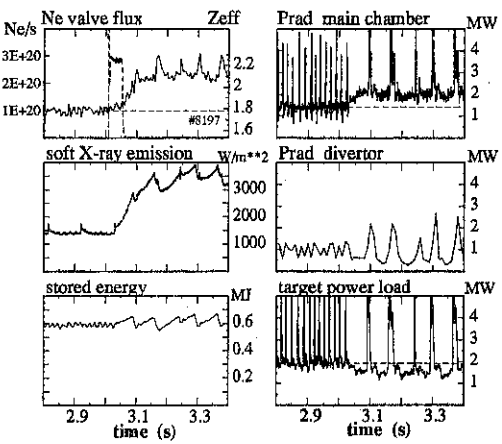

Figure 1: Time traces of a discharge with hot divertor, good energy confinement ($H^{ITER89p} = 2$) and moderate radiative cooling with neon. $P_{heat} = 5$ MW $D^0 \rightarrow D^+$ NBI.

frequency is 14 Hz throughout the discharge, after the neon puff, the sawteeth appear right after the ELM bursts. The improved confinement scenario exhibits a very thin and hot SOL and divertor plasma with an electron temperature $T_e \approx 40$ eV at the outer target.

Radiative efficiency transport modelling

The temporal development of impurity profiles is modelled with the impurity transport code STRAHL [2], using measured electron density and temperature profiles. The STRAHL output interface allows direct comparison with bolometry, spectroscopy, soft-X measurements and charge-exchange recombination spectroscopy (fully stripped impurity density profiles). The overall consistency of STRAHL output and measurements is typically within $\pm$ 30 % when all the diagnostics mentioned are adjusted simultaneously.

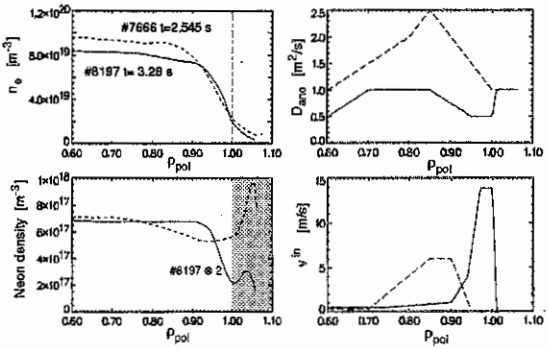

Figure 2: Edge electron and neon density profiles and transport parameters for modelling of the discharge shown in Fig. 1. Parameters of a 'standard' type-III ELMy discharge with moderate gas puffing are given in dotted lines for comparison.

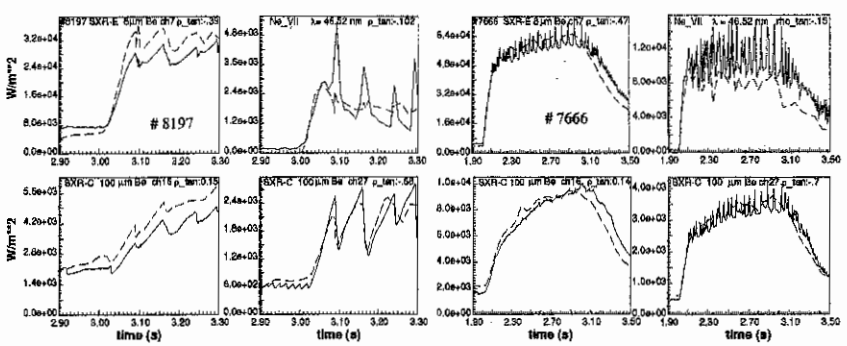

Figure 3: Time traces of soft-X emissivity and Ne^{VII} VUV line emissivity for the discharge shown in Fig. 1 and the reference discharge for comparison. (— model, - - - exp.)

Transport coefficients and density profiles in the outer plasma for the H* phase of Fig. 1 are shown in Fig. 2, values for a standard type-III ELMy discharge with neon cooling are given for comparison. Inside $\rho_{pol} = 0.8$, transport coefficients (D, v) are taken from dynamic pulse analysis using charge exchange recombination spectroscopy [3]. The transport coefficients for $\rho_p > 0.8$ are adapted for different discharge scenarios by matching the temporal evolution of SXR emissivities for various viewing lines and different filter thicknesses (8 and 100 μm Be). While with the 100 μm filters only continuum radiation is measured, with the 8 μm filters also line radiation of highly ionized species contributes.

The radiation profiles before the neon injection are simulated assuming carbon as single impurity (C concentration ≈ 2 %) and matching its influx. After the neon puff, the carbon influx is kept on its initial value, the transport coefficients (D,v) are taken identical to those of neon. The ELMs are simulated by increasing the diffusivity to D= 12 m^2/s over 5 cm inside the separatrix, the radiation during ELMs is not modelled due to the lack of fast enough $T_e(r)$, $n_e(r)$ diagnostics. Sawteeth are treated using an analytical model for the profile reorganization. Experiment and modelling are compared in Fig. 3. It should be noted, that the transport model shown in Fig. 1 represents a possible, but not the unique solution for the observed fluxes and profile shapes if the uncertainties of the measurements are taken into account (see, e.g., [4]). In fact, simultaneously doubling D and v for # 8197 over 3 cm inside the separatrix results in a prediction of the experimental data with a consistency which is similar to the results shown in Fig. 3. Fortunately, the ratio v/D is more robust than the individual values. The question arises, whether the strong neon inward drift during the H* phase is due to neoclassical effects. Fig. 4 shows the various contributions to v_{neo}, the density gradient driven Pfirsch-Schlüter term dominating the ∇T term. In combination with an anomalous D of 1 m^2/s (which is higher than what one would expect within a transport barrier), the neoclassical v_{neo} would fit the experimental data. However, there are uncertainties connected to v_{neo} since the C-Ne collisions and the influence of the radial electric field E_r are not considered in its calculation. Further, an anomalous inward pinch has to be used to reproduce the steep deuteron profile shown in Fig. 2 with simple 1-d modelling including the effect of charge exchange.

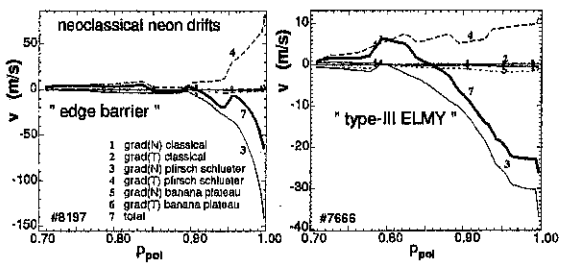

Figure 4: Neoclassical drifts of neon for the discharge shown in Fig. 1, t= 3.28 s and # 7666 for comparison.

We arrive at the following picture of the impurity transport: In the H-mode, D and v peak around ρ_{pol} = 0.8-0.9, and a transport barrier near the separatrix occurs during the H* phases. Between ELMs, anomalous diffusion is reduced within the barrier and a strong inward drift is seen just inside the separatrix. This inward drift leads to a fast impurity build-up close inside the separatrix, its magnitude is similar to the neoclassical level. The clearly anomalous inward drift around ρ_{pol}=0.85 does not lead to substantial impurity buildup since it is compensated by the large values of D. No distinct differences are seen in the radiative efficiencies of radiative type-III ELMy H- and L-modes, where the possible contribution of a neoclassical inward drift is masked by anomalous transport or ELMs.

Origin of the poor radiative efficiency with edge pedestal

The main reason for the poor radiative characteristics of the discharge with edge pedestal is the peaking of the impurity density profile with respect to its edge value. If the transport is characterized by diffusivity D and drift v, the relative profile shape is given by the peaking factor $F_{peak} = exp(-\int_a^r v/Ddr')$. High values of F_{peak} at radial positions with low specific emissivity means plasma pollution without radiative pay-off and

#	type	$H^{ITER89P}$	δ	n_0^{div}; $\overline{n}_e^{SOL}$		T_e^{div}	P_z	$P_z^{\rho<1}$	$F_{peak}^{\rho=0.9}$
				$[10^{19}\ m^{-3}]$		[eV]	[MW]	[MW]	
8197	edge pedestal	2	0.12	1.5	0.6	40	1.8	1.4	4.5
7666	type-III ELMs	1.6	0.09	10	1.0	7	3.5	2	1.1

Table 1: Comparison of radiative characteristics of two improved confinement scenarios with radiative cooling. δ refers to triangularity, T_e^{div} is the peak temperature from target Langmuir probes, P_z is total neon main chamber radiation per core neon Z_{eff} increase. I_p= 1 MA, q_{95}=4.

therefore low values of P_z. The situation for the discharges in comparison is illustrated in Fig. 5: A high drift velocity is only effective to produce profile peaking when connected to a region with low D.

Conclusions

The major drawback for radiative cooling of a discharge with edge pressure pedestal, expressed by the low radiative efficiency $\delta P_{rad}/\delta Z_{eff}$, originates from the large values of v_{in}/D close to the separatrix. Significant values of v_{in} are obtained from neoclassical effects, however, an anomalous contribution to v_{in} may be present. During type-III ELMy or L-mode phases, the neoclassical drifts are masked by other mechanisms and strong profile peaking near the edge is not observed. To obtain efficient radiative cooling, a radiator should be chosen which exhibits its peak emissivity just inside the transport barrier. Other means to increase the radiative efficiency would be density/temperature profile control to support neoclassical drift terms with outward direction. Since the power bursts connected to ELMs succeeding long quiescent H* phases will contradict lifetime requirements of the divertor in a reactor, rapid pellet injection could be used to trigger ELMs with controlled frequency which flatten the impurity profile shape over the pedestal region. The necessary frequency depends on the time scale for buildup of the impurity pedestal and on the width Δ of the pedestal $f \propto v/\Delta$. For designing a reactor scenario with 'edge pedestal', better estimates for the edge transport coefficients, including the neoclassical ones, are required to allow for calculation of the trade-off between confinement degradation and more efficient radiative cooling as well as helium exhaust. To achieve this, refinement of the edge diagnostics is highly desirable.

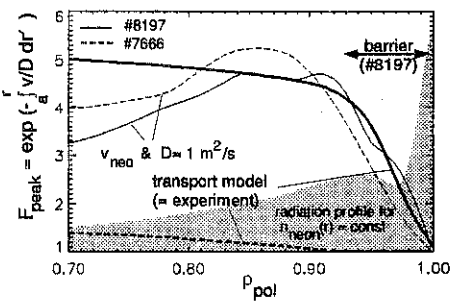

Figure 5: Impurity profile peaking factor F_{peak} for the anomalous transport model of Fig. 2 (fat lines) and for neoclassical drifts according to Fig. 4 and D= 1 m^2/s. The normalized neon radiation profile for #8197 is obtained by multiplication of F_{peak} with the specific emissivity (shaded curve)

References

[1] A. Kallenbach et al., Nucl. Fus. **35** (1995) 1231.
[2] R. Dux et al., PPCF **38** (1996) 989.
[3] S. de Peña Hempel et al., this conference.
[4] R. Giannella et al., Nucl. Fus. **34** (1994) 1185.

Physics of Perturbative Transport from Sawtooth Propagation and ECRH Modulation in ASDEX Upgrade

F. Ryter, F. Leuterer, G. Pereverzev, C.J. Fuchs,
J. Schweinzer W. Suttrop and ASDEX Upgrade Team

Max-Planck-Institut für Plasmaphysik, EURATOM Association, D-85748 Garching

1. Introduction

The understanding of transport in tokamak plasmas is expected to be improved by comparing results derived from steady-state and transient experiments. This is due to the different physical nature of the transport coefficients deduced in these two cases [1]. In this paper we analyse the electron heat conductivity (χ_e) in ASDEX Upgrade as deduced from power balance (χ_e^{PB}) and from heat pulses (χ_e^{HP}) caused by either sawteeth (ST) or ECRH power modulation. It has been previously shown for this tokamak that sawteeth and ECRH modulation yield different results: the latter yields χ_e^{ECRH} values close to power balance ($\chi_e^{ECRH}/\chi_e^{PB} \leq 2$) whereas the former yield χ_e^{ST} values without correlation with χ_e^{PB} and such that $1 \leq \chi_e^{ST}/\chi_e^{PB} \leq 6$, [2]. In this paper we present the χ_e profiles deduced from the three methods and discuss possible physical models.

2. Experiments

The ECRH system operates at 140 GHz in the second harmonic X-mode. This allows a thin deposition width, ≤ 5 cm to compared with a = 50 cm. The absorption is calculated to be 100% in the conditions of the experiments presented here and the supra-thermal population is negligible, the density being above 4 $10^{19} m^{-3}$. We analysed Ohmic and L-mode discharges with different heating powers, plasma currents, magnetic fields and densities, in deuterium and hydrogen. All the discharges were sawtoothing allowing systematic comparison between χ_e^{ECRH} and χ_e^{ST} [2]. We applied on/off ECRH power modulation with 50% duty cycle with P_{ECRH} up to 400 kW which is at most half of the heating power. The best results were obtained when the deposition is around mid-radius.
The essential diagnostic for these studies is the 45 channel ECE heterodyne radiometer which provides the electron temperature with a time resolution up to ≈ 30 kHz. Generally 30 channels at least were in the interesting plasma region. The radial resolution of each channel is under 1 cm and the distance between channels can be as low as ≈ 2 cm. These properties allow to analyse the heat pulse propagation over a large part of the plasma radius and to deduce radial profiles of χ_e^{HP}. It must be underlined that a careful independent calibration of the ECE system was performed and that the T_e measurement is in good agreement with the electron temperature from the Thomson scattering diagnostic. Therefore, both amplitude and phase of the Fourier analysis used below must be considered to have equal weight.

3. Analysis

The basis of the data analysis here is a Fourier transformation which yields amplitude and phase of the temperature perturbation for each ECE channel. The calculation of χ_e^{HP} follows the method described in [3]. At each radial point of the measurement a χ_e^{HP} value is calculated

with corrections for cylindrical geometry and density gradient. The gradient of the temperature perturbation necessary for the calculation of χ_e^{HP} is obtained from fit of the data. As usual, $\chi_e^{HP} = \sqrt{\chi_e^{Amp}\chi_e^{Phase}}$, χ_e^{Amp} and χ_e^{Phase} deduced from amplitude and phase.
The time-dependent transport code ASTRA is used to model the steady-state and transient experiments. This code uses the toroidal geometry, the damping (Ohmic power changes and electron-ion exchange) is calculated. The ECRH power modulation is included as a modulated heating term of the electrons with the corresponding frequency and wave form. The deposition is radially defined as a Gaussian with position and width corresponding to the experiment. The ion temperature profile is that of the experiment.
The sawteeth modelling is based on a Kadomtsev reconnection model. The frequency of the sawteeth is prescribed according to the experiment. In our discharges the inversion radius corresponds to the calculated q=1 radius within $\approx 20\%$. At each sawtooth crash the T_e profile is flattened and the energy is redistributed inside the mixing radius. Note that the exact modelling of the sawteeth is not essential in this study, the important part being the creation of a heat pulse outside the mixing radius which will then propagate towards the plasma edge, according to our transport model. The Fourier transformation of the ASTRA results and experimental data are compared to test the validity of different transport models.

4. Results

Examples of results from experiment and modelling are shown in Figs. 1 and 2 for ECRH modulation at 100 Hz and sawteeth respectively, during the same time period of the plasma. This is an L-mode discharge in hydrogen with 2 MW NBI heating, residual Ohmic power of 0.4 MW and line-averaged density of 5 $10^{19}m^{-3}$. The comparison of Figs. 1 and 2 clearly shows that χ_e^{ST} is larger than χ_e^{ECRH} and that both are larger than χ_e^{PB}. Note that is not due to a poor signal to noise ratio for the ST case because the amplitude of the ST perturbation is equal to or larger than that of ECRH and both are above the noise level, indicated in Figs. 1 and 2. It is also underlined that both amplitude and phase yield large χ_e^{ST} values. The difference between χ_e^{PB} and χ_e^{HP} is expected, as already mentioned above [1]. The fact that sawteeth and ECRH yield different values in the same discharge indicates that either the transport mechanism depends on the heat pulse or that two transport mechanisms are acting, depending on the nature of the perturbation. This is investigated in the following.
The first and simplest step in trying to model the transient experiments is to find a time-independent χ_e profile which reproduces the transient experimental results. This could be easily achieved for the ECRH modulation for which $\approx 2 \times \chi_e^{PB}$ gives good agreement with the amplitude and phase profiles of Fig. 1. This is a bench marking between ASTRA and the Fourier analysis and shows that a locally determined diffusive transport may well explain the data. However, this dose not include any physics model. For sawteeth it was not possible to find a time-independent χ_e yielding good agreement with both phase and amplitude. The disagreement is larger at higher frequency (3^{rd} harmonic). This suggests that a non-diffusive transport process is also involved. We tried to reproduce the experimental data from both ECRH and sawteeth with 3 transport models: a local model, a non-local model and a model combining both.
The local model is based on $\chi_e \sim \nabla T_e^{\alpha}$. According to [4] one may conclude from the ratio of about 2 between power balance and ECRH modulation that $\alpha \approx 1$. The simulation under this assumption gives rather good agreement for the ECRH case (Fig. 1) but also for the sawtooth case (Fig. 2). However in none of the cases the agreement is perfect. A more precise agreement is obtained for ECRH in Ohmic cases in which the χ_e profile is much flatter than in the auxiliary

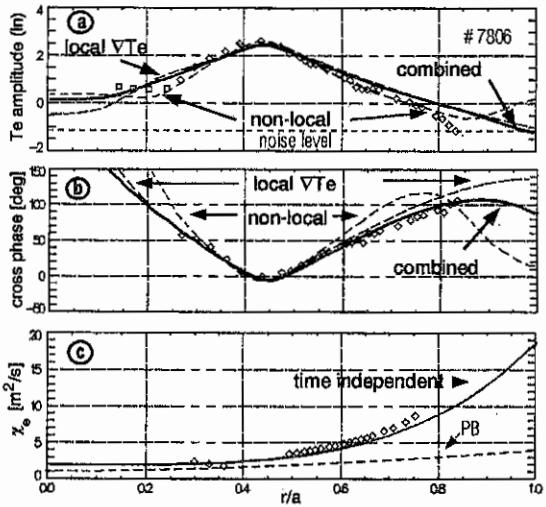

Fig 1. ECRH modulation: diamonds are experimental data. Dashed lines in a and b are simulations with local and non-local models. The third line is the combination of both local and non-local. The HFS region ($r/a \leq 0.3$) of the amplitude might be perturbated by the sawtooth underground noise.

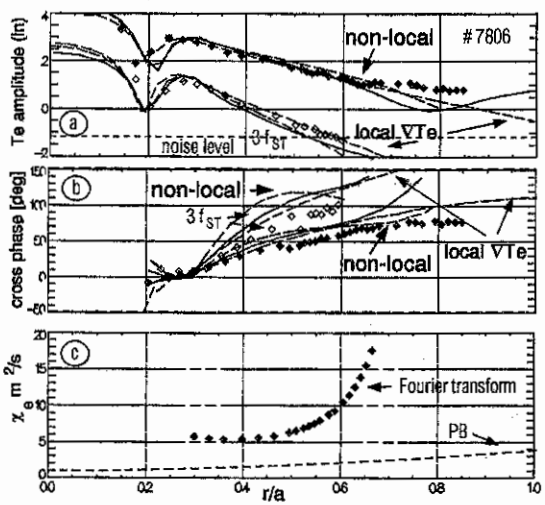

Fig. 2. Sawtooth analysis: Data points are diamonds: closed symbols for fundamental, open symbols for 3rd harmonic. The lines are the three simulation models as in Fig. 1.

heated discharge analysed here [5]. Figures 1 and 2 also show the comparison with our non-local model. Following the non-local power dependence of χ_e found for ECRH described in [4], we introduce here for sawteeth the model $\chi_e(t) = \chi_e^{PB} \times (\tilde{T}_{e0}^{ST}(t)/T_{e0})^{\beta}$, where $\tilde{T}_{e0}^{ST}(t)$ is the modulation of the central electron temperature caused by sawteeth and T_{e0} the time-averaged central electron temperature. For ECRH the amplitude of the perturbation is taken at the centre of the ECRH deposition profile. The exponent $\beta = 1.5$ yields good agreement with the experimental data, as shown in Figs. 1 and 2. Note the precise agreement of the amplitude for the ECRH but the poorer one for the phase. For the sawteeth the agreement for the amplitude is as good as obtained with the local model, but the agreement for the phase is poorer. The two models were combined: $\chi_e(t)=\chi_e^{PB} \times (\tilde{T}_{e0}^{ST}(t)/T_{e0})^{\beta} \times \nabla T_e$. The results in Figs. 1 and 2 were obtained with $\beta = 0.5$. The simulations are closed to the results from the local model. For ECRH the phase is somewhat better reproduced, for the sawteeth no significant difference appears. Clearly, based on this example non clear statement can be made on the character of the transport in these experiments.

5. Discussion and conclusion

The local ∇T_e model seems to explain our experimental data but the precision is not excellent. This leaves enough room for large variations in χ_e^{HP}, as this quantity depends on the square of the gradients of the phase and amplitude profiles. This is shown by the experimental χ_e^{HP} profiles which reach very large values, as shown in Figs. 1 and 2. A non-local model seems to able, even required to reproduce some features of our data, in particular outside r/a = 0.6. A non-local model excites an additional T_e perturbation along the radius where steady-state power exists, [4]. This creates a perturbation standing wave across the plasma. Our non-local model is very simple and uses the temperature change as a switch to vary χ_e in time. It clearly has the drawback that χ_e is changed instantaneously at the onset of the perturbation. This critically forces the phase of this standing wave to zero at the edge. A more realistic model with a radially dependent delay for reaction of χ_e to the perturbation is expected to change this situation. This will be the subject of future work.

6. Acknowledgement

It is a pleasure to acknowledge fruitful discussions with A. Jacchia, F. DeLuca, G. Gorini, N.J. Lopes Cardozo, P. Mantica and U. Stroth. We warmly thank P. Mantica for having cross-checked our Fourier analysis and χ_e calculation on some ASDEX Upgrade data sets with the methods used for JET and RTP data.

References

[1] LOPES-CARDOZO, N. J., Plasma Phys. Controlled Fusion **37** (1995) 799.

[2] RYTER, F. et al., IAEA, Montréal, 1996, F1-CN-64/AP1-5.

[3] JACCHIA, S. et al., Phys. Fluids B 3 (1991) 3033.

[4] STROTH, U. et al., Plasma Phys. Controlled Fusion **38** (1996) 611.

[5] RYTER, F. et al., Proceedings EPS 1996, **20C, part I, 11, 1996.**

Pellet refueling from the magnetic high field side

P.T.Lang, K.Büchl, M.Kaufmann, R.S.Lang, V.Mertens,
H.W.Müller, J.Neuhauser, F.Ryter, ASDEX Upgrade Team
Max-Planck-Institut für Plasmaphysik, EURATOM-IPP Association,
Boltzmannstr. 2, 85748 Garching, Germany

Introduction

Next generation fusion devices like ITER will have to operate at densities well beyond the Greenwald density limit enfaced with gas refueling [1]. It was shown that this empirical limit can be easily overcome by injection of frozen pellets, however in discharges with high heating power and especially in type-I ELMy H-mode plasmas a large fraction of the deposited material is rapidly expelled from the plasma [2], resulting in significantly reduced fueling efficiencies ε_f. In all these experiments, pellets were injected from the magnetic low-field side (LFS), i.e. from the torus outside, which is easily accessible in a tokamak. It was argued [3] that, because of the unfavourable toroidal curvature, part of the diamagnetic pellet plasma cloud could have been expelled before it was captured by the background plasma. In this case, injection from the magnetic high-field side (HFS), i.e. the torus inside, should be much superior, since the same effect would help to transport the pellet mass deeper into the bulk plasma. In order to clarify this question, experiments have been conducted in ASDEX Upgrade where pellets were injected from both sides into H-mode plasmas and ε_f as well as pellet penetration depths were compared.

Experimental setup

Pellet fueling experiments are executed on ASDEX Upgrade (R_0 = 1.65 m, plasma radius a_0 = 0.5 m, V_{Plasma} = 13 m^3, b/a = 1.6; tungsten-coated divertor target plates) plasmas with lower single null configuration, I_p = 0.8 - 1.2 MA, B_t = 1.7 - 2.5 T, q_{95} = 2.7 - 4.2 and P_{NI} up to 7 MW for H^0 and up to 10 MW for D^0 injection. Pellet injection was performed either with a centrifuge injector or a blower gun. The centrifuge injected only from the LFS. D_2 pellets of variable velocity (240 to 1200 m/s) and mass (1.4 to 3.8 x 10^{20} particles) can be delivered at repetition rates of up to 80 Hz. The blower gun injects D_2 pellets containing 3 x 10^{20} particles, accelerated by H_2 gas flow up to 130 m/s at repetition rates of up to 17 Hz. Pellets are delivered via guiding tubes optionally from the magnetic low- or high-field side. Switching from one track to the other is possible within 60 ms.

Pellet ablation is monitored by a CCD camera and photodiodes. Video pictures showing the ablation zone of the pellets are used to estimate the pellet penetration depths. A DCN interferometer, a Li-beam system, a Thomson scattering system and an ECE radiometer are applied to measure the density profile and determine the plasma particle content; the latter two are also used for temperature profile investigations. The measured increase of the number of particles in the target plasma (1-5 ms after ablation) divided by the number of particles contained in the pellet is defined as fueling efficiency ε_f. To calculate ε_f we used the maximum pellet mass found in testbed shots.

Experimental comparison of LFS and HFS pellet refueling

To demonstrate the enhanced refueling performance of HFS pellets, LFS and HFS pellets were injected into the same plasma discharge under practically identical conditions. Fig. 1 shows the temporal evolution of such a discharge (I_P = 0.8 MA, B_t = -1.9 T, q_{95} = 3.6, P_{NI} = 7.5 MW). During the whole sequence the discharge maintained type-I ELMy H-mode behaviour. Gas puffing was initially applied to control the line-averaged density at the required value of 7 x 10^{19} m^{-3}. The LFS pellet injection sequence was started after the density reached the preprogrammed value, and the HFS sequence was applied about 0.5 s after termination of the LFS pellet sequence, when the discharge had returned to identical starting conditions. Both sequences consisted of a nominal 10 pellets each with the same, relatively small nominal velocity of 130 m/s. A strong enhancement of ε_f with the HFS pellets in relation to the LFS pellets can be concluded from the increase in line-averaged density. The ε_f with the HFS pellets are about 4 times as high as the values obtained for LFS pellets. The higher efficiency with HFS pellets is also obvious from the particle flux applied as D_2 gas puff. Pellets launched into the plasma are monitored by the spikes they cause in the D_α radiation. Reduced intensities observed with some pellets are most probably due to mass losses on the external pellet path. The time averaged particle flux of the nominal pellet sequence is shown as dashed line in fig. 1. Whereas additional gas input is required by the plasma control system during the LFS sequence to reach the preset line density, gas valves close almost immediately after the start of the HFS pellet train. The divertor neutral flux density Γ_0^{div} gradually increases during the LFS sequence, whereas an almost constant lower value is maintained during the HFS sequence. With HFS pellet injection, significant density increase is achieved without deterioration of the plasma energy or energy confinement time τ_E. With LFS pellet injection, in contrast, no comparable density increase is observed. In earlier LFS experiments [4], density enhancement similar to that with present HFS injection was achieved only with 80 Hz pellet injection yielding approximately 6 times higher particle flux. This enhancement was always accompanied by a loss of plasma energy, a reduction of τ_E and strong cooling of the plasma. Evolutions of according discharges refueled by pellets are compared to data obtained for gas

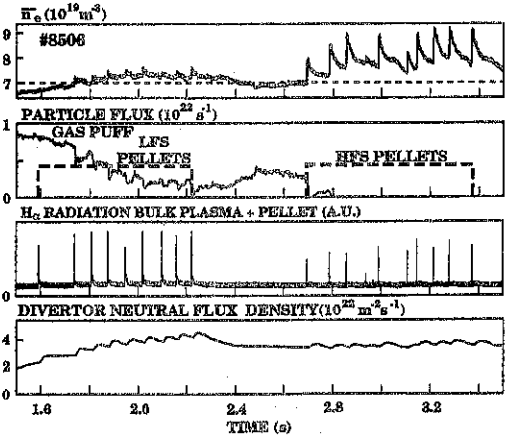

Figure 1: Temporal evolution of a discharge with LFS and HFS pellet injection applied performed with identical pellets and starting from almost identical plasma conditions.

puffed plasmas as shown in Fig.2. LFS pellet injection applying high particle flux to achieve high plasma densities causes a high neutral gas pressure P_{div} in the divertor. Increasing P_{div} however results, like in gas puffed discharges [5], in a degradation of the confinement. Reduced particle losses in the case of HFS injection allowed for a plasma density close to the Greenwald limit at lower divertor neutral pressure P_{div}, consequentely no significant confinement degradation occurs.

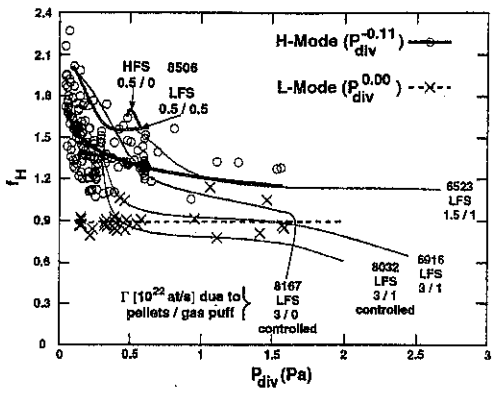

Figure 2: Enhancement factor f_H of energy confinement time relative to L-Mode scaling ITER89-P versus divertor pressure. Symbols and black curves: data for gas fueled discharges and according fits. Slim grey curves: evolution of LFS pellet refueled discharges to densities well above the Greenwald limit at different particle refueling flux rates. For LFS pellets, increasing plasma densities always are accompanied by high P_{div} and reduced f_H, whereas HFS injection (strong grey curve: evolution of #8506) approaches already $n_{e,Gw}$ at low P_{div} values without confinement degradation.

A series of pellet injections were performed under various plasma conditions to compare between LFS and HFS injection, Fig. 3 shows ε_f values for different P_{NI}. For $P_{NI} > 5$MW HFS pellets (filled symbols) showed efficiencies enhanced by up to four times that with equivalent LFS pellets (open symbols). With increasing P_{NI} and plasma temperature, HFS pellets show no significant power degradation of ε_f, whereas the maximum efficiency achieved using LFS pellets (solid line) is dropping. Even at the highest heating powers applied almost the same efficiencies are achieved for HFS pellets as in ohmic plasmas. The strong scatter of ε_f values is most probably an artefact caused by the external pellet mass losses mentioned earlier. This conclusion is further supported by the fact that reduced ε_f values were always accompanied by reduced ablation radiation. With the ablation radiation being assumed to be a good measure of the pellet mass [6], accordingly corrected ε_f values show a scatter reduced to ±10 % of the optimum value of ≈ 0.7 for the HFS pellets. For LFS pellets, however, a strong reduction in efficiency takes place despite the fact even bigger (3.8×10^{20} particles) and faster (1200 m/s) pellets were injected using the centrifuge at high heating powers, penetrating deep into the plasma. In the case of shallow penetration into type-I ELMy H-mode plasmas ε_f was even restricted to values below 0.2 [3]. Comparable conditions yielded the same result in the case of LFS pellet injection with the blower gun.

A striking difference in the pellet penetration depths Δ and ablation traces between LFS and HFS pellets became obvious from video observations. Whereas LFS penetration was rather

low ($\Delta \approx 8$ cm for the discharge shown in Fig.1), significantly deeper penetration ($\Delta \approx 19$ cm) was found with HFS pellets. This strong difference cannot be wholly attributed to different local target plasma conditions or different flux tube spacings (Shafranov shift); we estimate that these effects yield an enhancement of with HFS pellets less than 1.6 times as large as the LFS values. Whereas LFS pellet penetration depths Δ are in agreement with published ablation scalings, HFS pellets were found to penetrate considerably deeper into the plasma. Obviously, an additional shielding mechanism must be responsible for the enhanced Δ of HFS pellets, which we attribute to the diamagnetic pellet plasma cloud drift.

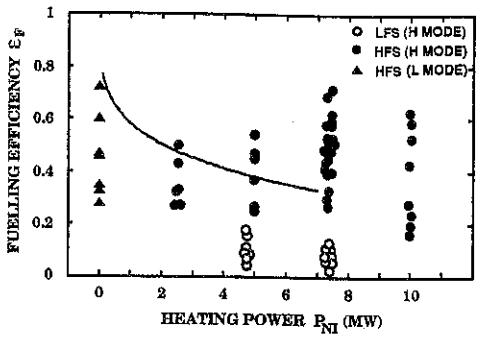

Figure 3: The triangles and circles show the fueling efficiency calculated on the assumption of maximum pellet masses versus additional heating power for LFS (open symbols) and HFS (filled symbols) pellets injected with the blower gun. Triangles: pellets into ohmic L-mode plasmas; circles: H-mode target plasmas. The solid line represents the upper limit of fueling efficiency in the case of LFS injection performed by the centrifuge.

Conclusions

Our experiments demonstrated that HFS pellet injection allows for efficient particle refueling of hot, high confinement plasmas relevant for next generation fusion experiments. The advantage over standard LFS injection seems to originate from the toroidal curvature, which tends to expell the diamagnetic ablation cloud from the LFS, while the same effect is highly beneficial for bulk refueling from the HFS.

References

[1] N. Greenwald et al., Nucl. Fusion, **28**, 2199 (1988).
[2] S.L. Milora, W.A. Houlberg, L.L. Lengyel, and V. Mertens, Nucl. Fusion **35**, 657 (1995).
[3] M. Kaufmann et al., Nucl. Fusion, **26**, 171 (1986).
[4] V. Mertens et al., in Controlled Fusion and Plasma Physics
(Proc. 23rd Eur. Conf. Kiev, 1996), European Physical Society, Geneva, June 1996.
[5] F. Ryter et al., IAEA paper F1-CN-64/AP1-5, Montreal 1996.
[6] C.A. Foster et al., Nucl. Fusion **17**, 1067 (1977).

Scaling of Thermal Energy Confinement in ASDEX Upgrade

O. Vollmer, F. Ryter, A. Stäbler, P.J. McCarthy and ASDEX Upgrade Team

Max-Planck-Institut für Plasmaphysik, IPP-EURATOM Association
Postfach 1533, D-85740 Garching bei München

1. Introduction

The thermal confinement time of the ELMy H-mode is an important issue for ITER [J. G: Cordey: Confinement understanding and extrapolation to ITER, this conf.]. It is therefore of interest to investigate the confinement dependence in individual devices, as recently underlined [D. Campbell, Physics Issues in ITER, ASDEX Upgrade Seminar April 1997] . Such studies have the advantage of being free from machine to machine differences and the dependencies can be investigated in detail.

2. Experimental Data

2.1 Database: The database contains 140 time slices from 75 ASDEX Upgrade H-mode discharges taken during steady-state phases with regular type I ELMs. The selection includes only deuterium discharges heated with co-injected deuterium neutral beams. As a consequence, the atomic mass dependence will not appear in the results. Excluded are time slices with high radiation (P_{rad}/P_{tot} < 45 %) - for instance induced by impurity injection - , with transient behaviour and near the ß-limit . Only discharges with deuterium gas puffing to vary the density have been selected.The plasma configuration was a single null with the ion gradB drift direction pointing towards the x-point in the standard geometry of ASDEX Upgrade R = 1.65 m, a = 0.5 m , κ = 1.7 and upper triangularity from 0 to 0.1. Geometrical dependencies are therefore not included in the derived scaling. The discharges were performed with boronized walls. The database combines operation periods with the divertor I equipped with carbon- (1995) and tungsten tiles (1996). The range of the main plasma parameters covered by the data base are indicated in Fig. 1. The Correlation Matrix of the database gives Table I.

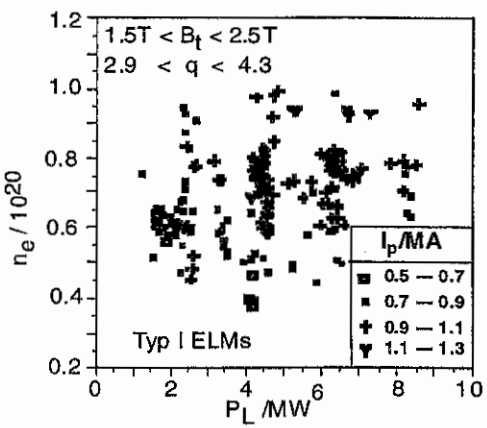

Fig.1: Database for the scaling

2.2 Recovery of neutral beam heating data: In order to evaluate thermal confinement data of neutral beam heated discharges the heating power coupled to the plasma as well as the

energy content of the fast ions have to be determined from the neutral power injected into the torus. Monte Carlo techniques are used for this purpose but due to the extrememly high CPU-times such codes are not practicable for a shot by shot analysis. A much faster method now available for ASDEX Upgrade plasmas is based on Function Parametrization of a statistically well designed database generated by several hundreds of runs of the Monte Carlo code FAFNER. However, plasma density and temperature profiles are required as an input, which are not always available for ASDEX Upgrade discharges.

Variable	P_{Div}	P_T	I_p	n_e	B_t
PDiv	1	0.49	0.44	0.63	0.31
P_T	0.49	1	0.42	0.23	0.23
I_p	0.44	0.42	1	0.52	0.69
n_e	0.63	0.23	0.52	1	0.05
B_t	0.31	0.23	0.69	0.05	1

Table I Correlation matrix of the database for the AUG typ I ELM discharges

In order to provide the fast ion losses and the energy content of the fast beam ion population for almost each of the ASDEX Upgrade discharges a fit procedure has been derived based on five plasma parameters readily available for most of the shots: line averaged density n_e separatrix density $n_e(a)$, SOL density fall-off length $\lambda_{n,SOL}$, total plasma energy content W_{mhd}, and plasma volume V_p. A subset of the FAFNER results produced for the Function Parametrization was used to find the following fit formulae for 60 kV D^0 beams:

Shinethrough: $\exp(-n_e/\alpha_i)$ Ripple Losses: η_i

Re-ionization in SOL: $\beta_i * (n_e(a) * \lambda_{n,SOL})$ Charge exchange losses: $\gamma_i * (\tau_{sd})^{\delta_i}$

Orbit Losses: $\varepsilon_i * (n_e(a) * < T_e >)^{\nu_i}$ Fast ion content: $\kappa_i * (\tau_{sd})$

where $\tau_{sd} = f(n_e, <T_e>)$ is the fast ion slowing down time and $<T_e>$ is estimated from the measured value of W_{mhd} by $<T_e> = (1/3) * W_{mhd} / (n_e * V_p)$. The coefficients ($\alpha_i, \ldots; i = 1, \ldots, 4$) have been determined individually for each of the four ion sources of the ASDEX Upgrade neutral beam injector. The ripple losses are only significant for the two ion sources injecting more perpendicularly and are calculated to be about 7% with neglegible dependence on edge parameters.

3. Thermal confinement scaling

For the described dataset we analyse the thermal confinement time. In our case of neutral beam heated plasma and time slices with stationary plasma energy content the thermal confinement time τ_{th} is calculated from

$$\tau_{th} = (W_{MHD} - W_{FAST\ IONS}) / P_L \quad \text{with } P_L = P_{OHM} + P_{INJ} - P_{LOSSES}$$

where the plasma energy W_{MHD} is corrected by the energy of the fast beam ion population $W_{FAST\ IONS}$. P_{LOSSES} represents all the fast ion losses. P_{LOSSES} and $W_{FAST\ IONS}$ are calculated by the fit procedure described above. Radiation losses are not taken into account, since the power radiated within the separatrix is in the order of only 15%. For the analysis by linear regression we use a power law assumption for the thermal confinement :

$$\tau_{th} = A * I_p^{\alpha_I} * P_L^{\alpha_P} * n_e^{\alpha_n} * p_{div}^{\alpha_{div}} \quad [s, MA, MW, ne10^{19}\ m^{-3}, P]$$

with the dependencies: Plasma current I_p, absorbed heating power P_L, line-density n_e and divertor neutral gas pressure p_{Div} .The gas pressure measured in the divertor region has been included because a pronounced influence of gas pressure on confinement has been found [1] , [5]. The gas pressure in the divertor is probably not the physical cause of the observed degradation but rather its influence on the edge parameters [2] . Pressure measurements in the main chamber could also be used, but the data in divertor are more complete and reliable. Pressures measured in main chamber and divertor are generally tightly coupled. The influence of the toroidal field is found to be low and could not be determined with reasonable precision from the database. The B_t dependence is therefore set to zero in the following analysis. This is roughly compatible with single shot to shot observations.

A regression has been performed including simultaneously the four above variables and the result are given in Table I. In spite of the size of the data base and the covered parameter range, the dependencies provided by the simultaneous regression might not be reliable, because of the correlation within the data (see Table II). Therefore a "regression by step" analysis has been performed as well, by windowing the database into fictive scans in which only one variable is varied whereas the other 3 are kept constant as much as possible. First the dependence on the divertor pressure is obtained from a scan at constant plasma current (Ip =1 MA) and narrow intervals for the density and the total heating power. The analysis is summarised in Table III, which gives the single regression steps and the parameter intervals used. The resulting dependence exponents are also given in Table I.

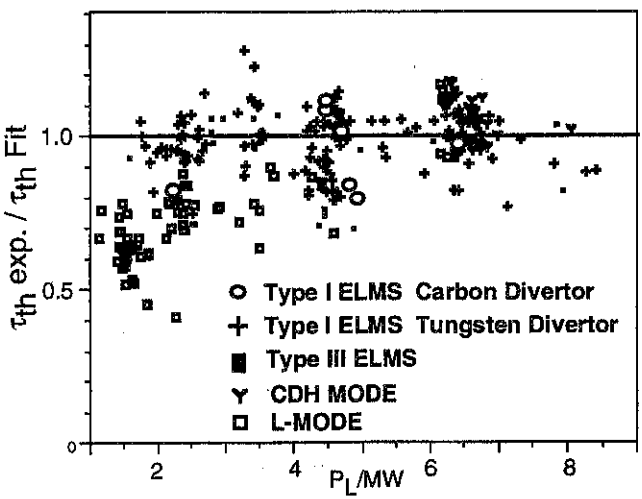

Fig.2: ASDEX Upgrade thermal confinement normalised by the scaling ("regression by step)"

The scaling provided by the "regression by step" is illustrated in Fig.2 where thermal confinement time normalised by the derived scaling is plotted versus the total input power P_L for the time slices of the database. The data are reasonably well represented with a standard deviation of 10%. For comparison, Fig.2 also includes data from other confinement regimes currently observed in ASDEX Upgrade. Discharges with type III ELMs do not significantly

differ from the type-I ELM fit. The thermal confinement of the L-mode approaches the H-mode confinement for higher P_L which is related to higher densities in our database. The CDH-mode points clustering around P_L=6.5 MW tend to slightly higher thermal confinement compared to the scaling. This is attributed to the density peaking caused by edge radiation which compensates the confinement degradation correlated by the required high divertor pressure.

4. Discussion

The majority of the data represent the operation of ASDEX Upgrade with the tungsten divertor in 1996. Only a few data points refer to the carbon divertor because of missing data for the divertor pressure. However no influence on the confinement appears for the operation with the two different materials in the divertor, in agreement with previous results [3].

Our results can be compared (Table II) to the thermal ELMy scaling obtained with the ITER H-mode database (ITER-92-P(y)) and recommended by the by ITER Modeling and Database Expert Group. [4]. A basic difference between the two expressions is that the neutral pressure is not included in the ITER-92-P(y) scaling. However this is not expected to have a major influence because most of the ELMy data included in the ITER database were not obtained with strong gas puffing but rather at the natural density for each device. The two scalings yield very similar dependencies for Ip, Bt. The difference on the density dependence might be attributed to the neutral gas pressure. In fact, the difference in the exponents is consistent with this assumption. The difference in the heating power exponent is outside the uncertainties.

Scaling	A	α_I (+/-)	α_P (+/-)	α_{Bt} (+/-)	α_n (+/-)	α_{div} (+/-)
AUG linear regression	0.21	0.59(0.08)	-0.53 (0.08)	(0)	0.5 (0.08)	-0.13 (0.02)
AUG lin. regress. "by steps"	0.19	0.85 (0.08)	-0.55 (0.05)	(0)	0.5 (0.05)	-0.2 (0.02)
ITER H-mode Database [4]	0.034	0.9	-0.65	0.05	0.3	(0)

Table II: Power law coefficients for thermal confinement scalings

Response	Variable	Parameter Range used for Regression
τ_{th}	P_{Div}	I_p = 1 MA / 7.5 < $n_e/10^{19}$ < 8.5 / 6.1 < PT/MW < 6.9
τ_{th} / $P_{Div}^{-0.2}$	P_T	I_p = 0.8MA / 5 < $n_e/10^{19}$ < 7 / 0.05 < P_{Div}/ Pasc.<0.3
τ_{th} / $P_{Div}^{-0.2} \cdot P_T^{-0.55}$	I_p	6 < $n_e/10^{19}$ < 8
τ_{th} / $P_{Div}^{-0.2} \cdot P_T^{-0.55} \cdot I_p^{0.65}$	n_e	

Table III : Sequence of the Regression by Steps

This question must be addressed in further work because it has a dramatic effect on the projection to ITER with 300 MW heating power.

Reference

[1] F. Ryter IAEA-CN-64-/AP1-5 1996 Montreal
[2] W. Suttrop / his conference
[3] R. Neu et al Plasma Phys. Control. Fusion38 1996 A165
[4] IAEA-CN-56/F-1-3 /1992/ H-Mode Database Working Group (Pres. O. Kardaun)
[5] O. Gruber / this conference

Broadband Reflectometry to Investigate Profiles and Fluctuations during ELMS on ASDEX UPGRADE

M. Manso, J. Santos, I. Nunes, F. Nunes, B. Kurzan*, F. Serra, A. Silva, W. Suttrop*

Associação EURATOM/IST, CFN, Instituto Superior Técnico - 1096 Lisboa Codex
**MPI fuer Plasmaphysik, EURATOMAssociation, D-85748 Garching, Germany*

Introduction

Plasma fluctuations "print" their signature on the reflectometry signals but for profile inversion only the average beat frequency f_B is extracted and the perturbations due to fluctuations are regarded (together with the noise from the system) as problems to the profile evaluation. Here we apply a method based on the estimation of the time-frequency distribution (TFD) of the energy of the reflectometry signals, that gives both f_B and the profile perturbations. The broadband signals are nonstationary because their spectral characteristics vary along the sweep and the method uses the concept of instantaneous frequency (*fi*) that was introduced to describe the frequency of nonstationary signals at a particular time [1]. The *fi* is the first moment of the TFD with respect to the frequency [1]. Several TFD's can be used to estimate the *fi*, in our study we used the simplest one, the periodogram. This can be computed with a sliding window Short-Time-Fourier Transform (STFT), being applicable as long as the signals are locally (in each window) quasistationary; the method and its application to broadband reflectometry is described in [2]. The analysis contributes to the study of the physical phenomena underlying plasma fluctuations and the understanding of the effect of fluctuations on the profile will improve the accuracy of profile measurement from reflectometry.

2. Evolution of density profile and fluctuations during ELMs

In the experiments we probe the ASDEX Upgrade plasma with the simultaneous operation of several O-mode reflectometry channels [3], in the frequency range *F*: 17-70 GHz corresponding to densities *ne*: 0.4 - 6.5 x 10^{19} m^{-3}. The measurements were performed at the high field side (HFS) during the ELMy phase of shot #8180. The interval between consecutive sweeps was 5 ms and the sweeping time 100 μs. The first time window under analysis is between 1.31 s (sweep 123) and 1.315 s (sweep 124) corresponding to the beginning of the ELMy phase ($\overline{n_e} \cong 6$ x 10^{19} m^{-3}). The periodograms obtained at the peak of the first ELM (Fig.1, sweep 123) and after the ELM (Fig.1, sweep 124), reveal that the plasma layers are mainly disturbed for *ne* below 2.5 x$10^{19}$$m^{-3}$ (F_l < 45 GHz). The profile shape can be inferred from the

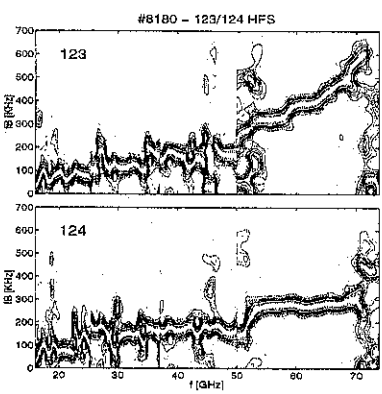

Figure 1

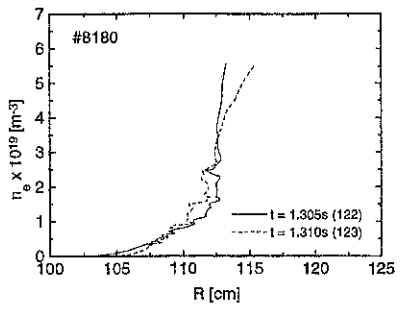

a) $n_{es} \cong 1.5 \times 10^{19}\ m^{-3}$

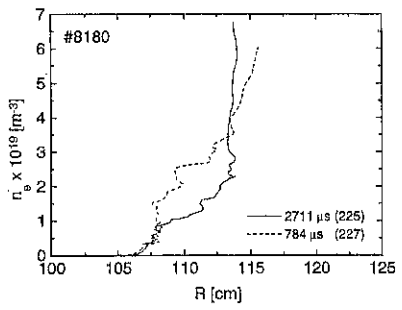

b) $n_{es} \cong 4.1 \times 10^{19}\ m^{-3}$

Figure 2

represented by plotting the amplitude of the D_α signal at the different sweeps. The time of reference for each sweep ($t' = 0$) is the rise time of D_α in the neighbouring ELM. The periodograms (Fig.4) reveal that the plasma is much more disturbed than in the previous case and the perturbations exhibits a rather different pattern, being stronger in the middle region, 30 - 55 GHz, 1 - 3.7 x 10^{19} m^{-3}. As in this case $n_{es} \cong 4.1 \times 10^{19} m^{-3}$, the disturbed region should be located close and outside the separatrix and may be associated with a satellite of the m=1 mode. In fact the same type of perturbation cannot be seen in the previous case where a large amplitude mode is not present. In addition, the perturbations are stronger even at inner plasma layers when the m=1 mode has the largest amplitude (sweep 227) and also when the mode ends at the

evolution of f_B, by taking into account that $F \propto \sqrt{ne}$, (horizontal axis) and f_B (vertical axis) can be converted into distance, after integration in F. During the ELM (Fig.1, 123) the profile flattens for $F > F_l$ (large increase of f_B), and it peaks (Fig.1, 124) in the same region after the ELM (very small increase of f_B). The density profiles (Fig.2 a) obtained directly from the first moment of the periodograms show that the profile flattening occur close and inside the magnetic separatrix, $n_{es} \cong 1.5 \times 10^{19}$ m^{-3}. Outside the separatrix the changes in the profile are very small, the plasma moves only slightly outward during the ELM.

The second window under analysis [1.815 s (sweep 224) - 1.845s (sweep 230)] is in the ELMy phase (see D_α signal in Fig.3 a), for $\overline{n_e} \cong 9 \times 10^{19}$ m^{-3}. In this interval the magnetic data shows that an m=1 mode is present, with increasing density (during the ramp up of a sawtooth event) until it ends at the sawtooth crash, occurring at 1.83s and preceding the peak of the ELM at 1.835s (sweep 228). The phases of the ELMs covered by the selected sweeps can be seen in (Fig.3.b), where a fictitious "ELM" is

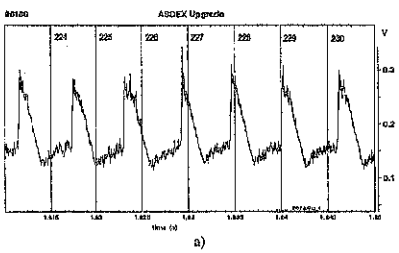

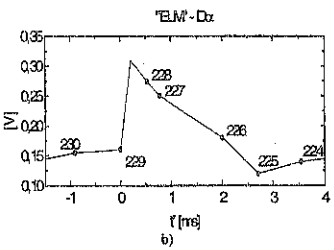

Figure 3

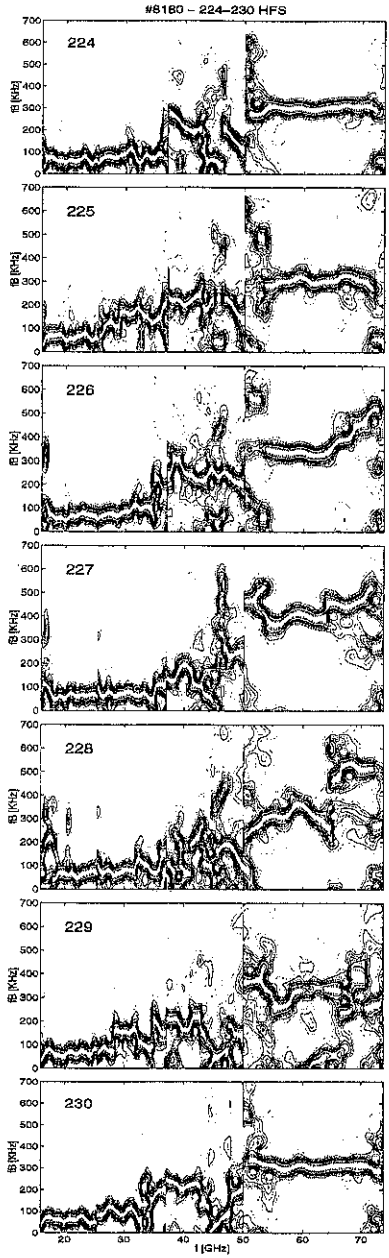

Figure 4

sawtooth crash (sweep 228). The changes of the density profile along the "ELM" observed in the periodograms (Fig.4), can be viewed in more detail from the evolution of the power spectrum at specific density layers, or frequencies F, (Fig.5). At the inner region, (Fig.5.e, f), the beat frequency (dashed line) increases abruptly at the onset of the ELM and decreases after, showing that the flattening of the profile coincides with the rise of the D_α signal. It should be noted that a low frequency perturbation appears at the onset of the ELM. For $t \geq$ 500μs the profile is already peaking whereas in the neighbouring layers, (Fig.5. g, h), the profile movements are less pronounced and are delayed by $\Delta\ t \approx$ 500 μs. This seems to indicate that the profile changes start inside the separatrix and "propagate" and damp towards the separatrix, $F(n_{es}) \cong 60$ GHz. At outer regions, $n_e \leq$ 0.65 x 10^{19} m^{-3} ($F \leq$ 23 GHz), the profile does not change significantly

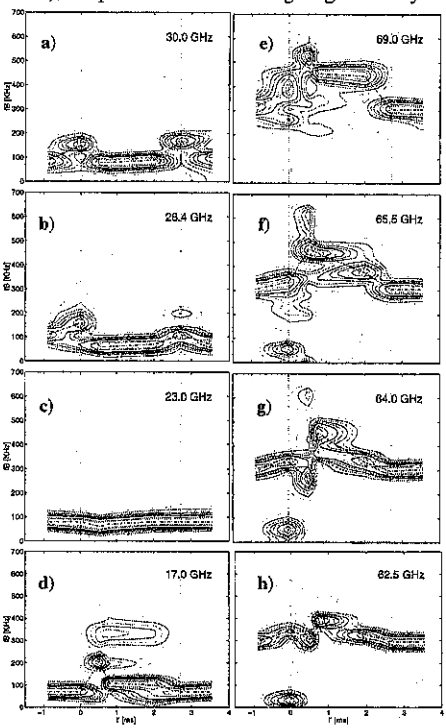

Figure 5

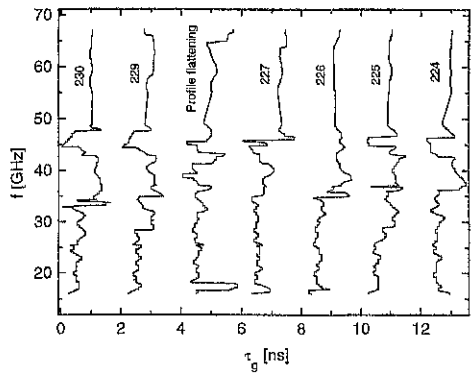

Figure 6

(Fig.5 c), suggesting that the separatrix region acts as a kind of "joint", for profile movements. Indeed, the crossing point of the profiles during an ELM and between ELMs in both studied cases, Fig.2 (a, b), occur at a density close to n_{es}. Outside the strongly disturbed zone, $F < 35$ GHz, the profile is quiescent except in a very narrow region (Fig.4, sweep 228), at the outer edge (F=17 GHz, ne= 0.37 x 10^{19} m^{-3}). The perturbations are observed coinciding with the profile peaking at the inner region (Fig.5 e, f), suggesting that there may be a link between inner and outer plasma layers. It should also be noted that at the edge, some layers (Fig.5 a, b) are displaced inwards at the beginning and at the end of the ELM. The changes of profile and perturbations along the "ELM" can be viewed simply in the τg curves (Fig.6) obtained from the maximum peak of the periodogram. This provides a direct tool for a first analysis of profile evolution.

3. Discussion

We applied a new data analysis method to broadband reflectometry which unfolds the energy associated with the reflection from the plasma and the energy scattered by fluctuations, giving its particular location in time (density) and frequency.

From the point of view of profile evaluation this is very important because it avoids the use of narrow digital filtering to extract τg and therefore retains details of the group delay curve that may be important for profile accuracy. It is also valuable when a significant part the energy is scattered by fluctuations and many spectral peaks exists. Profiles measured in ASDEX Upgrade during an ELM, show that the profile flattens inside the separatrix coinciding with the rise of the D_α signal; for $t \geq$ 500 μs the profile is already peaking and continues until a new ELM occurs. The profile changes in each density layer and the evolution of the local energy spectrum of plasma perturbations were obtained with great detail from the history of the energy spectrum in each window of analysis. Strong perturbations are present during ELMs and between ELMs, in the middle region of the plasma and at the onset of the ELM, in the inner zone where the profile flattens.

Further studies and more detailed experiments (with sweeps of 20μs, spaced by 30μs) are foreseen to determine if the observed perturbations can be attributed to MHD activity.

Acknowledgements - This work has been carried out in the frame of the Contract of Association between the European Atomic Energy Community and "Instituto Superior Técnico" and has also received financial support from JNICT and PRAXIS XXI.

[1] B. Porat (1994), Digital Processing of Random Signals, Prentice-Hall, Englewood Cliffs.

[2] J. Santos et al., (1997), III Reflectometry Workshop for Fusion Plasma, Madrid.

[3] A. Silva et al., (1996), Review of Scientific Instruments 67 (12), 1996.

Continuous tracking of density profile build-up during L-H transition on ASDEX Upgrade from microwave reflectometry

F.Serra, A.Silva, B.Kurzan*, M.E.Manso, T. Grossmann, J.Santos and W.Suttrop*

Associação EURATOM/ IST, Centro de Fusão Nuclear, 1096 Lisboa Codex, Portugal
** Max-Planck-Institut für Plasmaphysik, EURATOM Association, D-85748 Garching, Germany*

1. Introduction

The microwave reflectometry system on ASDEX Upgrade uses O-mode (at high-field (HFS) and low-field (LFS) sides), X-mode (low-field), and can operate at broadband ultrafast sweep ($\geq$ 20 μs) and at fixed frequency, probing densities up to ~ 6.5×10^{19} m^{-3} /1/. With fixed frequency specific plasma density layers are probed at a rate of 1 μs (sampling frequency: 1 MHz). A technique to track the plasma position of fixed density layers is presented and demonstrated for the density profile evolution during L- to H- transitions.

The temporal evolution of the frequency spectra of the reflected signals (with 300 kHz maximum imposed by the data acquisition rate) shows an abrupt reduction of the turbulent fluctuations at the L - H transition. The reduction is observed both at the high and low-field sides and permits to identify the time of transition (aside from the decrease of the D_α signal) with high temporal resolution. In the spectral content of the reflected signals a clear low-frequency oscillation ($\leq$ 500 Hz) is also observed around the L-H transition, due to the radial displacement outwards of the reflecting layer as the edge density gradient increases. From the corresponding phase and amplitude variations the incremental shift of the position of the reflecting layers can be inferred, with an accuracy (in the millimetre range) defined by the high temporal resolution of the detected fringes (3μs). Therefore, the profile build-up following the L-H transition can be tracked revealing the temporal development of the transport barrier.

2. Analysis of turbulence during an H-mode discharge

In a homodyne system the detected signal is sensitive to amplitude and phase fluctuations, such that $V(t) = A(t) \cos \phi(t)$, where $\phi(t)$ is the phase difference between the signals from the plasma and the reference arm. A reflection layer at a fixed equilibrium position leads to a constant phase angle. Density fluctuations will cause displacements and corrugations of the refractive index surfaces, leading to amplitude and phase variations that will have impact on the spectral components of the detected signal.

The temporal evolution of the power spectra is obtained using a FFT sliding technique. Fig. 1 c-e shows the contour plots , corresponding to three probing frequencies: 22.7 GHz ($n\sim0.64\times10^{19}$ m^{-3},at the HFS),31.7 GHz ($n\sim1.24\times10^{19}m^{-3}$,close to the magnetic separatrix, at the LFS), 45.7 GHz ($n \sim 2.58\times10^{19}$ m^{-3} , LFS), for # 8595; it is a discharge with unfavourable gradB drift direction (away from the X-point), where the H-mode is attained through ctr-NBI with high heating power (Fig. 1a). An abrupt reduction in the power spectrum of the turbulent fluctuations is observed both at the high and low field sides, that permits to identify the time of the L-H transition (t=1.704s) aside from the decrease of the Dα signal (Fig. 1b).

Although the reduction of density fluctuations occurs at the transition (simultaneously) for all the probed layers (that should therefore be located inside the suppression zone where the

transport barrier builds-up), there is a distinct behaviour when analysing the discharge from the OH to the H phases: at the HFS, outside the separatrix, the frequency spectrum extends up

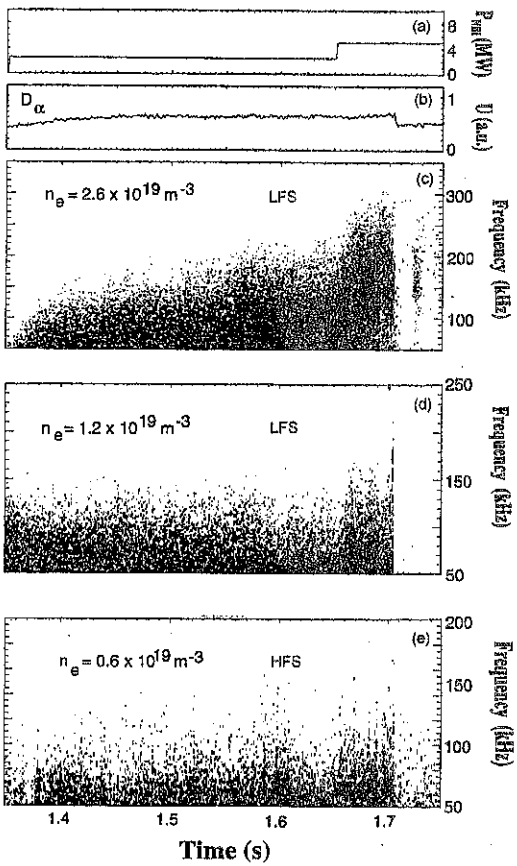

Fig.1

to ~ 100 kHz (Fig.1e); at the LFS, close to the separatrix, it extends to ~ 150 kHz (Fig. 1d)with an almost constant temporal behaviour until the transition; in contrast, inside the separatrix, at LFS,a broadening of the frequency spectrum occurs correlated with NBI, specially with high heating power (after 1.65 s) and reaching ~ 300 kHz just before the transition (Fig.1c). The observed broadening might be due to Doppler shift in the reflectometer signals induced by an E×B poloidal velocity rather than an increase of density fluctuations. The significant increase of the ExB velocity before the L-H transition inside the separatrix is consistent with the detected increase of the radial electric field (E_r) at the edge, as will be discussed in section 3. (see Fig. 2);the distinct behaviour at different radial positions suggests the existence of a highly sheared E×B flow leading to better confinement through the decorrelation of the turbulent fluctuations, the accepted scenario to trigger the L-H transition.

3. Detection of density profile modifications during the L - H transition

In the spectral content of the reflected signals a clear low-frequency oscillation ($\leq$ 500 Hz) is observed around the L-H transition; it is caused by movements of the reflecting layer associated with radial displacements of the layer during the density profile build-up associated with confinement improvement. In Fig.2 b , the low pass filtered reflectometry signal obtained from the raw data of Fig. 2a (referring to layer $n_e \sim 2.58\times10^{19}$ m^{-3} , LFS) is shown. Periodic oscillations start at t ~1.69s, coinciding with the slow increase of the radial electric field E_r before the transition; this rise in E_r is inferred from changes in the fluxes of ripple-trapped charge exchange (CX) neutrals /2/, (Fig. 2e),in parallel to the edge pressure gradient, revealing an improved confinement still in the L phase (with increasing $n_{e,edge}$ (Fig.2c), and with the presence of ELMs (Fig.2d)).

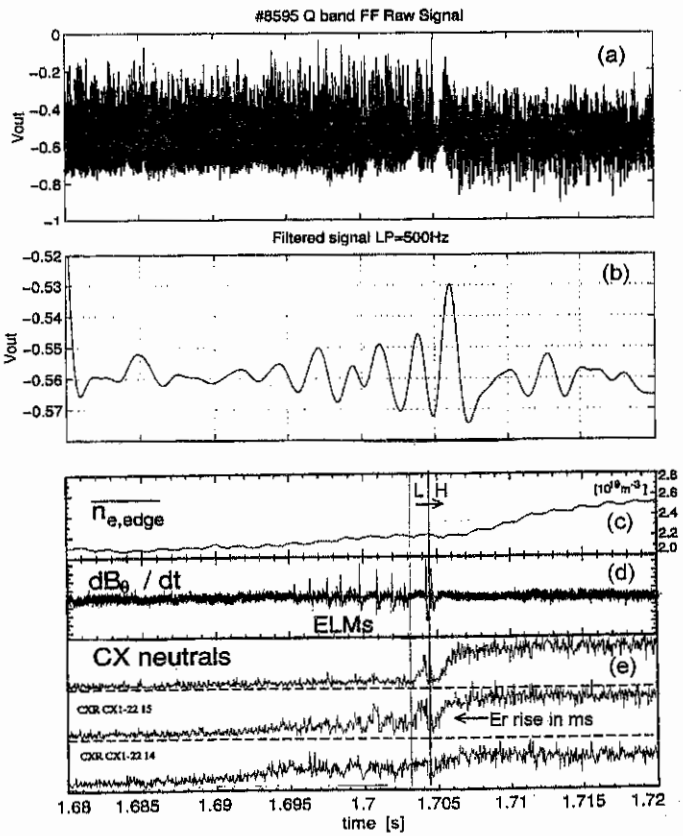

Fig. 2

After the L-H transition (t ~ 1.704s), a fringe with high amplitude is observed revealing a radial displacement outwards of the probed layer (towards the receiver antenna), corresponding to the profile build-up during a time interval of ~ 2.5 ms. On the same time

interval a fast increase of E_r occurs (Fig.2e), consistent with the build-up of the edge transport barrier following the abrupt drop in turbulence.

The profile evolution at the edge can be inferred by estimating the incremental displacements of the layer. Using a numerical code /3/ which takes into account the antenna-plasma geometry of the reflectometry system and assuming the shape of the evolving density profile (with increasing mean density and no global radial displacement) , the estimated displacement of the reflecting layer (ΔR_c) corresponding to one fringe variation is ~ 0.6 cm; a similar result is obtained through the relation $\Delta R_c \cong \lambda_0 \Delta\phi / (4\pi \overline{N})$, with the mean refractive index $\overline{N}$ = 0.6. Assuming as an initial profile the one from Li-beam at 1.7s, a radial displacement of 1.2cm (2 fringes) between 1.703s and 1.708s will lead to a steepening of the edge gradient from ~ 0.6×10^{21} m^{-4} to ~ 1.0×10^{21} m^{-4}.

The impact on the density profile of the full development of the transport barrier might therefore be tracked with the "continuous" temporal probing of several density layers (from the edge up to the bulk plasma), as foreseen for the next measuring campaign (with probed densities up to ~ 14×10^{19} m^{-3}). However, an heterodyne detection system for the direct measurement of the phase will be important in order to overcome ambiguities that might occur with fringe detection when the plasma layers move back and forth (as in the profile changes caused by ELMs).

4. Concluding remarks

In addition to information about the abrupt decrease of turbulence and about the increase of plasma rotation at the L - H transition, the spectral content of the reflected signals can also give insight about density profile changes. By low-pass filtering the spectra of the reflected signals, fringes due to radial displacement of the density layers during the profile build-up can be identified. With this technique the incremental shift of the position of the reflecting layer can be estimated with an accuracy in the millimetre range.

A new reflectometry channel has been recently installed for monitoring the L - H transition on ASDEX Upgrade, to operate in fixed frequency, independently of the other channels. Simultaneous measurements with fixed frequency and broadband operation in the same discharge (as foreseen for the next measuring campaign on ASDEX Upgrade), will provide density profile measurements with high temporal and spatial resolutions and further indication about the absolute position of the layers probed in fixed frequency. The potential of a such a highly performant reflectometry diagnostic suggests the possibility of tracking continuously the motion of plasma layers associated with important physical phenomena where fast profile changes occur (such as L-H transition, ELMs and MARFES).

Acknowledgments

This work has been carried out in the frame of the Contract of Association between the European Atomic Energy Community and "Instituto Superior Técnico" and has also received financial support from "Junta Nacional de Investigação Cientifica e Tecnológica" and PRAXIS XXI.

References

/1/ A. Silva et al., Rev. Sci. Instrum. 67 (12), 1996.
/2/ W. Herrmann et al., Phys. Rev. Lett. 75, 4401, 1995.
/3/ T. Grossmann et al., this Conference, 1997.

A 2-D Code for the Analysis of Microwave Reflectometry Measurements in Fusion Experiments

M.T. Grossmann, E. Holzhauer [1], M. Hirsch [2], F. Serra, M. E. Manso, I.Nunes

Associação EURATOM/IST, Centro de Fusão Nuclear, 1096 Lisboa Codex, Portugal
[1]Institut für Plasmaforschung, Universität Stuttgart, D-70569 Stuttgart, Germany
[2]Max-Planck-Institut für Plasmaphysik, EURATOM Association, D-85748 Garching, Germany

I - Introduction

In reflectometry experiments density fluctuations affect the propagation and reflection from a cut-off layer of electromagnetic waves. For a quantitative analysis of density fluctuations, 2-D effects (e.g. refraction and scattering) and the transverse field distribution of the microwave beam must be considered. The variation in the plasma parameters along the confining toroidal magnetic field can be neglected justifying a 2-D treatment. Several 2-D numerical codes (using finite difference methods) for the solution of the wave equation in plasmas have been recently developed /1/, /2/, /3/. Here we use a 2-D numerical code based on a spatially distributed RLC networks /4/ to model the full-wave equation in an inhomogenous plasma. The code is easily adapted to different antennae-plasma configurations and wave propagation in both O-mode and X-mode.

The code was applied to study the influence of poloidally propagating density fluctuations on reflectometry measurements at the W7-AS stellarator. A poloidal density modulation acts like a phase grating transferring part of the incident carrier into sidebands at different angles. A special feature of this experiment is the finite tilting angle of the symmetry axis of the transmitter/receiver antenna system versus the direction normal to the plasma surface. Therefore the reflected carrier and the sidebands are seen with different efficiency by the receiver antenna.

As observed experimentally, when there is asymmetry of the signal components, the numerical simulation reveals the existence of an anomalous drift of the phase ("phase runaway") above a given threshold value for the density fluctuation amplitude required.

II - Numerical code

The propagation of electromagnetic waves in an inhomogeneous medium can be described by an equivalent electric network consisting of inductance L, capacitance C and resistance R. The characteristics of the macroscopic density profiles and the small-scale fluctuations define the values of the network components./4/. If absorption processes in the plasma can be neglected the circuit reduces to a LC-network which, for the 2-D case, is shown schematically in Fig.1. The inductance in series is given by $L=\mu_0\Delta x$ and is kept constant. The spatial variation of the plasma parameters is contained in $\varepsilon(x)$ being the capacitance in parallel given by $C(x)=\varepsilon(x)\Delta x$, where Δx is the dimension of a plasma element with constant electron density n_e. In the calculations the grid size is $\Delta x \leq \lambda_0/12$.

The input impedance for every input node of the electrical network is calculated using matrix inversion programs. The transverse distribution of the input field is described by the input voltages (phase and amplitude). In analogy the individual return currents yield the transverse distribution (phase and amplitude) of the reflected filed.

The calculation has three basic steps: (i) Free-space propagating from transmitter antenna to plasma boundary. (ii) RLC-code for propagation and reflection in the plasma. (iii) Free-space propagation from plasma boundary to receiver antenna.

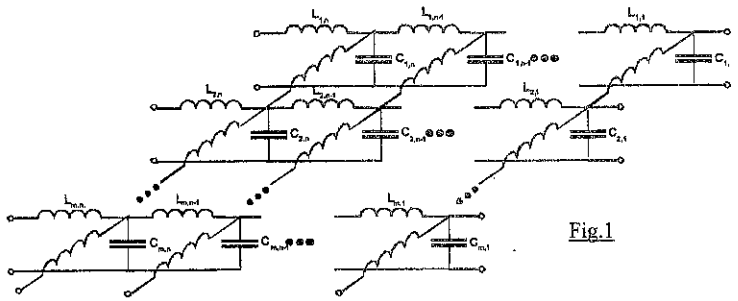

Fig.1

III - Phase runaway at the W7-AS reflectometry system

Depending on the operational range of the W7-AS stellarator a strong drift of the phase ϕ is observed ($d\phi/dt$ ~ 100 - 200 kHz) which is usually referred to as "phase runaway". It is too large to be originated by a realistic radial movement of the cut-off layer. To explain it, poloidally propagating fluctuations have to be included and therefore 2-D calculations must be performed.

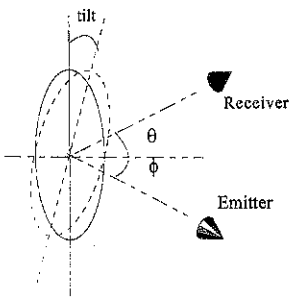

Fig.2

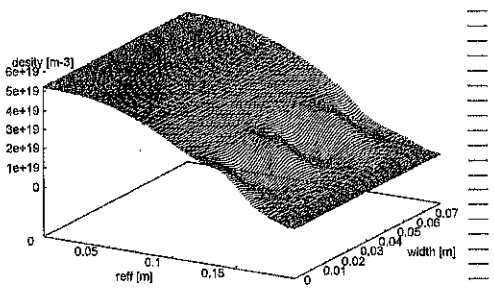

Fig.3

The reflectometry system installed at W7-AS /5/ operates with X-mode in the W-band (75-110) GHz . The two conical antennae use elliptical mirrors to produce a gaussian beam focused near the plasma edge. The antennas are oriented towards the torus axis and are separated by 12° with their symmetry axis in the equatorial plane. The plasma surface is not exactly perpendicular to the equatorial plane but is slightly tilted by 2.6°. In Fig.2 is shown schematically the antennae geometry considered in the 2-D simulation: tilt=2.6°, $\theta + \phi = 12°$. The radial density and magnetic field profiles represent typical operating conditions. Fig. 3 shows an example with $n_e(0)=5\times10^{19}m^{-3}$, and a periodic density modulation (with fixed amplitude and wavelength) propagating in the poloidal direction, radially localised around the reflecting layer (at r_{eff}~ 14 cm, for f = 85 GHz).

Calculations are performed for every time step of the poloidally propagating fluctuation. The receiver antenna signal is characterised by its complex amplitude (real and imaginary part).

Fig.4 shows the evolution of the complex amplitude during one cycle of the perturbation, for increasing amplitude of the fluctuations and tilt=2.6°. The threshold amplitude of the fluctuation for the onset of the phase runaway is 0.05 (normalised amplitude).

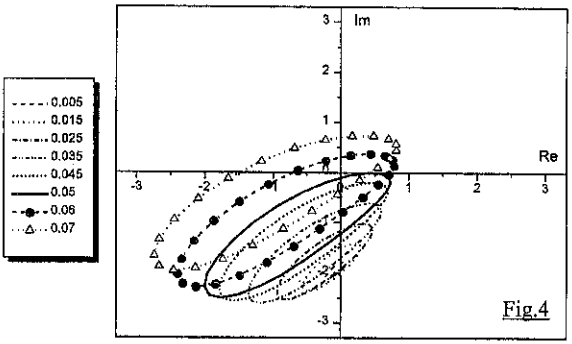

Fig.4

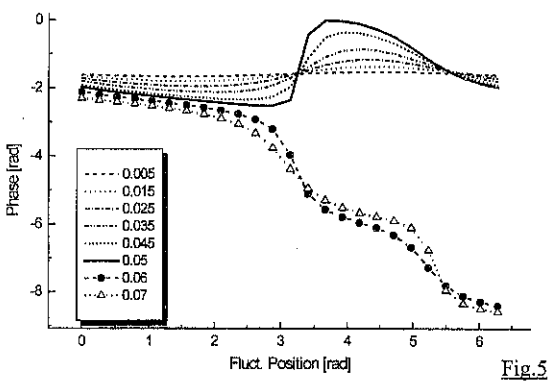

Fig.5

As can be seen from Fig.5, for small fluctuation amplitudes the output phase oscillates around its mean value. Once the threshold amplitude is reached, a jump of π in the phase occurs. As the amplitude increases further the phase continues to drift continuously in the same direction. In addition, the temporal behaviour of the signal amplitude (not shown here) is in agreement with experimental observations. The minimum of the amplitude occurs when the phase jumps by π due to destructive interference between signal carrier (ω) and sideband ($\omega \pm \Delta\omega(t)$).

The frequency shift of the scattered sideband signal is $\Delta\omega = \vec{k}_{pol} \cdot \vec{v}_{pol}$, where $\vec{k}_{pol}$ is the poloidal wavevector and $\vec{v}_{pol}$ is the poloidal propagation velocity of the fluctuation. A good agreement with theoretical predictions is found /6/. As expected, no phase runaway is found when the tilt angle is set to zero.

In. Fig.6, as the amplitude of the density perturbation increases beyond the threshold (up to 0.11), the receiver output is dominated by the frequency shifted component. The phase changes continuously as $\phi(t) = \Delta\omega t$, that is, the signal obtained at the antenna output is Doppler shifted by $\Delta\omega$ and therefore a drift of the phase with constant mean slope is detected by the reflectometer ("phase runaway").

The numerical results presented in Fig.6 predict that the mean slope of the phase drift reverses with the poloidal propagating velocity. Values of $d\phi/dt \sim \pm 100$kHz are obtained, with $k_f = 2\ cm^{-1}$, $V_{pol} \sim 3.2$ Km/s. This agrees with the results in the experiment where the

inversion of the plasma poloidal rotation direction is accomplished by inverting the magnetic field.

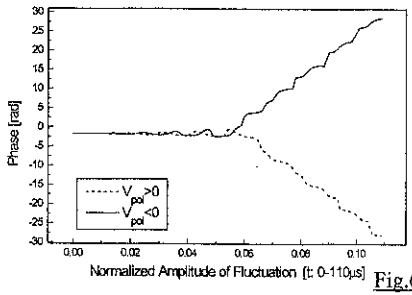

Fig.6

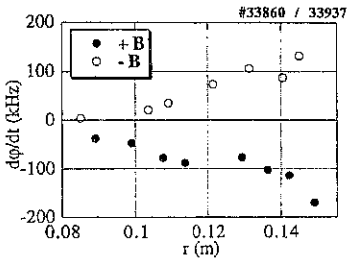

Fig.7

Fig. 7 shows the radial dependence of the phase drift measured at W7-AS for both signs of the magnetic field. For these experiments a direct comparison of the phase runaway (and the deduced poloidal propagation velocity) with spectroscopy measurements of the plasma rotation could be made /7/. The simulation results shown in Fig.6 fit the two symmetric experimental points obtained at $r_{eff} \sim 0.14$m shown in Fig.7.

IV- Concluding Remarks

A 2-D code based on spatially distributed RLC networks has been used to model the propagation of electromagnetic waves in a plasma with density fluctuations.

The code was applied to the study of poloidally rotating periodic structures in X-mode reflectometry experiments at the W7-AS stellarator. Good agreement with experimental results was found. The finite tilt angle of 2.6^0 from the vertical direction was identified as the necessary condition for the observed phase runaway. It could be shown that there exists a threshold value for the amplitude of the density fluctuation needed to observe the runaway phenomenon. The experiments performed with the reflectometer have showned that this value can easily be surpa ssed by the density turbulence in the L-mode or during ELMs.

Acknowledgments

This work has been carried out in the frame of the Contract of Association between the European Atomic Energy Community and "Instituto Superior Técnico" and has also received financial support from "Junta Nacional de Investigação Cientifica e Tecnológica" and PRAXIS XXI.

References

/1/ Fanak, I.Boucher, F.Clairet, S.Heuraux, G.Leclert, X.L.Zou, 22nd EPS IV-409, Bournemouth, 1995
/2/ G.D. Conway, L. Schott, and A. Hirose, Rev. Sci. Instrum. 67 (11), 1996
/3/ J.Irby, S.Horne, I.Hutchinson, P.Steek, Plasma Physics and Controlled Fusion 35 601, 1993
/4/ E.Holzhauer, G.Rohrbach, IAEA TCM on Microwave Reflectometry for Fusion Plasmas JET Joint Undertaking, March 1992
/5/ M.Hirsch, H.Hartfuss, T.Geist, E. de la Luna , Rev. Sci. Instrum. 67 (5), 1807, 1996
/6/ M.T.Grossmann, E.Holzhauer, M.Hirsch, F.Serra, M.E.Manso, I.Nunes, III Reflectometry Workshop for Fusion Plasmas. CIEMAT, Spain, May 1997.

Fast Determination of T_i-Profiles from Analysis of Neutral Flux Measurements

H.-U. Fahrbach, O. Kardaun, J. Stober, Yu.N.Dnestrovskij †,
W. Herrmann, A. Khutoretsky †, and the ASDEX-Upgrade team
Max-Planck-Institut für Plasma-Physik, EURATOM-Association,
D-85748 Garching, Germany
† RRC "Kurchatov-Institute", 123182, Moscow, Russia

1 Introduction

Up to now the determination of the radial ion temperature profile [1] in ASDEX-Upgrade from the energy spectrum of neutral particles uses the EIRENE Monte-Carlo code [2] for the calculation of the neutral density profile. This method is restricted to investigations of special interest, because of the necessary long computing time. For online evaluation during experiments a fast automatic procedure is needed. The classical logarithmic slope evaluation [3] is limited to low density and/or high temperature plasmas and does not provide profile information. Therefore a new computer code CENS [4] has been developed. It avoids specific Monte Carlo runs, but uses information about the neutral density obtained by such calculations in the past.

2 Measurements and method of evaluation

The energy spectra of hydrogen and deuterium neutrals are measured with two Neutral Particle Analyzers [5]. The neutrals are ionized in a hydrogen gas cell, separated in energy and mass by a magnetic and an electric field, and detected by 2 sets of 10 channeltrons. Figure 1 shows the geometry of the CX diagnostic at ASDEX-Upgrade.

The neutral flux emitted from the plasma is described by an integral over the line of sight [1]. The integral contains the profiles of the ion and electron temperature, T_i and T_e, the ion, electron and neutral density, n_i, n_e and n_n. The determination of the T_i profile is a difficult ill-posed non-linear problem, for which no simple method is available, and as much information about the other profiles as possible has to be taken into account. The n_e and T_e profiles and the magnetic flux surface geometry are taken from other diagnostics, but the neutral density cannot be measured until now and is the main obstacle for a straightforward determination of T_i.

Two groups of neutrals have to be distinguished: The 'wall' neutrals, which penetrate from the plasma boundary into the plasma and the neutrals due to volume recombination, which are calculated according to standard formulas [6] and added to the wall neutrals. In the central plasma region they can be the dominating part, when the density is high and/or the temperature low. In that case, the neutral problem is less severe. CENS uses a parametric representation of the wall neutral density, obtained from fits to Monte-Carlo calculated wall neutral profiles of discharges with very different properties. The following function was found to describe the profiles sufficiently well for our purposes [7,8]:

$$\ln n_{n,w}(\rho) = \ln n_{n,w}(1)(1 + k_n(1-\rho))^{-1/3} \qquad (1)$$

The parameters are $n_{n,w}(1)$, the wall neutral density at the edge, and k_n, a monotonic function of the dimensionless inverse fall-off length, which determines the shape of the profile. In Fig.2 the wall neutral density profile as obtained by EIRENE simulations and the approximation with the function above are shown for some ASDEX-Upgrade discharges.

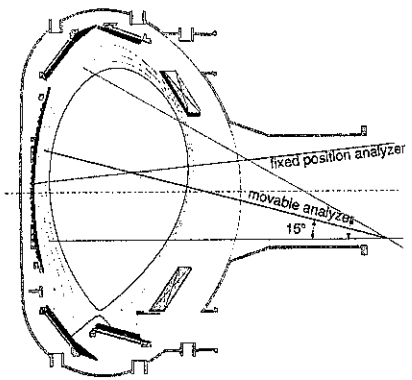

Figure 1: Viewing lines of the two Neutral Particle Analyzers in the poloidal plane. The movable analyzer can be turned also in toroidal direction.

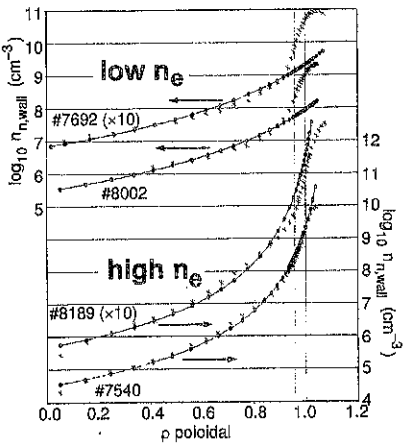

Figure 2: Density profiles of wall neutrals, calculated from simulation by the EIRENE code (stars) and fitted by the analytical function class (circles+line) in Eq.(1).

The CENS code fits the neutral profile simultaneously with a spline function model for the T_i profile by minimizing the deviation between the simulated and the measured fluxes. The parameters to be fitted are the T_i values at the knots, $\ln(n_{n,w}(1))$ and k_n. To get an estimate for the reliability and the accuracy of the results, pseudo-random noise according to the experimental errors is added to the neutral flux input data and the profiles are repeatedly calculated. In a first step the behaviour of CENS was studied in the so-called quasi-experiment mode [8], where the solution is known. Here we concentrate on processing of experimental data from plasmas in ASDEX-Upgrade.

3 Processing of experimental data

The program CENS provides a number of parameter options and modes, which make it a versatile tool and suitable for rather different conditions. The optimal operational range, where it recovers well the basic features of the T_i profile, but avoids the creation of oscillations and other artefacts, had to be found. For this purpose the following quantities were varied and the results compared with complete EIRENE simulations: 1. the number of spline knots, 2. the strength of Tikhonov regularisation, which favours solutions with low curvature, 3. the starting profiles, 4. the range of the flux spectrum 5. the amplitude of pseudo-random noise added to the experimental fluxes.

Satisfying results were obtained in a sufficient wide range of parameters. In particular the choice of the initial conditions is not critical. The optimal number of spline knots is 4 to 6. With 6 knots a moderate amount of Tikhonov regularisation is necessary; with a lower number of knots it can be reduced considerably.

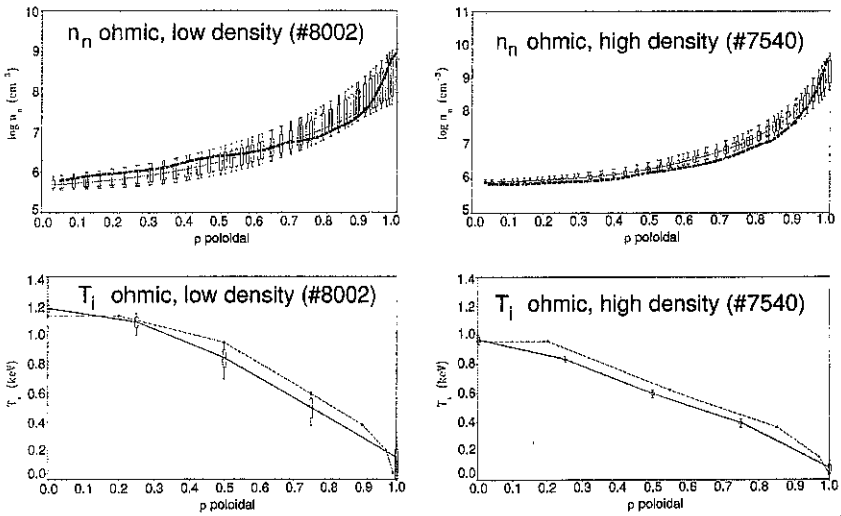

Figure 3: Ion temperature and neutral density profiles as a function of the normalised flux-surface radius ρ, for two ohmic discharges. The solid lines connect the median values. The boxes denote the interquartile ranges $Q_{75} - Q_{25}$, and the whiskers 90% interval estimates $Q_{95} - Q_5$. The dashed lines are a reconstruction based on EIRENE Monte Carlo simulations of the neutral density, in which additional measurements from the CX LENA diagnostic have been used. The accuracy (interquartile range) of latter reconstruction is in the order of 10% for the ion temperature and of 30% for the neutral density profile.

In Fig. 3 the results for two ohmic deuterium discharges are shown: #8002 has low density and current ($3 * 10^{19} m^{-3}$, 0.6MA), #7540 higher density and current ($6 * 10^{19} m^{-3}$, 1MA). The asymmetric position of the neutral density median at ρ *poloidal* > 0.7 for #8002 indicates, that there are two groups of solutions. The small interquartile distances in the central plasma region are due to the large contribution of neutrals from volume recombination.

Fig. 4 shows the recovered T_i profiles for a hydrogen discharge with increasing plasma density and Neutral Hydrogen Injection power, as given in the table within the figure. The evaluation uses the deuterium fluxes, which are not disturbed by the Hydrogen Injection. The steep rise between curves 3 and 4 and following slow decrease (curves 4 to 6) of the ion temperature reflects the switching on of the heating power and the continuously growing plasma density. At the end of the ohmic phase and at the highest densities essentially no particles from the plasma center contribute to the flux. The flux

birth profiles provide limits for the radius, below which the T_i profile has to be regarded merely as an extrapolation of the outer parts with no local information. In fig. 4 this is indicated by the change from solid to dashed lines.

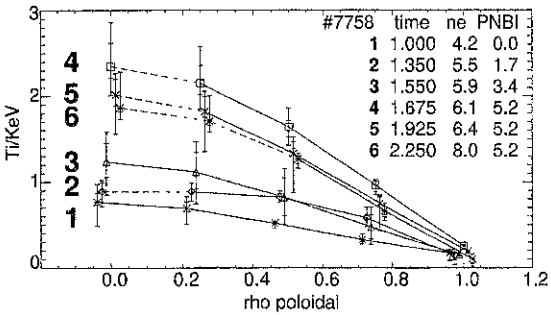

Figure 4: Ion temperature profiles of a discharge with increasing density and Neutral Beam heating power. The double error bars indicate the interquartile ranges $Q_{75} - Q_{25}$ and $Q_{90} - Q_{10}$, obtained from 80 realisations. Units: Time/s, $n_e/10^{19}m^{-3}$, PNBI/MW.

4 Conclusion

The CENS code allows fast determination of T_i profiles with an accuracy of 5 to 20 % over a reasonable range of plasma parameters. Simultaneously the wall neutral density can be determined with an accuracy of a factor of about 10. Regarding the huge dynamic range ($> 10^6$, see Fig.2,3) and the absence of measurements, such a determination of the neutral density profile may nevertheless be of interest. The computing time needed for one profile evaluation is about 1 minute on a standard workstation, depending on the desired accuracy of the interval estimates. Therefore, with CENS working in an automatic mode, it seems possible to provide temperature profiles for several selected intervals between two discharges. An overview about the T_i behaviour (about 10 profiles per discharge) for all discharges of a typical experimental day can be provided over night.

Part of this work was carried out under grant I/70032 of Volkswagen-Stiftung in 1995 – 1996.

References

[1] Stober J. et al., *Proc. of the 23nd EPS Conference on Controlled Fusion and Plasma Physics, Kiev, 1996,* **20C,III**, 1023 (1996), EPS

[2] Reiter D., *KFA Jülich reports*, **Jül-1947**, (1984), **Jül-2599**, (1992)

[3] Wagner F., *J. Vac. Sci. Technol.*, **20**, 1211 (1982)

[4] Yu.N. Dnestrovskij et al., IAE-5780/6, Russian Research Centre "Kurchatov Institute", Moscow, (1994)

[5] Bartiromo et al., *Rev. Sci. Instrum.*,**58**, 788 (1987)

[6] Yu.S. Gordeev et al., JETP. Letters, **25**, 204 (1977)

[7] O.J.W.F. Kardaun and A. Kus, IPP 5/68, (1996)

[8] A.V. Khutoretsky et al., Status Report of grant I/70032, Volkswagen Stiftung, 1997

Characterization of Edge Turbulence in Neutral Beam Injection and Ion Cyclotron Resonance Heated Plasmas in ASDEX Upgrade

B. Kurzan, T. Kass, M. Maraschek, J. Schweinzer, A. Silva*, W. Suttrop, ASDEX Upgrade-, ICRH-, NBI-Teams

Max-Planck-Institut für Plasmaphysik, EURATOM-Association, D-85748 Garching, Germany

**Centro de Fusão Nuclear, EURATOM-Association, Instituto Superior Técnico, 1096 Lisboa Codex, Portugal*

1) Introduction

With increasing additional heating power first a regime of low confinement, or L mode is reached, and beyond a certain threshold power the regime of high confinement or H mode is obtained [1, 2]. In neutral beam injection (NBI) heated L mode plasmas a density and magnetic fluctuation level higher than during Ohmic heating is observed in the plasma edge [3, 4]. A low turbulence level is obtained again in the H mode [3, 5]. With Ion Cyclotron Resonance Heating (ICRH) the fluctuations observed in the L mode on ASDEX Upgrade are lower than in NBI heated plasmas and are not suppressed during the L-H transition.

2) Diagnostics

For measuring the turbulence of the electron density and the radial magnetic field a reflectometry system in O mode polarisation [6] and small coils sensitive to high frequency magnetic fluctuations placed within a distance of 10 cm near to the plasma surface were used. Electron temperature and density profiles near the outer plasma edge are measured by a multichannel Electron-Cyclotron-Emission- and a Li-beam diagnostic [7] respectively.

3) Observation

The turbulence of the density and the magnetic field is visualized in the following (figs 1, 3) by contourplots after application of a sliding FFT to the signals. With the onset of the first NBI source a broadening of the bandwidth of the fluctuations of the radial magnetic field and of the electron density is observed (fig. 1). After the second beam source has been turned on an additional broadening of the fluctuation spectrum is observed, followed by a L-H transition clearly visible in the decreasing D_α intensity, after which the fluctuations are totally suppressed. The gradients of the electron density and temperature profiles do not change from the Ohmic to the first L mode phase (1.35 s – 1.40 s) at the position of measurement, fig. 2. Thus the turbulence driven by these sources should stay constant which, however, is not observed. The increase of the bandwidth until 1.7 s might be ascribed to an increase of the turbulence because of the then steeper edge gradients, or to a source which has its maximum at the plasma edge and is switched off at the L-H transition. When applying ICRH heating alone it is found that the turbulence level in a L mode plasma is lower than in a NBI heated L mode plasma. This turbulence is not suppressed at the L-H transition (fig. 3).

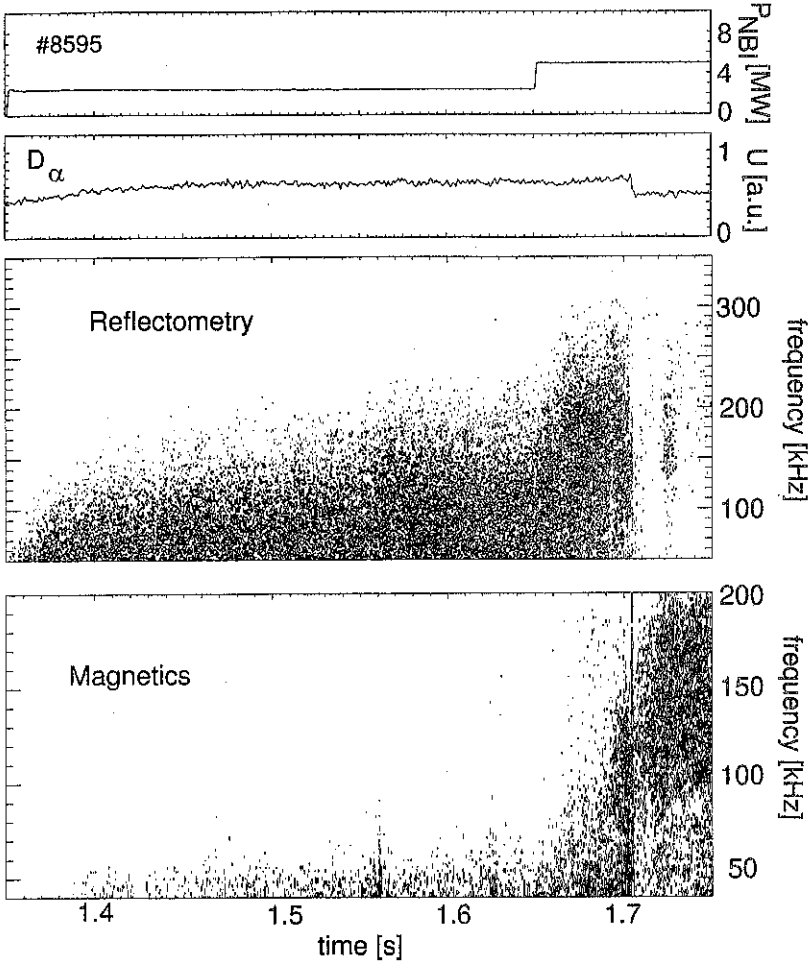

Fig. 1: The turbulence in a NBI heated L mode plasma is suppressed at $t = 1.704\,s$, *the time when also the* D_α *light at the divertor decreases, indicating the L-H transition. The turbulence quenching is observed both in the density, measured here by reflectometry (probed density* $2.6 \times 10^{19}\,m^{-3}$*) and in the radial magnetic field. In the H mode TAE modes with frequencies around 150 kHz are excited as clearly visible in the magnetic measurement.*

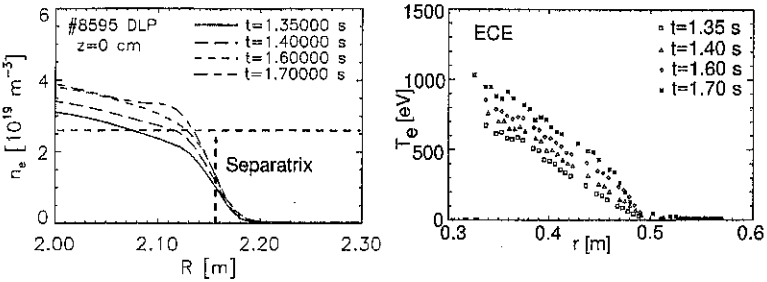

Fig. 2: Evolution of the profiles of the electron density and temperature at the plasma edge. The probed density layer in fig. 1 of $2.6 \times 10^{19}\,\mathrm{m}^{-3}$ *is indicated by a horizontal line.*

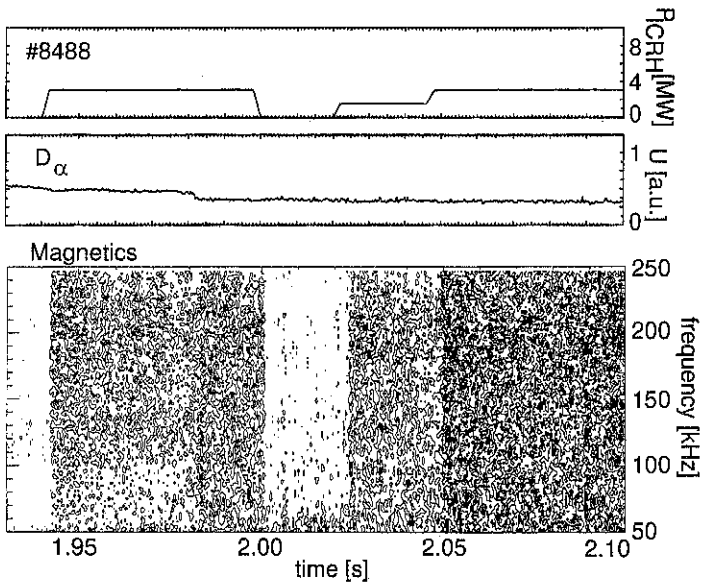

Fig. 3: The turbulence generated by ICRH is not reduced at the L-H transition at the time $t = 1.982\,s$ *as indicated by the decrease of the* D_α *light. In the Ohmic phase during the H mode where ICRH was switched off (2.000 — 2.020 s) the turbulence is reduced, confirming that the observed level is generated by ICRH.*

4) Characterization of the turbulence regimes with NBI heating

The neutral beam entering the fusion plasma is being partially ionized immediatally there. This zone of first ionization of the beam is one fast ion's gyroradius within the plasma because only there their space charge can be neutralized which is necessary for stable gyro orbits (degree of ionization there: 1%). The speeds of the slow, intermediate, fast Alfvén waves, c_{SL}, c_I, c_F were calculated at this position and compared with the beam speed v_b

resulting in $c_{SL} < v_b < c_I$ for the L mode (fig. 4). At the L-H transition the density profile

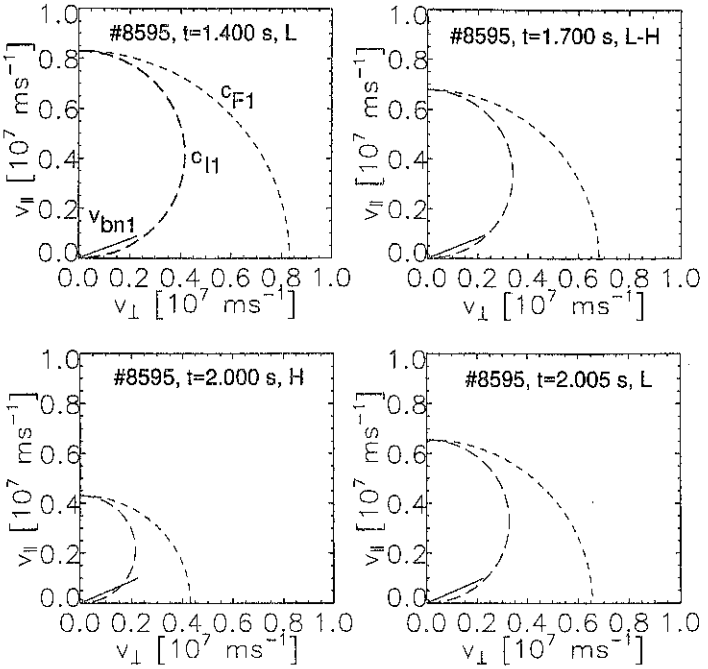

Fig. 4: Comparison of the beam speed (arrow) with the three Alfvén speeds at the plasma edge for the 3 phases L, L-H, H as indicated in the upper right corner of each plot (magnetic field 1.94 T, injection angle of the beam with respect to the magnetic field 72.8°, energy of the deuterium beam 60.5 keV, for the density and temperature of the deuterium plasma measured values were used).

steepens so that in the H mode $c_I < v_b < c_F$ is valid (fig. 4).

5) Conclusion

The different turbulence levels of the L and H mode observed only in NBI heated plasmas can be correlated with the relation of the beam speed with respect to the intermediate Alfvén speed at the plasma edge.

References

[1] F. Wagner, et al. Phys. Rev. Lett. 49 (19), 1408 (1982)
[2] D. W. Swain, Nucl. Fus. 21, 1409 (1981)
[3] ASDEX Team, Nucl. Fus. 29, 1959 (1989)
[4] O. J. Kwon, et al., Nucl. Fus. 28 (11), 1931 (1988)
[5] E. J. Doyle, et. al., Phys. Fluids B 3 (8), 2300 (1991)
[6] A. Silva, et. al., Fus. Techn. 1, 747 (1992)
[7] J. Schweinzer, et. al. Plasma Phys. and Contr. Fus. 31, 1551 (1989)

Motional Stark Effect Polarimetry for the Determination of the ASDEX Upgrade Current Density Profile

R. C. Wolf, P. J. Mc Carthy*, F. Mast, H.-P. Zehrfeld, and the ASDEX Upgrade Team

Max-Planck-Institut für Plasmaphysik, EURATOM
Association, D-85748 Garching, Germany
*University College Cork, Association EURATOM-DCU, Cork Ireland

1. Introduction. For the analysis of transport and stability of tokamak plasmas accurate knowledge of the current density profile and related quantities, such as safety factor and magnetic shear, is required. Motional Stark effect (MSE) polarimetry, which measures the internal local poloidal magnetic field, has become one of the most important methods for the determination of the current density [1, 2, 3]. At ASDEX Upgrade a 10-channel MSE polarimeter, using the modulation technique [4] and observing one of the 2.5MW, 65keV heating beams is under development.

2. Outline of diagnostic. The observation geometry crucially influences the performance of the polarization measurement. At ASDEX Upgrade the choice was to use one of four existing heating beams and to select one of 16 observation ports located every 22.5° between the toroidal field coils. As the heating beams are inclined at 4.9° to the midplane of the torus, a horizontal observation geometry could not be realized. For a selected, the three parameters pitch angle projection factor, spatial resolution, and spectral separation of full and half energy fractions have to be optimized simultaneously. An outline of the diagnostic with a planar view of the chosen observation geometry is shown in fig. 1. The resulting pitch angle projection factor, given by tan(polarization angle)/tan(pitch angle), ranges from 0.40 at the plasma centre to 0.75 at the plasma edge. The spatial resolution, determined by the angle between the viewing line and magnetic field, where the neutral beam volume intersects the viewing line, drops from 6cm at the plasma centre to 2cm at ρ=0.3 and rises again to 9cm at the plasma edge. The observation optics consists of a dielectric mirror followed by four lenses, which for each of the ten spatial channels images the neutral beam onto six vertically stacked 1mm diameter optical fibres. With a demagnification of 20 this corresponds to a 2cm wide and 12cm high spot in the plasma covering about 2/3 of the FWHM of the beam. The lens system exhibits an étendue of $\Omega A = 2.4 \times 10^{-6}$sr m^2 corresponding to f/1.4 at the fibre side, which is still below the theoretical limit of the fibres of f/1.

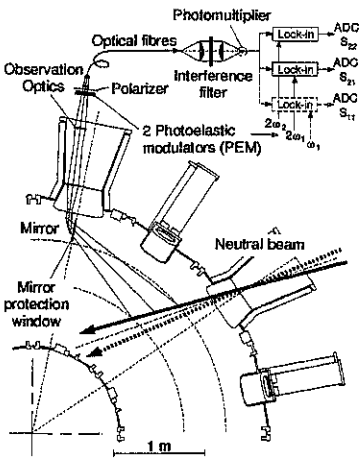

Fig. 1.: Outline of MSE diagnostic. The polarimeter design is similar to that described in [5].

3. Spectral simulation. A spectral simulation for the given geometry, taking beam and viewing line divergence as the main line broadening mechanisms, is shown in fig. 2. The

σ-component of the full energy fraction, which is to be used for the polarization measurement, is well separated from the π-component of the half energy fraction, which is the prime condition for a large polarization fraction at the σ-wavelength. In addition, the σ-component of the neutral beam used for MSE is, for all radii, sufficiently separated from the Stark spectrum of the other beam intersected by the viewing lines, to allow all heating beams to be operated simultaneously during MSE measurements. The optimum FWHM of the interference filters, derived from the spectral simulation, lies between 0.2 and 0.3nm depending on magnetic field and beam energy.

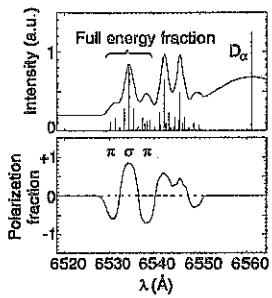

Fig. 2.: Spectral simulation of Doppler shifted Balmer-α beam emission spectrum and corresponding polarization fraction at ρ=0.3 for a 60keV deuterium beam, B_{tor}=2T, and T_i=3keV.

4. Faraday rotation. Faraday rotation in the MSE polarimeter, induced by the tokamak magnetic field, causes an offset in the polarization measurement. As suggested in [5], the use of Schott SFL6 glass with a Verdet constant of zero reduces the Faraday rotation significantly. For components not made of SFL6, such as the vacuum window or PEMs, a half wave plate positioned between the optical elements, so that the Faraday rotation angles before and after the half wave plate are equal, eliminates the net Faraday rotation. The condition of equal Faraday rotation angles means that in an inhomogeneous magnetic field B(x) using materials with different Verdet constants V(x) the integral along the optical axis $\int B(x)V(x)dx$ has to be the same before and after the half wave plate.

5. Influence of mirror. The use of a mirror is required, because a tangential access for the beam observation is not available. The polarization properties of the mirror, however, introduce a systematic error into the angle measurement (fig. 3). Here, the systematic error is the difference between the actual angle and that derived from the polarimeter signals. Two cases are distinguished in Fig. 3: (1) The apparent angle is deduced only from the ratio of the intensity modulation amplitudes at twice the PEM frequencies (dashed lines) and (2) in addition the phase shift is reconstructed from the modulation amplitude at the single PEM frequency (solid lines). It can be seen that for a horizontal viewing geometry, where the polarization angle of the σ-component is close to the mirror p-polarization, the systematic error approaches zero. At ASDEX Upgrade, however, due to the non-horizontal viewing geometry the polarization angle lies in the vicinity of 67° (shaded area), which requires corrections to the phase shift in order to minimize the systematic error.

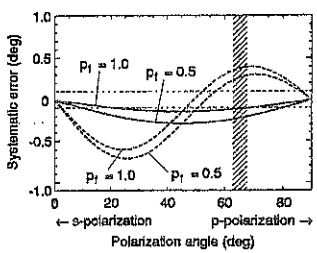

Fig. 3.: Systematic error introduced by a mirror (ρ_p=0.995, δ_p−δ_s=15°) as a function of polarization angle. The systematic error increases with decreasing polarization fraction p_f.

6. Current profile identification using MSE. To quantify the expected improvement in determining $j(R,z)$ with MSE measurements, a sensitivity study has been carried out using

a database of 1100 ideal MHD equilibria with 21 degrees of freedom, including I_p, B_t, 10 active and 2 passive poloidal field coil currents, and (with I_p scaled out) a 7-parameter $j_t = Rp'(\psi) + FF'(\psi)/(\mu_o R)$ profile family given by (with $\hat{\psi}$ the normalized poloidal flux)

$$p'(\hat{\psi}) \propto \hat{\psi}^{a_P} \exp\left\{b_P(1-\hat{\psi}) + c_P(1-\hat{\psi})^2\right\}$$

where a_P, b_P, c_P are randomly chosen for each $p'(\hat{\psi})$ profile, a_{FF}, b_{FF}, c_{FF} specify the $FF'(\hat{\psi})$ profile, and the 7th parameter determines β_{pol}. Reversed shear and edge pedestal profiles are easily generated with this family, and the wide range of current profiles in the database satisfies $0.5 < I_p < 2$MA, $1 < B_t < 4$T, $0 < \beta_{pol} < 2$, $0.5 < l_i < 2$, $0.5 < q_o < 4$, $2 < q_{95} < 6$, and reversed shear characterized by $1 \leq q_o/q_{min} < 4$.

6.1. Database Details. For each equilibrium in the database, all diagnostic data required for the study are calculated using the correct experimental geometry. These include 36 magnetic flux and field probes and 10 MSE channels. To gauge the usefulness of the MSE diagnostic compared to its main alternative, namely Faraday Rotation (FR) polarimetry (not to be confused with the nuisance effect of FR on the MSE measurements as outlined earlier), a hypothetical FR diagnostic on ASDEX Upgrade using the geometry of the 8-channel DCN (195 μm) interferometer is also simulated. For this purpose, a randomly generated $n_e(\psi)$ profile, chosen from a 5-parameter family, is assigned to each equilibrium and the differential equation describing the change in polarization along the beam path is integrated numerically so that Cotton Mouton effects are fully accounted for in the simulated FR measurements. Both MSE and FR geometries are shown in Fig. 4 and for the present database these yield angles with typical magnitudes of 5° for MSE and 8° for FR.

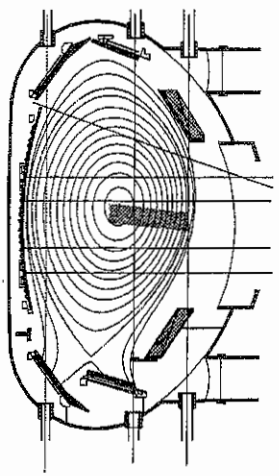

Fig. 4.: ASDEX Upgrade equilibrium flux surfaces. Shaded box near mid-plane indicates area spanned by 10 MSE channels. Geometry of 8 DCN channels is shown by straight lines criss-crossing the flux surfaces.

6.2. Identification Algorithm Starting from a baseline set of 36 equilibrium magnetic measurements and B_t, $j(R,z)$ identification representative of the entire database is monitored as MSE channels are progressively added to the baseline set. This is accomplished using the method of Function Parameterization [6] where here the current profile is regressed as a second degree polynomial whose arguments are B_t+16 principal components of the external magnetic measurements augmented by the MSE data. For the FR study, the MSE channels are replaced by the FR data consisting of two signals per channel, namely the line-integrated electron density and the rotation angle. The root mean squared errors (rmse) from the regressions are a measure of the recoverability of the current profile. For MSE, the finite spatial resolution of the viewing geometry (the horizontal resolution varies between 2 and 8 cm; the vertical resolution is 12 cm) is taken into account. For both MSE and FR, simulated measurement noise chosen from a uniform distribution in the range $\pm d°$ is added to the

"measured" angles. A sequence of runs was made with different values of d to determine the degradation of the recovery with increasing d.

6.3. Results. Fig. 5 shows 2×rmse, i.e. ≈ 95% confidence bands for $j(r,z)$ (where $r = (R-R_o)/a$ is a purely geometric quantity) identification along the $z = z_{mag.axis}$ plane (which spanned the range $0 \leq z_{mag.axis} \leq 0.2\,\mathrm{m}$ in the database) where both sets of data were perturbed by the experimentally expected noise level of ±0.2°. To facilitate the MSE/FR comparison, the outer two MSE channels were not used in this analysis. There is little to distinguish MSE and FR in the range $.5 < |r| < 1$. Near the plasma centre, however, the MSE identification is clearly better. For $j(r=0, z_{mag})$, the error reduction factor with respect to the baseline model is 4.2 for MSE, 3.1 for FR. The corresponding factors for $j(r=0.9, z_{mag})$ are 1.7 and 1.55. The localized nature of MSE may explain its superiority over FR at the plasma centre. Fig. 6 shows the effect of noise on the rms regression errors for the reversed shear indicator q_o/q_{min}. The rmse is trended for the cases of 3, 6 and all (9 for MSE, 8 for FR) channels included in the regressions (the point at infinity corresponds to the magnetics-only regression). As expected from their typical magnitudes (see 6.1.), the MSE measurements are more sensitive to noise than FR, although at a level of ±0.2° MSE is much more accurate than FR. Note the FR errors tend to reach a plateau. This was found to be due to the topological information present in the $\int n_e\, dl$ measurements, which were unperturbed by noise.

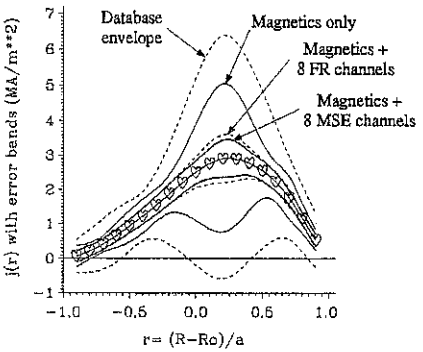

Fig. 5.: Mean $j(r, z_{mag})$ profile in the equilibrium database (♡) surrounded by (i) 2 × Std.Dev. envelope indicating the variation over the database of $j(r, z_{mag})$ about its mean, (ii) 2 × rmse confidence bands for the baseline (magnetics-only) regression, (iii) for the baseline set + all 8 FR channels, and (iv) for the baseline set + MSE channels 1-8, where noise of magnitude ±0.2° was added to both FR and MSE data.

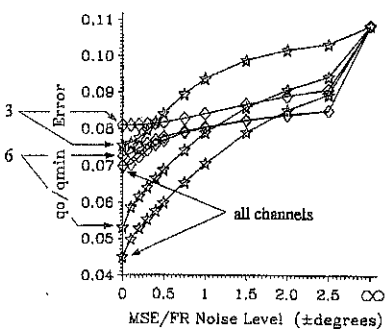

Fig. 6.: rmse for the parameter q_o/q_{min} versus error in the measured angle for MSE (⋆) and FR (◇) regressions with 3, 6, and all channels added to the Magnetics-only model.

6.4. Summary. Provided the experimental variation in $j(r,z)$ is described by the profile family used here, MSE is expected to reduce the uncertainty in $j(r,z)$ relative to a magnetics-only identification by a factor of ≈ 4 at the plasma centre and ≈ 1.5 near the edge.

7. References

[1] S. H. Batha et al., Nucl. Fusion 36, 1133 (1996)

[2] B. W. Rice et al., Phys. Plasmas 3, 1983 (1996)

[3] R. C. Wolf et al., Nucl. Fusion Lett. 33, 663 (1993)

[4] F. M. Levinton et al., Phys. Rev. Lett. 63, 2060 (1989)

[5] B. W. Rice et al., Rev. Sci. Instrum. 66, 373 (1995)

[6] P. J. Mc Carthy, Ph.D. thesis, University College Cork (1992)

Radially Propagating High-n/High-m Mode Cascades During Flattening or Inversion of Central q-Profile in ASDEX Upgrade

A. Gude, K. Hallatschek, M. Bessenrodt-Weberpals, S. Günter, A. Kallenbach, K. Lackner, S.D. Pinches, S. Sesnic, M. Sokoll, and the ASDEX Upgrade Team,
Max-Planck-Institut für Plasmaphysik, EURATOM-Association,
D-85748 Garching, Germany

1 Introduction

The discovery of neoclassical tearing modes ((3,2), (4,3), (5,4), etc.) has shown that modes of $n > 1$ can be excited in the core [1,2]. Moreover, advanced tokamak concepts with increased core confinement have opened new possibilities for higher-n modes in the vicinity of integer q surfaces and renewed the interest in core MHD modes [3,4]. This is especially true for reversed magnetic shear experiments, where q_{min} can be localized near $q = 1, 2$ or 3 [3,4]. In such a case, the local shear around these surfaces can be rather low. This, combined with the high β's in the modern experiments, could affect the stability of higher-n modes. The most probable modes to be destabilized in the area of an integer q surface ($q = k$, where $k = 1,2,3$), will have the poloidal and toroidal mode numbers linked by the expression $m = k \cdot n \pm 1$. In this paper we report on a new kind of high-n mode activity in the plasma core, which has similar attributes and is characterized by a cascading process.

2 Phenomenology of mode cascades

2.1 General properties of cascades

We define a cascade as a series of short mode bursts in order of increasing n. The cascade commences with the lowest n, typically 5 or 6, and can reach n values of 22 or higher. The relationship between the poloidal and toroidal mode numbers is given by $m = n + 1$, so that the q range of the cascade modes is $\approx 1.045 < q \leq 1.2$. This q range corresponds to a radial shell from $r = 11$ to 27 cm. At least two, sometimes even more, of the neighbouring modes in a cascade overlap partially in time, so that it can be assumed that the lower mode triggers the next higher one.

Fig. 1 gives examples for the two kinds of cascading processes observed in ASDEX Upgrade. In both cases the cascades begin with a mode of lower frequency, signifying a lower n number. The main difference between the two cases is that for co-injection a very low, but still positive, magnetic shear (PMS) develops in the central region and for counter-injection a low reversed magnetic shear (RMS) evolves. This low shear allows the cascades to appear in both PMS and RMS regions. The mode positions obtained from soft X-ray mode profiles differ for the two cases. The highest modes for PMS are established at lower minor radii and for RMS at larger radii than the lower cascade modes. There is also a difference in the radial progression of the cascades: In the PMS case, the cascading process (of a single cascade) advances from outside toward inside. For the RMS case the direction of progression is opposite. During the cascades, continuous low-n modes ((3,2), (4,3), (5,4)), not displayed in Fig. 1, appear. From their n numbers the lowest cascade n numbers (5 or 6) can be deduced using the fact that the frequency difference between two neighbouring modes does not change much with the n number.

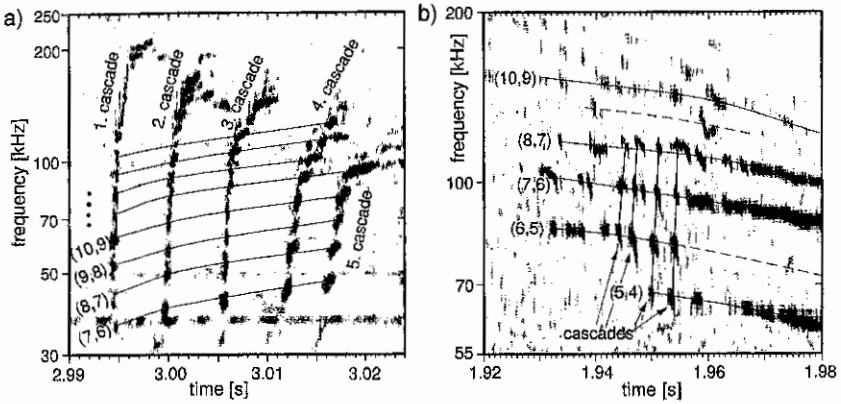

Figure 1: *MHD cascades observed in wavelet spectrum of soft X-ray radiation: a) positive magnetic shear case (co-injection) b) reversed magnetic shear case (counter-injection). Dark areas represent mode activity. Mode numbers for b) are estimated.*

Fig. 2 depicts the PMS cascading example of Fig. 1a, as observed in soft X-ray diodes. Cascades are indicated by different shadings. The shading marks two neighbouring diodes where the mode bursts cause a loss of energy and particles from inside (inner diode with a signal drop) to outside (outer diode with a signal rise). This also denotes the position of the modes. Due to the limited resolution of the diode array, several modes can be responsible for the signal drop. It is also evident from the figure that these cascades progress inward.

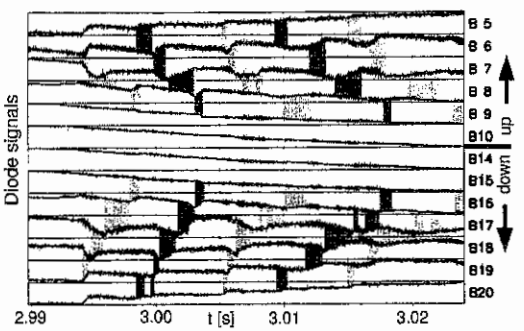

Figure 2: *Signals from a soft X-ray diode array showing the same cascades as in Fig. 1a. Shaded areas demonstrate inward progression of cascades.*

The mode cascading in ASDEX Upgrade occurs during a transient process in a discharge, where the central current profile is going through a strong modification brought about by low-Z (Ne, C) and/or high-Z (e.g., W) central accumulation. This accumulation leads to peaking of Z_{eff} (for low-Z) or flattening of the T_e profile caused by high central radiation (for high-Z impurities). In all discharges with cascades we observed both a peaking of Z_{eff} and a flattening of the T_e profile. During the later cascades the T_e profiles can even become hollow. The cascades are, therefore, observed in some of the CDH discharges, where Neon peaking sometimes occurs and in counter-injection discharges, which tend occasionally to accumulate impurities. All discharges where cascades

have been detected were auxiliary heated with a medium β_{pol} between 0.6 and 0.9.

2.2 Evolution of q profiles

Knowing the mode location, corresponding n number, and the relationship $m = n + 1$, one can construct the q profile in the cascade region. $m = n + 2$ or $m = n - 1$ are not applicable, because these relations would result in a large break in the q profile between low-n and cascade modes. The q profile including the $q = 1$ surface is shown in Fig. 3 for the PMS case for three times during the cascades. The modes at $q = 1.33$ and 1.25 are non-cascading low-n modes. This figure also demonstrates the inward movement of the central q profile. The magnetic shear, $s = r/q \cdot dq/dr$, becomes small in the region of cascade modes with values of $s = 0.5$ down to 0.26 for the (6,5) and 0.2 down to 0.07 for the (10,9) mode.

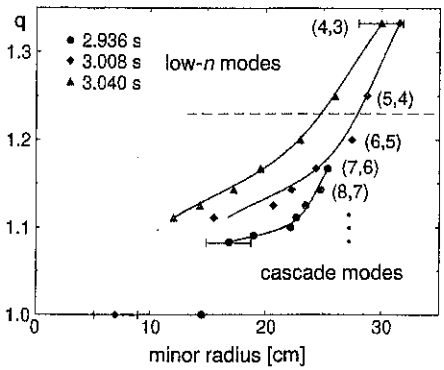

Figure 3: *Time evolution of the q profile during the cascading process determined from mode positions. The time sequence illustrates the inward movement of the q profile.*

From the change in mode location in the RMS case one can conclude that the RMS region progresses outward and most probably the q_{min} value increases. This can also be inferred from the lowering of the maximum and minimum n numbers observed for the cascades. In addition to the cascade modes there are low-n modes in the outer PMS region (of the RMS discharges). From the evolution of their location, we can conclude that this part of the q profile progresses inward as in the PMS case.

2.3 Frequency evolution of cascade modes

As can be seen from Fig. 1, there is a rather slow change in frequency of a given (m, n) mode from cascade to cascade but one can also notice a fast change of roughly 10 % during a mode burst. There are three contributions in the slow frequency change: an increase in the plasma rotation velocity, the inward (PMS) or outward (RMS) movement of the q surfaces, and the flattening of the pressure profile. These three terms contribute differently from discharge to discharge and from mode to mode. The pressure profile flattening decreases the electron diamagnetic drift contribution, f_{*e}, to the mode frequency. In the PMS case (co-injection) f_{*e} has a negative sign, which causes the mode frequency to increase. For RMS (counter-injection) the f_{*e} contribution has a positive sign, and, therefore, the frequency of the mode decreases. The same arguments apply for the fast change in frequency during the mode burst: the burst flattens the pressure profile in the mode region and the mode frequency increases for the co-injection (PMS) case and decreases for the counter-injection (RMS) case.

3 Theoretical considerations

Fig. 4 shows a spline-fitted q profile together with the inferred current density profile. High gradients at the outer edge of a peak in the current density meet very low shear right at the position of the cascading modes (between vertical lines). Cylindrical tearing mode calculations for the shown profiles result in instability for mode numbers up to $n \approx 12$, as observed in the corresponding discharge. Stability analysis of realistic ASDEX Upgrade equilibria with the same current profiles using the resistive MHD code CASTOR also proved instability up to high-n modes even at finite pressure. Moreover, with increasing pressure gradient, the high-n growth rate increases due to mode-coupling, yielding modified tearing modes [5].

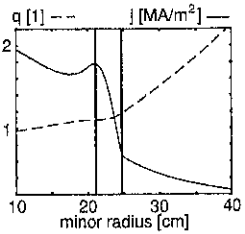

Figure 4: *q profile and corresponding current density*

For the development of a cascade an (m,n) mode has to destabilize the $(m+1,n+1)$ and stabilize the $(m-1,n-1)$. To model a cascading mechanism depending on the current, the evolution of a number of modes and their effect on the equilibrium current profile were calculated in a cylinder, neglecting higher harmonics, nonlinear coupling and pressure. That way, cascading could be simulated, which carries on over several stabilizing/destabilizing events (see Fig. 5). A detailed description of these findings will be published elsewhere.

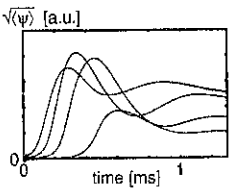

Figure 5: *Flux amplitudes of 4 cascading modes*

4 Summary

Core MHD cascades with a long series of mode bursts in order of increasing n have been observed in certain ASDEX Upgrade discharges. A cascade is initiated by a low-n mode, typically of $n = 5$ or 6, and can reach maximum n values of 22 or higher. Cascade modes satisfy the relationship $m = n+1$. They have been found in discharges with positive and reversed magnetic shear. In the positive shear case the cascade modes progress radially inward and in the reversed shear case outward. The common features of these cascades are that they are excited in a low magnetic shear region and that $0.6 < \beta_{pol} < 0.9$. Cascades are observed in discharges with high-Z/low-Z accumulation, where the current and the pressure profile are being rearranged. Parts of the q profile with positive shear are shifted inward and those with reversed shear outward. The frequency of the cascade modes changes due to the variation in the toroidal plasma rotation velocity and pressure gradient and because of the radial movement of the central q profile.

Acknowledgements

The authors want to thank D. Biskamp, J.C. Fuchs, O. Gruber, S. de Peña Hempel, and H. Zohm for helpful discussions.

References

[1] Z. CHANG et al., Phys. Rev. Letters **74**, 4663 (1995)
[2] H. ZOHM et al., Plasma Phys. Contr. Fusion **37**, A313 (1995)
[3] F.H. LEVINTON et al., Phys. Rev. Letters **75**, 4417 (1995)
[4] E.J. STRAIT et al., Phys. Rev. Letters **75**, 4421 (1995)
[5] S. GÜNTER, this conference

Differential Rotational Soft X-Ray Tomography of Coupled MHD Modes

M. Sokoll, M. Bessenrodt-Weberpals and the ASDEX Upgrade Team
Max-Planck-Institut für Plasmaphysik, EURATOM-Association,
D-85748 Garching, Germany

1. Introduction

Soft X-rays (SXR) emitted from a fusion plasma can be used to diagnose and interpret magnetohydrodynamic (MHD) plasma activities and their structure. At the tokamak ASDEX Upgrade the soft X-radiation is measured by 5 pinhole cameras with a total of 124 detectors. The detected signals are integrals along lines-of-sight, which lie in one poloidal cross-section of the tokamak. Thus, a tomographic reconstruction is a very important tool for the interpretation of the data.

For investigation of complex mode structures (higher poloidal mode number, several modes) the spatial resolution is too poor due to the low number of detectors ($\sim 10^2$), because of restricted space. On the other hand in the medical tomography some 10^5 chords are available [1].

To obtain sufficient spatial resolution tomography methods are adapted to the conditions in fusion plasmas. The method presented here is unique in its ability to reconstruct the soft X-ray emissivity of coupled MHD modes with high spatial resolution.

2. Differential Rotational Tomography

To improve the spatial resolution the well known method of rotational tomography can be used [2,3]. Here, time information is transformed into spatial information. Because of the toroidal and/or poloidal plasma rotation the mode rotates in the observation plane. Assuming a circular, rigid and concentric rotation of a stationary mode with constant angular velocity it is easy to correlate the data for one chord at different time points with the data for different chords at one time point.

To analyse noncircular and nonconcentric plasma shapes the rotational tomography was expanded by using an adaptive coordinate system $(\rho, \varphi, \theta^*)$. ρ is the radial poloidal flux coordinate. The toroidal coordinate φ is the Euclidean toroidal angle. The poloidal coordinate θ^* is the straight field line angle, i. e., the magnetic field lines are straight in the plane (φ, θ^*). The definitions are as follows:

$$\rho = \sqrt{\frac{\psi - \psi_A}{\psi_S - \psi_A}}, \quad \theta^* \sim \int_0^\theta d\theta' \frac{1}{R} \frac{\partial(R,z)}{\partial(\psi,\theta')} \quad \text{for } \rho = const. \tag{1}$$

θ^* is normalized to 2π. R and z are the Cartesian coordinates in the poloidal plane. θ is the Euclidean poloidal angle. ψ is the poloidal flux obtained from equilibrium calculations. It takes the value ψ_S on the separatrix and ψ_A on the magnetic axis. All lines-of-sight lie in the plane (ρ, θ^*) (or (R, z)) at one toroidal location (φ=0). The advantage of the coordinate system (ρ, θ^*) is that the motion of one mode is represented as a rigid, uniform, circular and concentric rotation. This simple properties are offset by complex representation of the lines-of-sight in these coordinates, confer figure 1.

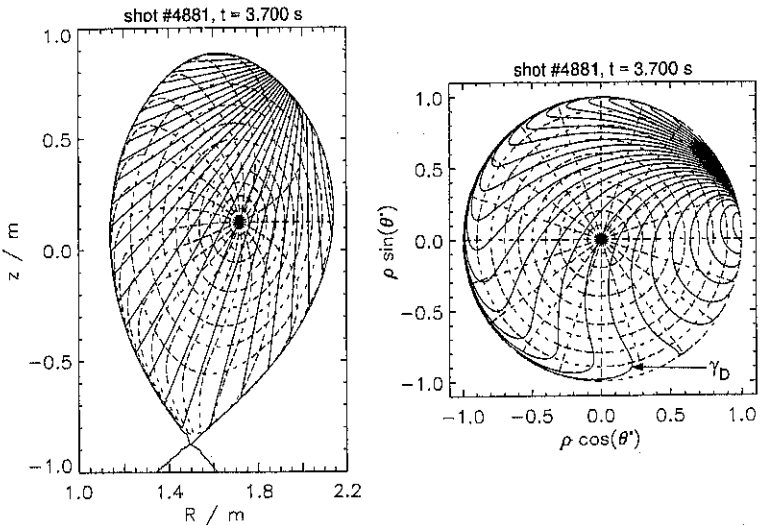

Figure 1: *Lines of constant ρ and θ^* (dashed), and lines-of-sight for camera D (solid), depicted in Euclidean (left) and adaptive (right) coordinates.*

Conventional rotational tomography fails if more than one mode is present. To deal with this difficulty we developed two complementary strategies. First, if the modes are uncoupled, i. e. if they correspond to different frequencies in the measured signal, we separate them in the Fourier space using the fast Fourier transform (FFT). Second, if they are coupled, we apply an ansatz which takes into account the corresponding different rotational velocities in the observation plane (ρ, θ^*). This will be developed step by step in the following paragraphs.

First, look at the ansatz for the soft X-ray emissivity of a pure harmonic mode (m, n):

$$g(\rho, \varphi, \theta^*) = A(\rho)\ e^{i(m\theta^* - n\varphi)} \tag{2}$$

Here, $A(\rho)$ is the complex radial function of this mode. Its absolute part corresponds to the radial amplitude function. Next, assume a rigid plasma rotation with the frequency ω and consider the time dependent ansatz at the toroidal location of the SXR diagnostic:

$$g(\rho, t, \theta^*) = A(\rho)\ e^{i(m\theta^* + n\omega t)} \tag{3}$$

The frequency $\omega = \omega_{tor} - \frac{m}{n}\,\omega_{pol}$ is composed of the toroidal and poloidal plasma rotation. Now, expand this ansatz to different frequencies ω_k and suppose for each of them a set of modes (m_{jk}, n_{jk}):

$$g(\rho, t, \theta^*) = \sum_{jk} A_{jk}(\rho)\ e^{i(m_{jk}\theta^* + n_{jk}\omega_k t)} \tag{4}$$

For each mode there is one radial function $A_{jk}(\rho)$. It is defined as an arbitrary cubic spline with h internal knots. Thus, it can be represented as a linear combination of real and well defined cubic B-splines [4]:

$$A_{jk}(\rho) = \sum_{l=1}^{h+4} c_{jkl} N_{jkl}(\rho) \tag{5}$$

Equations 4 and 5 give the total ansatz

$$g(\rho, t, \theta^*) = \sum_{jkl} c_{jkl} N_{jkl}(\rho)\ e^{i(m_{jk}\theta^* + n_{jk}\omega_k t)} \tag{6}$$

The measured signal $f_D(t)$ of a detector D is a line integral along a line-of-sight described by the curve γ_D (see figure 1):

$$f_D(t) = \sum_{jkl} c_{jkl} \left[\int_{\gamma_D} ds\ N_{jkl}(\rho)\ e^{i m_{jk}\theta^*} \right] e^{i n_{jk}\omega_k t} =: \sum_{jkl} c_{jkl}\, I_{jklD}\ e^{i n_{jk}\omega_k t} \tag{7}$$

This set of equations separates in the Fourier space with respect to $\omega := n_{jk}\omega_k$:

$$\tilde{f}_D(\omega) = \sum_{jkl} c_{jkl}\, I_{jklD}\ \delta(n_{jk}\omega_k - \omega) \tag{8}$$

Thus, for each ω we obtain one set of complex and linear equations. I_{jklD} depends only on the geometry of the diagnostic and on the coordinates ρ and θ^*. c_{jkl} are unknown and $\tilde{f}_D(\omega)$ are values from the Fourier transform of the measured SXR data. Solving equations (8) for c_{jkl} and substituting it in equation (6) one obtain the unknown emissivity g.

Furtheremore, we investigated errors and limits of our method. There are three main sources of errors: the measured line integrated intensities, the assumed geometry of the diagnostic and finally the magnetic equilibrium. The influence of these errors were investigated by tests, Monte Carlo simulations and calculations of error propagation. The approximate values of possible errors are listed in table 1, where the time variable emissivity Δg means the difference between the total emissivity g and the time independent emissivity, i. e. the (0,0) mode.

	g	Δg
measured intensity	1%	1%
geometry	0.5%	2%
equilibrium	2%	9%

Table 1: *Approximate values of possible errors of the emissivity g and Δg.*

For the splines we use mostly 11 knots ($\rho = 0.0, 0.1, 0.2, \ldots, 1.0$). It corresponds to a radial resolution of about 5 cm ($\Delta\rho = 0.1$) for each mode. The poloidal resolution is limited by the number of harmonics, i. e. by the band width of the data acquisition system. This is large enough, so that the poloidal resolution is limited only by the spatial extension of the lines-of-sight, which corresponds to a resolution of about 4 cm.

3. Results

With this new high resolution method we investigated the internal kink, the evolution of the sawtooth crash, the growth of the tungsten snake and coupled modes. An example for the studies of coupled mode structures in ASDEX Upgrade high-β discharges is shown in figure 2 [5]. Tomographic reconstructions of three phases of the discharge are depicted. In the first phase (left plots) the plasma does not reach the β-limit yet and a (1,1) mode is unstable. The radial mode amplitude and the contour plot of the time variable emissivity Δg can be seen. The next phase is at the beginning of the β-collapse. Here, we discovered a (4,3) mode with a toroidally coupled (3,3) mode. Finally, in the last phase during the β-collapse we reconstructed a (3,2) mode with a toroidally coupled (2,2) mode. The tomography procedure yields the m numbers while the n numbers are determined by the relations of the frequencies and by the Mirnov signals.

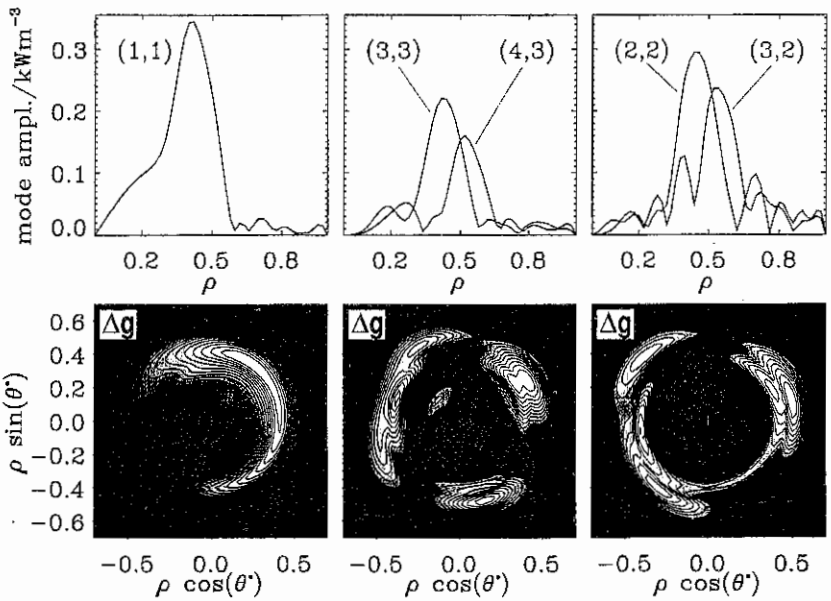

Figure 2: *Tomographic reconstruction of an high-β discharge in ASDEX Upgrade (shot #7694). Top: radial mode amplitudes. Bottom: contour plots of the time variable emissivity Δg. Left ($t = 1.831\,s$): (1,1) mode before the β-collapse. Middle ($t = 1.844\,s$): coupling of (4,3) and (3,3) modes at the beginning of the β-collapse. Right ($t = 1.887\,s$): coupling of (3,2) and (2,2) modes at the end of the β-collapse.*

4. Summary

An innovative tomography method was developed for interpretation of the soft X-ray data. It has high spatial resolution. For the first time, it is possible to reconstruct the soft X-ray emissivity of coupled MHD modes. The necessary assumption is a stationary mode structure on the time scale of one plasma rotation period (in ASDEX Upgrade: $\sim 100\,\mu s$). The main features are the use of rotational tomography in an adaptive coordinate system, an ansatz for coupled modes with the help of cubic splines and calculation in the Fourier space. Thereby the mode structures in high-β discharges have been clarified in detail.

References

[1] R. S. Granetz, P. Smeulders, Nuclear Fusion **28**, pp. 457, 1988

[2] N. R. Sauthoff, S. von Goeler, IEEE Transactions on Plasma Science **PS-7**, pp. 141, 1979

[3] Y. Nagayama, A. W. Edwards, Review of Scientific Instruments **63**, pp. 4757, 1992

[4] H. B. Curry, I. J. Schoenberg, Journal d'Analyse Mathématique **17**, pp. 71, 1966

[5] M. Sokoll *et al.*, to be published

Characteristics of type I and type III ELM precursors in ASDEX Upgrade

T. Kass, S. Günter, M. Maraschek, W. Suttrop, H. Zohm[1], ASDEX Upgrade Team
Max-Planck-Institut für Plasmaphysik, EURATOM Association, Boltzmannstr. 2, D-85748 Garching, Germany
[1]*Institut für Plasmaforschung, Universität Stuttgart, Pfaffenwaldring 31, D-70569 Stuttgart*

1. Introduction

So far, steady state H-mode has been achieved only with the presence of edge localized modes (ELMs) providing an efficient particle density and impurity control [1,2]. Following the classification based on the ELM frequency f_{ELM} dependence on the energy flux across the separatrix $P_{sep} = P_{heat} - P_{rad} - dW_{MHD}/dt$, where the radiated power P_{rad}, the heating power P_{heat} and the stored kinetic energy in the plasma W_{MHD} are considered [1], the ELM types observed in the ASDEX Upgrade tokamak are of type I ($df_{ELM}/dP_{sep} > 0$) and of type III ($df_{ELM}/dP_{sep} < 0$). It has been shown, that in ASDEX Upgrade type III ELMs are stabilized at edge electron temperatures somewhat above 300 eV [3]. Therefore their mechanism might be governed by resistivity. Type I ELMs on the contrary are found to be triggered at critical edge pressure gradients close to the ideal ballooning limit.

In this paper we will show, that an edge pressure gradient close to the ideal ballooning limit is not sufficient to trigger a type I ELM. In order to understand the ELM mechanism the MHD characteristic must be investigated further. The following discussion concentrates on the ELM precursor oscillation, as this phase of an ELM is not perturbed by turbulence emerging during the enhanced transport phase. Therefore the characteristics and experimental phenomenology of both types of ELM precursors observed in the ASDEX Upgrade tokamak (major radius R_0 = 1.65 m, minor radius a = 0.5 m, elongation κ = 1.6, triangularity δ = 0.1) are presented.

2. Experimental observations

2.1 Temporal evolution of the edge pressure gradient

First the temporal evolution of the edge electron pressure gradient $\nabla p_{e,edge}$ taken at r = a − 2 cm is investigated before and after a type I ELM. The electron pressure gradient shown in Fig. 1 is obtained from measurements of the electron density by means of DCN-Laser interferometry and Li-beam injection, and the electron temperature detected with the ECE-diagnostic. All data have been taken at the low-field side.

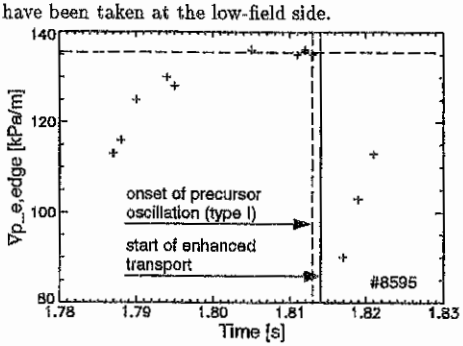

Fig. 1: The temporal evolution of the edge electron pressure gradient taken at r = a − 2 cm during a type I ELM shows that the pressure gradient recovers continuously from the drop caused by the preceding type I ELM (not shown). Several ms before the next type I ELM occurs (solid vertical line at t = 1.814 s) and well before the precursor oscillation arises (dashed vertical line at t = 1.813 s) ∇p saturates.

It can be observed, that $\nabla p_{e,edge}$ recovers continuously from the drop caused by the preceding type I ELM (not shown). Several milliseconds before the next type I ELM occurs (solid vertical line at t = 1.814 s) and well before the precursor arises (dashed vertical line at t = 1.813 s), $\nabla p_{e,edge}$ saturates at $\nabla p_{e,edge}$ = 136 kPa/m (dashed horizontal line). Thus, $\nabla p_{e,edge}$ remains approximately constant for a significant time period prior to the type I ELM. The normalized pressure gradient $\alpha = -2\mu_0 R q^2/B^2 \cdot \nabla p$ equals 2.57 at this time ($p = p_e + p_i \approx 2p_e$ is assumed).

Infinite-n ideal ballooning mode calculations (carried out with the help of the HELENA-code [4]) show that this value lies with an uncertainty of 30% close to the critical value α_{crit} given by the ideal ballooning limit. The main sources of error are the unknown ion pressure p_i and the uncertainty of the relative position of the profile. Another indication for ideal ballooning is the I_p^2-scaling of $\nabla p_{e,crit}$ found in the experiment [5]. Thus, in the considered case, the critical value of the edge pressure gradient is reached within the experimental accuracy well before the type I ELM occurs without immediately triggering a type I ELM. This indicates, that proximity to the ideal ballooning limit is not a sufficient to trigger a type I ELM, as suggested in [1]. Thus the MHD characteristic of ELMs must be further investigated. As the precursor phase of an ELM is not deteriorated by turbulence or non-linear effects, the following discussion is focused on their phenomenology as observed in ASDEX Upgrade.

2.2 Frequency of the ELM precursors

In Fig. 2 the result of a wavelet analysis (temporal evolution of the frequency spectrum) of a type I (Fig. 2a) and a type III ELM (Fig. 2b) together with their corresponding precursor oscillations during a discharge with counter-injection ($I_p = -1$ MA, $P_{NBI} = 5$ MW $D^0 \rightarrow D^+$) and the toroidal magnetic field ($B_t = +2.5$ T) in the unfavourable field direction (ion-∇B-drift away from the X-point) is shown. It can be seen, that in both cases the ELM precursor oscillation starts to grow about 1 ms before the transport increases (type III ELM precursors sometimes grow much faster). On the other hand the frequency of both types of ELM precursor oscillations differs considerably. Whereas type I ELM precursors exhibit a frequency of the order of 20 kHz, type III ELM precursors show a frequency of the order of 100 kHz during counter-injected discharges. Both frequency spectra exhibit quite a narrow band in contrast to the enhanced transport phase of the ELMs, which has a broad band spectrum.

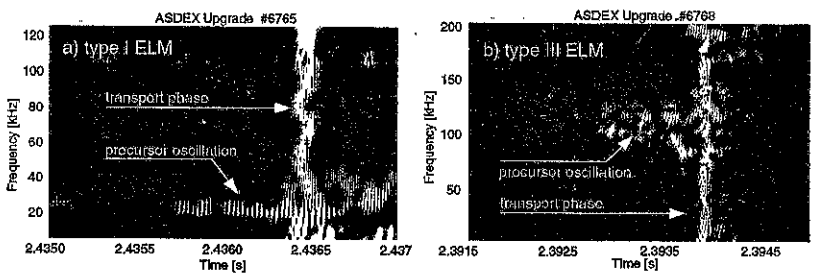

Fig. 2: The result of a wavelet analysis (differential Fourier analysis) of a type I (left plot) and a type III ELM (right plot) during two different counter-injected discharges shows, that both types of ELM precursor start to grow about 1 ms before the transport increases and that their frequencies differ considerably

In the case of co-injection the frequencies change significantly. The frequency of type III ELM precursors is then shifted to lower frequencies of the order of 60 kHz and type I ELM precursors are not observed. Despite the absence of a clear magnetic type I ELM precursor a slow electron temperature fluctuation around 5 kHz is detected by ECE channels resonant near the separatrix [6]. Here the question arises, whether the magnetic type I ELM precursor is indeed absent or only undetectable with magnetic probes.

Another feature of the ELM precursor oscillation, which can be seen for instance in Fig. 2b, is the presence of two apparently periodically alternating frequencies (100 kHz and 120 kHz in this example). The observation of two clearly separated frequencies in the Fourier spectrum appears sometimes also during type I ELM precursor oscillations and is also reported from the COMPASS-D experiment [7].

2.3 Mode structure of the ELM precursors

The mode structure of the ELM precursors can be inferred from an analysis of the magnetic signal [8]. In ASDEX Upgrade three pick-up coils each measuring $\dot{B}_r$ (a maximum sampling rate of 500 kHz is provided) are installed in different toroidal positions in the midplane ($z = 0$), thus enabling the determination of the toroidal mode number. A mode analysis of many ELM precursors of both types reveals that the toroidal mode number varies in the range of $n = 5 - 10$ for type I ELM precursors, whereas for type III ELM precursors $n = 10 - 15$ is found. Despite the obvious variation of n there is a significant global difference in the toroidal mode structure between both types of ELM precursors.

Since the type III ELM precursors are not detected by the poloidal Mirnov coil array positioned at the inside of the vacuum vessel and the radial pick-up coils are only available for one poloidal position (outer midplane), no reliable statement about the poloidal mode structure (m-number) can be given yet. But as a very rough approximation m can be estimated by the decay of the radial magnetic field $\tilde{B}_r$. As the three additional pick-up coils also have different radial positions ($R_1 = 2.267$ m, $R_2 = 2.301$ m, $R_3 = 2.386$ m) the decay of $\tilde{B}_r$ can be measured. In cylindrical and circular approximation $\tilde{B}_r(r) \sim (r_{res}/r)^{m+1}$ holds, where r_{res} denotes the radius of the resonant surface at which the mode is located. Thus, the following expression for the poloidal mode number m can be derived: $m = \{\ln(B_i/B_j)/\ln(r_j/r_i)\} - 1$, where i and j subscript different pick-up coils located at different radial positions. Note, that this method is not very exact and therefore afflicted with a significant uncertainty due to the poloidal variation of the pitch. Furthermore, the m-numbers are underestimated in this approximation, since only coils at the low-field side are used. Applying this method we find m varying from 10 to 15 for type I ELM precursors and m-numbers between 15 and 20 for type III ELM precursors.

The result that type I ELM precursors show significantly lower m-numbers compared to type III ELM precursors is also confirmed indirectly by the observation that these modes are also faintly visible on the coils mounted further away from the plasma. Thus the poloidal m-numbers of type I ELM precursors have to be smaller than for the type III ELM precursors, consistent with their lower n-numbers and reduced signal frequency.

Furthermore, both ELM precursor modes rotate in the electron diamagnetic drift direction consistent with observations from other experiments.

The radial extent of the layer in which the precursor oscillation occurs can be estimated from the time resolved measurement ($\Delta\tau = 4\ \mu$s) of the T_e at different radial positions in the plasma edge region. Such an investigation shows that the extent of the type I ELM precursor is restricted to a thin layer ($\Delta r \approx 1 - 2$ cm) close to the plasma edge as the precursor oscillation cannot be seen on the channels resonant deeper inside the plasma [6].

3. Discussion

The detected significant variation of the ELM precursor frequency can partly be understood by the different spatial structure of the ELM precursors. In the lab frame, MHD modes roughly rotate corresponding to the present radial electric field E_r, i.e. with the sum of the mainly poloidal diamagnetic frequency $\omega^* = 1/(eBrn) \cdot \nabla p$ and the frequency due to toroidal fluid rotation ω_{rot} driven by the tangential component of the neutral beam injection [8]. Thus, the detected signal frequency equals $\nu_{Mirnov} = (m \cdot \omega^* \pm n \cdot \omega_{rot})/2\pi$ („+/−“ for counter/co-injection). Consequently, the oscillation frequencies are generally higher in the case of counter-injection, consistent with the higher radial electric field E_r observed in these discharges (E_r is measured via the charge exchange flux [9]) [3].

However, the different n-numbers cannot fully explain the frequency difference between type I and type III ELM precursors. The frequencies differ by about a factor of $4 - 5$, whereas for the corresponding mode numbers only a factor of $2 - 3$ is found. This might point to a finite frequency of one of the modes in the fluid frame. In the case of type I ELMs with co-injection

(the usual case in ASDEX Upgrade), the effect of ω^* and ω_{rot} almost cancel (note the minus sign in this case in the above equation). Thus the fact that type I ELM precursors are not clearly visible under these circumstances is due to the resulting low frequency yielding a low Mirnov amplitude. Actually, the type I ELM precursor may also grow locked and therefore not be detected by magnetic probes at all. In these cases, they have a very high growth rate (on the sub-ms timescale), whereas the rotating precursors grow on a ms timescale. This may be due to the stabilizing effect of the wall on the rotating mode, which is absent for the locked precursor mode. In co-injected cases, where E_r vanishes in the steep pressure gradient region, the mode will be most unstable at this position, whereas in counter-injected discharges, E_r does not vanish in the region of high pressure gradient. This difference can explain why in ASDEX Upgrade generally, discharges with counter-injection have a significantly reduced ELM frequency (about a factor 10) compared to discharges with co-injection.

4. Summary

In this paper, we have shown that proximity of ∇p_{edge} to the critical value given by the ideal ballooning limit is not sufficient to trigger a type I ELM. In order to get more information about the ELM mechanism the MHD characteristic of ELMs is investigated. The present discussion is focused on the experimental phenomenology of type I and type III ELM precursor oscillation as observed in ASDEX Upgrade. Both types of precursor have a significant different oscillation frequency in co- ($f_I \lesssim 5$ kHz, $f_{III} \approx 60$ kHz) as well as in counter-injected discharges ($f_I \approx 20$ kHz, $f_{III} \approx 100$ kHz). The mode numbers found for type I (m, n = 10 − 15, 5 − 10) and type III ELM precursor (m, n = 15 − 20, 10 − 15) are consistent with the observed precursor frequencies, thus providing a third criterium, besides the ELM frequency scaling with P_{sep} and the peak power load on the divertor plates, to distinguish between type I and type III ELMs at ASDEX Upgrade. Furthermore, it has been shown, that the type I ELM precursor oscillation originates from a thin layer ($\Delta r \approx 1 - 2$ cm) close to the plasma edge.

5. Conclusions

From our point of view, it seems to be likely, that a coupling between the mode responsible for the ELM precursor oscillation and an ideal ballooning mode can trigger a type I ELM. A possible candidate for this ELM precursor mode would be the current-driven peeling mode, which has been shown can couple to an ideal ballooning mode at high plasma pressure and create a hybrid mode [10]. However, the major lack of this model is that the ELM-free regime experimentally found at ASDEX Upgrade is located right in the parameter space, which is calculated to be peeling unstable (compare Fig. 2 in Ref. 10). Further hints about the ELM mechanism may also be given by an observation recently reported from the TCV tokamak showing toroidally asymmetric precursor oscillations [11].

References

[1] H. Zohm et al., *Plasma Phys. Control. Fusion* **38** (1996) 105.
[2] E.J. Doyle et al., *Phys. Fluids B* **3** (1991) 2300.
[3] H. Zohm et al., *IAEA-F1-CN-64/A5-1*, Montreal, Canada, 1996.
[4] G.T.A. Huysmans et al., Proc. CP90 Conf. on Comp. Phys., 1991, p371.
[5] W. Suttrop et al., 23rd EPS Conf. in Kiev, Ukraine, A004, 1996.
[6] W. Suttrop et al., *Plasma Phys. Control. Fusion* **38** (1996) 1407.
[7] A.L. Colton et al., *Plasma Phys. Control. Fusion* **38** (1996) 1359.
[8] O. Klüber et al., *Nucl. Fusion* **31** (1991) 907.
[9] W. Herrmann et al., *Phys. Rev. Lett.* **75** (1995) 4401.
[10] C.C. Hegna et al., *Phys. Plasmas* **3** (1996) 584.
[11] H. Reimerdes et al., this conference.

Observation of TAE-modes in ohmically heated plasmas by drift wave excitation

M Maraschek, S Günter, T Kass, B Scott, H Zohm†, ASDEX Upgrade Team
MPI für Plasmaphysik, EURATOM-Association, Boltzmannstr. 2, D-85748 Garching
†*Institut für Plasmaforschung, Universität Stuttgart, Pfaffenwaldring 31, D-70569 Stuttgart*

The common understanding about the excitation of toroidicity-induced Alfvén Eigenmodes (TAE-modes) requires fast particles in the range of the Alfvén speed $v_A = B/\sqrt{\mu_0 n_i m_i}$ or in tokamaks one third of the Alfvén speed through sideband excitation.

Recently, in ASDEX Upgrade, TAE-modes have also been observed in purely ohmically heated discharges, where only fast particles from the Maxwellian distribution are present, which are not able to drive these modes unstable. Their frequencies scale with $f_{TAE} = \frac{1}{2\pi}\frac{v_A(r)}{2q(r)R}$, and they are located at the $q \approx 2.6$ surface. They can be observed on Mirnov and soft-X-ray measurements. A new excitation mechanism by coupling of the electromagnetic part of the drift Alfvén turbulence at the cold plasma edge to the ordinary Alfvén wave spectrum could explain their appearance.

Model of TAE-modes In the cylindrical large aspect ratio approximation two adjacent branches of the localized continuum shear Alfvén waves with the dispersion relation $\omega_A = v_A(r)\left|k_{\|}\right|$, $k_{\|} = (m-nq)/(qR)$ have a crossing point at the $q = (2m+1)/(2n)$ surface at which the modes with subsequent poloidal mode numbers m and $m' = m\pm1$ have degenerated energy states. Considering the toroidicity with a realistic aspect ratio of tokamaks, e.g. $R/a \approx 3.3$ for ASDEX Upgrade, the poloidal variation of the toroidal field B_t causes a coupling of the two adjacent branches and two standing waves are created. The degeneracy of the branches is resolved by these standing waves and at the corresponding frequency a gap is formed in which no radially localized continuum Alfvén wave can exist anymore. Within this gap a TAE-mode can exist with approximately the frequency of the former crossing point $f_{TAE} = \frac{1}{2\pi}\frac{v_A(q_{GAP})}{2q_{GAP}R}$.

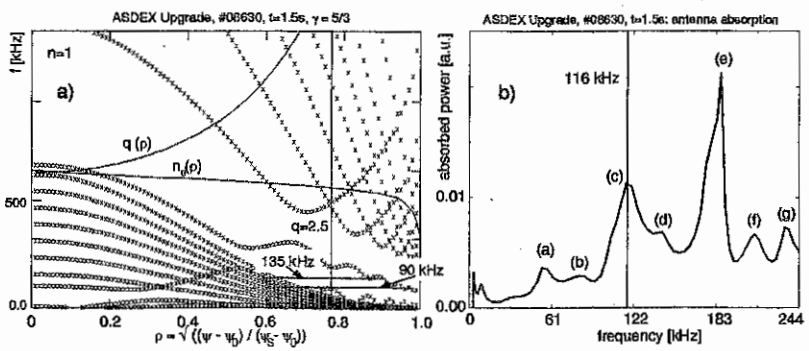

Figure 1: *a: Dispersion relations for continuum Alfvén waves for $n = 1$ calculated by CASTOR. b: Antenna absorption spectrum for the presented dispersion relations.*

To get an better description of TAE-modes, e.g. their exact frequencies and full radial structure, a toroidal resistive MHD-code like CASTOR [1] has to be used. This code solves

the linearized MHD equations in the full toroidal geometry and calculates the continuum Alfvén wave branches and in addition the frequencies and structures of the TAE-modes within the continuum gaps. The resulting dispersion relations are shown in Fig. 1a. The exact frequencies of the modes are determined by an extension of CASTOR in which the power absorbed by the plasma in response to a wave injected by external antennas is calculated as a function of frequency [2] (Fig. 1b). The maximum of the absorbed power gives the exact central frequencies of the TAE-modes at which the radial structure can then be calculated. The resulting eigenfunctions have a global structure and are spread over the minor plasma radius until they cross an Alfvén continuum branch. Their maximum amplitude is still localized at the position of the former crossing point of the continuum Alfvén waves at $q_{GAP} = (2m+1)/(2n)$ with a frequency of $f_{TAE} = \frac{1}{2\pi}\frac{v_A(r)}{2q(r)R}$.

Observation of TAE-modes in ohmic discharges Recently, at ASDEX Upgrade, TAE-modes with their characteristic structure in the Fourier spectrum of the Mirnov coils have also been observed in purely ohmically heated discharges. A typical spectrum of a Mirnov coil mounted at the high field side of the torus is shown in Fig. 2a.

A clear difference to the modes observed in NBI-plasmas (burst-like behaviour with approximately 1 ms duration) is their continuous appearance throughout the entire discharge with a modulation of the envelope. The amplitude is about one order of magnitude smaller compared to the modes with NBI. These TAE-modes rotate in the electron diamagnetic drift direction.

If the observed modes were TAE-modes, the frequencies should depend mainly on the magnetic field $B \approx B_t$, the mass of the ions m_i and the local density $n_e(q)$ on the relevant resonant surface. Comparing shots with different toroidal field B_t and different ion species m_i, e.g. hydrogen and deuterium shows a clear dependence of the form $f \sim B_t/\sqrt{m_i}$. A strong density variation through different rates of gas puffing has been applied to check the dependence of the frequency on the local density on flux surfaces. The observed frequencies scale with density as $f \sim 1/\sqrt{n_e}$, as shown in Fig. 2b for measurements of the soft-X-ray diagnostic. Combining the results leads to $f \sim B/\sqrt{m_i n_e} \sim f_A$.

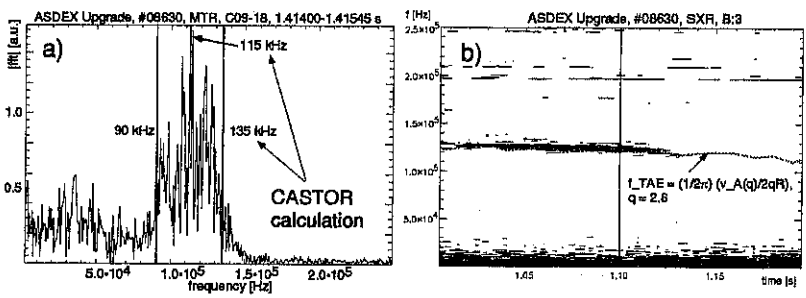

Figure 2: *a: A typical Fourier spectrum at the high field side of the torus. The broad spectrum has a significant amplitude in the range $f = 85 - 140$ kHz and reaches its maximum at $f \approx 115$ kHz. b: Dependence of the TAE-frequency upon the density as observed on the measurements from soft-X-ray.*

The remaining free parameter for calculating the location of the modes is the q-value q_{GAP} of the modes which can be fitted to the measured frequency by the equation $f_{TAE} = \frac{1}{2\pi}\frac{v_A(q_{GAP})}{2q_{GAP}R} = \frac{1}{2\pi}\frac{B_t}{\sqrt{\mu_0 m_i n_e(q_{GAP})}}\frac{1}{2q_{GAP}R}$, where $Z_{eff} = 1$ has been assumed. The density $n_e(q_{GAP})$ is taken on the flux surface for which $q = q_{GAP}$ holds. A fit of the q-value gives a value close to the plasma edge of $q_{GAP} \approx 2.6$ at $\rho_{TAE} \approx 0.84$ in a discharge with $q_{95} = 5$ (q-value at 95% of the poloidal flux).

Measurements of the soft-X-ray camera system show a clear frequency peak with $f_{TAE} = 127$ kHz at t = 1.0 s lying in the center of the observed multi peak structure of the Mirnov data for the corresponding time. The profiles reveals a $m = 0$ structure at this frequency. The maximum amplitudes are reached at the plasma edge consistently with the Mirnov data.

For these type of discharges for several time points a comparison with calculations of the resistive MHD-code CASTOR was done. The continuum spectrum for a typical time (#8630,t=1.5s) shows a gap in which TAE-modes can exist in the frequency range $f_{TAE,CASTOR} = 90 - 135$ kHz (Fig. 1). The spectrum of the absorbed power by external antenna excitation is shown in Fig. 1b. For the various peaks the resulting eigenfunctions have been analysed. All the eigenfunctions are radially peaked near the plasma center, where fast particles are normally present and are not excited. Only the frequency peaks (c) and (d) with $f \approx 115$ kHz show eigenfunctions, which are clearly peaked in the vicinity of the $q = 2.5$ surface. This frequencies are in perfect agreement with the observed frequencies and the mode location. For different times within the discharges the agreement also holds, besides the fact that different measured densities at the corresponding rational surface have to be applied to calculate the Alfvén frequencies.

At the L- to H- transition, the TAE-activity disappears or is strongly reduced in amplitude when the density fluctuation measured by reflectometry disappears (Fig. 3). During the H-mode the turbulence and also the TAE-modes reappear as bursts. Especially correlated with the ELM activity turbulence and TAE-mode activity reappears.

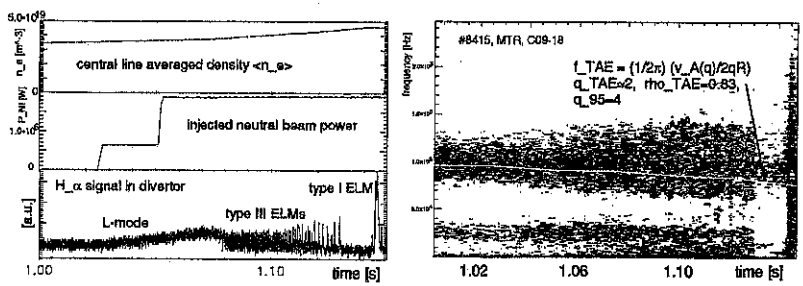

Figure 3: *Behaviour of the TAE-modes at the L- to H-transition. Correlated with the onset of the H-mode the TAE-modes disappear or are strongly reduced in amplitude.*

From TFTR similar mode activity observed on Mirnov coils has been reported [3]. The modes at TFTR were named Alfvén frequency mode (AFM) and were not consistent with the present TAE theory. In contrast to the results at TFTR the observed modes at ASDEX Upgrade could be identified as TAE-modes in the edge region of the plasma with the help of the resistive MHD-code CASTOR and the observation on the soft-X-ray diagnostic.

excitation by drift Alfvén turbulence A possible explanation for the excitation of these TAE-modes is the natural coupling to short wavelength drift Alfvén turbulence in the plasma edge. This mechanism would take place in two steps. In drift Alfvén turbulence, i.e. drift wave turbulence for which the magnetic induction associated with the fluctuating parallel current cannot be neglected, the parallel electric field is $E_{||} = -\partial A_{||}/\partial t - \nabla_{||}\phi$, with the induction term controlling the speed of the electron parallel dynamics [4,5,6]. This $E_{||}$ is coupled to the ExB turbulence by $\nabla_{||}p_e$ in the generalized Ohm's law. It is therefore unavoidable that electron drift turbulence and shear Alfvén waves are coupled at short perpendicular wavelength.

The second step is the transfer of this short wavelength Alfvén activity into global-scale modes via the well known 2D MHD inverse cascade in both ExB and magnetic energy. The finite range of both perpendicular and parallel wavelengths excited in the three dimensional turbulence makes it likely that some of this Alfvénic activity can find its way into the TAE-modes, since the curvilinear flux surface geometry prevents any particular mode number from being isolated. A broad interaction spectrum is consistent with both the CASTOR antenna spectrum (Fig. 1b) and the observations (Fig. 2a).

In addition, the TAE-modes are observed to propagate in the electron drift direction, which is consistent with the tendency of drift Alfvén turbulence as electron drift dynamics, and the tendency of edge fluctuations in general to be suppressed in the H-mode is consistent with the observation that the TAE activity becomes much less prominent in the H-mode.

All of this differs from the mechanism of the so called AFM activity in the absence of fast particles proposed by the TFTR group [3]. The activity seen in ASDEX Upgrade can be confidently identified as TAE activity which could be correlated with plasma edge turbulence.

Summary and conclusions The observation of TAE-modes in ohmically heated plasmas without fast particles has been reported. A consistent picture of the continuous TAE-modes in ohmically heated discharges with the help of the CASTOR code has been presented. A new idea has been proposed how TAE-modes could be excited without nonthermal fast particles by drift Alfvén turbulence in purely ohmically heated discharges.

Acknowledgment
The authors are grateful to the developers of the CASTOR code, in particular to W. Kerner, for making it available to us. Also we want to thank the continuous help and patience of G. Huysmanns. Discussions with A. Boozer, M. Kaufmann, K. Lackner and A. Weller about TAE-modes and their excitation are also gratefully acknowledged.

References

[1] W. Kerner et al., Contr. Fusion and Plasma Phys. **Part IV**, 89 (1992).
[2] G. T. A. Huysmans et al., Phys. Plasmas **2**, 1605 (1995).
[3] Z. Chang et al., Nucl. Fusion **35**, 1469 (1995).
[4] S. Camargo et al., Phys. Plasmas **3**, 3912 (1996).
[5] B. Scott et al., 13th Int. Conf. on Plasma Phys. Contr. Fusion, Montreal **IAEA-CN-64/DP-18** (1996).
[6] B. Scott, Three-Dimensional Computation of Drift-Alfvén Turbulence, submitted to Plasma Phys. Contr. Fusion (1997).

Modified high-n/high-m tearing modes in low shear regions with high pressure gradients and high resistivity

S. Günter, S.D. Pinches, A. Gude, K. Hallatschek, K. Lackner,
and the ASDEX Upgrade-Team
MPI für Plasmaphysik, EURATOM-Association, D-85748 Garching, Germany

1 Introduction

Recently at ASDEX Upgrade modes with high toroidal mode numbers n and probably $m = n + 1$ have been observed in discharges with high impurity accumulation [1]. In Fig. 1 of [1], a wavelet analysis of the soft X-ray data for the modes of a typical shot is given. Whereas the lower (m, n) modes can be observed continuously, one finds a cascading behaviour for the higher mode numbers ($n \geq 5$). Within one cascade the modes follow each other in such a way that each subsequent mode has its own mode number raised by 1. Comparing different cascades within one shot, one finds that the highest reachable n-number decreases with time. The aim of this paper is to investigate the nature of these modes and to find out for which conditions these modes appear. These theoretical investigations have been performed using the resistive MHD code CASTOR [2].

2 Theoretical investigations of the observed modes

Once the mode numbers and the location of the modes are known from SXR measurements, one may infer the q-profile. A typical q-profile just before the first cascade is given in Fig.1 together with the corresponding current and shear profiles. The locations of the (3,2) and the (11,10) modes are shown. The q-profiles of the shots considered have a characteristic flat region near the $q = 1$ surface where the high (m, n) modes are located.

Due to the large current gradient and the small shear all modes $(m, n) = (n + 1, n)$ with $2 \leq n \leq 10$ are tearing mode unstable in a circular cylinder. However, in a toroidal plasma, even for vanishing pressure, only those modes up to medium mode numbers are tearing mode unstable if one neglects mode coupling. Adding only a very small pressure, these modes also become stabilized.

Including the coupling between modes with different poloidal mode numbers m, however, the pressure dependence of all considered modes changes dramatically. The growth rates for various mode numbers (m, n) versus pressure are given in Fig. 2. As can be seen, modes with low mode numbers are not influenced by pressure at all, except for very low pressures. For medium mode numbers one finds a stabilizing effect due to pressure only for extremely low pressures. With increasing pressure mode coupling becomes more important and leads to rising growth rates.

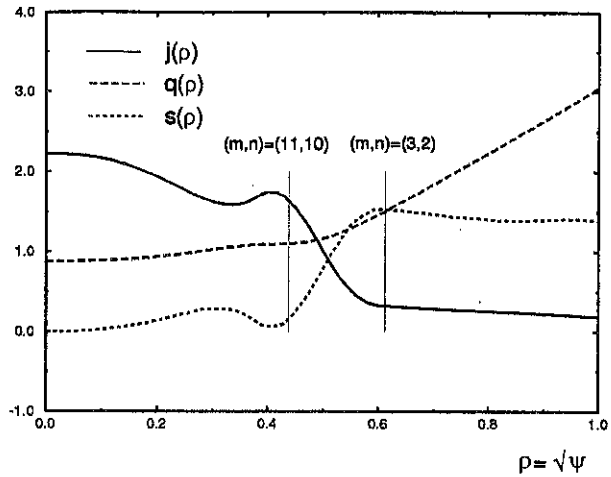

Fig. 1. Typical profiles for current (j), safety factor (q), and shear (s) for ASDEX Upgrade discharge 8529.

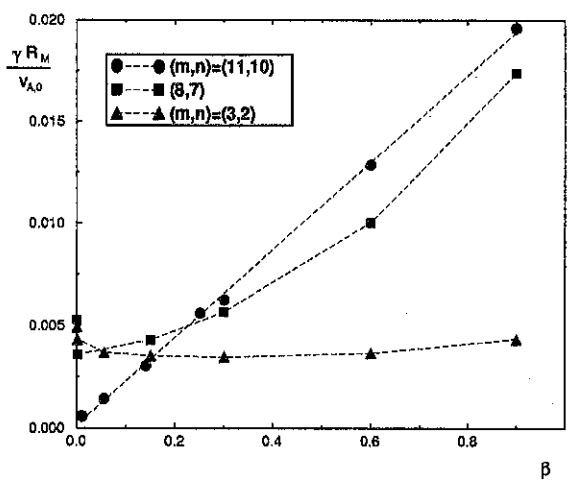

Fig.2. The pressure dependence of the growth rate for the modes $(m, n) = (3, 2), (8, 7), (11, 10)$. The growth rate is normalized to $1/\tau_{A,0}$, where $\tau_A, 0$ is the Alfvén time.

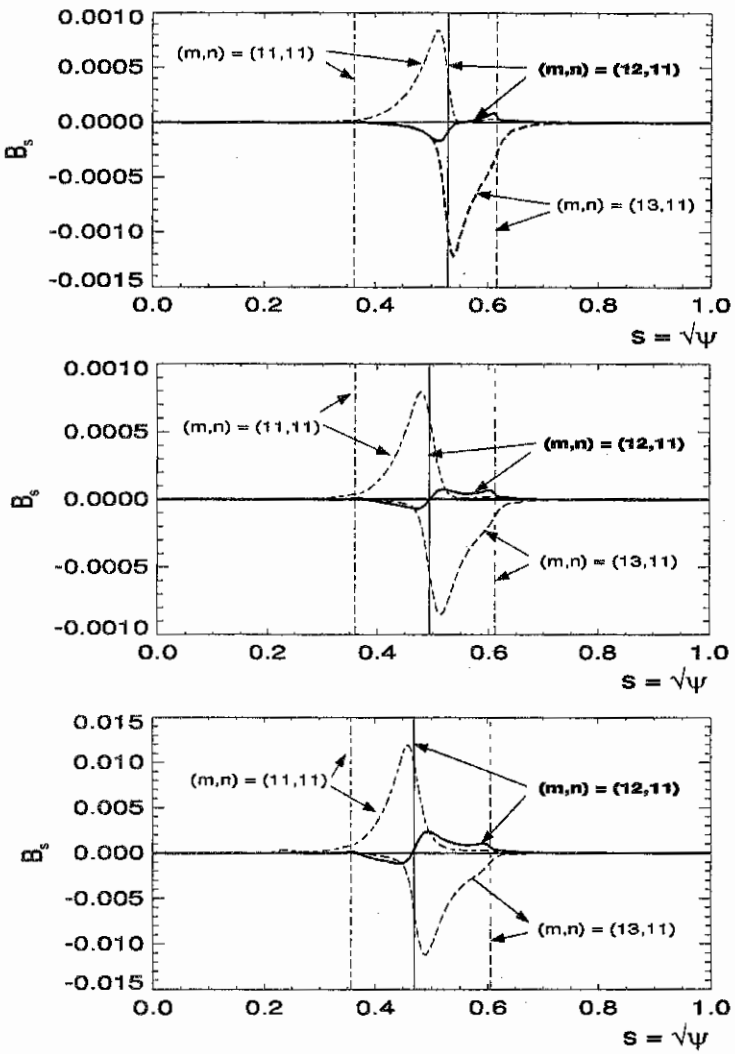

Fig. 3. The radial magnetic field B_s for the $(12, 11)$ mode. The Fourier components $(11, 11)$ and $(13, 11)$ together with their corresponding rational surfaces are included. The pressure rises from top to buttom: $\beta_{pol} = 0.05, 0.3, 0.6$.

Modes with very high mode numbers would be stable in a torus without mode coupling even for vanishing pressure. Due to mode coupling, however, their growth rates rise proportional to β_{pol}. Varying the pressure gradient at the rational surface, keeping β_{pol} constant, one again finds a linear dependence between growth rate and pressure gradient. One may conclude, therefore, that the pressure dependence of the growth rate is mainly caused by the pressure gradient at the corresponding rational surface.

In order to study the properties of the observed modes one has to consider their eigenfunctions. The most dramatic change due to mode coupling can be seen in the radial magnetic field B_r. The influence of the mode coupling rises with increasing mode number and with higher pressure. The influence of the pessure is shown in Fig. 3 for the (12, 11) mode. It becomes obvious that the radial fields of the neighbouring Fourier components ($m = n, n+2$) become very important at the $q = (n+1)/n$ surface. For very high mode numbers such as that shown in Fig. 3, the radial field at this rational surface predominantely is given by the harmonics $m \neq n+1$. The radial field of the component with $m = n+1$ may become zero or even change the direction at its rational surface if the pressure becomes high enough. In this case there would be no radial magnetic field with the right helicity at the considered rational surface that could cause a tearing of the magnetic field lines. Thus, through mode coupling the classical tearing modes change their properties completely. Nevertheless, the variation of the growth rates with respect to resistivity of the modes considered is proportional to $\eta^{3/5}$ corresponding to the well known tearing mode scaling.

The investigation of tearing modes with high mode numbers requires the inclusion of many poloidal harmonics as well as a high radial resolution. To ensure that the results are reliable, convergence studies have been carried out. Taking the experimental pressure it has been shown that the inclusion of 12 poloidal harmonics and 100 radial grid points is sufficient even for the highest mode numbers.

3 Conclusions

The observed high-n/high-m modes in ASDEX Upgrade discharges with high impurity accumulation have been shown to be modified tearing modes. These modes are unstable in low shear regions due to mode coupling. High resistivities, high pressure and current gradients at the corresponding rational surfaces as well as low shear support the mode growth.

[1] A. Gude, K. Hallatschek et al., this conference

[2] W. Kerner et al., JET report JET-P(97)04, submitted to J. Comp. Phys. (1997)

Localized ECRH Power Deposition in ASDEX Upgrade

F. Leuterer, A.G. Peeters, G. Pereverzev, F. Ryter,
and ASDEX Upgrade Team
Max Planck Institut für Plasmaphysik, IPP-EURATOM Association
Garching, Germany

1) Introduction

For ASDEX Upgrade an ECRH system with 140 GHz, 2 MW, 2 sec is in construction [1]. Up to now experiments with 0.4 MW, 0.5 sec, 2nd harmonic x-mode were performed, mainly for heat wave studies, where amplitude and phase of the heat wave are evaluated outside of the power deposition zone to deduce the electron heat conductivity [2]. In this paper we want to examine how and which information can be deduced from the temperature rise in the deposition region.

2) The heat diffusion equation

We assume the plasma as homogeneous within the considered volume and apply the linearized heat diffusion equation with constant coefficients to describe the temperature rise after switch-on of the ECRH

$$v_t(x,t) = \frac{2}{3}\chi v_{xx}(x,t) - bv(x,t) + f(x,t) \qquad (1)$$

The subscripts denote differentiation with respect to time or space. The damping term b describes changes in the local Ohmic power input and in the electron-ion collisions. For the driving term $f(x,t)$ we assume a Gaussian profile of amplitude $f_0(t)/(w\sqrt{\pi})$, width w, and a step function $f_0(t)$ in time centered at $x = x_0$. The solution to this equation is

$$v(x,t) = ac\frac{e^{ab}}{\sqrt{ab}}\left\{\Psi\left(\sqrt{ab(1+t/a)},\sqrt{abg}\right) - \Psi\left(\sqrt{ab},\sqrt{abg}\right)\right\} \qquad (2)$$

with $a = w^2/(8\chi/3)$; $c = f_0/w$; $g = (x - x_0)^2/w^2$; and the function

$$\Psi(\mu,\nu) = \frac{2}{\sqrt{\pi}}\int_0^{\mu}\exp(-\xi^2 - \nu^2/\xi^2)d\xi \qquad (3)$$

The quantity a is a characteristic time depending on the heat conductivity χ and the deposition width w, while c is the temperature rise per time unit at $x = x_0$ and $t = 0$, and g is a normalized space coordinate. The function $\Psi(\mu,\nu)$ can be expressed in the form of usual errorfunctions as

$$\Psi(\mu,\nu) = \frac{1}{2}\left\{e^{-2|\nu|} - e^{2|\nu|} + e^{2\nu}\Phi(\mu+\nu/\mu) + e^{-2\nu}\Phi(\mu-\nu/\mu)\right\} \qquad (4)$$

Fig.1 shows the calculated time evolution of temperature at different locations g. The time is normalized to the characteristic time a. Within the power deposition region, $g \leq 4$, the temperature rises instantaneously, outside the temperature rise is increasingly delayed. Nonzero

damping, $b \neq 0$ acting as a sink of energy, leads asymptotically to a finite temperature increase. Evaluations of equ. (2) show that it takes about 10 characteristic times for the profile to expand in space by about a factor of 2.

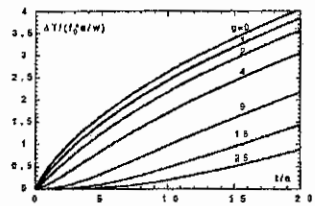

Fig. 1: Normalized temperature rise at zero damping (b = 0), at different locations g = ((x-x0)/w)^2

The temperature rise given by equ.(2) depends on the width w of the deposition profile. However, for $t/a \gg 1$ the temperature evolution becomes independent of w. Therefore the temperature evolution contains information on the initial power deposition profile only for times $t/a < 1$.

3) Application to ASDEX Upgrade shots

In ASDEX-Upgrade we apply ECRH in the 2nd harmonic x-mode to achieve a stronly localized power deposition. In addition the Gaussian microwave beam is focused such that also for off-axis heating by poloidal beam deflection the power deposition remains very localized. Ray tracing calculations, including diffraction effects to describe the Gaussian beam [3], result in power deposition profiles with widths w from 3 mm to 15 mm. Assuming a heat conductivity of $\chi = 1$ m^2/sec this corresponds to characteristic times of $a = 3.5$ to 80 μsec. With such a focused deposition at half radius in ASDEX Upgrade it takes about 50 μsec in a 1 keV plasma to distribute the energy around the flux surface. We will therefore not be able to measure deposition profiles with $w < 10$ mm. In addition, for $t/a < 1$ the temperature rise is very small and comparable to the noise level, and we need a much longer time ($\approx$ 1 msec) to determine the rate of change of the temperature. Therefore we cannot expect to reliably determine such narrow deposition profiles from the slope of the temperature rise in a single switch-on event.

However, assuming that locally a homogeneous plasma slab model is applicable, we may use equ.(2) and fit it to the experimentally measured temperature rise (by ECE) over a time span $\Delta t/a \gg 1$. From such a fit we can determine the quantities a, b, c and x_0, but not w. For the fit we use several adjacent ECE channels at known positions x in and close to the deposition region, and assume a deposition profile w as calculated from ray tracing, but not narrower than 10 mm. The fit is done over a time span of 10 msec so that magnetic field diffusion can be neglected. Furthermore, to get unperturbed data during the switch-on of the ECRH heating, we used a time interval in ohmic discharges at the end of the plasma current ramp-up when sawtooth oscillations did not yet set in.

An example of such a fit is shown in fig.2. The fit was applied to all temperature signals simultaneously. According to the applied model, we require the quantities a and c to be constant for all channels, but let b free for each channel. The heat conductivity χ is then calculated from

the fit parameter a and is multiplied by κ (κ = elongation) to take into account the variation of the temperature gradient around a poloidal circumference of a flux surface.

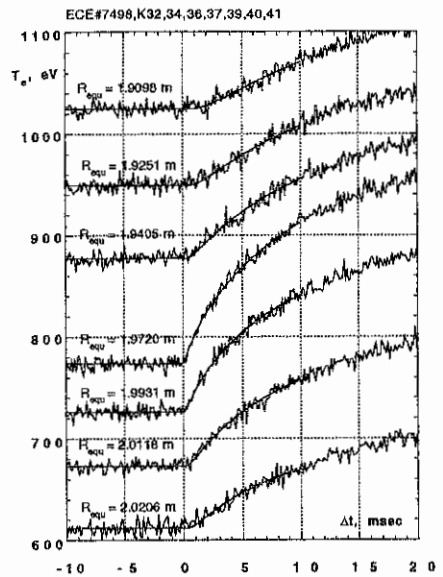

Fig. 2: Fitted ECE-temperature signals. All channels are fitted simultaneously

Values of χ thus obtained at different radial deposition centers are shown in fig.3. Most χ values are in the range of 1 m^2/sec and thus close to the values obtained from power balance analysis, but lower than those obtained from heat wave studies [2,4]. In some of the shots the power was deposited close to a resonant q-surface and did excite an mhd-mode.

From the central temperature rise c as obtained from the fit we can calculate the absorbed power

$$P_{abs} = \frac{3}{2} n_e c\, 2\pi R_0\, 2\pi r_{dep} w \kappa \qquad (5)$$

with R_0 = major radius, r_{dep} = minor radius of deposition centre. The results are shown in fig. 4 and compared with the launched power.

The centre of deposition x_0 is also obtained from the fit. These results are compared in fig.5 with those calculated with ray tracing for different poloidal launch angles and on-axis resonant magnetic field. These results depend on the precision of the magnetic field reconstruction.

The damping term b was treated as a free fit parameter. So it was different for each ECE channel. The values were in the range 0.01 to 0.1 $msec^{-1}$, and thus of the order as expected from the local drop in ohmic heating power and the electron-ion energy exchange. The values of b tend to be higher on the low field side of the deposition centre, as expected because of the electron temperature gradient.

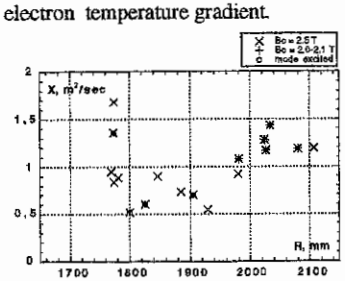

Fig. 3. Heat conductivities determined from the fit parameters as function of the major radius

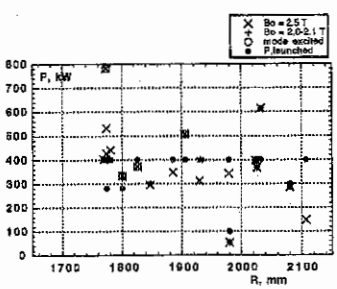

Fig. 4 Absorbed power as obtained from the fit parameter c (R_0 = 1650 mm, a = 500 mm)

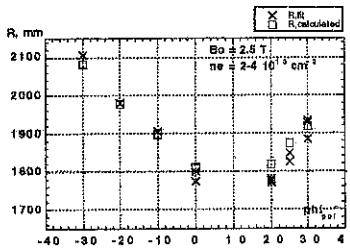

Fig. 5. Deposition centres as obtained from the fit compared to ray tracing results for different poloidal launch angles

Fits like in fig.2 are not uniquely determined. As explained above, for $t/a >> 1$ the information on the initial deposition profile is lost. Consequently we can get nearly equally good fits for different values of the profile width w. These fits differ mainly in the first millisecond, where an instantaneous rise or also a delayed rise can be fitted to the data within their fluctuations. Choosing smaller/larger w would lead to higher/lower values for the heat conductivity, but the product c^*w stays nearly constant. We consider our choice of the width obtained from ray tracing, but $w \geq 10$ mm, a reasonable one.

This fitting procedure was also applied to a test data set, which was created from a modelling of an ASDEX-Upgrade shot with the ASTRA transport code [5], specifying for χ a constant value of 0.8 m^2/sec. Two cases with deposition (width $w = 5$ mm) centered at r/a = 0.5 and r/a = 0.8 were fitted. The value of x_0 was in both cases within 1 mm of the specified deposition centre. The value of χ was within 10% of the specified one. The damping term b was as expected with a radial dependence because of the existing temperature gradient.

4) Summary

The response of the electron temperature upon the switch-on of very localized ECRH heating with Gaussian spatial profile can be well fitted to the heat diffusion equation with constant coefficients. To extract an electron heat conductivity from such a fit one needs to know the deposition profile width. This can in principle also be obtained from the fit. However, for narrow profiles, as we have them in ASDEX Upgrade, this requires better space and time resolution than available. Taking calculated values for the deposition width we arrive at heat conductivities close to those obtained from power balance.
The location of the deposition is within a few centimeters at the calculated position. The absorbed power is of the order of the launched power.

[1] Leuterer F., et al., Proc. 9th worksh. ECE and ECH, Borrego Springs, 1995, p. 529
[2] Ryter F., et al., 23rd EPS Conf. Contr. Fus. and Plasma Phys. Vol.1, 11, Kiev 1996
[3] Peeters A.G.,Phys. Plasmas 3, 4396 (1997)
[4] Ryter F., this conference
[5] Pereverzev G., et al., IPP - report IPP 5/42 (August 1991)

Scale lengths of current flow in magnetized plasmas

M. Weinlich, A. Carlson, V. Rohde, and the ASDEX Upgrade and NBI Teams
Max-Planck-Institut für Plasmaphysik, EURATOM Assoc., 85748 Garching, Germany

I. INTRODUCTION

When a current is driven from an electrode into a plasma, part of the voltage will drop across the sheath, the rest in the bulk. It is not uncommon in the ASDEX Upgrade divertor for an I–V characteristic to show a slope near floating of $I_{\mathrm{sat}}/(1\,\mathrm{V})$, even at densities as high as $10^{20}\,\mathrm{m}^{-3}$. The slope expected if all the voltage were dropped in the sheath is $I_{\mathrm{sat}}/(k_B T_e/e)$, so the electron temperature cannot then be higher than 1 eV. This puts an upper limit of about $\lambda_{\mathrm{resist}} = (\sigma_\parallel k_B T_e)/(n_e e^2 c_s) \approx 13\,\mathrm{mm}$ on the length of the current path, since otherwise more than the full voltage would have to be dropped in the bulk. For typical 1 mm probe dimensions, we see that the cross field current density can be no more than one order of magnitude smaller than the parallel current density. Current flowing across a magnetic field produces a force, which must be compensated by an equal and opposite force or an acceleration. If we can identify the nature of this compensating force, we may also find out whether and how Langmuir probe analysis needs to be modified to take the voltage drop in the bulk into account.

There are a number of approaches to these questions. Although it would be difficult to measure directly, the parallel path is certainly shorter than the connection length if all the current from a probe returns to the surrounding surface. Another indirect indication of the parallel path is the perpendicular distribution of the return current, which can be measured directly with passive probes or indirectly through the ratio of electron to ion saturation current. The connection between the parallel and perpendicular scales can be understood by considering a small perturbation on a uniform background plasma. Expressing the solution in terms of Fourier modes, larger $k_\parallel$ will be associated with larger $k_\perp$, although the exact relationship will depend on the details of the physics. Modes with a parallel scale longer than $\lambda_{\mathrm{resist}}$ will be dominated by the bulk resistance. Probes larger than the corresponding perpendicular scale will thus be affected by the bulk resistivity, although they will seek to minimize the cost by giving more weight to smaller scales, so that most of the current will flow near the edges of the probe. Probes smaller than this scale will be dominated by the sheath resistance and may be evaluated using the classical formulas. Since modes up to the characteristic scale are associated with little bulk resistance, the probe will use these to minimize the sheath resistance of the return current, spreading it over a distance given by the characteristic perpendicular scale. These ideas can be formulated and solved within the framework of magnetohydrodynamics (MHD) since the ion gyroradius is small compared to the

perpendicular scale and the parallel mean free path is about $\sqrt{m_i/m_e}$ times smaller than λ_{resist}. Comparison with experimental results on the current distribution and saturation current ratio will help determine what force balances $j \times B$.

II. MEASUREMENT OF RETURN CURRENTS

The first study [1] to measure the pattern of current flow from Langmuir probes in a tokamak used the divertor plate probe arrays in ASDEX Upgrade. One element was driven actively, and a passive current was looked for on elements in the surrounding and the opposing target plates. At most a few percent of the current was found to reach the opposing surface. The bulk of the current returned to the surrounding surface within about 2 mm as measured perpendicular to the magnetic field. A later study used a specially constructed Checkerboard Probe (CBP) [2] on a manipulator in the midplane of ASDEX Upgrade. This probe consisted of several elements which could optionally be driven together to vary the active area. The surrounding elements were maintained at vessel potential to measure the magnitude and distribution of the return current. In addition, the assembly could be rotated to vary the angle relative to the field and consequently the projected area. Within the experimental accuracy of about 10%, all of the current was found to return to the surrounding surface (Fig. 1) despite the relatively short connection length of $L_c = 3\,\text{m} \approx 10\lambda_{e,mfp} \approx 1/5\lambda_{\text{resist}}$. The distribution of current as a function of angle varied in a way that suggests that the width of the return area does not follow the width of the active area but is characteristic of the plasma conditions.

III. MEASUREMENT OF CURRENT RATIOS

The first investigation [3] of the ratio of electron to ion saturation current as a function of probe size was performed with the Tilting Probe Array (TPA) on DITE. A tendency of the current ratio to rise with projected probe size was found. A study done with the CBP on ASDEX Upgrade showed similar results where the projected areas were the same, but with larger projected areas, the reverse tendency was found (Fig. 2). The transition between small and large probes in this sense was found to occur when the projected length was a few ion gyroradii or a few tens of local Debye lengths. We note here that no promising ansatz has been found to explain a rise of the current ratio with probe size, and potential orbit and kinetic effects make this branch more difficult to handle theoretically. If we concentrate on the large probe branch, which is e.g. valid for the target plate probes at ASDEX Upgrade, we see that the current ratio is inversely proportional to the projected probe size (Fig. 2). If the saturation of the electron current is caused by ion saturation in the return area, then the current ratio can be taken as a measure of the ratio of the return area to the probe area. These results are again consistent with a 2 mm return current scale which is a characteristic of the plasma.

IV. ANALYTICAL SOLUTION OF MHD EQUATIONS

The linearized MHD equations reveal three candidates for the effect opposing $j \times B$: Braginskii viscosity [4], convective acceleration [5], and interaction with neutrals [6,7]. Viscosity turns out to be too weak to explain most of the I–V characteristics seen in the ASDEX Upgrade divertor. A convection of plasma across the probe, as would be produced by turbulence, can be thought of as the polarization drift of the ions, which see a changing electric field as they move across the probe. This mechanism is much stronger than viscosity, but is not able to explain measurements at the lowest temperatures and highest densities. In this regime the most powerful mechanism turns out to be interaction with neutrals. Under most conditions the dominant process is charge exchange with atoms, but under certain circumstances elastic collisions with molecules and ionization can be of a similar magnitude. Analysis of the MHD equations coupled with estimates of the neutral interaction obtained from Monte Carlo simulations yield a characteristic perpendicular scale of about 1 mm for electron temperatures below 5 eV. This is consistent with the observation in the ASDEX Upgrade divertor of I–V characteristics with slopes of $I_{\mathrm{sat}}/(1\,\mathrm{V})$ at all densities and a 2 mm return current perpendicular scale length.

It is important to point out that no "anomalous" diffusion was added to the MHD equations, as has been done in some other analyses [4,6,7]. Tokamak scrape-off layers are known to exhibit strong turbulence with a scale length of about 1 cm, which can be understood in terms of nonlinear solutions of the MHD equations. On a scale larger than 1 cm, the effects of this turbulence may well be described by an anomalous diffusivity. A Langmuir probe with a perpendicular dimension of only 1 mm, on the other hand, does not see turbulence, but only a more or less uniform convection of the plasma which changes its direction with time.

V. IMPLICATIONS FOR ANALYSIS OF PROBE DATA

Whether a correction is necessary to account for bulk resistivity is closely related to the question of whether the perpendicular extent of the probe is larger or smaller than a characteristic scale determined by plasma parameters. We have estimated that probes used in tokamaks are typically smaller than this scale, but not necessarily by a large factor, so moderate corrections may be necessary. We have also suggested that the ratio of electron to ion saturation current may be an indication of the ratio of characteristic scale to probe size. If this is so, then the temperature determined from the slope near floating and the saturation current might have to corrected downward more strongly when the current ratio is low. If the I–V characteristic is evaluated as that of an asymmetric double probe [8], this will occur automatically. In fact, where they showed lower current ratios, the measurements made with the TPA and the CBP both showed higher apparent temperatures as determined by a traditional analysis using the data

below or near floating. A double probe analysis shows a constant temperature (Fig. 3) in both data sets, regardless of whether the data are taken from the small probe or large probe branch. Whether or not the fluid analysis above is the entirely correct explanation, this establishes empirically that the double probe analysis is a necessary and adequate procedure for I–V characteristics with low electron current.

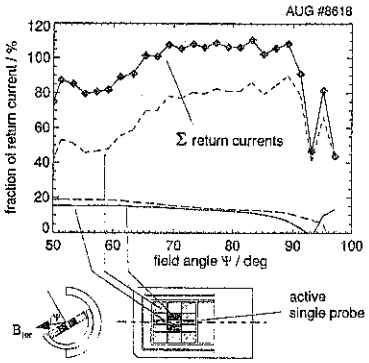

Fig. 1: *measurement of return currents*

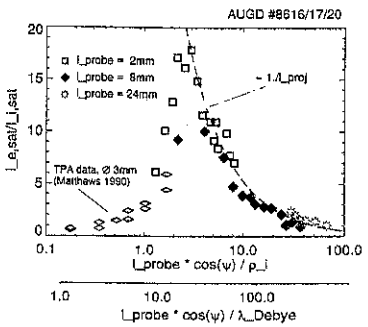

Fig. 2: *current ratios at different projected probe sizes*

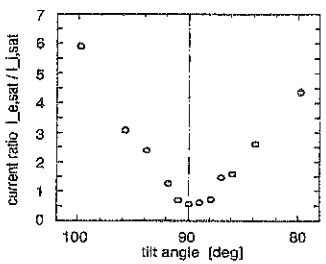

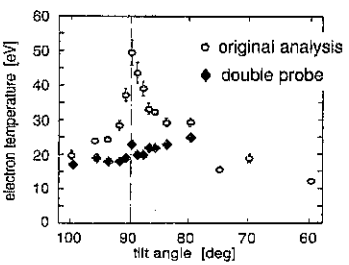

Fig. 3: *small current ratios require a double probe analysis to reproduce constant plasma parameters (TPA data points marked with open circles are out of [3]).*

[1] WEINLICH, M., report IPP V/64 (1995), Max-Planck-Institut für Plasmaphysik.
[2] CARLSON, A. et al., Journal of Nuclear Materials (1996), Proceedings of the 12th International Conference on Plasma Surface Interaction, to be published.
[3] MATTHEWS, G. et al., Plasma Physics and Controlled Fusion **32** (1990) 1301.
[4] ROZHANSKY, V. et al., Contributions to Plasma Physics **36** (1996) 391.
[5] CARLSON, A. et al., in *Europhysics Conference Abstracts* (1993) 17C/III, pp 1103.
[6] GÜNTHER, K. et al., Contributions to Plasma Physics **34** (1994) 484.
[7] GÜNTHER, K., in *Europhysics Conference Abstracts* (1995) 19C/I, pp 433.
[8] WEINLICH, M. et al., Physics of Plasmas **4** (1997) 2151.

Three-dimensional simulations of two-fluid drift-Braginskii turbulence

A. Zeiler, J. Bowman, D. Biskamp
Max-Planck-Institut für Plasmaphysik, EURATOM Association
85748 Garching, Germany

1. Introduction

A physics-based understanding and prediction of plasma-edge confinement requires the investigation of the complete two-fluid drift-Braginskii equations [1] in realistic geometry. In this paper we extend previous approaches (see Refs. [2,3] and citations within) in two ways. *(a)* Ion temperature dynamics are self-consistently taken into account. This allows us to study, within the same system, turbulence driven by resistive modes, which was previously treated in the cold ion limit, and η_i-mode turbulence. It also enables us to check whether the nonadiabatic electron response at the plasma-edge modifies the η_i-mode, since resistive effects usually are neglected in simulations of η_i-mode turbulence (see e.g. Refs. [4-6]). *(b)* To account for the fully nonlinear self-consistent evolution of the plasma-edge profile and to make efficient use of parallel computers with distributed memory architecture, we have developed and applied an anisotropic multrigrid Poisson solver to simulate resistive drift-wave turbulence in sheared magnetic geometry.

2. Ion temperature fluctuations

Our investigations of ion temperature effects are based on the electrostatic drift-Braginskii equations [1] in a flux-tube domain with field-aligned coordinates [3],

$$\nabla_\perp \cdot \frac{d}{dt}\nabla_\perp(\phi + \tau\alpha p_i) + \hat{C}\frac{p_e + \tau p_i}{1+\tau} + \frac{\partial^2 h}{\partial z^2} = 0, \tag{1a}$$

$$\frac{dn}{dt} + \frac{\partial \phi}{\partial y} - \left[\epsilon_n \hat{C}(\phi - \alpha p_e) - \alpha\epsilon_n(1+\tau)\frac{\partial^2 h}{\partial z^2}\right] = 0, \tag{1b}$$

$$\frac{dT_e}{dt} + \eta_e\frac{\partial \phi}{\partial y} - \frac{2}{3}\left[\epsilon_n \hat{C}(\phi - \alpha p_e) - 1.71\alpha\epsilon_n(1+\tau)\frac{\partial^2 h}{\partial z^2} + \kappa_\parallel \frac{\partial^2 T_e}{\partial z^2}\right] = 0, \tag{1c}$$

$$\frac{dT_i}{dt} + \eta_i\frac{\partial \phi}{\partial y} - \frac{2}{3}\left[\epsilon_n \hat{C}(\phi - \alpha p_e) - \alpha\epsilon_n(1+\tau)\frac{\partial^2 h}{\partial z^2}\right] = 0, \tag{1d}$$

with $p_e = n + T_e$, $p_i = n + T_i$, $h = \phi - \alpha(p_e + 0.71T_e)$, and $\nabla_\perp^2$, the total time derivative d/dt, and the curvature operator $\hat{C}$ defined as in [3]. The time and space units

$$t_0 = \left(\frac{RL_n}{2}\right)^{1/2}\frac{1}{c_s}, \quad L_\perp = 2\pi q_a \left(\frac{\nu_{ei} R\rho_s}{2\omega_{ce}}\right)^{1/2}\left(\frac{2R}{L_n}\right)^{1/4}, \quad L_z = 2\pi q_a R,$$

chosen to balance the three terms in Eq. (1a), are the natural choice for the resistive ballooning mode (but not for the η_i-mode which scales like ρ_s, as we will show). This normalization yields the dimensionless parameters $\alpha = (\rho_s c_s t_0)/[(1+\tau)L_n L_\perp]$, $\epsilon_n = 2L_n/R$,

$\tau = T_{i0}/T_{e0}$, $\kappa_\parallel = 1.6\alpha^2\epsilon_n(1+\tau)$, $\eta_e = L_n/L_{T_e}$, $\eta_i = L_n/L_{T_i}$ with $c_s^2 = (T_{e0}+T_{i0})/m_i$, $\rho_s = c_s/\omega_{ci}$, the profile e-folding lengths L_n, L_{T_e}, and L_{T_i}, and the magnetic shear parameter $\hat{s}$.

To calculate the linear properties of resistive ballooning and toroidal η_i-modes we drop the electron temperature fluctuations and Fourier-transform Eqs. (1a), (1b), (1d) in x and y keeping only the modes with $k_x = 0$. Along the magnetic field we expand in the orthogonal functions $\psi_n(z) = \exp\{-(\lambda z)^2/2\}H_n(\lambda z)$ where H_n are the Hermite polynomials. This leads to a generalized matrix eigenvalue problem for the growth rate γ, which we solve by standard numerical techniques.

We perform the eigenvalue calculations in the range of typical edge parameters $\alpha \sim 1$, $\epsilon_n \sim 0.05$, $\eta_i \sim 1$, $\hat{s} = 1$. Three main results are obtained: First, the resistive ballooning and the curvature driven η_i-mode appear as two different branches at comparable wavelengths, depending on the parameters. Second, the η_i-mode is unaffected by the non-adiabatic electron response. Its growth rate agrees surprisingly well with the one obtained without parallel resistivity. Third, the ion pressure gradient strongly supports the resistive ballooning mode. Consistent with Ref. [7] the resistive ballooning mode has a wavelength which scales like $L_\perp$ and is restricted to the low-α regime ($\alpha \leq 0.5$) by electron and ion diamagnetic effects. The η_i-mode is compared to the adiabatic limit ($\phi = \alpha n$) where the dispersion relation can be solved analytically. The analytic solution matches the numerical result obtained for arbitrary resistivity. The analytic solution allows us to show that unstable roots exist if and only if $\eta_i > 2/3$. Furthermore, we obtain the approximate scaling for the spectrum of unstable modes $k_y^2\rho_s^2 \sim 1/[\tau(\eta - 2/3)]$. This shows that η_i needs to be sufficiently larger than $2/3$ to destabilize the mode in the transport relevant long wavelength regime. The characteristic wavelength of the η_i-mode scales like ρ_s, in contrast to the $L_\perp$-scaling of the resistive ballooning mode. Thus, we conclude that the relative importance of resistive ballooning and η_i-modes is largely controlled by the ratio of the two scale lengths $\rho_s/L_\perp = \alpha(1+\tau)\epsilon_n^{1/2}$ and by the parameter η_i, since steepening the temperature gradient boosts the η_i-mode due to an increased growth rate at larger wavelength.

In order to check the relevance of the linear results we proceed to direct numerical simulation of the complete set of nonlinear equations (1) using the numerical methods described in Ref. [3]. In the low-α regime the ratio $\rho_s/L_\perp = \alpha(1+\tau)\epsilon_n^{1/2}$ is always small for realistic values of ϵ_n, hence we do not expect the η_i-mode to contribute unless $\eta_i \gg 1$; this result is confirmed by the numerical simulations. In the high-α regime ($\alpha = 1.25$), where the resistive ballooning mode is stable, the η_i-mode can become important for realistic values of ϵ_n. At $\epsilon_n = 0.2$, corresponding to large $\rho_s/L_\perp$, the transport rates are high and strongly peaked at the torus outside, demonstrating the importance of the toroidal η_i-mode. Consequently the turbulence level is strongly altered if η_i is changed. If ϵ_n is reduced ($\epsilon_n = 0.1$), the ratio $\rho_s/L_\perp$ becomes smaller and the transport coefficients are lower until, at $\epsilon_n = 0.05$, the transition to nonlinearly driven drift-wave turbulence

occurs (*cf.* Ref. [3] and citations within). A further reduction to $\epsilon_n = 0.02$ again strongly drives the transport. In this regime the inside/outside asymmetry is weak, reflecting the fact that the nonlinear drive does not depend on toroidicity.

3. Anisotropic multigrid Poisson solver

We have developed an object-oriented three-dimensional anisotropic multi-grid Poisson solver for simulating nonlocal collisional electrostatic drift-wave turbulence. In the design of this solver considerable effort was made to ensure that the presence of anisotropy (eg., arising from magnetic shear) does not lead to a significant degradation in performance. A three-dimensional slab version of the solver, which can be readily extended to more realistic geometries, has already been implemented for the Hasegawa–Wakatani equations. The code has been designed in a manner so that the complete nonlinear reduced Braginskii equations (*cf.* Sec. 2), including ion thermal dynamics, can be readily incorporated.

For nonlocal simulations of resistive drift-wave turbulence, we normalize (x, y, z, t) to $(\rho_s, \rho_s, L_\parallel, \Omega_i^{-1})$ and the total fields (ϕ, n) to $(T_e/e, \bar{n})$. Here $\rho_s = c_s/\Omega_i$, $\Omega_i = eB/(m_i c)$, $c_s = (T_e/m_i)^{1/2}$, T_e is the electron temperature, m_i is the ion mass, $L_\parallel = \rho_s[B/(ec\eta_\parallel \bar{n})]^{1/2}$, and $\bar{n}$ is some characteristic density. In this normalization, the coupled set of equations for the potential and density studied by Hasegawa and Wakatani (Ref. [8]) appear as

$$\nabla_\perp \cdot \left(n \frac{d}{dt} \nabla_\perp \phi \right) + \nabla_\parallel \cdot \left(\nabla_\parallel \phi - \frac{\nabla_\parallel n}{n} \right) = D_\phi \nabla_\perp{}^8 \phi, \tag{2a}$$

$$\frac{dn}{dt} + \nabla_\parallel \cdot \left(\nabla_\parallel \phi - \frac{\nabla_\parallel n}{n} \right) = D_n \nabla_\perp{}^6 n. \tag{2b}$$

In terms of the shear scale length L_s one may express

$$\nabla_\perp = \left(\frac{\partial}{\partial x} + z \frac{L_\parallel}{L_s} \frac{\partial}{\partial y} \right) \hat{x} + \frac{\partial}{\partial y} \hat{y}, \qquad \frac{d}{dt} = \frac{\partial}{\partial t} + \hat{z} \times \nabla \phi \cdot \nabla. \tag{3}$$

The hyperviscosity coefficients D_ϕ and D_n are chosen to minimize the range of scales devoted to modelling small-scale dissipation.

The coupled equations (2) are solved as an initial value problem, using a second-order predictor-corrector scheme. To avoid unnecessary restriction of the time step by the parallel-gradient terms, we treat these terms implicitly with a second-order trapezoidal approximation. At the i^{th} time step, this requires the inversion of an anisotropic elliptic operator of the form

$$\nabla_\perp \cdot (n_{i-1} \nabla_\perp \phi_i) + \frac{\Delta t}{2} \nabla_\parallel \cdot \left(\nabla_\parallel \phi_i - \frac{\nabla_\parallel n_i}{n_{i-1}} \right) = f_i^\phi, \tag{4a}$$

$$n_i + \frac{\Delta t}{2} \nabla_\parallel \cdot \left(\nabla_\parallel \phi_i - \frac{\nabla_\parallel n_i}{n_{i-1}} \right) = f_i^n; \tag{4b}$$

The advective nonlinearities, treated explicitly, are incorporated into the right-hand side. The resulting operator, linear in n_i and ϕ_i, is inverted with an anisotropic multigrid solver.

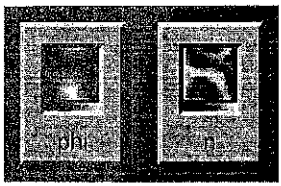

Figure 1: Typical xy-cross section of ϕ and n in the absence of magnetic shear.

This solver, which is based on an xy-zebra-surface Gauss-Seidel smoother, in turn requires the solution of

$$\nabla_\perp \cdot (n_{i-1} \nabla_\perp \phi_i) = f_i. \tag{5}$$

Solutions to this 2D anisotropic Poisson equation are obtained with a secondary multigrid solver based on an y-zebra-line Gauss-Seidel tridiagonal smoother (*cf.* Ref. [9]).

Our algorithm has distinct advantages relative to a pseudospectral Poisson solver. On a scalar machine, the computation time for our anisotropic multigrid solver is comparable to that of a pseudospectral code. However, a multi-grid solver parallelizes much more effectively over a distributed memory architecture (a parallel version of the code is currently being developed for a Cray T3E computer). A multigrid algorithm also allows the use of more general boundary conditions. Furthermore, all nonlinear terms can be retained in a straightforward manner; in contrast, pseudospectral solvers require linearization of the n_{i-1} factor appearing in (5). While the execution time for a single step of our semi-implicit algorithm is not substantially greater than that for an explicit code (based on a 2D Poisson solver), we have found that the implicit treatment of the parallel-gradient terms typically permits a time step of about four times larger. In Fig. 1 we illustrate a typical turbulent state obtained with our multigrid solver.

References

[1] A. Zeiler, J. F. Drake, B. Rogers, "Nonlinear reduced Braginskii equations with ion thermal dynamics in toroidal plasma", Phys. Plasmas, in press (1997).

[2] B. Scott, Plasma Phys. Control. Fusion **39**, 471 (1997).

[3] A. Zeiler, J. F. Drake, D. Biskamp, Phys. Plasmas **4**, 991 (1997).

[4] R. E. Waltz, Phys. Fluids **31**, 1962 (1988).

[5] M. Ottaviani, *et al.*, Phys. Fluids B **2**, 67 (1990).

[6] H. Nordman, J. Weiland, Nuclear Fusion **29**, 251 (1989).

[7] S. V. Novakovskii, *et al.*, Phys. Plasmas **2**, 781 (1995).

[8] A. Hasegawa and M. Wakatani, Phys. Rev. Lett. **50**, 682 (1983).

[9] W. Hackbusch, Multi-Grid Methods and Applications, Springer (1985).

Three Dimensional Computation of Fluid and Kinetic Drift Alfven Turbulence in Tokamak Geometry

B. Scott and F. Jenko

Max Planck Institut für Plasmaphysik
Euratom Association
D-85748 Garching, Germany

June 1997

A two-fluid moment model for drift Alfvén turbulence is constructed, in which the electron temperature is allowed to be anisotropic. For weakly collisional edge plasmas, the fact that only the parallel temperature is coupled through the Alfvenic dynamics to the ExB flows is quantitatively significant. Electron dominated edge turbulence throughout typical edge operation space is drift Alfven turbulence, with weak dependence on either collisionality or ballooning effects. ExB flow generation is significant if the collisionality is low enough or the plasma beta is high enough, suggesting an important role for magnetic flutter, or magnetic Reynolds stress, in the L-H transition.

In the construction of fluid drift turbulence models which are valid in hot tokamak regimes, the fact that the electron collisional relaxation frequency is slow compared to the turbulence has to be faced in some reasonable way, even if a fully rigorous fluid model may not be possible to construct [1]. For the purposes of electron pressure gradient driven turbulence it is sufficient to carry the temperature and parallel heat flux as self-consistent, time-dependent variables in order to capture the correct time scales of the processes involved in the coupling of ExB flows to the things they transport [2]. The type of "mode" most prominent in this process is the drift Alfven wave system, in whose most basic form with $\widetilde{n}$, $\widetilde{\phi}$, and $\widetilde{A}_{\parallel}$ as dependent variables the three eigenmodes are an almost electrostatic drift mode and two almost ideal shear Alfven waves — at finite $k_{\perp}\rho_s$ each eigenmode has a small amount of admixture from the other two [3]. In turbulence all these are coupled, and while there are no well-defined eigenmodes *per se*, the turbulence is still well-described as an almost electrostatic ExB turbulence doing the transport coupled through thermal/kinetic Alfvenic dynamics to two electromagnetic transients which do all the dissipation and control the amplitude of the turbulence. Additional effects such as magnetic flutter or curvature (*i. e.*, ballooning) may be important in deciding the level of the turbulence but have no qualitative effect on its mode structure [2].

In this work the drift Alfven turbulence model is further extended to weak collisionality by allowing the parallel and perpendicular temperatures to differ. Each is coupled to dissipation through the corresponding parallel flux of parallel or perpendicular energy, respectively, in what can be called a six moment closure [4]. The only important differences to [4] is that the equation system is not a guiding center system, so that it must reduce to the Braginskii equations [5] in the collisional limit, and that since the field lines can be perturbed, $k_\parallel$ may not be used as a parameter in the model for Landau damping. For the present, Landau damping is modelled via direct damping of the two heat flux moments.

Under drift ordering, with the usual normalisations of drift-wave, drift-Alfvén, or universal-mode turbulence (t to $L_\perp/c_s$ and perpendicular coordinates to ρ_s), and under the cold-ion restriction (in which the polarisation drift divergence reduces to ExB advection of the ExB vorticity and the parallel ion velocity is forced by the electron pressure), this version of the fluid drift system becomes

$$\frac{d}{dt}\nabla_\perp^2\phi = \nabla_\parallel J_\parallel - \mathcal{K}\left(T_\perp + n\right) \tag{1}$$

$$\frac{d}{dt}n = -\omega_n\frac{\partial\phi}{\partial y} + \nabla_\parallel\left(J_\parallel - u_\parallel\right) - \mathcal{K}\left(T_\perp + n - \phi\right) \tag{2}$$

$$\frac{1}{2}\frac{d}{dt}T_\parallel = -\frac{1}{2}\omega_t\frac{\partial\phi}{\partial y} + \nabla_\parallel\left(J_\parallel - u_\parallel - q_{\parallel\parallel}\right) - \mathcal{K}\left(0.5T_\parallel\right) - \nu\left(T_\parallel - T_\perp\right) \tag{3}$$

$$\frac{d}{dt}T_\perp = -\omega_t\frac{\partial\phi}{\partial y} - \nabla_\parallel q_{\perp\parallel} - \mathcal{K}\left(3T_\perp + n - \phi\right) + \nu\left(T_\parallel - T_\perp\right) \tag{4}$$

$$\hat{\beta}\frac{\partial}{\partial t}A_\parallel + \hat{\mu}\frac{d}{dt}J_\parallel = \nabla_\parallel\left(T_\parallel + n - \phi\right) - \hat{\mu}\nu\left[J_\parallel + \frac{0.71}{1.6}\left(q_{\parallel\parallel} + q_{\perp\parallel} + 0.71J_\parallel\right)\right] \tag{5}$$

$$\hat{\mu}\frac{d}{dt}q_{\parallel\parallel} = -\frac{3}{2}\nabla_\parallel T_\parallel - \hat{\mu}a_L q_{\parallel\parallel} - \hat{\mu}\nu\frac{5/2}{1.6}\left[q_{\parallel\parallel} + \frac{3}{5}0.71J_\parallel + 1.28\left(q_{\parallel\parallel} - 1.5q_{\perp\parallel}\right)\right] \tag{6}$$

$$\hat{\mu}\frac{d}{dt}q_{\perp\parallel} = -\nabla_\parallel T_\perp - \hat{\mu}a_L q_{\perp\parallel} - \hat{\mu}\nu\frac{5/2}{1.6}\left[q_{\perp\parallel} + \frac{2}{5}0.71J_\parallel - 1.28\left(q_{\parallel\parallel} - 1.5q_{\perp\parallel}\right)\right] \tag{7}$$

$$\hat{\epsilon}\frac{d}{dt}u_\parallel = -\nabla_\parallel\left(n + T_\parallel\right) - \mu_\parallel\nabla_\parallel^2 u_\parallel \tag{8}$$

where d/dt includes advection by the ExB velocity, $\nabla_\parallel$ includes the contribution from magnetic fluctuations, $J_\parallel = -\nabla_\perp^2 A_\parallel$, and $\mathcal{K}$ is the magnetic curvature operator.

This set is similar to that for transcollisional drift Alfvén turbulence with an isotropic temperature [2], and the parameters in the equations are the same. The main ones are those controlling the ratios of important frequencies:

$$\hat{\beta} = \frac{4\pi nT}{B^2}\left(\frac{qR}{L_\perp}\right)^2 \qquad \hat{\mu} = \frac{m_e}{M_i}\left(\frac{qR}{L_\perp}\right)^2 \qquad \nu = \frac{\nu_e}{(c_s/L_\perp)} \tag{9}$$

giving the relative speeds of the Alfvén, thermal transit, and collision frequencies, respectively. The ion mass in these units, $\hat{\epsilon}$, is also normalised by the same two factors of $qR/L_\perp$, reflecting the field line connection length as $2\pi qR$ and baseline parallel wavenumber of $k_\parallel qR \approx 1$. The other parameters are secondary; ω_n and ω_t give the relative strengths of the density and temperature gradients and $\mu_\parallel$ is an artificial parallel viscosity, all of order unity. The Landau damping parameter is set to $\hat{\mu}^{-1}$.

In these equations it is important to note the different roles for $T_\parallel$ and $T_\perp$ — $T_\parallel$ participates in the parallel Alfvenic dynamics (through $J_\parallel$) while $T_\perp$ is directly coupled to $\widetilde{\phi}$ through the magnetic curvature. With finite collisionality, however, the distinction between $T_\parallel$ and $T_\perp$ or $q_{\parallel\parallel}$ and $q_{\perp\parallel}$ disappears and we revert to the isotropic model of [2].

The computations are done in a flux-tube model tokamak geometry, with the coordinates aligned to the magnetic field; the treatment is as in [6], but the x-dependence of the geometric coefficients is dropped as in The parallel boundary condition is maintained as in [6], due to the importance of having the correct discrete spectrum for $k_\parallel$ in the parallel electron dynamics. This self-consistent dynamics is responsible for the basic mechanism of the nonlinear drift wave [7,8], or drift Alfvén [2], instability.

Computations in the slab geometry of [2] show the effects of the anisotropy in the temperature and heat flux. The comparison was done for the nominal case of [2], with $\hat{\beta} = \hat{\mu} = 10$, $\nu = 0.5$, and $2L_\perp/R = 0.03$ corresponding to the pre-transition parameters in ASDEX Upgrade, and also for a "low-density" case with $\nu = 0.1$. The same drift Alfvén mode structure emerges, and the transport difference at $\nu = 0.5$ is only about 6 to 5, with the anisotropic case lower. At $\nu = 0.1$ the difference is greater, 4 to 3, so the dependence on ν is slightly greater with the anisotropic temperature. This is consistent with the departure of $T_\perp$ from $T_\parallel$, and the thermal wave in the $T_\parallel, q_{\parallel\parallel}$ pair is faster than that in the $T, q_\parallel$ pair by a factor of $\sqrt{9/5}$, which slightly reduces the total drive due to the temperature gradient. This is not a sharp contrast, but it is enough of one to affect comparisons between theory and experiment in the serious first-principles L-H computations of the near future. A tokamak like ASDEX Upgrade should be more affected by this in edge turbulence than one like Alcator C-Mod.

Another process affected by the anisotropy is the generation of sheared ExB flow by magnetic flutter, again because this is mediated by $\nabla_\parallel J_\parallel$ (the magnetic Reynolds stress) as well as $\mathbf{v}_E \cdot \nabla\nabla_\perp^2\phi$ (the ExB Reynolds stress), and only $T_\parallel$ affects $J_\parallel$. The comparative studies show that a well-formed shear layer — a vorticity profile nearly flat and a ϕ profile nearly parabolic — forms most likely for $\nu < 0.2$ and $\hat{\beta} > \hat{\mu} = 10$.

A parabolic $\phi(x)$ is significant since the effects of the boundaries in the x-domain can be judged less important than if $\phi(x)$ has many local extrema (one of the undesirable effects of periodic boundary conditions in too small a domain). Although these runs have not yet produced a self-consistent L-H transition, this effect may have an important role in one.

We are also developing a drift-kinetic electron model to more solidly ground the fluid model in the collisionless regime. This is done by replacing Eqs. (2–7) with the drift kinetic equation:

$$\frac{df_e}{dt} = -\omega_T \frac{\partial \phi}{\partial y} - \alpha_e w_\parallel \nabla_\parallel f_e - \alpha_e E_\parallel \left(w_\parallel f^M - \frac{\delta}{2} \frac{\partial f_e}{\partial w_\parallel} \right) \tag{10}$$

where $\alpha_e = \sqrt{2/\hat{\mu}}$, $\omega_T = \omega_n + \omega_t(w^2 - 3/2)$, and $\delta = \rho_s / L_\perp$. So far, this has been done with $\hat{\beta} \to 0$ and $\nu \to 0$ and no curvature; extension to tokamak geometry is in progress. We have found that the velocity space nonlinearity in Eq. (10) has a strong effect in the absence of magnetic shear, because it damps the higher $k_\parallel$ modes which populate the $k_\parallel = 0$ portion of ϕ required for significant transport [9]. With moderate shear ($\hat{s} = 1$), however, there are no purely $k_\parallel = 0$ modes and therefore ϕ is coupled to f_e at al degrees of freedom. The portion with $|k_\parallel q R| < 1/2$ then does the transport more or less by itself and the damping of higher $k_\parallel$ modes has little effect. In this case, the Landau resonance is smeared out by ExB turbulence [10]. Since this effect is captured in the fluid model by the presence of ExB advection in Eqs. (6,7), there is genuine hope that a relatively simple fluid model can capture the important processes in fluid drift turbulence in the weakly collisional regime, even quantitatively.

References

[1] G. Hammett and F. Perkins, *Phys. Rev. Lett.* 64 (1990) 3019.

[2] B. Scott, submitted to *Plasma Phys. Contr. Fusion* March 1997.

[3] A. B. Mikhailovskii and L. I Rudakov, *Sov. Phys. JETP* 17 (1963) 621; J. T. Tang and N. C. Luhmann, Jr., *Phys. Fluids* 19 (1976) 1935; J. D. Callen, *Phys. Rev. Lett.* 39 (1977) 1540. K. T. Tsang, J. C. Whitson, J. D. Callen, P. J. Catto, and J. Smith, *Phys. Rev. Lett.* 41 (1978) 557.

[4] M. A. Beer and G. W. Hammett, *Phys. Plasmas* 3 (1996) 4046.

[5] S. I. Braginskii, *Rev. Plasma Phys.* 1 (1965) 205.

[6] B. Scott, *Plasma Phys. Contr. Fusion* 39 (1997) 471.

[7] B. Scott, *Phys. Rev. Lett.* 65 (1990) 3289; *Phys. Fluids B* 4 (1992) 2468.

[8] D. Biskamp and A. Zeiler, *Phys. Rev. Lett.* 74 (1995) 706.

[9] C. Z. Cheng and H. Okuda, *Phys. Rev. Lett.* 41 (1978) 1116.

[10] W. W. Lee, Y. Y. Kuo, and H. Okuda, *Phys. Fluids* 21 (1978) 617.

Drift motion in the scrape-off layer during hard disruptions

L.L. Lengyel*, V.A. Rozhansky**, I.Yu. Veselova**

*Max-Planck-Institut fur Plasmaphysik, Euroatom Association, D-85748 Garching, Germany
**St.Petersburg State Technical University, St.Petersburg, Russia

1. Introduction

During hard disruptions, intense vaporization of the divertor plates takes place. The process is accompanied by the formation of a dense and partially ionized vapor layer over the plates, which significantly reduces the particle and heat fluxes reaching the divertor tiles and thus determines the evaporation rate of the surface. The energetic plasma particles moving along the skewed magnetic field lines are stopped inside the layer at different depths. Hence, in order to produce a return current that compensates the current carried by the plasma particles, a self-consistent electric field is generated (ambipolarity constraint). Since the temperature of the vapor plasma is of the order of some eV-s, the electrical conductivity is rather low and the resulting electric field is of considerable strength. In a tokamak with conducting divertor plates, the local electric field has to be normal to the plates, thus creating plasma drift across the flux surfaces. This electric field and the resulting drift motion are modelled in a self-consistent manner. In the code applied, the deceleration of hot particles of different energy groups is calculated, while the cold layer is described by means of resistive MHD equations by taking into account all important elementary processes taking place in the plasma [1]. In the present 1-D model, the electric field is calculated from the condition of zero net current through the plates. The analysis shows that drift velocities of the order of 10^3 to 10^4 m/s may be expected, which may notably impair the shielding characteristics of vapor layers and may thus increase the erosion rate of the divertor plates. Under analogous conditions, this type of drift may become relevant also for detached divertor plasmas in normal tokamak regimes.

2.Model

The 1D geometry is considered, Fig. 1, $\partial/\partial z = \partial/\partial x = 0$, B_x is assumed to be zero. The current of hot particles $e\Gamma_i(y)$-$e\Gamma_e(y)$ is parallel to $\vec{B}$, and its projection on y direction is $e(\Gamma_i - \Gamma_e)\sin\alpha$. It is calculated by tracing the depletion of particle groups of different energies [1]. The potential drop between the cold and the hot plasmas [2], [3] is also taken into account.

The current has to be balanced by the return current created by the self-consistent electric field E_y. The return current j_y is the sum of the projections of the B-parallel current $j_{||}\sin\alpha$ and the B-perpendicular current $j_{\perp}\cos\alpha$. The parallel current is primarily the electron current driven

by the parallel projection of electric field $E_{||}=E_y\sin\alpha$. The perpendicular current $j_\perp$ is associated with $E_\perp$. The condition of vanishing net current in the y-direction throughout the vapor layer can be written as

$$j_{||}\sin\alpha+j_\perp\cos\alpha+e(\Gamma_i-\Gamma_e)\sin\alpha=0. \quad (1)$$

It differs from the corresponding condition discussed in [3] by the second term. The component $j_{||}$ is determined from the parallel projection of the electron momentum balance equation

$$j_{||} = \sigma_{||}\sin\alpha(E_y + eT_e\partial\ln n_e / \partial y + g_T e\partial T_e / \partial y), \quad (2)$$

where $\sigma_{||}$ is the electrical conductivity which depends both on Coulomb and electron-neutral collisions [3], the coefficient g_T is larger than unity due to the thermal force. From the perpendicular component of the electron momentum balance equation (neglecting the perpendicular thermal force), we have

$$\vec{j}_\perp + \beta_e[\vec{j}_\perp \times \frac{\vec{B}}{B}] = \sigma_\perp(\vec{E}_\perp + [\vec{V}\times\vec{B}] + \frac{\nabla_\perp p_e}{en_e}), \quad (3)$$

where the Hall parameter $\beta_e=\omega_{ce}/\nu_e$; ω_{ce} is the electron cyclotron frequency, ν_e is the electron collision frequency, and $\vec{V}$ is the ion velocity, $\sigma_\perp=const\sigma_{||}$. Due to high collisionality, the ion and neutral gas velocities are assumed to be equal.

Another relation between the perpendicular current and plasma velocity is given by the x-component of the momentum equation

$$\frac{\partial\rho V_x}{\partial t} + \frac{\partial(\rho V_y V_x)}{\partial y} = [\vec{j}_\perp \times \vec{B}]_x. \quad (4)$$

The velocity component V_y is calculated from the y component of the momentum equation by solving simultaneously the complete set of resistive MHD conservation equations, thus determining the evolution of the vapor layer. The electric field component E_x is assumed to be zero.

3. Results of calculations

A set of typical results is presented for a scenario in which a carbon (or carbonized) divertor plate is exposed to a thermal disrupting plasma at t=0. The following input parameters were assumed: T_{e0}=5keV, $n_{e0}=5.5\times10^{18}m^{-3}$, B=6T, $\alpha=5^0$. A cold and dense shielding layer is evolving at the surface. The temperature (electron temperature being equal to the heavy particle temperature) and the density distributions, monitored at t = 50μs , are shown in Figs. 2

and 3. At this time instant, ionization degrees significantly less than unity only exist in a narrow vapor layer adjacent to the surface (y less than 2 cm) in which the neutral atom density is of the order of $10^{24}m^{-3}$. The corresponding potential distribution is shown in Fig. 4. The divertor plate as well as the vapor layer are biased negatively with respect to the rest of the SOL. The potential difference is of the order of the energy of the incident hot electrons. In Fig. 5, the calculated velocity component V_x is displayed for three different time instants. As can be seen, large lateral velocities may exist. Outside of the weakly ionized region the value of V_x practically coincides with the drift velocity $V_{drift}=E_\perp/B\approx E_y/B$. In another scenario calculations with T_{e0}=1keV, $n_{e0}=6x10^{19}m^{-3}$, which correspond to larger Hall parameter values β_e, lateral velocities of the same order of magnitude were obtained. Within the ionized part of the vapor layer, the values of V_x are found to be close to the values of V_{drift}.

4. Conclusions

Drift velocities of the order of 10^3 to 10^4 m/s may be expected during hard disruptions. This effect may notably impair the shielding characteristics of the vapor layer and increase the erosion rate of the divertor plates.

Acknowledgment

The study was supported in the framework of the German-Russian Scientific Technical Cooperation in the Field of Peaceful Use of Atomic Energy, Project No. RUS-554-96; by the RFFI, Grant No. 96-02-16919.

References.

1. Lalousis, P. et al. in Controlled Fusion and Plasma Physics (Proc. 22nd Eur. Conf. Bournemouth, 1995), Vol. **19C**, Part II, European Physical Society, Geneva (1995) 285.

2. Lengyel, L.L., Rozhansky, V.A., Veselova, I. YU., Nucl. Fusion **36**, No. 12 (1996).

3. Rozhansky, V.A., Lengyel, L.L., Calculation of Electric Fields in Vapor Shields Evolving at Ablating Surface, Tech. Rep. IPP 5/53, Max-Planck Institut fur Plasmaphysik, Garching (1993).

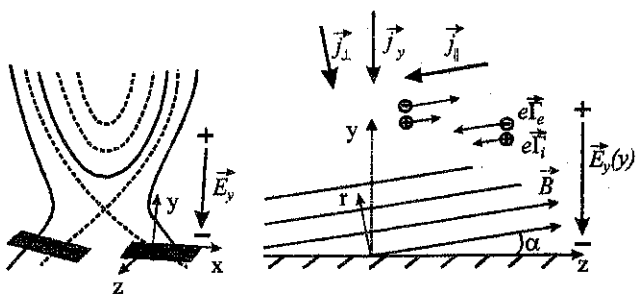

Fig.1 The geometry considered

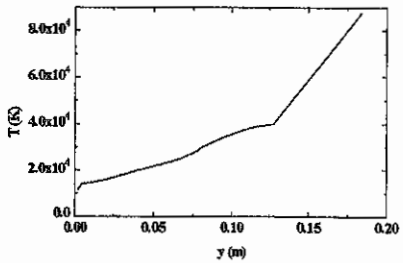

Fig.2 5 keV disrupting plasma: temperature distribution in the vapour layer 50 μs after plasma-wall contact.

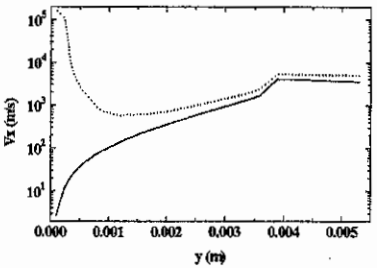

Fig.5 5 keV disrupting plasma: distributions of V_x (solid lines) and and $E_\perp/B$ (dotted lines) in the vapour layer

a) t = 3 μs.

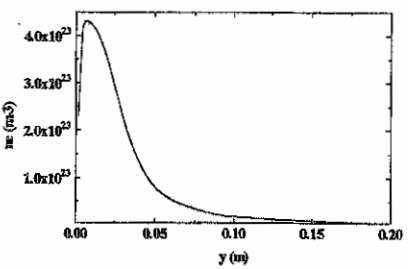

Fig.3 5keV disrupting plasma: density distribution in the vapour layer 50 μs after plasma-wall contact.

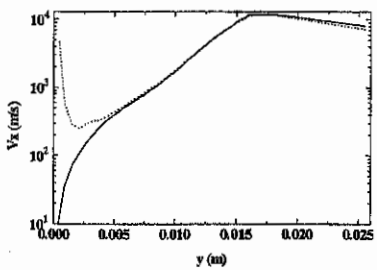

b) t = 10 μs.

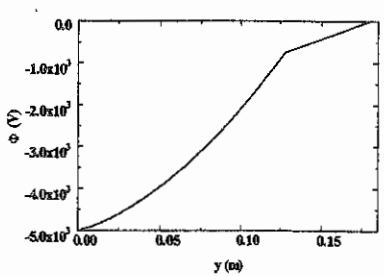

Fig.4 5 keV disrupting plasma: potential distribution across the vapour layer, t=50 μs

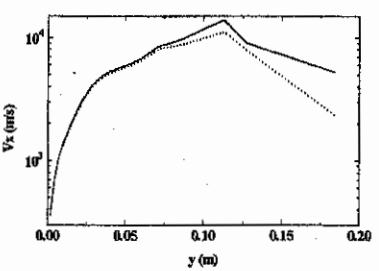

c) t = 50 μs.

Two-fluid MHD simulation of confinement of pellet-produced hydrogen clouds in hot magnetized plasmas

G. Kristof[a] and L. Lengyel

Max-Planck-Institut für Plasmaphysik, Euratom Association, D-85478 Garching, Germany
[a]Permanent address: Technical University Budapest, Department of Fluid Mechanics, H-1111 Budapest, Hungary

The structure of dense particle clouds surrounding ablating hydrogen isotope pellets is investigated, with particular emphasis on the B-perpendicular expansion, ionization, and deceleration dynamics. A time-dependent single-temperature two-fluid 1.5-D Lagrangian model is used in which the neutral and ionized fluid components are allowed to move with different velocities.

As is well known, the H_α and H_β emission patterns of excited neutrals residing in hydrogen pellet clouds are cigar-shaped, elongated in the direction of the magnetic field lines (see, for example, Durst [1]), although the expansion of the neutrals is not affected by the presence of magnetic fields. Accurate determination of the confinement radii of pellet clouds is of relevance from the point of view of up-to-date pellet ablation models, in which the magnetic constriction of the cloud expansion plays an important role [2,3,4]. The objective of the present work was to obtain quantitative information on the magnitude of collisional coupling between the neutral and ionized species of pellet clouds and on some phenomena not considered in previous cloud studies such as the inductive electric field associated with the time variation of the magnetic field during the high-beta cloud expansion phase. The analyses available on pellet cloud evolution and pellet cloud properties, with magnetic field effects properly taken into account, are usually based on single-velocity approximations [3,4,5,6,7,8] and therefore yield no information on the magnitude of collisional effects. For this reason, a time-dependent two-fluid single-temperature Lagrangian MHD model was developed in which the neutral and ionized components are allowed to move with different velocities but are collisionally coupled. The cloud is heated by the background plasma: the energy input along the magnetic field lines is specified in terms of the thermal energy flux carried by the plasma electrons (with a flux-limiting factor of 0.50), and by anomalous heat conduction in the **B**-perp direction ($\chi_e = 1\ m^2/s$ was assumed). The ablated particles are released as neutrals, their ionization being followed up by finite-rate calculations. The model is based on the usual MHD conservation equations, Maxwell's equations, and various rate equations. The details can be found elsewhere [9].

With respect to the geometry and scenario considered, the fact that the ablated particles leaving the pellet surface expand with a velocity that is about an order of magnitude larger than typical pellet flight-velocities (10^4 m/s compared with 10^3 m/s) [10] offers a convenient way of analysis: the pellet velocity is ignored and the analysis is carried out in a cylindrically symmetric, stationary coordinate system whose axis is aligned with the magnetic field. A disc-shaped mass-source of infinitesimal thickness is placed at the centre, which represents the ablating pellet. The size (radius) and the strength of the mass-source are given. The space is filled with a homogeneous hot background plasma of given temperature and density. At time = 0 the mass-source is turned on and cold neutral particles are blown into the plasma at a given rate and continuously heated by the incident hot particles. The evolution of the cloud forming around the mass-source is followed up by numerical means. The Lagrangian cells (coaxial annuli) receive cold neutral particles as long as they are in contact with the source. The cell boundaries are propagated in the radial direction with the particular velocity at which the neutral particle flux crossing the boundary from one side is balanced by the ion flux coming from the other side, the absolute value of the ion velocity being, in general, smaller than or equal to the neutral velocity. Hence at each cell interface one has

$$n_a(v_{ar} - v_r) + n_i(v_{ir} - v_r) = 0$$

where v_{ar} and v_{ir} are the radial velocities of the neutral and ionized components, computed by solving the respective momentum equations, and v_r represents the velocity of the cell boundary considered. Defining the degree of ionization α as $\alpha \equiv n_i/(n_a + n_i)$, the grid velocity can readily be expressed as a weighted function of the ion and neutral velocities:

$$v_r = \alpha\, v_{ir} + (1-\alpha) v_{ar}.$$

As can be seen, in the case of fully ionized and/or neutral clouds, the radial component of the grid velocity converges to the velocities of the ionized and/or neutral components, respectively.

In the axial (field-aligned) direction, it is assumed that, due to sufficiently high collisionality, the neutral and ionized species move with the same velocity: $v_{az} = v_{iz} = v_z$. The axial expansion velocity is calculated in terms of the cloud - background plasma pressure difference affecting the **B**-perp interface of each annular cell. To assure approximately equal cell masses, the number of cells can be increased during the computations. Artificial viscosity is used, if needed, in the numerical scheme. The input parameters of the model thus defined are T_{e0}, n_{e0}, B_0, size and strength of the mass-source (pellet radius and ablation rate), respectively.

Scenario calculations were performed with systematic variation of the input parameters. In the following, some representative results are described.

In FIG.1, the radial distributions of some cloud parameters (heavy-particle density in m^{-3} (a), ionization degree (b), temperature in K(c), Mach number of the radial expansion

velocity (d)) are given for the following set of input parameters:

$n_{e0} = 5 \cdot 10^{19}\,m^{-3}$; $T_{e0} = 500\,eV$; $B_0 = 2\,T$; $\dot{n}_s = 2 \cdot 10^{23}\,s^{-1}$; $r_s = 1\,mm$

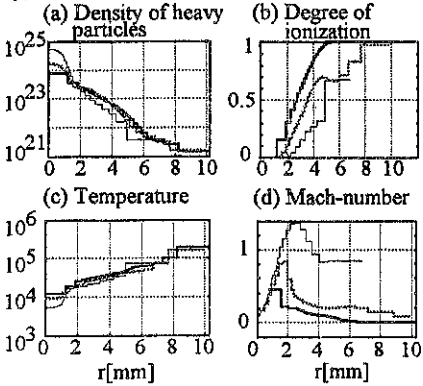

FIG.1.

The three curves shown correspond to three different time levels: 0.3 μs (thin solid line), 0.6 μs (dotted line), and 0.9 μs (heavy solid line). (The horizontal sections of the curves represent the thickness of the Lagrangian cells.) The asymptotic radial flow pattern is inherently subsonic, in disagreement with earlier steady-state transonic neutral shielding ablation models [11,12].

Since the radial expansion of the ionized matter is first stopped at the periphery and this deceleration 'wave' propagates from the periphery into the cloud interior, the effective channel cross-section for the axial (**B**-parallel) momentum transfer defined by the ratio of the volume integrals $R_{eff} = \int r \cdot v_z(\rho_a + \rho_i)dV \;/\; \int v_z(\rho_a + \rho_i)dV$ may change in time. For the scenario shown in FIG.1 the asymptotic value of the 'effective radius' $R_{eff}(\tau \geq 10\,\mu s)$ is about 68% of its initial (maximum) value. The constricted flow of the ablated material in channels whose effective cross-sections are less than those defined by the respective confinement radii may be responsible for the striated structure of pellet wakes observed in tokamaks [10].

At the beginning of the ionization process, the neutral fluid component may move significantly faster than the ionized component. In FIG.2, the specific radial momenta of the two components (given in $kg \cdot m^{-2} \cdot s^{-1}$) are plotted as functions of the radius at two time levels: 0.3 μs and 20 μs.

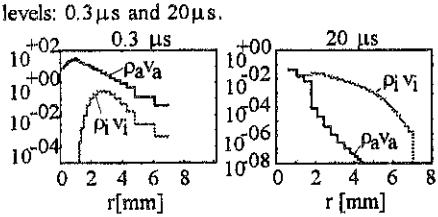

FIG.2.

As can be seen, prior to substantial ionization, the momentum of the neutral component significantly exceeds the ion momentum. During a time interval comparable to the residence time of the pellet in its own magnetically confined cloud, the neutrals lose practically all their radial momentum because of collisions with ions (except in a small region adjacent to the neutral source).

With regard to the effect of the inductive E-field on the cloud evolution, different approximations were used for calculating the $\mathbf{j} \times \mathbf{B}$ force appearing in the momentum equation [9].

With regard to the confinement radius, numerous scenario calculations were carried out with systematic variation of the input parameters [9]. At low plasma temperatures, the radial extension of the cloud is determined primarily by the ionizaton time: an increase of the input plasma temperature causes a decrease of $R_{99\%}$ (99 % mass, low-temperature regime: LTR). At high plasma temperatures, $R_{99\%}$ is controlled by the internal pressure evolving in the cloud: typical high-beta interaction takes place. The pressure is able to push the ionized outermost layer of the cloud outward against the $\mathbf{j} \times \mathbf{B}$ force. In this case an increase in the plasma temperature is associated with a corresponding increase in $R_{99\%}$ ($\dot{n}_s$ and B_0 are kept constant, high temperature regime: HTR). Unlike $R_{99\%}$, the ionization radius (the outermost radius where $\alpha = 0.99$) was found to be a monotonic function of T_{e0}. The cloud radius was found to be proportional to $B_0^{-1/6}$ in LTR and proportional to $B_0^{-1/2}$ in HTR ($\dot{n}_s, T_{e0}$ constant). Another power-law dependence of $R_{99\%}$ on the ablation rate ($\dot{n}_s$) was found to be $R_{99\%} \propto \dot{n}_s^{1/3}$ in LTR and $R_{99\%} \propto \dot{n}_s^{1/4}$ in HTR.

Concerning the calculated confinement radii, good agreement was found between the present results and some experimental measurements [9]. There is reasonably good agreement between the results obtained with the present two-fluid model and those stemming from simpler approximations: single-cell Lagrangian model [4], or multi-cell single-fluid model [3]. The two-fluid model consistently calculates stopping radii somewhat larger than the above approximations. On the other hand, the ionization radii computed with the present model are very close to the confinement radii of the other models. At higher plasma densities, the calculated values of the ionization radius, electron density, cloud temperature, etc., agree well with experimental observations in the case of both two-fluid and single-fluid models. Further checks against experimental data, particularly in the low plasma density domain, are needed.

REFERENCES

[1] R. D. Durst, W. L. Rowan, M. E. Austin, R. A. Collins, et al., Nucl. Fusion **30**, 3 (1990).

[2] W. A. Houlberg, S. L. Milora, S. E. Attenberger, Nucl. Fusion **28**, 595 (1988).

[3] L. L. Lengyel and P. Spathis, Nucl. Fusion **34**, 675 (1994).

[4] B. Pegourie, J.-M. Picchiottino, et al., Nucl. Fusion **33**, 591 (1993); see also B. Pegourie and J.-M. Picchiottino, Plasma Phys. Contr. Fusion **35** paper B157 (1993).

[5] L. L. Lengyel, Phys. Fluids **31**, 1577 (1988).

[6] G. G. Zavala, Max-Planck-Institut für Plasmaphysik, Garching, Rept 5/33, Dec. 1989 (see also Ph.D. Thesis, The University of Michigan, Ann Arbor, 1990); see also Nucl. Fusion **31**, 1107 (1991).

[7] J.-M. Picchiottino, Injection de glasons dans un plasma chaud de tokamak: theorie et experience, Ph.D. Thesis, Universite de Provence, Marseille, 1994.

[8] P. B. Parks, Nucl. Fusion **31**, 1431 (1991).

[9] G. Kristof, Rept 5/73, Max-Planck-Institut für Plasmaphysik, Garching, Dec. 1996.

[10] S. L. Milora, W. A. Houlberg, L. L. Lengyel, and V. Mertens, Review Paper, Nucl. Fusion **35**, 657 (1995).

[11] S. L. Milora and C. A. Foster, Technical Report ORNL/TM-5776, Oak Ridge National Laboratory (1977).

[12] P. B. Parks and R. J. Turnbull, Phys. Fluids **21**, 1735 (1978).

TAE Studies in ASDEX Upgrade

S. D. Pinches, S. Günter, M. Maraschek
and the ASDEX Upgrade Team
MPI für Plasmaphysik, EURATOM-Association, D-85748 Garching, Germany

1 Introduction

The effect of toroidicity within tokamak plasmas leads to a coupling between neighbouring poloidal harmonics and enables the formation of Toroidicity induced Alfvén Eigenmodes (TAE). These are generally weakly damped Alfvén waves with phase velocities comparable with those of energetic plasma particles.

Energetic particles arising from external heating schemes may resonately exchange energy with a series of Alfvén resonances present in the plasma. These resonances will approximately occur when

$$v_{\parallel} \approx \frac{v_A}{|2l-1|},$$

with the strength of the interaction decreasing for increasing l.

The neutral beam injection (NBI) system in ASDEX Upgrade produces a population of energetic particles with characteristic birth energy of 60 keV. For typical ASDEX Upgrade parameters this corresponds to a birth velocity of $v = 0.85\, v_A$ indicating that these particles will be resonant for $l > 1$. The exchange of energy between particles and waves enables either wave growth or decay to be obtained.

Recently in ASDEX Upgrade, TAE have also been found in purely ohmically heated discharges [1]. Since only thermal particles are present in this case, an excitation by fast particles as described above is impossible.

2 NBI driven TAE in ASDEX Upgrade

In ASDEX Upgrade TAE are routinely observed in NBI heated plasmas. The HAGIS code [2, 3] has been used to study the interaction between the population of energetic deuterons arising from the NBI system and a single TAE in a shaped ASDEX Upgrade plasma. HAGIS is a self-consistent nonlinear code developed for the purpose of studying the interaction of fast particles with AEs. It evolves both the waves and particles in time allowing the linear growth rates and saturation amplitudes to be calculated as well as the fast particle redistribution/losses resulting from the wave-particle interactions.

The shot investigated is #7692. The plasma parameters were chosen to simulate the injection of 60 keV deuterons into a pure D plasma with the fast particle distribution function used found by splining the experimental NBI deposition profile in radius and assuming a slowing down distribution in energy. The distribution in pitch angle is assumed to be isotropic. The radial structure of the $n = 3$ TAE calculated using CASTOR [4] for this shot is shown in Fig. 1, whilst the growthrate of this mode is presented in Fig. 2.

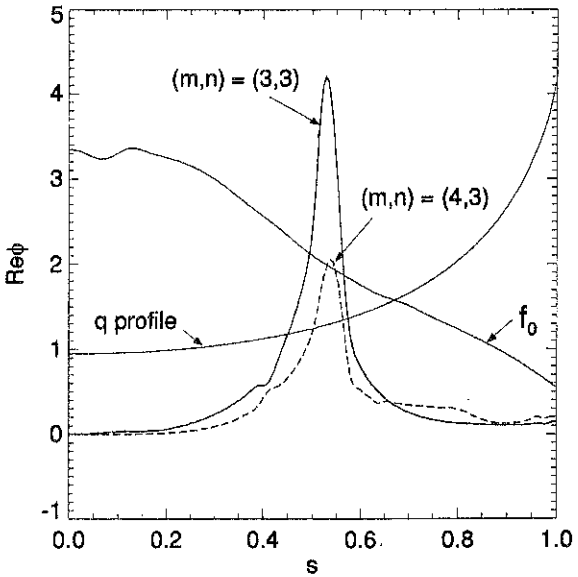

Figure 1: Plot showing TAE eigenfunctions together with the radial fast particle distribution and q-profile.

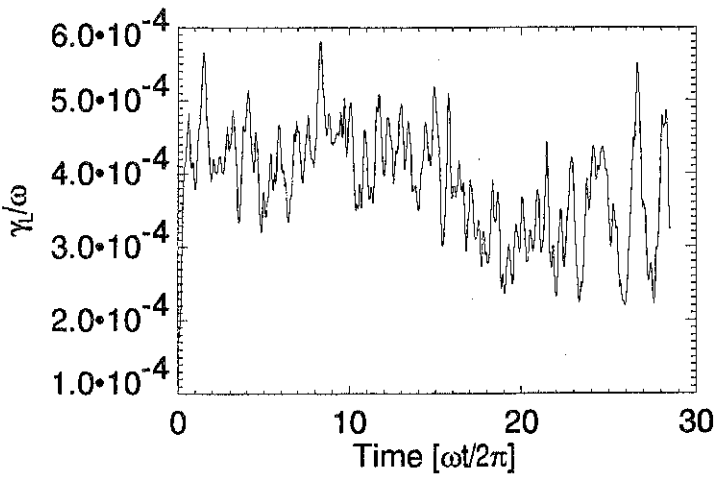

Figure 2: Growthrate of $n = 3$ TAE driven by NBI ions in ASDEX-U.

3 TAE in Ohmically Heated Plasmas

Besides the well known TAE in additionally heated plasmas, similar modes have also been observed in purely Ohmically heated plasmas.

In contrast to the bursting nature of the modes in NBI heated plasmas, in Ohmic shots the modes appear continuously throughout the discharge. Their amplitude is about one order of magnitude smaller than those in NBI heated plasmas [1]. Investigating shots with different toroidal fields B_ϕ and different ion species (mass m_i) one finds the expected frequency scaling for Alfvén modes $f \propto B_\phi/\sqrt{m_i}$. The same is true for the density dependence ($f \propto 1/\sqrt{n_e}$) which has been checked via a strong density variation within one shot.

For the theoretical investigation of these modes the resistive MHD code CASTOR [4] has been applied. In Fig. 3 the continuous spectrum for a typical ASDEX Upgrade

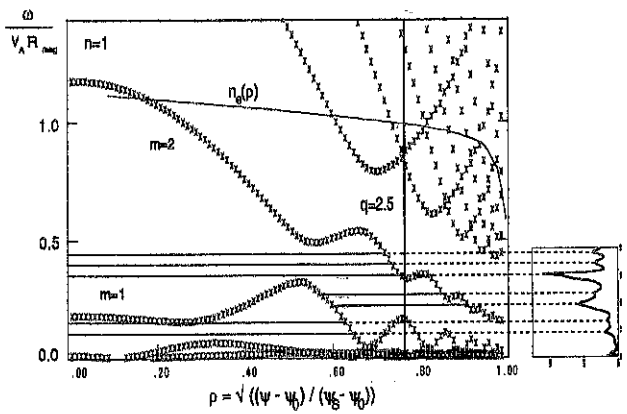

Figure 3: The Alfvén continuum frequencies for $n = 1$ of ASDEX Upgrade discharge #8630 as a function of the radius for a compressible plasma. (The slow continuum is not given here.) On the right hand side the power absorbed by the plasma as a function of the antenna frequency is drawn.

shot without additional heating is given. On the right hand side the power absorbed by the plasma as a function of the driving frequency of an external antenna is shown. The resonances in this spectrum correspond to the global Alfvén waves. In Fig. 4 the same spectrum is compared to a Fourier spectrum measured by Mirnov coils at the high field side. It is apparent that only those waves with a frequency of about 115 kHz have been observed on the Mirnov diagnostics. Considering Fig. 3 and the corresponding eigenfunctions one finds that the observed modes are located near the plasma edge (at about $q \approx 2.5$) which is in agreement with soft X-ray measurements.

A possible excitation mechanism for these modes is through drift wave turbulence at the plasma edge [5]. Such an explanation seems to be reasonable since the observed modes disappear at the L-H transition where the turbulence vanishes. Additionally the rotation

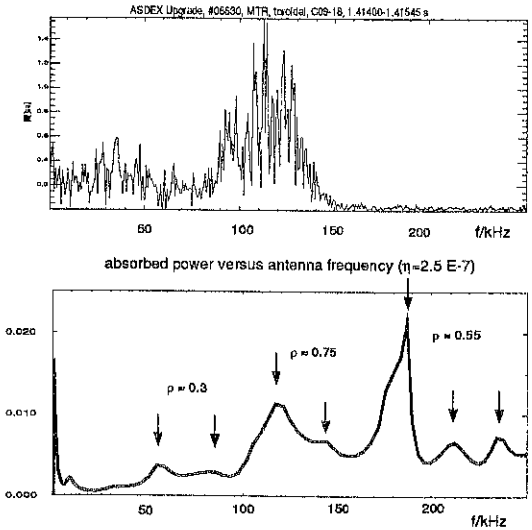

Figure 4: The Fourier spectrum measured by Mirnov coils at the high field side compared to the antenna absorption spectrum. The arrows indicate the radial location of the corresponding Alfvén wave.

of the modes in the electron diamagnetic drift direction further supports this idea since the drift waves are coupled to the plasma electrons.

Acknowledgements

The authors gratefully acknowledge the many useful conversations with Dr. A. Stäbler regarding the radial distribution of NBI ions in ASDEX-Upgrade.

References

[1] M. Maraschek, S. Günter, T. Kass, B. Scott and H. Zohm, submitted to Phys. Rev. Lett. 1997

[2] S. D. Pinches, PhD Thesis, University of Nottingham.

[3] L. C. Appel, H. L. Berk, D. Borba, B. Breizman, T. C. Hender, G. T. Huysmans, W. Kerner, M. Pekker, S. D. Pinches and S. E. Sharapov. Nuclear Fusion, **35** p.1697 (1995)

[4] W. Kerner, J. P. Goedbloed, G.T.A. Huysmans, S. Poedts, and E. Schwarz, JET report JET-P(97)04, submitted to J. Comp. Phys. (1997)

[5] B. Scott, S. Camargo, and F. Jenko, 13th Int. Conf. on Plasma Physics and Controlled Nuclear Fusion Research, IAEA-CN-64, D-3-4, DP-18, Montreal (1996)

Growth Rates of Resistive Ballooning Modes in ASDEX Upgrade and W7-AS

H.P. Zehrfeld, J. Geiger

Max-Planck-Institut für Plasmaphysik, EURATOM Association,
D-85748 Garching

Introduction

Being pressure gradient driven, resistive ballooning modes limit the achievable beta values in toroidal devices. In particular, the pressure gradient formation will depend on their growth rates so that it is of interest to calculate the latter in regions with large gradients. This paper presents the results of such calculations for the tokamak ASDEX Upgrade and for the low shear stellarator W7-AS using a general treatment which merges approaches described elsewhere [1, 2].

For ASDEX Upgrade we are interested in the high confinement phases where the plasma equilibrium is characterized by steep pressure gradients at the plasma edge. We concentrate on the immediate neighbourhood of the separatrix with a plasma pressure profile characteristic for ASDEX Upgrade.

For W7-AS we consider a sequence of finite β-equilibria. We look at the dependence of the real growthrate on the Lundquist-Reynolds number and discuss the marginality of the equilibria at different β-values.

Theory Background

The investigation of the stability behaviour of a toroidal plasma against resistive ballooning modes [3] requires the solution of a Sturm-Liouville problem in two complex functions $\mathbf{w} = (w_1, w_2)$ (the modes) with nonlinear dependence on the complex growthrate γ. The equations – written in a form suitable for stellarators as well as for tokamaks – are

$$\mathbf{B}\cdot\nabla\left\{\frac{(1+S^2)}{D|\nabla\Psi|^2}\mathbf{B}\cdot\nabla w_1\right\} - \left\{2\mu_0\frac{dp}{d\Psi}\frac{\kappa_n - S\kappa_g}{|\nabla\Psi|} + \mu_0\rho\gamma^2\frac{1+S^2}{|\nabla\Psi|^2}\right\}w_1 - 2\mu_0\frac{dp}{d\Psi}\frac{\kappa_n - S\kappa_g}{|\nabla\Psi|}w_2 = 0$$

$$\mathbf{B}\cdot\nabla\left\{\frac{1}{B^2}\mathbf{B}\cdot\nabla w_2\right\} + 2\mu_0\frac{dp}{d\Psi}\left(\frac{4\pi^2 n^2\eta}{\mu_0\gamma} + \frac{\rho\gamma^2}{\mu_0(dp/d\Psi)^2}\right)\frac{\kappa_n - S\kappa_g}{|\nabla\Psi|}w_1 +$$

$$+\left\{\frac{4\pi^2 n^2\eta}{\mu_0\gamma}\left(2\mu_0\frac{dp}{d\Psi}\frac{\kappa_n - S\kappa_g}{|\nabla\Psi|} - \mu_0\rho\gamma^2\frac{1+S^2}{|\nabla\Psi|^2}\right) - \frac{\mu_0\rho\gamma^2}{B^2}\frac{1+\beta}{\beta}\right\}w_2 = 0$$

where we have used the following abbreviations and definitions

$$D \equiv 1 + \frac{4\pi^2 n^2\eta}{\mu_0\gamma}\frac{B^2(1+S^2)}{|\nabla\Psi|^2} \tag{3}$$

$$S = S(\mathbf{x}_0, \mathbf{x}) \equiv \frac{|\nabla V|^2}{B}\int_{\mathbf{x}_0}^{\mathbf{x}}\frac{(\nabla V\times\mathbf{B})\cdot\mathbf{rot}(\nabla V\times\mathbf{B})}{|\nabla V|^4}\frac{\mathbf{B}\cdot d\mathbf{x}'}{B^2} \tag{4}$$

$$\kappa_g \equiv \frac{\underline{\kappa}\cdot(\nabla V\times\mathbf{B})}{|\nabla V|B}, \quad \kappa_n \equiv \frac{\underline{\kappa}\cdot\nabla V}{|\nabla V|}, \quad \underline{\kappa} \equiv \frac{1}{2}\left\{\frac{2\mu_0\nabla p}{B^2} + \frac{1}{B^2}\nabla_\perp B^2\right\} \tag{5}$$

They must be considered along the field line (described by the position vector $\mathbf{x}$) passing through the mode-localization point $\mathbf{x}_0$. V is the volume enclosed by the magnetic surface containing$\mathbf{x}_0$, Ψ the poloidal flux, n the toroidal mode number and ρ the mass density. Further, $\beta = \mu_0\gamma_T p/B^2$ with $\gamma_T = c_p/c_v$. All other quantities have their usual meaning. Note that no assumptions on axisymmetry have to be made.
We define small and large radii r_s and R_s, respectively, the poloidal Alfvén transit time τ_A used for the normalization of γ, the resistive time τ_R and an effective Lundquist-Reynolds number according to

$$\tau_A = \frac{(\mu_0\rho)^{1/2}r_s}{B_s}, \quad \tau_R = \frac{r_s^2\mu_0}{\eta}, \quad L_{eff} = \frac{\tau_R}{4\pi^2 n^2 \tau_A} \tag{6}$$

where $B_s = 2\pi R_s\Phi' \simeq B_T$. Further, we transform to 4 real modes $\mathbf{u}$ by $\mathbf{w} \mapsto \mathbf{u} = \{\mathrm{real}(w_1), -\mathrm{imag}(w_1), \mathrm{real}(w_2), -\mathrm{imag}(w_2)\}$ and introduce a parameter t along the localization field line by $\Phi'\partial/\partial t \equiv \mathbf{B}\cdot\nabla$, where Φ is the toroidal flux and $\Phi' = d\Phi/dV$. The problem to be solved can then be shown to be equivalent to a consideration of the quadratic functional in $\mathbf{u}$

$$F(L_{eff}, \gamma, \mathbf{x}_0) = \int_{-\infty}^{+\infty} \mathcal{L}(L_{eff}, \gamma, \mathbf{x}_0, t, \mathbf{u}(t), \dot{\mathbf{u}}(t))dt \tag{7}$$

with the Lagrange density $\mathcal{L} = \frac{1}{2}(\dot{\mathbf{u}}\cdot\mathbf{P}\cdot\dot{\mathbf{u}} - \mathbf{u}\cdot\mathbf{Q}\cdot\mathbf{u})$: Satisfying the stationarity conditions of F with respect to $\mathbf{u}$ is equivalent to the solution of the transformed ballooning mode equations

$$(\mathbf{P}\cdot\dot{\mathbf{u}})^{\cdot} + \mathbf{Q}\cdot\mathbf{u} = 0 \tag{8}$$

with the boundary conditions $\mathbf{u}(t = \mp\infty) = 0$. For a given equilibrium the 4x4-matrices $\mathbf{P}$ and $\mathbf{Q}$ have the parametric dependence $\mathbf{P} = \mathbf{P}(L_{eff}, \gamma, \mathbf{x}_0)$ and $\mathbf{Q} = \mathbf{Q}(L_{eff}, \gamma, \mathbf{x}_0)$. Their dependence on $\mathbf{x}_0$ is due to the accumulated shear S (4). Using a magnetic coordinate system (V, θ, φ) S can be written as

$$S = -\frac{|\nabla V|^2}{B}\left[X + \sqrt{g}\,\frac{B^\varphi g^{\theta V} - B^\theta g^{\varphi V}}{|\nabla V|^2}\right]_{\mathbf{x}_0}^{\mathbf{x}} \tag{9}$$

where X is determined solving the 3 ordinary differential equations

$$\frac{d\theta}{dt} = \frac{B^\theta(\theta,\varphi)}{\Phi'}, \qquad \frac{d\varphi}{dt} = \frac{B^\varphi(\theta,\varphi)}{\Phi'}, \qquad \frac{dX}{dt} = \frac{\sqrt{g}}{\Phi'}\left\{B^\theta\frac{\partial B^\varphi}{\partial V} - B^\varphi\frac{\partial B^\theta}{\partial V}\right\} \tag{10}$$

with the initial conditions $\theta_0 = \theta(\mathbf{x}_0)$, $\varphi_0 = \varphi(\mathbf{x}_0)$ and $X_0 = 0$.

Computational Setup

Limiting the size of the integration region of the Lagrangian to a sufficiently large value and discretizing on M intervals leads to an approximation of (7) of the form $F_M = \mathbf{y}^T\cdot\mathbf{G}_M\cdot\mathbf{y}$. Here $\mathbf{y}$ comprises function values of $\mathbf{u}$ on the localization field line. This way the stationarity conditions for the Lagrangian make up a system of $4(M-1)$ homogeneous equations for $\mathbf{y}$: $\mathbf{G}_M\cdot\mathbf{y} = 0$, where $\mathbf{G}_M = \mathbf{G}_M(L_{eff}, \gamma, \mathbf{x}_0)$. In order to find – with L_{eff} and the localization point $\mathbf{x}_0$ as parameters – those values of γ for which there are non-trivial solutions we have used the method of inverse vector iteration. This way, for a given plasma equilibrium, the growthrate of resistive ballooning modes can be obtained in the form $\gamma = \gamma(L_{eff}, \mathbf{x}_0)$.

Application to Tokamaks: ASDEX Ugprade

For a particular equilibrium with a steep pressure profile near the plasma boundary a localization point (LP) of the resistive ballooning modes with a distance of 0.44 cm from the outer side of the separatrix was chosen.

In this region of high shear ($d(\ln q)/d(\ln\rho) \simeq 16$, $\rho = ((\Psi_{LP} - \Psi_A)/(\Psi_B - \Psi_A))^{1/2}$, Ψ_A – flux on axis, Ψ_B – at plasma boundary) we started with a study of the ideal ballooning limit $L_{eff} \to \infty$ and $\gamma \to 0$. In this case the half-bandwidth of the symmetric system matrix G_M reduces to one and the stability boundaries correspond to vanishing eigenvalues in the method of inverse vector iteration. Fig.1 shows that the plasma is stable for a value of the pressure gradient of 238 kPa/m. Scaling the explicitly appearing pressure derivative in the ideal ballooning mode equation with a factor of about 1.52 causes transition into the first unstable regime. This result was confirmed by calculations using equilibria with correspondingly higher edge pressure gradients.

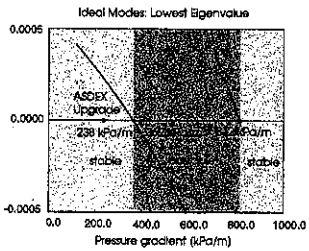

Figure 1: Actual pressure gradient at x_0 and its values at the stability boundaries of ideal modes.

Another confirmation was found in full resistive calculations (Fig.2). With an effective Lundquist-Reynolds number of $L_{eff} = 1.2 \times 10^5$ the plasma is nearly ideal and ballooning-stable for an unscaled pressure.

Estimates of the ideal ballooning limit using the simple $\alpha - s$ model – depending still on how α and s are generalized to be acceptable for a toroidal noncircular plasma – indicate lower critical values for the edge pressure gradient. This fact must be ascribed the combined effects of finite aspect-ratio and ellipticity of the magnetic surfaces, which are significant for ASDEX Upgrade. For an axisymmetric configuration the accumulated shear S (4) has the form

$$S = -\frac{|\nabla V|^2}{B}\left[X - \frac{B_T}{|\nabla V|^2}\frac{\Psi_R \sin\theta + \Psi_z \cos\theta}{\Psi_R \cos\theta - \Psi_z \sin\theta}\right]_{\theta_{LP}}^{\theta}$$

It secular part is

$$S_s = -s(\theta - \theta_{LP}), \qquad s = -\frac{\nabla\Psi \cdot \nabla q}{2\pi B} \qquad (11)$$

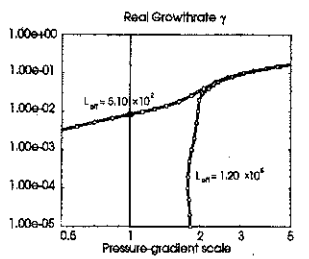

Figure 2: Resistive growth rates for scaled pressure derivatives and different values of L_{eff}.

It can be shown that particularly the second term in (11) describing the effects of toroidal shift and ellipticity and the shear parameter s in S_s have considerable influence on the ballooning stability of ASDEX Upgrade.

Application to Stellarators: W7-AS

From the variety of magnetic configurations allowed by the coil system of W7-AS we chose a typical one at $\iota_{vac} \approx 0.34$ with no vertical field applied. We investigate a sequence of equilibria with increasing plasma pressure ($\beta_o \approx 0.1 - 1\%$) calculated with the equilibrium code NEMEC [4]. The pressure profile used is $p = p_o(1 - \Phi/\Phi_B)$, the

toroidal current vanishes within each flux surface. A stability analysis with respect to ideal and resistive interchange modes shows stability for the considered β-range. The following investigations is limited to real γ.

First we consider the dependence of γ on L_{eff}. Analytic theory predicts $\gamma \sim L_{eff}^{-1/3}$. For a standard extension of the field line of 24 times the long way around the torus the behaviour of γ with L_{eff} is shown in Fig. 3 (thick curve). For values of $L_{eff} > 260$ we find no solution, although analytic theory predicts solutions for finite resistivity in any case. However, deviations from the simple power law for small L_{eff} have been reported earlier [1], but, it was also noticed that for small growthrates the mode's extension along the field line grows. Increasing the field line range by a factor of 8 ($24 \rightarrow 192$), we find solutions with γ approaching the scaling law for $L_{eff} > 60$ and, additionally, there are now solutions for $L_{eff} > 260$. This means that for low resistivity the modes need a considerable range along the field line to be excited. In the case of low L_{eff} no change in γ appears with increasing extension of the field line range. Thus, the deviation from the power law for high resistivity is real.

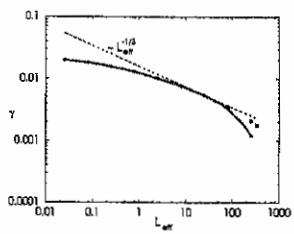

Figure 3: Growthrate of resistive ballooning modes as function of L_{eff} in W7-AS.

Next, we discuss an intuitive pressure scaling in the resistive ballooning equations. To predict behaviour of γ with increasing pressure gradient we considered a sequence of equilibria. In order to keep the number of equilibria small, one would like to predict the behaviour at higher gradients from equilibria with lower ones or vice versa by scaling the explicitly appearing pressure gradient in the equations (1,2). To check the applicability of this scaling we investigated the appearence of resistive ballooning solutions in 6 equilibria with different central pressures for $L_{eff} = 253$, the same field line as above with an extension of 24. Fig.4 shows that in our case equilibria with pressure gradients lower than the marginal one overestimate the pressure where the first solutions appear whereas equilibria with higher gradients stay "unstable".

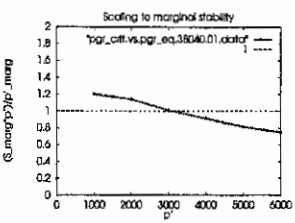

Figure 4: Scaling to marginal: $p'_{marg} = 3200$

[1] H. P. Zehrfeld and K. Grassie, Resistive Ballooning Stability of ASDEX Equilibria, Nucl. Fusion **5**, 891 (1988).

[2] H. Zehrfeld, J. Kisslinger, and H. Wobig, Resistive Ballooning Stability of Advanced Stellarators, in *IAEA Conference*, Venice, Italy, 1989.

[3] D. Correa-Restrepo, Z. Naturforschung **37**, 848 (1982).

[4] S. Hirshman, W. van Rij, and P. Merkel, Three-dimensional free boundary calculations using a spectral Green's function method, Comput. Phys. Comm. **43**, 143 (1986).

Bolometer measurements and transport simulations of the density limit on the W7-AS stellarator

L. Giannone, E. Bellido, R. Brakel, R. Burhenn, R. Dux, A. Elsner, S. Fiedler, T. Geist, P. Grigull, H. Hacker, H. Hartfuss, A. Herrmann, J.P.T. Koponen, F. Penningsfeld, G. Pereverzev, U. Stroth, F. Wagner, NBI Team and the W7-AS Team.

Max-Planck-Institut für Plasmaphysik, EURATOM Association, D-85748 Garching, Germany

1. Introduction

A theoretical basis for understanding the density limit is of importance for a fusion reactor as high edge densities will be needed for power handling. Basic aspects of the density limit can be described by a simple two point power balance of the scrape off layer (SOL) [1,2]. This model assumes pressure constancy and classical parallel electron thermal conductivity along field lines and stable thermal equilibrium in front of divertor/limiter plates with detachment at the density limit when power balance in front of the limiter can no longer be supported. The radiation term in the power balance equation assumes radiation from carbon (coronal equilibrium) in the SOL. The electron density and temperature measurements at the limiter and last closed flux surface, together with the bulk density, temperature and radiation profiles are the experimental quantities of interest. Using the 4 equations of the two point model for a limiter machine [2] , the edge density, n_S, as a function of electron temperature at the limiter, T_{lim}, for a given temperature fall off length, Δ_T, and net power flux at the last closed flux surface, $q_\perp$, can be predicted.

In W7-AS a discharge with rising line integrated electron density reaching a density limit is shown in Fig.1. The sudden degradation in confinement leading to a decrease in the diamagnetic energy indicates the density limit. In contrast to tokamaks [3,4], current free stellarators at the density limit do not suffer from MHD disruptions and can even recover to a steady state.

This paper is a first attempt to apply the simple two point model to density limit experiments in the W7-AS stellarator. The time dependent ASTRA code [5] was coupled to the impurity transport code STRAHL [6] to facilitate modelling of the radiation profile measured by bolometry. The addition of the simple two point model to ASTRA allowed time dependent simulations of the measured density and temperature at the limiter.

2. Experiments and comparison with the two point model

A magnetic field scan from 0.6 T to 2.5 T in NBI discharges with 1100 kW absorbed power, a rotational transform, ι, of 0.43 and an upward density ramp was performed. At the lowest and highest magnetic field the total radiated power is 35% and 70% of the input power respectively. This procedure was repeated in discharges at 1.25 T and 2.5 T for absorbed powers from 380 kW to 1440 kW with $\iota = 0.34$. The edge densities were taken to be 0.25 of the line averaged density and these values are in good agreement with those from the lithium

beam and Thomson scattering diagnostics.

The two point model was adapted for W7-AS and compared with data from these power and magnetic field scans. From the difference between the input power and bolometer measurements of the bulk radiated power, $q_\perp$ can be calculated. The experimental observation of rising radiated power and decreasing $q_\perp$ with rising line integrated density means that a critical edge density will be reached where $q_\perp$ is no longer sufficient to maintain power balance. Shown in Fig.2, for a typical case in W7-AS with Δ_T = 1,2 or 3 cm, and a connection length to the limiter plate, L_c, of 18 m, this maximum n_S at the density limit is plotted. It can be seen from the magnetic field scan that for low magnetic field a $\Delta_T > 3$ cm is suggested, well above the maximum indicated by scaling studies.

3. Scaling

The scaling of n_S with $q_\perp$ and B_o found by regression analysis, as shown in Fig. 3, is $n_S = 0.52\ q_\perp^{0.5+/-0.2}\ B_o^{0.8+/-0.15}$. This scaling can be compared to that found in density limit studies for JET limiter discharges with coefficients of 0.66 and 0.33 respectively [2]. The JET scaling is close to that expected when Bohm diffusion is assumed for the scaling of Δ_T. In the case of the B_o scan on W7-AS, the plasma is pushed up against the inboard limiters. To first order it is expected that L_c remains constant as a function of B_o so that the geometrical heat flux enhancement factor, L_c/Δ_T, on the left hand side of the power balance equation is not varying significantly with B_o. In the case of the power scan series, obtaining probe measurements at the limiter involves the compromise of using the up/down limiters which are tangential to the last closed flux surface. This introduces the complication that L_c will be a function of Δ_T and B_o. It may be possible to explain the stronger n_S scaling with B_o in W7-AS and the apparently large Δ_T inferred in the above section by a detailed consideration of the L_c dependence of Δ_T and B_o.

Compared to ASDEX and ASDEX Upgrade density limit discharges, the Greenwald limit for W7-AS in the large aspect ratio, low beta circular approximation appears to be at least a factor of 2 greater but because of the discussed configuration considerations in W7-AS, the usual scaling may not be valid.

4. Transport simulations

The values of n_S from the lithium beam and the measured radiation profiles to calculate $q_\perp$ were taken as inputs while a constant Δ_T = 1.5 cm was assumed. The time evolution of temperature and density measured by Langmuir probes in front of the limiter in the density limit discharge at 2.5 T with 380 kW NBI input power can then be predicted and are compared to the Langmuir probe measurements in Fig.4. The general features of a rising electron density and falling electron temperature at the limiter can be reproduced and the collapse of the discharge begins as the temperature at the limiter reaches 10 to 20 eV in both the simulation and experiment. From the lithium beam measurements it is clear that the edge density rises continuously to the point of the collapse in diamagnetic energy and that a sudden increase in the density fall off length occurs in the collapsing phase of the discharge, while Langmuir probe measurements indicate that the edge density remains constant for a further 50 ms in the collapsing phase of the discharge.

Impurity puffing experiments were conducted to increase the radiated power and reduce

the power flux so that a density limit could be reached in a similar discharge at a lower edge density. In NBI discharges with 380 kW of deposited power at 2.5 T, nitrogen gas was introduced. For this impurity, the radiation rate coefficient is strongest at 10 eV and with a second maximum at 100 eV and total radiation is proportional to the impurity ion and electron density. The impurity ion density profile for a given impurity flux rate assuming a diffusion coefficient of 0.2 m^2/s and an inward pinch of 5r/a m/s as calculated by STRAHL and the electron density profile measured by Thomson scattering or an 8 channel microwave interferometer allows the radiated power to be calculated. In discharges without nitrogen gas puffing, carbon was assumed to be the dominant impurity. Impurity concentrations of 15% and 5% in discharges with and without impurity puffing were necessary to reproduce the total radiated power preceding the collapse of the discharge at the density limit. In discharges with impurity puffing, toroidally separated bolometer cameras indicate that impurity gas injection produces significantly more radiation in the vicinity of the gas inlet valve and MARFE formation was observed. In discharges where the impurity gas puffing was systematically increased the density limit decreased.

5. Conclusions

Density limit discharges in power and magnetic field scans in W7-AS have been compared to the predictions of the two point model. At low magnetic field, a Δ_T greater than 3 cm is inferred, well above the maximum indicated by scaling studies. A stronger n_S scaling with B_o compared to JET is found. It is speculated that these two observations can be accounted for by variations in L_c as a function of Δ_T and B_o. Transport simulations of the time evolution of the density and temperature in front of the limiter according to the two point model were found to reproduce the experimental features of a rising density and falling temperature preceding the density limit. This implies that the limit to the maximum allowable edge density for a given $q_\perp$ necessary to satisfy power balance, with the collapse occurring for a temperature at the limiter of 10-20 eV, is the relevant mechanism determining the density limit in W7-AS.

Helpful discussions with K.Borrass and R.Schneider are gratefully acknowledged.

6. References

[1] D.E.Post and K.Lackner, „Physics of Plasma Wall interactions“, Plenum Press,New York, 1986.

[2] K.Borrass, D.J.Campbell, S.Clement and G.C.Vlases, Nuclear Fusion, 63, **33**, 1993

[3] A. Stäbler et al., Nuclear Fusion, 1557, **32**, 1992

[4] W.Suttrop et al., Nuclear Fusion, 119, **37**, 1997

[5] G.Pereverzev, P. Yushmanov, A. Dnestrovskii, A. Polvoi, K.Tarasjan and L. Zakharov, „An Automatic System for Transport Analysis in a tokamak“, IPP Report 5/42, 1991.

[6] K.Behringer, „Description of the Impurity Transport Code STRAHL“, JET Report, JET-R(87)08, 1987.

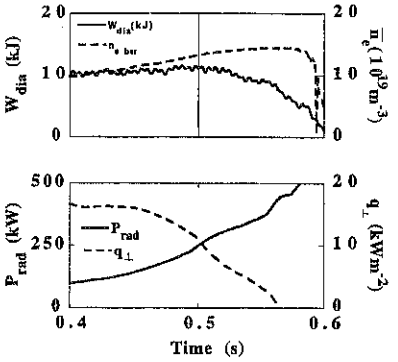

Fig 1. Diamagnetic energy, line integrated density, radiated power and net heat flux at the plasma edge for a density limit shot. Discharge reaches density limit at 0.5 s with a sudden fall in the diamagnetic energy.

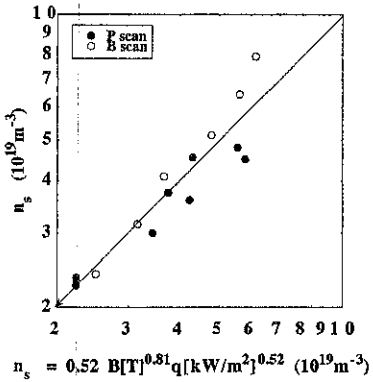

Fig. 3. Edge density at the density limit scaling with repect to the magnetic field and perpendicular heat flux with errors of +/-0.15 and +/-0.2 respectively in the power law coefficients.

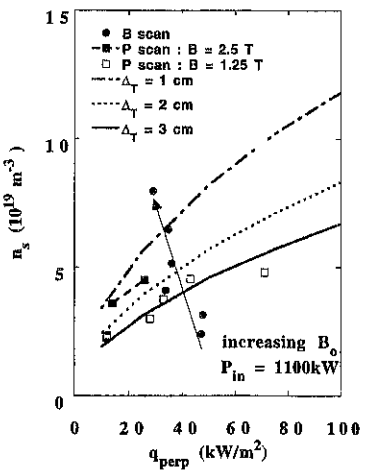

Fig 2. Predicted maximum edge density as a function of heat flux value at the last closed flux surface for various values of the temperature fall off length, Δ_T, and L_c = 18 m with experimental point from the power and B scan.

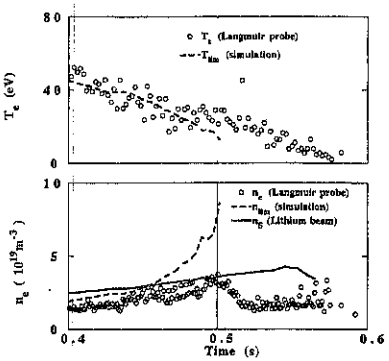

Fig 4. Time evolution of limiter temperature and density compared to the calculated values from the two point model. At 10-20eV, the maximum allowable edge density, n_S, is reached and the discharge collapses.

The effects of field reversal on the W7-AS island divertor at low densities

Y. Feng, G. Herre, P. Grigull, F. Sardei and W7-AS Team

Max-Planck-Institut für Plasmaphysik, EURATOM Ass.
D-85748 Garching, Germany

1. Introduction

In the last years, considerable effort has been made on W7-AS to explore the diversion properties of the boundary magnetic islands in high ι ($\geq$0.5) configurations for control and exhaust of the edge plasma [1]. Besides investigating basic aspects of divertor operation, such as high recycling, detachment and impurity control, understanding the drift effects on the particle and energy balance between the contacting plates is essential to improve the divertor performance.

Poloidal asymmetry of the plasma distribution in the island SOL of low density discharges has been observed for W7-AS divertor configurations at ι=5/9, with the inboard plates intersecting the islands through the O-point. Unlike in most single-null tokamak divertors where, generally, higher density is found on one divertor plate while higher power flux on the other, the W7-AS divertor experiments show that the density, the power flow and the particle flux distributions have the same phase shifts in the island SOL. After reversing the magnetic field, the observed asymmetry is reversed. This asymmetry can be explained by an $\mathbf{E}_r\mathbf{x}\mathbf{B}$ drift in the island SOL as follows. The radial temperature gradient within the open island surfaces, which are intersected and radially linked by the electrically conducting plates, leads to a radial gradient of the plasma electrostatic potential and hence to a radial electric field inside the islands. The $\mathbf{E}_r\mathbf{x}\mathbf{B}$ drift delivers additional particles and energy in the island SOL along the upper or lower island fans to the targets, depending on the direction of the toroidal field. This picture is in good agreement with the experimental observations. In order to understand the drift effects quantitatively, in a first step the 3D Monte Carlo transport code EMC3/EIRENE [2] has been extended to allow the treatment of the poloidal drift. Calculations show the same phase shift of the density contours as observed.

2. Experimental observations

At high ι ($\geq$0.5), the edge magnetic structure of W7-AS is governed by inherent magnetic islands. Having a considerable size and an appropriate internal rotational transform, the ι=5/9 islands have been chosen for the divertor experiments. Ten symmetric divertor plates are installed on the inboard side of the wall with a toroidal location which is symmetric to the triangular cross sections (Fig. 1). Each plate intersects poloidally two islands and the radial intersection position can be easily changed by application of a vertical field shifting the magnetic flux surface configuration horizontally with respect to the plates. In this work, however, only a configuration with the plates cutting the islands through the O-point is considered, which allows easy estimation of the radial electric field throughout the islands. Each divertor plate is poloidally segmented into 8 tiles and calorimetry measurements on each tile give a poloidal

distribution of the power load. In addition, a two-dimensional H_α diode array is fixed horizontally at the outside of the torus, looking at a plate poloidally.

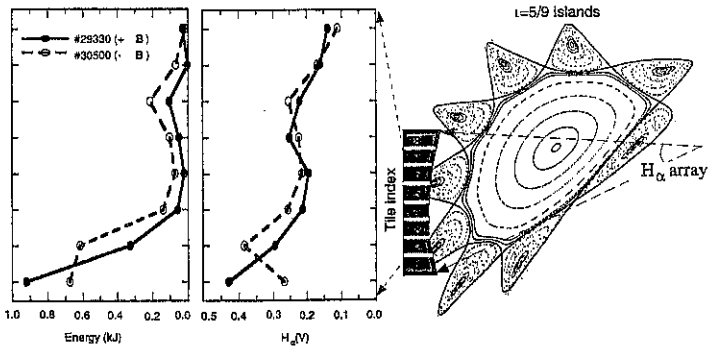

Fig.1 Right: poloidal cross section of the ι=5/9 configuration at the toroidal plane of an inboard plate. Left: calorimetry and H_α data for two discharges with B-field reversal.

The discharges investigated are at extremely low density ($\langle n_e \rangle_{line} < 10^{19}$ m^{-3}) with ECR heating power of about 200 kW. The results for two discharges with B-field reversal are compared in Fig. 1, in which the interaction of the two islands with the plate is well reflected by the diagnostics. It should be mentioned that the present inboard plates are not yet the optimized ones for W7-AS divertor operation. This explains why the power load and recycling are strongly inhomogeneous between the two islands. However, this does not affect the investigation of the drift problem addressed in this paper. We pay our attention only to the lower island, which, due to the longer connection length, carries higher particle and power flows to the plate. This island is cut by the two lowest tiles of the plate. Therefore, the two lowest diagnostic channels of the calorimeter and the H_α array are best suited to verify the differences in particle and energy flows between the upper and lower island fans. In the positive B-field case, higher energy and particle

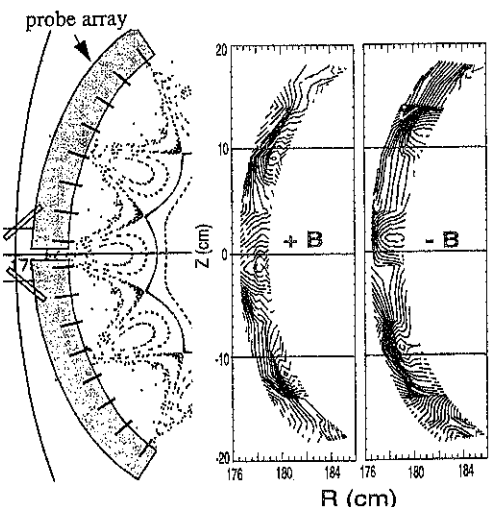

Fig.2. Left: Arrangement of the Langmuir probe array and the vacuum structure of the touching islands.
Right: Measured density contours for two low density discharges with B-field reversal.

outflows are found at the lower island fan, shifting to the upper one as the B-field is reversed.

A Langmuir probe array consisting of 16 probes is used to measure the density distribution of the edge plasma. The probe array is poloidally shaped to follow the main edge structure of the configuration and toroidally placed on a triangular cross section (Fig. 2). It can be shifted horizontally inward and outward by a few cm, thus providing 2D plasma density distribution in the region of interest. The resulting density contours from the probe array for the two field cases are illustrated in Fig. 2, in which the poloidal structure of the island chain is clearly identified. However, up/down asymmetries in the density contours emerge, showing a strong dependence on the field direction. Comparing density contours for the positive B-field with the vacuum island structure, we find that the plasma density is higher on the lower island fan than on the upper one. As the B-field is reversed, the higher plasma density shifts to the upper island fan, showing a simple correlation with the B-field direction.

3. Theoretical considerations and 3D simulations

As the observed asymmetries change with B-field reversal, the classical drifts are reasonably considered to play an important role because of their close dependence on the B-field direction. We examine the classical drifts, in order to isolate the candidates which can explain our experimental observations. The classical drift terms contributing to the fluid equations of Braginskii [3] are the electric drift $\mathbf{E}\times\mathbf{B}$ and the diamagnetic drift $\mathbf{B}\times\nabla P$. As has been shown by Chankin [4], the diamagnetic drift and the corresponding diamagnetic energy flux are dominated by divergence-free parts which do not deliver particles and energy to the target, nor give rise to any particle or energy accumulation or sink. The non-divergence-free components are due to spatial variations of the magnetic field, i.e. $\mathbf{B}\times\nabla B$ and $\nabla\times\mathbf{B}$. In a net-current-free stellarator such as W7-AS, the latter term is directly related to the plasma diamagnetic current and, in practice, can be neglected for the low density discharges involved in this paper. The $\mathbf{B}\times\nabla B$ term is a vertical drift and, therefore, its effect on the asymmetries in the islands is strongly reduced by the helical path of the islands around the torus.

According to these considerations, we can restrict our attention to the electric field drifts $\mathbf{E}_r\times\mathbf{B}$ and $\mathbf{E}_\theta\times\mathbf{B}$. The former is related to the radial gradient of the sheath potential due to the temperature drop towards the O-point. The latter is due to the potential drop along the B-field line from up- to downstream, associated with the parallel E-field arising from the thermal force. Following the particle flux estimation made by Chankin for tokamak divertors [5], we have the total radial and poloidal particle drift fluxes:

$$\Gamma_r \approx N2\pi R(kT_{e,up}-kT_{e,down})n_e/eB \text{ and } \Gamma_\theta \approx N2\pi R3kT_{e,down}n_e/eB,$$

where N is the poloidal periodicity of the configuration. Since N=1 for single-null divertor tokamaks, the drift effects in N>1 island divertors like W7-AS (N=9) are more pronounced than in tokamaks. Comparing the radial and poloidal drift fluxes, we find that the condition for Γ_θ dominating over Γ_r is $T_{e,down} >> (T_{e,up}-T_{e,down})/3$. This is the case for the low density discharges discussed here. Heat transport simulations with the EMC3/EIRENE code showed that the temperature is about 90 eV at upstream position, dropping to 60 eV at the target, which agrees with the downstream temperature deduced from the Langmuir probe array data. A radial drop in temperature of about 20 eV was estimated from the Monte Carlo code. The resulting positive and negative poloidal drift velocities were inserted into the code, leading to the same

phase shift of the density contours as observed (Fig. 3), which can be briefly explained as follows. In the picture assumed here, the particles created by low recycling in the main plasma and diffusing outside across the LCFS experience a poloidal drift in addition to the parallel montion along the island fans. A particle accumulation results in the upper or lower island fan, depending on the B-field direction.

The convective power flux driven by the poloidal drift is estimated to be ~90 kW, which is about half of the total heating power. This implies stronger asymmetry of the power fluxes between the upper and lower island fans than the one observed. One reason for the discrepancy is that the power fluxes along the upper and lower island fans cannot be sharply resolved by the two lowest channels of the calorimeter. Secondly, due to the large ratio of connection length to island size, a significant fraction of the drift power flux can circulate around the island between the discontinuous plates without reaching them. A quantitative assessment of these effects for island divertors needs a selfconsistent 3D treatment of the drifts, which is beyond the present capability of the EMC3/EIRENE code.

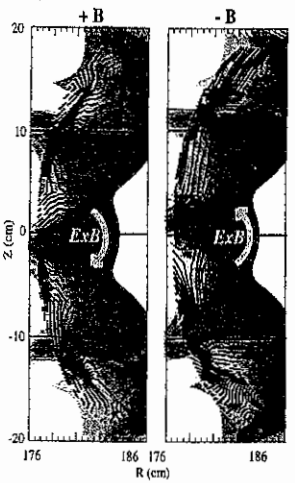

Fig. 3. Density contours from the probe array (curves) compared with the EMC3/EIRENE results for positive and negative B-field.

4. Conclusions

For low density, low recycling discharges, poloidal asymmetries in the island SOL have been observed for the W7-AS divertor configurations at ι=5/9, with the islands deeply cut by the present inboard plates through the O-point. Higher density, power flow and particle flux are measured for the lower or upper island fans, depending on the direction of the toroidal magnetic field. The asymmetries are considered to be driven by an $\mathbf{E}_r\mathbf{xB}$ drift resulting from the radial temperature gradient in the island. The $\mathbf{E}_r\mathbf{xB}$ drift delivers additional particle and energy fluxes along the island fans to the divertor plates, leading to the same phase shift of the density, energy and particle flux distributions in the island. 3D Monte Carlo calculations including the poloidal drift can well reproduce the density asymmetries measured by the 2D Langmuir probe array.

5. References

[1]. F. Sardei et al., Proc. 12th int. Conf. on Plasma Surface interactions in Controlled Fusion Devices, Saint Raphael, France, 1996 (to be published in J. Nucl. Materials).

[2]. Y. Feng et al., Proc. 12th int. Conf. on Plasma Surface interactions in Controlled Fusion Devices, Saint Raphael, France, 1996 (to be published in J. Nucl. Materials).

[3]. S. I. Braginskii, Reviews of Plasma Physics, Vol.1, ed. by M.A. Leontovich, Consultants Bureau, New York (1965) p.205.

[4]. A. V. Chankin and P. C. Stangeby, Plasma Phys. Control. Fusion, 36 (1994) 1485.

[5]. A. V. Chankin et al., Plasma Phys. Control. Fusion, 36 (1994) 1853.

Feedback controlled radiative edge cooling experiments in the Wendelstein 7-AS stellarator

P. Grigull, R. Brakel, K. Borrass, J. Baldzuhn, A. Elsner, S. Fiedler, H. Hacker, H. J. Hartfuß, D. Hildebrandt[1], R. Schneider, U. Stroth, F. Wagner, A. Weller, X. D. Zhang[2], W7-AS Team, ECRH Group

Max-Planck-Institut für Plasmaphysik, EURATOM Ass., D-85748 Garching, Germany
[1]Bereich Plasmadiagnostik, D-10117 Berlin, Germany
[2]Institute of Plasma Physics, Academia Sinica, Hefei, P. R. China

Introduction. Radiative edge cooling by seeded impurities with appropriate radiation characteristics is widely considered as an option to protect targets in fusion experiments from thermal overloading. In devices with active pumping capability (divertors, pump limiters), noble gases (e.g. Ne) are preferred as edge radiatiators due to both, their favourable radiation characteristics as well as their recycling properties [1, 2]. They are not pumped by plasma facing materials and, consequently, do not build up long-term reservoirs leading to uncontrollable release in particular during long-pulse or steady state discharges. In devices without active pumping capability as W7-AS, on the other hand, the seeded impurity has to be sufficiently pumped by the walls to allow control of the concentration. As was shown in Ref. [3], nitrogen is relatively well suited. It has favourable radiation characteristics, and its capability to be pumped by the walls enables feedback control of the radiation level over typical discharge durations ($\approx$1-2s) in W7-AS. A shot-to-shot build-up of an intrinsic nitrogen reservoir was found to settle at a very low, stationary background radiation level which could be completely removed by ECRH discharges without nitrogen puff. In continuing a previous study [3], this paper reports results from a nitrogen concentration scan with improved feedback control of the nitrogen radiation levels and with extended target diagnostics.

Experimental. The study in W7-AS (R = 2 m, a = 0.18 m) was performed at B = 2.5 T and ι = 0.34 with the configuration bounded by two horizontal graphite limiters at the top and bottom of an elliptic cross section. Nitrogen was injected into net current free ECRH (140 GHz, 430 kW) discharges with flat-top phases of 1.5 s at a line-averaged density $\overline{n}_e = 4\times10^{19}m^{-3}$. Feedback control of the radiation levels was performed via VUV line emission (N IV, 765 Å). Compared to Ref. [3], the control spectrometer was now positioned further away from the nitrogen inlet thus actually enabling quasi-stationary radiation levels. In addition to the diagnostics mentioned in [3], limiter-integrated, poloidal Langmuir probe arrays allowed to study in particular downstream parameters in more detail. The limiters are poloidally segmented by ten tiles per limiter, each equipped with thermocouples allowing poloidally resolving target calorimetry.

Results and discussion. Stationarity within the injection phase of 0.7 s could be obtained up to a central nitrogen concentration of about 2.5% (estimated from CXRS) corresponding to a radiated power fraction of about 60% (from bolometer), Figs.1, 2. Attempts to exceed this limit lead to radiative instability and to feedback induced oscillations of the discharge parameters rather than to a complete collapse. CCD camera observations covering three of the five torus modules indicated strong shrinking of the hot plasma cross section, but did not give any evidence for MARFE formation during the radiative excursions. Decreasing the prescribed nitrogen radiation level and thus the nitrogen influx within the discharge duration to below this stability limit leads to re-establishment of stationary conditions. It was found that relatively

small nitrogen concentrations (≈1%) already effectively suppress medium-Z radiation from the core which is primarily ascribed to lower impurity release from stainless steel components due to lower edge temperature.

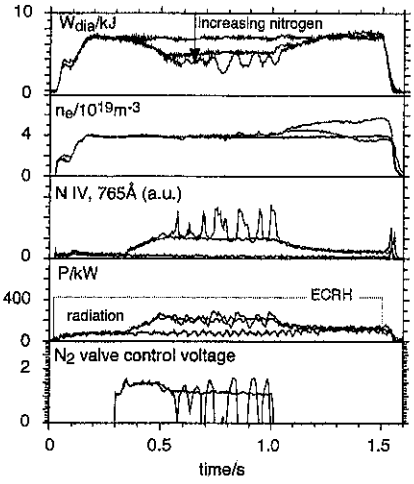

Fig.1: Stored energy, line-averaged density, nitrogen radiation intensity, total radiative power (bolometer) and N_2 valve control voltage versus time for a reference discharge without nitrogen and for nitrogen concentrations marginally below (≈ 2.5%) and above the thermal stability limit, respectively.

Under quasi-stationary conditions, the stored plasma energy degrades approximately linearly with the radiated power fraction (Fig. 2) because, due to the small size of W7-AS, the nitrogen radiation zone extends inward to $r/a \approx$ 0.4 (Fig. 3). The electron temperature T_e is decreased only at the profile wings, whereas the value at the centre is not affected by the nitrogen radiation. A transport analysis (from power balance, Fig. 3c) indicates slightly improved confinement rather than a degradation. The density profiles (not shown) are flat inside $r/a \approx 0.7$ with steep gradients at the outside (from multi-channel interferometer and Li-beam). They are, within the error limits, not altered by the nitrogen radiation which means that the improvement of the central confinement does no coincide with density profile peaking as is often observed in tokamaks.

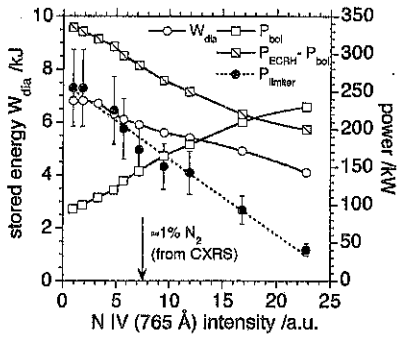

Fig.2: Stored energy from diamagnetic signal W_{dia}, total radiated power P_{bol} from bolometer, power flow P_{ECRH}-P_{bol} across the LCMS, and total power flow $P_{limiter}$ onto both limiters from calorimetry versus the NIV radiative intensity from SPRED spectrometer.

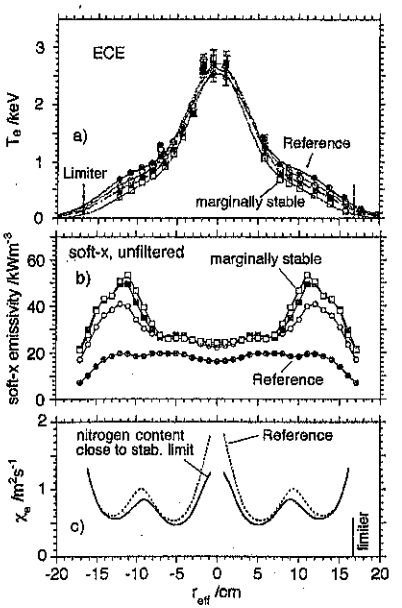

Fig. 3: Radial profiles of a) the elctron temperature T_e, b) the soft-x emissivity and c) the electron heat diffusivity χ_e (from power balance) for discharges with nitrogen concentrations from zero (reference) to slightly below the stability limit.

Calorimetric measurements at the two limiters (corrected for the injection phases being shorter than the pulse lengths) show much stronger reductions of the total power onto limiters than expected from bolometry, Fig. 2. The power accountability referred to P_{ECRH}-P_{bol} (with P_{ECRH} and P_{bol} being the heating and radiated power, respectively) is about 70 - 80% without nitrogen and decreases towards higher nitrogen content. This seems to indicate increasing toroidal asymmetry of the radiation shell not registered by the bolometers. CCD camera observations support this conjecture, but due to the lack of toroidally distributed bolometer cameras there is not yet direct quantitative evidence.

Data from the limiter-integrated Langmuir probe arrays show that the downstream electron temperature T_{ed} (measured at about 2 mm outside the last closed magnetic surface, LCMS) nearly linearly decreases fom about 90 eV without nitrogen to 20 eV slightly below the stability limit, whereas the downstream density n_{ed} stays approximately constant, Fig.4. The upstream temperature T_{eu} at the LCMS is decreased from about 90 to 40 eV (from a fast reciprocating Langmuir probe close to the stagnation plane). In order to check the consistency with calorimetric data, a simple two-point model of the scrape-off layer (SOL) power balance [4, 5, 6] was applied to estimate T_{eu}, T_{ed} and n_{ed} from the upstream density n_{eu} and the calorimetric power onto the central limiter tile which determines the LCMS. It includes parallel heat transport by classical parallel electron heat conduction, pressure constancy along field lines and the sheath boundary condition for the heat transfer to the target:

$$T_{eu} = \left(T_{ed}^{7/2} + \frac{7}{4\kappa_0} q_{\|} L_c \right)^{2/7}; \quad n_{ed} = n_{eu} T_{eu} / 2T_{ed}; \quad q_{\|} = n_{ed} c_s \gamma_s k T_{ed} \qquad (1)$$

k, c_s, γ_s, L_c and κ_0 are the Boltzmann factor, ion sound speed, heat transfer factor (≈8), connection length and parallel heat conductivity coefficient, respectively. The parallel power flux was derived from the fitted calorimetric power onto the central limiter tile, $q_{\|} = P_{target}/\lambda_q w$. For the power flux decay length λ_q an average value was inferred from the poloidal (representing also radial) power deposition profiles on the flat limiters, and w is the poloidal tile width (2.7 cm). The upstream density n_{eu} at the LCMS was kept fixed at 10^{19} m^{-3} (from upstream probe and Li-beam). The results (lines in Fig. 4) satisfactorily agree with the probe data thus indicating basic consistency.

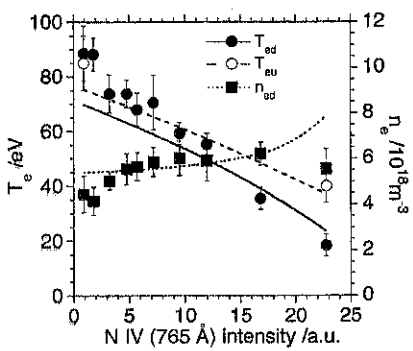

Fig.4: SOL upstream and downstream parameters close to the LCMS calculated by the two-point model (lines, see text) in comparison with probe data (symbols) versus the NIV radiation intensity from SPRED spectrometer. The upstream density n_{eu} is 10^{19}m^{-3}. Error bars are from statistics only.

In order to check the conditions near the stability limit towards smaller T_{ed} in somewhat more detail, the sheath boundary condition was extended to include energy losses to hydrogen, $q_{\|} = n_{ed} c_s k(\xi + \gamma_s T_{ed})$ with the temperature and density dependence of ξ fitted according to Ref. [7]. These losses could be neglected for calculating the results in Fig. 4, but become increasingly important towards smaller T_{ed}. The above model was then applied to calculate densities as functions of T_{ed} for calorimetric $q_{\|}$ values of the discharges without nitrogen and with the highest nitrogen

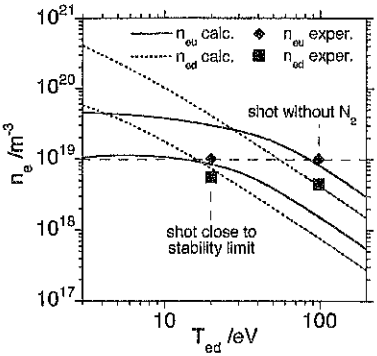

Fig.5: LCMS upstream and downstream n_e values calculated as functions of the downstream T_{ed} for $q_{\parallel}$ values from two shots, and probe data for comparison. The lower curve set indicates that further reduction of the power crossing the LCMS at fixed density would lead to thermal imbalance.

content below the stability limit (upper and lower curve set, respectively, in Fig. 5). Fig. 5 suggests that the marginally stable discharge closely approaches to the SOL thermal instability associated with the existence of a local maximum of n_{eu} versus T_{ed} [6]. Considering nitrogen radiative losses at coronal equilibrium from the SOL does not significantly affect this result. The deviation of the measured T_{ed} from the critical value at the maximum of the calculated upstream density is not too much of a concern because probe data generally tend to over-estimate T_{ed} in the presence of strong T_e parallel gradients. This SOL instability may destabilize the core radiative mantle with respect to radial shrinking as is seen in the experiments (see also Ref. [8]). However, to definitely confirm this interplay, a more refined analysis is needed which will be given elsewhere.

Summary and conclusions. Radiative edge cooling experiments have been performed in W7-AS by feedback controlled nitrogen injection into limiter-bounded, net current-free ECRH discharges. Within injection phases of 0.7s, quasi-stationarity was obtained up to central nitrogen concentrations of about 2.5%. Bolometer data indicate radiated power fractions up to about 60% whereas calorimetric data, together with downstream probe results, indicate target load reductions by up to factors of five to six. This discrepancy may indicate asymmetries of the radiation shell not registered by the bolometers. Though the plasma stored energy degrades with increasing nitrogen content due to the small machine size, the central T_e is not affected. A transport analysis shows improved confinement at $r/a < 0.3$. Exceeding the nitrogen level mentioned leads to radiative instability. Downstream data combined with model estimates suggest that this instability coincides with a SOL thermal instability. More detailed studies in particular on this latter issue including B2/EIRENE code analysis with selfconsistent treatment of impurity radiation are in preparation.

References:

[1] U. Samm et al., Plasma Phys. Control. Fusion 35 (1993) B167
[2] A. Kallenbach et al., Nucl. Fusion 35 (1995) 1231
[3] R. Brakel et al., Proc. 23rd Eurp. Conf. on Contr. Fusion and Plasma Physics, Kiev, Ukraine,1996, ECA, 20C, Vol. II, p. 495-498
[4] D. E. Post, K. Lackner, Physics of Plasma-Wall Interactions in Controlled Fusion, D. E. Post and R. Behrisch editors, Plenum Press, New York, London 1986, p. 627
[5] K. Borrass et al., Nucl. Fusion 33, 1 (1993) 63-76
[6] K. Borrass et al., Nucl. Fusion 31, 6 (1991) 1035
[7] M. F. A. Harrison, P. J. Harbour, E. S. Hotston, Nucl. Technol./Fusion 3 (1983) 432
[8] F. Castejon et al., this Conference

Plasma Radiation with Local Impurity Injection into a Magnetic Island of W7-AS Stellarator and at the separatrix of AUG Tokamak

D. Hildebrandt [1], V. Rohde [1], R. Brakel [2], A. Elsner [2], S. Fiedler [2], J.C. Fuchs [2], L. Giannone [2], C. Görner [2], P. Grigull [2], H. Hacker [2], G. Herre [2], H. Kastelewicz [1], B. Napiontek [1], D. Naujoks [1], R. Neu [2], W. Suttrop [2] and W7-AS-Team and AUG-Team

Max-Planck-Institut für Plasmaphysik, EURATOM Association

[1] Bereich Plasmadiagnostik , D-10117 Berlin, Germany

[2] Garching, Boltzmannstr.2, D-85748 Garching, Germany

Introduction

Energy dissipation by impurity radiation at the plasma edge has become the preferred solution for reducing the heat loads of divertor plates in tokamaks and stellarators. However the magnetic configuration at the plasma boundary is quite different for the proposed ITER-tokamak and the W7-X-stellarator [1]. Whereas in ITER open magnetic field lines outside the separatrix are guided to a divertor chamber being locally separated from the main plasma magnetic islands at the plasma edge are intersected by target plates in the main chamber with relatively small radial separation from the separatrix in W7-X. While impurity radiation cooling in the tokamak edge configuration has been studied already extensively, the influence of magnetic islands on the properties of the edge plasma is still quite unknown. First investigations on the stellarator W7-AS are reported in this paper. For this purpose nitrogen pulses of a few ms duration have been injected into natural islands at the plasma edge of W7-AS discharges by a reciprocating erosion probe with a radial precision of injection of about 5 mm [2]. The cylindrical probe head consists of a boronnitrid casing of 5 mm diameter and length and a small electrode of titanium or carbon of 2 mm diameter and length on the front side. For comparison similar experiments with nitrogen injection were also made in the tokamak ASDEX-Upgrade. In this case a boronnitrid probehead of 30 mm diameter was exposed near the separatrix on the outboard side for 10 ms several times during a discharge using the midplane manipulator.

Modelling of Nitrogen radiation from a magnetic island

The power which can be stationarily radiated by nitrogen from a magnetic island region has been studied using a simple particle transport model. A continous impurity source at the centre of a circular plasma region, representing the island with density n_e, electron temperature T_e and impurity residence time of $\tau = r^2 / D$ is considered where D is the cross field diffusion coefficient. The temporal evolution of the impurity charge states in this region is calculated from the equation

$dn_q/dt = n_e (S_{q-1}n_{q-1} - (S_q+R_q)n_q + R_{q+1}n_{q+1}) - n_q/\tau_q$

with n_q being the density of the impurity species, q the ionization state; S and R are the rate coefficients for ionization and recombination, respectively. The radiated power density has been calculated from the relation $p = \Sigma L_q(T_e)\, n_q\, n_e$ in which L_q is the radiation rate function. Assuming $n_e = 1*10^{19} m^{-3}$, r = 2 mm and an atomic nitrogen source strength of $1*10^{22}\ m^{-3}\ s^{-1}$ the results shown in fig.1 are obtained. Considerable nitrogen radiation from a magnetic island can only be expected if T_e is about 15 eV and if furthermore the diffusion coefficient within the island is smaller than 0.2 m^2 / s. Using the values of fig.1 a radiated power from the magnetic island of a 5/9-configuration up to 400 kW are predicted in case of W7-AS.

Experiments in the stellarator W7-AS

The experiments were performed in NBI-heated discharges with a 5/9- island configuration and limiters on the inboard side [2]. The nitrogen was injected with the reciprocating probe in upstream position (bottom side). Due to the injection the electron temperature within the island of W7-AS measured by the probe itself decreased from values up to 80 eV to about 10 eV. The total radiation raised up to 90 % of the input power, however, particular enhancement of radiation from island region could not be observed. The spatial distribution of the radiation after injecting nitrogen was found to be only slightly dependent on the location of the injection (X- or O-point). Enhanced radiation mainly occurred on the inboard side. When the density was increased, plasma shrinking induced by impurity injection was observed to start at densities of about $1 \times 10^{20} m^{-3}$. This shrinking was accompanied by partial transient plasma detachment from the inboard limiters. However, there are strong indications for poloidal asymmetries in connection with plasma shrinking. In fact, at plasma densities of $1.6 \times 10^{20} m^{-3}$, the ion current measured by probes near the O-point decreased by more than an order of magnitude on the outboard side (upstream) and less than a factor of two in the equatorial plane on the inboard side (downstream). Strongly localized radiation zones at the inboard side (MARFE s) were induced by the impurity injection at this density. In contrast to tokamaks the radiating region is not toroidally symmetric but seems to follow a helical line within a modular section similar to the helical edge observed earlier on the outboard side of W7-AS [3]. The power load to the inboard limiters measured by thermography was reduced by less than 25 % when a Marfe was formed in front of these limiters. The close proximity of the radiating region to the limiters possibly prevent a stronger reduction of the limiter load.

Besides the radiation from nitrogen a considerable enhancement of radiation from intrinsic impurities occurred. This observation is explained by the increase of radiation with decreasing plasma edge temperature and a deeper penetration of intrinsic impurity atoms due to the low edge plasma density and temperature.

Experiments in the tokamak ASDEX-Upgrade

Nitrogen was repeatedly injected just inside the separatrix in a 2 MW neutral beam heated L-mode discharge with programmed increasing plasma density from 4 to $8*10^{19}$ m^{-3}. During the injections the electron temperature at the separatrix measured by ECE on the outboard side decreased to values between 30 eV and 10 eV depending on the density (see fig.3) while the line averaged plasma density was transiently affected by less than 10 %. Radiation measured by the bolometer at a toroidal distance of 2.5 m from the impurity source was enhanced mainly above the X-point and on the inboard side. The fraction of the total radiated power in the main chamber to the input power reached about 0.8. Divertor detachment is indicated by the CII-signal of the divertor spectrometer at all plasma densities. The particle and the power fluxes to the target plates measured by Langmuir probes and thermography were also found to be strongly reduced during the injection (not shown here). Most remarkable is the following observation: Despite the fact that the carbon flux released from the target plates of the divertor was strongly reduced the concentration of carbon and oxygen in the main chamber increased as evidenced by the signals from the monitor for these impurities.

Modelling of the plasma boundary of AUG

In order to model the AUG-experiment descibed above an artificial carbon or boron ion source inside the separatrix on the outboard side was introduced in the B2/Eirene-code for a discharge with a plasma density of $5*10^{19}m^{-3}$ at the separatrix and 3 MW heating power. The diffusion coefficient was assumed to be 0.2 m^2s^{-1}. With increasing strength of the artificial impurity source and decreasing edge temperature the carbon radiation has been found to shift continously from the divertor to the X-point. Generally, when a MARFE is formed with an electron temperature of 1-2 eV finite temperature gradients exist along the separatrix. Thus the electron temperature varies between 1 and 20 eV on the inboard side whereas the value on the outboard side is still 30 eV (see fig.4). This is consistent with the observed radiation pattern. Evidently, the intrinsic impurity fluxes of carbon and oxygen produced at the inner wall shield can penetrate much deeper into the plasma at temperatures below 10 eV; i.e. the screening of the SOL-plasma due to ionization is reduced. This reduced screening may explain the experimental observation of enhanced C and O concentration in case of strong nitrogen injection into the edge plasma of AUG.

Summary:

Despite the quite different magnetic configurations in the stellarator W7-AS and the tokamak AUG the radiation pattern is similar when the electron temperature at the separatrix is decreased to values lower than 30 eV. A particular radiation from island regions at the plasma edge is not observed even after injecting nitrogen into a magnetic island of the stellerator W7-AS. The experiments in AUG have revealed that a too extensive radiation cooling should be avoided in order to prevent an increase of the intrinsic impurities caused by loss of screening.

References :

[1] J. Kisslinger et al., Proc. of the 22nd EPS Conference on Controlled Fusion and Plasma Physics, Bournemouth, ECA, Vol.19c, Part III (1995) 149

[2] D. Hildebrandt et al., Proc. XII. PSI, St. Raphael, 1996, to be published in J. Nucl. Mater.

[3] P. Grigull et al., J. Nucl. Mater.176&177 (1990) 975

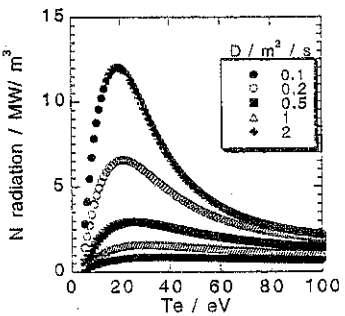

fig.1 : Calculated power density radiated during nitrogen injection into a magnetic island in dependence on the electron temperature with the diffusion coefficient as parameter

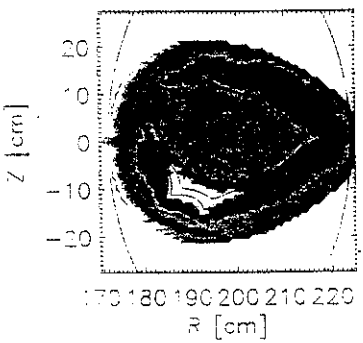

fig. 2 : 2D-plot of radiated power (bolometer) during nitrogen injection showing a MARFE on the inboard side below the equatorial plane of W7-AS

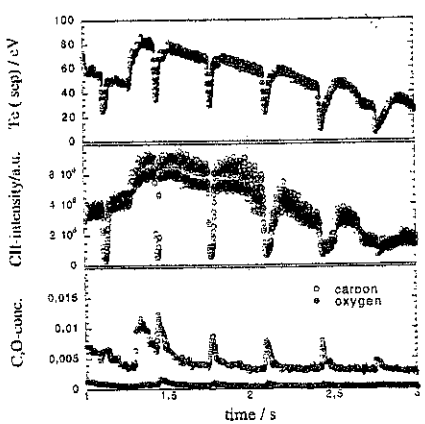

fig. 3 : Temporal traces of diagnostic signals of the AUG-discharge # 7738. From top to bottom:
electron temperature at the separatrix
C-II-signal of the divertor spectrometer,
C-and O-concentration inside the separatrix

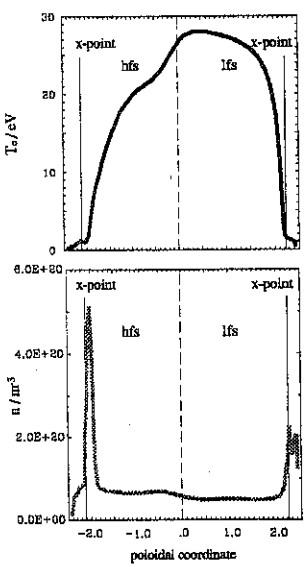

fig.4 : Electron temperature and plasma density at the separatrix in dependence on the poloidal position for a discharge with a MARFE near the X-point as calculated from B2/Eirene

RADIATIVE INSTABILITIES IN W7-AS PLASMAS WITH HIGHLY RADIATING BOUNDARIES

F. Castejón, M. A. Ochando
Asociación Euratom/CIEMAT para Fusión, Av. Complutense 22, 28040 Madrid, Spain
R. Brakel, W7-AS Team, ECRH Group
Max-Planck-Institut für Plasmaphysik, EURATOM Association, D-85748 Garching, Germany

Introduction

In low radiation ATF (Advanced Toroidal Facility [1]) stellarator plasmas it was concluded that the lack of efficiency in the radial energy transfer to sustain the local energy balance in regions with enhanced losses leads to plasma collapse [2]. The Proctr code [3] was used to analyse NB heated ATF collapsing discharges with moderate radiation levels (Prad/Pin $\approx$ 30 %) finding that radiative instabilities near the plasma periphery may be the trigger mechanism. On the other hand, low to intermediate Z impurity injection is being considered as a suitable procedure to cool the plasma edge region and, therefore, protect divertor plates in high power fusion experiments from thermal overloads. Then, the dominant plasma contaminant must be the adequate in every device for radiative edge cooling purposes, since cooling rate profiles determine the local energy lost by radiation.

Nitrogen is widely considered as an appropriate impurity for those purposes because of its radiative properties and its capability to be sufficiently pumped by the wall, especially when no active pumping is available [4]. In particular, it is used in tokamaks [5] to get the so called detached plasmas.

Experimental

In a previous work [6], nitrogen was confirmed to be an adequate impurity to effectively cool the edge region of Wendelstein 7-AS stellarator (R = 2.0 m, a = 0.18 m, no active pumping capability). However, steady state complete detachment from the limiters could not be established due to the onset of a radiative instability at a radiation level of about 60 % of the heating power. Further nitrogen injection experiments have been performed in W7-AS stellarator with feedback control of the radiation levels, via VUV line emission (N IV, 765 A), to maintain the impurity concentration under the limit of radiative collapse [7].

For the present studies a series of net current free ECRH discharges are considered, with flat-top of 1.5 s, at B=2.5 T, Iota/2π=0.34, injected power about 430 kW and electron density $n_e = 10^{19}$ m^{-3}. Transport analysis have been done with the predictive transport code Proctr. Here we are presenting the results obtained for three representative discharges, with no N_2 injection, 1 % and 2.5 % N_2 concentrations, shots # 36770, 36780 and 36783, respectively. In Figure 1 time evolution of line density, plasma stored energy and radiated

power are plotted for the three mentioned discharges. A fraction of about 60 % radiated power (measured from bolometry) is reached in discharge 36783 and the attempts to exceed this limit lead to a radiative instability and to feedback induced oscillations of the discharge parameters rather than to a collapse. Decreasing the nitrogen influx and, thus, the radiation level within the discharge duration leads to re-establishment of stationary conditions.

W7-AS is operated with two carbon limiters and so a moderate concentration of carbon is considered to be present in discharge 36770. The experimentally measured density profile is flat up to r/a=0.5, whereas the electron temperature profile is rather peaked for the three discharges.

Transport Analysis

To simulate the discharge dynamics the following experimental parameters have been used as inputs for Proctr: total radiated power, stored energy, heating power, line density, and the dominant species. Density is feed-back maintained with gas puffing plus limiter recycling. Power deposition is notably localized, according to [8]. The experimental electron temperature and density profiles have been used to benchmark the transport models chosen. The modelled temperature and density profiles can be seen in Figure 2, marked with the nitrogen concentration of the discharge.

In Figure 3 the radial profiles of loacal and integrated power electron balances are plotted for the three discharges in steady state regime, at time t = 700 ms. Again every plot is marked with the nitrogen concentration. It can be seen the very different behaviours of the radiated power profiles, depending on the nature and concentration of the impurity. In discharge 36770 carbon impurities are accumulated mainly at r/a = 0.6, and the radiation profile is rather flat. When about 1% of nitrogen is injected (discharge 36780) the global radiated power increases in the whole plasma column, mainly due to a small increase of Z_{eff}, but this increment is more pronounced at the edge, where the radiation profile becomes clearly peaked. For this nitrogen concentration only slight changes appear in plasma transport. Further nitrogen injection notably modifies the power balance at the outermost region of the plasma. Due to the strongly localized ECR absorption in these plasmas, almost no changes in the power deposition profile are seen because 100 % single pass absorption is reached, since the temperature is still high enough. Differences are found mainly in particle convection and in the power interchanged with ions by collisions. The edge radiation peak propagates inwards and increases in intensity. This nitrogen concentration somehow represents the maximum admissible limit beyond which a steady state discharge cannot be held.

Surpassing this limit leads to a sudden plasma contraction together with an accumulation of impurities in the plasma core. That is, a thermal collapse occurs. An artificial discharge has been modelled based on the data and transport parameters considered in

discharge number 36783. Concentration of nitrogen, radiated power, and stored energy have been proportionally modified to provoke the appearance of radiative instabilities.

Discussion

Nitrogen injection has been demonstrated as a good procedure for edge cooling in W7-AS, provided that feed-back is used to maintain the plasma under the limit of radiative collapse. In spite of the high radiated power, energy confinement time is only slightly degraded in discharge 36783 as compared with the reference one. This fact is confirmed by the diminishing of the estimated heat conductivity in the bulk plasma. This result agrees with the one presented in [7].

When comparing these results with the ATF NB-heated discharges [2] a difference is found in the plasma behaviour. As was concluded there, the detailed radial profile of the electron thermal conductivity plays a key role to supply power to the place where is needed. In the plasmas studied here this term is not able to cure the local increase of power losses and so the plasma can only reacts by modifying convection and power transmission to ions, i. e., particle transport must be mainly involved. One possible reason for these diverse behaviours can be found in the plasma heating method, since NBI power deposition profile is wider than ECRH (for high electron density and temperature) and changes according to the evolution of plasma parameters, such as density and temperature, higher power density is available near the maximum radiative losses region. Another likely cause may be that the magnetic configuration, strong sheared in ATF torsatron and almost shearless in W7-AS helias, is the responsible of the different transport regimes that appear in the two devices.

To clarify this problem simulations of ECR heated ATF discharges are underway. In particular the formation of transport barriers is planned to be studied.

References

[1] J. F. Lyon et al., Fusion Technol. **17** (1990) 33.

[2] M. A. Ochando et al., Nucl. Fusion. **37** (1997) 225

[3] H. C. Howe, "Physics models in the toroidal transport code Proctr". Oak Ridge National Laboratory Report ORNL /TM-11521 (1990)

[4] U. Samm et al., Plasma Physics Control. Fusion **35** (1993) B167

[5] G. F. Mathews and the JET Team, Plasma Physics Control. Fusion **37** (1995) A227.

[6] R. Brakel et al., "Radiative boundary studies in the Wendelstein 7-AS stellarator". to be published in the Proc. of 23rd EPS Conference on Plasma Physics and Controlled Fusion, Kiev (1996).

[7] P. Grigull et al., Poster at this conference.

[8] V. Erckmann, Plasma Physics Control. Fusion **36** (1994) 1869

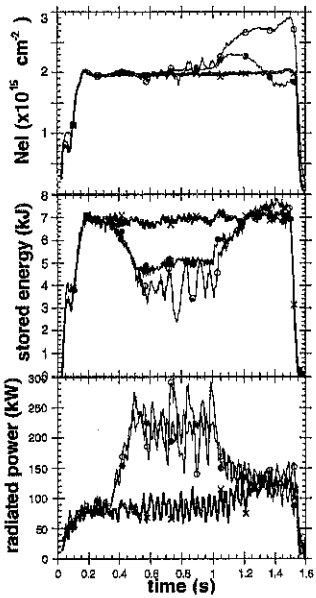
Nel (x10^15 cm^-2)
stored energy (kJ)
radiated power (kW)
time (s)

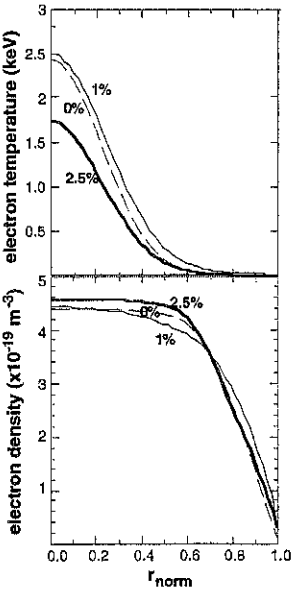
electron temperature (keV)
electron density (x10^19 m^-3)
0%
1%
2.5%
r_norm

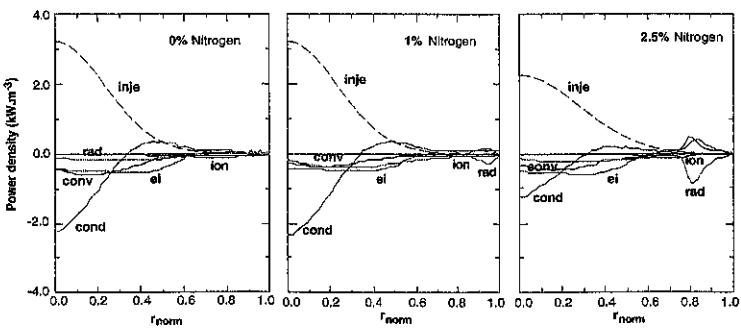
0% Nitrogen
1% Nitrogen
2.5% Nitrogen
Power density (kW.m^-3)
inje
rad
conv
ei
ion
cond
r_norm

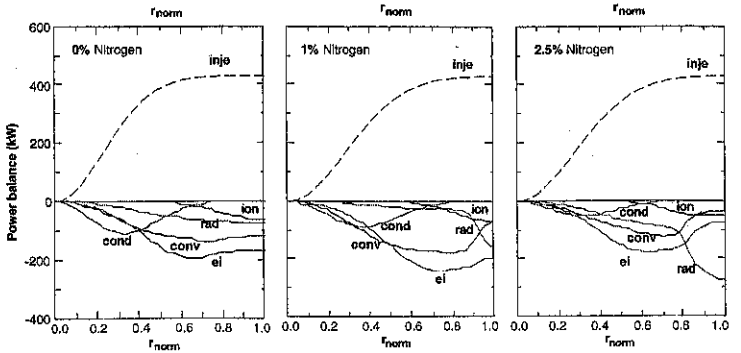
0% Nitrogen
1% Nitrogan
2.5% Nitrogen
Power balance (kW)
inje
ion
rad
cond
conv
ei
r_norm

The role of the radial electric field and plasma rotation for the W7-AS stellarator confinement

J. Baldzuhn, R. Burhenn, O. Heinrich, J. Hofmann, M. Kick,
H. Maassberg, W. Ohlendorf, W7-AS Team
Max-Planck-Institut für Plasmaphysik, EURATOM-Association,
85748 Garching, Germany

Experimental principles and neoclassical calculations

In the advanced stellarator W7-AS [1], the toroidal and poloidal plasma rotation velocity is measured by charge exchange recombination spectroscopy CXRS [2] on impurity ions, mainly on Helium. For that sake, two different spectroscopic systems are available [3], the first one with observation chords in one poloidal plane, the second one with viewing lines with an angle of roughly 50 degrees to the magnetic field lines. The CX light intensity is excited in the beam of a modulated diagnostic neutral beam injector.

From the spectral CX line intensity, Doppler line broadening and line shift, the impurity density n_{I+1} (r), the impurity ion temperature T_I (r) and the rotation velocities V_ϕ and V_θ (r) are determined, respectively. Here, ϕ and θ are the toroidal and poloidal angle co-ordinates. The CX reaction changes the impurity charge state Z from I+1 to I. It is assumed that T_i (r) = T_I (r) = T_{I+1} (r). The radial electric field profile E_r (r) is calculated from the simplified radial force balance equation [4]:

$$E_r = \frac{\partial (n_{I+1}(r) \cdot T_{I+1}(r))}{\partial r} \cdot \frac{1}{e Z_{I+1} n_{I+1}(r)} + \frac{T_I(r)\gamma}{e Z_I} \cdot \frac{\partial \zeta_I / \partial r}{\zeta_I} + (B_\theta V_\varphi - B_\varphi V_\theta) \qquad (1)$$

Here, B stands for the magnetic field, e for the elementary charge, ζ_I is the excitation probability for the CX spectral line under consideration. The lifetime τ_I of the excited state and the ion gyro frequency ω_I are taken into account for the factor γ:

$$\gamma = \frac{(\omega_I \tau_I)^2}{1+(\omega_I \tau_I)^2} \qquad (2)$$

In eq. (1), the first term on the right hand side gives the impurity ion pressure gradient contribution to E_r. The second term arises from finite lifetime of the excited electronic state during the ion gyro motion after CX, for the case that the spectroscopic line of sight $\vec{l}$ is perpendicular to the magnetic field, and a gradient of the excitation probability exists, perpendicular to $\vec{l}$ and $\vec{B}$. In W7-AS this direction is parallel to the minor radius r, therefore the derivatives are with respect to r. Eq. (1) holds for CX approximately for $\gamma << 1$, as this is given in our case for He^+, and therefore that second term is small. The third term is the $\vec{J} \times \vec{B}$ force. In stellarators, the toroidal and poloidal rotation are de-coupled, in contrast to tokamaks [14]. It is found experimentally for W7-AS that the main contribution to E_r comes from the poloidal rotation, the toroidal rotation is strongly damped because of

the missing axi-symmetry of the magnetic stellarator field. A fast toroidal plasma motion can be provoked only by non balanced neutral beam heating NBI, with counteracting toroidal viscosity which is found to be in good agreement to neoclassical calculations [9]. But even then its contribution to E_r is negligible (typically < 5%), because $B_\theta << B_\phi$.

In non-axisymmetric devices like stellarators a strong dependence of transport from E_r is expected from neoclassical theory. The formation of E_r is determined by the radial particle fluxes Γ from the ambipolarity condition:

$$\Gamma_e(r, E_r) + \Gamma_i(r, E_r) + Z_I \Gamma_I(r, E_r) = 0 \qquad (3)$$

Especially in the long mean free path regime LMFP, the differences between tokamaks and stellarators are essential, because in LMFP the ripple of the magnetic field along the field lines produces large populations of trapped particles in stellarators, with different trapping types (toroidally, helically or combinations) with an enhanced radial drift. With respect to the development of a stellarator-reactor this unfavourable effect has to be minimized, as this is done by the so-called optimization concept for the advanced stellarators W7-AS and W7-X [12]. These drifts are also strongly reduced by the ambipolar E_r, an effect which is for the ions much more pronounced than for the electrons.

The neoclassical definitions for the particle fluxes Γ and heat fluxes Q are given by:

$$\Gamma_\alpha = -n_\alpha \left\{ D_{11}^\alpha \left(\frac{n'_\alpha}{n_\alpha} - \frac{q_\alpha E_r}{T_\alpha} \right) + D_{12}^\alpha \frac{T'_\alpha}{T_\alpha} \right\}$$

$$Q_\alpha = -n_\alpha T_\alpha \left\{ D_{21}^\alpha \left(\frac{n'_\alpha}{n_\alpha} - \frac{q_\alpha E_r}{T_\alpha} \right) + D_{22}^\alpha \frac{T'_\alpha}{T_\alpha} \right\} \qquad (4)$$

The subscript α stands for ions or electrons, respectively, q for their electric charge, D are the coefficients of the transport matrix. For the definition of Γ, a possible Ware's pinch term proportional to D_{13}^α is neglected. Besides the linear dependence of Γ and Q from E_r, also the D's are functions of E_r, for the ions much stronger than for the electrons. For E_r, an odd number of solutions is expected from neoclassical theory [13]. Two of them should be stable, the others are unstable.

For the neoclassical calculation of E_r the numerical DKES code [5] is used. Starting from the specific magnetic configuration, represented by Fourier modes of the magnetic field, DKES calculates the mono-energetic transport coefficients by solution of the drift-kinetic equation, as function of the effective minor radius, the collisionality and E_r. By energy convolution, the 3×3 thermal transport matrix D_{ij}^α is then obtained, which is used to calculate the radial particle fluxes following eq. (4). The solution of the ambipolarity condition (3) provides then the solutions for the neoclassical E_r, which are finally compared to the measured one.

E_r and transport in W7-AS

For the case of low electron collisionality (low electron density $n_e(0)$ below $3 \cdot 10^{19}$ m^{-3}, high electron temperature $T_e(0)$ above 2 keV) only one strong positive solution is expected in W7-AS near the plasma center, the "electron root", with $E_r \approx +400$ V/cm. For that particular case, the central electron heat transport is considerably reduced [10], allowing experimentally for maximum $T_e(0)$ up to 4 keV. This situation can be obtained only in conjunction with rather low T_i, typically below 400 eV.

For the case of higher $n_e(0)$ (between $4 - 12 \cdot 10^{19}$ m^{-3}), only one negative solution is expected near the plasma edge, the "ion-root". For that type of discharge, with combined NBI and ECRH heating and high power > 1 MW, maximum negative $Er \approx -1000$ V/cm are obtained in the gradient region which act as a potential barrier, together with maximum $T_i(0)$ up to 1.5 keV. The global energy confinement time exceeds the prediction from the ISS95 regression database [11] by more than a factor of two.

Multiple field solutions are expected for medium $n_e(0)$ between $2 - 5 \cdot 10^{19}$ m^{-3} and lower heating power, typically with negative E_r values ("ion-root") near the plasma edge but smaller values than described above for $E_r \approx -100$ to -400 V/cm, and either strong positive E_r ("electron-root") near the plasma center for sufficiently high $T_e > 2$ keV, or small positive $E_r \approx +20$ V/cm for lower T_e (positive "ion-root").

The comparison between the measured and calculated E_r is a sensitive means to investigate the mutual interference between E_r and the particle transport in detail [6]. It is found that the measured and the neoclassically calculated E_r are in general consistent to each other [7]. Thus, the validity of the neoclassical particle transport model for the prediction of E_r in W7-AS is demonstrated, at least for the central part of the plasma up to $r < 0.7 \cdot a$. The most striking feature appears when investigating the impact of E_r on the shape of impurity density profiles because of the higher Z. This point is of particular interest for a future stellarator reactor, because impurity accumulation has to be prevented, and efficient Helium exhaust is desired. For the calculation of the impurity density profiles, the SITAR code [8] is used which employs a tokamak axisymmetric magnetic field model. The flux ansatz $\Gamma_I = -D_I \cdot n_I' - V_I \cdot n_I$ with diffusion and convection is used in SITAR in the form:

$$\Gamma_I = \frac{\rho^2}{Z_I \tau}\,(0.5+q^2)\left(B\frac{\partial n_I}{\partial r} - \frac{n_I}{Z_I n_I}\frac{\partial n_I}{\partial r} - A\frac{n_I}{T_I}\frac{\partial T_I}{\partial r} - \frac{n_I}{T_I} e Z_I E_r\right) \qquad (5)$$

where ρ stands for the mean path length between two collisions, τ is a mean collision time, q is the tokamak safety factor, A and B are collisionality dependent factors [15]. SITAR fulfils internally the ambipolarity condition, thus taking into account the E_r influence implicitly. The detailed information on the stellarator magnetic field as required for the explicit calculation of the transport coefficients for W7-AS, however, is taken into account only by DKES. For some discharges, which in principle allow for multiple solutions as described above, small positive $E_r \approx +10$ V/cm (positive "ion-root") are predicted by DKES

in W7-AS near the plasma center. In the gradient region, the "ion-root" is negative with values $E_r \approx -100$ V/cm. The spectroscopic E_r measurement bars in this case are, however, too large to confirm the small central positive E_r from the evaluation following eq. (1) alone, see fig. 1 on the left side.The spectroscopic measurement by CXRS in fact shows a hollow He^{++} density profile for that type of discharge, as plotted in fig. 1 below on the right side (dots and broken line). With the small positive $E_r \approx +10$ V/cm taken into account in SITAR in eq. (5), the calculated He^{++} density profile also shows that hollow shape. Thus, an outward convection for He^{++} is confirmed, as a consequence of the positive E_r.

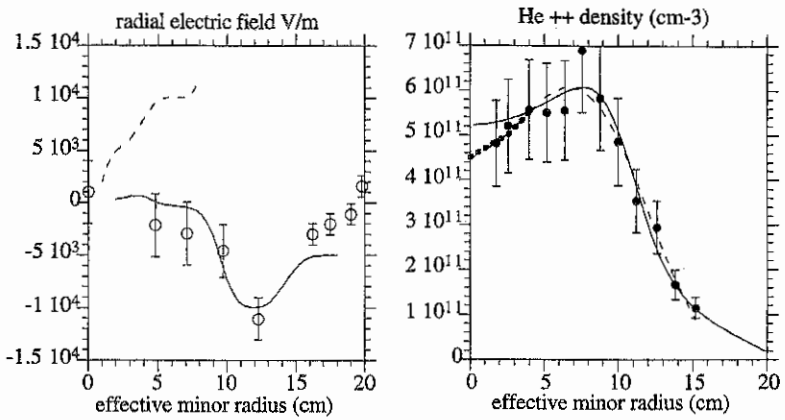

Fig. 1: Left plot: E_r profile: CXRS measurement (circles), DKES calculation for the ion-root (solid line) and the electron-root (broken line) which is not realized. The ion-root solution is positive for $r < 6$ cm. Right plot: He^{++} density profile measured by CXRS (dots), least squares fit of a generalized Gaussian function to the measured points (thin broken line), result of the SITAR transport calculation without the small positive E_r taken into account (solid line), the SITAR result with E_r reproduces the outcome of the Gaussian fit (thick dotted line).

References

[1] Sapper J, Renner H 1990 *Fusion Technol.* **17** , 62
[2] Fonck RJ, Darrow DS, Jaehnig KP 1984 *Phys. Rev.* A **29** , 3288
[3] Baldzuhn J, Ohlendorf W, W7-AS Team 1997 *Rev. Sci. Instr.* **68** , 1020
[4] Field AR, Fussmann G, Hofmann JV, ASDEX Team 1992 *Nucl. Fus.* **32** , 1191
[5] van Rij W, Hirshman S 1989 *Phys. Fluids* B **1** , 563
[6] Baldzuhn J et al 1995 *10th Int. Conf. Stell. Madrid* EUR-CIEMAT **30** , 144
[7] Baldzuhn J et al, to be published
[8] Weller A et al 1991 *Plasma Phys. Contr. Fus.* **33** , 18th EPS Conf. Berlin 1559
[9] Hofmann JV et al 1994 *Proc. 21th EPS Conf. Montpellier* , I - 392
[10] Brakel R, this conference; Maassberg H to be published
[11] Stroth U et al 1996 *Nucl. Fusion* **36** , 1063
[12] Grieger G et al 1992 *Phys. Fluids* B **4** , 2081
[13] Mynick HE, Hitchon WNG 1983 *Nucl. Fusion* **23** , 1053
[14] Kim YB, Diamond PH, Groebner RJ 1991 *Phys. Fluids* B **3** , 2050
[15] Hirshman SP, Sigmar DJ 1981 *Nucl. Fusion* **21** , 1079

Study of density turbulence and coherent mode activity in W7-AS by microwave reflectometry

M. Francés, M. Hirsch*, M. Anton*, T. Geist*, H. J. Hartfuss* and E. Holzhauer**

Asociación EURATOM-CIEMAT, Madrid, Spain
**Max-Planck-Institut für Plamaphysik, Association EURATOM-IPP, Garching, Germany*
***Institut für Plasmaforschung, Universitat Stuttgart, Stuttgart, Germany*

Abstract - In the context of transport investigations different heating scenarios have been studied in W7-AS. When the plasma is heated by NBI (pure as well as combined with ECRH) the signals from the microwave reflectometer show coherent mode activity in the frequency range of 20 to 90 kHz depending on the iota profile. These modes have been observed for all the radial positions probed by the reflectometer and are identified as global Alfvén modes.

Experimental system - At W7-AS ($R = 2$ m, $a < 0.17$ m, 5 field periods, modular stellarator coil system) a reflectometer is installed [1,2] for density profile and fluctuation measurements. The system uses X-mode propagation in the W-band (75-110 GHz) for probing radial positions corresponding to densities between 1 to 6 10^{19} m^{-3}. At the toroidal position where the reflectometer is installed the plasma has a nearly elliptical shape with the minor axis along the equatorial plane of the torus. Corrugated horns in combination with elliptical mirrors are used as emitting and receiving antennas resulting in a focused Gaussian beam of 2 cm diameter at the reflecting layer. Heterodyne detection allows to measure phase and amplitude fluctuations separately. An Amplitude Modulation (AM) system [2] integrated into the reflectometer provides a time delay measurement which is used to obtain electron density profile information. This time delay of the signal depends on the cutoff position and on the local density gradient being, in most of the cases, more sensitive to the latter one. Therefore the time delay signal can be considered as a monitor of the local density gradient.

Experimental results - In the context of transport investigations the microwave reflectometer was operated in discharges with different heating scenarios: ECRH, NBI, and combined NBI+ECRH. Two types of discharges are studied in this paper. (1) Plasmas with combined, ECRH (500 kW) and NBI (1.5 MW), heating which show a very high ion temperature, reaching values up to 1.5 keV [3]. (2) Discharges with pure NBI heating with lower injected power (0.5 MW), which reach energy confinement times about twice as large as predicted by neoclassical theories [3]. Both improved confinement scenarios are achieved under low wall-recycling conditions and are characterized by a low edge density and high density peaking factor [4]. Electron density profiles from Thomson scattering and AM-reflectometer for these two types of discharges are shown in Figure 1. The radial positions probed by the microwave reflectometer are between 11 cm and 15 cm. Shots with pure NBI heating and very

high energy confinement time show an electron density profile steeper than shots with combined heating (ECRH+NBI) and very high ion temperature.

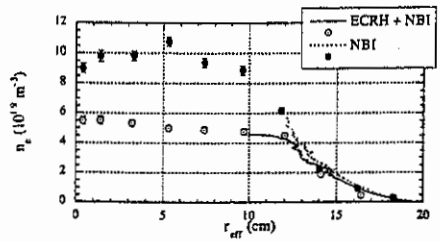

Figure 1: Electron density profiles from Thomson scattering (circles) and from microwave reflectometer (lines) in the discharges of interest: combined ECRH+NBI heating and pure NBI.

In general, if the plasma is heated by NBI (pure as well as in combination with ECRH) the reflectometer signals show coherent mode activity. Other diagnostics (X-ray, ECE, Mirnov coils, etc.) also observe these modes depending on the iota profile, and have been identified as global Alfvén modes [5].

The interpretation of reflectometry phase measurements is complicated by an asymmetry in the phase fluctuation spectra, called „phase runaway" [6]. Under both plasma conditions discused in this paper this effect is several times lower than in pure ECRH plasmas, therefore the measured phase fluctuations mainly can be interpreted in terms of density fluctuations.

Figure 2-a: Phase fluctuation spectra during a purely NBI heated plasma for different radial positions.

Figure 2-b: Time delay spectra during a purely NBI heated plasma for different radial positions.

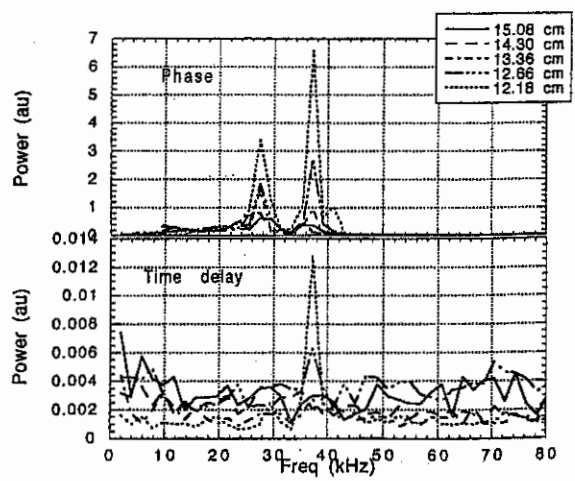

During pure NBI heating the coherent modes observed by reflectometry appear in the frequency range of 10-40 kHz. As an example Figure 2-a shows the power spectra of the reflectrometer phase. Two different modes with frequencies of 27 kHz and 37 kHz are present

simultaneously in the spectra. The frequency of these modes is independent of the radial position probed by the reflectometer (r_{eff} = 11-15 cm) and their amplitude increases towards the plasma centre.

The time delay signal has been measured simultaneously. The dispersive effects, associated with the local density gradient, represent the largest contribution to the measured time delay. Therefore, fluctuations in the time delay signal can be considered as a monitor of the local density gradient. The spectral analysis of this signal, shown in Figure 2-b, does not always show the coherent modes. Only in the most inner radial positions probed with the reflectometer, the highest frequency (f = 37 kHz) coherent mode is seen. This absence of coherent modes in the time delay signal can be interpreted as a movement of the density profile.

During discharges with combined heating, P_{ECRH} = 400 kW and P_{NBI} = 1.5 MW, where the ion temperature reaches values of about 1.45 keV, the frequency of the observed modes is higher than during pure NBI heating, appearing modes up to 90 kHz. Similarly to purely NBI heated discharges, the amplitude of these modes also increases towards the plasma centre and their frequency is constant along all the probed radii. As an example Figure 3-a shows the spectra of the phase signal where several global modes are observed at different frequencies. The coherent mode with the highest frequency appears at 85 kHz in all the probed positions. The spectra of the time delay signal, Figure 3-b, shows this highest frequency coherent mode in most of the radii tested while the lower frequency modes are not observed.

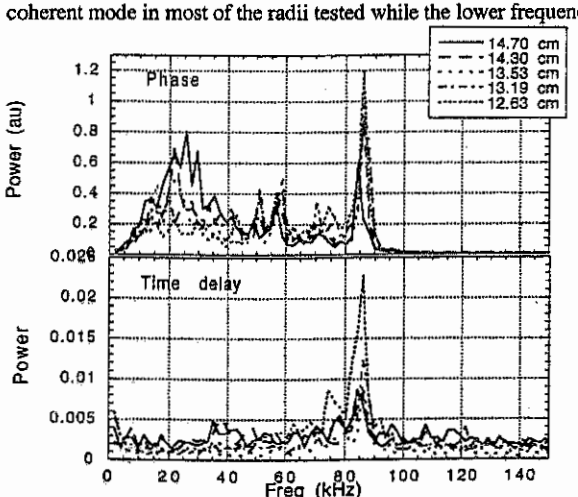

Figure 3-a: Phase fluctuation spectra during a combined NBI + ECRH heating for different radial positions.

Figure 3-b: Time delay spectra during a combined NBI + ECRH heating for different radial positions.

Microwave reflectometer results were also obtained during discharges in which the heating was switched from pure NBI (0.5 MW) to pure ECRH (0.4 MW). In contrast to the purely NBI heated phase in the purely ECRH heated plasma these coherent modes disappear in the reflectometer signal in all of the probed radii, indicating that the heating and not the magnetic configuration is related with the origin of the modes. Similar radial positions were probed by

the reflectometer in the two heating scenarios. In the NBI heating regime (Fig. 4-a) a coherent mode with a frequency of about 45 kHz can be observed in all the probed radii while with ECRH (Fig. 4-b) this mode does not appear. The absence of the 45 kHz coherent mode in the ECRH regime has been also observed by other diagnostics, e.g. Mirnov coils as shown the figure 5.

Figure 4-a: Phase fluctuation spectra during a purely NBI heated plasma for different radial positions.

Figure 4-b: Phase fluctuations spectra during a purely ECRH heated plasma for different radial positions.

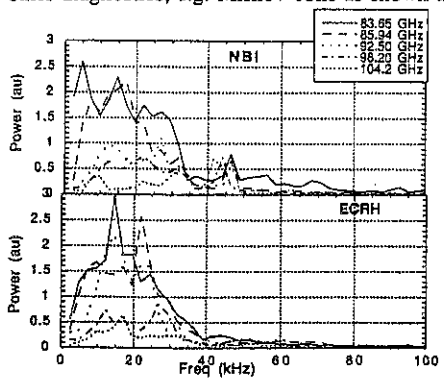

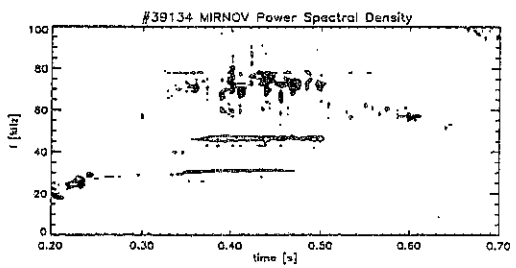

Figure 5: Temporal spectrum evolution of Mirnov coil signal in a shot where the heating was switched from pure NBI to pure ECRH. The 45 kHz coherent mode disappears when the heating scenario is changed at 0.5 s.

In both heating regimes the low frequency broadband incoherent density fluctuations (f < 40 kHz) decrease as positions futher inside are probed. In contrast the power of the 45 kHz coherent mode observed with NBI is nearly independed of the probed positions.

Conclusions - In NBI heated plasmas coherent mode activity is observed which shows up as coherent oscillations in the reflectometer signal if the phase runaway is low. The spectral analysis of the phase signals shows very sharp frequency lines. The modes decay with about 200 μs after NBI is switched-off and their frequencies scale roughly with the Alfvén velocity [5]. They are observed in all the probed radial positions indicating a global mode structure. These observations are in agreement with an interpretation as global Alfvén eigenmodes.

[1] H. J. Hartfuss, T. Estrada, M. Hirsch et al., Rev. Sci. Instrum. 65(7), 2284 (1994)
[2] M. Hirsch, H. J. Hartfuss, T. Geist, E. de la Luna, Rev. Sci. Instrum. 67(5), (1996)
[3] M. Kick, J. Baldzuhn et al. Proc. IAEA 16th Internacional Conference on Plasma Physics and Controlled Nuclear Fusion Research, IAEA-F1-CN-64/C1-4 (1996)
[4] U. Stroth, M. Anton et al. this conference
[5] A. Weller, D. A. Spong et al. Proc. 21st Eur. Conf. on Controlled Fusion and Plasma Physics (Montpellier, 1994) Vol 18B Part I, 408
[6] B. Branas, M. Hirsch et al. Submited to Plasma Physics and Controlled Fusion (1997)

Role of recycling to achieve high $nT\tau_E$ in W7-AS

O. Heinrich, H. Maaßberg, J. Baldzuhn, S. Fiedler and the W7-AS Team
Max-Planck-Institut für Plasmaphysik, EURATOM Association,
D-85748 Garching, Germany

Introduction High $nT\tau_E$ at W7-AS in pure or combined NBI and ECRH discharges is only obtained for low edge density. In the case of combined heating, steep temperature gradients (T_e' as well as T_i') in the region of low densities in connection with strongly negative radial electric fields are observed [1]. In the bulk plasma, both energy balances (electrons and ions) and particle balance are in good agreement with the neoclassical fluxes. In the gradient region the particle fluxes are still anomalous, but are much lower than in discharges with higher edge densities and lower confinement. Central values of high confinement plasmas with e. g. 825 kW NBI and 370 kW ECRH absorbed power are $n_e = 1 \cdot 10^{20}\,\mathrm{m}^{-3}$, $T_i = 1$ keV and $\tau_E \approx 22$ ms. This is by a factor of about 2 larger than the one from the International Stellarator Scaling [2].
The same relation between confinement and profile characteristics appears if one considers the dependence of confinement on rotational transform ι or density in W7-AS. The variation of the latter leads partly to remarkable transitions in confinement. This points to a crucial dependence of global confinement quality, edge profiles and recycling.

Particle Transport The influence of recycling and particle transport is studied in ECRH deuterium discharges with moderate heating power (≈450 kW) where either ι or the averaged line density was varied between shots. In addition, discharges with a density ramp were performed and these are discussed in the next section. The plasmas were limiter bounded ($B_z = 23$mT) by the symmetric inboard limiters [3], which allows particle transport analysis with defined sources. ι was in the range around 1/3, which shows a resonance-like dependence of confinement and ι in W7-AS (upper part of Fig. 1) [4]. At first sight this behaviour might indicate a *direct* influence of magnetic islands on transport, but neither this nor MHD activity seem to explain the observations. Possible explanations are given on the basis of anomalous transport effects induced by rational ι-surfaces and/or ι-shear [5-7]. The H_α-signal (lower part of Fig. 1), which roughly corresponds to the particle flux at the edge, shows a strong anti-correlation to W_{dia}. This means that the particle transport is very important in this resonant phenomenon.

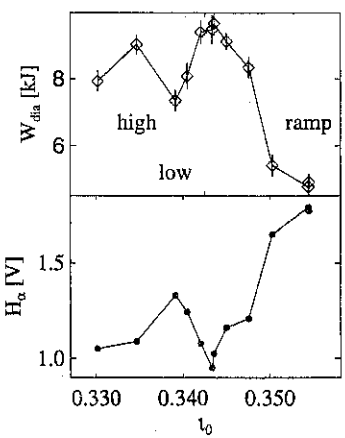

Fig. 1: Diamagnetic energy W_{dia} and H_α-signal at the inboard limiter vs. central ι_0. The shadowed lines mark the ι_0-values of the discussed discharges with low or high confinement and density ramps.

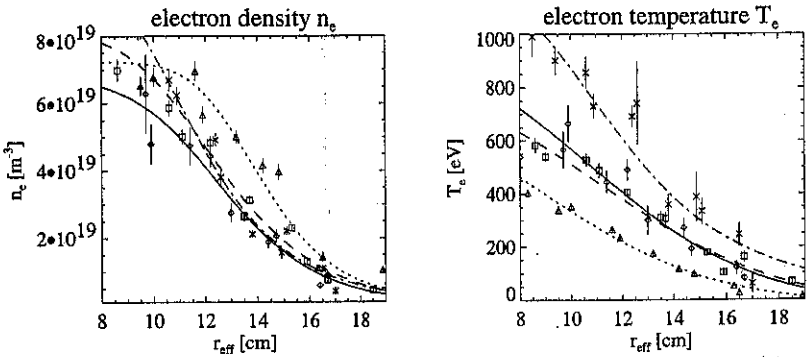

Fig. 2: Plasma profiles in the gradient region for low and high confinement. Below (#29925, solid line, ◇) and above (#29927, dotted, △) density threshold at $\iota_0 = 0.338$. At $\iota_0 = 0.335$ (#29928, dashed, □). High $nT\tau_E$ NBI discharge (#34609, dash dot, ×). Explanation see text.

Besides ι the density has an equivalent influence on confinement. This can be shown as follows: if at $\iota_0 = 0.338$ the line density is increased the confinement suddenly decreases at a certain density. Fig. 2 shows the profiles near the confinement transition. Above the density threshold the density at the limiter increases and the density profile broadens; also the particle edge flux (H_α) increases. Simultaneously the temperature significantly lowers over the entire plasma radius and as a consequence the energy content decreases by almost 20%. If then ι is decreased to a high confinement value ($\iota_0 = 0.335$, same line density), the former state with a narrow density profile and good confinement is re-established. Therefore at this point a slight change in ι or n_e have the identical effect. The comparison with the high confinement NBI heated discharge shows a nearly identical density profile at the edge ($r_{eff} \geq 12$cm) although the central density is almost twice as high. So low edge densities seem to be a necessary condition for obtaining high confinement.

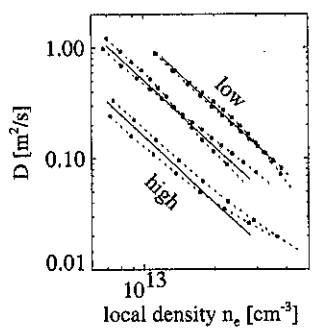

Fig. 3: Effective diffusion coefficient D vs. local density. Given are the "experimental" radial D's between $r_{eff} = 12$ and 17 cm for discharges (dots, dashed) of low (e. g. #29927) and high (e. g. #34609) confinement and between them (#29925,#29928). The lines are rough fits to $(cn_e)^{-2}$ with $c \cdot 10^{13} = 0.92, 1.4, 2.5$ from low to high confinement.

The particle transport is investigated with the help of the 3D Monte-Carlo code EIRENE [8], which provides the particle sources. The adaption to the experimental conditions was done with a similar procedure as formerly [9]. From a radial 1D diffusion equation (n_e-distribution in cylindrical symmetry) radially resolved particle fluxes and an effective diffusion coefficient are obtained. In fig. 3 the diffusion coefficients D of the discharges of fig. 2 are shown. It clearly can be seen that the relative density dependence is the same for all types of confinement. The n_e^{-2}-dependence found here is in contrast to earlier observations, which scale with n_e^{-1} [10],

but the discrepancy is not understood so far. However the absolute value of D differs according to the quality of confinement: better confinement means lower D. The same applies to the edge particle flux, which in the high $nT\tau_E$ NBI discharges with $\sim 10^{21}$ part/s is very low compared to $\sim 5 \cdot 10^{21}$ part/s in the low confinement case. A more astonishing point is that the differences in D can be resolved, if the local T_e is also taken into account. Then the diffusivities can be described by $D \sim (n_e T_e)^{-1}$. However the implication is not clear: there could e. g. exist a mechanism, which acts both on n_e and T_e profiles, or there is some direct relation between energy and particle transport. Therefore it should carefully be interpreted as some additional parameter whose value effects D.

Density ramps In order to investigate the dynamic behaviour of the confinement transition, discharges with positive and negative density ramps were performed. In fig. 4 the difference of a density ramp discharge with low and high confinement is shown. While in high confinement the energy content increases linearly with density, in the other case the diamagnetic energy deteriorates above the density threshold again. Both energy loss and edge flux are increased by a factor of 2 compared to high confinement. Due to the excellent wall conditions the typical time scale of a density ramp-up (~0.5s) could also be obtained in ramp-down discharges. Since in both cases the transition occurs at the same line density, the density can be clearly identified as the transition parameter. Fig. 5 shows a discharge with a density ramp-down at low confinement $\iota_0 \approx 0.354$ (see fig. 1). It exhibits a very sharp transition to high confinement as the density decreases. This can be seen especially in the edge flux (H_α), which drops on a ms-scale, but also in n_e- and T_e-profiles. After the transition the profiles evolve over 150 ms until a new quasi-stationary state is formed. The energy content increases (due to T_e) up to the value, which is observed in an equivalent discharge at high confinement ι. At the same time the density profile at the edge stays nearly constant, but the line density still decreases. This indicates the change of the density profile shape. The transition is not always as fast as in Fig. 5. A higher wall recycling e. g. smoothes the transition, because it influences the edge density profile.

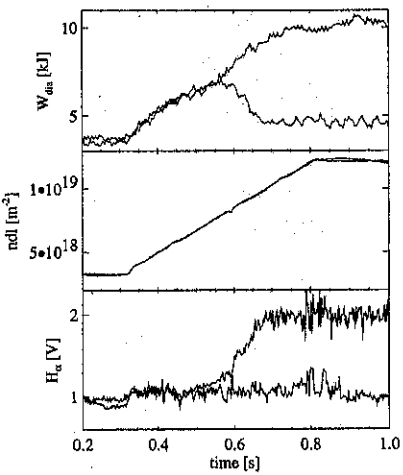

Fig. 4: Density ramp-up for two different ι at low ($\iota_0 = 0.354$) and high ($\iota_0 = 0.344$) confinement. In the low conf. case the edge flux (H_α) increases with the confinement decrease, whereas in the other case the particle confinement stays constant.

From the data, no clear causality between the influence of n_e and T_e can be drawn. At the transition the edge n_e-profile (by Li-beam) decreases, which marks the lower edge density with better confinement. Simultaneously the particle flux is reduced, which corresponds to the lower D in high confinement (see fig. 3). Also the sudden increase of T_e as well as the increased negative radial E-field (v_{pol}) indicate the better confinement.

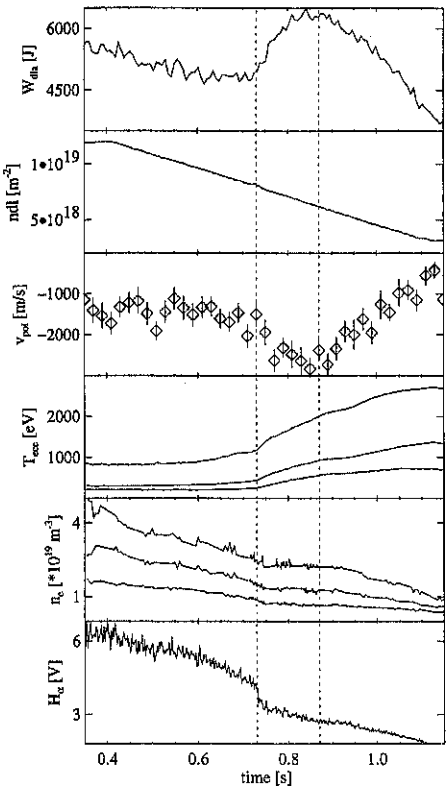

Fig. 5: Time evolution of discharge #39258 ($\iota_0 = 0.354$) with a negative density ramp. Shown are from top to bottom: diamagnetic energy, central line density from microwave interferometry (line of sight = 50 cm), pol. rotation speed (by CXRS), T_e by ECE at $r_{eff} = 1, 7, 10cm$, n_e by Li-beam at $r_{eff} = 12, 14, 16cm$, H_α-signal at the inboard limiter. The transition occurs at 0.73s; only after 150ms the energy content reaches its maximum.

To elucidate the relation between particle flux and the edge density, the radial diffusion equation in cylindrical coordinates has been solved. For the diffusion coefficient typical "experimental" diffusivities as shown in fig. 3 were used. The simple $\frac{1}{n^2}$-dependence can reproduce broad and narrow density profiles similar to the experimental ones. However the edge fluxes were about 10% higher in the case of a narrow profile. It was not possible without additional assumptions to bring down the fluxes as found in the experiment. This corresponds to the observation of the last section, that a $D = D(n_e)$ description is not sufficient to explain the different particle confinement.

Conclusions A low edge density seems to be a prerequisite for high confinement in W7-AS. This applies also to the resonance-like dependence of confinement with ι. The strong anti-correlation of edge fluxes and W_{dia} shows the close connection of particle transport and this resonant phenomenon. There exists a density threshold, where a fast transition of confinement occurs. The particle transport analysis of different confinement states gives to the known n_e-dependence an additional T_e-dependence for the "experimental" diffusivities. However this should be interpreted as the influence of a parameter, which *could* be the temperature or a related quantity. A causal influence of n_e or T_e cannot be distinguished.

References

[1] Kick M et al., F1-CN-64/C1-4, IAEA 1996, Montreal, Canada
[2] Stroth U et al., *Nucl. Fusion*, Vol. 36, (1996), 1063
[3] Das J et al., *Proc. 22nd EPS Conf.*, Bournemouth, Vol. 19C, Part IV, 313, (1995)
[4] Jänicke R et al., *Nucl. Fusion*, Vol. 33, No. 5 (1993), 687-704
[5] Brakel R et al., invited paper of this conference, to be publ. in *Plasma Phys. Contr. Fus.*
[6,7] Weller A et al., Stroth U et al., this conference
[8] Reiter D, *report of KFA Jülich*, No. 2599, Institut für Plasmaphysik, (1992)
[9] Fiedler S et al., *Proc. 23rd EPS Conf.*, Kiev, Vol. 20C, Part III, 1011, (1996)
[10] Maaßberg et al., *Plasma Phys. Control. Fusion*, Vol. 35, (1993), B319-B332

High-Confinement NBI Discharges in W7-AS

U. Stroth, M. Anton, J. Baldzuhn, R. Burhenn, M. Francés[1)], J. Geiger, T. Geist, L. Giannone, H. Hartfuß, M. Hirsch, R. Jänicke, J.P.T. Koponen, M. Kick, G. Kühner, F.-P. Penningsfeld, F. Wagner, A. Weller

Max-Planck-Institut für Plasmaphysik, EURATOM Association, D-85748 Garching, [1)]EURATOM-CIEMAT Association, Madrid, Spain

Abstract: In W7-AS, the longest energy confinement times were achieved in NBI-heated discharges under low wall-recycling conditions. Low recycling is needed to control the density at line averaged values of $\bar{n}_e \approx 10^{20}$ m^{-3}. Under these conditions, electron and ion temperatures of up to 1 keV and confinement times of 55 ms were obtained with an absorbed heating power of $P \approx 0.35$ MW. In NBI discharges without density control, the density rose up to typically 2×10^{20} m^{-3} and the temperatures remained at 0.3 keV only.

From the H-mode, where after a fast transition the profiles broaden, these discharges can be distinguished by low edge densities and a rather gradual improvement of energy confinement. The reduction of transport is concentrated to a layer at about 2/3 of the plasma radius. In this region steep temperature gradients and a strong gradient in the radial electric field develop. In this respect the discharges are similar to discharges with stronger NBI and additional electron cyclotron resonance heating (ECH), where the highest ion temperatures were achieved [1].

What is specific for the discharges here is the gradual transition. Since the measured electric field is consistent with the neoclassical ambipolar field, this high-confinement mode could be an example where the neoclassical electric field leads to a suppression of anomalous transport, this in turn produces steeper gradients which lead according to neoclassical theory again to a stronger field. This loop is interrupted when transport reaches the neoclassical level. The result is a transport barrier similar as in high performance tokamak discharges like in JET [2].

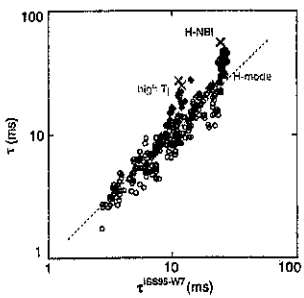

Fig. 1: Diamagnetic confinement times of high-confinement NBI, high ion temperature and H-mode discharges compared with the ISS95 scaling (W7-AS pre-factor) and W7-AS data contributed to the ISS95 database (open symbols). Crosses: kinetic values.

Global Energy Confinement Time: In Fig. 1, we compare the energy confinement time τ_E of high-confinement discharges with the W7-AS dataset contributed to the ISS95 scaling [3], which covers our previously accessible parameter range. In the ISS95 dataset a trend was already observed of the kinetic confinement times, as deduced from profiles, being about 15% higher then the diamagnetic ones. For the discharges here, the kinetic confinement time is about 35% higher than the diamagnetic one. A 15% discrepancy can be understood in terms of the diamagnetic loop picking up a component of the vertical field generated by Pfirsch-Schlüter currents. The 35% difference remains unclear at the moment. Since the profiles are well documented for

these discharges, we have added the kinetic confinement times to the plot. The figure underlines that the confinement time of these discharges is a factor of 2 above our standard confinement level.

Characteristics: In Fig. 2, the main characteristics of a high-confinement NBI discharge are depicted. The distinct feature is the continuous increase from 0.25 to 0.4 s of the energy content at constant heating power and line density. During this phase, which corresponds to three energy confinement times, electron and ion temperatures increase. Simultaneously, a reduction in the H_α light indicates improving particle confinement. The slow increase of the impurity content in the core is consistent with impurity transport studies [4] yielding a very low particle diffusivity of 0.07 m^2/s and inward convection of $5r/a$ (m/s).

The improvement is accompanied by a reduction in the density fluctuation amplitude, which is partly due to the fact that the reflecting layer moves 1.5 cm inward during the measurement. We observe the reduction primarily in the frequency range below 60 kHz. The radial electric field at a location close to the minimum of the thermal diffusivity becomes continuously stronger while confinement is improving.

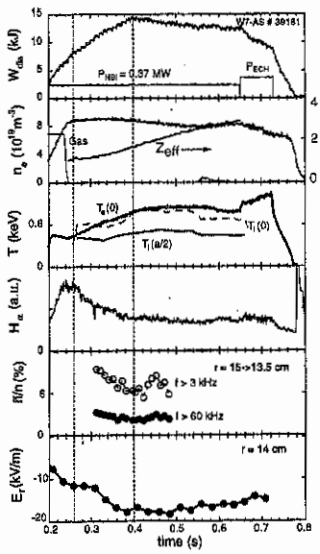

Fig. 2: Time traces of discharge 39181: Diamagnetic energy content and heating power, line averaged density and Z_{eff} from soft X-ray emission, electron temperature from ECE and ion temperature from a neutral particle analyzer, H_α light from a limiter, density fluctuation amplitudes from reflectometry integrated over the entire spectrum and over higher frequencies only, radial electric field from passive charge-exchange spectroscopy.

In Fig. 3, the temporal evolution of electron density and temperature profiles of this discharge can be studied. The increase of the electron temperature occurs over the entire cross-section and stops at around 0.4 s first in the outer region and later in the core. The increase of the energy content can be partly attributed to the broadening of the profile. The evolution of the density profile continues up to 0.55 s. After an initial evolution from a broad to a more peaked profile, it is primarily the edge density which continues to decrease. We see that a continuing reduction of the edge density does not lead to a further improvement of energy confinement. The possibility of controlling the density seems to be the crucial element rather than the low edge density. Radial derivatives of the data in Fig. 3 show a pronounced steepening of both temperature and density gradients in the radial zone between 10 and 14 cm during the initial phase where confinement improves. The gradients remain unchanged after 0.4 s. The bolometric

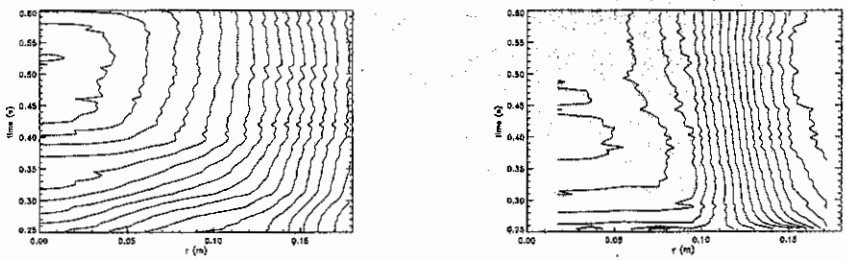

Fig. 3: Temporal evolution of the electron temperature profile from fits to 24 ECE radiometer channels (left) and the density profile unfolded from 8 interferometer channels (right).

radiation profiles are hollow with a maximum at about 0.14 m and start slowly to fill up in the center. At the end of the discharge, this process is not yet completed.

Power Balance Analyses: The transport properties of a high-confinement NBI discharge are compared with those of an ECH discharge at similar density and a heating power of 0.5 MW. The ECH discharge serves as "normal" confinement case. Although the absorbed power is higher, the kinetic energy content is only 13 kJ compared to 17 kJ of the NBI discharge. The power balance analyses shown in Fig. 4 were carried out with the same heat diffusivity $\chi \equiv \chi_e = \chi_i$ for electrons and ions. Electron temperature and density profiles from Thomson scattering serve as input and χ as well as the ion temperature profile are derived from the power balance. They are compared with measurements and neoclassical predictions from the DKES code [5]. For both discharges, the calculated ion temperature agrees with the measurements.

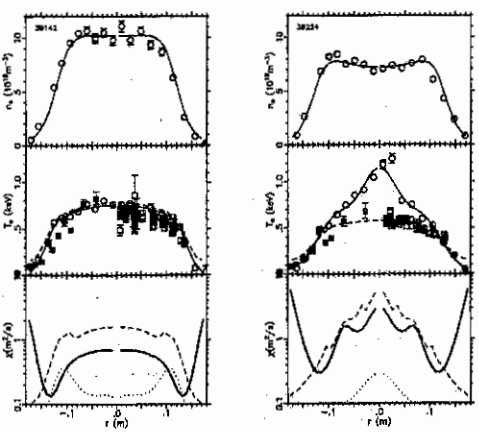

Fig. 4: Comparison of power balance analyses of a high-confinement NBI discharge (left) with an ECH discharge (right). Thomson electron density and temperature (open circles) and fits (solid lines), ion temperature as result from the power balance (dashed lines in the middle) and from charge-exchange spectroscopy (solid squares) and neutral particle analysis (open squares). Heat diffusivity from the power balance (solid line) compared to the equivalent neoclassical estimates for electrons (dotted) and ions (dashed).

The neoclassical diffusivities in Fig. 4 are total energy fluxes divided by the temperature gradients, hence the same quantity which is extracted from the power balance. In case of the ECH discharge, χ agrees well with the neoclassical estimate for the ions and is well above the electron value. Hence, if the ions behave

neoclassically, the electron heat diffusivity must be strongly anomalous.

In case of the NBI discharge, there is an overall reduction of the diffusivity. χ is below the neoclassical ion diffusivity and touches at its minimum the neoclassical electron diffusivity. From this result for χ for $r < 10$ cm, we cannot conclude that χ_i is below the neoclassical value. A two fluid power balance showed that using the neoclassical prediction for χ_i is also consistent with the central ion temperature measurements. In such an analysis in the core , χ_e drops only by 20%. At the transport barrier ($r \approx 12$ cm), however, the two fluid analysis fails to reproduce the data. Either the ion temperature is predicted as too high or, if in this region additional anomalous losses are added to the ion channel, χ_e drops well below its neoclassical value. The result at the barrier is that either χ_e or χ_i or both are below the neoclassical prediction. Hence this region satisfies the criteria of a transport barrier in which anomalous transport seems to be suppressed.

E × B and Magnetic Shear: The slow temporal evolution of confinement could also point to current penetration and magnetic shear as an important ingredient. The ι profile of the high-confinement NBI discharge has a low magnetic shear zone in the outer half of the plasma. By adding positive and negative currents to the discharge it was shown, that the magnetic shear was not the key parameter. It can be ruled out too that the existence of negative shear is, as in tokamaks, a pre-requisite of achieving the high confinement times.

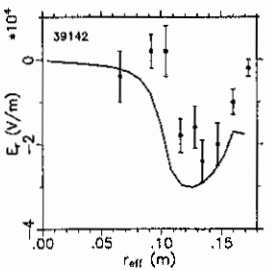

Fig. 5: Radial electric field as deduced from charge-exchange spectroscopy [6] and neoclassical theory.

In comparison with the transport barriers observed in the H-mode and in high performance tokamak discharges the role of the radial electric field is of special interest. In W7-AS in general, there is agreement between the electric field as deduced from spectroscopy and from the ambipolarity of the neoclassical fluxes [6]. Fig. 5 shows that this also holds for the high-confinement NBI discharges. The radial zone of low transport is characterized by strong gradients in the radial electric field and hence strong shear in the perpendicular plasma flow.

In Fig. 2, it was shown that the electric field increases together with electron and ion temperatures. The fact that confinement improves gradually rather than through a fast transition could point to a causality loop where transport is reduced by sheared flow generated by the neoclassical electric field. The reduction of transport steepens the gradients, which increase again the neoclassical electric field etc. This loop would stop when anomalous transport is suppressed and transport is on the neoclassical level. The time constants of the process would be in the order of the confinement time.

References

[1] KICK, M. et al., Proc. 16^{th} Int. IAEA Conf., Montreal, 1996.
[2] NAVE, M. F. F. et al., Nucl. Fusion **32** (1992) 825.
[3] STROTH, et al., Nucl. Fusion **36** (1996) 1063.
[4] BURHENN, R. et al., this conference.
[5] MAASSBERG, H. et al., Phys. Fluids, **B5** (1993)3627
[6] BALDZUHN, J. et al, this conference.

Dynamic behaviour of the H-mode edge transport barrier in the W7-AS stellarator

M. Hirsch, E. Holzhauer *, J. Baldzuhn, R. Brakel, S. Fiedler, T. Geist, P. Grigull, H. J. Hartfuß, J. Hofmann, R. Jaenicke, J. Koponen, F. Wagner, A. Weller, H. Wobig and the W7-AS team

Max-Planck Institut für Plasmaphysik, EURATOM Ass., D-85748 Garching, FRG
** Institut für Plasmaforschung, Univ. Stuttgart, 70569 Stuttgart, FRG*

Introduction

In the stellarator W7-AS the H-mode is characterized by an edge transport barrier which is associated with a strong reduction of magnetic and density turbulence and a sheared poloidal rotation in the electron diamagnetic direction [1,2,3]. A specific feature of W7-AS is the restriction of the H-mode operational range to narrow windows of the edge rotational transform where the H-mode is obtained even at the lowest available heating power. The quiescent ELM-free H-mode is always obtained through a phase with quasi periodic ELMs [3]. Once the quiescent state is reached, edge profile gradients and the spectroscopically measured poloidal plasma rotation develop on a timescale of about 20 ms while the energy confinement improves by $\Delta W/W \approx 30\%$.

Influence of edge parameters on the H-mode operational range

In the low-shear stellarator W7-AS H-mode operation is obtained within narrow windows of the edge rotational transform ι_a (e.g. at $\iota_a = 0.525 \pm 0.005$ and $\iota_a \approx 0.48$) at the lowest available heating power, 200 kW of ECRH (one gyrotron) or 340 kW of NBI (one source), respectively. The actual power threshold might even be lower. At the onset of an ELM-free quiescent H-mode the energy flux density across the separatrix is comparable or less to that found for the L-H transition in tokamaks [4].

The magnetic field topology within the operational windows is characterized by a comparatively large plasma minor radius and a plasma boundary determined by the inner separatrix of a natural island chain (e.g. 5/10 and 5/9). The limiter does not disturb this LCFS. Under these conditions two mechanisms are believed to contribute to the easy access into the H-mode: (1) outside the LCFS the connection lengths decrease to a value of some meters within a radial distance $\Delta r \approx 1$ cm. This allows for the development of a strong radial variation of the radial electric field and a corresponding velocity shear layer already before a fully developed H-mode is achieved [5]. (2) the poloidal viscosity is lower than for other values of ι_a, as the island structures which create strongly corrugated flux surfaces increasing the magnetic pumping are shifted out of the confinement region [2,6].

The quiescent H-mode is always reached through a phase with quasi periodic ELMs [2] with a typical repetition frequency f_{ELM} > 1kHz. Between the ELMs turbulence is strongly reduced and indistinguishable from the quiescent H-mode phase. Global confinement in this ELMy H-mode is close to the L-state which only exists outside the H-mode operational range. Within the H-mode operational windows no stationary turbulent L-mode is found to preceed the transition. Instead short (<1ms) quiescent phases and sequences of periodic ELMs are observed intermittently even in the early phase of the discharge. For the onset of an ELM-free quiescent H-mode a threshold density n_{th} is required which depends on the edge rotational transform as an important parameter. In Fig.1a the operational window around $\iota_a = 0.525$ is marked by the hatched area and the observed values of n_{th} are given by the squares. The numbers inserted in the Figure indicate the repetition frequencies f_{ELM} observed in ELMy H-modes. As the density approaches the threshold f_{ELM} decreases to a minimum of 1 kHz. Stationary ELMy H-modes have been obtained below the threshold for up to 700 ms if the line averaged density was kept constant. In Fig.1b the same range of the total edge rotational transform ι_a is scanned continuously within 130 ms in a single discharge by adding a small ohmic current (0 kA < I_{tor} < 5 kA). The average density is kept constant at <n>=4 10^{19} m^{-3}. ELMs appear as ι_a crosses the operational range and f_{ELM} approaches a minimum as the chosen density is close to the corresponding threshold density for a quiescent H-mode.

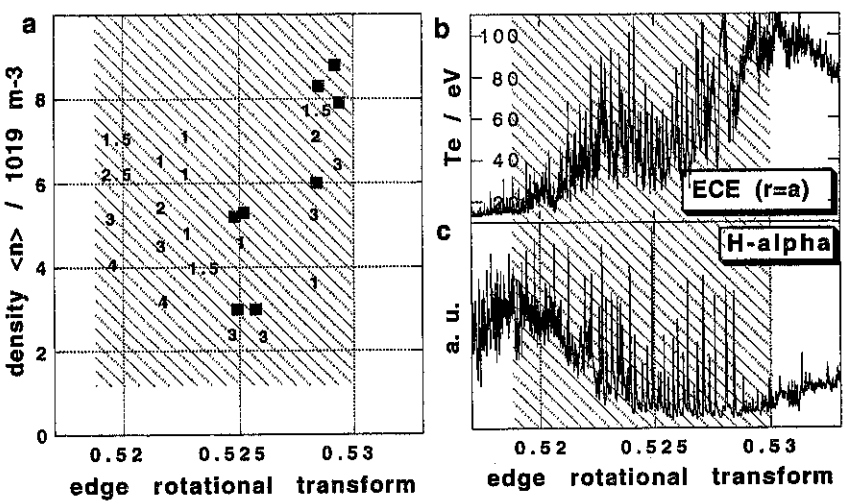

Fig. 1a: Operational range (hatched area) and threshold density (squares) for the quiescent H-mode in the ι_a window around ι_a=0.525. The numbers inserted indicate ELM repetition frequencies of ELMy H-modes in kHz.

Edge electron temperature from ECE (Fig. 1b) and H_α-signal (Fig. 1c) as the total edge rotational transform is tuned over the operational window shown in Fig 1a by adding an increasing ohmic current. <n> is kept constant at 4 10^{19} m^{-3}. The time window shown lasts 130 ms.

The influence of magnetic shear

The H-mode can also be achieved if positive or negative magnetic shear is induced in addition to the vacuum configuration by positive and negative ohmic currents. An improvement of the edge confinement can be obtained by magnetic shear even outside the H-mode operational windows [7]. With increased shear the fluctuation spectra observed with reflectometry are found to broaden and shift further into the electron diamagnetic drift direction.

Dynamic behaviour of edge parameters

The ELMs within the ELMy H-mode display characteristics similar to type III ELMs found in tokamaks [8]. They show up as bursts of magnetic and density turbulence with a repetition frequency >1kHz and a typical length of 200μs followed by an interval with strongly reduced turbulence identical to that in the quiescent H-mode phase. In most cases at the onset of the ELM magnetic coils measure a quasi coherent precursor activity with a frequency around 400 kHz. Edge profiles of T_e and n_e are obtained with high time resolution from EC- and SX-emission, reflectometry and a 10 channel mm-wave interferometer, respectively. As the broadband magnetic and density turbulence level starts to grow the edge profiles of T_e and n_e flatten over the first 3 cm inside the separatrix, emphasising the edge localized character of the phenomenon and the associated loss of confinement. As soon as the level of turbulence begins to decrease edge gradients again begin to steepen.

The *radial propagation* of the change of density perturbations is followed with reflectometry on a shot to shot basis using the onset of the H_α-burst as reference. Over a distance from 3 cm inside to 1 cm outside the separatrix the increase of the density fluctuation level occurs within a time interval as short as 20 μs.

The *poloidal propagation* of density perturbations can also be measured with the reflectometer system since the antenna beams are tilted with respect to the normal of the magnetic surfaces. The measured Doppler-shift of the reflected mm-wave results from the selected poloidal wavevector component and the poloidal propagation velocity of the density perturbation [9]. As an example Fig.2 shows a frequency power spectrum of the reflected wave during an ELMy H-mode. The spectrum is scanned over 20 ms, therefore about 30 ELMs and intermitted quiescent phases are covered. Selecting only time intervals during ELMs Fig.3 shows the radially resolved Doppler-shift on a shot to shot basis. The observed Doppler-shift towards negative frequencies is due to the poloidal propagation of the density perturbations in the electron diamagnetic drift direction. The poloidal propagation velocity of fluctuations derived from the Doppler-shift depends critically on the resulting tilt angle i.e. on the details of the complex edge topology. For positions inside the separatrix region a maximum poloidal velocity of about 20 km/s is estimated. Note that the observed velocity of the turbulence structures v_{pol} is the sum of poloidal plasma rotation and the intrinsic phase velocity of the turbulence itself.

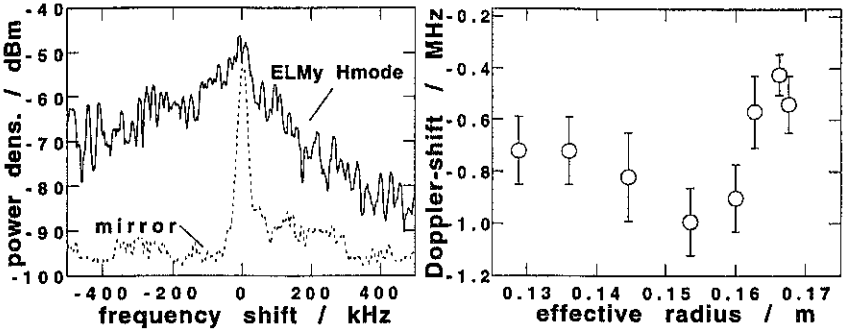

Fig 2 : Power spectrum of a reflected mm-wave measured over 20ms of an ELMy H-mode consisting of about 30 ELMs and intermittent quiescent intervals. The unshifted line reflected from the rear torus wall is given as a reference.

Fig 3 : Doppler-shift of the reflected signal during ELMs. Each point is an average over 20 ELMs. Different radial positions have been probed on a shot to shot basis. The separatrix position estimated from an interpolation of equilibrium calculations is 16 cm. For the steep edge gradients observed the actual separatrix may be shifted more outward.

Termination of the quiescent H-mode

After a quiescent H-mode of more than about 50 to 100 ms confinement tends to degrade which is accompanied by an increase of bolometry and SX radiation. During this phase strong *isolated* ELMs can appear as a distinct (duration less than 300μs) burst of magnetic and density turbulence associated with a huge spike in H_α-emission and a reduction of n_e and T_e gradients at the edge (i.e. less than 3 cm inside the separatrix). In contrast to the quasi periodic ELMs found in the ELMy H-mode the edge gradients do not recover immediately after the event but remain flat for a typical period of several ms. During that time the decrease of n_e and T_e propagates to the inner part of the plasma. In comparison to the quiescent H-phase the fluctuation level at the plasma edge in most cases remains significantly higher during this period.

References

[1] Wagner et al., Plasma Phys. Control. Fusion 36 A61 (1994).
[2] Holzhauer et al., Plasma Phys. Control. Fusion 38 1267 (1996).
[3] Hirsch et al., Proc. of the 16th IAEA Conference, Montreal, 7-11 Oct 1996.
[4] Ryter et al. Plasma Phys. Control. Fusion 36 A99 (1994).
[5] Wagner et al, Proc. of the IAEA Conference, Sevilla, V1.1 559 (1994).
[6] Wobig and Kißlinger, this conference.
[7] Brakel et al. this conference.
[8] Zohm, Plasma Phys. Control. Fusion 38 105 (1996).
[9] Hirsch, Holzhauer, Proc. of III Workshop on Reflectometry, Madrid, May 5-7 1997.

The Neoclassical "Electron-Root" Feature in W7-AS

H. Maaßberg, J. Baldzuhn, C.D. Beidler, K.S. Dyabilin[1], *V. Erckmann, U. Gasparino, N. Marushchenko*[2], *S. Murakami*[3], *N. Nakajima*[3], *M. Romé, and the W7-AS Team*

Max-Planck-Institut für Plasmaphysik, EURATOM Ass., D-85748 Garching, Germany
[1] *High Energy Density Research Center, Moscow, Russia*
[2] *Institute of Plasma Physics, NSC-KhPTI, Kharkov, Ukraine*
[3] *National Institute for Fusion Science, Nagoya, Japan*

Introduction: The confinement properties of stellarators in the long mean free path regime are determined by the radial component of the ∇B-drift of particles trapped in local ripples. In the worst case, the unfavourable neoclassical temperature dependence of the heat flux, $q \propto T^{9/2}$, leads to rather poor confinement properties. Optimisation of the magnetic configuration - e.g., as performed for W7-X - can significantly reduce the averaged radial drift of these localized particles leading to an essential confinement improvement. A sufficiently strong radial electric field (the poloidal $E \times B$-drift) will force the trapped particle orbits close to the flux surfaces also leading to significantly reduced transport. With the neoclassical transport coefficients in the *lmfp* regime depending on E_r, multiple roots of the ambipolarity condition, $\Gamma_e = Z_i \Gamma_i$, may exist: the "ion root" solution with weak E_r for which only the ion transport coefficients are reduced, and the "electron root" solution at strongly positive E_r with additionally improved electron confinement. For classical stellarators (without optimisation of the magnetic configuration) the "electron root" scenarios are mandatory to obtain acceptable confinement properties. Furthermore, operation with the positive E_r may turn out to be essential for preventing neoclassical impurity accumulation.

Experimental Findings: Recently, strongly positive radial electric fields have been measured at W7-AS in low density discharges at high ECRH power level ($\geq$ 400 kW) with 2nd harmonic X-mode (140 GHz). The electron temperature profiles are highly peaked (with $T_e(0)$ up to 4 keV), and the ion temperatures (with T_i of several 100 eV) fairly flat, see Fig. 1. The density profiles are flat or even slightly hollow. The finding of the strongly positive E_r is related to an additional peaking of the central T_e profile indicating improved electron energy confinement. The corresponding experimental heat diffusivity, χ_e , from the power balance is much lower than the neoclassical one for $E_r \simeq 0$. E_r simulations based on the neoclassical ambipolarity condition with only thermal fluxes taken into account predict only the "electron root" in the inner plasma region. The predicted neoclassical χ_e with these E_r are, however, smaller than the experimental ones.

This "electron root" feature at sufficient ECRH power is only found for W7-AS configurations where a significant fraction of the ECRH power at 2nd harmonic X-mode is absorbed by ripple trapped electrons close to the magnetic axis. For 70 GHz O-mode launching, an "electron root" feature was not observed, so far [1]. Equivalent experiments in a configuration without trapped electrons in the ECRH launching plane neither show these strongly positive E_r nor the additional peaking of the T_e profile. In spite of the fact that this specific magnetic configuration is neoclassically improved, the central T_e are lower than the ones of the "electron root" feature at equivalent power levels. A strong indication, that the ECRH driven electron flux (related to the generation of suprathermal electrons as shown by bounce-averaged Fokker-Planck calculations [2]) is responsible for the "electron root" feature, is found from the ECE temperature measurements after the ECRH is switched off, see Fig. 2. For the configuration with significant trapped particles in the launching plane (even more than in the "standard" configuration of Fig. 1), the decay of the central T_e is characterized by two different time scales. After a very fast decay (within less than 1 ms immediately after switch-off), the central T_e relaxes on a time scale similar to that slightly outside of the "electron root" region. For the "neoclassically improved" configuration, the initial fast decay is not found, and the central T_e is lower although the confinement (reflected by the time scale of $T_e(r,t)$) is clearly higher. Furthermore, the confinement

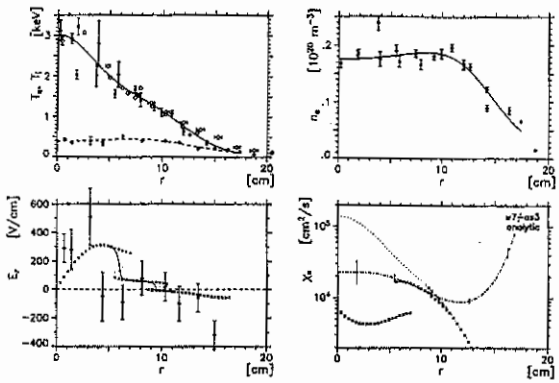

Fig. 1 *Temperature and density profiles for an ECRH discharge (X-mode at 140 GHz with 400 kW) in the W7-AS "standard" configuration. The E_r profile is simulated by means of the ambipolarity condition with only the thermal neoclassical fluxes taken into account (experimental E_r data from active CXRS, lower left plot). The electron heat diffusivities (lower right plot): the neoclassical ones with the simulated E_r (×), and with $E_r = 0$ (dotted line); the χ_e from power balance (dot-dashed line) is given for reference.*

properties of high energetic electrons found in the strongly down-shifted ECE channels (with small reabsorption by the plasma at outer radii on low-field side) also show the fast response, depending on the magnetic configuration.

Monte Carlo Simulations: The "convective" contribution of the ECRH driven electron flux is estimated by Monte-Carlo simulations in 5D phase space [3]. The quasi-linear diffusion term describing the ECRH in the Fokker-Planck equation is approximated by an explicit source term, $\underline{\nabla}_v \cdot (\underline{\underline{D}} \cdot \underline{\nabla}_v f_{\mathrm{Max}})$. The quasi-linear diffusion coefficient, $D_{\perp\perp}(v_\parallel, v_\perp)$, is obtained from ray-tracing calculations for the different heating scenarios. In this linear approach, the driven electron flux is proportional to the heating power. Quasi-linear degradation effects at higher ECRH power can only be treated by means of the bounce-averaged Fokker-Planck code [2]. The effect of the different magnetic configurations, however, is completely taken into account.

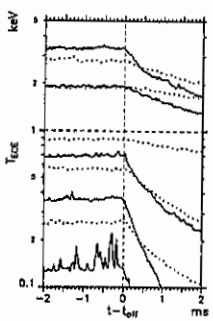

Fig. 2 *ECE electron temperatures after the ECRH is switched off for ECRH discharges (400 kW, X-mode at 140 GHz) with $n_e \simeq 1.5\ 10^{19}\ m^{-3}$ for configurations with slightly increased (solid lines) and nearly without ripple (neoclassically improved, dotted lines) at the ECRH launching: central, intermediate (from high field side) and outer channels (from low field side).*

The electron fluxes driven directly by the ECRH are shown in Fig. 3 in comparison with the neoclassical ambipolar fluxes for the discharge parameters of Fig. 1. These ECRH driven fluxes are significantly decreased by E_r, but less than the neoclassical ones at the transition region to the "electron root". Consequently, these "convective" electron fluxes dominate at high E_r in the ambipolarity condition. Within the traditional neoclassical transport theory (which is

the basis for the DKES code [4] used at W7-AS), this discrepancy cannot be resolved since all fluxes are decreased with increasing E_r (e.g., the electron transport coefficients in the $\sqrt{\nu}$ regime scale with $E_r^{-3/2}$ which is the case in the "electron root" region). Due to the higher absorption for the X-mode scenarios, the $D_{\perp\perp}(v_\parallel, v_\perp)$ has a maximum closer to the thermal bulk than for the O-mode case. In case of X-mode, however, the power is mainly absorbed by deeply trapped electrons whereas in the O-mode case mainly by barely trapped electrons. In addition to the $v_{\nabla B}$ drift being proportional to energy, the energy dependence of the collisional detrapping leads to the broadening of the electron fluxes in the O-mode case. These results are well in agreement with the findings from the "effective power deposition" profiles by the electron heat wave propagation analysis [2].

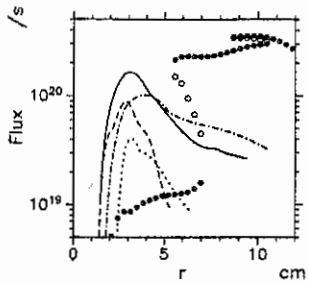

Fig. 3 *ECRH driven fluxes from Monte Carlo simulation for $n_e \simeq 2\ 10^{19}\ m^{-3}$, $T_e \simeq 3.5$ keV, and 400 kW heating power in the W7-AS "standard" configuration: with $E_r = 0$ (X-mode: solid, and O-mode: dot-dashed line), and with E_r corresponding to Fig. 1 (X-mode: dashed, and O-mode: dotted line). The ambipolar neoclassical fluxes (purely thermal) are given for reference (open circles: unstable root).*

Effects of strong poloidal rotation: The strongly positive radial electric field within the region of the "electron root" feature leads to complex effects on the flux surfaces. In the continuity equation, the inhomogeneity of B with $\underline{\nabla} \cdot \underline{v}_{E\times B} \simeq -2\underline{v}_{E\times B} \cdot \underline{\nabla} ln B$ drives a parallel flow (which is the equivalent to the Pfirsch-Schlüter current) as well as a (1*st* order) density inhomogeneity, n_1. In the ion force balance equation, the $(\underline{v} \cdot \underline{\nabla})\underline{v}$ term is approximately given by the gradient of the kinetic energy related to the poloidal rotation as well as the parallel flow. Viscous damping of this parallel flow by, e.g., ripple trapped particles leads to an enhanced density disturbance n_1 which, in turn, has to be compensated by a (1*st* order) potential, Φ_1, in the electron force balance equation. These effects can play an essential role mainly in the poloidal component of the force balance, and an external energy flux seems to be necessary to drive a strong poloidal rotation, i.e., the "electron root" feature.
On the other hand, the strong E_r leads also to modifications in the neoclassical transport. In the "usual" ordering, the $E \times B$ drift is assumed to be constant on flux surfaces (and terms of the order of $(\underline{B} \times \underline{\nabla} B) \cdot \underline{E}_r$ are neglected to allow for a mono-energetic solution). The only mode coupling in the Fourier expansion of the drift-kinetic equations appears due to the mirror term, $\underline{B} \cdot \underline{\nabla} B\, \partial f_1 / \partial p$ (with f_1 the 1*st* order distribution function, and $p = v_\parallel / v$), leading to all the neoclassical transport in the *lmfp* regimes. In addition to the $\underline{B} \cdot \underline{\nabla} \Phi_1\, \partial f_1 / \partial p$ in the self-consistent approach [5], also the $\underline{v}_{E\times B} \cdot \underline{\nabla} f_1$ term leads to mode coupling, and, as a consequence, to a 1*st* order density and potential, n_1 and Φ_1, respectively. As this $\underline{v}_{E\times B}$ is partly counteracted by the $v_\parallel$ term, this effect will be dominant in the ion drift-kinetic equation, whereas the 1*st* order potential affects both equations. Although no particle fluxes are driven by the Φ_1 with respect to (the 0*th* order) f_0, the energy flux is directly affected. With respect to f_1 (which leads to the usual neoclassical transport), the strong E_r will modify the particle and energy transport both for electron and ions in this self-consistent approach.

The bifurcation in the radial electric field: After flux-surface averaging of the poloidal component of the combined electron and ion force balance equation, the contributions of the pressure as well as of the kinetic energy (from rotation and parallel return flow) vanish. In this context, only the neoclassical predition of an "ion/electron root" transition based on the local ambipolarity condition is analyzed. With the shear viscosity in the divergence of the pressure

tensor taken into account, the transition between both roots is smoothed out leading to a local violation of the neoclassical ambipolarity condition, i.e., to a radial current, $e(Z_i\Gamma_i - \Gamma_e)$, of different sign on both sides of the poloidal rotation shear layer. With the $\partial v/\partial t$ term from ion inertia, the (time dependent) diffusion equation equivalent to Ref. [1] is obtained (for simplicity, $\partial\hat{\eta}/\partial E_r = 0$ is assumed here for the normalized shear viscosity coefficient $\hat{\eta}$)

$$\frac{nm_i}{B^2}\frac{\partial}{\partial t}E_r = \frac{2}{r^2}\frac{\partial}{\partial r}r^2\hat{\eta}\left(\frac{\partial E_r}{\partial r} - \frac{E_r}{r}\right) - e(Z_i\Gamma_i - \Gamma_e).$$

Under the assumption of a stationary E_r, this diffusion equation leads for small $\hat{\eta}$ to the shear layer position, r_{SL}, within the region of several roots, see the solid line in the E_r plot in Fig. 1. With the current density, $e(\Gamma_i - \Gamma_e)$, roughly of the form $\propto (E_r - E_r^{i})(E_r - E_r^{un})(E_r - E_r^{e})$ where the index refers to the "electron", an unstable, and the "ion root", the diffusion eq. for E_r leads to a "bifurcation" problem which is quite similar to 1*st* order phase transitions in non-linear thermodynamics, e.g., see Refs. [6,7]. Within the poloidal rotation shear layer, the rotation energy is dissipated by viscosity leading to a damping mechanism adding to the one discussed in the previous section. Here, however, only the radial motion of r_{SL} can be analyzed (i.e., the flux-surface averaged force balance has one degree of freedom).
For the special scenarios with $T_i \ll T_e$ and the pronounced *lmfp* transport in W7-AS at the inner radii (here, the "effective" helical ripple is mainly determined by the toroidal mirror terms) the region with multiple roots of the ambipolarity condition is radially restricted. The thermodynamic arguments can only be applied in this region for estimating r_{SL}, i.e., in this picture the viscous damping of the poloidal rotation within the shear layer cannot be the main reason for the total disappearence of the "electron root". Then, in both the transition and the "electron root" region, the crucial point is related to the "current dependence" on E_r within the "electron root" region, i.e., the neoclassical $Z_i\Gamma_i(E_r) - \Gamma_e(E_r)$ dependence.

Conclusions: The "electron root" feature found at W7-AS with strongly positive radial electric fields is driven by the ripple-trapped suprathermal electrons generated by the ECRH. After switching-off the heating, the "electron root" feature disappears nearly immediately, i.e., on the same time scale as this ECRH driven flux. Monte Carlo simulations in 5D phase space clearly indicate that the additional "convective" electron fluxes are roughly of the same order of the ambipolar neoclassical prediction for the "ion root" at much lower E_r. For the predicted "electron root" E_r, the ambipolar fluxes predicted by the traditional neoclassical ordering are much too small. These findings indicate strongly, that the traditional neoclassical theory (at least for the ions) has to be checked in case of very strong radial electric fields.
Due to the variation of the magnetic field strength, a strong poloidal plasma rotation drives also a Pfirsch-Schlüter-like parallel flow on the flux surfaces, and, as a consequence, density and potential variations. This parallel flow velocities can give a significant contribution to the inertia term in the ion force balance. Although experimental indications of instabilities affecting the central confinement properties are missing so far, the "free energy" related to the strong poloidal plasma rotation as well as the parallel return flow may also be responsible for an "electrostatic" instability which superposes the neoclassical transport in the central region. All these features of the "electron root" at W7-AS, however, cannot be extrapolated to the high density scenarios with $T_e \simeq T_i$ in next generation stellarators. One essential aspect is the questionable reliability of the traditional neoclassical transport predictions for very strong radial electric fields as obtained in the "electron root" scenarios.

References

[1] H. Maaßberg et al., Phys. Fluids B **5** (1993) 3728.
[2] M. Romè et al., Plasma Phys. Contr. Fusion **39** (1997) 117.
[3] S. Murakami et al., Proc. ICPP, Nagoya 1996 (to be published)
[4] W.I. van Rij and S.P. Hirshman, Phys. Fluids B **1** (1989) 563.
[5] C.D. Beidler and H. Maaßberg, *Theory of Fusion Plasmas (Varenna)*, (1996) 375.
[6] L. Shimansky-Geier and W. Ebeling, Ann. Physik **40** (1983) 10.
[7] S.K. Chan, J. Chem. Phys., **60** (1977) 5755.

Investigation of impurity tracer transport in high density plasmas at the stellarator Wendelstein 7-AS

R. Burhenn, M.Anton, J. Baldzuhn, R. Brakel, L. Giannone, H. Hacker, M. Hirsch, L. Ledl, M. Maassberg, U. Stroth, A. Weller,
W7-AS Team, ECRH Group[1], NI Group
Max-Planck-Institut für Plasmaphysik, EURATOM Ass., D-85748 Garching, FRG
[1]Institut für Plasmaforschung, Universität Stuttgart, D-70569 Stuttgart, FRG

Introduction - For the decay time of injected tracer impurities (aluminum laser blow-off) in W7-AS, the electron density is, among others, an important scaling parameter [1], indicating improved confinement of impurities towards high electron density. Previous impurity injection experiments (H_2S gas oscillation and Al laser blow-off) [1] at medium density (n_{e0}=2-5·10^{19} m^{-3}) could partially be simulated within the errors by the one-dimensional radiation and transport code SITAR [2], based on neoclassical and Pfirsch-Schlüter transport for axisymmetric devices. At low density, the transport was found to be significantly higher than predicted, whereas at high density (n_{e0}=6.5·10^{19} m^{-3}), the neoclassical fluxes had to be reduced to fit the experimental data. Analysis of further discharges at different electron densities, using a simple transport model (diffusion coefficient D(r)=const, inward velocity $v(r)=(r/a)v_{(r=a)}$, a: plasma radius), supports the trend of decreased diffusion coefficients towards higher density, which cannot be attributed simply to a decrease in Z_{eff}. A similar dependence of D on electron density was already observed in ECF heated Heliotron E plasmas [3] and supposed to be caused by changes in D rather than in the flow velocity, the latter being close to the classical expectations. In order to elucidate the density dependence in W7-AS, discharges with densities varied by a factor of 2 (n_{e0}=3.5/7·10^{19} m^{-3}) are analyzed in more detail (fig.1), together with fluctuation- and MHD-diagnostics and measurement of the radial electric field. Especially in non-axisymmetric devices like stellarators, the latter can play an important role for impurity transport [4], but is not yet included in SITAR.

Simulations with simple assumptions about D(r)- and v(r)-profiles might mask possible local changes in transport. Therefore, the radial transport coefficients were tried to be directly derived from the temporal and radial behaviour of spectral radiation, detected by the SX-camera during the penetration process of injected aluminum by laser blow-off. Indications were expected, whether the modification of the transport coefficients happens in the core plasma or somewhere in the plasma boundary.

Transport analysis - Because of its good radial and temporal resolution, the SX-camera is a proper diagnostic tool at W7-AS for transport investigation. In spite of its energy-integrated information, the use of a 25µm Be-filter in front of the camera offers the possibility to restrict the number of ionization states contributing to the measured intensity and simplifies the reconstruction of the total impurity density profiles. For total impurity density reconstruction during the penetration process of injected aluminum, the radial intensity profile at each time-step was abel-inverted (figs.1b,e) and converted to a total impurity density profile assuming coronal equilibrium (quasi-stationary condition) in a first step. This is considered to be applicable in

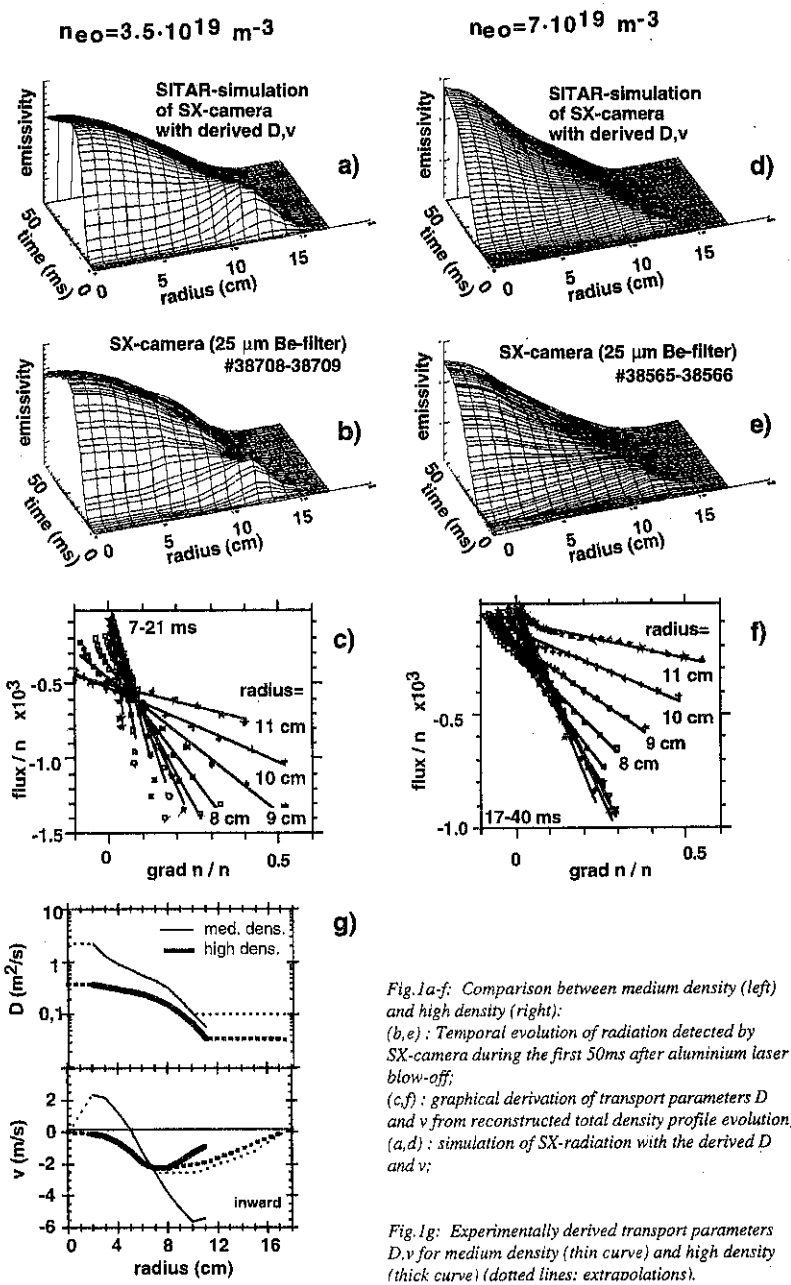

Fig.1a-f: Comparison between medium density (left) and high density (right):
(b,e) : Temporal evolution of radiation detected by SX-camera during the first 50ms after aluminium laser blow-off;
(c,f) : graphical derivation of transport parameters D and v from reconstructed total density profile evolution;
(a,d) : simulation of SX-radiation with the derived D and v;

Fig.1g: Experimentally derived transport parameters D,v for medium density (thin curve) and high density (thick curve) (dotted lines: extrapolations).

low-transport discharges at high electron density. The transport coefficients at a certain radial position can then be derived from the local temporal evolution of the total impurity density profiles n(r,t) [5]. With the ansatz Γ=-D grad(n)+vn, D and v can be determined by fitting a straight line, when plotting the normalized total impurity fluxes Γ/n vs. the normalized total density gradients grad(n)/n for all time points at this radial position (figs.1c,f). The flux Γ can be estimated from the density profile evolution using the continuity equation dn/dt=-div(Γ) with restriction to radial regions where external sources and sinks can be neglected.

In cases where the assumption of quasi-stationarity might not hold, the reconstruction with coronal equilibrium can cause errors. Therefore, the radial density profiles for each time step were reconstructed again, now using a reconstruction factor ß(r,t)=n(r,t)/P(r,t) (P:total local emissivity contributing to SX-camera) obtained from a transport and radiation calculation with SITAR, using the D- and v-values derived in the first step as input. A repeated derivation procedure for D and v, but now with the corrected density profile evolution as described above provides new transport coefficients (fig.1g) which, in fact, fit the SX-camera better in most cases (fig.1a,d). The accuracy of this iterative method strongly relies on the quality of abel-inversion and atomic data base. Possible errors have to be discussed in this context.

Results and discussion - In order to study the density dependence of impurity confinement at W7-AS, ECF-heated discharges (P_{ECF}=400kW) at two different densities (figs.1a,b,c: $n_{e0}=3.5\cdot10^{19}$ m^{-3}; figs.1d,e,f: $n_{e0}=7\cdot10^{19}$ m^{-3}) were compared. The transport coefficients were derived according to the procedure described above and are plotted in fig.1g for both densities.

For the outer plasma region, the last reliably determined value of the diffusion coefficients at r=10-11cm were kept constant up to the plasma edge. They represent average diffusion coefficients for this region, determining essentially the central time behaviour during the inflow phase. The extrapolated average diffusion coefficient for medium density approaches values consistent with neoclassically predicted ones (0.09m^2/s≥D≥0.04m^2/s, 10cm≥r≥17cm), but falls below the predictions (0.2m^2/s≥D≥0.07m^2/s, 10cm≥r≥17cm) for the high density case. This trend is even more pronounced at higher electron densities of $n_{e0}=1.2\cdot10^{20}$m^{-3}, e.g. in high confinement neutral-beam heated discharges [6], where transport coefficients were derived (D(r)=0.07m^2/s, v(r)=5m/s·(r/a), #38551), being clearly smaller than predicted by SITAR, in which the fluxes are already reduced by 50% to account for the W7-AS transport optimization.

The convection velocity was extrapolated to vanish in the plasma center and was adjusted in the outer part to fit better the temporal decay of spectral line intensities from different ionization states of aluminum, observed by central-line-of-sight crystal- and VUV-spectrometers (fig.2). For the high density discharge, only a slight correction in the derived v (fig.1g) was necessary to excellently fit all experimental data. In the case of medium density, D(r=10cm) was used for extrapolation and v has to be reduced by a factor of 2 for a good compromise in fitting the experimental data radially as well as temporally. A reduction of D in the outer region down to the value D(r=11cm) would fit the time traces of the spectrometers only for the case of vanishing convection velocity, but will lead to a misfit of the radial profiles.

In the two ECF-heated discharges under investigation, no substantial changes as well in the radial electric field E_r (within the error) as in MHD-activity and electron density profile shape

could be observed from which the difference in transport can be deduced. However, previous measurements of the density fluctuation level as a function of electron density [7] show some inverse dependence, but an effect on the impurity transport cannot simply be concluded.

In the case of high electron density, D is overall lower by a factor of 2-3 compared to the medium density discharge, v being quite similar. The resulting difference in confinement can be illustrated quite impressively by the change in decay time for the injected aluminium (fig.2). Consequently, also the time evolution of intrinsic impurity radiation and Z_{eff} is remarkably different during the flat-top phase for this two densities (fig.3). However, assuming a constant impurity influx of, e.g. intrinsic chlorine from the walls and using just the derived set of transport parameters, the difference in the time traces of Cl-XIV can be qualitatively well described (fig 3, fits): compared to medium electron density, where stationary conditions were achieved well within the pulse length (fig.3 curve b, arrow) due to higher transport, the reduced transport in the high density case causes longer times to establish stationarity (fig.3 curve a).

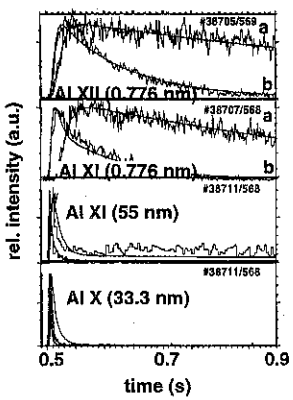

Fig.2: Time traces of spectral lines from different ionization states of aluminum fter injection by laser blow-off: (a) n_{eo}=7·0^{19}m^{-3}, (b) n_{eo}=3.5·10^{19} m^{-3}

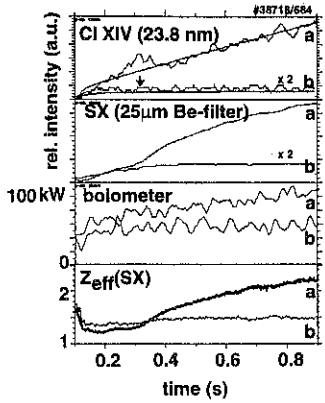

Fig.3: Temporal evolution of impurity radiation and Z_{eff}(SX) for (a) n_{eo}=7·10^{19}m^{-3}, (b) n_{eo}=3.5·10^{19} m^{-3} and simulations for Cl-XIV.

Similar behaviour for other intrinsic impurity species might explain the signals of the SX-camera, the bolometer and Z_{eff}. Nevertheless, at high density (n_{eo}=7·10^{19}m^{-3}) the extrapolated total radiation (bolometer) at the time when the Cl-XIV radiation should reach 90% of its stationary level (approx. at 1.7s, from simulation), stays well below the critical value of 60% of the heating power [8], where the plasma is severely affected by radiation.

References

[1] R.Burhenn et al., 22nd EPS Conf. on Contr. Fus. and Plasma Physics, Vol.19C, part III, p.145-148, Bournemouth 1995
[2] WVII-A Team, NI Group, Nucl. Fusion 25(11) 1593 (1985)
[3] H.Kaneko et al., Nucl. Fusion 27(7) 1075 (1987)
[4] A.Baldzuhn et al., this conference
[5] A.Weller et al., Plasma Physics and Controlled Fusion 33(13) (1991),1559
[6] U.Stroth et al., this conference
[7] U.Stroth, Report IPPIII/216
[8] P.Grigull et al., this conference

Structure of the edge fluctuations in the W7-AS stellarator

J. Bleuel, M. Endler, H. Niedermeyer, G. Theimer,
W7-AS Team
Max-Planck-Institut für Plasmaphysik, EURATOM Association, Garching, Germany

1. Introduction. The turbulent fluctuations in the SOL and the outer confinement zone of the W7-AS stellarator are spatially and temporally resolved using Langmuir probe arrays. The main topic is the investigation of the structure of these fluctuations both perpendicular to and along the magnetic field.

Perpendicular to the magnetic field we apply two different techniques to obtain a 2d - representation of the fluctuations' structure. A right angled probe array, with legs in the radial and the poloidal direction, allows the calculation of a 2d - correlation function under the assumption of poloidal homogeneity of the turbulence. A 2d - representation is also derived using one poloidal probe array and one single probe toroidally separated for conditions where a high correlation along the connecting field line exists as in our earlier experiments [1]. Generally, a 2d - analysis is necessary for the investigation of radial properties of the fluctuations like the radial size or the radial propagation velocity.

Formerly, a very high correlation of about 90% for floating potential and ion saturation current fluctuations over a distance of about 6 m along a magnetic field line [1] was found. In these experiments two toroidally separated Langmuir probes were connected by a field line that stayed on the outside of the torus, where fluctuations are known to be driven unstable, over the whole connection length. In this paper, measurements along a field line that passes the inside, where fluctuations are partly suppressed, are presented. In general the maximum correlation is observed along the wavefront which is nearly parallel to the magnetic field since $k_{\parallel}$ is usually very small. The inclination between wavefront and magnetic field can be observed in our experiments and therefore $k_{\parallel}$ can be calculated.

2. Structure in the radial-poloidal plane. The derivation of a 2d-correlation function from a measurement using an angled probe array is described in [1]. The second method uses an experimental setup with two toroidally separated probes connected by a field line of 6 m connection length. One of them is a single probe, while the other is a poloidally resolving probe array. Since for this configuration a correlation of about 90% was observed along the field line [1] the fluctuations undergo nearly no change along the field. Thus the signal observed by the single probe is nearly the same as it would be in the toroidal plane of the probe array at the point where the projection of the single probe along the field line is situated. This point is used as a reference point and therefore defines the

origin of the 2d-correlation function. During the shot the probe array is moved radially about 6 cm into the plasma. This movement is relatively slow (400 ms) so that the probe movement is negligible within time windows of 10 ms, which are necessary to obtain a statistically stable correlation function. All the correlation functions between the single probe and the probe array that can be calculated for the different radial positions of the array can be combined into a 2d-correlation function depending on time-delay, the radial distance and - due to the poloidal resolution of the array - also on the poloidal distance from the reference point. The experimental flexibility of this method is quite restricted since it needs a specific magnetic field geometry to connect both probes. Nevertheless it is possible to measure 2d - correlation functions that are extended across the LCFS in the radial direction.

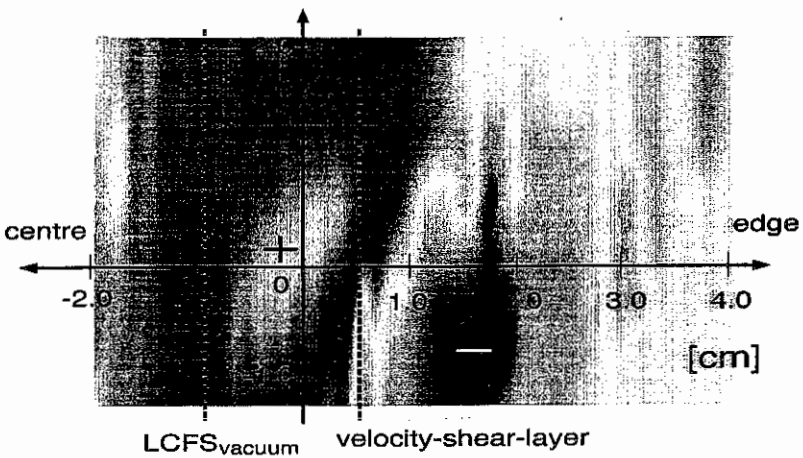

Figure 1: *2d-correlation function that extends over the LCFS for constant time-delay τ=0. Radial-poloidal plane.*

In the case shown in fig. 1 the origin is very close to the LCFS indicated both by the LCFS from a vacuum-field calculation which is typically 1 cm inside the LCFS corrected for finite β and by the velocity-shear-layer which is typically 0.5 cm outwards respectively. The fluctuating structure of fig. 1 is clearly extended both into the confinement zone and the SOL.

The 2d correlation analysis in the SOL by use of an angled probe array [1] shows quite similar structures for both floating-potential- and ion-saturation-current-fluctuations. Both

have the well known oblique structure in the radial-poloidal plane as it has been observed before in case of floating-potential-fluctuations [1]. Setting up the probe array such that the radial probe tips measure floating-potential and the poloidal ones ion-saturation-current, the 2d cross-correlation between potential and density fluctuations can be obtained. The maximum correlation is hereby shifted in time and space indicating a phase shift between potential and density which causes transport due to these fluctuations. The obliqueness in the radial-poloidal plane means that the particle flux by fluctuations is not purely radial but that is has a significant poloidal component.

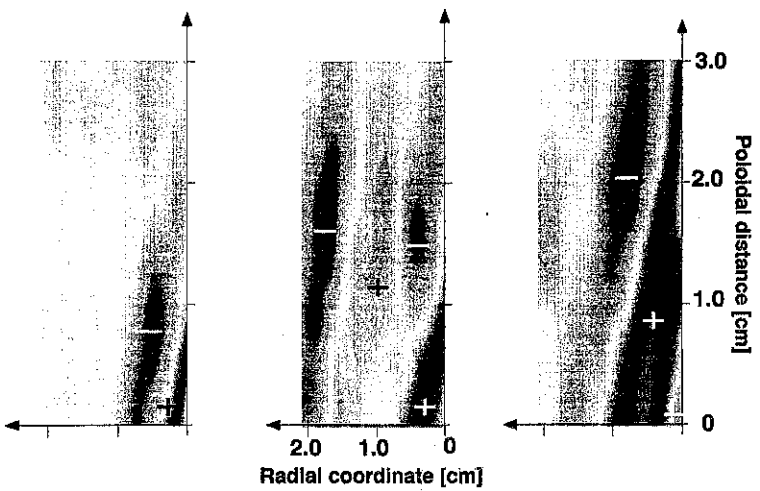

Figure 2: *2d-correlation functions ($\tau = 0$) obtained by an angled probe array for floating-potential (left) and ion-saturation-current (middle). The cross-correlation between floating-potential and ion-saturation-current is shown right.*

3. Correlation along field lines passing the torus inside. The experimental setup at W7-AS allows connection of two toroidally separated probes by a magnetic field line that passes the inside of the torus and has a connection length of 32 m. Due to the suppression of fluctuations in the regions of good magnetic curvature and due to the long connection length the correlation observed is only around 40% for both floating-potential and ion-saturation-current. In these experiments the connection between both probes is

only possible within the confinement zone of W7-AS.
In this case the correlation is no longer along the computed magnetic field line but there is a shift in the poloidal direction observed. This shift can be explained by a nonzero $k_{||}$ since the correlation is observed along the wavefront which is no longer along the magnetic field, if $k_{||}$ is different from zero.

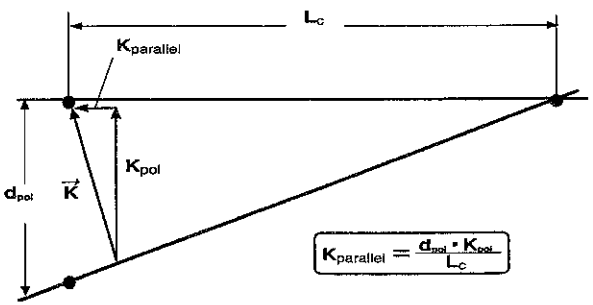

Figure 3: *Schematic view of the experimental setup for the measurement of* $k_{||}$.

The experimental results give $k_{||} = 0.0098\frac{1}{m}$, which corresponds to a parallel wavelength of $\lambda_{||} \approx 320\,m$.

4. Conclusion. Analysing the structure of edge fluctuations in the W7-AS stellarator we found that in the radial-poloidal plane these fluctuations look like deformed convective cells with a longer half width in the poloidal than in the radial direction. As mentionend earlier [1], these fluctuations are oblique in the radial-poloidal plane. The potential-density cross-correlation showed in addition that the fluctuation-induced particle flux is not purely in the radial direction but that is has a significant poloidal component. Along the magnetic field we observed very long wavelengths of the fluctuations in the order of some 300 meters. Good curvature does not suppress fluctuations completely.

5. References

[1] J. Bleuel et. al., Proc. 23rd EPS Conference on Controlled Fusion and Plasma Physics, Kiev 1996, volume 20C, part II, pp. 727–730

Review of 3-D equilibrium calculations and reconstructions for W7-AS

H.Callaghan†, J.Geiger, C.Görner, J.V. Hofmann, R. Jaenicke, P.J.McCarthy†, A. Weller

Max-Planck-Institut für Plasmaphysik,Euratom-IPP Association,
85748-Garching,Germany
†Dept. of Physics, University College Cork, Association Euratom-DCU,
Cork, Ireland

Abstract

Knowledge of the 3-dimensional structure of the plasma equilibrium is a prerequisite for experiments in stellarators and for the interpretation of the results. Therefore, since the calculation of equilibria consistent with the experimental data is an important task, we review the calculations done for W7-AS with applications to high β and large toroidal currents for stellarator-tokamak hybrid operation. We also present a novel method for fast equilibrium reconstruction for stellarators based on function parameterization.

Introduction

Although the geometry of the flux surfaces of a stellarators is largely determined by the external coil system, the plasma current densities induced by finite β, internal or external current drive (bootstrap-, Okhawa-, ohmic- and ECCD currents) may lead to considerable changes in the equilibrium fields.

To calculate 3-D MHD equilibria with free boundary, we use the NEMEC-code [1] assuming nested flux surfaces. The input consists of profiles for pressure and toroidal current, an estimate of the magnetic axis position and the plasma boundary, and the vacuum magnetic field. Based on an energy principle the equilibrium is determined iteratively using a steepest gradient method. The equilibrium quantities like flux surface geometry and magnetic field are given in Fourier series with respect to the cylindrical toroidal angle and a poloidal angle coordinate on a radially discretized grid.

An equilibrium reconstruction of a discharge at a given time point clearly implies an iterative process of adjusting the input parameters such that the resulting equilibrium data best match the experimental ones.

Equilibrium Calculations(1) : β effects

Usually, the pressure induced current densities dominate the changes in the magnetic configuration in net toroidal current free discharges. Although the reduced average toroidal curvature of W7-AS leads to smaller Pfirsch-Schlüter (PS) currents (a factor $\sqrt{2}$ compared to a conventional stellarator) they may give rise to appreciable Shafranov shifts, changes in the rotational transform (ι) profile and a displacement of the plasma as a whole in the accessible ι-range of W7-AS ($0.26 < \iota_{vac} < 0.56$). Very good agreement of the NEMEC calculations with experimental data was shown in Refs 2 and 3 for the high β cases. For W7-X the higher reduction of the average toroidal curvature as well as the higher operational range in ι ($\iota_{vac} \approx 1$) leads to much more stable magnetic configurations in the sense of finite-β equilibrium changes.

Equilibrium Calculations(2) : Toroidal current effects

Internally or externally driven net toroidal currents also affect the ι-profile and the geometry of the equilibrium flux surfaces, depending on their magnitude and distribution. At W7-AS, the usual operation is net current free, which means that the toroidal plasma current is kept at zero by inductive compensation. However, the toroidal current (I_{pl})

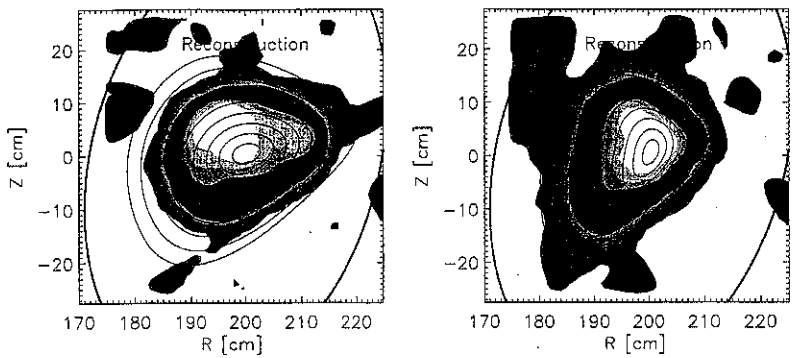

Figure 1: Comparison of Soft-Xray emissivity with NEMEC flux surfaces for $I_{pl} = 30$kA (right) and -30kA (left) shows good agreement in the gradient regions. A very flat central emission profile dominates the central contours for $I_{pl} = 30$kA.

within each flux surface does not vanish and thus alters the ι-profile. A large aspect ratio estimate for the change in ι is given by $\Delta\iota(r_{eff}) = I_{pl}(r_{eff})R/(2\Phi(r_{eff}))$ with r_{eff} and R the minor and major radii, respectively, and Φ the toroidal magnetic flux. Nevertheless, for vanishing net current there is generally no influence on the flux surface geometry. Therefore, to evaluate ι-profiles in net-current free discharges, it is sufficient to know the finite β changes on ι and then correct the profile using the toroidal current profile deduced from neoclassical theory and deposition profiles.

Introducing a net toroidal current also changes the flux surface geometry depending on the current's magnitude. Calculations show that the excursion of the flux surfaces in R increases with positive net current (the shape tends to be more oblate) and decreases with negative net current (higher vertical elongation). Good agreement of the calculated flux surfaces in 2 cases with large toroidal currents ($\pm$30kA at B=2.5T, $\iota_{tot} \approx 0.4$) with the tomographically reconstructed soft X-ray emissivity measured by the new MiniSoX camera system [4] is shown in Fig. 1.

Discussion of NEMEC calculations

Up to high β and rather high currents, the equilibrium calculations for W7-AS with NEMEC are in good agreement with the experiment. However, the computational effort is orders of magnitude higher compared to the calculation of tokamak equilibria. For fast reconstructions accompanying the experiment on a shot to shot basis or even online, NEMEC is not suitable with present-day computing power. Therefore, other approaches like function parameterization, which is discussed below, have to be explored.

Despite the good agreement with the experiment, there are limitations in the NEMEC applications. The assumption of nested flux surfaces excludes the detection of ergodic regions or islands. For this, more advanced equilibrium solvers have to be applied, like HINT or PIES. However, their computational requirements are orders of magnitude higher again than that of NEMEC. Furthermore, the Fourier representation of the equilibrium quantities together with the energy minimization method applied limits the resolution of boundary structures which require high Fourier harmonics and contain comparably small energies. Such 5/m resonant structures ($m \geq 12$) have been seen by video observations of visible light in high β discharges. Nevertheless, NEMEC shows a smooth plasma boundary without the actual indentation.

A hybrid FP/interpretive method for equilibrium recovery

Interpretive methods for determining plasma equilibria are widely used in tokamak analysis. Input parameters to an equilibrium code are iteratively adjusted such that simulated diagnostic signals from the resulting equilibrium best match experimental data. These methods are generally unsuitable for stellarators since each iteration involves the full solution of a 3D equilibrium code, a task requiring roughly one hour of CPU time on the Cray J-90 at IPP for standard W7-AS equilibrium calculations using NEMEC.
The application of function parameterization[5] (FP) to W7-AS is under development. FP seeks simple functional relationships between plasma parameters and diagnostic measurements over a database of simulated equilibria. This facilitates rapid equilibrium reconstruction, here in terms of magnetic data and a prescribed pressure profile. We have developed a novel interpretive method for equilibrium identification based on FP reconstructions that can be performed in the order of a few tens of seconds on a workstation.

FP database

Here, the database consists of *circa* 400 NEMEC equilibria with zero net toroidal current. They are chosen by randomly varying 8 input parameters over ranges appropriate to W7-AS, namely 3 ratios of the 4 field coil currents, a limiter position and a 4-parameter pressure profile chosen from the following family (s is normalized toroidal flux):

$$p(s) = p_0\,(1-s)^2\,\exp(as + bs^2 + cs^3)$$

Interpretive scheme

The Thomson scattering diagnostic on W7-AS gives electron temperature and density (and thus the electron pressure p_e) on ≤ 20 channels along a horizontal line-of-sight through the magnetic axis in a symmetry plane (ϕ=0) at a single timepoint during a discharge, i.e. $p_e = p_e(R_i)$, R_i being the major radii of the Thomson channels. A smoothing polynomial in R is fitted to the p_e data, allowing evaluation between channels. The iterative procedure attempts to reproduce the spatial to flux transformation $s(R)$ in $p_e(R)$ since p_e is constant on flux surfaces. Starting from an initial guess, the equilibrium pressure profile $p_{eq}(s)$ is varied to minimize the quantity

$$\int \left(p_e[R_{in}(s)] - p_e[R_{out}(s)]\right)^2 \, ds$$

subject to the constraints that $p_{eq}(s)$ is non-hollow and the boundary flux surface coincides with the zeroes of $p_e(r)$. An additional restriction that the kinetic energy content match the diamagnetic energy from the experiment can be optionally enforced.
The interpreted fit thus depends only on the topology of the $p_e(R)$ profile and not on its magnitude. In fact, it could be done separately for the Thomson temperature and density profile. Clearly, mismatches between the theoretical and physical magnetic configurations could falsify both the present scheme and the standard calculations. Consistency checks with additional spatially resolved or global diagnostic data would reveal such discrepencies, if present.

Comparison with standard calculations

Results from the interpretive method and the standard NEMEC simulation for shot 31909 are illustrated. The upper plots show the Thomson $p_e(R)$ with smoothing polynomial and the interpreted $p_{eq}(s)$ together with the standard NEMEC profile. The lower plots show the equilibrium flux surfaces in the Thomson ($\phi = 0$) plane and the final asymmetry error in $p_e(s)$.

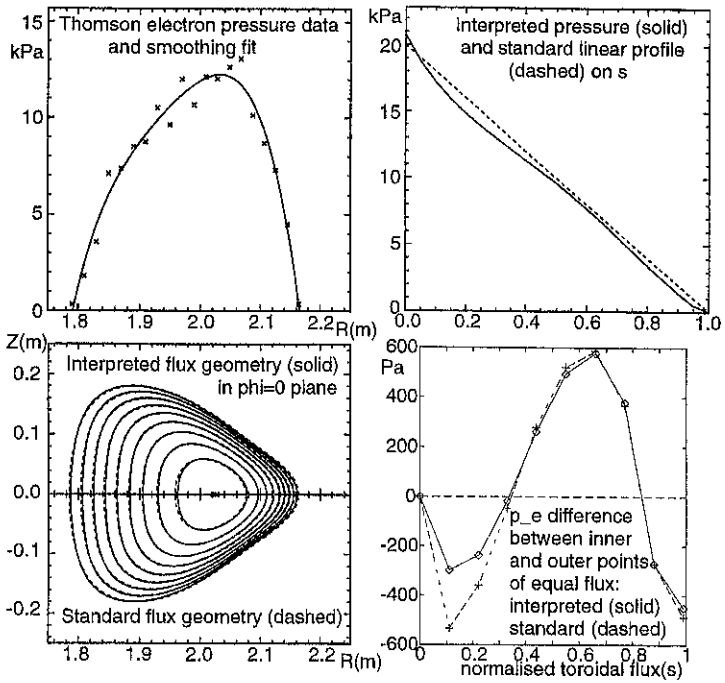

Though the two fits are of comparable quality, the interpreted fit is better than the standard calculation in the inner half of the plasma. This is not unexpected since the standard calculation uses the same optimization criterion with manual intervention required between iterations, rather than an automated least-squares fit. The p_e symmetry can be further improved by varying additional pressure parameters during iterations. Only three of a possible six were varied here to prevent overfitting. The interpretation for this case took roughly 20 seconds on a workstation, whereas the standard simulation required several NEMEC calculations.

Work in progress includes investigation of the effects of signal noise on the recovery. Moreover, although scalar equilibrium parameters and flux geometry are well recovered, a model that reproduces the ι-profile well has so far proved elusive. Once this is achieved, the procedure will be applied to equilibria with finite net toroidal current.

Acknowledgement

J.G. is thankful for the fruitful discussions and advices in the use of NEMEC by J. Nührenberg, P. Merkel, E. Strumberger and S. Gori of the W7-X Group.

References

1. Hirshman S.P., van Rij W.I. and Merkel P., Comput.Phys.Comm.**43** (1986)143
2. Jaenicke R. et al,Plasma Phys. Control. Fusion **37**,(1995),163
3. Kick M. et al,Proc. 16th IAEA Conf. on Plasma Phys. and Contr. Nucl. Fusion Research, Montreal (1996) to be published
4. Görner C. et al, this conference
5. Mc Carthy P. J., 'An Integrated Data Interpretation System for Tokamak Discharges' Ph.D. thesis, University College Cork, 1992

Simulation and analysis of neutral particle spectra from W7-AS in combination with neutron activation measurements

N. Rust, G. Beikert, K. Hübner*), M. Kick, F.P. Penningsfeld, U. Stroth, A. Weller, B. Wolle*)
Max-Planck-Institut für Plasmaphysik
Association EURATOM-IPP, D-85748 Garching, Germany
*)Institut für Angewandte Physik, Universität Heidelberg, D-69120 Heidelberg, Germany

For the investigation of confinement of fast ions we present results of an experimental and theoretical study at W7-AS. It consists of the analysis of non-thermal neutral particle spectra and absolute neutron yield measurements combined with theoretical calculations.

The fast ion distribution function is measured with the neutral particle diagnostics. It consists of four neutral particle energy analysers for spatially resolved measurements. The lines-of-sight of the analysers cross a neutral particle diagnostic beam which is passing vertically through the plasma centre. For absolute neutron yield measurement indium activation samples are used which are irradiated inside the vacuum vessel near the plasma. Their γ-activation is measured with a calibrated germanium detector. Using a fluence factor which is calculated with the Monte Carlo code MCNP, the volume integrated absolute neutron yield of the plasma discharge is determined. - For the numerical simulation of the neutral particle spectra and the neutron yield the time-dependent 2D Fokker-Planck code NRFPS is used.

The local charge-exchange particle flux $S(v,\mu,t)$ from the plasma is given by

$$S(v,\mu,t) = g\, n_i\, n_0\, f(v,\mu,t)\, \langle\sigma v\rangle_{cx} \cdot \exp\left[-\int_0^a \frac{1}{v}\left(n_i \langle\sigma v\rangle_{cx} + n_e \langle\sigma v\rangle_e + n_i \langle\sigma v\rangle_i\right)\right] . \quad (1)$$

Here, $f(v,\mu,t)$ is the ion velocity distribution, v the particle velocity, $\mu = v_{\parallel}/v_{\perp}$ the pitch-angle, g a geometrical factor, n_i and n_0 are the ion and neutral particle densities, $\langle\sigma v\rangle_{cx}$ and $\langle\sigma v\rangle_e$ are the rate coefficients for charge-exchange and for electron impact ionisation. The exponential factor describes the absorption of the particles on their trajectory through the plasma and is calculated with respect to the real stellarator geometry.

The local neutron rate Q from the plasma is given by

$$Q(t) = \frac{n_i n_j}{1+\delta_{ij}} \iint f_i(v,t)\, f_j(v',t)\, \sigma(|v-v'|)\, |v-v'|\, d^3v\, d^3v' , \quad (2)$$

where $f_i(v,t)$ and $f_j(v',t)$ are the velocity distributions for the ion species i and j, $|v-v'|$ the relative velocity and σ the fusion cross section, respectively

Measurements and calculations have been carried out for a variety of W7-AS discharges with H^0 and D^0-injection with average electron densities ranging from 2.8×10^{19} to $7\times10^{19}\,m^{-3}$, electron temperatures from 0.5 to 2.8 keV and ion temperatures of about 0.32 to 1 keV. Electron temperatures and densities were taken from the Thomson scattering and ion temperatures from the neutral particle diagnostics. The deposition profile for the injected particles was calculated with the 3D FAFNER code.

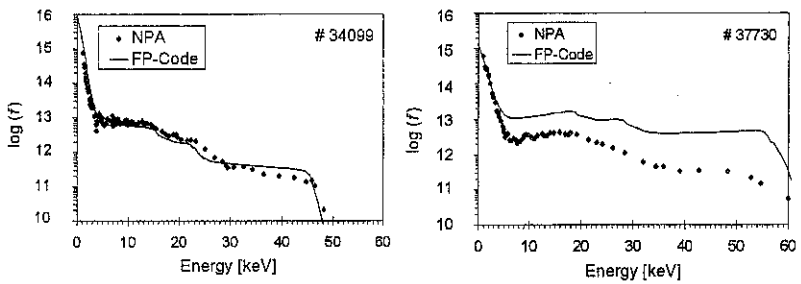

Fig. 1: Comparison of calculated neutral particle flux with experimental data.

1a: $n_e = 7{,}3\times10^{19}\ m^{-3}$
$T_e = 0.5$ keV
Ti = 0.44 keV
$\tau_W = 3.5$ ms

1b: $n_e = 3{,}7\times10^{19}\ m^{-3}$
$T_e = 2{,}8$ keV
Ti = 0.83 keV
$\tau_W = 52$ ms

Fig.1 shows as an example the calculated and measured neutral particle flux for two different plasma discharges. For the high density discharge the measurement and the calculation agree rather well. However, discrepancies occur for lower densities. The smaller the density becomes in a discharge, the larger becomes the neutral gas density and the higher the electron temperature. Increasing electron temperature and decreasing density result both in an enlargement of the energy relaxation time of the fast particles. As shown in fig.2 the discrepancies increase strongly with increasing classical energy relaxation time τ_W.

In principle, the observed discrepancies can be caused by three different processes, namely by reduced particle deposition owing to the high neutral gas density, and by particle or energy loss mechanisms with time scales comparable to the classical relaxation times.

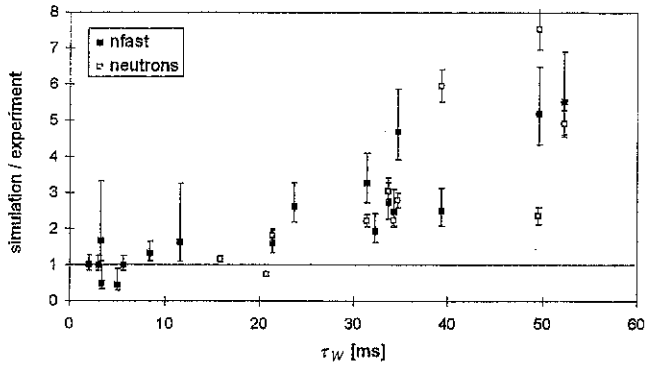

Fig.2: Comparison between calculated and measured fast particle density and between calculated and measured neutron yield in dependence of τ_W.

These three processes will influence the time behaviour of the plasma signals in a different way. First of all it is of interest to investigate the initial rise of the plasma signals at the onset of the injection. To that end it is sufficient to use the relaxation time model which takes into account only the relaxation of energy $dW/dt = -W/\tau_W^*$ and leads to the simple approximation

$$f(W) = \frac{dn(W)}{dW} = \frac{\tau_W^*}{W}\left(S - \frac{n(W)}{\tau_n}\right) \tag{3}$$

for the energy distribution function of fast particles. Here, τ_W^* is the total energy relaxation time, resulting from classical and anomal energy losses ($1/\tau_W^* = 1/\tau_W + 1/\tau_{W,anomal}$). S is the density of injected particles per second and τ_n the time constant of direct particle losses. From this expression follows that the initial rises of the plasma energy E_f and of the neutron-rate Q at the onset of the neutral beam injection are solely determined by the particle injection properties:

$$\left.\frac{dE_f(t)}{dt}\right|_{t\to 0} = S W_0, \qquad \left.\frac{dQ(t)}{dt}\right|_{t\to 0} = S n_e \sigma(W_0)\sqrt{\frac{2W_0}{m}}. \tag{4}$$

Here, W_0 is the injection energy, m_f the mass of the injected ions. An example for the initial rise of the plasma energy and the neutron signal. is shown in fig.3. The dotted lines indicate the theoretical rise according to eq.4. Agreement with the measured signals is obvious for the high density discharge but - owing to the statistical fluctuations in the signals - not as clear for the low density one.

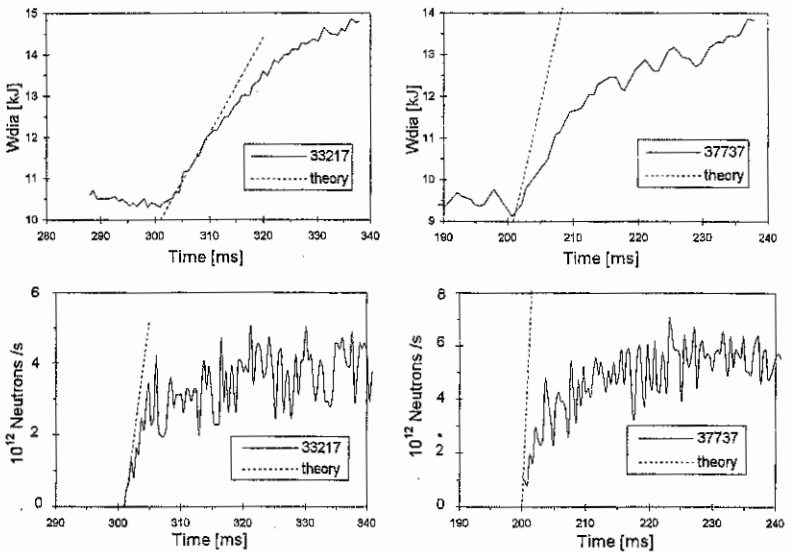

Fig. 3: Initial rise of the plasma energy and the neutron signal.

3a: n_e=5.7x10^{19} m^{-3}
T_e=1.2 keV
τ_W= 21 ms

Fig.3b n_e=3.9x10^{19} m^{-3}
T_e=2.7 keV
τ_W= 50 ms

Although further investigations are required this may be an indication that the observed discrepancies are not caused by a reduced deposition but by a loss mechanism. Moreover, from the FAFNER calculations it follows that the neutral gas density at the plasma edge has to be at the level of 2.5x10^{10}cm^{-3} in order to explain the observed effects. This seems to be a rather high value. On the other hand, a direct particle loss owing to radial diffusion would require a diffusion coefficient in the order of 1 m^2/s, this may be a reasonable value. Finally, up to now we have not detected plasma mode activities which correlate with the observed discrepancies and thus could lead to an anomal energy relaxation by ion-plasmon interactions. Thus, in conclusion, though we can presently not exclude definitely the other two processes, it seems that enhanced radial diffusion of the fast ions may be the reason for the observed reduction in fast particle density and neutron emission in low density discharges.

Tomographic Reconstruction of Plasma Equilibria and MHD-Modes at WENDELSTEIN 7-AS

C. Görner, M. Anton, J. Geiger, W. von der Linden, A. Weller, S. Zoletnik❖, W7AS-Team

Max-Planck-Institut für Plasmaphysik, EURATOM Association, D-85748 Garching

❖ KFKI-Research Inst., Dept. of Plasma Physics, P.O. Box 49, Budapest-114, HUNGARY

I. Introduction

The usage of soft-X radiation for detection of MHD-activities in a plasma and for mapping of plasma equilibrium flux surfaces is a widely applied method on fusion devices. The specific magnetic configuration of W7-AS is the result of the optimization procedure for the stellarator design and, compared with the axial-symmetric tokamak configuration, the flux surfaces are three-dimensional and are characteristically shaped in a poloidal plane, such that a tomographic system needs an enhanced poloidal resolution. To achieve proper plasma imaging for the soft-X radiation, a small sized camera system was installed inside the vacuum vessel to overcome the technical restriction of access from the inboard side of the torus. The system consists of 10 cameras with a total sum of 320 channels and therefore a good spatial resolution in both the radial and poloidal direction is obtained. Together with a well balanced distribution over the poloidal plane, tomographic reconstruction of the soft-X emissivity distribution (6μm Be filter) can be done without additional assumptions about the topology.

In this paper we introduce the camera system and the numerical algorithm, applied for the tomographic reconstruction. Additional data processing is also presented. With the whole tomographic system, comprising the hard- and software, we show some applications to

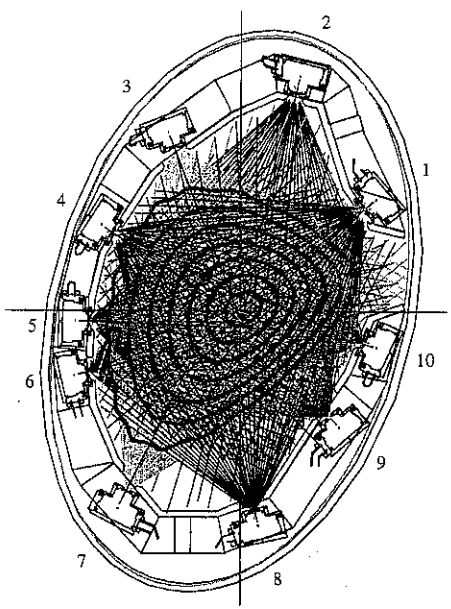

Fig. 1: 10 camera tomographic system at W7-AS. All 320 lines of sight are drawn. Typical $\iota \approx 1/3$ flux surfaces are additional plotted. The surrounding ellipse is the W7-AS vessel.

measurements of the equilibrium flux contours and MHD-activities, seen in the stellarator W7-AS.

II. The 10-camera tomographic system at W7-AS

Figure 1 shows an overview of the hardware of the tomographic system together with the idealized lines of sight of the X-ray detectors. The spatial resolution is comparable with the separation between two neighbouring lines. Data acquisition is performed with a sampling rate of up to 200kHz in time windows with a typical duration of about 50ms (defined by a maximum total data amount of 8MByte per shot).

Three different algorithms for the 10-camera tomography and additional techniques to extract the relevant physical data are used, because different reconstruction problems may require an appropriate algorithm. A choice can be made between algorithms using first order regularisation [1], which tries to avoid steep gradients, a minimum Fisher-information regularisation scheme [2] and the maximum entropy [3, 4] solution.

$$\Lambda_{\mathrm{LinReg}} = \frac{1}{2}\chi^2 + \alpha_R R \qquad R = \int \|\nabla \rho\|^2 \qquad \text{1. order regularisation}$$

$$\Lambda_{\mathrm{MinFisher}} = \frac{1}{2}\chi^2 + \alpha_R I_F \qquad I_F = \int \frac{g'(x)^2}{g(x)} dx \qquad \text{min. Fisher-information}$$

$$\Lambda_{\mathrm{MaxEnt}} = \frac{1}{2}\chi^2 - \alpha_R S \qquad S = \sum_{i=1}^{N_p} \left[\rho_i - m_i - \rho_i \ln \frac{\rho_i}{m_i} \right] \qquad \text{max. entropy}$$

Maximum Entropy is not a widely used algorithm, because of the long numerical calculations. On the other side, it is the only algorithm, implemented such, that the result is a real mathematical result without the need of guessing the regularisation parameter. Additionally, error bars for the reconstructed distribution are obtained by this method.

For visualisation and quantitative analysis, additional processing is necessary. This includes the implementation of different meshes and expansion functions of the emissivity to be reconstructed, singular value decomposition (SVD), filtering in the frequency-space and error calculations for the case of maximum entropy reconstructions. SVD thereby is the most important method, to extract the fluctuating part of the emissivity attributed to MHD-modes from a sequence of reconstructions. In order to check the reliability, simulated plasma radiation distributions were used.

III. Equilibrium reconstructions

Concerning equilibrium effects, quantitative measurements of the magnetic surface struc-

ture were made. Two effects have been investigated in particular: the change of the plasma shape due to toroidal currents and the effect of the Shafranov-shift, depending on the plasma beta. The minimization of the Shafranov-shift is one of the most important optimization criteria of W7-AS. The comparison between reconstructions and equilibrium calculations [5] was made for a mean plasma radius were SX-profiles have steep gradients. For both cases very good agreement was observed. Only minor differences in the reconstructions was observed in comparing the three tomographic algorithms mentioned above.

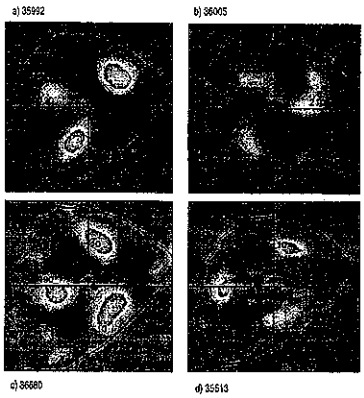

Figure 2: Four different modes with poloidal mode number m = 3. *a) and b) GAE, c) pressure driven mode and d) tearing mode. The plotted flux surface is at normalized radius of 0.75.*

IV. MHD-activities

The physics issues addressed in this paper comprise, firstly, different kinds of MHD-instabilities including pressure- and current-driven modes and fast particle driven global Alfvén eigenmodes (GAE). An example is shown figure 2, where different modes are plotted for the case of m = 3. GAE-modes usually extend over a large part of the plasma cross section, whereas tearing modes and pressure driven modes are localized around a rational surface.

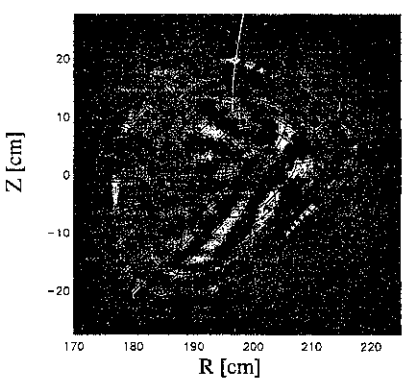

Figure 3: GAE with m=9. *Fourier-expansion in the magnetic angle is used. There for only the radius-dependent phase is a measured quantity. The phase agrees with lines of constant magnetic angle.*

In the case of GAE modes, the reconstruction of the radial and poloidal mode structures, i.e. the determination of the poloidal mode number (m) and the radial eigenfunction, a variety of peaks found in the Alfvén spectrum were analysed. Most of the peaks correspond to the lowest (m,n)-modes expected from theory, but also higher m-numbers and modes with different radial structure were observed. At Wendelstein 7-AS, GAE-modes are commonly seen with neutral beam heating, and the main features are compatible with theoretical predictions, see [6]. With the new tomographic system,

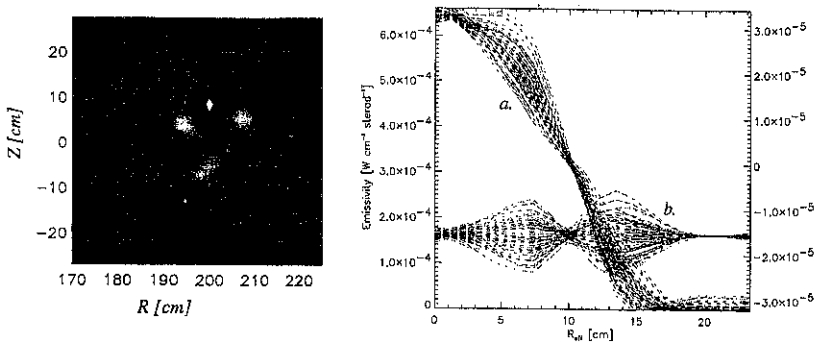

Figure 4: Radial mode structure found in shot #35982. *Left: SVD-filtered picture of the fluctuating emissivity. The solid line corresponds to magnetic angle of* $\theta = 40^{\circ}$.
Right: Profiles of the total emissivity profile (a., left axis) and the fluctuations (b., right axis) at different time points (at $\theta = 40^{\circ}$*). For the total profile, the fluctuations are magnified by a factor of 10.*

more complex mode structures can be assessed. For example, figure 3 shows an (m=9)-GAE mode that shows up together with a (m=3) and (m=6) mode (not plotted). Another example, Figure 4, shows two (m=3)-GAEs: one with a radial node at about R_{eff}=10cm and the second without node are observed simultaneously. In both discharges, m = (3,6,9) and m = (3,3 with radial node), the modes propagate at different frequencies, that seem to develop independently during the live time of the modes.

References

[1] S. Zoletnik and S. Kálvin. *Rev. Sci. Instrum.*, **64**(5):1208–1212, 1993.

[2] M. Anton, H. Weisen, M. J. Dutch, W. von der Linden, F. Buhlmann, R. Chavan, B. Marletz, P. Marmillod, and P. Paris. *Plasma Physics of Controlled Fusion*, **38**:1849 – 1878, 1996.

[3] W. von der Linden. *Applied Physics A*, **60**:155 – 165, 1994.

[4] K. Ertl, W. von der Linden, V. Dose, and A. Weller. *Nuclear Fusion*, **36**(11):1477 – 1488, 1996.

[5] H. Callaghan, J. Geiger, C. Görner, J. V. Hofmann, R. Jaenicke, and A. Weller. *this conference.*

[6] A. Weller, D. A. Spong, R. Jaenicke, A. Lazeros, F. P. Penningsfeld, S. Sattler, W7-AS Team, and NBI-Group. *Physical Review Letters*, **72**(8):1220, 1994.

Analysis of D Pellet Injection Experiments in the W7-AS Stellarator

J. F. Lyon and L. R. Baylor, *Oak Ridge National Laboratory, Oak Ridge, TN, 37831 U.S.A.*
J. Baldzuhn, S. Fiedler, M. Hirsch, G. Kühner, and A. Weller,
Max-Planck-Institut für Plasmaphysik, EURATOM Association, 85748 Garching, Germany

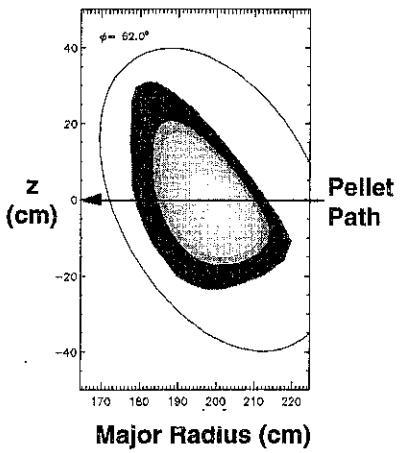

Fig.1. Typical flux surfaces and the pellet injection path in W7-AS.

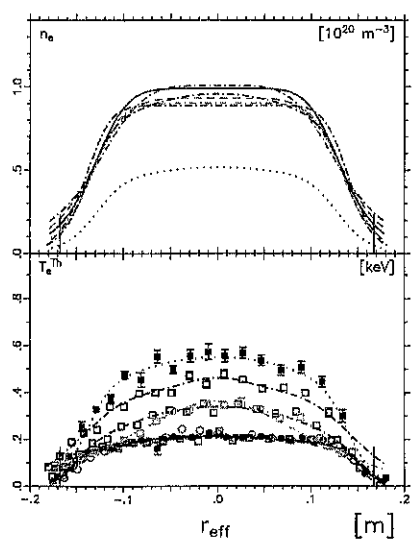

Fig. 2. Thomson scattering profiles from before pellet injection (highest T_e , lowest n_e curves) to 18.5 ms after the pellet (second highest T_e curve).

A centrifugal injector was used to inject deuterium pellets (with 3–5 × 10^{19} atoms) at ≈600 m/s into currentless, nearly shearless plasmas in the Wendelstein 7-AS (W7-AS) stellarator. The D pellet was injected horizontally at a location where the noncircular and nonaxisymmetric plasma cross section is nearly triangular (Fig. 1.) Visible-light TV pictures usually showed the pellet as a single ablating mass in the plasma, although the pellet occasionally broke in two or splintered into a cloud of small particles.

Density Evolution Following Pellet Injection in W7-AS

Figure 2 shows Thomson scattering profiles for the electron density n_e and temperature T_e immediately before and at times shortly after pellet injection (at 0.4 ms, 0.5 ms, 0.65 ms, 5.7 ms, 7.6 ms, and 18.5 ms) for a neutral-beam-heated plasma. Pellet injection leads to a rapid (< 400-μs) rise in n_e in the main part of the plasma and to a slow increase in the plasma edge on a longer (>20-ms) timescale. Microwave reflectometer measurements of the time delay (which reflects the density gradient) and FIR interferometer measurements of the line-average density also indicate that the density rises in <500 μs (Fig. 3) and then remains unchanged. The same behavior is seen in the soft X-ray intensity profiles in Fig. 4 (with 1.4 ms between curves); this signal is more influenced by density than by temperature because there was no

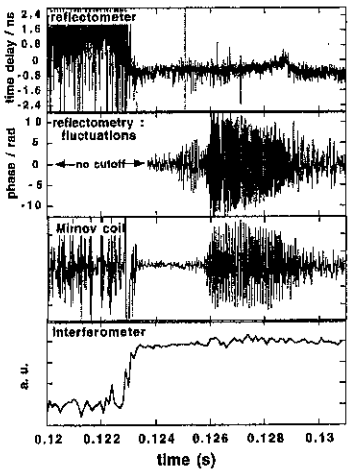

Fig. 3. Time delay and fluctuation level from a microwave reflectometer, MHD oscillations from a Mirnov coil, and line-average density around the time of pellet injection.

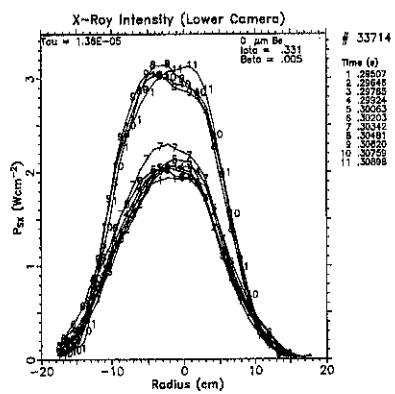

Fig. 4. Soft X-ray intensity profiles from 6.5 ms before pellet injection to 8.4 ms after a pellet.

filter in front of the soft X-ray diode array. Neutral lithium beam measurements of n_e at radii r >12.5 cm (Fig. 5) show that the outer density rises slowly after pellet injection (on a 60-ms timescale), presumably due to recycling from the wall. The increase in n_e decreases with distance into the plasma.

Pellet ablation calculations using the standard neutral gas shielding model and the $n_e(r)$ and $T_e(r)$ profiles before injection indicate that the increment in density should be peaked. However, this is not seen in W7-AS on the timescale of any of the measurements. The change in the $n_e(r)$ profile in Fig. 2 is not diffusive. If it were, then the particle diffusivity would have to increase by a factor of >100 for a relatively short time (<400 μs, about the transit time for the pellet through the plasma). There was not a significant loss of injected particles during the fast density change: comparing the number of particles in the pellet with the increase in the number in the plasma after pellet injection indicates that >60% of the pellet is retained in the plasma for times >20 ms. This behavior, where the density profile after pellet injection assumes the shape of the preexisting profile without significant loss, is not seen in tokamaks. Either the ablation model is not correct and the deposition profile is the same as the initial density profile for different initial densities and field values, or a fast density redistribution occurs in these experiments in W7-AS.

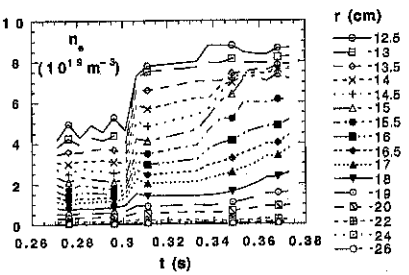

Fig. 5. Increase in the plasma density in the edge region from 30 ms before to 70 ms after a pellet.

Effect of Pellet Injection on Energy Confinement and Fluctuations in W7-AS

Figure 2 shows a rapid drop in T_e after pellet injection because the stored energy W does not change immediately. Although the $n_e(r)$ profile remains at the new (higher) value for the duration of the discharge following pellet injection, $T_e(r)$ gradually returns toward its preinjection value, indicating an increase in the energy confinement time τ_E. This is illustrated in Fig. 6 where W and τ_E increased by a factor of 2.7 for a factor of 1.7 increase in n_e. From the W7-AS τ_E scaling expression [1] $W = P\tau_E^{W7\text{-}AS} \propto n_e^{0.5}p^{0.46}$, the increase in n_e should lead to a factor of ≈1.3 increase in the stored energy because $P = P_{absorbed}$ is approximately constant at the densities in these experiments. The additional factor of 2 improvement in τ_E is due to an increase in confinement: $\tau_E/\tau_E^{W7\text{-}AS}$ is 0.7 before the pellet and 1.4 afterward. In Fig. 2, the confinement improvement (1.35) is less: $\tau_E/\tau_E^{W7\text{-}AS}$ was 0.8 before the pellet and 1.1 afterward.

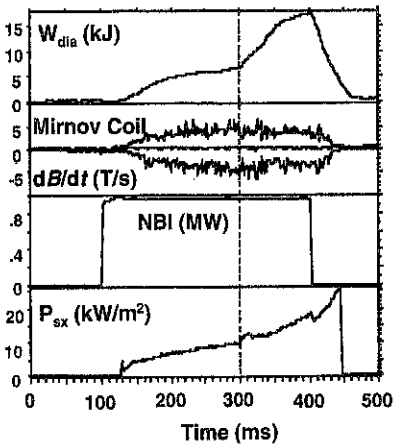

Fig. 6. Response of the plasma to pellet injection at t = 300 ms.

A few-ms quiescent period is sometimes seen in the MHD signals on Mirnov coils following pellet injection when the stored energy starts to increase, as seen in Fig. 3. In all cases, the Mirnov loop signal (often associated with degraded confinement) is reduced, and $\tau_E/\tau_E^{W7\text{-}AS}$ is >1 after a pellet. Low density fluctuation levels, followed by a decaying high-frequency burst in several discharges, were seen with the microwave reflectometer after the rapid density rise (Fig. 3). These oscillations are correlated with the Mirnov coil signal. An example of pellet injection suppressing MHD activity for a longer period with a resultant increase in τ_E is shown in Fig. 7. Without the pellet, the MHD activity and the associated enhanced energy loss persist for a longer time. It is thought that the pellet rapidly depletes the fast particle population that drives the instability [2].

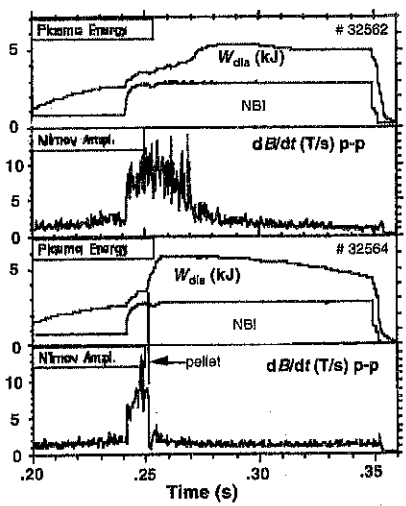

Fig. 7. MHD activity that retards transition to a high-β phase (2 top traces) is suppressed by pellet injection (2 bottom traces).

The soft X-ray (and MHD loop) signals in Fig. 8 show short-duration oscillations (for ≈300 μs) immediately after pellet injection, followed by slow (650-Hz) oscillations that damp out after a few ms and are in phase across the plasma ($m = 0$). The phase velocity of the slow oscillations indicates a disturbance propagating outward at 350 m/s. The initial burst is coincident with the fast change in n_e in the bulk of the plasma seen in Fig. 2. If the rapid change in $n_e(r)$ is due to a fast density relaxation rather than an anomalous particle deposition profile, then this burst may be evidence of an instability that causes the fast radial spreading of the high-β pellet blob. The magnetic field has low shear, a relatively weak radial gradient along the pellet path, and stronger field regions some distance toroidally on either side, which may allow a radial mixing to occur. The process may be different than in tokamaks because of the low $B \times \nabla B$ radial drift in W7-AS. In earlier experiments in W7-AS [3], the density profile became more peaked, and soft X-ray tomographic reconstruction showed small-amplitude (≈2-mm) internal oscillations in the location of the peak of the soft X-ray emission following pellet injection. In that case, the soft X-ray oscillations showed a different ($m = 1$) mode structure. Experiments with higher shear and the opposite toroidal variation of the magnetic field strength are needed to understand these observations.

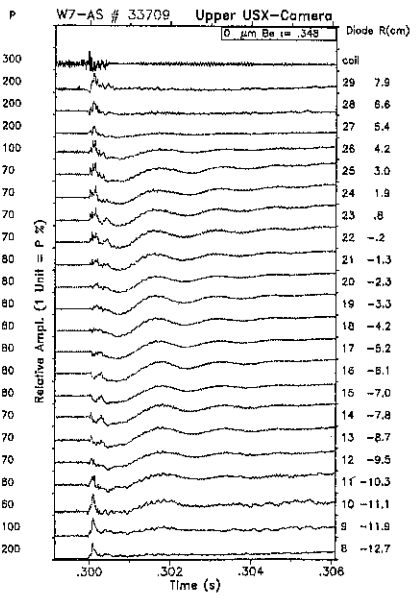

Fig. 8. Damped soft X-ray intensity oscillations following pellet injection.

The next steps involve use of a one-dimensional transport code to model the evolution of the density profile and experiments with a more versatile gas gun that allows injection with a larger range of pellet masses. Improved diagnostics — Thomson scattering triggered by the pellet, fast multichannel ECE and microwave and FIR interferometers, a Cotton-Mouton-effect polarimeter, an extensive soft X-ray array that surrounds the plasma poloidally, improved MHD loop arrays — should allow better study of the evolution of $n_e(r)$ and the associated transport.

References

[1] U. Stroth et al., *Nucl. Fusion* **36**, 1063 (1996).
[2] Max-Planck-Institut für Plasmaphysik, *IPP Annual Report 1995*, p. 59.
[3] A. Weller et al., *17th EPS Conf. on Controlled Fusion and Plasma Heating, Amsterdam*, Part II, 479 (1990).

*Research sponsored in part by the Office of Fusion Energy Sciences, U. S. Department of Energy, under contract DE-AC05-96OR22464 with Lockheed Martin Energy Research Corp.

ICRF Experiments on the Stellarator W7-AS

D.A. Hartmann, G.Cattanei, J.F. Lyon*, V. Plyusnin†, ICRF-Group, W7-AS Team

Max-Planck Institute for Plasma Physics, EURATOM Ass., 85478 Garching, Germany
*Oak Ridge National Laboratory, Oak Ridge, Tennessee 37831
†Institute for Plasma Physics, 310108 Kharkov, Ukraine

INTRODUCTION

The first successful ICRF plasma heating experiments in the W-7AS stellarator [1] have demonstrated effective plasma heating and plasma sustainment, for 2nd harmonic and two-ion hybrid heating regimes without significant increase of impurity radiation. The results presented in this paper establish ICRH as an attractive method to heat and sustain the plasma in stellarators under steady-state conditions.

TECHNICAL SETUP

The RF system of W7-AS consists of two RF generators with a nominal power of 1.5 MW that are connected to two antennas. For the experiments to be described the RF power was launched with a broad four-port antenna exciting a narrow $k_{||}$-spectrum around $k_{||} = 6\mathrm{m}^{-1}$ for $\pi-$phasing [2,3] After a faster arc protection system (full power switch-off within $20\mu s$ of an arc) and a section of lossy transmission line to avoid generator self-oscillations [4] had been installed more effective conditioning of the antenna became possible. Thus RF pulse lengths longer than one second with voltages in the transmission lines up to 70 kV were reached.

EXPERIMENTAL RESULTS

Plasma heating, sustainment and startup from a seed discharge were investigated for the two-ion hybrid heating scenario for hydrogen minority in a deuterium and ^{4}helium plasma. Good absorption of the RF power radiated from the antenna was observed only if the hydrogen concentration was less or about 10%. Such low hydrogen concentrations were obtained after boronization of the vessel interior with B_2D_6 or after helium glow discharges with about 5% deuterium. The hydrogen concentration was infered from comparison of the intensity of the H_α and D_α lines and comparison of the CX hydrogen and deuterium fluxes. This ratio was uncontrolled and only determined by wall recycling. Good wall conditions (obtainable only after many hundreds of plasma discharges) were imperative for keeping the hydrogen concentration sufficiently low during the ICRF experiments.

ECRH generated deuterium and helium plasmas (P_{ECRH}=500 kW, $n_e(0) = 3. \times 10^{19}\mathrm{m}^{-3}$, $T_e(0)$=2.5 keV, $T_D(0)$=450eV, ι=0.34, W_{diam}=5 kJ, central heating) were used as targets. Antenna loading approximately doubled with plasma compared to vacuum

loading. Thus half of the generator power was radiated into the plasma, the remainder was ohmically dissipated in the antenna.

Fig. 1 shows the temporal evolution of an ICRF-heated ECRH plasma. During the ICRF pulse an increase of about 25% of the diamagnetic energy was observed. The dominant part of this increase is due to an increase in deuterium temperature. Fig. 2a shows the deuterium temperature profiles with and without ICRF. An overall increase from 400 eV to 550eV is observed. Fig. 2b shows the electron temperature profiles with and without ICRF. The strongest increase in electron temperature was observed off-axis at the approximate location of the two-ion hybrid resonance and was mainly due to direct electron heating.

Fig. 3 shows the radial profile of the RF power density absorbed by the electrons. This was evaluated from the change in slope of the ECE electron temperature and the Thomson electron density profile at the turn-on time of the RF power. The total RF power absorbed by the electrons was around 30 kW for this case.

The transient drop of the central electron temperature within the first 50μs is not understood. It cannot be attributed to a central density increase or an increase in impurity radiation.

For RF powers up to about 400 kW the increase in diamagnetic energy followed the stellarator confinement time scaling [5]. From this one can conclude that most of the radiated power is absorbed in the plasma. For higher RF powers the diamagnetic energy increased less than expected as can be seen in Fig.4 . There the increase in diamagnetic energy is shown for different ICRF powers radiated from the antenna. The solid line is the prediction based on the confinement time scaling for W7 -AS [5]. For RF powers larger than 400kW, which corresponds to $P_{ICRF}/P_{ECRH} \approx 0.6$, a saturation in the relative increase of the diamagnetic energy is observed. Data at higher ICRF power that should be available now are necessary to clarify this point.

Bulk hydrogen temperature up to 1.2 keV was measured at the plasma center with active CX whereas the deuterium temperature was about 400 eV. Hydrogen fluxes with energies up to 45 keV were observed at an angle of about 45° to the magnetic field lines. At RF powers less than about 400 kW an increase of the tail temperature with RF power was observed. However, the tail temperature saturated at about 7 keV for RF powers greater than 400 kW.

It was possible to sustain the plasma solely with ICRF. Pulse lengths up to 1 sec (>50 energy confinement times) at RF powers of 500 kW were achieved. Fig. 5 shows the time evolution of such an ICRF plasma. The achieved plasma parameters were: $W_{diam} \leq 4.2$ kJ, $T_e(0) \leq 800$ eV, $T_D(0) \leq 500$ eV, $n_e(0) \leq 4.5 \times 10^{19}$ m^{-3}, $P_{RF} \leq$ 700 kW. Good wall conditions facilitated density control over the length of the discharge. After some slightly transient behavior steady-state was reached where all measured plasma parameters were constant. In particular, no increase of impurity radiation was observed.

The total radiation as determined by bolometry remained comparable to ECRH plasmas. VUV measurements showed a slow increase of iron and chromium radiation that saturated after a few hundred milliseconds in agreement with the long particle confinement times expected at these densities and power levels.

It was also possible to generate the plasma with ICRF starting from a seed plasma given by the afterglow of a discharge. The time evolution of such a discharge is shown in Fig. 6. At the start of the ICRF pulse the density of the seed plasma was less than the cut-off density for the fast wave and the antenna loading was equal to the vacuum loading. Within 100 msec of the start of the RF pulse typical ICRF-plasma parameters were recovered. The stub tuners of the system had to be set to a compromise setting to ensure sufficiently low VSWR during the whole discharge.

CONCLUSIONS

Plasma heating, sustainment and generation from a seed plasma is possible with ICRF for the two-ion hybrid heating scenario in an advanced stellarator. ICRH-sustained plasma parameters were comparable to those achieved with ECRH. The experiments showed, however, that the heating efficiency degraded rapidly if the hydrogen concentration increased beyond 20-30 %. Therefore, control of the minority concentration is of crucial importance for this heating scenario in a large aspect ratio device as the W7-AS stellarator. A viable alternative to hydrogen minority could be ^{3}He, whose concentration can easily be controlled.

REFERENCES

1. G. Cattanei et al., *EPS Conf. on Controlled fusion and Plasma Physic, Kiev, 1996*,20C part II, 499
2. G. Cattanei et al., *Nucl. Fus.* **29**, 15 (1989).
3. G. Cattanei et al., *EPS Top. Conf. on Radiof. Heating and Current Drive, Brussels, 1992.*
4. D.A. Hartmann et al., *EPS Top. Conf. on Radiof. Heating and Current Drive, Savannah, 1997.*
5. U. Stroth et al., *Nucl. Fus.* **36**,1063 (1996).

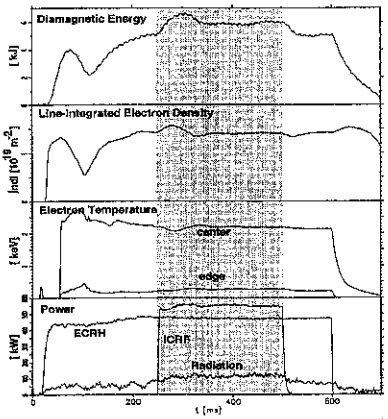

FIGURE 1. Shot 37298. ICRF heating of ECRH plasma.

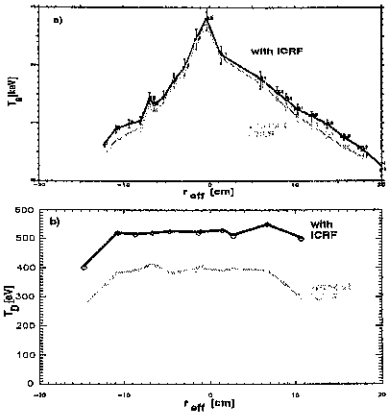

FIGURE 2. Electron and deuterium temperature profile for shot 37298.

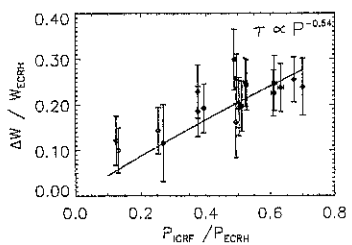

FIGURE 3. Relative increase in diamgnetic energy versus the ratio of ICRF power radiated from the antenna to ECRH power.

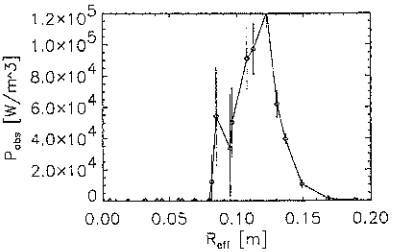

FIGURE 4. Radial profile of RF power density absorbed by electrons.

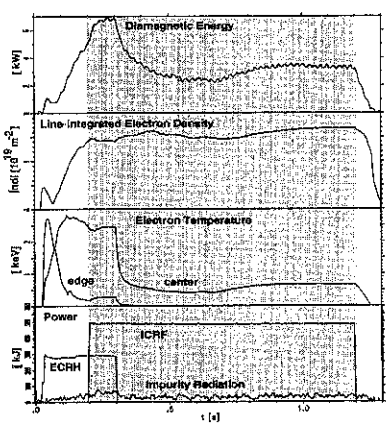

FIGURE 5. Shot 39387. ICRF sustained plasma.

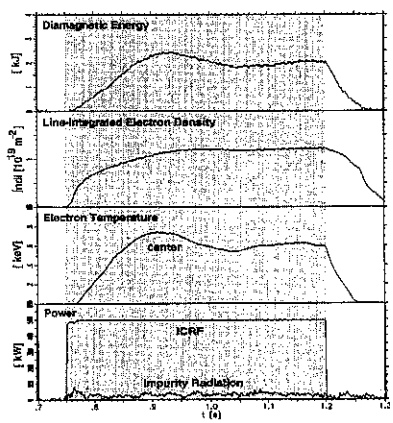

FIGURE 6. Shot 39389. ICRF generated plasma.

ENERGY and DENSITY INHOMOGENEITIES DRIVEN by TOROIDALLY LOCALIZED ECRH in W7-AS

U. Gasparino, H.J. Hartfuß, H. Maaßberg, N. Marushchenko*, W. Pernreiter, M. Romé

Max-Planck Institut für Plasmaphysik, *EURATOM Ass., D-85748 Garching, Germany*
* Institute of Plasma Physics, NSC-KhIPT, *310108 Kharkov, Ukraine*

W7-AS is a modular stellarator with 5 field periods. Close to the plasma axis the poloidal Fourier components of the 3-D magnetic field tend to vanish and the configuration becomes similar to five "toroidally linked mirrors". During on-axis ECRH, the highly focused injected beam interacts, besides passing particles, with only the trapped particle population confined in the mirror where ECRH is launched. In low density ECRH discharges in magnetic configurations with high fractions of trapped particles, strong toroidal anisotropy in the electron distribution function may arise. Aim of this paper is the quantitative evaluation of the collisional redistribution of the deposited power between the different classes of trapped particles and an investigation of the possibility to detect experimentally the ECRH driven toroidal inhomogeneities by means of the ECE diagnostic.

• ECRH DRIVEN TOROIDAL ANISOTROPIES •

The problem has been investigated by means of the bounce-averaged Fokker-Planck code FPTM /1/ suitable for the study of ECRH in periodic magnetic fields. The analyzed scenarios refer to second harmonic on-axis heating by a collimated beam of X-mode polarized waves injected perpendicularly from low-field-side in the "minimum B" and the "maximum B" magnetic configurations characterized by a local minimum or a local maximum, respectively, in the toroidal plane where the ECRH beam is injected /2/. While in the case of "maximum B", the power is mainly deposited to passing particles and redistributed toroidally in a rather uniform way, in the case of "minimum B" strong local perturbations of the distribution function can arise for the population of electrons trapped in the local toroidal mirror where ECRH is injected, as shown in Fig. 1 (for a target plasma with density $n_0 = 1 \cdot 10^{13}$ cm^{-3}, temperature $T_0 \simeq 1400$ eV, ECRH power density 5 W/cm^3). In this mirror, the deviations from the Maxwellian distribution are considerably stronger than those found in the other mirrors where heating appears only due to collisional energy transfer from passing particles.

In steady-state, the redistribution of density and energy between the different populations of particles is mainly determined by the balance between ECRH and collisions. The increase of the perpendicular energy of the electrons resonant with the ECRH beam, has two main consequences: the power absorbed by "barely" passing particles can cause their trapping, while the power deposited in the trapped particle region of velocity space tends to create an enhancement of trapped particles at higher energy and a depletion at lower energy. Due to the velocity dependence of pitch angle scattering, the anisotropy at low velocity is more efficiently counteracted than at high velocities, causing a net flux through the boundary between trapped and passing particles. On the other side, as trapped particles of higher perpendicular energy are poorly confined in Stellarators, losses will also play a role in the redistribution.

The ECRH driven density perturbation is shown in Fig. 2. In the "minimum B" configuration, the density of the population of directly heated trapped particles is increased mainly due to the collisional redistribution driven by ECRH. In the other mirrors loss effects are dominant and the number of trapped electrons is slightly reduced.

In the "maximum B"-scenario, the deviations are considerably smaller in amplitude (different scales are used for the ordinates in Fig. 2), as most of the power is now absorbed by passing particles and homogeneously redistributed toroidally. A qualitative similar toroidal dependence is obtained for the ECRH driven energy perturbation (the relative energy perturbation being three times greater in magnitude for the case under examination).

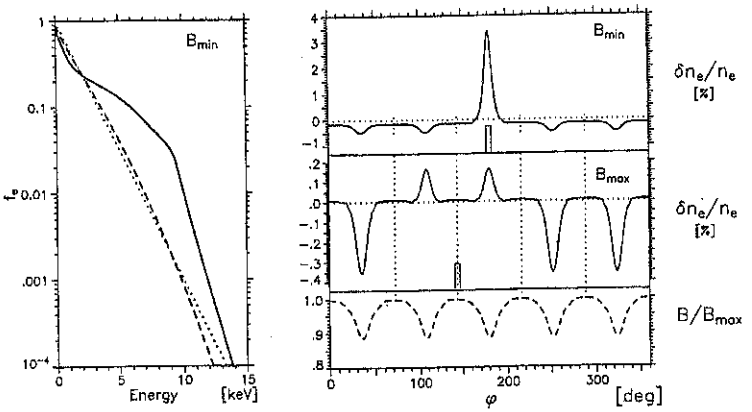

Fig. 1 *Energy spectra, along the line $v_{\|} = 0$, of the bounce-averaged distribution function. Solid line: toroidal mirror with ECRH launch; dashed-line: other mirrors; dotted line: initial Maxwellian (for reference).* **Fig. 2** *Toroidal dependence of the relative density perturbation driven by ECRH for the "minimum B"* (**top**) *and for the "maximum B"-scenario* (**center**). *The small rectangle in these figures indicates the toroidal position of the launching system. On the* **bottom** *the normalized magnetic field used for the bounce-averaging is shown.*

The inhomogeneity in the electron density generates toroidal electric fields. The density perturbation under stationary conditions is determined by the balance between the particle fluxes driven by ECRH and by these electric fields. As ions remain unperturbed, any perturbation of the electron density results in the generation of an electric field (proportional to the density gradient), that, in a self-consistent treatment, would tend to reduce the ECRH driven density perturbation.

• DETECTION BY ECE •

The ECE intensity, I, can be evaluated from the "radiative transfer equation" /3/:

$$N_r^2 \frac{d}{ds}\left\{\frac{I}{N_r^2}\right\} = \eta - \alpha I \qquad \Rightarrow \qquad \frac{I(s)}{N_r^2} = \int_0^s ds' \frac{\eta(s')}{N_r^2(s')} e^{-\int_{s'}^{s} \alpha(s'')ds''} \tag{1}$$

where N_r is the ray refractive index, η and α, the emission and absorption coefficients, respectively, and s the space coordinate along the ray trajectory.

For a Maxwellian distribution function, η and α are related by a simple multiplicative constant, in agreement with Kirchhoff's law:

$$\frac{\eta(\underline{k},\omega)}{\alpha(\underline{k},\omega)} = N_r^2 \frac{\omega^2 T}{8\pi^3 c^2}. \tag{2}$$

In the general case the evaluation of η and α requires the determination of the (warm) polarization of the wave and an integration along the resonance curve $\omega - k_{\|} v_{\|} - \frac{n\omega_{ce}}{\gamma} = 0$ in velocity space /4/. While for the emission coefficient the integrand is proportional to the electron distribution function, in the expression for the absorption coefficient a differential operator appears (corresponding to the derivative of the distribution function along the "diffusion path" in velocity space) /4/. In this paper the wave polarization has been evaluated from the Maxwellian bulk, while for the integration in velocity space the deviation of the electron distribution function predicted by the FPTM-code has been taken consistently into account.

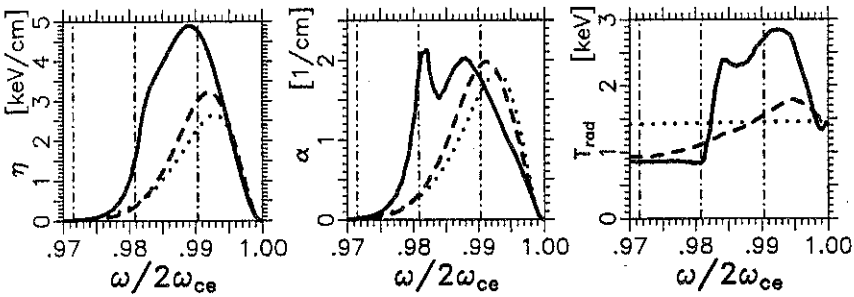

Fig. 3 **left** *(normalized) emission coefficient,* **centre** *absorption coefficient and* **right** *"radiative temperature" for the scenario of Fig.1. The same line notation as in Fig.1 is used and the vertical lines corresponds to resonant electrons with energy 15,10,5 keV, respectively.*

The normalized emission $\bar{\eta}(\underline{k},\omega) = \eta(\underline{k},\omega) \cdot (8\pi^3 c^2)/(N_r^2 \omega^2)$ and the absorption coefficients are shown in Fig.3, together with the "radiative temperature", $\bar{\eta}(\underline{k},\omega)/\alpha(\underline{k},\omega)$, for the distribution function in Fig.1.

In the ECRH injection plane ("elliptical plane") the magnetic field topology is rather similar to that found in a Tokamak ($B \propto 1/R$). Two viewing geometries have been investigated for the ECE-antenna. The first refers to perpendicular viewing from the low-field-side and the second to vertical viewing. Low-field-side observation is characterized by a rather strong gradient of the magnetic field, while for vertical observation the changes in B are weaker and a local maximum appears close to the crossing of the viewing chord with the plasma axis /5/. In order to integrate Eq.(1), the distribution function, determined by the Fokker-Planck code only close to the plasma axis, has to be extended radially. The dominant broadening mechanism is related to ∇B-drift of ripple trapped particles. This kind of "convective losses" were examined in /2/. In this paper we use a simple analytical model, $f(r,\underline{v}) = f_{Max}(r,v) + [f_{FP}(0,\underline{v}) - f_{Max}(0,v)] \cdot exp(-r^2/\sigma^2)$, where f_{Max} is the Maxwellian, f_{FP} the Fokker-Planck distribution and σ a "broadening parameter" ($\sigma = 3$ cm, in this paper). The deviation of the distribution function from the Maxwellian is therefore distributed on the magnetic surfaces in a poloidal uniform way, only the amplitude of the ECRH-driven perturbation decreases with increasing radii.

The emission spectra obtained integrating Eq.(1) along these viewing chords, for the case of 2^{nd}-harmonic X-mode emission, are shown in Fig.4. Together with the emission of a Maxellian plasma the spectra for an antenna localized in the ECRH injection mirror and in a mirror where no ECRH is injected are shown too. As the deviations expected by Fokker-Planck simulations are found at relatively low energies (see Fig.1), the emission detected by the low-field-side antenna, sensitive to the bulk properties of the distribution function, can be strongly perturbed, especially for the mirror where ECRH is injected. On the other side, the vertical observation is generally "insensitive" to perturbations in the bulk of the distribution close to the plasma axis, as this emission tends to be reabsorbed by thermal optically thick plasma at outer radii, during its propagation towards the ECE antenna. Only emission at sufficiently down-shifted frequencies can reach the antenna. No ECRH power is expected to be directly absorbed at these resonant energies and collision and radial losses mainly determine the tail population /2/. The vertically observed ECE-spectrum is therefore determined by the balance between collisions and radial losses. The response to sudden changes in the injected ECRH power (switch-on, -off, modulation) can in principle be used to separate the two mechanisms, due to the different time scales and energy dependencies /6/.

In case of ECE at optically thin harmonics, reabsorption becomes negligible and the emission from the central region, where the deviation from Maxwellian are expected to be stronger, can reach the ECE antenna under any viewing geometry. Fig.5 refers to the case of emission at

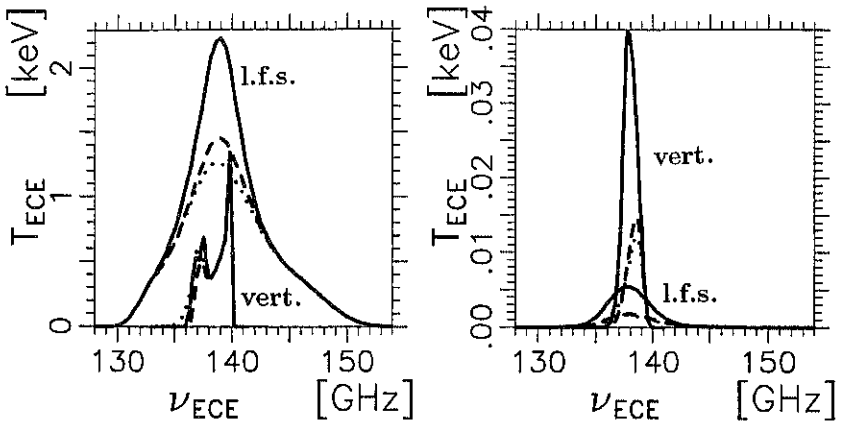

Fig. 4 *Simulated ECE-spectra for perpendicular viewing of X-mode 2^{nd} harmonic from a low-field-side antenna (l.f.s.) and for a vertically viewing antenna (vert.). The same line notation as in Fig.1 is used.* **Fig. 5** *Same as Fig. 4 but for X-mode 4^{th} harmonic emission.*

the (optically thin) 4^{th} harmonic (the magnetic field has been reduced from 2.5 to 1.25 T). The radiation temperature is relatively weak for these frequencies. The interpretation of the signals related to optically thin harmonics can be made critical due to possible contributions from wall reflection, making the presence of a "beam dump" mandatory.

• CONCLUSIONS •

Strong ECRH driven toroidal anisotropies are predicted by Fokker-Planck modelling. The deviations in the bulk of the distribution function in the toroidal mirror where ECRH is injected are expected to be strong enough to affect the ECE detected from low-field-side. The detected "radiation temperature" is expected to be substantially higher than the one detected in the other toroidal mirrors. Vertical ECE, along $B \simeq const$, due to the relation between emitting frequency and energy ($\omega - \frac{n\omega_{ce}}{\gamma} \simeq 0$) allows a more direct interpretation of the observed ECE-spectrum in terms of the "line averaged" distribution function. However, while emission at optically thin harmonics and/or high enough resonant energies can reach the vertical antenna, at optically thick harmonics, the emission related to low energy electrons located close to the plasma axis, i.e., where Fokker-Planck simulations predict the strongest deviations from Maxwellian, is generally reabsorbed during its propagation towards the antenna.

• REFERENCES •

/1/ N. Marushchenko et al., *accepted for publications in Comp. Phys. Comm.*

/2/ M. Romé et al., *Plasma Phys. Control. Fusion*, **39** (1997) 117

/3/ G. Bekefi, *Radiation Processes in Plasmas* (John Wiley & Sons, New York, 1966)

/4/ U. Gasparino, *proc. of the 8th joint workshop on ECE and ECRH, Gut Ising, (1992), IPP Report III/186, Vol. 1, p. 19*

/5/ U. Gasparino et al., *proc. of the 19th EPS Conf. on Contr. Fusion and Plasma Physics, Innsbruck (1992), Vol. 16C, Part II, p. 1001*

/6/ W. Pernreiter et al., *to be published in the proc. of the 10th joint workshop on ECE and ECRH, Ameland, (1997)*

RESONANT ELECTRON BERNSTEIN WAVE HEATING VIA MODE CONVERSION IN W7-AS

H.P. Laqua, V. Erckmann, W7-AS Team
Max-Planck-Institut für Plasmaphysik, EURATOM Ass.
D-85748 Garching, FRG,

ECRH-Group
Institut für Plasmaforschung, Univ. Stuttgart, D-70569 Stuttgart, FRG

Abstract

Electron cyclotron resonance heating (ECRH) above the plasma cutoff density with electron Bernstein waves (EBW) was investigated and successfully demonstrated at W7-AS stellarator. The EBW's were generated via O-X-B mode conversion heating from an O-wave to an X-wave and, finally, to an electron Bernstein wave. A narrow power deposition profile could be determined from a careful analysis of the soft-X emission at the power switch-off. The deposition could be shifted by changing the position of the cyclotron resonance layer.

Introduction

ECRH with electromagnetic waves is a very efficient method to heat magnetically confined fusion plasmas. However, the accessible plasma density is limited by a critical density (cutoff density). On the other hand, the prospected large stellarator W7-X will have operational regimes above the cutoff density of the proposed ECRH heating system. A possibility to overcome the density limit is the O-X-B mode conversion process proposed by J.Preinhaelter and V.Kopecký [1] in 1973. This process is a general physics phenomenon of EC-waves propagating in hot magnetised plasmas, such as ionospheric or fusion plasmas. Here O, X, and B represent the ordinary, extraordinary and electrostatic mode, the so called electron Bernstein mode. The essential part of this scheme is the conversion of an O-wave launched by an antenna from the low field side into an X-wave at the O-wave cutoff layer. This mode conversion requires an O-wave oblique launch near an optimal angle. The transverse refractive indices N_x of the O-wave and X-wave along a wave trajectory in a density gradient are connected at the optimal launch angle with a corresponding longitudinal (parallel B_0) index $N^2_{z,opt}=(Y/(Y+1))$ with $Y=\omega_{ce}/\omega$ (ω is the wave frequency, ω_{ce} is the electron cyclotron frequency) without passing a region of evanescence ($N_x^2<0$). Therefore power can be transmitted through the plasma cutoff and a fast X-wave is generated. At the upper hybrid resonance (UHR), where the X-mode branch is connected to the electron Bernstein branch, EBW's are generated and propagate, since for EBW's no density limit exists, toward the dense plasma center. A detailed description of the O-X-B mode conversion experiments at W7-AS is found in [2]. In this paper the propagation and cyclotron absorption of the EBW's in W7-AS was investigated and successfully demonstrated.

Ray tracing

Ray tracing calculations were performed in order to get a more detailed insight into the O-X-B-scheme and to show the propagation and absorption of the EBW's. Density, temperature and magnetic field profiles similar to that of a typical neutral beam sustained W7-AS plasma were used for model calculations in a torus. We use the nonrelativistic hot dielectric tensor with a correction for electron ion collisions given by [3] and an isotropic electron temperature. The ray trajectories in the equatorial plane are shown in Fig. 1. The beam is launched from the low field side and propagates through the cutoff, where it is converted into an X-mode. Then it moves back to the UHR-layer, where the X-B-conversion takes place. The EBW's are absorbed near the cyclotron resonance at the plasma centre. A small fraction of the beam power is lost at the UHR due to finite plasma conductivity. The power deposition zone for resonant heating strongly depends on the magnetic field and electron temperature as shown in Fig.1.

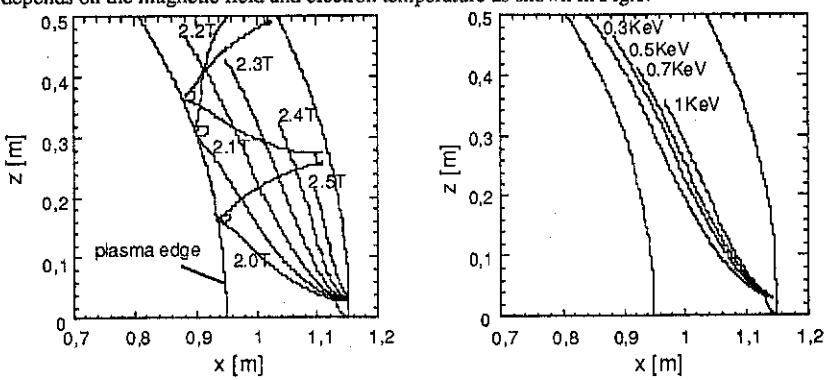

Fig.1 Results of ray tracing calculations.
Left picture: Ray trajectories of 70 GHz EBW's in a plasma torus for different magnetic fields. The central density was 1.5 $10^{20}m^{-3}$ and the central temperature was 500 eV. In the resonant case the trajectory was calculated until 99% of the power was absorbed.
Right picture: Ray trajectories for different central plasma temperatures at a central magnetic field of 2.2 T and a density of 1.5 $10^{20}m^{-3}$.

EBW's experience a cutoff layer ($N \rightarrow 0$) at the UHR surface, which in the nonresonant or higher harmonic ($\omega_{ce}/\omega < 1$) field totally encloses the inner plasma. The radiation is then trapped inside the plasma like in a hohlraum. The EBW's are either reflected at the UHR surface in the case of an oblique angle of incidence or are back converted to X-waves which are converted again to the EBW's at their next contact with the UHR. Radiation can only escape through the small angular window for O-X- and X-O-conversion, respectively. In the absence of an electron cyclotron resonance in the plasma the EBW's may be absorbed due to finite plasma conductivity after some reflections at the UHR-layer. In the resonant case due to the nonvanishing parallel component $N_{\parallel} \approx N_{z,opt}$ of the refractive index in the oblique launch the cyclotron absorption is strongly Doppler shifted.

Experimental set-up

The experiments were performed at the W7-AS stellarator (major radius R= 2.0m , minor radius a= 0.18m) with two 70 GHz gyrotrons with 170 KW power each. A detailed description of W7-AS and its 70 GHz ECRH system can be found in [4]. The central magnetic field was set between 2.0 and 2.5T and the edge rotational transform ι, taken from the magnetic reconstruction, near 0.35 according to the experimental requirements. The central density of the neutral beam injection (NBI) sustained target plasma was up to 1.5 10^{20} m^{-3}, which is more than twice the 70 GHz O-mode cutoff density. The NBI power was 360 KW in co-injection. At the ECRH launch position the stellarator plasma has an elliptical shape similar to D-shaped tokamak. In the equatorial plane the magnetic field as a function of the effective radius r_{eff} is approximately given by the following relation: $B(r_{eff}) = B_0 A / (A - r_{eff} / a)$ with A= 10.5. The power deposition was estimated from the change of the temperature profile at the power switch-off. Since the density was far above the ECE cutoff, the temperature profiles were calculated from the soft-X emission and the Thomson scattering diagnostic. The central temperature was 500 eV. The X-ray emission was monitored by an array of 36 silicon detectors with a 25 µm beryllium filter. To obtain the radial X-ray emission profile the signals were inverted to the magnetic flux co-ordinates. The time resolution was 0.1 ms and the radial resolution was about 1cm.

Experimental results

The soft-X intensity I_{SX} at the detector is approximately given by the following formula:

$$I_{sx}(T_e) = c_{fit}\, n_e^2 Z_{eff} \sqrt{T_e}\, \exp\left(-\frac{E_{filter}}{T_e}\right),$$

where n_e is the electron density, which we take from the Thomson scattering diagnostic, T_e is the temperature, and E_{filter} is the cutoff energy of the filter (1keV for 25 µm Be). Z_{eff} is assumed to be constant over the radius. At the time of Thomson scattering the linearity of this relation was checked with the Thomson temperature over the full temperature range and a proportionality factor c_{fit} was estimated. Assuming that n_e and Z_{eff} do not change during the ECRH power switch-off the temperature difference is then

$$\Delta T_e = \left(\frac{dI_{sx}}{dT_e}\right)^{-1} \Delta I_{sx}.$$

Since for small time scales the radial heat transport is low, the difference of two soft X-ray profiles with Δt=3ms immediately after the ECRH switch-off represents the upper limit of the relative ECRH absorption profile. The local power deposition was estimated from the heat wave at the power switch-off taking into account the radial symmetry of the temperature profile. In Fig.2 the absorption profiles for different magnetic fields are shown. The absorption is strongly Doppler shifted due to the oblique launch and moves from the high field side at 2.0T through the center (2.2T) to the low field side at 2.3T with increasing magnetic field, which clearly demonstrates the propagation and the local cyclotron absorption of the EBW's for the

first time. In comparison with the ray tracing results the experimental absorption is more Doppler shifted than the calculated one, which may be related to an only rough modelling of the stellarator magnetic field geometry in the ray tracing code.

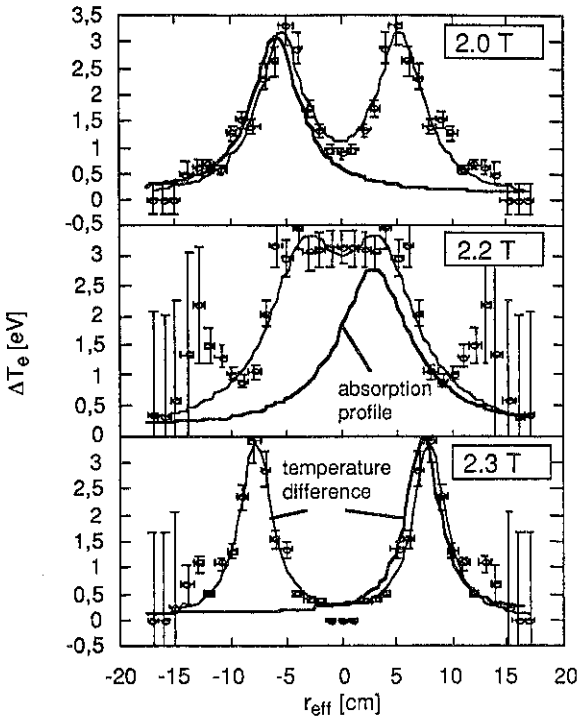

Fig.2
Changes of temperature 3ms after O-X-B heating switch-off and the related ECRH absorption profiles different central magnetic fields.

Conclusions

ECRH of an overdense plasma with 70 GHz electron Berstein waves was clearly demonstrated in W7-AS. The EBW's were generated via mode conversion in the O-X-B process. The position of the narrow absorption profile, estimated from the soft-X emission, could be changed by a shift of the cyclotron resonance layer. Thus the propagation and the local resonant cyclotron absorption of EBW's was shown, which is an excellent test of hot plasma wave theory.

References

[1] J.Preinhaelter and V.Kopecký , J. Plasma Phys. 10 (1973) 1;
[2] H.P. Laqua et al., Phys. Ref. Let. Vol. 78, No.18, pp.3467-3470, 1997
[3] T.H.Stix:"THEORY OF PLASMA WAVES"; McGraw-Hill, 1962
[4] H. Renner et al., Plasma Phys. and Contr. Fusion, Vol.31, No.10, pp.1579-1596, 1989.

Analysis of W7-AS Mirnov data using SVD and correlation techniques

M. Anton, R. Jaenicke, A. Weller, J. Geiger, W7-AS-Team, NBI- and ECRH-Groups
Max-Planck-Institut für Plasmaphysik, EURATOM Association,
Boltzmannstr. 2, D-85748 Garching, Germany

Introduction: The modular stellarator W7-AS is equipped with three poloidal arrays of Mirnov probes, two with eight, one with sixteen coils measuring the rate of change of the poloidal magnetic field. Data are acquired at a rate of $333kHz$ and $250kHz$, respectively. Analysis comprises SVD, correlation and Fourier techniques. The aim is to identify MHD instabilities, the influence of which on stellarator confinement is often unclear.

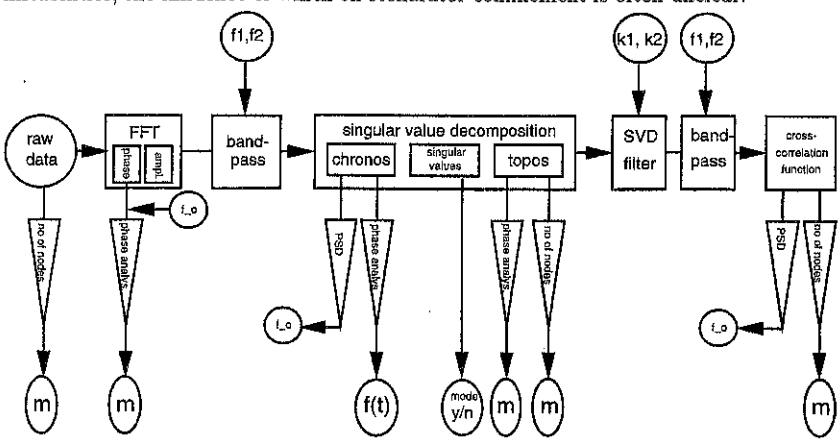

Fig. 1: Schematic of mode analysis: circles indicate input data/parameters, boxes represent entities of different decompositions. Triangles describe ways to analyse the decomposition entities, e.g. *power spectral density or phase analysis of SVD chronos. Output data are represented by 'eggs'. Further explanations see text.*

Data Analysis: Raw data are FFT'd and band-passed to eliminate parasitic signals such as pick-up from the thyristors of W7-AS' power supply.

Singular value decomposition (SVD) or biorthogonal decomposition (BD) [1] splits a matrix $\mathbf{X}$ $(M \times N, M > N)$, containing N time series of M samples of N probes into three matrices: $\mathbf{U}(M \times N)$, $\mathbf{V}(N \times N)$. and a diagonal $\mathbf{S}$.

$$\mathbf{X} = \mathbf{U} * \mathbf{S} * \mathbf{V}^{\dagger} \tag{1}$$

The columns of **V** are spatial "eigenvectors" or *topos* (figs. 2c, d), the columns of **U** are temporal "eigenvectors" or *chronos* (figs. 2e, f), ordered with respect to variance ("importance") which is reflected by the monotonuously decreasing singular values contained in **S** (fig. 2b).

If two of the singular values are approximately equal, the corresponding *topos* and *chronos* describe one single, but rotating perturbation. In that case, the *topos* reveal the dominant m (figs. 2c, d), as does the relative phase of the two neighbouring *topos* (figs. 2g, h), which is analysed in the same manner as phases obtained from FFT [3] The relative phase of the corresponding *chronos* yields a time–resolved frequency [1] (figs. 2i, j).

In our example, SVD components with $k \geq 4$ will contain mostly noise (see the discussion in [1]). A non-Fourier noise–filtering may thus be obtained if the higher order singular values are set to zero when reconstructing **X** according to eq. (1).

The normalised cross correlation function (NCC) [2] is calculated from SVD–filtered data using selected *topos* and *chronos* $k_1 \ldots k_2$ *. Probe 1 (outboard midplane, fig.3a) serves as a reference channel and $j = 1 \ldots N$:

$$c_{1j}(p) = \frac{1}{2\,M+1} \sum_{i=-M}^{M} x_1(i) x_j(i-p) \qquad (2)$$

The correlation diagram, *i.e.* a plot of $c_{1j}(p)$ *vs.* the time lag p and the probe position reveals the frequency, the sense of rotation and the dominant poloidal harmonic m (figs. 2k, l, o, p).

For the frequencies of maximum power spectral density yielded by the coherence spectra and the spectra of the relevant *chronos*, m is obtained by FFT phase analysis** [3].

A comparison with calculated phases or correlation diagrams which are obtained using the assumed m and the straight field line angle θ^* from the vacuum configuration is often extremely helpful. Such calculations are shown in figs. 2g, h, o, p as dashed curves and in figs. 2k, l as overlayed solid curves.

Result of the analysis example: We state the presence of two different modes. The first one rotating in the *ion* diamagnetic drift direction (fig. 2k) is possibly a beam-driven GAE mode. The power spectral density of its two *chronos* is very sharply peaked at $37kHz$. The poloidal structure appears to be more consistent with $m = 4$ (see figs 2g,

*An FFT band-pass filter may be used additionally.

**This is not shown here, but looks essentially the same as figs. 2g, h

k, o), although the correlation diagram exhibits some distortions (fig. 2k). The second mode with $m = 3$ rotates in the *electron* diamagnetic drift direction (fig. 2l). The power spectrum reveals a rather broad peak about $25kHz$.

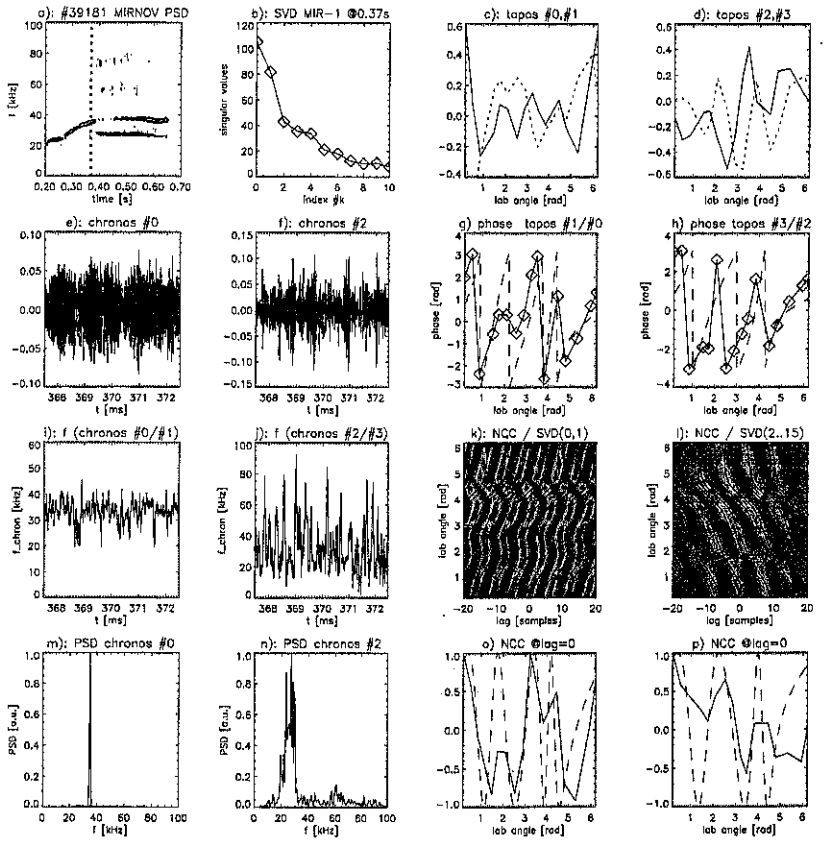

Fig. 2: Mirnov analysis of W7-AS discharge # 39181, a purely NBI heated D plasma: $P_{NBI} = 0.5MW$, line density $\approx 4 \cdot 10^{19}m^{-2}$, central electron temperature $\approx 700eV$, extraordinary good energy confinement of $\tau_E \approx 40ms$ [4] in spite of comparatively strong MHD activity. Data were taken with the 16-probe array (compare fig. 3a) at a sampling rate of 250kHz. 1000 samples centered about 370ms were selected. Further explanations see text.

Reliability: Any difficulties arising from noisy data are presumably circumvented by the use of the analysis procedure described above. Persisting problems are essentially caused by geometry, *i.e.* by a too high m, a too great distance between the probes and the source of the magnetic signal or by inadequate poloidal positions of the probes.

In order to quantify these limitations, time series of simulated Mirnov signals have been produced for the 16-probe array (fig. 3a). Based on theoretical equilibria, modes with $m-$ numbers between 2 and 6 at different radial positions $2cm \leq r_{eff} \leq 15cm$ have been simulated. The degree of agreement of the analysis result with the actual m is displayed in fig. 3b. Identification of modes with $m \geq 6$ is impossible, due to the short decay lengths of high multipoles. It is feasible to identify $m = 5$ if the perturbation is located at $r_{eff} \geq 12cm$. If the mode is located inside $r_{eff} \approx 10cm$ which is frequently the case for GAE modes [5,6], $m = 3$ and $m = 4$ may already be hard to distinguish.

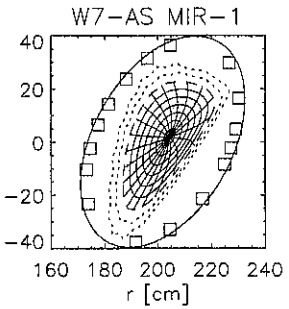

Fig. 3a: array of 16 $\dot{B}_\theta$-probes (MIR-1). Contours indicate flux surfaces of a sample vacuum configuration. The dashed contour corresponds to $r_{eff} \approx 17cm$.

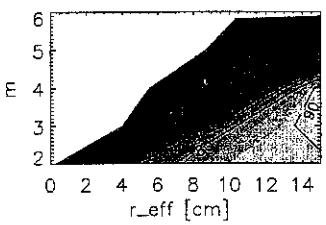

Fig. 3b: fraction of correctly determined poloidal harmonics m as a function of r_{eff} and m. Contours represent levels of 10% to 90% agreement.

References:

[1] **Dudok de Wit, T** et al.: Phys. Plasmas **1** (10) p3288 (1994)

[2] **Press, W H** et al.: "Numerical Recipes in FORTRAN", 2nd Ed., Cambridge (1992)

[3] **Harley, T R** et al.: Nuclear Fusion, **29** (5) p771 (1989)

[4] **Stroth, U** et al., this conference

[5] **Weller, A** et al., this conference

[6] **Goerner, C** et al., this conference

Correlation between MHD-activity, energetic particle behaviour and anomalous transport phenomena in WENDELSTEIN 7-AS

A. Weller, M. Anton, J. Geiger, C. Görner, R. Jaenicke,
C. Konrad, F.P. Penningsfeld, N. Rust, D.A. Spong*), C.Y. Teo
W7-AS Team, NBI Group, ECRH Group**)

Max-Planck-Institut für Plasmaphysik, EURATOM-Association, D-85748 Garching, Germany
*) *Oak Ridge National Laboratory, Oak Ridge, Tennessee, USA*
**) *Institut für Plasmaforschung, Universität Stuttgart, D-70569, Germany*

Introduction - Energy and particle transport in W7-AS exhibits a resonance-like dependence on the edge rotational transform (iota) as long as the magnetic shear is relatively weak (low β, no significant net toroidal currents). MHD modes at resonant surfaces may cause enhanced radial transport depending on the magnitude and radial extent of the magnetic perturbations. In many cases discharges in W7-AS are very quiescent, or in case of mode activity, often no influence on energy and particle confinement is found. In the high beta regime ($\langle\beta\rangle \leq 1.8\,\%$) shear is increased due to the effect of the Shafranov shift leading to the formation of low order rational surfaces inside the plasma. Pressure driven mode activity appears at corresponding resonant surfaces. These modes could be resistive interchange instabilities since the respective stability criterion can be violated at least in the outer part of the plasma. Only around the highest beta values and in cases, where the magnetic well of the configuration was reduced, relaxations of the plasma energy are observed, indicating the vicinity of a soft beta-limit. In most cases, however, the maximum achievable beta is determined by the available heating power.

Effect of NBI driven global Alfvén Eigenmodes on plasma confinement - Most of the MHD activity observed occurs during neutral beam injection (NBI) in the lower beta regime, where low order rational surfaces can be avoided due to the very low shear of the configuration. Away from but close to resonant surfaces gaps in the shear Alfvén spectrum are present, where global Alfvén eigenmodes (GAE) can be excited by resonant fast ions of the beam distribution. In NBI heated plasmas GAE activity often coincides with the iota-range of degraded confinement. However, this is also the range where formation of low (m,n) Alfvén gaps becomes possible. Since the resonant confinement degradation also occurs during ECRH, where no fast ion population is present and only very weak MHD-activity is observed, it is conjectured, that magnetic turbulence phenomena around the dense high (m,n) resonant surfaces are causing this effect. From the analysis of iota-profiles it is concluded, that the main low (m,n) resonances are less unfavourable because their neighbourhood is free of resonances. In the period after switch on of NBI very pronounced GAE activity causing enhanced transport can be excited due to transiently unstable fast ion velocity distributions. In particular, when the target plasma has very low density or the discharge is initiated by the

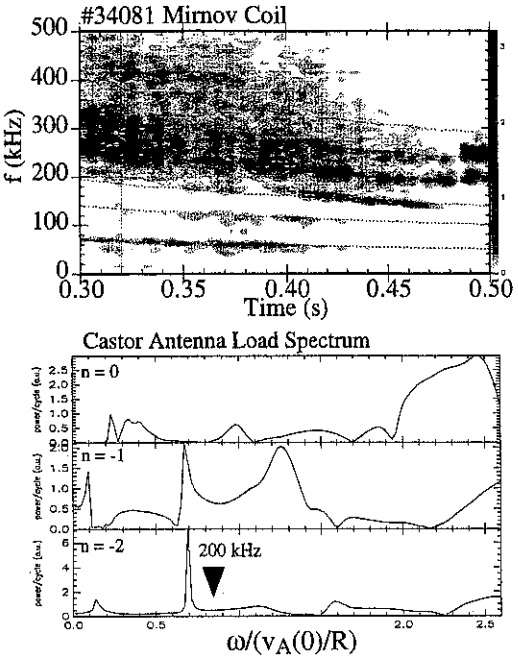

Fig. 1: Global Alfvén frequency contours (top) during NBI density ramp. The dashed lines indicate the temporal evolution of the Alfvén speed. Bottom: antenna loading spectrum calculated with the CASTOR code for n=1,2,3.

neutral beams, even more unfavourable fast ion distributions can be formed due to charge exchange effects. In this case in addition to the low frequency (20 - 40 kHz), low (m,n) GAE-activity a broad frequency range of activity extending up to 500 kHz is found by magnetics and various fluctuation diagnostics. The origin of this activity can be explained by Alfvén modes of higher mode numbers. GAEs, but also global Alfvén modes in gaps induced by ellipticity or higher non-symmetry (EAE, NAE) could play a role. Fig. 1 shows the change of the frequency spectrum (Mirnov coil) with the change of the Alfvén speed. Simulations of a (virtual) antenna loading spectra with the CASTOR code [1] reveal a number of resonances in the frequency range of the experimental data. The high frequency activity has set in later than the low (m,n) GAE's, which can already be excited by sub-Alfvénic beam ions via toroidal sideband excitation. For a number of cases also MHD calculations of Alfvén instabilities were performed with a gyrofluid model for the fast particles [2], which are consistent with the observed MHD activity. The analysis of mode structures, which is important for comparisons with theory, has been improved by a 10-camera soft X-ray system with 320 channels [3] and new analysis techniques for the magnetic probes [4].

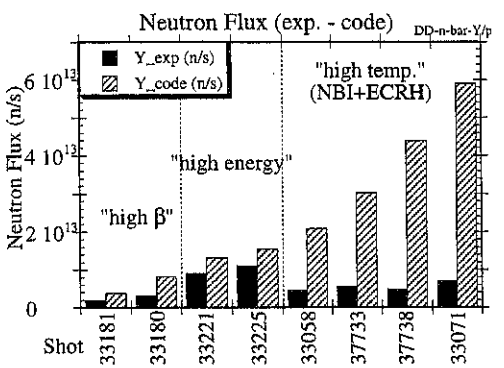

Fig. 2: The discrepancy between measured and calculated neutron rates increases at low collisionalities with increasing slowing down times(selected shots)

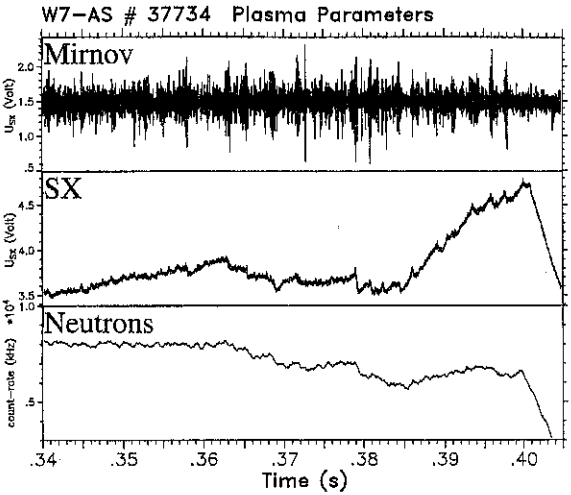

Fig. 3: Correlation between GAE bursts and reaxations of the soft X-ray intensity and neutron rate

Another regime where strong effects on transport are caused by beam driven Alfvén modes is at low electron collisionality achieved with combined ECRH and NBI heating. Under these conditions the classical slowing down time can be up to 50 ms exceeding clearly the energy confinement time. A transition from continuous GAE modes to bursting GAE activity occurs, which is accompanied by losses of fast particles and thermal plasma energy. This has been inferred from data obtained with deuterium injection using the neutron rate as a measure of the fast particle density since beam-target reactions are the dominating neutron production process. The magnitude of the stationary neutron flux was found to be significantly lower than predicted values (fig. 2), and in addition, relaxations of the D-D neutron rate and soft X-ray signals in correlation with the MHD bursts are observed (fig. 3). The loss rate of energetic particles, can be estimated roughly from $\tau_{fast} \approx \Delta t \cdot (\Delta\phi/\phi)^{-1}$, where Δt and $\Delta\phi/\phi$ are the average time between bursts and the average relative drop of the neutron flux, respectively. The fast particle confinement times derived in single cases are of the order of the slowing down time. Since resonances often occur with ions of relatively low velocities (< 1/3 injection velocity), which do not contribute to the neutron production, this analysis may underestimate the total loss rate.

Alfvén modes in the absence of fast particles - MHD activity presumably due to GAE modes is also observed in ECRH plasmas without NBI. These modes are weaker as compared with NBI driven GAE modes and are preferentially seen under degraded confinement conditions without being the direct cause of enhanced thermal transport. Whereas during NBI the propagation is in the (fast) ion diamagnetic drift direction as expected from the ion drift excitation process, it is opposite during ECRH only. The frequencies are consistent with GAE modes inside the lowest Alfvén continuum gap (fig.4). The observations are similar to results of TFTR [5] and ASDEX Upgrade [6] where TAE modes were found in the OH phase. A possible excitation mechanism considered recently is the coupling of $\mathbf{E} \times \mathbf{B}$ turbulence to

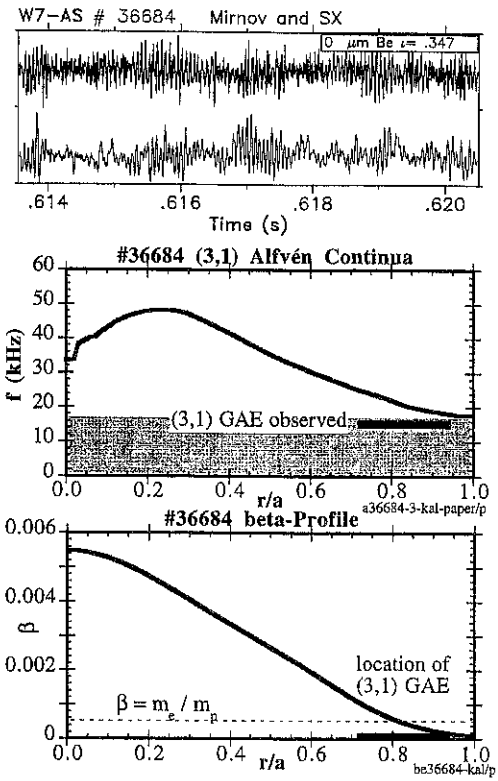

Fig. 4: Global Alfvén Eigenmodes (GAE) in ECRH plasma (Mirnov and SX signals top), Alfvén gap structure (middle) and beta profile (bottom).

electromagnetic drift Alfvén turbulence cascading into low $k_\parallel$ Alfvén waves [7,6]. The local β-values at the location of the modes is in the range where such coupling is expected (fig. 4, bottom). A correlation between MHD-activity, broadband turbulence and enhanced transport is found in many cases including NBI discharges.

Conclusions - The dependence of the confinement on the magnetic configuration cannot be explained simply by low (m,n) magnetic field resonances ("natural" islands and other static field perturbations) or mode activity. Global Alfvén modes emerge from the multiformity of MHD activity in W7-AS as most prominent instabilities. Since their propagation requires finite $k_\parallel$ (or a gap in the continuous Alfvén spectrum), GAE modes with mode numbers (m,n) cannot be easily suppressed by avoiding the corresponding rational surface iota=n/m in the confinement region. The effect of Alfvén modes on energy and particle transport is significant only during transient phases of bursting modes and in the low collisionality regime with NBI. Drift Alfvén turbulence is considered to be an important process to explain both, the resonant anomalous transport and the excitation of GAE's in ECRH plasmas.

References

[1] G.T. Huysmans et al., Physics Plasmas 2, 1605 (1995)
[2] D.A. Spong, B.A. Carreras and C.L. Hedrick, Phys. Fluids **B 4**, 3316 (1992)
[3] C. Görner et al., this conference
[4] M. Anton et al., this conference
[5] Z. Chang et al., Nuclear Fusion 35, 1469 (1995)
[6] M. Maraschek et al., this conference
[7] B. Scott et al., 16th IAEA Fusion Energy Conf., Montreal, 1996, IAEA-CN-64/D-3-4

The Shear Alfvén Continuum of an Ideal MHD Equilibrium without Spatial Symmetry

A. Salat
Max-Planck-Institut für Plasmaphysik, Euratom Association, Postfach 1533,
85740 Garching bei München, Germany
J. A. Tataronis
University of Wisconsin-Madison, 1500 Engineering DR, Madison, WI 53706, USA

The Shear Alfvén continuum in an *asymmetric* plasma configuration that is an exact solution of the equilibrium equations of ideal magnetohydrodynamics is treated. It is found that the Alfvén continuum has two components: a continuous component that is characterized by modes defined over the entire magnetic surface, and a discrete component characterized by modes localized with a finite decay length on specific magnetic field lines. The localized modes, the *nonsymmetry induced Alfvén eigenmodes* (NAE), do not occur in symmetric plasmas.

The shear Alfvén continuum of ideal magnetohydrodynamics has received considerable interest in the past because of its potential importance for plasma heating and current drive, and because of its possible effects on plasma stability. The key feature of the shear Alfvén wave in the continuum is its spatial singularity about surfaces of constant pressure. What is known about the Alfvén continuum has arisen principally from studies of Alfvén wave phenomena in MHD equilibria with spatial symmetries, such as the one-dimensional cylindrical screw pinch and the two dimensional toroidal tokamak. Equilibria without symmetries have received minimal attention, in part because the existence of asymmetric MHD equilibria has not been clearly established. Recently, however, several classes of asymmetric ideal MHD equilibria have been found [1]. These particular equilibria are parallel to a straight, infinite, magnetic axis (z axis). The magnetic lines of force twist about the axis and form closed magnetic surfaces. In the limit of plasma $\beta \ll 1$ the Cartesian components of the magnetic field $\mathbf{B}$ are

$$\begin{aligned} B_x &= -B_0\, \mathrm{e}^{\kappa z} \sin(\kappa x)\,/\,2, \qquad B_y = B_0\, \mathrm{e}^{-\kappa z} \sin(\kappa y)\,/\,2\,, \\ B_z &= B_0\,[\,\mathrm{e}^{\kappa z} \cos(\kappa x) + \mathrm{e}^{-\kappa z} \cos(\kappa y)\,]\,/\,2\,, \end{aligned} \tag{1}$$

where B_0 is the value of magnetic field at $z = 0$ on the axis $x = y = 0$, and κ is a length scale parameter. The magnetic field lines are embedded in the surfaces $F = \text{const}$, i.e. $\mathbf{B} \cdot \nabla F = 0$, with

$$F(x,y,z) \equiv \mathrm{e}^{2\kappa z} \sin^2(\kappa x) + 2[1 - \cos(\kappa x)\cos(\kappa y)] + \mathrm{e}^{-2\kappa z} \sin^2(\kappa y)\,. \tag{2}$$

see Fig. 1. In the limit $z \to \pm\infty$ the cross section condenses into an infinitely thin sheet.

The Alfvén continuum, i.e. its frequencies and modes, in the limit of small plasma β, is governed by a single second-order ordinary differential equation along the magnetic field lines [2]. If z is used as a label along the field line chosen the mode equation becomes

$$\frac{\mathrm{d}}{\mathrm{d}z}\left[p(z)\frac{\mathrm{d}u}{\mathrm{d}z}\right] + \Lambda s(z)u(z) = 0\ , \tag{3}$$

where $p = \hat{B}_z/Q$, $s = 4/(\hat{B}_z Q)$, $Q = \hat{B}^2/(\nabla F)^2$ and $\Lambda = \mu_0\rho\omega^2/B_0^2$. In these definitions, μ_0 and ρ are, respectively, the vacuum permeability and the plasma mass density, while $\hat{B}_z$ and $\hat{B}$ are, respectively, the z component and the magnitude of $\mathbf{B}$ normalized with respect to $B_0/2$. For the time dependence of the mode the ansatz $u(z,t) = u(z)\exp(i\omega t)$ was made. Λ equals the frequency squared divided by the square of the Alfvén speed on the magnetic axis. The coefficients $p(z) \equiv p(x(z), y(z), z)$ and $s(z)$ in Eq. (3) have to be taken along the magnetic field line $x = x(z)$, $y = y(z)$. The field line orbit is determined by the coupled system of differential equations

$$\mathrm{d}x/\mathrm{d}z = B_x(x,y,z)/B_z(x,y,z)\ , \qquad \mathrm{d}y/\mathrm{d}z = B_y(x,y,z)/B_z(x,y,z)\ . \tag{4}$$

If $\Lambda \sim \omega^2$ is real, Eq. (3) is self-adjoint, provided $R \equiv \lim_{a\to\infty} pu^*\mathrm{d}u/\mathrm{d}z|_{-a}^{+a}$ is bounded. The latter condition in practice reduces to the requirement that $u(z)$ be bounded asymptotically, as $z \to \pm\infty$.

Within these premises, the nature of the Alfvén spectrum still depends on the details of the asymptotic behavior of $u(z)$. Two general classes of solutions and therefore spectral components can be identified according to whether the integral $I \equiv \int_{-\infty}^{+\infty} u^2(z)\,\mathrm{d}z$ is bounded or not. If I is bounded, Λ is a *discrete eigenvalue*. The associated mode $u(z)$ is a *discrete* or *localized eigenfunction* which falls off to zero asymptotically for $|z| \to \infty$. If I is unbounded, Λ is in the *continuous spectrum* and the associated mode $u(z)$ is an *extended eigenfunction* which stretches along the whole infinite length of the field line.

On magnetic surfaces close to the axis, $|\kappa x|$, $|\kappa y| \ll 1$, Eqs. (4) can be solved analytically. There results $x(z) = x_0\left[2\mathrm{e}^{-\kappa z}/(\mathrm{e}^{\kappa z} + \mathrm{e}^{-\kappa z})\right]^{1/2}$, $y(z) = y_0\left[2\mathrm{e}^{\kappa z}/(\mathrm{e}^{\kappa z} + \mathrm{e}^{-\kappa z})\right]^{1/2}$, where x_0 and y_0 are the transverse coordinates of the field line in the plane $z = 0$. Equation (3) becomes

$$\frac{\mathrm{d}}{\mathrm{d}z}\left[\left(\mathrm{e}^{\kappa z}x_0^2 + \mathrm{e}^{-\kappa z}y_0^2\right)\frac{\mathrm{d}u}{\mathrm{d}z}\right] + \frac{\mathrm{e}^{\kappa z}x_0^2 + \mathrm{e}^{-\kappa z}y_0^2}{\cosh^2(\kappa z)}\,\Lambda\,u(z) = 0\ . \tag{5}$$

For $\alpha \equiv y_0^2/x_0^2 = 1$, Eq. (5) can be solved by substituting $\kappa\tau(z) = \arctan[\sinh(\kappa z)]$. This yields the equation, $\mathrm{d}^2u/\mathrm{d}\tau^2 + \Lambda\,u = 0$, which, for Λ real, has the solutions,

$$u(z) = d_1 \sin\left[\sqrt{\Lambda}\arctan(\sinh z)\right] + d_2\cos\left[\sqrt{\Lambda}\arctan(\sinh z)\right], \quad \text{for } \Lambda > 0\ , \tag{6}$$

$$u(z) = d_3 \exp\left[\sqrt{-\Lambda}\arctan(\sinh z)\right] + d_4\exp\left[-\sqrt{-\Lambda}\arctan(\sinh z)\right], \quad \text{for } \Lambda < 0\ , \tag{7}$$

where (d_1, d_2, d_3, d_4) are integrating constants, and κ has been set equal to 1.

On the stable side of the spectrum, where $\Lambda > 0$, localized eigenmodes do exist. The boundary conditions $u(\pm\infty) = 0$ for Eq. (6) are satisfied with $\Lambda = \Lambda_m = m^2$, $m = 1, 2, 3, \ldots$ with the corresponding eigenfunctions $u_1(z) = 1/\cosh z$, $u_2(z) = \sinh z/\cosh^2 z$, $u_3(z) = (1 - 3\sinh^2 z)/\cosh^3 z$, etc. In Fig. 2, the eigenfunctions $u_1(z)$ and $u_{10}(z)$ are shown. Note that the analogue of Eq. (3) does not have localized solutions in axisymmetric configurations as follows from the theory of differential equations with periodic coefficients. In nonaxisymmetric toroidal MHD equilibria, however, provided such equilibria exist, localization seems to be possible again [3].

In addition to discrete modes, the $\alpha = 1$ solutions also yield continuum modes. For $\Lambda \neq \Lambda_m$ all solutions (6) and (7) asymptotically tend towards a nonvanishing constant, at least at one end of the configuration. This implies the divergence of the integral I. Consequently, the continuous spectrum consists of the entire complex ω plane. If $\mathrm{Im}(\omega) < 0$, the continuum modes are unstable. Symmetric and antisymmetric stable continuum modes are shown in Fig. 3, while examples of unstable continuum modes are shown in Fig. 4. The occurrence of an unstable Alfvén spectrum characterized by $\mathrm{Im}(\omega) < 0$ in a static equilibrium contradicts conventional results. However, modes in the unstable continuum generally will not contribute to the wave dynamics of the plasma equilibrium because they are tied to specific inhomogeneous boundary conditions that must be specified at the singular ends of the equilibrium, $z \to \pm\infty$. If these conditions are not satisfied, the unstable continuum modes do not appear.

For field lines with $0 < \alpha < 1$ the spectrum and the modes have to be determined numerically. The dependence of the eigenvalues $\Lambda_1 - \Lambda_3$ on α is shown in Fig. 5. For a fixed value of Λ a sequence of continuum modes is shown in Fig. 6, displaying a smooth transition as α varies from zero to one. For $1 < \alpha < \infty$ the spectrum and the modes can be obtained by replacing α with $1/\alpha$ and z with $-z$.

Concerning the global behaviour of modes on the whole magnetic surface the following picture emerges from Figs. 5 and 6. There are frequency domains ($\omega^2 \sim \Lambda$) in which a single Alfvén continuum mode, i.e. with fixed frequency, is able to cover smoothly the whole surface, $0 \leq \alpha \leq \infty$, just as in, for example, axisymmetric equilibria. A phase on each field line and a poloidal mode number at one arbitrary position $z = \mathrm{const}$ are free. Interspersed between these continuum domains there are frequency domains in which on at least one field line the mode extension shrinks to a finite value. It is conceivable that the interaction of the plasma with e.g. externally applied waves or fast particles is concentrated in or excluded from this region.

[1] R. Kaiser, A. Salat, Phys. Rev. Lett. **77**, 3133 (1996).

[2] M. P. Bernardin, J. A. Tataronis, Phys. Fluids **27**, 133 (1984).

[3] A. Salat, Plasma Phys. Contr. Fusion **34**, 1339 (1992).

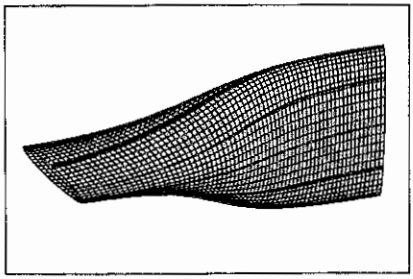

Fig. 1: *Magnetic surface* $F = 1.0$ *for* $-2.3 < z < 2.3$. *With four field lines.*

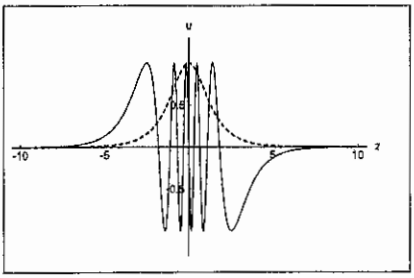

Fig. 2: *Eigenfunctions* $u_1(z)$ *(dashed) and* $u_{10}(z)$ *(solid).*

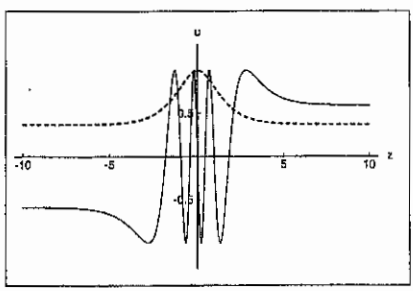

Fig.3 : *Stable continuum modes* $u(z)$ *for eigenvalue parameter* $\Lambda = 1/\sqrt{3}$ *(dashed) and* $\Lambda = 100/\sqrt{3}$ *(solid).*

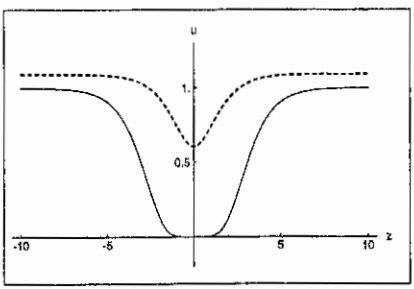

Fig. 4: *Unstable continuum modes* $u(z)$ *for eigenvalue parameter* $\Lambda = -1/\sqrt{3}$ *(dashed) and* $\Lambda = -100/\sqrt{3}$ *(solid).*

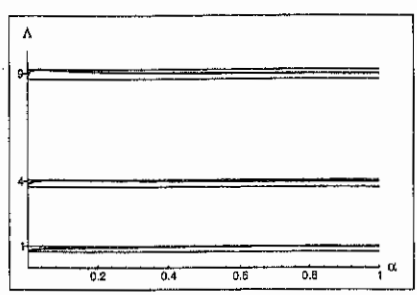

Fig. 5: *Dependence of* Λ_1 *(lower curve),* Λ_2 *(middle curve) and* Λ_3 *(upper curve) on field line position* α.

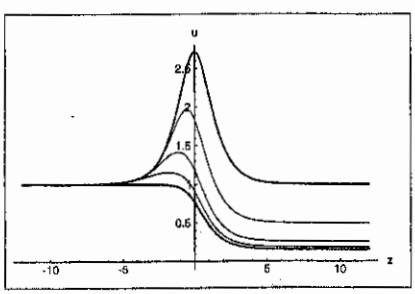

Fig. 6: *Dependence of continuum modes* $u(z)$ *on field line position* α: $\alpha = 1$ *(upper thick curve),* $\alpha = 10^{-1}$, 10^{-2}, 10^{-3} *(curves in descending order) and* $\alpha = 0$ *(lower thick curve). With* $\Lambda = 1/\sqrt{3}$ *fixed.*

Analysis of a kinetic energy principle for a 3D plasma equilibrium

Axel Könies
Max-Planck-Institut für Plasmaphysik, Teilinstitut Greifswald,
IPP-EURATOM-Association, Koitenhäger Landstr., D-17491 Greifswald

1. Introduction

Fast α-particles from fusion may destabilize toroidal Alfvén eigenmodes and ballooning modes in tokamaks, as was found e.g. in ref. [1]. In a 3D plasma confinement device there are reflected particles which are restricted to the period of the magnetic field. The latter have also been shown to be destabilizing if they are energetic [2].
Thus, a stability analysis of 3D plasma equilibria from the kinetic point of view is highly desirable.

2. Ideal MHD Energy Principle

The plasma potential energy of ideal MHD is given as [3,6]:

$$W_p = \frac{1}{2}\int\int\int d^3r \left[|C|^2 - \mathcal{A}(\vec{\xi}\cdot\nabla s)^2 + \gamma p(\nabla\cdot\vec{\xi})^2\right] \tag{1}$$

Clearly, the stabilizing terms are the fluid compression term proportional to γp and $\vec{C} = \nabla\times(\vec{\xi}\times\vec{B}) + \frac{\vec{j}\times\nabla s}{(\nabla s)^2}\vec{\xi}\cdot\nabla s$, with ξ the perturbation and s the flux label. The fluid compression term can be minimized to zero [6].
The only possibly destabilizing term $\mathcal{A}$ contains the curvature, local shear and parallel current density as destabilizing contributions.

3. Kinetic Energy Principle

The guiding center description of a plasma yields an energy principle for low frequency perturbations similar to the MHD one [4,5]. The kinetic energy principle is equivalent to the adiabatic conservation of the magnetic moment μ, the longitudinal action invariant $J = m\oint v_\parallel dl$, and - in the case of energetic particles - the flux through the drift orbit, the so called third adiabatic invariant $\Phi = \oint \alpha d\beta$ [5]. The triple (α,β,l) forms a coordinate system of flux, poloidal and field line coordinates, respectively.
This energy functional differs only in its kinetic term from the MHD result, i.e. the latter replaces the fluid compression term in eq. (1):

$$W_p = \frac{1}{2}\int\int\int d^3r \left[|C|^2 - \mathcal{A}(\vec{\xi}\cdot\nabla\alpha)^2 + W_k\right] \tag{2}$$

In the case of thermal plasmas where the particles can be assumed to be attached to the field lines the energy principle reduces to the well known Kruskal-Oberman result [4] in which the kinetic term is stabilizing. This kinetic term is given by:

$$W_k = -\frac{1}{2}\int d\alpha\, d\beta\, d\mu\, dJ \left(\frac{\partial F}{\partial \epsilon}\right)_{\alpha,\mu,J} \langle H\rangle^2 \tag{3}$$

The quantity $\langle H \rangle$ is the mean variation of the particle kinetic energy between the reflection points whereas F denotes the distribution function of the plasma with ϵ the particle energy.

Introducing the perturbation $\vec{\xi}$, the field line curvature vector $\vec{\kappa}$ and $\nu = \epsilon/\mu$ one obtains:

$$W_k = \frac{1}{2}\int d\alpha \frac{15}{8} p(\alpha) \sum_k \int d\beta \int_0^{1/B_{min}} d\nu \left(\oint \frac{dl}{\sqrt{1-\nu B}} \right)^{-1} \times$$
$$\times \left(\oint dl \left[\sqrt{1-\nu B}(2\vec{\kappa}\cdot\vec{\xi}_\perp + \vec{\nabla}\cdot\vec{\xi}_\perp) - \frac{\vec{\nabla}\cdot\vec{\xi}_\perp + \nu B \vec{\kappa}\cdot\vec{\xi}_\perp}{\sqrt{1-\nu B}} \right] \right)^2 \qquad (4)$$

This kinetic energy principle (eq.(2)) is investigated for a sequence (with sequence parameter t) of 3D magnetic field configurations interpolating between an unstable l=1,2 stellarator ($t = 0$) and the stable Wendelstein 7-X ($t = 1$). The details of the interpolation are given in ref. [7].

The stability analysis has been done with a kinetic generalization of the CAS3D code [6], the numerical field line integration scheme has been adopted from NOVA-K [8]. The eigenvalue problem corresponding to eq. (2) has been solved.

4. Results

For the computation of eq.(4) the possible particle trajectories along the field lines have to be catalogued. The torodial periodicity and the special magnetic field structure of W7-X like configurations allow a categorization of reflected particles on surfaces of constant s and ν in not more than three groups (Fig. 1).

The by far most important contributions to the kinetic energy term stem from the reflected particles. The passing particles average over the whole flux surface and are therefore almost negligible, see Fig.2. The eigenvalues of the kinetic energy principle

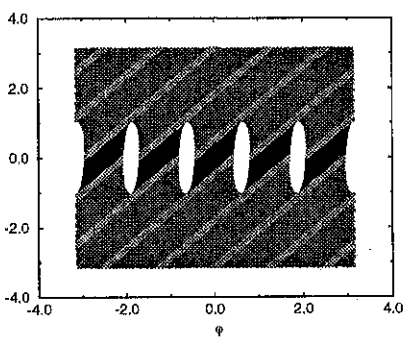

Fig.1: *shows a cut through the magnetic field strength at the $s = 0.343$ surface at $1/\nu = B_{ref} = 1.6080$. The mean B is $\langle B \rangle = 1.4752$. At the white spots $B > B_{ref}$ is valid. Their edges form the reflection points of the trajectories. It can be seen that 3 groups of particles exist: reflected within 1/5 (black), 4/5 (dark gray), 5/5 (light gray) of the torus*

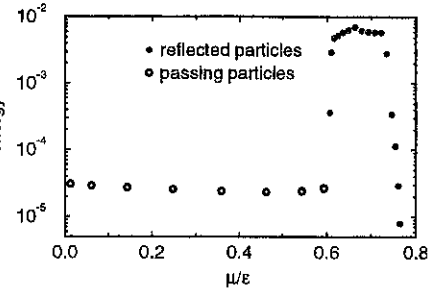

Fig.2: *The main contributions to the kinetic energy term arise from the reflected particles which are characterized by an ϵ/μ value between $1/B_{max}$ and $1/B_{min}$ on a flux surface. (here, for example the contribution from the $s = 0.34$ surface is given).*

have been calculated extending the CASSD code with eq. (2).

It can be shown that although the structure of the functional of the kinetic term is completely different from the MHD structure there exist so called mode families [6] as in the MHD analysis. The toroidal Fourier indices within a mode family differ by an integral multiple of the number of field periods. A coupling between modes of different families does not exist. Also, the so called phase factor transformation [6,7] to deal with high mode numbers can be performed as in ideal MHD.

The inclusion of the kinetic energy term into the eigenvalue problem tends to shift the main contributions from the perturbation to the plasma edge and, simultaneously, to lower them (Figs. 3,4).

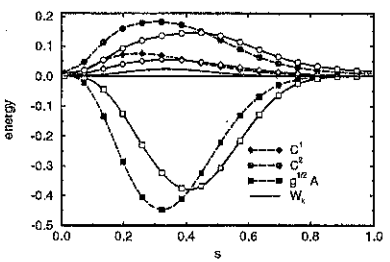

Fig.3: *Contributions to the plasma energy for the unstable $t = 0.4$ configuration and for both the ideal MHD case (broken lines) and the kinetic energy principle (full lines).*

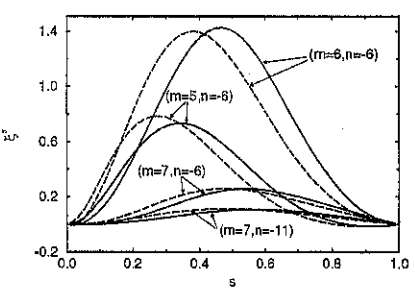

Fig.4: *The radial dependence of the four most prominent ξ^s perturbation modes (out of 12) for the sequence parameter $t = 0.4$. The ideal MHD modes are those with broken lines*

The point of marginal stability is shifted by approximately 0.1 towards lower values of the sequence parameter t compared to the ideal MHD due to the stabilizing kinetic term (Fig. 5).

A perturbative treatment of W_k with ideal eigenfunctions yields an eigenvalue which is approximately 10% larger than that from the exact solution.

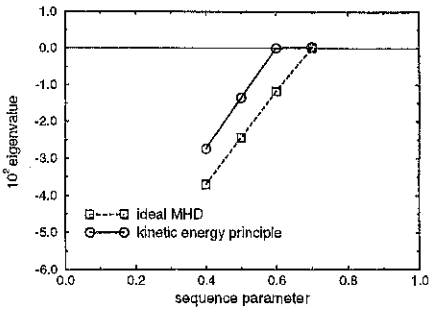

Fig.5: *Eigenvalues calculated with the CAS3D-K code for a sequence of 3D plasma equilibria.*

5. Conclusions

A kinetic energy principle for thermal plasmas (neglecting drifts) has been investigated in a 3D magnetic field and the according eigenvalue problem has been solved.

In comparison to ideal MHD the kinetic energy principle is more stable leading to a small shift of the point of marginal stability in a sequence between stable and unstable equilibria. The reflected particles have been found to be the most important contributors to the kinetic energy term in the functional.

The energy functional will serve as starting point for the investigation of hot particle instabilities. For the latter particle drifts have to be included as outlined in [5].

6. References

[1] D. Spong, et al. Fusion Technology, **18**, 496 (1990).

[2] J. Nührenberg and L.-J. Zheng, *Proc. 20th EPS Conf. Contr. Fusion Plasma Phys.* ECA17c I-413 (1993).

[3] I.B. Bernstein, E.A. Frieman, M.D. Kruskal, and R.M. Kulsrud, Proc. R. Soc. London Ser. A **244**, 17(1958).

[4] M.D. Kruskal and C.R. Oberman, Phys. Fluids **1**, 275 (1958).

[5] J.W. Van Dam, M.N. Rosenbluth, and Y.C. Lee, Phys. Fluids **25**, 1349 (1982).

[6] C. Nührenberg, Phys. Fluids B **5**, 3195 (1993).

[7] C. Nührenberg, Phys. Plasmas **3**, 2401 (1996).

[8] C.Z. Cheng, Phys. Fluids B **2**, 1427 (1990).

[9] A. Könies, DPG-Frühjahrstagung, Mainz 1997.

Computation of Stellarator Equilibria with the PIES Code Using Input of VMEC Results

S. Arndt [*], D. A. Monticello [**], A. H. Reiman [**]

[*] Max-Planck-Institut für Plasmaphysik, Teilinstitut Greifswald
IPP-EURATOM Association
D-17491 Greifswald, Federal Republic of Germany

[**] Princeton Plasma Physics Laboratory, Princeton, N. J. 08543, U. S.

Introduction

Codes for solving the MHD equilibrium equations

$$\mathbf{J} \times \mathbf{B} = \nabla p, \ \nabla \times \mathbf{B} = \mathbf{J}, \ \nabla \cdot \mathbf{B} = 0 \tag{1}$$

for finite-aspect-ratio, high-beta, 3-D configurations are necessary for the design of fusion machines and analysis of experimental data.

Due to the absence of symmetries, which guarantee the existence of nested magnetic surfaces, in stellarators the treatment of magnetic fields with islands and/or stochastic regions is required.

The **VMEC** code [1] solves the equilibrium equations by a variational method in which the total plasma energy is minimized. The VMEC code presumes a nested toroidal flux surface geometry, and hence can not deal with the magnetic islands and stochastic regions mentioned above. However, it is generally believed that the solutions found by the VMEC code represent good approximations to the solutions including islands and stochastic regions. The VMEC code is robust and yields an accurate description of the flux surfaces with a minimum of computational effort and a minimum number of poloidal and toroidal harmonics. These features make the VMEC code the the most widely used of the 3-D equilibrium codes

The **PIES** code [2] solves the MHD equilibrium equations (1) by a Picard-like iteration scheme

$$\nabla \times \mathbf{B}^{(n+1)} = \mathbf{J}(\mathbf{B}^{(n)}). \tag{2}$$

$\mathbf{B}^{(n)}$ is the magnetic field at the start of the nth iteration. The computationally intensive part of the code is the calculation of the current density $\mathbf{J}(\mathbf{B}^{(n)}) = \mathbf{J}_\perp + \mathbf{J}_\parallel$ from the equilibrium equations (1) and $\nabla \cdot \mathbf{J} = 0$. Here, $\mathbf{J}_\perp$ is the diamagnetic part and $\mathbf{J}_\parallel$ is the parallel part of the current density. These current densities are found from

$$\mathbf{J}_\perp = -\frac{\nabla p \times \mathbf{B}}{B^2}, \tag{3}$$

$$\mathbf{B} \cdot \nabla \mu + \nabla \cdot \mathbf{J}_\perp = 0 \quad \text{with} \quad \mathbf{J}_\parallel = \mu \mathbf{B}. \tag{4}$$

Using this non-variational method, the PIES code is able to handle systems which do not have a nested toroidal flux surface geometry.

Due to the use of the Picard iteration scheme, the PIES code shows a very slow convergence rate, especially when large blending parameters (see below) have to be used to avoid numerical instabilities. In this work, finite-beta solutions obtained with the VMEC code are used as initial guesses for the PIES code in order to accelerate the convergence.

PIES convergence

Using magnetic coordinates (ρ, θ, ψ) and solving the equilibrium equations (1),

$$\mathbf{J} = \nabla\psi \times \nabla\theta \left(I'(\psi) + \frac{dp}{d\psi} \sum_{m,n}{}' \frac{m\mathcal{J}^{\rho}_{m,n}}{(n - \iota m)} \cos(n\phi - m\theta) \right)$$
$$+\nabla\phi \times \nabla\psi \left(-g'(\psi) + \frac{dp}{d\psi} \sum_{m,n}{}' \frac{n\mathcal{J}^{\rho}_{m,n}}{(n - \iota m)} \cos(n\phi - m\theta) \right). \qquad (5)$$

$I(\psi)$ and $g(\psi)$ are the net toroidal and net poloidal current, respectively, $\mathcal{J}^{\rho}_{m,n}$ are the Fourier coefficients of the Jacobian between laboratory and magnetic coordinates. m, n label the poloidal and toroidal mode number, respectively. As seen from equation (2) and depending on the shape of the local pressure profile, there may occur current density resonances near rational surfaces with $\iota = m/n$. The observed numerical instabilities mentioned often appear close to these resonances.

It was found to be useful or even necessary in this connection to blend the Fourier coefficients of the coordinates and fields with those of the previous iteration(s). This blending is accomplished with the algorithm, $A(n+1) = \bar{A}(n+1) + b_A \cdot (A(n) - A(n+1))$. A are the coefficients to be blended, e. g. coefficients of B^{ϕ}, x and ι, and b_A is the blending parameter for A. Particularly in the case of low shear and/or high values of $\langle\beta\rangle$, large values of blending parameters are necessary to avoid instability and to achieve convergence. The result is a very slow convergence rate. This slow convergence can be illustrated by the computation of W7-X equilibria (for W7-X, see e. g. [3]). For an equilibrium with islands, $\langle\beta\rangle = 3.75$ %, and using the vacuum field as initial guess, several hundred iteration are needed for convergence [4]. Generally, blending factors of 0.950 to 0.995 are found to be necessary for W7-X configurations.

It is possible to improve the convergence rate by using of 'Chebychev' periodic sequences of iterations with various blending parameters. Such a sequence allows the algorithm to perform one iteration step with a rather small blending parameter after some steps with large blending parameter without loss of stability.

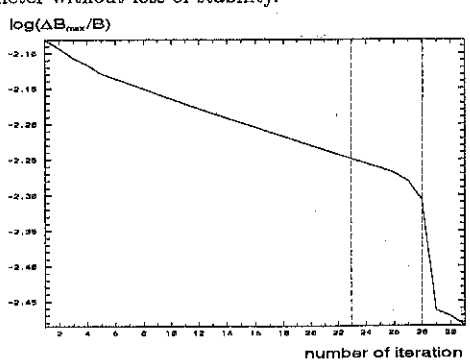

Figure 1: *max. correction $\Delta B_{max}/B$ versus the number of iterations. Iteration # 2 to # 31 with a Chebyshev sequence from # 24 to # 28 are shown. W7-X configuration, $\langle\beta\rangle = 4.1$ %.*

In fig. 1, the convergence of the magnetic field B is shown by plotting the change ΔB of B versus the number of iterations. One Chebychev sequence with a period of $N = 5$

from iteration No. 24 to iteration No. 28 is shown. Iteration No. 28 is the one with the smallest blending factor, the acceleration of the convergence is clearly visible.

Fixed-boundary results

Another method to improve the convergence rate is to improve the initial guess for the magnetic field. Here, VMEC results are used as initial guess. The field resulting from a VMEC run is transformed into PIES coordinates via an interface code. To illustrate this method of accelerated convergence, extensive computations of fixed-boundary W7-X equilibria with $\langle\beta\rangle$ from 3 to about 5 % with and without islands were done. The number of iterations necessary for a PIES run to converge with a VMEC field as initial guess was found to decrease by nearly one order of magnitude compared with corresponding PIES runs using the vacuum field as initial guess. For W7-X configurations without islands, about 30 to 40 iterations were found to be necessary to compute a equilibrium, in cases with islands, about 70 to 110 iterations were required depending on island size and possibilities to use Chebychev sequences. The number of toroidal and poloidal mode numbers used were $|n| \leq 8$ and $|m| \leq 10$ to 16. The numbers of radial points used were from 33 for configurations without islands up to 65 in cases with islands. For all considered W7-X configurations, the island widths were found to be very small compared with the plasma radius although the islands were located in the low-shear region of the ι profile, for example at $\iota = 5/6$. Typical values are in the region of a few percent.

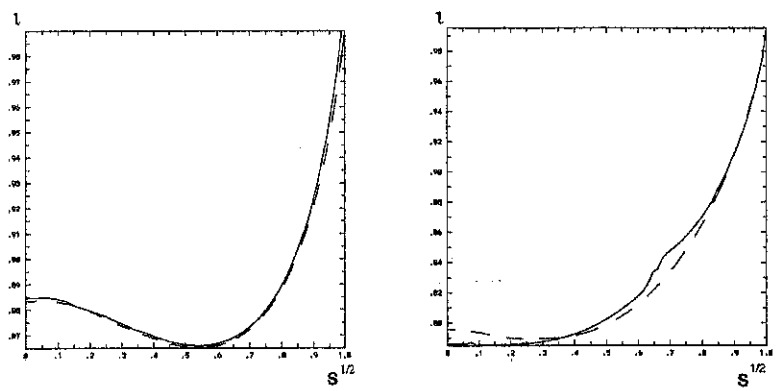

Figure 2: *Rotational transforms ι versus the normalized radius for W7-X equilibria with $\langle\beta\rangle$ = 3 % (left) and $\langle\beta\rangle$ = 5 % (right).*
Dashed line: VMEC calculations, full line: PIES calculations.

In fig. 2, the rotational transforms ι versus the radial flux label for a W7-X equilibrium with $\langle\beta\rangle = 3$ % and no islands (more specifically, with islands which size are below the discretization length) and for a case with $\langle\beta\rangle$ = about 5 % and (small) islands are shown. Both PIES and VMEC profiles are plotted in order to illustrate the practicality of using VMEC inputs. The profiles are quite similar for these configurations. In fig. 3, flux surfaces of a W7-X equilibrium with $\langle\beta\rangle = 5$ % obtained from PIES for three different iterations are shown. The left one is the field obtained from VMEC, the right one is the converged equilibrium field. The corresponding ι profile is on the right side of fig. 2. The island chain is associated with a transform of $\iota = 5/6$.

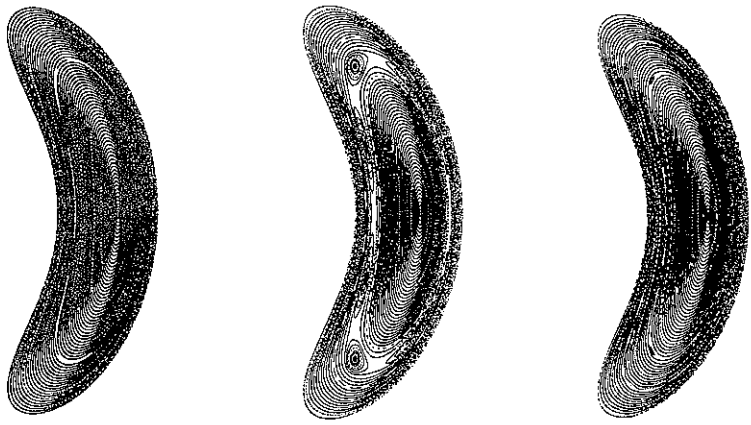

Figure 3: *Flux surfaces of a W7-X equilibrium with $\langle\beta\rangle = 5$ %, obtained from PIES after the 0th (left), the 11th (center) and the 96th (right) iteration.*
Number of poloidal, toroidal modes: $m \leq 10$, $|n| \leq 8$, 65 radial mesh points.

Conclusions

Using VMEC equilibria as PIES input, a considerable acceleration of the fixed-boundary PIES convergence has been realized. This makes the PIES code a suitable tool to perform equilibrium and, particularly, island studies for W7-X and other configurations.
Our next step, is the calculation of free-boundary equilibria. The **NEMEC** code combines the VMEC fixed boundary code and the **NESTOR** code [5]. The NESTOR code is used to calculate the Neumann problem in the vacuum region. The NEMEC code can thus be used to solve the free-boundary MHD equilibrium equations assuming 'good' flux surfaces in the plasma region. Combining the PIES code and the NESTOR vacuum code, one gets a **free-boundary PIES** code that solves the free-boundary equilibrium problem for a given external magnetic field.
The use of NEMEC W7-X results as input for the free-boundary PIES code is under development in order to accelerate convergence as in the fixed-boundary case.

Acknowledgments

We would like to thank P. Merkel for his many helpful suggestions.

References

[1] Hirshman, S. P., Lee, D. K., Comput. Phys. Commun. **39**, 161 (1986), Hirshman, S. P., et al., J. Comput. Phys. **87**, 396 (1990).
[2] Greenside, H. S., Reiman, A. H., Salas, A., J. Comput. Phys. **181**, 102 (1989), Reiman, A. H., Greenside, H. S., J. Comput. Phys. **87**, 349 (1990).
[3] Grieger, G., et al., Plasma Physics and Controlled Nuclear Fusion Research 1990 (Proc. 13th Int. Conf., Washington, DC, 1990) **2**, 655 (IAEA, Vienna, 1991).
[4] Merkel, P., et al., Plasma Physics and Controlled Nuclear Fusion Research 1994 (Proc. 15th Int. Conf., Seville, 1994) **3**, 621 (IAEA, Vienna, 1996).
[5] Merkel, P., J. Comput. Phys. **66**, 83 (1986).

Sheared Poloidal Flows and Turbulence in the Edge Plasma Region of Stellarator and Tokamak Devices

R. Balbín, C. Hidalgo, E. Sánchez, M.A. Pedrosa, B. van Milligen
Euratom-Ciemat Association, Madrid, Spain

J. Bleuel, H. Niedermeyer
Euratom-IPP Association, Garching, Germany

G. Fiksel
Department of Physics, University of Wisconsin, US

I. Introduction

It is known that a poloidal shear flow in a magnetically confined plasma has in general a stabilizing effect[1,2]. Recent calculations have shown that the dependence of the phase angle between density ($\tilde{n}_e$) and electric field fluctuations ($\tilde{E}_\theta$) on flow shear may be an important aspect of the $E_r \times B$ shear flow suppression[3]. Simultaneously it is known that poloidal acceleration will occur if there are radial gradients in the turbulent Reynolds stress[4]. The aim of the presented experiments is to investigate the effect of sheared $E_r \times B$ flow on turbulent fluxes (coherence and phase angles between density and electric field fluctuations) and the interaction between poloidal flows and turbulence. The radial behaviour of the Reynolds stress (both electrostatic and magnetic) in the proximity of the velocity shear layer in the TJ-IU torsatron has been investigated.

The turbulence (fluctuation levels, cross phase, cross coherence) in the proximity of the naturally occurring velocity shear layer in the TJ-I tokamak (R = 0.3 m, $\bar{a}$ = 0.1 m, $\bar{n}_e$ ≈ (1 - 3) × 10^{19} m^{-3}, B_t ≈ 1 T, I_p ≈ 30 kA), in the TJ-IU torsatron (P_{ECRH} = 200 kW, $\iota(0)$ ≈ 0.23, R = 0.6 m, $\bar{a}$ ≈ 0.1 m, $\bar{n}_e$ ≈ 0.5 × 10^{19} m^{-3}, B_t = 0.67 T) and in the W7-AS stellarator (P_{ECRH} = (200 - 400) kW, $\iota(0)$ ≈ (0.24 - 034), R = 2 m, $\bar{a}$ ≈ 0.17 m, $\bar{n}_e$ ≈ 2 × 10^{19} m^{-3}, B_t = (1.25 - 2.56) T) have been studied.

II. Turbulence and sheared poloidal flows

Data analysis has focused in the evaluation of the coherence and phase angle between $\tilde{E}_\theta$ and $\tilde{n}_e$ at the plasma edge of the W7-AS stellarator. Fig. 1a shows the radial profiles of mean values of ion saturation current (I_{sat}) and floating potential (ϕ_{fl}), measured with a fast reciprocating Langmuir probe and referred to the velocity shear layer position. The fluctuating poloidal electric field ($\tilde{E}_\theta$) is calculated as the difference of two ϕ_{fl} separated 4 mm in the poloidal direction and the density fluctuations are taken to be proportional to the $\tilde{I}_{sat}$ assuming negligible temperature fluctuations. Fig. 1b shows the

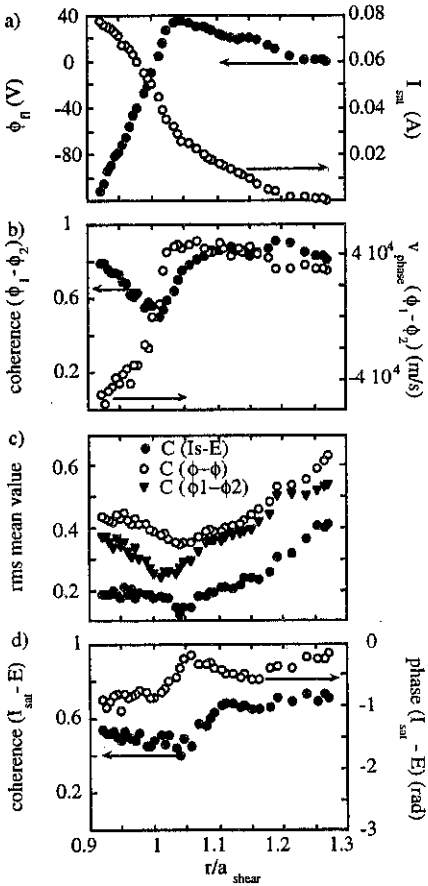

Figure 1: Radial profiles of plasma parameters measured with a fast reciprocating Langmuir probe at the plasma edge of W7-AS during a typical shot with 1.26 T and 180 kW ECR heating

poloidal coherence of the ϕ_{fl} measured with two tips placed 4 mm apart in the poloidal direction as well as phase velocity of fluctuations (v_{ph}) deduced from the ϕ_{fl} measurements. As expected, the poloidal coherence (fig 1.b) and rms cross-correlation $C(\phi 1-\phi 2)=\left\langle C^2_{\tilde{\phi}1\tilde{\phi}2}(\tau)\right\rangle^{1/2}$, being $C_{\tilde{\phi}_1\tilde{\phi}_2}(\tau)=\left\langle\tilde{\phi}_1(t)\tilde{\phi}_2(t+\tau)\right\rangle/\sigma(\tilde{\phi}_1)\sigma(\tilde{\phi}_2)$ (fig. 1.c) between floating potential signals decrease at the velocity shear layer location where $v_{ph} \approx 0$. It is interesting to note that the rms value of cross correlation $C_{\tilde{I}\tilde{E}}(\tau)$ (fig. 1.c) shows a minimum at the radial location $r/a_s \approx 1.05$ that cannot be explained as a Doppler shift effect because in the radial region $1 < r/a_s \leq 1.15$ the v_{ph} is rather constant within the error bars. Note that $\tilde{I}_{sat}$ and $\tilde{E}_\theta$ are measured at exactly the same poloidal position. Fig. 1d shows the coherence between $\tilde{I}_{sat}$ and $\tilde{E}_\theta$, and the cross phase between these magnitudes. A decorrelation and a phase change between $\tilde{n}_e$ and $\tilde{E}_\theta$ are observed related to the maximum change in E_r, whereas the level of fluctuations does not significantly change. The spectrally resolved analysis shows that these changes occur mainly for frequencies above 25 kHz.

Statistical analysis of the probability distribution function (PDF) of the $\tilde{I}_{sat}$ signal has been done and a clear departure from gaussian behavior is observed in the SOL. In the plasma edge the PDF tends to show a more gaussian behavior, in consistency with previous experiments in the TJ-I tokamak and the TJ-IU torsatron[5].

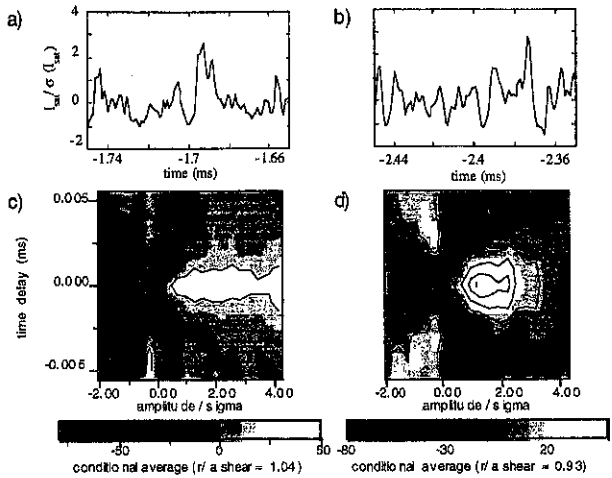

Figure 2: Normalized I_{sat} raw data and its conditional average at two radial positions at the SOL (a) and the plasma edge (b) in the TJ-1 tokamak. At the SOL burst of turbulence growing faster than decaying are clearly observed. The conditional average plot abciss (c and d) display the amplitude of the pulses and ordinate the time delay with respect to the position of the maximum/minimum of the pulse. The raw data has been normalized removing the DC component and making the rms equal 1.

In the TJ-I tokamak the structure of the $\tilde{I}_{sat}$ fluctuations is strongly intermittent in the proximity of the velocity shear layer. That might suggest a competition between the driving and damping mechanisms of turbulence. A systematic analysis of the degree of asymmetry in the shape of the temporal pulses using a conditional averaging method has been done. Fig. 2 shows the raw data at two radial positions, the SOL and the plasma edge, and the resulting statistical average over different amplitudes of the pulses. The asymmetry (in the sense that low frequency pulses have faster growth than decay time constants) is significant in the SOL while the asymmetry disappears inside of the velocity shear layer. Similar features have

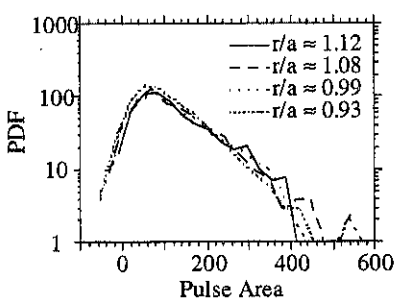

Fig 3. PDF of the I_{sat} pulse time integral at three radial positions in W7-AS showing an exponential decay at high amplitudes

been found in the TJ-IU torsatron and the W7-AS stellarator.

The better statistics of data from W7-AS have allowed the study of the PDF of pulse time integrals (areas). The decay of the PDF is aproximately exponential outside the velocity shear layer and at the plasma edge as can be seen in Fig. 3.

III. Reynolds stress measurements in the edge region of the TJ-IU torsatron

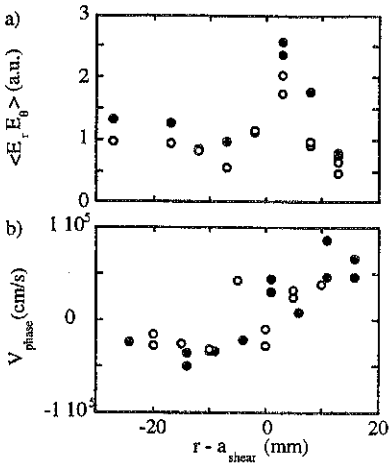

Fig. 4 Radial profiles of Reynolds stress and velocity propagation of fluctuations measured at the TJ-IU torsatron using a radial-poloidal array of Langmuir probes.

The radial profile of the cross-correlation between $\tilde{E}_\theta$ and $\tilde{E}_r$, and $\tilde{B}_\theta$ and $\tilde{B}_r$ have been investigated in the TJ-IU torsatron. The coherence between $\tilde{B}_\theta$ and $\tilde{B}_r$ is quite high (close to 0.8 for frequencies below 70 kHz). The magnetic component of the Reynolds tensor, proportional to $< \tilde{B}_\theta \tilde{B}_r >$, was measured and found to be negligible due the low fluctuation amplitude and the fact that the poloidal and the radial component of the fluctuating magnetic field are shifted by $\pi/2$. Fig. 4 shows the radial profile of $\langle \tilde{E}_r \tilde{E}_\theta \rangle$ (Fig. 4a) and v_{ph} (Fig. 4b) obtained from two floating potential measurements of tips placed 2 mm apart in the poloidal direction and 6 mm in the radial direction. It can be argued that the radial derivative of $\langle \tilde{E}_r \tilde{E}_\theta \rangle$ evolves in the proximity of the velocity shear position. Further analysis of the experimental results are in progress to quantify the importance of poloidal flow driven by (electrostatic) Reynolds stress.

1T. Chiuen, P.W. Terry, P.H. Diamond and J.E. Sediak, Phys. Fluids **29**, 231 (1986)

2 K.H. Burrell, E.J. Doyle, P. Gohil et al. Phys. Plasmas **1**, 1536 (1994)

3 P.W. Terry, et al. Proc. 16th IAEA (IAEA-CN-64/DP-20) (1996)

4 P.H. Diamond and Y.B. Kim. Phys. Fluids **B3**, 1626 (1991)

5 E. Sánchez, C. Hidalgo, M.A. Pedrosa, R. Balbín, I García-Cortés, T. Estrada and B. van Milligen. Transport, Chaos and Plasma Physics 2. S. Benkadda, F. Doveil and Y. Elskens Eds. World Scientific Publishing Co. (1996)

Viscous Damping and Plasma Rotation in Stellarators

H. Wobig, J. Kisslinger

Max-Planck-Institut für Plasmaphysik, EURATOM-Ass., Garching, Germany

Poloidal rotation with shear flow is one of the key elements in the theory of H-mode confinement in toroidal systems. There are various driving forces which may excite poloidal and toroidal rotation: Stringer spin-up, turbulent Reynolds stresses and lost orbits. Viscous damping is the main candidate to retard the rotation. In a collision dominated plasma viscous damping is provided by the magnetic pumping effect which arises from the variation of the magnetic field strength along the stream lines of rotation. It only depends on the Fourier spectrum of B on magnetic surfaces and not on the details of particle orbits. A comparison of viscous damping rates of various toroidal configurations has been given in [1]. The non-axisymmetric components in the Fourier spectrum of B lead to extra maxima in the poloidal force which complicates the bifurcation problem as compared to axisymmetric tokamaks. Enhanced poloidal damping also occurs if magnetic islands exist in the confinement region. In stellarators islands occur on rational magnetic surfaces if there exists a resonant field perturbation. Such perturbations always exist on "natural surfaces with the rotational transform $\iota = M/k$, k=1,2,3,..M is the number of field periods. The denominator indicates the number of islands. Symmetry breaking field perturbations introduce another class of islands which can easily dominate over the natural islands.

In general there is a combination of natural islands and symmetry breaking islands. Examples are given by the Wendelstein stellarators W 7-A and W 7-AS [2] Islands lead to enhanced radial transport and therefore also to enhanced poloidal damping. In the neighbourhood of islands magnetic surfaces are modified and the Fourier spectrum of B exhibits harmonics with the periodicity of the island. Due to toroidal curvature the field variation on magnetic surfaces is roughly $\delta B/B = r/R$.

Even if no islands are present in the plasma region magnetic surfaces at the plasma edge are modified by resonant Fourier harmonics. This in particular occurs in the boundary region of Wendelstein 7-AS, where the last magnetic surfaces exhibit the M/k structure of the natural islands.

---

[1] J. Kisslinger, H. Wobig , " On rotation of collisional plasmas in toroidal systems ", Plasma Phys. Contr. Fusion 37 (1995) 893 - 922

[2] R. Jaenicke, K. Schwoerer, E. Ascasibar, P. Grigull, I. Lakicevic, M. Zippe, Proc. of 16th EPS-Conf. on Contr. Fus. and Plasma Phys. Venice 1989, Pt II, 627

Fig. 1: Magnetic islands in the boundary region of a stellarator.

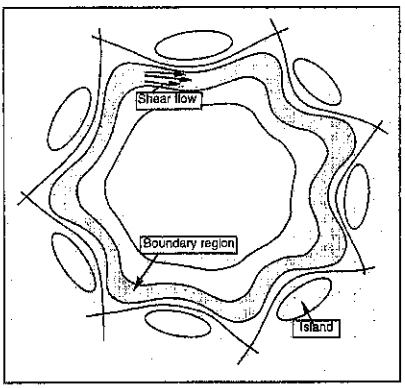

In the following we start from a magnetic field configuration with nested magnetic surfaces which satisfies the condition of ideal equilibrium. On these nested magnetic surfaces the Hamada coordinate system is introduced which is characterised by straight magnetic field and a Jacobian equal to unity. In this coordinate system the base vectors are defined by $\mathbf{e}_p = \nabla s \times \nabla\varphi$, $\mathbf{e}_t = -\nabla s \times \nabla\theta$. $\mathbf{e}_p$ is the poloidal base vector and $\mathbf{e}_t$ the toroidal base vector. s is the volume of the magnetic surface. The lowest order rotation $\mathbf{v}_0 = -E(\psi)\mathbf{e}_p + \Lambda(\psi)\mathbf{B}$ stays on magnetic surfaces and satisfies the equation $\nabla\mathbf{v}_0=0$. The two flux functions E and Λ describe the poloidal and the parallel motion on magnetic surfaces. E is the radial electric field.

In a toroidal plasma the forces by magnetic pumping inhibit the rotation of the plasma, these forces are

$$<\mathbf{e}_p\bullet\nabla\bullet\pi> = <\left(p_{\parallel}-p_{\perp}\right)\mathbf{e}_p\bullet\frac{\nabla B}{B}> \quad ; \quad <\mathbf{B}\bullet\nabla\bullet\pi> = <\left(p_{\parallel}-p_{\perp}\right)\mathbf{B}\bullet\frac{\nabla B}{B}>$$

In a collisional plasma these equations reduce to (see ref. 1)

$$\begin{pmatrix} -<\mathbf{e}_p\bullet\nabla\bullet\pi> \\ <\mathbf{B}\bullet\nabla\bullet\pi> \end{pmatrix} = 3\tau P \begin{pmatrix} C_p & C_b \\ C_b & C_t \end{pmatrix} \begin{pmatrix} E \\ \Lambda \end{pmatrix}$$

P = plasma pressure, τ = collision time. The coefficients are

$$C_p = <\left(\mathbf{e}_p\bullet\frac{\nabla B}{B}\right)^2> \; ; \; C_t = <\left(\mathbf{B}\bullet\frac{\nabla B}{B}\right)^2> \; ; \; C_b = <\left(\mathbf{e}_p\bullet\frac{\nabla B}{B}\right)\left(\mathbf{B}\bullet\frac{\nabla B}{B}\right)>$$

Thus the damping forces are the product of plasma parameters and geometrical coefficients. In the following numerical computations of these coefficients C_p,C_t, and C_b are shown. The poloidal coefficient C_p is of particular interest, since a small poloidal damping facilitates poloidal rotation and poloidal shear flow. The results of numerical calculations show large damping coefficients in standard l=2 stellarators and torsatrons in contrast to optimised stellarators of the Helias type.

Fig. 2: Poloidal damping C_p coefficient in l=2 stellarators and the optimised stellarator W 7-X. In W 7-X the coefficient is roughly a factor 2 smaller than in W 7-AS and standard stellarators. A similar result exists for the threshold $D=C_p - C_b*C_b/C_t$ of poloidal spin-up. These coefficients increase towards the plasma boundary. However, since these coefficients are multiplied by τP which decreases strongly towards the boundary the viscous forces are small in the boundary region. This may explain why plasma rotation is mainly observed in the boundary regions.

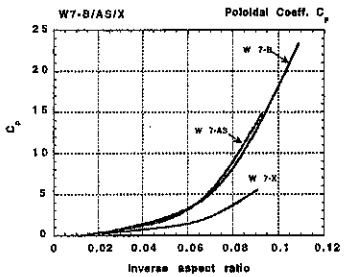

Magnetic islands may arise in the boundary region of some stellarators like Wendelstein 7-AS. These islands distort the magnetic surfaces in the neighbourhood and lead to an enhanced viscous damping (or magnetic pumping). Inside the island region the plasma equilibrium is not represented by the ideal MHD-theory, therefore the coefficients given here are only relevant in the region outside magnetic islands.

Fig. 3: Poloidal viscous damping rate C_p (collisional regime) in Wendelstein 7-AS. The regime of the rotational transform is between 5/10 and 5/9. The absissa is the average radius of the magnetic surface. Close to the island the damping rate is en-hanced by a factor of 2. The coefficient C_b exhibits a similar enhancement. Little effect of magnetic islands is seen in the toroidal coefficients C_t. In conclusion, mainly poloidal rotation will be inhibited by magnetic islands.

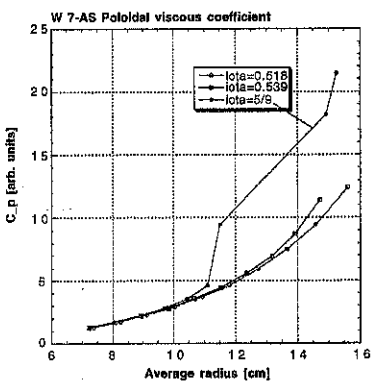

The standard case of Wendelstein 7-X has 5 islands at the boundary. These islands are the base of the divertor concept and the issue arises whether these islands suppress plasma rotation in this region. The following figure shows that only in a small neighbourhood of these islands enhancement of the poloidal damping coefficient occurs.

Fig. 4: Comparison with tokamak. Poloidal viscous coefficient. The gray rectangular region is the island at the boundary of W 7-X. Enhancement of viscous damping in W 7-X

occurs in a few cm distance from the islands. The two curves of W 7-AS differ by the rotational transform. Poloidal damping in W 7-X and a tokamak (Tore Supra) are nearly equal at equal plasma radii.

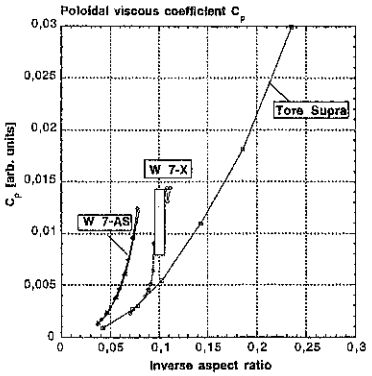

Discussion

The viscous damping of poloidal and toroidal plasma rotation depends on two factors, one factor is τ P - collision time times plasma pressure - and the other factors are geometrical factors C_p, C_t and C_b. With respect to the geometrical factor significant differences among the various stellarators exist. C_p is the relevant geometrical factor of poloidal rotation. In axisymmetric devices only the toroidal curvature effect gives rise to magnetic pumping and a finite coefficient C_p. In stellarators, however, additional helical harmonics lead to increased poloidal viscous damping . Reducing the poloidal variation of B - as has been done in optimised configurations of the Helias type - also reduces the poloidal viscous damping. In the neighbourhood of magnetic islands enhanced viscous damping arises due to the distortion of magnetic surfaces. This effect may be of importance in Wendelstein 7-AS, where magnetic islands in the boundary region strongly corrugate the surfaces. The viscous damping coefficients C_p and C_b are enhanced in the neighbourhood of the islands. In comparison to axisymmetric configurations standard stellarators exhibit a more complex Fourier spectrum of B and therefore magnetic pumping effect is larger. The optimisation scheme realised in Wendelstein 7-X, however, reduces the poloidal damping rate to the level of axisymmetric configurations. As seen in Fig. 4 the coefficient C_p is nearly the same in both configurations The present analysis is based on a collisional plasma model. Such a model is applicable to a plasma boundary, where the temperatures are below 100 eV and the densities above 10^{19} m^{-3}. At higher temperatures the plateau regime is reached and the viscous damping must be computed from a kinetic equation. This will be done in a subsequent paper.

Time–resolved Transport in W7–X as predicted by Neoclassical Theory

E.E. Simmet, C.D. Beidler, H. Maaßberg

Max-Planck-Institut für Plasmaphysik, IPP-EURATOM Association
D-85748 Garching bei München, Germany

In next–genaration stellarators such as W7–X, recycling and gas puffing affect only the edge of the plasma. Hence, an active density profile control via central particle sources, e.g., NBI and/or pellets, is needed. To reach a certain experimental plasma density, the central particle source is not only determined by diffusive losses due to the density gradient as for instance in tokamaks. The off–diagonal elements of the neoclassical transport matrix become essential in the stellarator long mean free path (LMFP) regime which is mandatory for the central region of W7–X plasmas. Especially the off–diagonal term which is related to the particle balance predicts additional particle losses due to the temperature gradient.[1] Hence, strong temperature gradients together with too small a central gas refuelling rate will drive the density hollow, i.e. a positive density gradient has to compensate the off–diagonal losses to fulfil the particle balance. On the other hand, too large a filling rate may give rise to increasing density and decreasing temperature.

Neoclassical Transport Matrix

The neoclassical particle and energy flux densities, Γ_α and Q_α, with $\alpha = e, i$, are given by

$$\Gamma_\alpha = -n_\alpha \{ D^\alpha_{11} (\frac{{n_\alpha}'}{n_\alpha} - \frac{q_\alpha E_r}{T_\alpha}) + D^\alpha_{12} \frac{{T_\alpha}'}{T_\alpha} \}$$

$$Q_\alpha = -n_\alpha T_\alpha \{ D^\alpha_{21} (\frac{{n_\alpha}'}{n_\alpha} - \frac{q_\alpha E_r}{T_\alpha}) + D^\alpha_{22} \frac{{T_\alpha}'}{T_\alpha} \}$$

with q_α being the particle charge and with the "convective term" $(3/2) T_\alpha \Gamma_\alpha$ included in Q_α. The radial electric field E_r is determined by the roots of $Z_i \Gamma_i = \Gamma_e$. The neoclassical transport coefficients D^α_{jk} (with j,k=1,2) are determined from the mono–energetic transport coefficients, e.g., $D_{1/\nu} \sim 1/\nu$, $D_{\sqrt{\nu}} \sim \sqrt{\nu}$ and $D_\nu \sim \nu$ with ν being the collision frequency [2,3].

In order to show the time evolution of the density and the temperature profile, the ASTRA code [4] is used in a stellarator specific version [5] with the full neoclassical transport matrix for the W7–X high–mirror configuration [6] (see Fig. 1). The ambipolar E_r is calculated by direct iteration yielding the so–called "ion root" which is expected for the plasmas of interest here. For simplicity, $n_e = n_i = n$ is used in all cases. To yield quantitative estimates about the central refuelling rate which is needed to reach a scenario with non–hollow density and pressure profiles calculations are performed at various heating powers of up to 20 MW (electron heating only) and for different initial conditions of densities and temperatures.

Need for Central Particle Refuelling

As can be seen from Fig. 2, too large a central heating and too small a central refuelling rate produces a hollow density profile as expected from theory [1]. In this case, the start conditions are $n = 1 \times 10^{20}$ m^{-3}, $T = 1$ keV, $P = 10$ MW. The filling rate is 1×10^{20}

s^{-1}. Here, a strong temperature gradient driven by the heating cannot be balanced or exceeded by the external particle source. While the density gradient becomes positive, the negative electron temperature gradient is increased by the increased value of heating power per particle, driving the density gradient more and more positive. Hence, no stationary situation is reached here and the whole central density may be lost within a few hundred milliseconds. In this case also an inverted pressure profile occurs with $p' > 0$, which may drive MHD instabilities.

Enlarging the central refuelling rate to over–compensate the particle losses which are caused by the strong off-diagonal term of the transport matrix coupled to the temperature gradient yields an almost contrary situation. The hollow density profile is observed only at the beginning of the discharge owing to the start conditions. At later times, when the influence of the start conditions is more and more lost, the high refuelling rate is able to drive a steep density profile. Close to the plasma edge, however, the high temperature together with an unfavourable scaling of the transport coefficients result in local particle fluxes which generally are less than the central refuelling rate. A transport barrier occurs. Due to this barrier, the central density increases and becomes more and more peaked. Both temperatures decrease slowly and become identical, as can be seen from Fig. 3 (refuelling: 15×10^{20} s^{-1}; n: 2×10^{20} m^{-3}; T: 1 keV; P: 10 MW). As far as an active control of the central particle source is possible, e.g. via pulsed pellet scenario, this behaviour is less critical than the case shown in Fig. 2. This situation does not differ much by changing the density and temperature start conditions, as can be seen from Fig. 4. This figure shows also that independent from the start situations three different regimes can be distinguished: The low rate regime, where the whole central density may be lost within less than a few hundred milliseconds; the high rate regime with highly peaked and increasing densities and lifetimes of a few seconds before the pressure profile becomes hollow due to almost vanishing central temperatures; and the intermediate regime with almost constant plasmas. The rate needed for this intermediate regime is almost proportional to the heating power, i.e. the filling rate must be close to 1×10^{20} m^{-3} per second per MW heating power according to the value determined in [1] with stationary calculations.

Further, simulations show that not only the total particle source is linked to the total heating power. To reach non–hollow pressure profiles, the radial profile of the particle deposition must be strongly correlated to the power deposition profile. In all cases with almost stable conditions, both profiles are nearly identical. With a too narrow or too broad particle source, either the density or the temperatures are driven hollow, depending on the total refuelling rate. The reason for this behaviour can be found from the strong coupling of the transport equations in the central region. Assuming sufficiently high temperatures, the radial electric field can be neglected. Solving the stationary equations for the filling rate yields an ambipolar particle flux which is roughly proportional to the energy fluxes of the electrons and the ions. Here the radial dependences of the transport coeffiecients cancel each other. Hence, the particle refuelling profile is similar to the power deposition profile.

In W7–X, this strong coupling is necessary for the high–mirror configuration. Lowering the toroidal mirror term will change the local behaviour of the transport coefficients with the effect of broader refuelling profiles which are less coupled to the heating profile. Central refuelling, however, will be mandatory.

Transport Barrier at outer Radii

At outer radii, the neoclassical particle flux must exceed at least the central particle source. Otherwise the outer density increases and the global density control is lost. In

this region, however, the neoclassical transport coefficients of the electrons are much smaller than those of the ions. Solving the transport equations for the particle flux at outer radii shows that the ambipolar partical flux can simply be described as being proportional to D^e_{11} and the normalized temperature gradient. For the same reason, the ion energy flux is close to the whole energy flux, which should be equal to the central heating power in stationary plasmas. As far as both the central heating and the central particle source have to be strongly coupled, a strong constraint between the particle flux at the edge and the central heating power can be found which mainly depends on the ratio D^e_{11}/D^i_{11}. In terms of temperatures, a critical temperature for the edge region can roughly be estimated (mainly proportional to D^e_{11}/D^i_{11} and to the central temperature) which defines a transport barrier. For T exceeding this critical value, the outer particle flux is less than the central refuelling rate, and the outer density increases. Additional moderate anomalous heat conductivity (up to 1 m^2/s) or radiative losses (up to 3 MW) will amplify the problem.

In Fig. 5, the time evolution of density and particle flux is shown for such a plasma (refuelling: $15\times\ 10^{20}\ s^{-1}$; n: $10^{20}\ m^{-3}$; T: 1 keV; P: 10 MW). At the beginning, the whole refuelling rate is balanced by particle losses. The transport barrier which occurs at about 100 milliseconds reduces the particle losses to nearly two third of the central filling rate.

The ratio of both transport coefficients depends, in principle, on the magnetic configuration. Hence, in W7-X this problem can be analyzed by varying the toroidal mirror term over a wide range.

References

[1] H. Maaßberg et al., EPS 1996, ECA **20C II** (1996) 487.

[2] W.I. van Rij and S.P. Hirshman, Phys. Fluids B 1 (1989) 563.

[3] C.D. Beidler et al., EPS 1994, ECA **18B II** (1994) 568.

[4] G.V. Pereverzev et al., *ASTRA - An Automatic System for Transport Analysis in a Tokamak*, (1991) IPP-Report 5/42.

[5] N.E. Karulin, *Transport Modelling of Stellarators with ASTRA*, (1994) IPP-Report 2/328.

[6] C.D. Beidler et al., EPS 1996, ECA **20C II** (1996) 479.

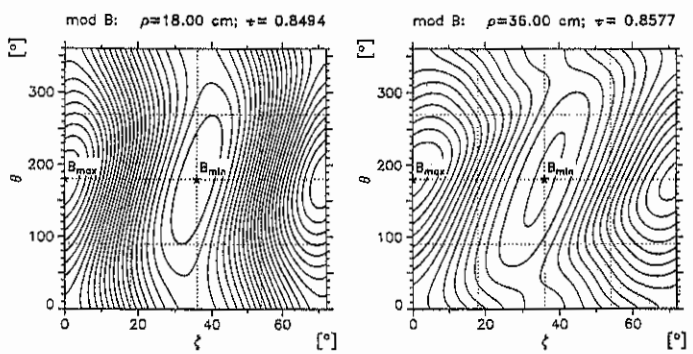

Fig. 1: Magnetic field topology of the W7-X high mirror configuration [6] at two radii with ζ and Θ being the toroidal and poloidal angle.

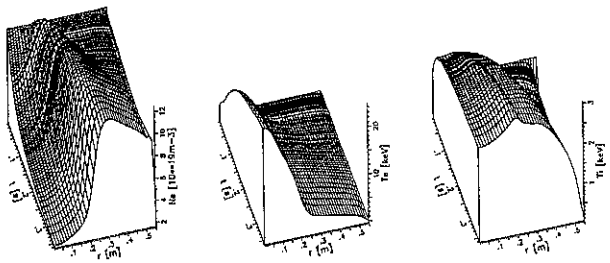

Fig. 2: Density and temperatures of a discharge with low particle refuelling rate ($P = 10$ MW).

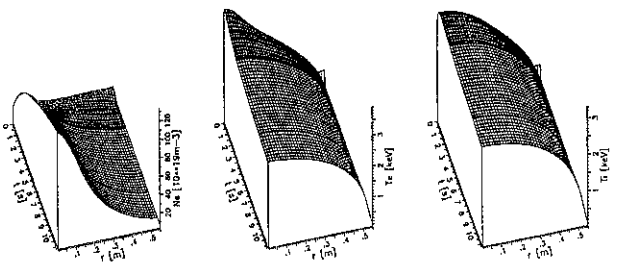

Fig. 3: Density and temperatures of a discharge with high particle refuelling rate ($P = 10$ MW).

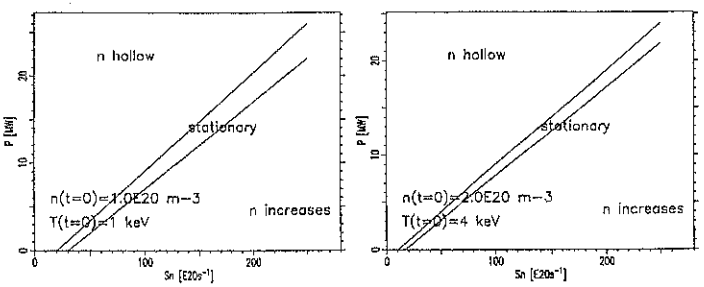

Fig. 4: Operational regimes for different heating powers and refuelling rates.

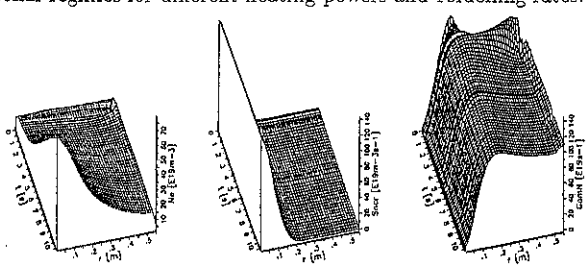

Fig. 5: Time evolution of density (left), particle source (middle) and particle flux (right) for a discharge with occuring transport barrier.

FIRST SURVEY OF FINITE-β MAGNETIC FIELDS OF W7-X

E. Strumberger

IPP-Euratom Association, Max-Planck-Institut für Plasmaphysik,
Garching, Federal Republic of Germany

The optimized Wendelstein 7-X (W7-X) Helias stellarator is expected to reach volume averaged β-values of up to 5%. Part of the experimental flexibility will be achieved by modifying the rotational transform in the range $5/6 \leq \iota \leq 5/4$. In order to optimize the divertor geometry for various plasma equilibria and to improve SOL studies, a detailed knowledge of the corresponding magnetic field structures is necessary. For this purpose, magnetic fields are calculated for finite-β equilibria up to $\langle\beta\rangle = 5\%$ and rotational transform values of $\iota = 5/5,\ 5/6,\ 5/4$ in the edge region.

For these first computations the following system of numerical codes is used. The GOURDON code calculates the vacuum magnetic field, traces field lines and computes the rotational transform and the magnetic well. Further, the last closed magnetic surface (lcms) is determined. It lies inside the macroscopic islands (5/6, 5/5 or 5/4 islands) because these islands are intersected by divertor plates (see e.g. [1]). The data of the coordinates along the field line forming the lcms are used in the DESCUR code [2] to approximate the lcms by a set of Fourier coefficients, which serve as initial guess of the plasma boundary in the three-dimensional free-boundary equilibrium NEMEC code [3]. The NEMEC code is a synthesis of the VMEC code (**V**ariational **M**oments **E**quilibrium **C**ode) and the NESTOR (**NE**umann **S**olver for **TO**roidal **R**egions) vacuum code. It computes free-boundary finite-β Helias equilibria. Using the results obtained with the NEMEC code the MFBE code (**M**agnetic **F**ield Solver for **F**inite-**B**eta **E**quilibria) [4] calculates the magnetic field of the finite-β equilibrium on a grid inside and outside the plasma boundary. This magnetic field serves as input to the GOURDON code, which is used to determine the lcms of the finite-β equilibrium. If this lcms does not coincide with the plasma boundary obtained by the NEMEC code, the toroidal flux, which is a free parameter in the NEMEC code, is modified, that is, the toroidal flux is determined iteratively [4]. Finally, the JMC code [5] yields the Fourier spectrum of the magnetic field and the stability of the three-dimensional finite-β equilibrium with respect to Mercier [6] and resistive interchange modes [7] is studied.

Figure 1 shows the resulting magnetic fields in their dependence on the volume averaged β-value for the low-iota case (case A: $\iota = 5/6$), the standard case (case B: $\iota = 5/5$) and the high-iota case (case C: $\iota = 5/4$). For case C, which has the largest aspect ratio (see Fig. 3), finite-β equilibria could only be obtained up to $\langle\beta\rangle = 4\%$ in the framework of the used method (NEMEC + MFBE code), but $\langle\beta\rangle = 5\%$ may be reached by a more appropriate choice of the coil currents. The width of the 5/5 islands (case B) increases with increasing β, while the remnants of the 5/4 islands (case C) become

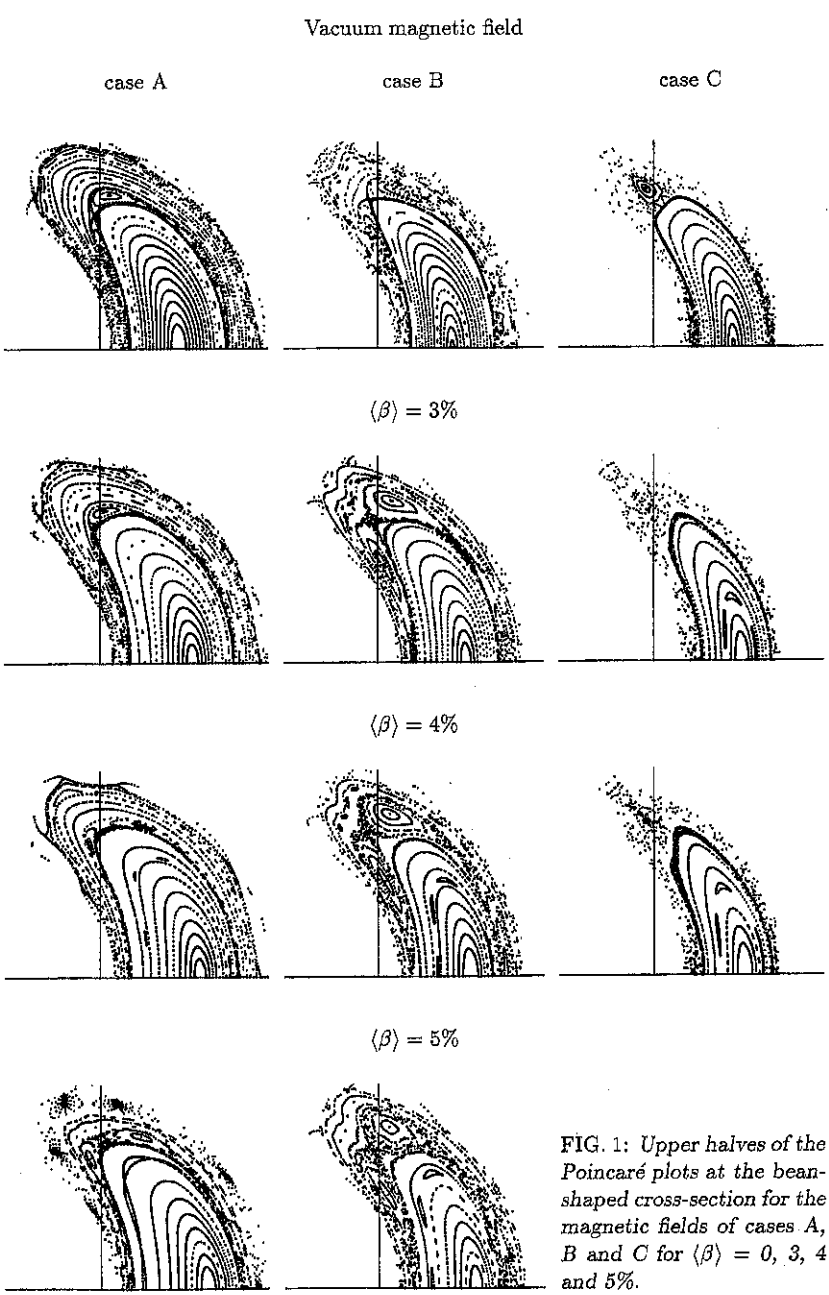

FIG. 1: *Upper halves of the Poincaré plots at the bean-shaped cross-section for the magnetic fields of cases A, B and C for* $\langle\beta\rangle = 0$, 3, 4 *and* 5%.

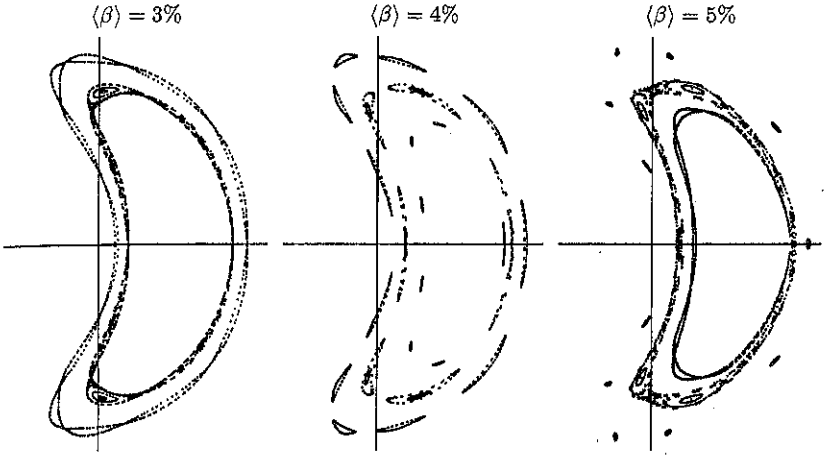

FIG. 2: *Case A: phase shift of the 5/7, 5/6 and 10/11 islands. The islands are plotted for* $\langle\beta\rangle = 3$, *4 and 5%.*

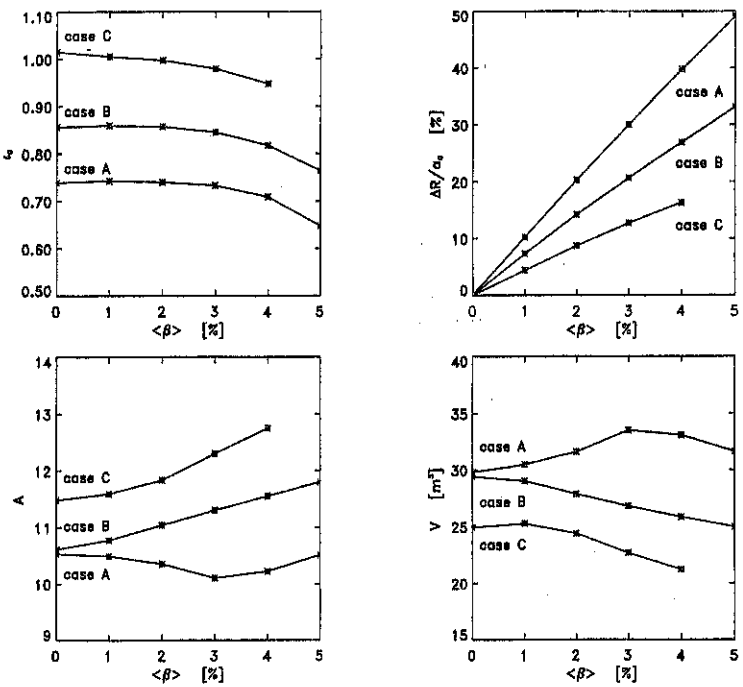

FIG. 3: *Rotational transform* ι_0 *on the magnetic axis, normalized shift of the magnetic axis* $\Delta R/a_0$ *(*ΔR *= mean shift of the magnetic axis, plasma radius:* $a_0 = 0.55$ *m), aspect ratio* A *and volume* V *enclosed by the lcms versus* $\langle\beta\rangle$.

smaller because of the increasing ergodization of the edge region. The positions of the X- and O-points of these macroscopic islands are almost unchanged. The width of the 5/6 islands (case A) decreases up to $\langle\beta\rangle = 3\%$. For $\langle\beta\rangle \geq 4\%$ phase shifts of these macroscopic islands and also of the 5/7 and 10/11 islands are observed. As shown in Fig. 2, the phase shifts of the 5/6 and 10/11 islands occur between $\langle\beta\rangle = 3$ and 4%, while the phase shift of the 5/7 islands takes place between $\langle\beta\rangle = 4$ and 5%. It will be interesting to compare these results with those obtained by other codes, e.g. the PIES code [8].

The $\langle\beta\rangle$-dependences of the rotational transform ι_0 on the magnetic axis, the normalized shift of the magnetic axis $\Delta R/a_0$ (ΔR = mean shift of the magnetic axis, plasma radius: $a_0 = 0.55$ m), the aspect ratio A and the volume V enclosed by the lcms are summed up in Fig. 3. For case A the aspect ratio A and the plasma volume V as functions of $\langle\beta\rangle$ show a behaviour different from those of case B and case C because of the phase shift of the macroscopic islands. The mean shifts of the magnetic axes and the rotational transform profiles of cases A, B and C slightly depend on the mass profile used in the NEMEC code as input [9]. Here a mass profile of the form $m(s) \approx 1 - 2s + s^2$ (s = flux lable with $s = 0$ at the magnetic axis and $s = 1$ at the plasma boundary) has been chosen.

Finally, cases A, B and C are stable with respect to the Mercier[6] and resistive interchange [7] criteria up to $\langle\beta\rangle = 3\%$. For higher β-values formal instability prevails around the 5/7, 5/6 and 5/5 resonances. The formation of these resonances may be suppressed by suitably chosen coil currents [10] and also depends on the mass profile.

A more detailed representation of the computations described in this paper will be given in [9].

REFERENCES

[1] Strumberger, E., Nuclear Fusion **36**, 891 (1996).

[2] Hirshman, S.P., et al., Phys. Fluids **28**, 1387 (1985).

[3] Hirshman, S.P., et al., Comput. Phys. Commun. **39**, 161 (1986); Comput. Phys. Commun. **43** 143, (1986).

[4] Strumberger, E., Nucl. Fusion **37**, 19 (1997).

[5] Nührenberg, J., et al., Phys. Lett. A **114** (1986) 129; Proc. 12th EPS Conf. on Contr. Fusion and Plas. Phys., Budapest 1985, EPS, Vol **9F**, Part I, 445.

[6] Mercier, C., in Plas. Phys. and Contr. Nucl. Fusion Res. 1961, Nucl. Fusion 1962 Suppl. 2, IAEA, Vienna, 801 (1962).

[7] Glasser, A.H., et al., Phys. Fluids **18** 875 (1975).

[8] Reiman, A.H., et al., J. Comput. Physics **87**, 349 (1990); Comput. Phys. Commun. **43**, 157 (1986); Arndt, S., et al., this conference.

[9] Strumberger, E., IPP Laboratory Report, will be published.

[10] Strumberger, E., et al., Laboratory Report IPP 2/333, Garching 1996.

Physics and Engineering Studies of a Helias Reactor

C. D. Beidler, G. Grieger, E. Harmeyer , F. Herrnegger, J. Kisslinger , E. Strumberger , H. Wobig, A.V. Zolotukhin
Max-Planck-Institut für Plasmaphysik, EURATOM-Ass., Garching bei München
N. Karulin, *Nuclear Fusion Institute, Moscow*

Introduction

Helias (Helical Advanced Stellarator) configurations have been developed at the IPP Garching in a long phase of analytical and numerical studies to improve the reactor prospects of a classical stellarator. The current Helias reactor is an extrapolation of the W 7-X configuration to reactor dimensions. The basic physical features of a Helias configuration are: its capability to confine an MHD-stable plasma up to $<\beta>=5\%$, the low neoclassical losses which are not prohibitive to ignition and the good confinement properties of highly energetic alpha-particles. The paper summarizes the computational results of various activities to improve the concept of the advanced stellarator reactor:

> Forces and stress analysis of the coil system, self-consistent computation of plasma equilibria, a concept of divertor action on the basis of magnetic islands, neoclassical transport and investigation of alpha-particle confinement, start-up scenarios of the Helias reactor using ECRH and pellet injection and confinement studies using empirical scaling laws.

Coil system

The coil system of the Helias reactor consists of 5 field periods with 10 coils per period. In comparison to a previous design [1] the magnetic field on the coils has been reduced using a trapezoidal shape of the coil cross section and by reducing the average field by 5%. The winding pack is split in two parts in order to reduce the overall current density at the location of maximum magnetic field.

The maximum field on the coils is now 10 T which is in the range of NbTi-technology at a temperature of 1.8 K. Furthermore, slight modifications of the coil geometry have been made to account for the necessary space for blanket and intercoil support elements. Each coil is enclosed in a steel case, which is designed as a box-type profile with a central web for mechanical stiffening.

A 0.04 T vertical field is provided by the modular coils and compensates the Shafranov shift at the outermost surfaces. The minimum bending radius of the superconducting cable is 1.4 m. Force and stress analysis of the Helias coil system have been reported in [2]. An optimized design of the intercoil support system is in progress.

Table 1: Parameters of the HSR coil system

Major radius	22 m	Windings per coil	288
Number of coils	50	Current in winding	37.5 kA
Average coil radius	5 m	Magnetic energy	100 GJ
Max. field on coils	10 T	Weight of one coil	300 - 350 tonnes
Current density	29.5 MAm^{-2}	SC winding pack	4000 tonnes

Finite-beta-equilibrium

The magnetic field of a finite-beta-equilibrium is computed iteratively using the free-boundary equilibrium code NEMEC [3] inside the last magnetic surface and the code MFBE [4] in the region outside the plasma. Starting from a vacuum field with inward-shifted magnetic surfaces, a finite-beta equilibrium with $<\beta> = 5\%$ was computed. As can be seen from Fig. 1 there is a finite Shafranov shift, however the radiating plasma center is still centered with respect to the first wall, thus avoiding large hot spots from neutron irridiation. The Shafranov shift is in the expected range of Helias configurations. The effective plasma radius shrinks slightly at finite beta leading to a modification of the island region at the boundary. The remnants of the $\iota = 1$-islands determine the pattern of plasma flow to the divertor plates. As shown in Fig. 1 by Monte-Carlo calculations of particle orbits, divertor target plates collect the outstreaming plasma. The finite beta-plasma at $<\beta> = 5\%$ is stable according to both Mercier and resistive interchange criteria.

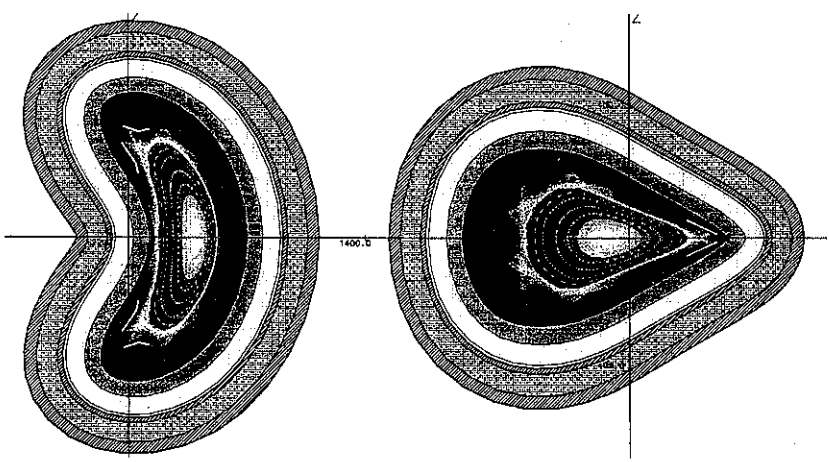

Fig. 1: Cross section of plasma and coils at $<\beta> = 5\%$. Left: $\varphi = 0^{o}$, right $\varphi = 36^{o}$. Width of blanket and shield is 1.2 m at all locations around the torus.

Neoclassical transport

The neoclassical transport charactristics of the new configuration are very similar to those of its predecessors. To summarize briefly, the vacuum magnetic field has an effective helical ripple (for 1/ν-transport) of 2.5% or less over the entire plasma cross section. Neoclassical electron losses are thereby small enough to allow ignition even for the "ion root" solution of the ambipolarity constraint. This is a critical point as the envisaged plasma parameters do not allow operation at the more favourable " electron root". Finite plasma pressure introduces two transport-relevant changes of the magnetic field spectrum: the reduction of the mirror term on the magnetic axis and a significant radial variation of the flux-suface-averaged value of B. The first is a relatively modest effect and actually reduces the effective helical ripple to 2% and less by means of improved drift optimization. The second is critical for the confinement of highly energetic α-particles but of only minor importance for bulk plasma transport.

Alpha-particle studies

Confinement of trapped α-particles is a critical issue in HSR, however, finite plasma pressure produces a true minimum -B-configuration in which the majority of reflected α-particles are confined for at least one slowing-down time [5]. Nevertheless, modular-coil ripple leads to a small fraction of "very prompt" losses (with confinement times less than 10^{-3} sec), potentially resulting in " hot spots " on the first wall of the reactor. To estimate the severity of the problem, the α-particle birth profile is combined with the fraction of phase space in which the birth takes place in a modular ripple. For the $<\beta>=5\%$ case, the total heat load on the first wall due to very prompt losses is estimated to be ≤ 2.2 MW.

Ignition scenarios

The ignition phase of the Helias reactor has been computed using the 1-D time-dependent ASTRA-code [6]. The transport model uses the neoclassical model including the non-diagonal transport coefficients and the anomalous thermal conduction corresponding to ASDEX-L-mode scaling. The radial electric field results self-consistently from the ambipolar condition. In the envisaged parameter regime ($T = 14$ keV, $n(0) = 3 \times 10^{20}$ m^{-3}) the ion root determines the electric field. Fuelling of particles is provided by D-T-pellet injection. The results of the computations show that ignition can be achieved within 10 seconds using a net heating power of 70-80 MW. Typical confinement times of steady-state operation are 1.6 - 1.8 s which coincides very well with the predictions of Lackner-Gottardi scaling. A critical parameter is the fraction of cold alpha-particles which must not surpass 5 - 6%.

Another approach to ignition is the extrapolation on the basis of empirical scaling laws [7] which are deduced from the international stellarator data base. On the the basis of ISS-scaling (International Stellarator Scaling which averages over all stellarator systems) ignition cannot

be achieved; as with the LHD-scaling an improvement factor is needed. However, Lackner-Gottardi scaling and the W7-AS-scaling, which describe the data in Wendelstein 7-A and Wendelstein 7-AS, predict ignition without any improvement factor.

Table 2: Plasma parameters in a Helias reactor

Major radius	22	[m]	Max. beta	15.6	[%]
Average plasma radius	1.8	[m]	Average beta	4.6	[%]
Field on axis	4.75	[T]	Alpha power	608	[MW]
Temperature T(0)	14	[keV]	Fusion power	3040	[MW]
Av. temperature	4.9	[keV]	Confinement time τ_E	1.8	[s]
Electron density n(0)	3.15	10^{20} m^{-3}	Fraction of α-particles	5	[%]

The wall loading by 14 MeV neutrons has been computed taking into account the geometry of the finite-β-plasma. Consistent with the data in Table 2 the peak neutron wall load is 1.6 MWm^{-2} and the average value 0.8 MWm^{-2}. In the region of the divertor plates (see Fig. 1) radiation by fast neutrons is rather weak at about 0.6 MWm^{-2}.

Conlusions

First results of finite-β-equilibria computations in a Helias reactor have verified that the Shafranov shift at $<\beta>$ =5% is acceptable and that neutron emission is distributed equally to the inboard and outboard sides. The magnetic field has been reduced slightly compared to previous concepts to accomodate the requirements of NbTi-superconductor. Ignition in the Helias reactor can be achieved on the basis of empirical scaling laws from present-day stellarator experiments; assumptions about improvement factors are not needed. In conclusion, Helias reactor studies made to date have confirmed the viability of the advanced stellarator reactor concept.

References :

[1] C.D. Beidler et al., 16th IAEA Fusion Energy Conference, Montreal ,Oct. 1996, paper CN-64/G1-4

[2] E. Harmeyer, N. Jaksic, J. Simon-Weidner, 19th Symposion on Fusion Technology, Lisbon 1996

[3] S.P. Hirshman et al. Comput. Phys. Commun. 434 (1986) 161

[4] E. Strumberger, Nucl. Fusion 37, (1997) 19

[5] W. Lotz et al. Plasma Phys. Controlled Fusion, 34 (9192), 1037

[6] G.V. Pereverzev et al. IPP-report 5/42 (1991)

[7] U. Stroth. M. Murakami, R.A. Dory, H. Yamada, S. Okamura, F. Sano, T. Obiki, Nucl. Fusion, Vol. 36, 1063 (1996)

Statistical Properties of the Ergodic Layer in TORE SUPRA and the DED of TEXTOR

Ph.Ghendrih, A.Grosman
Association Euratom-CEA, DRFC, CE Cadarache,
F-13108 St Paul lez Durance, Cedex, France.

A.Kaleck
Institut für Plasmaphysik, Forschungszentrum Jülich,
Association EURATOM-KFA, Partner in the Trilateral Euregio Cluster (TEC)

To create a region of enhanced cross field transport at the plasma edge, coil systems were introduced into TORE SUPRA and planned for TEXTOR generating helical magnetic fields which are resonant on several of the unperturbed flux surfaces. The destruction of the magnetic surfaces due to this helical field determines a divertor volume with a radial extent of roughly 5 cm in the TEXTOR DED and 16 cm in the ergodic divertor of TORE SUPRA.
Some general properties of the resultant divertor are reported. They relate the degree of stochastization to the design values of the coils and to variations of the equilibrium parameters. This analysis is performed with the spectrum of the perturbation field [1] using proper magnetic coordinates which enables a statistical analysis of the field lines by the amplitudes of the resonant modes. Full calculations with these coordinates were done with the code SPECTRE.

The statistical properties of an ergodic layer can be analyzed by the island width δ, the Chirikov parameter σ_{Chir}, which is a measure of overlapping of the islands and of the ergodization, the Kolmogorov length L_k and the field line diffusion coefficient DFL:

$$\delta_{m,n}/2 = \left[\frac{8qrR}{ms}\frac{b_{m,n}}{B_{tor}}\right]^{1/2}; \qquad \sigma_{Chir} = \frac{\delta_{m,n}+\delta_{m+1,n}}{\Delta_{m,m+1}} \approx \delta_{m,n}\frac{ms}{r};$$

$$L_k = \pi q R_0 \left(\frac{\pi q \sigma_{Chir}}{2}\right)^{-4/3}; \qquad DFL = \pi q R_0 \left|\frac{b_{m,n}}{B_{tor}}\right|^2;$$

Here $s = r/q\,\frac{dq}{dr}$ is the shear parameter, $\Delta_{m,m+1} = \frac{r}{ms}$ is the distance between two adjacent resonant surfaces and the $b_{m,n}$ are the Fourier coefficients of the radial component of the perturbation field. This field is created by helical coils having the same pitch angle as the field lines of a given magnetic surface of a fixed equilibrium. In general the coil system has a finite toroidal and poloidal extent and therefore produce a spectrum of many harmonics. Essentially the poloidal spectrum of one toroidal component determines the properties of the ergodic layer. The resulting sine cardindal spectrum is plotted in fig.1.

The center m and the width δm are given by:

$$m = m_{geom}\frac{\Delta\theta}{\Delta\theta^*} = \frac{2\pi}{\Delta\theta^*}m_{coil}$$

$$\delta m = \frac{2\pi}{\Delta\theta^*} = \frac{m_{geom}}{m_{coil}}\left(\frac{\Delta\theta}{\Delta\theta^*}\right) \quad \Rightarrow \quad \frac{\delta m}{m} = \frac{\delta q}{q} = \frac{1}{m_{coil}}$$

with $\Delta\theta$ the poloidal extension and m_{coil} the number of periods in the coil system. m and m_{geom} are the mode numbers in intrinsic and geometric coordinates resp. θ^* is the intrinsic poloidal coordinate. The actual value of $q(r) = m'/n$ determines the decisive component $b_{m,m'}$. The width of the ergodic layer is bounded to

$$\Delta_{ergodic} \leq \left(\frac{dq}{dr}\right)^{-1}\delta q = \frac{r}{sq}\delta q \approx \frac{a}{s\,m_{coil}}$$

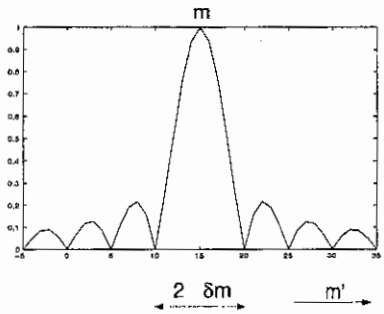

Figure 1: sine cardinal spectrum of finite sin-periods $\frac{\hat{b}_{m,m'}}{\hat{b}(r)} = \frac{\sin(m-m')\,\Delta\theta^*/2}{(m-m')\,\Delta\theta^*/2}$

and also by the radial decay of the amplitude $\hat{b}(r) \sim r^{m_{geom}-1}$.
For circular cross sections the ratio $H = \frac{\Delta\theta}{\Delta\theta^*} \approx (1+\varepsilon\cos\bar{\theta})^2 \cdot (1+\Lambda\varepsilon\cos\bar{\theta})$ varies slowly with r but significantly with Λ, ($\Lambda = \beta_{pol} + l_i/2 - 1$ and $\varepsilon = r/R$) thus we have:

$$\frac{\delta m}{m} = \frac{\delta q}{q} = -\frac{\delta(\Delta\theta^*)}{\Delta\theta^*} \approx \frac{\varepsilon\cos\theta}{(1+\Lambda\varepsilon\cos\theta)} \quad \delta\Lambda$$

$\bar{\theta}$ corresponds to the poloidal location of the coil system. To ensure the same resonance conditions while varying Λ or β_{pol} for TORE SUPRA ($\theta = 0$) q has to be increased for increasing β_{pol} and vice versa for TEXTOR ($\theta = \pi$).

The **TEXTOR DED** is designed for $B_{tor} = 2.25Ts, a = 46cm, R_0 = 1.75m, r(q = 3) = 0.43m, I_{pl} = 441kA, \beta_{pol} = 1$ and for $m/n = 12/4$. For more details see [2]. Sine $m_{coil} = 4$ the spectra (see fig.2) are quite narrow $\delta m = 3$. Optimum resonance q = 3 at r = 43 cm leads to a small value of $\hat{b}_{m,n}$ at the boundary (r = 46 cm) and for this case we have $\sigma_{Chir} \leq 1.5$ and $DFL \leq 10^{-6}$ for $43cm \leq r \leq 46cm$..

Changing the q-profile to $q(r = 46) = 3$ moves the resonant point to the maximum of the right spectrum and this succeeds in a maximum Chirikov parameter of 2.7 and $DFL = 10^{-5}$ at $r = a$.
A numerical study by the SPECTRE code confirms that the latter values can be maintained during a β_{pol}-variation from 0 to 2.0 by adjusting q at the boundary from 3.5 to 2.5 resp. The DED coil system can be fed by current distributions which excite also lower modes like the $m/n = 6/2$ or 3/1 modes. Since the lower modes penetrate deeper into the plasma a small admixture of 25% of the 6/2 mode to 75% of the 12/4 mode leads to larger islands at the r = 43 cm surface without destroying the q = 2 surface (r = 39 cm). The Chirikov parameter is now $\sigma_{Chir}(r = a) = 4$. It has to be proved wether the field line diffusion coefficient is also improved compared to the application of the pure modes.

On **TORE SUPRA**, the magnetic perturbation is generated by 6 octopolar coils equally spaced toroidally. The optimum magnetic configuration is therefore such that the unperturbed magnetic surface tangent to the CFC protection tiles of the coil casing has the same curvature as the coil, hence $R = 2.38m, a = 0.79m$. The plasma current and toroidal field are then governed by the resonant criterion which is determined by the Shafranov parameter $shv = \beta_{pol} + li/2$. Routine operation for ohmic shots, $shv \approx 0.7$, is performed with $B_T \approx 3T$ and $I_p \approx 1.5MA$. The maximum current in the ergodic divertor is $I_{ED} = 45kA$ leading to values of $DFL \cdot v_{the} = 300m^2/s$ at the boundary. The main toroidal wave number of the perturbation spectrum is induced by the coil periodicity,

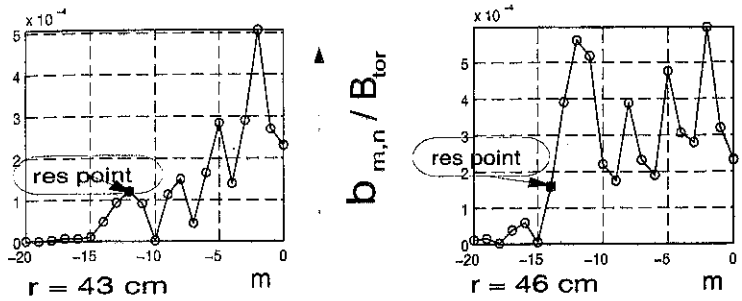

Figure 2: TEXTOR-DED: spectra of the design case for n = 4

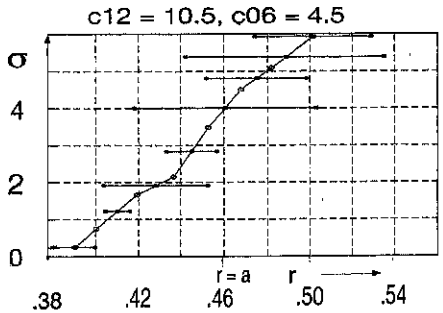

Figure 3: TEXTOR-DED: Chirikov parameter of the mixed mode, the horizontal bars indicate the island widths

$n = 6$. The poloidal spectrum, fig.(4), is close to the sum of two sine cardinal functions (fig.(1)), the useful part being centred on $m = -18\,(q_{res} = -m/n = 3)$. The width of the main component is $\delta m \approx 6$. The fit of the resonant boundary safety factor in terms of shv has been computed in [3], $q_{res} = 9.589/(3.86 - shv)$. The resonance width is defined by the coil design, $\frac{\delta q_{res}}{q_{res}} = 1/3.5$, in good agreement with experimental evidence [4, 5]. The Chirikov parameter allows one to define the location of the separatrix $\rho_{sep}, \sigma(\rho_{sep}) \approx 1$, fig.(5). One finds $\rho_{sep} \approx 0.8$ for ohmic shots and somewhat smaller values, $\rho_{sep} \approx 0.7$, with increasing shv, fig.(5). The design parameters of the ergodic divertor are such that the $q = 2$ surface remains unperturbed, $\sigma(q = 2) \leq 1$, while maximising the size of the stochastic boundary. As a result, the relationship, $\rho_{sep} \approx \rho_{q=2}$ generally holds. In the divertor volume, $\rho \geq \rho_{sep}$ transport is governed by the field line diffusion which was computed with the spectrum of the perturbation, fig.(6). For free particles streaming at thermal velocity along the field lines the ratio of ionic transport to electronic transport is $(me/mi)^{1/2}$ (assuming $T_e \approx T_i$). As a consequence, electronic transport is expected to be perturbed throughout the divertor volume $DFL \cdot v_{the}(\rho \gg \rho_{sep}) \geq 1m^2/s$, while ionic transport only exceeds $1m^2/s$ over half of the divertor volume, fig.(6).

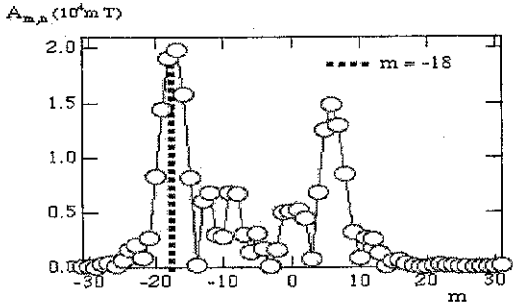

Figure 4: Poloidal spectrum of the perturbation for n = 6,. resonance at m = -18.

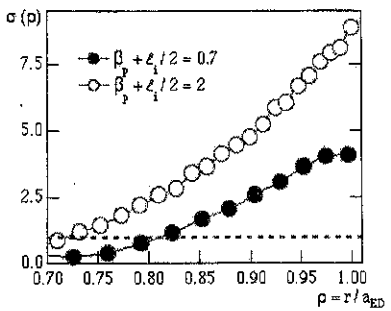

Figure 5: Chirikov parameter profile for low and high β_{pol}

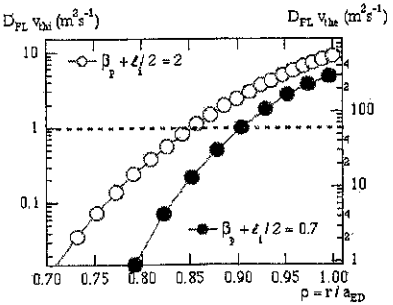

Figure 6: Free particle diffusion coefficient $DFL \cdot v_{th}$ for deuterium ions and electrons.$(mi/me)^{1/2} \approx 60; T_e, T_e = 100eV$).

References

[1] Ph. Ghendrih, H. Capes, F. Nguyen, A. Samain
Contrib. Plasma Phys. **32** (1992) 3/4, 179–191 ·

[2] A. Kaleck, K.H. Finken, M.Haßler
Magnetic Field Line Properties of the Dynamic Ergodic Divertor for TEXTOR-94 at this conference

[3] Ph. Ghendrih, report EUR-CEA-FC-1537.

[4] Ph. Ghendrih, A. Grosman H. Capes, Plasma Phys. Contr. Fusion, 38(1996)1653.

[5] Equipe Tore Supra, presented by Ph. Ghendrih, "High power ergodic divertor operation of Tore Supra", this conference, submitted to Plasma Phys. Contr. Fusion.

Magnetic Field Line Properties of the Dynamic Ergodic Divertor for TEXTOR-94

A.Kaleck[1], K.H.Finken[1], M.Hassler[1], M.Baelmans[1], P.Börner[1],T.Eich[1], T.Evans[4], D.Faulconer[2], B.Giesen[1], R.Koch[2], B.Küppers[1], A.Montvai[3], A.Nicolai[1], D.Reiter[1], A.Rogister[1], M.Tokar'[1], G.Van Oost[2], G.H.Wolf[1]

[1]Institut für Plasmaphysik, Forschungszentrum Jülich GmbH, EURATOM Association D-52425 Jülich, Germany*

[2]Laboratoire de Physique des Plasmas - Laboratorium voor Plasmafysica ERM/KMS, EURATOM Association, B-1000 Brussels,Belgium*

[3]FOM Instituut voor Plasmafysica 'Rijnhuizen', EURATOM Association, Nieuwegein, The Netherlands*

[4]General Atomics, San Diego USA

* Partner in the Trilateral Euregio Cluster (TEC)

For TEXTOR-94, a Dynamic Ergodic Divertor (DED) is proposed which generates a helical perturbation field. This field is either static (DC-operation) or propagating with rotation frequencies of 50 Hz and 7 further frequencies in the range of 1 kHz to 10 kHz. During static operation, similarities and differences with respect to other devices will be studied. The DED is unique in its long continuous windings located at the high field side.The poloidal spectrum of the perturbation field is narrower than that of other machines. In front of the DED-coils a helical near field divertor is built. Important goals of this project are to optimize the radiative mantle of TEXTOR (RI-mode) and to enhance the particle removal by the pump limiter ALT-II.

During the 50 Hz operation, the divertor strike points are smeared out over the relatively large area of the divertor target plate (several square meters). Since the higher frequency rotation is a new aspect, it is more speculative than the more established DC-operation. It is expected that the inertia of the plasma particles (rotation frequency in the order of the diamagnetic rotation frequency) adds a "temporal ergodization" to the spatial one. At f=1 kHz, the DED-fields may sweep the plasma particles into the throat of the pump limiter. It is estimated [1], that at highest frequencies the DED induces a toroidal torque on the plasma of about 1 Nm which is about the same as the one from NBI. The induced rotation may unlock modes, delay the onset of disruptions, improve the confinement (due to sheared rotation) and stabilize dynamically ballooning modes.

The DED coils consist of four quartets of single turn conductors mounted at the HFS with a helical pitch such that the magnetic field lines of the q=3 surface ($\beta_{pol} = 1$) are in parallel. All coil endings are fed through the TEXTOR flanges such that any connection of the wiring is possible. The coils are supplied by 4 phases establishing the rotation pattern mentioned above.

In the present contribution the ergodic structure is discussed by field line tracing calculations. From Poincaré plots characteristics like the Chirikov parameter and the field line diffusion coefficient are deduced. The results are compared to the results of the harmonic analysis of [2] and also complement it.

First attempts are described to start modelling of the helical near field divertor.

The coil system is sketched in fig.1 and the currents in the coils are:

$I_j = \sin\left[2\pi\frac{m}{3}\frac{j-1}{16} + \omega t\right]$ with $m = 12, 6, 3$ or a mixture of theses modes.

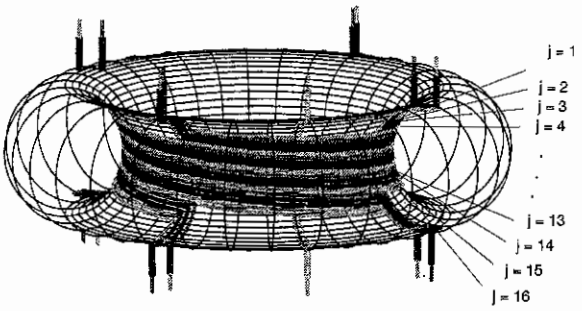

Figure 1: sketch of the DED coils

Fig.2 shows the Poincaré plot of the $m/n = 12/4$ mode at a moderate perturbation level. Because of the finite poloidal extension of the coils, also the m = 10,11,13,14 island chains are directly induced and by nonlinear interaction of neighbouring chains higher harmonics appear such as m/n = 25/8, 29/8, or even 37/12, which leads to stochastization before the main islands overlap.

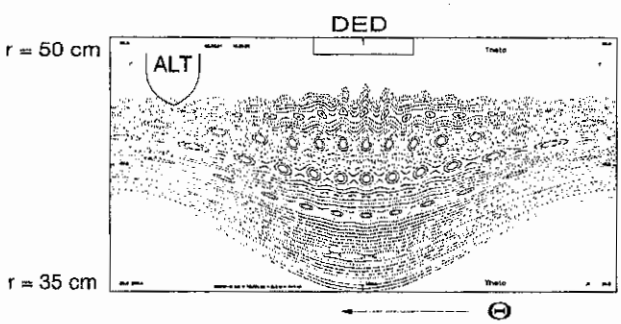

Figure 2: Poincaré plot of the m/n = 12/4 operation mode; $I_{DED} = 5kA$

By measuring the island widths of a series of low level perturbations and extrapolating to the maximum current $I_{DED} = 15kA$ we found a Chirikov parameter of $\sigma_{Chir} = 1...2$ in the ergodic region $43cm \leq r \leq 46cm$ of fig.3 which is in good agreement with harmonic analysis calculations [3].

There are still remnant islands and a barrier was found which hinders field lines to move from the interior to the divertor target plate. Moving the plasma by $\approx 2cm$ toward the coils or moving the resonant q-surface (q=3) more to the plasma boundary will break this barrier.

Since the lower modes (such as m/n = 6/2) can penetrate deeper into the plasma, a mixture of the 12/4 and the 6/2 operation mode can widen the stochastic layer (see fig.4).

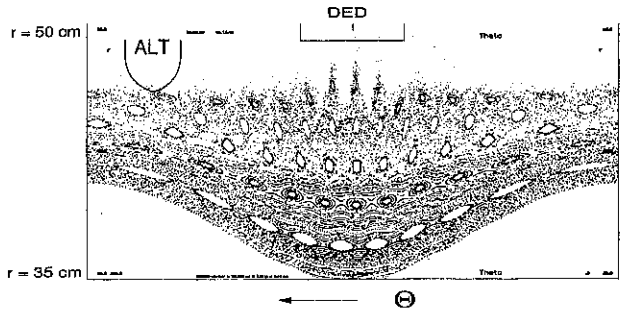

Figure 3: $m/n = 12/4$ operation mode at maximum perurbation level

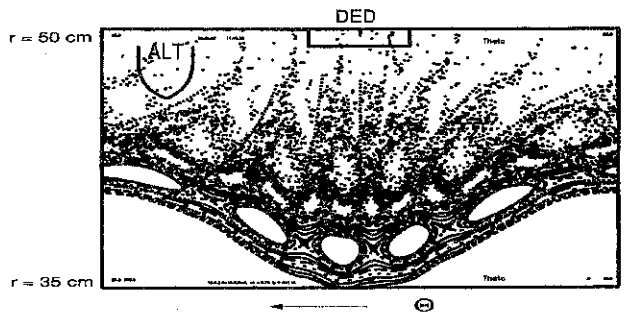

Figure 4: mixed mode $m/n = 12/4(75\%) + 6/2(25\%)$

For an estimation of the field line diffusion coefficient DFL which is described in [2] and evaluated for several DED situations in [3] we start with an ensemble of field lines equally distributed along the toroidal angle at $r = const$ and following it one poloidal turn (i.e. ≈ 3 toroidal turns). Passing the perturbation zone the lines are spread; using the standard deviation of the r-distribution δ in the expression $DFL = \delta^2/(2\pi q R_0)$ we get results comparable to those evaluated from [3]. For the mixed mode we get at $r = 46cm(q_{bound} = 3) : DFL = 2 \cdot 10^{-5} m$, which is about twice larger than the result from [3] adding the squares of the two relevant perturbation components.
It has been shown in cylindrical approximation that the near field of the DED creates a multipolar divertor [4] in front of the perturbation coils. The current required for establishing a helical near field divertor is about one order of magnitude smaller than the one required for a classical poloidal divertor. The complicated field line topology resulting from the ergodization suggests that the modelling is by far more demanding than the one of a poloidal divertor.

To investigate the structure of the magnetic field, the field lines are traced during one poloidal rotation. Depending on whether the field lines intersect a material object (liner, divertor target plate or toroidal pump limiter ALT-II), or not the field lines are marked differently. As a starting plane for the field line tracing, a radial-toroidal cut at the low field side is chosen. Fig.5 shows the starting points (left) and the end points (right) of the

field lines for the path along the top part of TEXTOR. One finds three disjunct areas: The starting points from area (I) do not intersect an object during their path, the field lines from area (II) hit the divertor target plate and the field lines of area (III) hit the liner. A similar picture is found for the path along the lower half of TEXTOR. The combination of both paths finally provides continuous (i.e. non fractal) characteristic areas with the property that a) the field lines do not intersect any object (ergodic area), b) field lines connect the ergodic zone with a material object, or c) material objects are interconnected (like in the normal SOL). For a first step of the modelling it is assumed that the source terms for field lines from the ergodic zone (b) are homogeneous; for area of interconnected magnetic field lines (c) the source terms are assumed to decrease exponentially with the distance from the boundary of this zone.

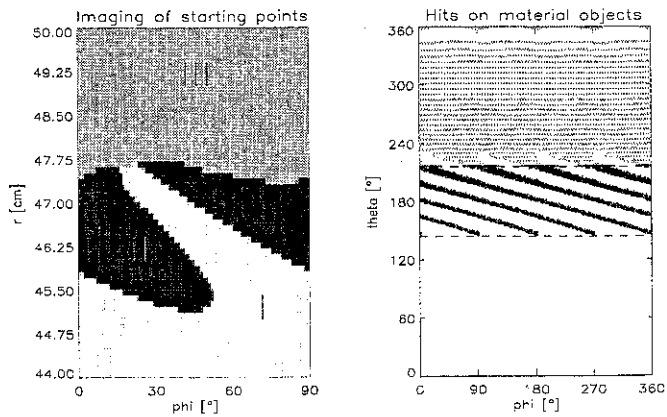

Figure 5: Starting points of field lines (left), starting in a $r-\varphi$-plane, and their intersection points (right) with the divertor target plate $144^0 \leq \theta \leq 216^0$ and the liner $216^0 \leq \theta \leq 360^0$

References

[1] T.Jensen in "Dynamic Ergodic Divertor (DED) for TEXROR-94, Berichte des Forschungszentrum Jülich: 3285,1996

[2] Ph. Ghendrih, H. Capes, F. Nguyen, A. Samain
Contrib. Plasma Phys. **32** (1992) 3/4, 179–191

[3] Ph. Ghendrih, A. Grosman, A.Kaleck
Statistical Properties of the Ergodic Layer in TORE SUPRA and the DED of TEXTOR at this conference

[4] K.H.Finken, Nucl.Fusion.37 (1997) 583

Confinement in discharges with impurity seeding in TEXTOR-94 and TFTR.

J.ONGENA[1*], R.V.BUDNY[2], C.E.BUSH[2], K.HILL[2], A.M.MESSIAEN[1], D.MUELLER[2], A.RAMSEY[2], B.UNTERBERG[3], P.E. VANDENPLAS[1], G.VAN WASSENHOVE[1], R.R.WEYNANTS[1], G.BONHEURE[1], P.DUMORTIER[1], TEXTOR-94 and TFTR teams

(1) Laboratoire de Physique des Plasmas-Laboratorium voor Plasmafysica, Association "EURATOM-Belgian State", Ecole Royale Militaire-Koninklijke Militaire School, B-1000 Brussels, Belgium**

(2) Princeton University, P.O. Box 451, Princeton NJ, 08543, USA, supported by the US DoE Contract No. DE-AC02-76-CH03073

(3) Institut für Plasmaphysik, Forschungszentrum Jülich, GmbH, Association "EURATOM-KFA", D-52425 Jülich, FRG**.

* Researcher at NFSR, Belgium
**Partner in the Trilateral Euregio Cluster (TEC)

A new confinement regime has been established in 1993 on TEXTOR and confirmed on the upgraded TEXTOR-94, a tokamak with a circular cross-section, equipped with the toroidal pump limiter ALT-II, and with a heating system consisting of 2 tangential neutral beam lines (1 co and 1 counter) and 2 antenna pairs. This new regime is called the Radiative I-Mode or RI-Mode. Originally intended to show the possibility of a radiating zone confined to the edge of the plasma in order to cool the edge of the plasma and thus to reduce the maximum heat flow to the wall components, many additional characteristics of interest to a future fusion reactor have been discovered in these discharges : quasi-stationarity of the plasma parameters, high confinement close to ELM-free H-mode confinement, high plasma density near the Greenwald limit, high normalised β, and the possibility to operate at low edge q. The RI-Mode has been obtained in deuterium discharges heated with NBI-co ($D^\circ \rightarrow D^+$), combined with ICRH and/or NBI-counter heating ($D^\circ \rightarrow D^+$) and with (i) a minimum of $P_{NI\text{-}co}/P_{tot} \geq 20\text{-}25\%$ (ii) at sufficiently large central line-averaged densities $\bar{n}_{eo}$ such that the Greenwald number $\bar{n}_{eo}/\bar{n}_{eo,Gr} \geq 70\%$ (where $\bar{n}_{eo,Gr} = I_p/(\pi a^2)$ with as units $10^{20} m^{-3}$, MA, m [1]) (iii) with impurity seeding such that the radiated power fraction exceeds about 50%. The quasi-stationarity has been obtained with the feedback control of (i) the radiating power and (ii) the plasma energy content by acting on the ICRH power level.

This paper will address questions related to the choice of the impurity which can be used for the edge cooling, to the global confinement of the RI-Mode scaling expressed in engineering and non-dimensional parameters and to extrapolating the RI-Mode to larger machine sizes.

1. RI-Mode obtained with Ar seeding in TEXTOR-94

RI-Mode characteristics obtained with Ne cooling have been extensively discussed in previous papers [2-3]. New experiments have been performed with Ar as a radiating impurity and a summary of the effects observed is given in Fig. 1, where a comparison of the time evolution of basic plasma parameters of two discharges at a plasma current $I_p = 350$ kA, with and without Ar cooling is shown. The discharges are heated by the combination of NBI-co and ICRH, and the diamagnetic energy content E_{dia} was kept constant by a feedback control of the ICRH heating power. From t=1.5 to t=3.8s Ar seeding is applied and the intensity of the Ar-VIII line is feedback controlled. Note the similarity to RI-Mode discharges on TEXTOR-94 obtained with Ne cooling : (i) increase in the central line-averaged density $\bar{n}_{eo}$ to values close to the Greenwald limit, (ii) increase in the diamagnetic energy E_{dia} triggered shortly after the start of the Ar seeding together with (iii) a decrease in the ICRH power (at t = 3.2s), when the preset value of E_{dia} of about 120kJ is reached, resulting in (iv) a value for the enhancement factor versus ELM-free H-mode $f_{H93} \cong 1$; (v) increase of the deuterium particle confinement time; (vi) no degradation of the neutron yield [4] but on the contrary, a large increase in the presence of

Ar seeding resulting mainly from the density increase at rather constant temperatures and from the (vii) low central dilution [5]. In addition, a decrease of the safety factor on axis is observed, and an increase in the peaking of the electron density profile. Note also the long duration of the high confinement phase which is about 50 confinement times ($\tau_E \cong 42$ ms), which is terminated on purpose at $t \cong 3.8$s, where the Ar inlet valve is closed and simultaneously a fast ramp down of the plasma current is started, which helps to decrease the density and to terminate the discharge without disruption.
The principal difference between Ar and Ne cooled discharges is the extent of the radiating mantle, which is broader in the case of Ar [5]. In addition, from the present experimental data, γ-values close to 90% and densities above the Greenwald limit seem more difficult to obtain than in discharges with Ne seeding.

2.Confinement behaviour in RI-Mode discharges seeded with Ne and Ar in TEXTOR-94

Previous studies [6] have shown that the confinement of RI-Mode discharges seeded with Ne is well approximated by :

$$\tau_{RI} = (\bar{n}_{eo}/\bar{n}_{eo,Gr})\ \tau_{ITERH93\text{-}P} \qquad (1)$$

where $\tau_{ITERH93\text{-}P}$ is the confinement time as given by the ITERH93-P ELM-free H-mode scaling law. The resulting confinement scaling expression is given by :

$$\tau_{RI} = 0.0113\ \bar{n}_{eo}^{1.17} I_p^{0.06} R^{1.9} a^{1.89} B_t^{0.32} P_{tot}^{-0.67} A_i^{0.41} \qquad (2)$$

(where A_i is the atomic mass and where the units used are's, 10^{19}m^{-3}, MA, m, m, T, MW). Note the linear dependence on the density (as for ohmic discharges) and the near absence of a current dependence. The usual power degradation remains however. Note also that up to now only the dependence on $\bar{n}_{eo}$, I_p and P_{tot} has been checked experimentally.

A similar confinement scaling is found for Ar seeded discharges. This is illustrated in Fig.2, where data points are selected with $f_{H93} \geq 0.8$ for a broad parameter range, obtained from discharges seeded with Ar and Ne.

An interesting question is how the RI-Mode can be expressed as a function of non-dimensional variables. It is well known that the ELM-free H-mode scaling is of the Gyro-Bohm type ($B\tau \propto \rho^{*-2.70}\nu^{*0.28}\beta^{-1.23}$). If one considers ρ^*, β and ν^* as the only significant dimensionless parameters [7], then one would obtain for the RI-Mode $(B\tau)_{RI} \propto \rho^{*-4.23}\nu^{*0.48}\beta^{1.04}a^{0.87}$. Note (i) that we have retained the dependence on the minor radius a, because the scaling (2) does not fulfil the Kadomtsev constraint, in contrast to ITERH93-P; (ii) the ρ^* dependence which is even stronger than Gyro-Bohm and (iii) the increase of confinement with β, in contrast with the usual L- and H-Mode scalings.
However, this choice of non-dimensional variables overlooks a possible role of atomic processes in confinement [7]. A way to take these into account is to use the Hugill number H_u, as an additional dimensionless parameter, proposed by Kadomtsev [8]. This is easily done in our case, since $\bar{n}_{eo}/\bar{n}_{eo,Gr} = 5/\pi\ H_u$ and we propose : $\tau_{RI} \propto H_u\ \tau_{ITERH93\text{-}P}$.

This scaling retains the gyro-Bohm property of the ELM-free H-Mode and takes into account the influence of atomic processes on transport in the RI-Mode.

3. Experiments with Ne and Ar cooling in TFTR.

In view of the extrapolation to a device of the size of a future fusion power reactor, an important question is whether the RI-Mode can be obtained in devices larger than TEXTOR-94. To this

end, experiments have been performed recently in TFTR with both Ne and Ar cooling in deuterium discharges heated with deuterium NBI-co injection.
In Fig.3, a comparison is given of two discharges with similar basic plasma parameters, with and without Ne seeding and heated with 9.5 MW NBI-co at a plasma current I_p =1.6 MA and a toroidal field B_t = 3.9T (corresponding to q_a = 3.6). The plasma density obtained in these discharges corresponds to $\bar{n}_{e0}/\bar{n}_{e0,Gr} \approx 70\%$. It was difficult in the short time available to obtain larger densities. In order to get a 'soft landing', a simultaneous ramp-down of the plasma current, magnetic field and the NBI-co power was pre-programmed at the end of the discharge.. Ne injection was not feedback controlled, and a short puff of Ne (injecting about 0.75 Torr l) was given at t= 3.4s. Due to the absence of a sink for Ne the radiation stayed more or less constant during the phase were the flattop values for I_p, B_t, and $P_{NBI\text{-}co}$ were maintained (t = 3.4 - 4.3s).
Note the similarities with the RI-Mode observed in TEXTOR-94 during Ne puff [2,3] : (i) no decrease of the stored energy E with large values of γ but on the contrary, an increase of E of about 10% corresponding to $\tau_E \approx 1.1 \times \tau_L$ (ii) increase in $\tau_{p,D}$ (iii) decrease in the carbon flux, as seen from the intensity of a C-II line (iv) increase in the peaking factor of the density profile $\gamma_n = n_e(0)/\langle n_e(r)\rangle$ (v) increase in the central electron temperature T_{e0} (vi) no decrease in the neutron reactivity (vii) low central Z_{eff} value leading to a low central concentration of the seeded impurity of about 0.7-0.8 %.

Experiments with feedback controlled Ar cooling have also been performed on TFTR at higher plasma current, heating power and toroidal field (I_p = 2.0MA, $P_{NBI\text{-}co}$ =14.0 MW, B_t = 4.75T) and confirm the observations made in the Ar seeded RI-Mode discharges on TEXTOR-94. They also show a similar signature of RI-Mode physics as the discharges obtained with Ne in TFTR. A wall retention of Ar has been observed, also found in TEXTOR-94, making Ar seeded operation more difficult.
Ne and Ar seeding experiments have been also been performed on TFTR with He as the main discharge gas. In contrast to the Ne or Ar seeded deuterium discharges, no improvement in confinement, but sometimes even a degradation in confinement has been observed.

It is important to note that a large confinement enhancement as in RI-Mode experiments on TEXTOR-94 has not been observed on TFTR (see Fig.4, showing f_{H93} as a function of the Greenwald number for TFTR and TEXTOR-94 discharges with Ar and Ne seeding) as densities around the Greenwald limit could not be realised in the very short experimental time available. However, the many similarities between the TFTR discharges and the RI-Mode discharges on TEXTOR-94 with Ne and Ar seeding seem to justify hopes that the physical mechanisms at work in the RI-Mode can be extended to larger machines. A new series of experiments with Ne seeding is foreseen in the near future on DIII-D, in order to try to show the full performance of the RI-Mode in larger machines.

REFERENCES :

[1] M.Greenwald, J.L.Terry et al., Nucl.Fusion **28**, 2199 (1988).
[2] A.M.Messiaen, J.Ongena, et al., Phys. Rev. Lett. **77**, 2487 (1996).
[3] A.M.Messiaen, J.Ongena et al., Phys. Plasmas **4**, 1690 (1997).
[4] G.Van Wassenhove, S.Helbing et al., this conference
[5] B.Unterberg, A.Messiaen et al., this conference
[6] A.M.Messiaen , J.Ongena et al., *"Recovery of a Neo Alcator type scaling with auxiliary heating in radiatively cooled discharges on TEXTOR-94"*, Comments Plasma Physics Contr. Fusion, in print.
[7] J.G.Cordey, B.Balet et al., Plasma Physics Control. Fusion, **38**, A67-A75 (1996)
[8] B.B.Kadomtsev, *"Tokamak Plasma : a complex physical system"*, Plasma Physics Series, IOP Publishing Ltd., Bristol and Philadelphia, 1992, pp 100-101.

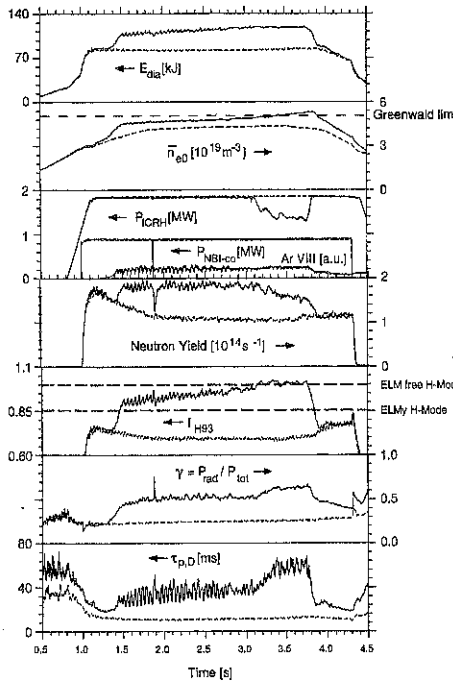

Fig. 1: Comparison of a discharge with (#70688, plain curves) and without (#70666, dashed curves) Ar seeding on TEXTOR-94

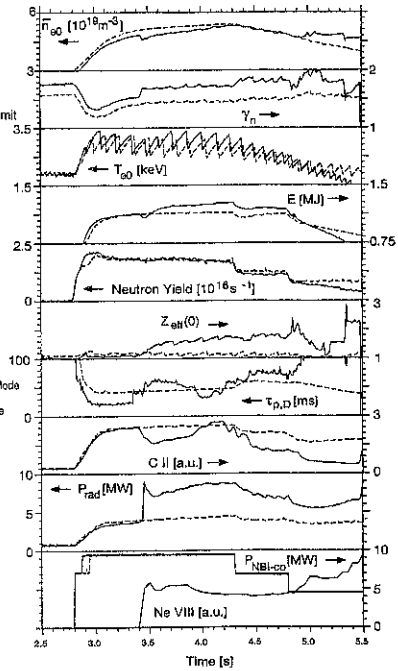

Fig. 3: Comparison of a discharge with (#101948, plain curves) and without (#101947, dashed curves) Ne seeding on TFTR

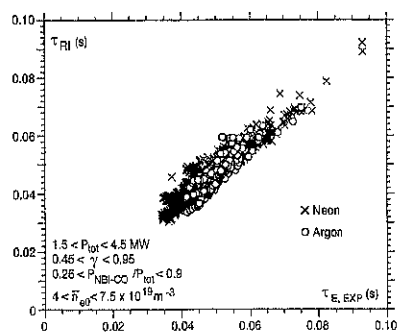

Fig. 2: Confinement as given by the RI-Mode scaling versus experimentally observed confinement time for Ne (crosses) and Ar (circles) cooled discharges in TEXTOR-94. All datapoints satisfy H_{93} > 0.8

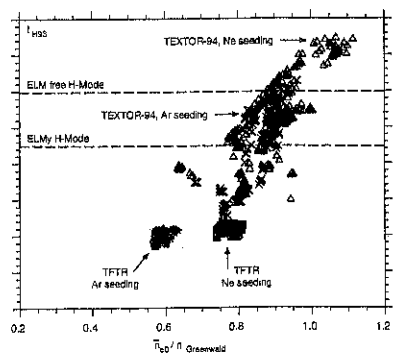

Fig. 4: Enhancement factor w.r.t. ELM-free H-mode versus Greenwald number for Ne and Ar cooled discharges in TEXTOR-94 (open triangles : Ne, crosses : Ar) and TFTR (full squares : Ne, stars : Ar)

Dilution and electron temperature determination from neutron rate measurements during RI mode discharges in TEXTOR.

G. Van Wassenhove[1], S. Helbing[2], G. Bonheure[1], F. Gadelmeier[4], R. Jaspers[3], A. Kramer-Flecken[2], A. Messiaen[1], J. Ongena[1+], G. Telesca[1], B. Unterberg[2], M. Vervier[1], B. Wolle[4]

1 Laboratoire de Physique des Plasmas / Laboratorium voor Plasmaphysica, ERM / KMS, EURATOM Association, B-1000 Brussels, Belgium *
2 Institut für Plasmaphysik, Forschungszentrum Jülich GmbH, EURATOM Association, D-52425 Jülich, Germany *
3 FOM Instituut voor Plasmaphysica Rijnhuizen, EURATOM Association, Nieuwegein, The Netherlands *
4 Institut für Angewandte Physik, Universität Heidelberg, D-69120 Heidelberg, Germany.

* Partner in the Trilateral Euregio Cluster (TEC)
+ Researcher at NFSR, Belgium

Recently, a new confinement regime called radiative I-Mode (RIM) has been observed on the limiter tokamak TEXTOR-94 [1,2]. This regime is obtained by impurity seeding (Ne, Ar) of a plasma of D heated with NBI-co injection of D eventually combined with ICRH. The study of the central impurity content of those plasmas is of particular importance. The analysis of neutron production during the discharges offers a very straightforward way to study the evolution of $< n_D / n_e >$ in the central part of the plasma during impurity injection.

Experimental results

The neutron yield is measured using 6 detectors of different types BF3, He 3 counters and liquid scintillators surrounded with lead. The calibration of the detectors was carried out using a reference neutron source and is controlled regularly using activation probes [3]. We present in figure 1 the time evolution of the neutron yield as function of time for 4 consecutive discharges with increasing level of injection of neon. Similar results are obtained with injection of argon. The neutron rate increases at the start of the impurity injection and remains almost constant during the impurity injection phase. In some shots with intense Ar injection where the power radiated reach values as high as 88 % the neutron yield may decrease during the phase of impurity injection but this decrease is accompanied by a continuous increase in density (fig. 2).

Discussion

For the shot of fig. 2 the neutron production calculated from TRANSP code and from a simple 1D model are compared using the $T_e(r)$ profile from ECE measurements and $T_i(r)$ from CXES. In this 1D model the neutron density production is decomposed into the neutrons produced by collisions of thermal deuterium ions y_{th} and the neutrons produced by beam-target interaction y_{bt}.

$$y(r) = y_{th}(r) + y_{bt}(r)$$

with $y_{th}(r) = (\frac{n_D}{n_e})^2 \frac{n_e^2}{2} < \sigma v >$ and $y_{bt}(r) = 0.24 j(r) \frac{n_D}{n_e} K(T_e)$

The reactivity $<\sigma v>$ is a function of the ion temperature T_i of the plasma, n_D and n_e are the deuterium ion and electron density, T_e is the electron temperature, $K(Te) = T_e(r)^{3/2} \int_0^{v_b} \frac{v^2}{v^3 + v_c^3(T_e)} (\sigma v) dv$ with v_b the injection velocity of the ions (corrected to take into account the toroidal rotation of the plasma), $(\sigma v)(T_i, v)$ the average value of σv for mono-energetic ions of velocity v interacting with a maxwellian target plasma of temperature T_i. The beam power deposition profile j(r) is calculated using the DEPON code. The time dependence of neutron yield is neglected in those high density discharges because the slowing down time is of the order of 40 ms at the beginning of the injection for the Deuterium deposited in the centre of the plasma and, due to the increase in density, is becoming lower than 20ms after 100ms of beam injection. The slowing down time for the ions deposited at higher r is even smaller. This is the reason why we can also neglect the beam beam interaction and the density of the beam ions. The critical energy of the plasma is such that the beam ions, during their slowing down, loose first thier energy in collision with the electron and the isotropisation of the beam can be neglected. The density of the beam target neutrons is maximum at a radius of 17 cm,the thermal neutrons are produced at an average radius of 10 cm.

The results of the integration K shows that for the beam injection and plasma conditions of RI mode of TEXTOR, K is almost proportional to T_e. We made the hypothesis $T_i = T_e$, which is justified because the energy equipartition time is much smaller than the energy confinement time of the particles [1]. The total number of neutrons produced in the beam target reaction Y_{bt} is therefore proportional to $<Te> = \int_0^a j(r) T_e(r) r dr \Big/ \int_0^a j(r) r dr$.

The comparison of the evolution of $Te(r=15cm)$, $<T_e>$ and an average temperature given by the ratio of diamagnetic energy and line averaged central density $Tedia = \frac{E_{dia}}{n_{e0}}$ shows that the evolution of $\int_0^a j(r) T_e(r) r dr$ is better approximated by $\frac{E_{dia}}{n_{e0}}$ than by Te(r=15cm). For discharges where the y_{bt} >> y_{th} it is therefore possible to have direct information on the evolution of the dilution $< n_D / n_e >$ by comparison of Tedia and Y.

The comparison between the run of TRANSP and the 1D model is presented in fig.3. The results are similar all along the time of the discharge for rather different plasma conditions. The remaining difference can be attributed to the following differences between 1D model and TRANSP simulation: i) 1D model calculates neutron production at constant n_D/n_e=0.9 while n_D/n_e is varying between 0.95 and 0.85 in the run of TRANSP in order to match the measured plasma resistivity, ii) the power deposition profiles given by TRANSP and by DEPON are sligthly different, (TRANSP code gives a more central power deposition, y_{bt} is proportional to the temperature so y_{bt} (TRANSP) is higher), iii) the impact of the rotational velocity on the beam target neutron production is overestimated in the 1D code. The increase in neutron yield at the

beginning of the injection of impurities is due to the increase of its thermal component: the deuterium density increases at almost constant ion temperature. Using the 1D code the evolution of n_D/n_e during the shot 70287 can be evaluated,with the hypothesis that n_D/n_e in the plasma core is independent of r and taking into account that y_{th} is proportional to n_D/n_e and that y_{bt} is proportional to $(\frac{n_D}{n_e})^2$. The result of this dilution determination is presented in fig 4. The value of n_D/n_e stays almost constant at .9 during the injection phase. The drop in neutron rate observed all along the shot is due to the change of the power deposition profile and of the temperatures but not to the change of the dilution. The absolute error bar on the value of n_D/n_e is of the order of 30% due to the uncertainty in the calibration of the neutron detector and on the value of electron and ion temperatures and error on code predictions. The relative error bar on the evolution of n_D/n_e during injection is smaller but remains nevertheless dependent on the absolute value of measured T_i (For Shot 70287 an increase of T_i of 10% will decrease n_D/n_e by 10%).

As shown in a sensitivity study [4] the electron temperature has a very strong influence on the neutron yield for TEXTOR conditions. Therefore it is the plasma parameter best suited for a determination by use of the fast Fokker-Plank-code NRFPS [5], assuming that the dilution is known. If the electron density is so high that a determination of T_e from 2nd harmonic electron cyclotron emission (ECE) is impossible, it is especially usefull to calculate T_e by that method. The results of the calculation of T_e using NRFPS for discharge #67130 are shown in fig. 6 (with some parameters of that discharge in fig. 5). They differ substantially from the also shown 2nd harmonic ECE measurement for which the cut-off density in the center of 8.95 10^{19} m^{-3} is reached at t=1.7 s. However, they are close to the values from 3rd harmonic ECE which were available for that shot. In this shot neon injection starts at t=1.5s.This agreement can therefore be interpreted as a proof of the validity of the hypothesis that n_D/n_e was not changing in the plasma during the neon injection.

Analysis of the neon scan and conclusion

In the RIM mode shots of TEXTOR with NB injection power of 1 MW the thermal neutron production can become a substantial fraction of the total neutrons production. This is due to the rather high ion and electron temperature accompanied with very high densities at moderate beam energies.

The 1D code was run to determine the evolution of n_D/n_e as a function of time for different levels of Ne injection. The uncertainties in the measurement of T_i are quite high but the change in n_D/n_e when the Ne injection is increased is not larger than 10% .This result is in agreement with results of bremsstrahlung and charge exchange measurements.

References

[1] A.M.Messiaen, J.Ongena et al., Phys. Rev. Lett. **77**, 2487 (1996).
[2] A.M.Messiaen, J.Ongena et al., Phys. Plasmas **4**, 1690-1698 (1997).
[3] F. Gadelmeier , private communication (1997).
[4] Wolle B,Helbing S. et al, Plasma Phys. Control. Fusion **39**, 541-547 (1997).
[5] Wolle B, Eriksson L-G, Gerstel U and Sadler G Plasma Phys. Control. Fusion **36**, 1051 (1994)

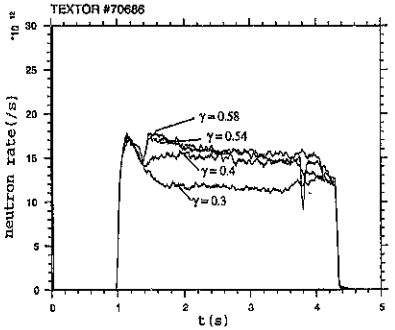

Fig. 1 : Neutron rate as function of time without and with different level of injection of Ne.Ne injection starts at t=1.3 s until t=3.7 s. γ is the ratio between radiated power and total power injected in the plasma. γ = 0.3 is the case without Ne injection.

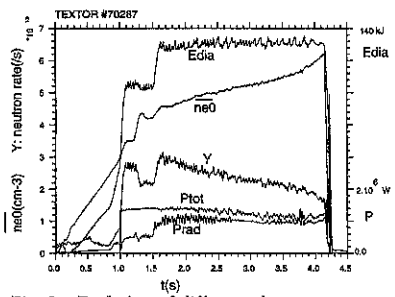

Fig. 2 : Evolution of different plasma parameters for a discharge with Ar injection. (# 70287). Shown as function of time are the diamagnetic energy E_{dia}, the central line averaged density $\overline{n_{e0}}$, total neutron rate Y, the total heating power P_{tot}(Ohmic+ NBI + ICRH).

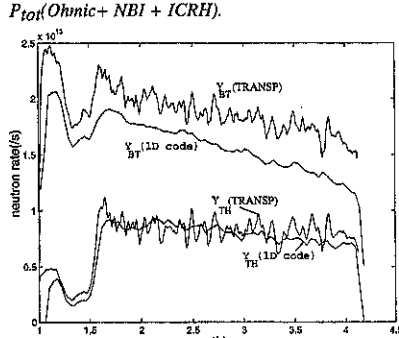

Fig.3 : Comparison of total neutron rate components evaluated using TRANSP or the 1D code (shot 70287).

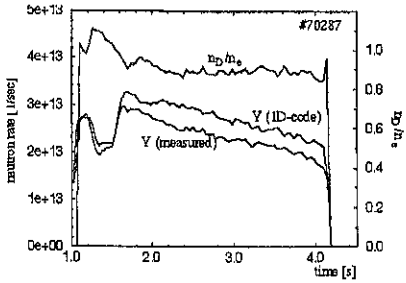

Fig. 4 : Measured and predicted neutron rate Y as function of time (Shot 70287),with hypothesis n_D/n_E=1 and evolution of n_D/n_e deduced from comparison of measured and predicted neutron rate.

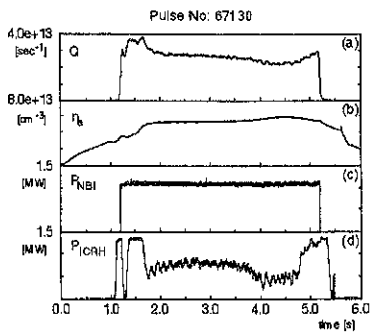

Fig. 5 Time evolution of (a) neutron emission, (b) line-averaged electron density, (c) neutral beam power and (d) coupled RF power, for discharge #67130. The cut-off density for 2nd harmonic ECE is reached at t=1.7 s.

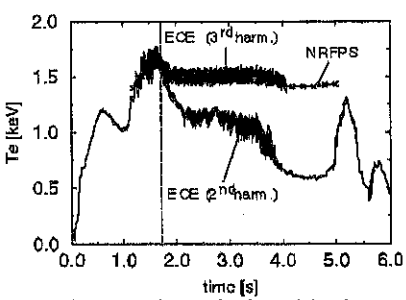

Figure 6: Measured central values of the electron temperature from 2nd and 3rd harmonic ECE emission together with the results of a time-dependent T_e interpretation calculation with the NRFPS-code for discharge # 67130.

Experimental investigations on the effect of $\vec{E}\times\vec{B}$ flow shear on edge transport in improved confinement at TEXTOR–94

St. Jachmich[1], G. Van Oost[2] and R.R. Weynants[2]

Partners in the Trilateral Euregio Cluster:

[1] Institut für Plasmaphysik, Forschungszentrum Jülich GmbH, EURATOM Association, D–52425 Jülich, Germany

[2] Laboratoire de Physique des Plasmas – Laboratorium voor Plasmafysica, Association "Euratom – Belgian State", Ecole Royale Militaire – Koninklijke Militaire School, B–1000 Brussels, Belgium

Abstract

Edge transport and confinement changes induced by radial electric fields, externally imposed in TEXTOR–94 by means of electrode biasing, were investigated. A particle transport barrier is found to be built up as the electric field gradient increases, thus strengthening the conjecture that $\vec{E}\times\vec{B}$ stabilization of turbulence is a viable mechanism for improved confinement in tokamaks.

1 Introduction

In the enduring effort to explain the mechanism of high confinement modes in tokamaks, many theories on the creation of transport barriers have dedicated a decisive role to radial electric fields [1–6]. The hitherto favoured explanation for the confinement improvement in all these circumstances is the stabilization of turbulence [2,4] by the shear rate $\omega_{\vec{E}\vec{B}}$ in the $\vec{E}\times\vec{B}$ flow induced by E_r [7]

$$\omega_{\vec{E}\vec{B}} = \left|\frac{dv_{\vec{E}\vec{B}}}{dr}\right| = \left|\frac{(RB_\theta)^2}{B}\frac{\partial}{\partial\Psi}\frac{E_r}{RB_\theta}\right| \quad , \tag{1}$$

where R is the major radius, B_θ is the poloidal field and Ψ is the poloidal flux.

According to the radial momentum equation

$$E_r = \frac{1}{en_i}\nabla_r p - v_\theta B_\phi + v_\phi B_\theta \quad , \tag{2}$$

the electric field can have its cause either in the plasma rotation or the pressure gradient, such that the verification of the causality between the shear of $\vec{E}\times\vec{B}$ and confinement changes is aggravated. In the "natural" H–mode, for instance, it was found that E_r, which is in those cases negative, can quite often be upheld by the pressure gradient, such that the discrimination whether E_r is the cause or the result of the confinement improvement is impeded. In our experiments [8] we can avoid this inauspicious circumstance by imposing positive electric fields in the plasma edge using electrode biasing. Since the contribution of $\nabla_r p_i$ is in such regimes always negative, the electric field is then a consequence of strong poloidal and toroidal rotation in the plasma edge.

2 Experimental set–up and Results

The experiments were performed at TEXTOR–94 in deuterium discharges with the parameters as follows: $B_T = 2.33$ T, $I_P = 210$ kA and a pre–bias central line–averaged electron density $\overline{n}_{e,0} = 1.0 \cdot 10^{13}$ cm^{-3}. The mushroom–shaped electrode is introduced into the plasma 5 cm beyond the LCFS and is biased positively with respect to the toroidal belt limiter ALT–II. The resulting radial electric field profiles were measured by a recently developed nine–tip probe (henceforth called rake probe) continuously during the whole discharge. The edge density and temperature profiles were obtained by means of Li– and He–beam diagnostics, which are located at the same outboard port as the rake probe with a connection length of 12 cm.

Figure 1 shows time traces of important parameters for a typical discharge, where the electrode voltage V_E is slowly ramped up to 600 V. The electric field, represented by its maximum, develops gradually until a sudden jump of $E_{r,max}$ occurs in conjunction with a sudden drop in the electrode current I_E (not shown). This bifurcation of E_r is attributed to a dramatic decrease in the parallel viscosity [9]. Although the gas–feed of the density control is closed, the total number of electrons $N_{e,tot}$ starts already growing at low fields ($t_1 = 1.5$ s) and its growth accelerates upon the field bifurcation ($t_2 = 2.1$ s). Also shown is the H_α emission summed over the total plasma periphery (limiter, wall and biasing electrode) from which, in combination with $N_{e,tot}$, the particle confinement time τ_p can be obtained. Increasing E_r apparently improves the particle confinement time.

Detailed edge measurements show the confinement improvement to be the result of the formation of a transport barrier (i.e. a zone of finite extent where the particle diffusivity D is depressed) at the plasma edge, coincident with the radial region where the imposed electric field is located (the electrical layer). As a measure of D we take the ratio of Γ (the net outflow of particles through a magnetic surface and which must be proportional to H_α) to the local density gradient ∇n. Assuming Γ in first approximation to be constant with radius, a relative decrease in the local diffusivity due to the imposed field can then be inferred from a relative increase in the local ∇n, a measure of which is ξ, the ratio of $\nabla n_{bias}/\nabla n_{prebias}$.

In Fig.2b a contour plot of $\xi - 1$ in the edge region is shown, indicating an enhancement of ξ in a zone which turns out to have the radial extent of the electrical layer. Note that there are two regions of enhanced ξ, meaning that the density gradient steepens in two zones and develops a minimum in between (see also [8,10]). We generally find the radially innermost maximum to be 2 to 4 times higher than the outer one. Because of this fine structure, it is impossible to attribute the observed changes directly to E_r. If the latter one were indeed the responsible acting parameter, a single zone of enhanced ξ should be present. However a clear correlation is found with the gradient of E_r, the absolute value of which is shown as a contour plot in Fig.2a. The minimum in ξ, in between the maxima discussed earlier, is closely correlated with the location of $E_{r,max}$, which is indicated by the thick solid line in Fig.2b. The obvious temporal link between ∇n and ∇E can still better be appreciated when showing in Fig. 1 the temporal evolution of both quantities at the radius of 43.9 cm where the radially innermost maxima of ξ and of ∇E are found. Indications are that there might exist a threshold value of ∇E before ξ reacts, but this threshold is by no means sharp.

The observed spatial and temporal link between ∇n and ∇E is found to be very robust. On the one hand, it is found that in discharges where the plasma position is

changed, both the electrical layer and the enhanced layer move together. Their temporal sequence, on the other hand, is maintained even for very short voltage ramps. One is forced to conclude that ∇E, which is the imposed quantity in this experiment, is the cause and ∇n the effect in this causal link.

3 Discussion and conclusion

In these polarisation experiments the radial electric field is imposed in a controlled fashion. The positive sign of the field allows to rule out that the field is developing as a result of improved confinement. If the local ∇n , as we have argued, is a reliable measure of the local diffusivity, the observed spatial and temporal link between ∇E and ∇n allows to conclude that particle transport is indeed improved by shear in the $\vec{E}\times\vec{B}$ flow, as theory predicts. As an important test for said theory, we find however that both positive and negative field gradients can affect diffusivity.

The local imposition of shear in the edge region leads to the formation of a particle barrier in the electric layer. This barrier has an internal structure such that the density profile steepens at two radial locations with a minimum in the gradient in between. As the radially outermost density steepening in our experiments is found to be weaker than the innermost, and in addition its effect on the bulk plasma is attenuated by the adjacent minimum, it is found (see Fig. 1) that the time and rate of increase of the total number of particles is practically set by the behaviour of the innermost steepening. Because of this, we are not in a position to decide on the relative effectiveness of positive or negative shear in shaping transport. Forthcoming polarisation experiments with imposed negative field are likely to further improve our understanding.

Acknowledgement

The authors like to thank the ERM/KMS–staff and the TEXTOR–Team, especially J. Boedo, M. Brix, A. Huber, A. Lyssoivan, A. Pospieszczyk, B. Schweer, H. Van Goubergen and F. Weschenfelder for their assistance.

References

[1] E.J. Doyle et al., Paper IAEA–CN–64/A6–4, Montreal, Canada, Oct. 1996.

[2] S.–I. Itoh and K. Itoh, *Phys. Rev. Letters*, **60** (1988), p. 2276.

[3] K.C. Shaing and E.C. Crume, Jr., *Phys. Rev. Letters*, **63** (1989), p. 2369.

[4] H. Biglari, P.H. Diamond, and P.W. Terry, *Phys. Fluids B*, **2** (1990), p. 1.

[5] B.A. Carreras et al., *Phys. Plasmas*, **1** (1994), p. 4014.

[6] G.M. Staebler et al., *Phys. Plasmas*, **1** (1994), p. 909.

[7] T.S. Hahm and K.S. Burrell, *Phys. Plasmas*, **2** (1995), p. 1648.

[8] R.R. Weynants et al., *Nuclear Fusion*, **32** (1992), p. 837.

[9] J. Cornelis et al., *Nuclear Fusion*, **34** (1994), p. 171.

[10] R. Van Nieuwenhove et al., *Proc. of 18th EPS-Conf. on Contr. Fus. and Plasma Phys.*, Berlin, **15C** part I (1991), p. 405.

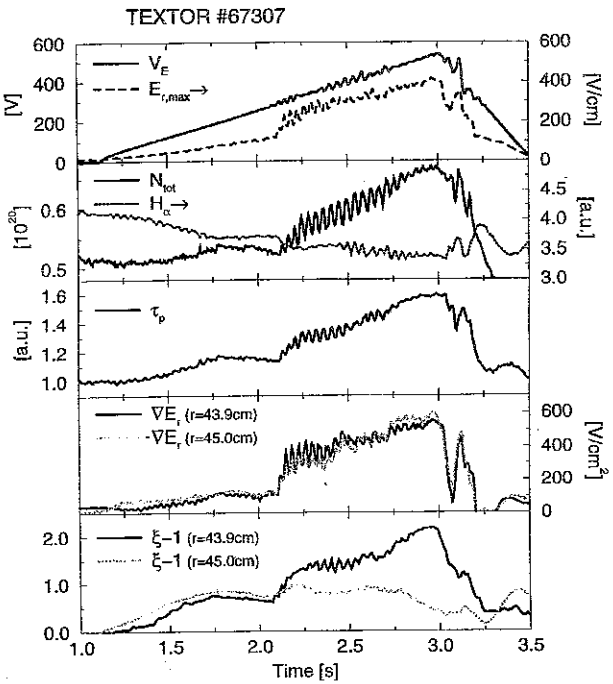

Fig. 1: Time traces of the electrode voltage V_E, electric field maximum $E_{r,max}$, total number of electrons N_{tot}, H_α–light, particle confinement time τ_p, field gradient maxima ∇E and the relative change of the density gradient $\xi - 1$ at the corresponding radii.

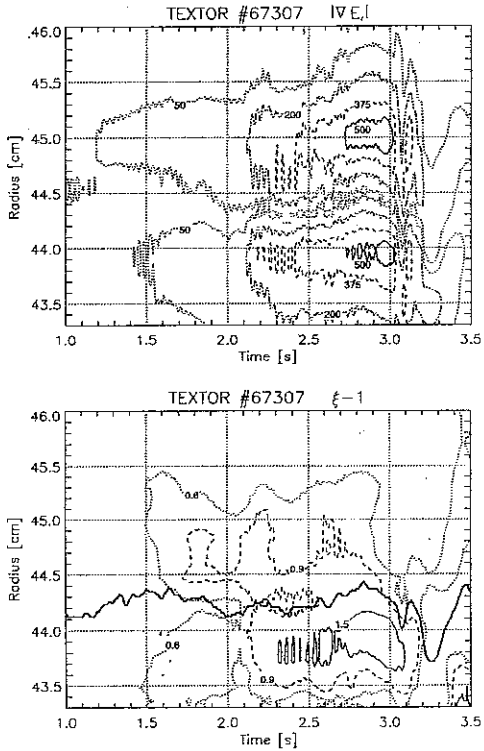

Fig. 2: Contour plots of a) the absolute value of the electric field gradient ∇E (the outer maxima corresponds to the negative field gradient side) and of b) the relative change of the density gradient $\xi - 1$. The thick solid line indicates the position of the electric field maximum.

Runaway diffusion in TEXTOR-94

I. Entrop[1,2], R. Jaspers[1], K.H. Finken[2], N.J. Lopes Cardozo[1]
Partners in the Trilateral Euregio Cluster:
[1]FOM Instituut voor Plasmafysica Rijnhuizen, EURATOM Association, Nieuwegein, Netherlands
[2]Institut für Plasmaphysik, Forschungszentrum Jülich GmbH, EURATOM Association, D-52425 Jülich, Germany

1 Introduction

Thermal electron diffusivity in tokamak plasmas is much larger than neoclassical theory predicts. Possible cause of this anomalous loss are magnetic field perturbations. Because high energetic runaway electrons are effectively collisionless, their dynamics is mainly determined by these perturbations and could, therefore, be helpful in the study of those. Difficulties with deriving magnetic turbulence levels from runaway diffusion arise, however, from the difference between the topology of runaway orbits and that of magnetic field lines, as well as the large drifts that could decouple the runaways from the field lines and make them less sensitive to magnetic perturbations [1–3].

In TEXTOR-94, runaways in the plasma core with energies up to 30 MeV are detected by measuring the synchrotron radiation these highly relativistic electrons emit. Previous experiments on runaways in TEXTOR [4] were limited by the fact that only a small part of the plasma cross section could be viewed. Here, we report on experiments in which the field of view was expanded to a full cross section. That allows us the determination of radial profiles of runaway densities, from which the profile of the radial runaway diffusion coefficient $D_r(r)$ is determined for the Ohmic case. Furthermore, the effect of additional heating (NBI and ICRH) on runaway diffusion is investigated.

2 Experiments

Experiments were performed at the TEXTOR-94 tokamak, which has major radius $R_0 = 1.75$ m and minor radius $a = 0.46$ m. Typical plasma parameters for Ohmic runaway discharges are: toroidal magnetic field $B_t = 2.25$ T, plasma current $I_p = 350$ kA, line averaged density $\bar{n}_e < 1.0 \times 10^{19}$ m^{-3}, flat-top loop voltage $V_{loop} \approx 1$ V. A power scan was made with NBI (co-injection, with respect to plasma current) and ICRH.

The synchrotron radiation is detected with an infrared (IR) camera, which scans one image in 16 ms (NTSC-TV standard). The working wavelength range of the detection system is $3 - 8$ μm. The line of sight of the camera is tangential to the plasma in the direction of electron approach.

The IR images are processed afterwards. With help of software defined integration boxes, the evolution of the synchrotron radiation can be determined from subsequent pictures. With a narrow slit-shaped box at the equatorial plane, a radial profile is obtained for each image. Note that only runaways with energy $W_r > 20$ MeV are detected with the above set-up, i.e. all derived quantities are valid only for these high relativistic runaways.

3 Results and interpretation

Fig. 1(a) and 1(b) show synchrotron radiation evolution and radial profiles of an Ohmic runaway discharge, reaching a steady state at about $t \approx 4$ s.

We assume that the runaway transport is diffusive. A diffusion coefficient can be determined from the diffusion equation

$$\frac{\partial n}{\partial t} = -\nabla \cdot \mathbf{\Gamma} + S \tag{1}$$

including a source term S, and the relation between particle flux $\mathbf{\Gamma}$ and particle density gradient ∇n. In steady state, with cylindrical coordinates, D_r follows from

$$D_r(r) = \frac{\frac{1}{r}\int_0^r S(r')r'dr'}{-\frac{\partial n}{\partial r}(r)} \tag{2}$$

where S is the runaway source density and n the runaway electron density. To derive these quantities from the measured synchrotron radiation, several assumptions have to be made. The intensity from the radiation is proportional to the number and energy of runaways. In [4], Monte Carlo simulations show a rather peaked energy dependence in the synchrotron radiation and also the estimation of the energy distribution with help of different filters do not show a strong sensitiveness to the exact shape of the energy distribution. We, therefore, assume a monoenergetic energy distribution, so that the intensity evolution is a measure of runaway density evolution. This assumption implies a constant energy profile, needed to interpret the intensity profiles as runaway density profiles.

The strength of the source density S follows directly from (1) in case $-\nabla \cdot \mathbf{\Gamma} = 0$, i.e. when the synchrotron radiation starts to develop. For the shape of the source density, first a δ-function is assumed, leading to an upper limit of the runaway diffusion coefficient $D_{r,upper}$, then a constant source density leading to a lower limit $D_{r,lower}$. A self-consistent solution is found by iteration converging to $D_{r,it}$, when we assume that the runaway distribution has a given width at the critical energy (from [4], $\Delta r = 7$ cm) and that this profile broadens during the acceleration due to diffusion with a constant D_r. It is likely that the diffusion coefficient is a decreasing function of runaway energy, so $D_{r,it}$ is still an upper limit. Based on measurements at $r \in [20, 35]$ cm, Fig. 1(c) shows the result of these three different approximations. At half radius, $D_r < 0.01$ m^2/s.

The power scan shows both for NBI and ICRH (Fig. 2(a) and 2(b)) a transient phase of approximately 300 ms after the heating is turned on. Then, the evolution of radiation continues to rise or decays dependent on the power of NBI or ICRH. A very coarse estimate is made of the rise (decay) times τ determined after the transient phase. The inverse of τ is shown in Fig. 2(c). Unfortunately, in the absence of a steady state, the method used in the Ohmic case to determine the diffusion coefficient cannot be applied to the case with additional heating.

4 Discussion

The runaway diffusion is best compared to thermal transport instead of particle transport, because runaways are effectively test particles, are not subjected to ambipolar diffusion

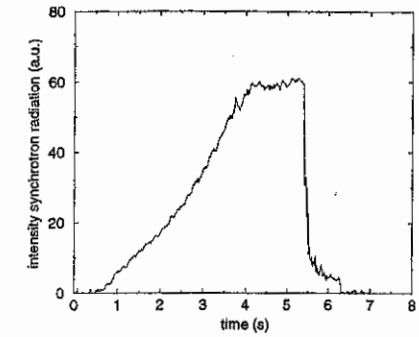

(a)

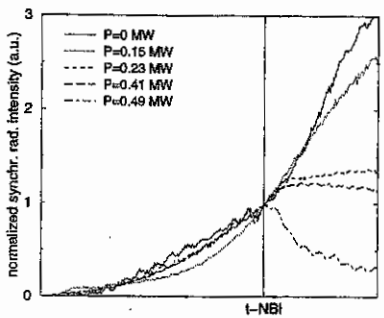

(a)

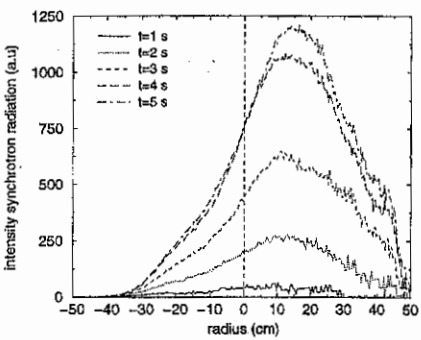

(b)

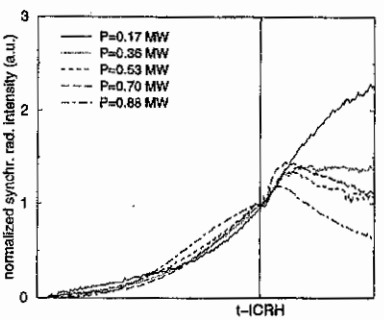

(b)

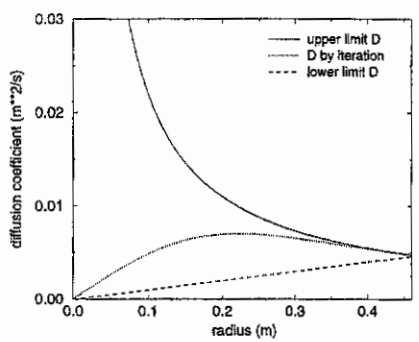

(c)

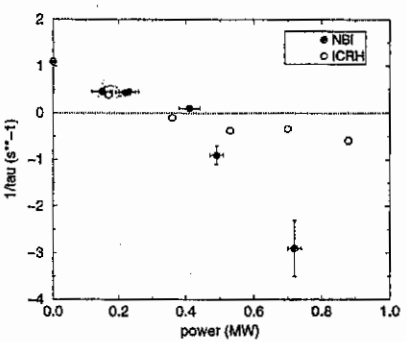

(c)

Figure1:
(a) Evolution of synchrotron radiation.
(b) Radial profiles of synchrotron radiation at different time.
(c)Profile of radial diffusion coefficient.

Figure 2:
(a) Evolution of synchrotron radiation at different NBI power.
(b) Evolution of synchrotron radiation at different ICRH power.
(c) Inverse of rise (decay) time for both NBI and ICRH.

and do not experience recycling effects as thermal particles do. In TEXTOR-94, electron heat transport typically has $\chi_e \sim 1$ m^2/s (χ_e the electron diffusivity) [5]. The measured runaway diffusion coefficient is found to be two to three orders smaller than χ_e. In case of classical diffusion, a similar difference would be expected, but then, both D_r and χ_e would be orders of magnitude smaller than the measured values. Magnetic turbulence is often suggested to explain this difference. However, from the commonly used estimate of test particle diffusion $D \sim v_{\|} D_M$ with $v_{\|}$ the velocity along the magnetic field lines and $D_M = \pi q R_0 \langle b_r^2 \rangle$ [6] ($\langle\rangle$ denotes flux surface average, b_r the radial component of the perturbing magnetic field normalized to B_t, q the safety factor) it would follow that $b_r < 10^{-6}$ which is low compared to [7]. An explanation could be, that for low levels of magnetic turbulence, still chains of islands and good surfaces will remain which will determine the net diffusion [8]. This could explain the large difference between D_r and χ_e. Because no quantitive theory for test particle transport in mixed magnetic field topologies exists, no estimation of the magnetic turbulence level can be made based on runaway confinement measurements. Differences between the topology of runaway orbits and magnetic field, and averaging effects due to the drift displacement could also enhance the difference between D_r and χ_e.

In case of additional heating, the τ is only a very rough measure for the runaway confinement. From Fig. 2(a) and 2(b), it may be stated that runaway diffusion is increasing with increasing input heating power, which is also measured for χ_e [5]. Changes in electron temperature T_e and Z_{eff}, dependent on input power, effecting the accelerating electric field $E_{\|}$, i.e. the runaway radiation level, could play a roll too. A deterioration of runaway confinement can result either from an increase of the turbulence level or an increase of the correlation length of the turbulence. Remarkable is the difference in τ between NBI and ICRH at higher power. This could be ascribed to the different nature of heating mechanism and its effect on the plasma (e.g. toroidal rotation effects) and on magnetic field turbulence.

References

[1] M. de Rover, N.J. Lopes Cardozo, A. Montvai, Phys. Plasmas.**3** (1997) 4468; M. de Rover, N.J. Lopes Cardozo, A. Montvai, Phys. Plasmas.**3** (1997) 4478.

[2] J.R. Myra, P.J. Catto, Phys. Fluids B **4** (1992) 176.

[3] H.E. Mynick, J.D. Strachan, Phys. Fluids **24** (1981) 695.

[4] R.J.E. Jaspers, Ph.D. thesis, Technical University Eindhoven, 1995.

[5] A. Krämer-Flecken, G. Waidmann, *Proc. of 21st EPS Conference on Controlled Fusion and Plasma Physics* (1994) 122.

[6] A.B. Rechester, M.N. Rosenbluth, Phys. Rev. Lett. **40** (1978) 38.

[7] X.L. Zou, L. Colas, M. Paume, J.M. Chareau, L. Laurent, P. Devynck, D. Gresillon, Phys. Rev. Lett. **75** (1995) 1090.

[8] C.C. Hegna, J.D. Callen, Phys. Fluids B **5** (1993) 1804.

Xe injection experiments in TEXTOR-94.

G. Bertschinger, W. Biel, G. Fuchs, E. Graffmann, L. Könen, H. R. Koslowski, A. Krämer-Flecken, J. Rapp, M. Tokar'

Institut für Plasmaphysik, Ass. Euratom-Forschungszentrum Jülich GmbH, 52425 Jülich

1. Introduction

For future fusion experiment, the choice of the materials for the plasma facing components is still an open question. Until now, usually low-Z elements have been used for limiter, divertor and wall materials, for ITER, both low and high-Z materials as Mo or W are discussed. To determine the transport properties of high-Z elements in TEXTOR-94, Xe injection experiments have been performed. Both short single pulses as well as multiple pulses have been used. Gas injection is utilised for the transport studies, as due to the high reproducibility the influx of impurities can be controlled precisely.

Short single pulses (in TEXTOR-94 FWHM < 2.5 ms), as well as pulse trains have been used. Single injection pulses behave similar to laser blow off and depend mainly on the properties of the background plasma, whereas multiple injection pulses also depend on the Xe recycling.

2. Experimental set-up

In TEXTOR-94 the plasma dimensions (R_0 = 175 cm, a = 46 cm) are determined by the toroidal belt limiter ALT II. In addition poloidal limiters can be inserted. The gas is injected by a fast gas injection system, located at the position of the liner (r = 55 cm). The gas flow is controlled by a piezo valve, the tube guiding the gas to the liner position has an exponentially increasing diameter. The exponential gas inlet system used in TEXTOR-94 is 2.4 times faster than a tube with a constant diameter of the same length. The gas flow is measured by the pressure decrease in a buffer volume. To overcome nonlinearities of the valve, the gas flow is controlled by pulse width modulation with a base frequency between 5 Hz and 200 Hz. The gas inlet is reproducible to 2 %. The confinement property of the plasma is determined from the intensity of the Xe XXVI radiation at 17.4 nm, measured by a gracing incidence monochromator. The detector is a high count rate channeltron, operated in pulse counting mode. The same equipment is used to measure the quasicontinuum of W^{30+} in the laser blow off experiments.

If the concentration of Xe is sufficiently high, the Xe density is evaluated from the increase of total radiation due to the injection, measured by a 26-channel bolometric system. The line

integrated emission is inverted to get local values [1], the Xe concentration is then calculated assuming coronal equilibrium and using the emissivity data of Post [2].
Changes of the density- and the q- profile after injection are determined from the 9 channel Interferometer/Polarimeter[3]. The electron temperature profile is measured by the ECE system.

3. Injection of single Xe pulses and comparison with W laser blow off.

To study the confinement properties of TEXTOR-94 we injected single pulse of Xe into plasma heated by neutral beam injection and varied the amount of injected Xe and the edge cooling by Ne. The plasma current : I_p = 350 kA, the electron density : $n_e = 3 * 10^{13}$ cm^{-3}, and the heating power : P_{NI} = 1.4 MW were kept constant. For short pulses, the radiation behaves similar to W radiation, indicating that Xe is pumped off quite efficiently by the plasma facing components (fig 1). The intensity increases by less than 3 % due to Xe recycling compared to the amplitude of the injection pulse. The pumping decreases if poloidal limiters with higher thermal load are used (see multiple pulse injection). The discharges are characterised by the ratio $\gamma_{rad} = P_{rad} / (P_{NI} + P_{OH})$, the total radiated power over total heating power. γ_{rad} temporarily exceeds 1. The decrease of plasma energy is not taken into account. Above γ_{rad} = 80% the confinement time increases for some shots. For Xe two branches are separated: for edge cooling by Ne, i. e. $\gamma_{rad} > 80\%$, the confinement increases by up to a factor of 5. For discharges with low edge cooling, the confinement increases only slightly, even though the amount of injected Xe is much higher (fig 2).
For discharges with low edge cooling, Xe accumulation with strong peaking in the center was observed, the maximum concentration exceeded $1.5 * 10^{-3}$. With rising impurity density, the sawteeth disappear and the safety factor in the center q(0) increases. The concentration decays with a time constant comparable to the Xe XXVI signal. (115 ms vs. 85 ms) (fig 3).

4. Multiple Xe pulse injection

Multiple (5 with frequency of 5 Hz) pulses of Xe behave similar to single pulses. A strong signal appears immediately after injection followed by a small background due to recycling. Whereas the recycling fraction in single pulses does not depend on the amount of Xe, the background increases from pulse to pulse in the multiple injection. The decay time rises from pulse to pulse as well. Compared to single pulse injection experiments with low edge cooling the maximum confinement time is larger, but it is lower than with edge cooling by Ne. Accumulation occurs at lower values of γ_{rad}, the maximum γ_{rad} reached was 86 % (fig 4).

Both, the direct signal and the recycling fraction, depend on the limiter configuration. If the poloidal limiters are inserted at the same radial position as the ALT II belt limiter, the recycling is increased by about 50 %, indicating that the pumping of Xe depends on the load of the plasma facing components (fig 5).

Two different behaviours for the impurity accumulation have been observed. When the amount of Xe is increased gradually, accumulation occurs with impurity peaking in the center and concentrations up to 0.2 %. Sawteeth disappear and q(0) increases, reaching values above 3. With the decay of the impurity concentration, q(0) drops again, after about 500 ms the sawteeth reappear. This behaviour is similar to one pulse injection (fig 6).

For some discharges peaked profiles have been observed, stable for more than 0.5 s. The Xe injection was smaller than in the previous shot, the concentration reached 0.1 %. After the concentration had decreased to 0.05 % it remained constant until this condition was teminated by a break down in the heating beam. The q(0) increased to about 1.5 and remained well above one. During the whole phase, no sawteeth occured. This phase is characterised by mode activity with frequencies above the Nyquist frequency of the ECE system (fig 7).

5. Summary

Xe injection with fast pulses is shown to be a powerful tool to study transport properties of high-Z impurities. Due to the high precision of the amount of impurities added to the plasma it is possible to reproduce discharges with prescribed impurity concentration. From experiments with pulsed injection it is found that the particle confinement strongly depends on the edge cooling by Ne. For strong edge cooling impurity confinement is increased by an order of magnitude. For low cooling and high impurity injection accumulation is observed. γ_{rad} is found to be close to 100 %.

If Xe is injected into a plasma with a higher background concentration of Xe, accumulation occurs at a level of γ_{rad} well below 100 %. The accumulation leads to loss of sawtooth activity and an increase of the safety factor q(0). In some cases stable sawtooth free discharges with peaked concentration profiles have been produced.

6. References

[1] J. Rapp et al. this conference, Poster P 4.094, p. 521

[2] D. E. Post et al. Atomic Data and Nuclear Data Tables **20,** (1977)

[3] H. R. Koslowski et al. this conference Lecture TL 16, p. 429

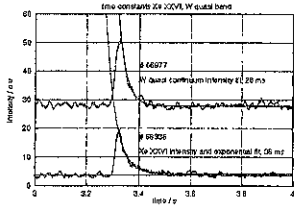

Fig 1 W quasi continuum radiation and Xe XXVI radiation.

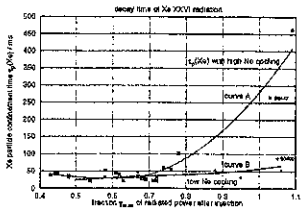

Fig 2 decay times of Xe XXVI for different radiation cooling. Curve A for high Ne edge cooling, curve B for low Ne edge cooling.

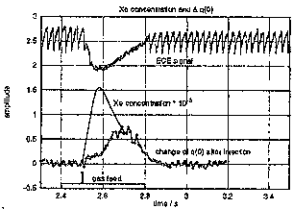

Fig 3 accumulation behaviour after single pulse Xe injection (#68400, curve B)

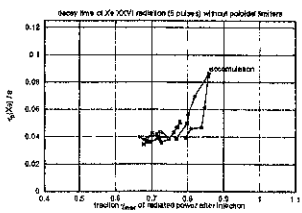

Fig 4 decay times of Xe XXVI for multiple pulse Xe injection with low Ne edge cooling. Compare to Fig 2 curve B

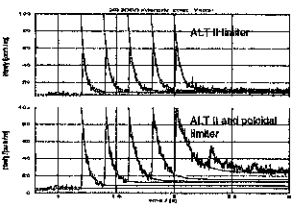

Fig 5 Comparison of Xe XXVI signal for similar discharges with toroidal and poloidal limiter at the same rad. position (r_s = 46 cm)

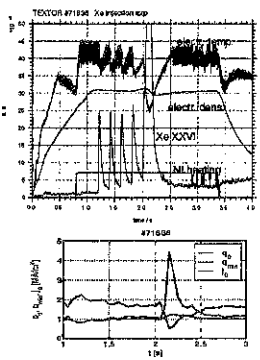

Fig 6 Impurity accumulation and evolution of the safety factor q(0). During the accumulation q(0) increases strongly, leading to reversed magnetic shear in the center.

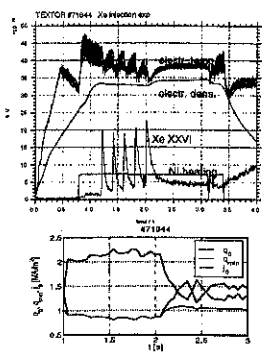

Fig 7 Impurity accumulation and evolution of q(0) in discharge with a sawtooth free period. q(0) remains well above 1.

Neon profiles and concentrations under radiative edge cooling conditions in TEXTOR-94

R. Jaspers[1], E. Busche[2],T. Krakor[3], B. Unterberg[2]

Partners in the Trilateral Euregio Cluster
[1]FOM-Instituut voor Plasmafysica 'Rijnhuizen', Association EURATOM-FOM
P.O.Box 1207, 3430 BE Nieuwegein, The Netherlands.
[2]Institut für Plasmaphysik, Forschungszentrum Jülich GmbH,
Association EURATOM-KFA, P.O.Box 1913, D 52425 Jülich, Germany.
[3]Experimentalphysik V, Ruhr-Universität Bochum, Germany.

1. Introduction

The scenario of a radiative boundary exhibits some attractive features and is therefore included in the ITER operational scheme. First of all the power load on the plasma facing components is reduced after injection of a suitable impurity (either Neon or Argon). The line radiation distributes the power flux more uniformly onto the wall thereby cooling the plasma edge. Additionally, with this edge cooling operation TEXTOR-94 reaches under certain conditions a better confinement regime, the Radiative Improved (RI) mode [1]. However, the RI mode or the radiative boundary scenario is only a valid option if the central dilution, depending on the transport parameters of the seeding impurity, is tolerable.

The determination of this impurity concentration from CXRS measurements at TEXTOR-94 is the subject of this paper. After a short overview of the used equipment, we introduce in section 3 the method employed to obtain the impurity concentration. In section 4 this method is applied for RI-mode discharges. In the next section a first attempt is made to measure several ionization stages of Neon simultaneously. Comparing these profiles with code calculations could provide us some information about the impurity transport.

2. Setup of CXRS diagnostic at TEXTOR-94

The experiments reported in this paper are performed on the limiter tokamak TEXTOR-94 ($R_o = 1.75m$, $a = 0.46m$, $B_\phi = 2.25T$) and mainly focuss on the results of the charge exchange recombination spectroscopy (CXRS). TEXTOR-94 is equipped with two neutral beams (NBI) which inject tangentially into the plasma in opposite directions. One of these beams, which for the experiments reported here inject in the direction of the plasma current (co-injection), is used for the CXRS measurements. The CXRS diagnostic consists of four sets of spectrometers with each 15 lines of sight into the plasma covering the range $r = [-0.02 - 0.43]m$. This allows us to measure full profiles of four different impurity densities, rotation and temperature with a time resolution of typically 50 ms. Since the lines of sight are almost tangential to the magnetic surfaces, the radial resolution is between 3 and 8 cm for the different lines, although the beam has a FWHM of about 20 cm. The NBI can be operated at 20-50 kV acceleration voltage with hydrogen, deuterium or helium. The power can be varied by changing this voltage or by partly closing the beam aperture. The maximum injected power of one beam is about 1.5 MW. The carbon measurements reported here were performed on the $C^{5+}(n = 8 \rightarrow 7)$ transition at $\lambda = 529.0nm$ and for the neon the $Ne^{9+}(n = 11 \rightarrow 10)$ transition at $\lambda = 524.9nm$ was used.

3. Cross sections and effect of excited beam particles

To obtain the impurity density n_z from the measured CX-radiance L_z^{cx} and the neutral beam density n_b one has to calculate:

$$n_z = \frac{4\pi L_z^{cx}}{\sum_{i=1}^{3} \int n_b(E_b/i) dl q_{eff}^z(E_b/i)} \qquad (1)$$

where the integration is along the line of sight and the beam density for all three beam species at full, half and third beam energy E_b can be either calculated with a beam at-

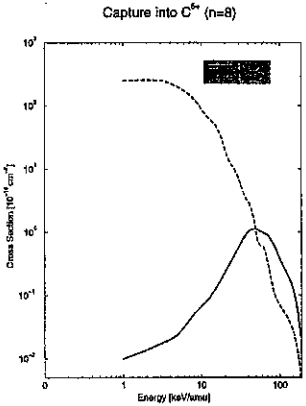

Figure 1: *Cross-sections for the charge exchange process between hydrogen atoms in ground state (1s) and first excited state (n=2) and C^{6+} as a function of beam energy. (Data from R. Hoekstra, KVI-Groningen, The Netherlands).*

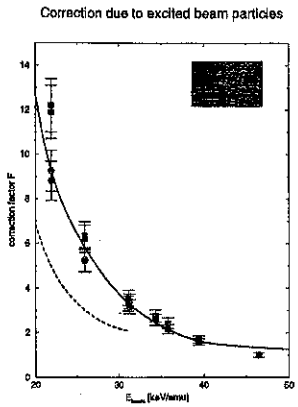

Figure 2: *Enhancement of the calculated n_z as a function of E_b when only CX from H(1s) is taken into account. The solid line results of a calculation of the contribution of CX from H(n=2) with C^{6+} in case of an H-beam, the dashed line for a D-beam, where the species mix is different.*

tenuation code or determined from measurements of the Doppler shifted Balmer-α line of hydrogen. The effective emission rate $q^z_{eff}(E_b)$ is given by the product of the CX cross-section (corrected for cascade processes) and the beam velocity. This is in our case taken from the atomic data base ADAS [2]. However, by applying eq. 1 to determine the C^{6+} and Ne^{10+} concentrations at TEXTOR-94 in the case of a D-beam (E_b=20-25 keV/amu) unrealistic high values emerged. Since it is known that at lower beam energies the cross-section for the charge exchange process with beam particles in the ground state sharply drops, whereas the same process with the excited hydrogen atoms strongly increases (see Fig. 1), it is hypothesized that the emission from this latter process has a non-negligible contribution to the measured L_z^{cx} and should be taken into account. To test this, experiments were performed where identical discharges where made differing only in the beam energy of NBI-1. The change in power for different energies was compensated by partly closing the aperture, keeping the input power almost equal ($P_{NBI-1} = 0.4MW$). Moreover, a second beam at P_{NBI-2} was the main heating device and operated at 1.2 MW. The bremsstrahlung level was identical for the whole series of discharges, so the determined C^{6+} and Ne^{10+} concentrations should be the same for all shots. Nevertheless, large deviations at lower beam energy were found by using eq. 1. The resulting n_z, normalised to the value at the highest beam energy (46 keV/amu) is plotted in Fig. 2, which can be interpreted as a plot of a correction factor F. Making use of the cross-section data of figure 1, the species distribution of the beam and an estimate of $n_b(n = 2)$, this correction factor for C^{6+} can be calculated as well for our hypothesis. The excited beam population was computed with the ADAS package by taking into account only electron impact excitation. This resulted in a correction factor with a similar trend as the experimental data, but a somewhat lower value. However, ion impact collisions, which were neglected in the ADAS calculation since not all cross-sections were available, will enhance the excited beam pop-

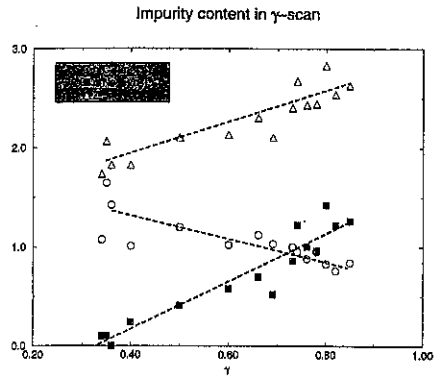

Figure 3: *Results of Charge exchange measurements in the RI-mode. As a function of the radiated power fraction γ is plotted: a) the central C^{6+} concentration (circles, b) the central Ne^{10+} concentration (squares) and c) Z_{eff} calculated from CX-measurements on carbon, neon and oxygen. The dashed lines are only intended to guide the eye.*

ulation appreciably since for this energy range this process has the same importance as electron impact excitation. By multiplying therefore $n_b(n = 2)$ by 2 the experimental F could be reproduced as shown by the solid line in Fig.1b. Note that this calculation depends on the density and the species mix of the beam neutrals. For a deuterium beam at TEXTOR-94, where a larger fraction of beam particles is at the full beam energy, the correction factor is expected to be smaller (dashed line in Fig. 2). Because the experiment shows only little difference in F for C^{6+} and Ne^{10+}, we take for neon the same F in the following.

On several other machines like DIII-D and ASDEX-U conflicts were found in neon concentrations as determined from CXRS measurements (using the ADAS cross-sections) and Z_{eff} measurements [3]. They introduced also a cross-section correction factor for E_{beam} below 50 keV/amu. The excited beam neutrals might be the physical justification for this.

4. Neon Concentrations in the RI mode

Having found in the previous section a method to obtain impurity concentrations and profiles, one can study the dilution of the plasma in the so-called Radiative Improved (RI) mode at TEXTOR-94. Simultaneously achieving high confinement, high n_e, high β, high radiative power fraction and quasistationarity makes this RI-mode an attractive alternative to the H-mode regime of divertor machines, provided the impurity (i.e. neon) concentration stays tolerable. To address this, a scan was made in a typical RI-mode discharge ($I_p = 400kA$, $\overline{n_e} = 6 \cdot 10^{19} m^{-3}$, $P_{NBI} = 1.5MW$ (deuterium beam at 24 keV/amu) $P_{ICH} < 1.6MW$). The neon seeding was varied to increase $\gamma = P_{rad}/P_{tot}$. The result is plotted in Fig. 3. It is shown that even for the highest γ of 85% the neon concentration stays below 1.5 % and $Z_{eff} < 3$. Comparison of the dilution calculated with neutron measurements [4] gave similar results. Also the values determined for Z_{eff} were for this scan within 15% in agreement with bremsstrahlung results (the latter being somewhat higher). Finally, for few shots a Z_{eff} was calculated from polarimetry data giving again the same results [5]. This shows the reliability of the used method of correction the CX-cross-section as described in the previous section.

Even for the highest radiation fraction in the RI-mode the neon concentration stays limited. No accumulation of neon under normal RI-mode conditions was observed and Z_{eff} could be kept below 3. Although rather speculative one might extrapolate this to ITER, assuming $Z_{eff} - 1$ scales with $P_{rad}/(S\overline{n_e^2})$ [6], where S is the radiating surface. This would yield a tolerable Z_{eff} of 1.5.

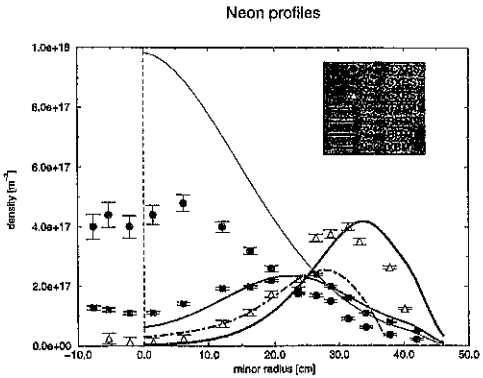

Figure 4: *Neon profiles from CXRS (data-points), RITM calculations (solid lines) and XBM (dashed line).*

5. Neon Profiles

To deduce some information about transport parameters of Neon in edge cooled discharges profiles of Ne^{8+}, Ne^{9+} and Ne^{10+} were measured by CXRS and compared with results of an x-ray Bragg monochromator(XBM) (measuring Ne^{9+} and Ne^{8+}) and with calculations of the selfconsistent 1D impurity transport code RITM [7]. For the CX of Ne^{8+} we have taken the cross-sections for O^{8+} which has the same isoelectronic structure. The contribution of oxygen which radiates at the same $\lambda = 607nm$ is subtracted from the signal before neon was injected. For $Ne^{9+}(\lambda = 648nm)$ no cross-sections were available, but a relative profile could still be obtained. Discharges were performed in the L-mode confinement regime. Here we could use a 50 keV/amu H-beam to maximise the CX signal and minimise the contribution of excited beam particles. Furthermore the XBM signal is not disturbed by the large neutron flux of the RI-mode. The radiated power fraction γ is around 80% for this series, $\overline{n_e} = 3.0 \cdot 10^{19} m^{-3}$, and $P_{NBI} = 1.2MW$. The results are plotted in Fig. 4. Although the absolute values differ by a factor 1-2 between the different methods, the similarity is sufficiently close between CX and RITM to continue to study more systematically the neon profiles for impurity transport investigations.

6. Conclusions

The concentration of Neon in discharges in TEXTOR-94 with radiative edge cooling has been measured with charge exchange spectroscopy. It has been experimentally demonstrated that the cross-sections for Neon have to be modified, due to the effect of excited beam particles. The neon concentration in the Radiative Improved mode amounts to $1.2 - 1.4\%$ for a radiated power fraction of 85%. Profiles of Ne^{10+}, Ne^{9+} and Ne^{8+} have been measured with CXRS and compared with results of an x-ray Bragg monochromator and the 1D impurity transport code RITM, giving a rather consistent result.

References

[1] A. Messiaen et al., Phys. Rev. Lett. **77**, (1996) 2487.
[2] H.P. Summers, JET-IR(94)06, 1994.
[3] S. de Peña Hempel, PhD-thesis, Technische Universität München, Germany, 1997.
[4] G. van Wassenhove et al., this conference.
[5] R. Koslowski, this conference.
[6] G. Matthews, Proceedings of 12^{th} PSI-conference, in press, (1996).
[7] M. Tokar',Plasma Phys. and Control. Fusion **36** (1994) 1819.

Rotational Differences between MHD instabilities and Plasma in TEXTOR-94

P.C. de Vries and R.J.E. Jaspers

Partners in the Trilateral Euregio Cluster

FOM-Instituut voor Plasmafysica 'Rijnhuizen', Association EURATOM-FOM
P.O.Box 1207, 3430 BE Nieuwegein, The Netherlands
Institut für Plasmaphysik, Forschungszentrum Jülich, GmbH.
EURATOM Association, P.O.Box 1913, D 52425 Jülich, Germany

The core plasma and the MHD rotation frequency have been determined independently by CXRS and ECE diagnostics. A differential rotation between plasma and MHD mode rotation was observed in NBI heated discharges which is expected to be due to the diamagnetic drift. This difference disappeared in case of large MHD modes which locally flattened the pressure gradient.

1 Introduction

Individual particle drifts or fluid mechanical properties will cause a toroidal (ϕ) or poloidal (θ) rotation of the plasma. Furthermore, the injection of neutral beams (NBI) will add momentum to the plasma.

The plasma rotation causes, for example, temperature profile perturbations due to MHD instabilities, like magnetic islands, to appear as oscillations on the time traces of the electron cyclotron emission (ECE) diagnostic. In this paper we present an investigation into plasma and MHD mode rotation on the TEXTOR-94 tokamak ($R_o = 1.75, a = 0.46$m, $B_\phi = 2.25$T, $I_P = 350$kA and $q_a = 3.8$). The purpose is to reveal the different contributions to the magnetic island rotation and MHD frequency.

The toroidal ion rotation profile, representative for the bulk plasma rotation, has been determined by Charge eXchange Recombination Spectroscopy (CXRS) and the MHD mode rotation frequency has been derived from the $m/n = 1/1$ precursor oscillations, usually observed prior to sawtooth crashes. The toroidal rotation could be modified in TEXTOR-94 by means of tangential NBI with a variable beam aperture. In the next section a short summary on the theory of plasma and MHD mode rotation will be given. Thereafter the measurements will be presented and discussed.

2 Plasma and MHD mode rotation

Drifts of electrons and ions in poloidal and toroidal direction result in a plasma rotation. The momentum balance of a separate particle species, α, predicts drifts due to an electric field and pressure gradient perpendicular to the magnetic field [1],

$$\frac{1}{n_\alpha q_\alpha}\frac{\partial}{\partial r}p - E_r = v_\theta^\alpha B_\phi - v_\phi^\alpha B_\theta, \qquad (1)$$

where n and q are the density and charge of the particle. The first contribution differs in direction for electrons and ions due to the difference in charge while the second, due to the radial electric field, is equal to both electrons and ions. A difference in ion and electron rotation results in a current in the plasma. The pressure gradient drives a diamagnetic current [1]. This current opposes the magnetic field in the plasma and is perpendicular to

the field, hence, mainly in poloidal direction. This is added to the usual toroidal plasma current in a tokamak.

The rotation of MHD modes is observed as an MHD frequency on the time traces of various diagnostics. This MHD frequency is due to the plasma or ion rotation in toroidal and poloidal direction. However, if the MHD mode is coupled to the electrons, it moves, furthermore, due to plasma currents with respect to the plasma ions [2]. The observed MHD mode rotation is expected to differ from the ion rotation. As the wave vector of a magnetic island parallel to the magnetic field lines is zero, it is expected that the plasma current parallel to the field lines will not affect the differential rotation. The diamagnetic current, however, which is perpendicular to the field lines, might provide an additional component to the mode rotation and MHD frequency. This movement is mainly in poloidal direction.

Under these assumptions the MHD frequency may than be given by,

$$f_{MHD} = n\frac{v_\phi^i}{2\pi R_o} \pm m\frac{v_\theta^I}{2\pi r} + f^*, \tag{2}$$

where m, n are the poloidal and toroidal mode number of the mode. The $\pm$ gives the orientation of the toroidal current with respect to the magnetic field. Assuming that the diamagnetic current is mainly poloidal, f^* can be given by [1],

$$\omega^* = 2\pi f^* \approx \frac{m}{en_e}\frac{j^*}{r} = \frac{m}{en_e}\frac{1}{Br}\frac{\partial}{\partial r}p, \qquad \omega^* \approx 4mq_a\frac{T_e(eV)}{a^2 B_\phi(T)}. \tag{3}$$

The last formula represents the diamagnetic frequency which has been obtained by assuming natural profiles [4]. For an $m = 1$ mode in the centre of the TEXTOR-94 tokamak ($T_e^{q=1} = 900$eV) one finds $f^*_{m=1} \approx 4.5$kHz. The MHD frequency for an $m/n = 1/1$ mode can then be approximated by,

$$f_{MHD} \simeq |\frac{v^\phi}{2\pi R_o}(1 \pm \frac{R_o}{r}\frac{v^\theta}{v^\phi}) - f^*_{m=1}|. \tag{4}$$

By measuring the toroidal plasma rotation, v^ϕ, and the MHD frequency the separate contributions in eq. 4 may be determined.

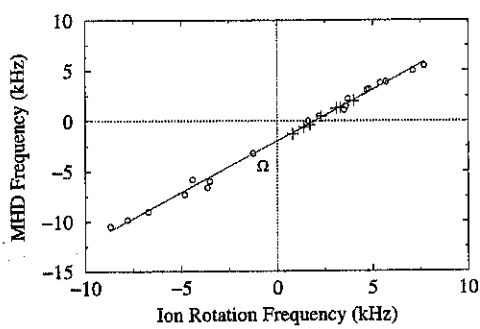

Figure 1: *The $m/n = 1/1$ MHD rotation frequency, versus the toroidal ion rotation frequency $v_{CXRS}/2\pi R_o$. The crosses represent data obtained by injection of both co- and counter-NB while the circles are obtained by using only one injector. In the last case the the current direction was reversed to switch between co- and counter injection. The Ω marks the point given by the ohmic precursor frequency of 3.3kHz (where v_{CXRS} has not been measured).*

3 Experimental observations

The toroidal plasma rotation profile is measured by CXRS via the C^{VI}-line at 529nm The Carbon and Hydrogen rotation velocity can be assumed to be equal in the TEXTOR-94 core plasma [3]. Several discharges have been produced with a similar density of $\bar{n}_e = 2.5 \cdot 10^{19} m^{-3}$ but with different toroidal rotation. The toroidal rotation was varied by injecting different amounts of NBI power. Both co- and counter- current NBI have been obtained by reversing the current direction or using a second injection beam in opposite direction.

The MHD frequency has been determined from the sawtooth precursors on the ECE signals. According to the reaction of the frequency at switch-on of, either a co-, or counter-current NBI the 'sign' of the MHD frequency has been determined.

In fig. 1 the plasma and MHD mode rotation frequency are compared. According to eq. 4 one expects that an offset due to the diamagnetic frequency while the slope of the curve might depend on a possible poloidal plasma rotation. An offset of 2.5 ± 0.1kHz between plasma and MHD mode rotation frequency is indeed observed which might resemble the diamagnetic frequency. The diamagnetic frequency is expected to depend on the temperature according to eq. 3. This is experimentally confirmed in fig. 2. A specific discharge is shown where, due to a drop in the central temperature, the offset between the toroidal plasma rotation and MHD frequency decreases.

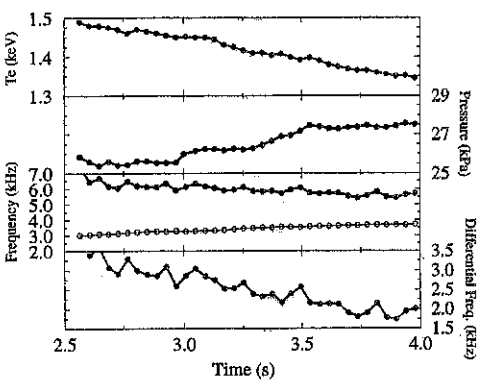

Figure 2: *Rotation properties during part of discharge 63816. The co and counter beams (P_{co} = 800kW and P_{ct} = 1320kW) were switched on at t = 2 and 2.5s, respectively. The plasma current was I_p = 350kA. Plotted are from top to bottom; the central temperature, pressure, the ion and MHD rotation frequencies (closed and open circles) and the differential frequency, respectively. The global temperature drop causes a decrease in this offset.*

The slope of the curve in fig. 1 was found to be: 0.98 ± 0.02. According to eq. 4 a slope so close to unity indicates that the poloidal rotation, v_θ is negligible. However, note that the diamagnetic frequency is mainly due to a poloidal movement of the MHD mode with respect to the plasma.

In case of a zero poloidal rotation the momentum balance equation (eq. 1) can be simplified. The toroidal rotation then will be inverse proportional to B_θ and, hence, the toroidal plasma rotation is therefore expected to be inverse proportional to the plasma current also in case the pressure gradient, radial electric field and other forces remain approximately constant. Hence, the momentum and energy confinement time should be constant during the ramp. This is experimentally observed by ramping up the current from I_p = 250 to 475kA during NBI in a single discharge. The confinement time (≈ 50ms) was found to be constant during the ramp phase (≈ 2.5s).

In fig. 3 the dependence of the central toroidal plasma rotation versus q_a ($\sim I_p^{-1}$) is plotted. During a small time window also sawtooth precursor activity has been observed. Again an offset has been found with the plasma rotation which was independent of the

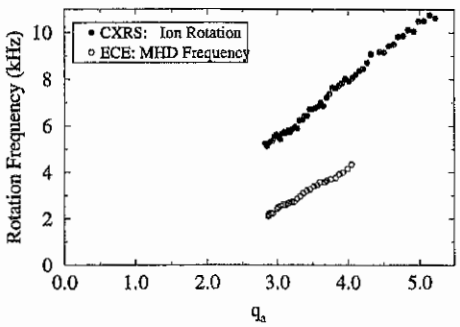

Figure 3: *The toroidal ion rotation frequency as a function of* $1/I_{plasma}$. *The data have been obtained by ramping up the plasma current from* $I_p = 200$ *to* $475kA$ *during NBI* (P^{co}_{NBI}) *in discharge 67520. The ion rotation is measured by CXRS.*

plasma current. During the ramp phase the central pressure increased less than 20%. Because of the broadening of the density and velocity profiles at higher current the total moment remain approximately constant during the current ramp.

4 Discussion

The observed offset between the MHD mode and plasma rotation can be explained by the diamagnetic current. It scales with the plasma temperature. The experimentally observed offset (2.5kHz) is smaller than expected (4.5kHz), however, the local diamagnetic drift may be reduced due to the presence of the magnetic island which may locally perturb the pressure gradient. For large MHD modes, observed prior to major disruptions, no offset is found, which can be explained by the fact that the pressure is flattened over the magnetic island [5,6]. The toroidal plasma current did not affect the MHD frequency.

The diamagnetic frequency is mainly due to a poloidal movement of the island with respect to the plasma ion fluid. The poloidal ion rotation was found to be negligible in the core. This can be explained by the phenomenon of poloidal flow damping [7]. The central toroidal plasma rotation varied with the plasma current in case the momentum and energy confinement time remained constant. This was expected according eq. 1.

As the ohmic precursor frequency is known to be approximately 3.3kHz in TEXTOR-94 the rotation of the plasma in the ohmic case can be derived to be 0.8kHz ($\approx$ 9km/s). Using the toroidal momentum balance equation and assuming natural profiles an averaged ohmic radial electric field is found of about 2kV/m, pointing radially inward. Because NBI increases the toroidal rotation, the radial electric field will be affected too. The field strength can be increased more than one order of magnitude with respect to the ohmic level. The observation of the absence of a diamagnetic offset between plasma and mode rotation frequencies might be an indication of a flattening of the pressure profile over the rotating magnetic island.

References

[1] F.F. Chen, *Plasma Physics and Controlled Fusion* (Plenum Press: New York)(1993)
[2] O. Klüber, *et al.*, Nucl. Fusion **31** (1991) 907.
[3] R. Tammen, *et al.*, Phys. Rev. Lett. **72** (1994) 356.
[4] F.C. Schüller, *et al., in the Proc of the* 18^{th} *Conf. on Plasma Phys. and Contr. Fusion, Berlin* (1991) Vol. IV, p183.
[5] P.C. de Vries, *et al.*, Plasma Phys. Control. Fusion **38** (1996) 467.
[6] D. Stork, *et al. in the Proc of the* 14^{th} *Conf. on Plasma Phys. and Contr. Fusion, Madrid* (1987) Vol. I, p206.
[7] R.C. Morris, *et al.*, Phys. Plasmas **3** (1996) 4513.

Helium exhaust under radiative I-mode conditions at TEXTOR-94

G. Mank[1], K.H. Finken[1], A.M. Messiaen[2,*], J. Ongena[2,*], B. Unterberg[1], J.A. Boedo[3], M. Brix[1], T. Denner[1], D.L. Hillis[4], R. Jaspers[1], U. Samm[1], M.Z. Tokar'[1]

[1]Institut für Plasmaphysik, Forschungszentrum Jülich, Ass. Euratom-KFA, Germany[#]
[2]Laboratoire de Physique des Plasmas - Laboratorium voor Plasmafysica, Ass. Euratom-Belgian State, ERM-KMS, Brussels, Belgium[#]
[3]FERP, University of California, San Diego, CA, USA
[4]Oak Ridge National Laboratory, Oak Ridge, TN, USA
[*]Researcher at NFSR (Belgium)
[#]Partner in the Trilateral Euregio Cluster (TEC)

Recently on TEXTOR-94 a new regime of improved confinement under radiative edge conditions (RI mode) has been found [1]. In this RI regime the energy confinement time τ_E increases with density and high radiation level up to 90 % of the total input power is possible. Quasistationary conditions for these discharges are sustained. In a future fusion reactor the maximum amount of seed impurities depends strongly on the rate at which the helium ash is removed. As a strong radiative edge may be advantageous for a future reactor, the helium exhaust for RI mode conditions is investigated for different line averaged electron densities and pumping conditions for the first time.

For this investigation TEXTOR-94 is operated at a plasma current of 400 kA and a toroidal magnetic field B_T=2.25 T. The radiation level is increased by injection of neon as a seed impurity. Particles - i.e. here deuterium, neon and helium - are removed by the toroidal pump limiter ALT-II [2].

At First the exhaust for different limiter positions is studied. The pump limiter has been positioned at a minor plasma radius of either 44 cm or 46 cm. Mostly TEXTOR is operated with a plasma radius of 46 cm; nevertheless the tiles of the limiter system are optimized with respect to the heat flux distribution for 44 cm. Despite the different pitch of the field lines ($q_{edge}(I_P$=400 kA, a=46 cm) = 3.4, $q_{edge}(I_P$=400 kA, a=44 cm) = 3.1) the pumping performance of the ALT-II pump limiter should not change [2]. Due to the different limiter position the plasma location had to be shifted in order to optimize the RI mode. Figure 1 shows the edge profiles for the electron density n_e (solid line) and the electron temperature T_e (dashed line) for the different limiter radii. The last close flux surface (LCFS) which is the limiter surface corresponds to 0 cm. The throat of the limiter is located 2 - 5 cm behind the LCFS. Figure 2

compiles the results for different ratios γ of the radiated power to the total heating power at a line averaged electron density of $5 \cdot 10^{13}$ cm^{-3}. For all radiation levels the density decay length (λ_n) between the limiter surface and the limiter throat length is about 1 cm. The temperature decay length is lower for the reduced plasma diameter (open symbols). A reason for this decrease may be the repositioning by 2 cm of the plasma which was necessary to reestablish the good RI mode confinement. Following the analysis in [3], which illustrates the salient features of the scrape-off layer transport phenomena, an estimate of the change of the fraction of helium entering the throat of the limited ($\varepsilon_{collection}$) can be given. Due to the shorter temperature decay length, the calculated collection efficiency is about 20 - 30 % lower. In addition, the absolute value of the electron temperature is 5 - 10 eV lower (r_{ALT-II} = 44cm). This lower T_e leads to a reduced amount of helium that is actually trapped in the throat. Assuming the same conditions as in [4] and taking an electron density in the throat of the limiter of $1.5 \cdot 10^{12}$ cm^{-3} the removal efficiency (ε_{rem}) is reduced by about 5%. Thus the exhaust efficiency ($\varepsilon_{exh} = \varepsilon_{coll} \cdot \varepsilon_{rem}$) is about 25% lower for the reduced plasma radius. This tendency is found experimentally by measuring $\varepsilon_{exh} = \tau_{He} / \tau^*_{He}$ with τ_{He} as the particle confinement time and τ^*_{He} as the effective particle confinement time.

In a second investigation τ^*_{He} is measured in a series of discharges where the radiation level is increased from 30% to 90% while keeping the total diamagnetic energy to about 120 kJ. Three different methods have been used to determine the decay of the helium signal after the helium gas-puff: the change of the neutral helium flux on the limiter blades, the change of the charge exchange resonance spectroscopy signal, and the change of the partial helium pressure in the pumping duct. The three methods agree within the experimental errors. However, since the neutral helium flux at the limiter is used to determine the particle confinement time τ_{He} the values given in this paper refer to this measurement. For comparison a discharge with and without helium injection has always been performed. τ^*_{He} increases from ca. 800 ms at the lowest radiation level to about 1600 ms at $\gamma = 0.9$ as shown in figure 3. For the high density discharges, the energy confinement time increases with the radiation level from 35 ms to about 60 ms. This leads to an increase of critical ratio [5] $\rho^* = \tau^*_{He}/\tau_E$ of about 20%. This ratio ρ^* results from the balance between He-ash production and exhaust and is considered to be about 5 - 10 for ITER [6]. The absolute value of ρ^*, which is between 23 and 28 in this experiment, is e.g. dependent on how far the limiter blade extends into the SOL. In order to have a safety margin the limiter tiles have been chosen to 20 mm thickness to accomodate the

increased heat load to the belt limiter. However, previous experiments on TEXTOR with 12 mm thick tiles show that the collection of particles can be increased by a factor of 2 [7] so reducing τ^*_{He} and therefore ρ^* by the same amount. This agrees with calculations for the collection efficiency following the considerations of [3].

The increase of τ^*_{He} with higher radiating boundary can be interpreted in the following way: As the temperature decay length increases from about 2 cm to 5 cm the collection efficiency increases by about 20 % [3], improving the exhaust. However, at the same time the temperature at the throat is reduced from 40 eV to less than 30 eV for the discharges quoted here. This reduces the removal efficiency by 10 % [4]. Furthermore a steepening of the density profiles is observed for the RI-mode and the edge density is slightly reduced, reducing the total particle flow into the throat. Due to the lower edge temperature τ_{He} increases with the penetration depth of the neutrals and a decrease of the particle diffusion coefficient in the edge [1]. This leads experimentally to an increase of ρ^* of 20 %.

A possibility to improve the exhaust could be to apply a dynamic ergodic divertor [8]. This would increase the radiation potential and together with the higher diffusion coefficient due to the ergodicity of the plasma edge the particle flow to the limiter edge should be improved. Furthermore a rotating magnetic field could probably influence the recycling and the local diverting field structure could possibly improve the particle transport to the edge.

The radiative improved (RI) mode is in reasonable agreement with sufficient helium exhaust. The increase of ρ^* is about 20 %, but as the heat flux is distributed more uniformly new designs of toroidal belt limiters are possible thus increasing the exhaust. Additionally new concepts like the dynamic ergodic divertor (DED) could furthermore improve the exhaust. However, the compatibility of the DED with the RI mode has to be investigated.

References

[1] G.H. Wolf et al., 16th IAEA Fusion Energy Conf., Montreal 1996, IAEA-CN-64/O2-5.
[2] K.H. Dippel et al., J. Nucl. Mater. **145-147**, 3 (1989).
[3] R.W. Conn, J. Nucl. Mater. **128&129**, 407 (1984).
[4] G. Mank et al., 23rd EPS, Kiev 1996, Europhysics conf. abstr. Vol. **20C, II,** 815 (1996).
[5] D. Reiter et al., Nucl. Fusion **30**, 2141 (1990).
[6] G. Janeschitz and ITER team, Plasma Phys. Controlled Fus. **37**, Suppl. 11A, A19 (1995).
[7] J.A. Boedo, priv. communication.
[8] Berichte des Forschungszentrums Jülich; # **3285** (1996).

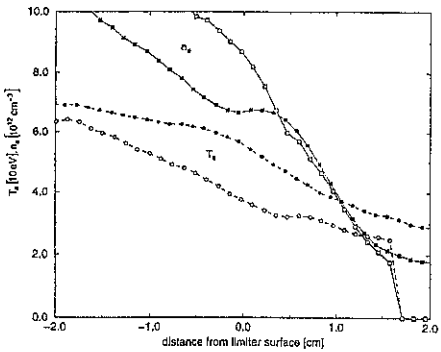

Figure 1: Radial profiles for the edge electron temperature (○: a=44 cm, ●: a=46 cm) and electron density (□: a=44 cm, ■: a=46 cm) relative to the last close flux surface.

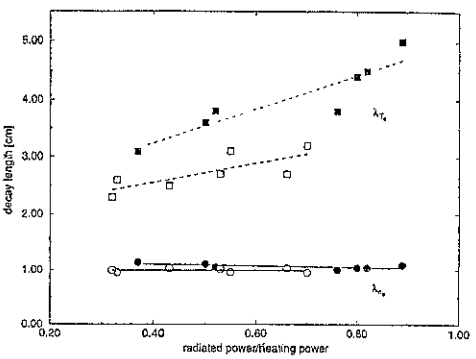

Figure 2: The density and temperature decay lengths (λ_n, λ_T) for different radiation levels and different limited radii (λ_n : ○: a=44 cm, ●: a=46 cm; λ_T : □: a=44 cm, ■: a=46 cm).

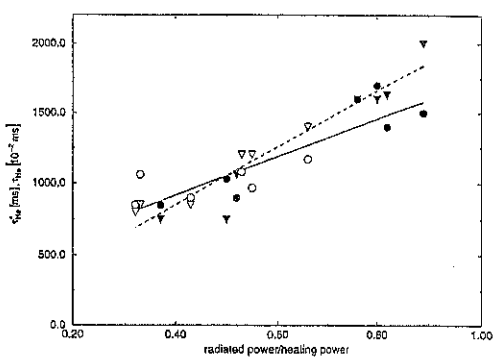

Figure 3: The effective helium particle confinement time (τ^*_{He}, ○: a=44 cm, ●: a=46 cm; solid line) and the helium particle confinement time (τ_{He}, ▽: 44 cm, ▼: a=46 cm; dahed line) versus the radiation level.

OPTIMIZATION OF NEON EDGE COOLING ON TEXTOR-94

G. Telesca, A.M.Messiaen, J. Ongena, J. Rapp*, U. Samm*, N Schoon, B. Unterberg*, G. Van Oost

Partners in the Trilateral Euregio Cluster:
Laboratoire de Physique des Plasmas / Laboratorium voor Plasmafysica, ERM / KMS, EURATOM Association, B-1000 Brussels, Belgium
* Institut fuer Plasmaphysik, Forschungszentrum Juelich GmbH, EURATOM Association, D-52425 Juelich, Germany.

1. INTRODUCTION

The main aim of impurity seeding is the enhancement of the level of the power radiated (P_{rad}) which can be beneficial for the operational conditions of the next step tokamak generation. Indeed, if the radiation properties of the selected seeded impurity are such that the power is radiated predominantly at the plasma periphery, the goal of protecting the targets from highly localized power loading can be achieved without excessive reduction of the central plasma reactivity. This might be possible only if the central plasma Z_{eff} is maintained low (typically below 2 for an ITER-like reactor) at high radiation fraction $\gamma = P_{rad}/P_{\alpha}$ (typically above 0.6).

On the pumped limiter tokamak TEXTOR-94 radiative scenarios are being established since many years by injection of neon and recently of argon. A wide range of the operational parameter space of the machine has been explored including low and high β operation and low and high confinement regimes. In ref.[1] it is shown that the ratio between the incremental P_{rad} (ΔP_{rad}) and the incremental Z_{eff} (ΔZ_{eff}) arising from the injection of an impurity is the figure of merit for the assess ment of a radiative scenario. This ratio does not only depend on the radiation function of the considered impurity (L_Z) and on its charge (Z), but also on the plasma parameters. Indeed, it depends on the transport properties of the main and impurity ions (which are represented for brevity by τ_p) as well as on the electron density $\bar{n}_{eo}$ and on the edge electron temperature $T_e(a)$ according to:

$$[\Delta P_{rad}/\Delta Z_{eff}(0)] / \bar{n}_{eo}^2 = V L_Z(T_e(a), \tau_p) / [Z^2 - Z] \qquad (1)$$

where the plasma volume V where line radiation is emitted is a function of the other quantities. When, at high level of radiation, the contribution of the intrinsic impurities to P_{rad} and to Z_{eff} is marginal compared to that of the seeded impurity, one has:

$$[\Delta P_{rad}/\Delta Z_{eff}(0)] / \bar{n}_{eo} = [P_{rad}/(Z_{eff}(0)-1)] / \bar{n}_{eo}^2 \qquad (2)$$

The quantity $[P_{rad}/(Z_{eff}(0)-1)] / \bar{n}_{eo}^2$ which does not depend explicitly on the electron density will be referred as the quality of impurity cooling.The quality of neon cooling (q.n.c.) measured on TEXTOR-94 depends strongly on particle transport and increases when trasport is enhanced. It can be a factor of 2-3 higher for auxiliary heated L-mode discharges (high transport) as compared to ohmic heating (low transport), as it is shown in ref. [2].
In this paper we report and discuss measurements of the quality of neon cooling during the high confinement radiative regime, Radiative Improved-mode [3], of TEXTOR-94 . P_{rad}, poloidally and radially resolved, is measured with a 26 channel bolometric system and the radial Z_{eff} profile from visible continuum with a new 7 channel diagnostic. However, since the level of confidence of the reconstructed bremsstrahung emissivity is acceptably high only in the central plasma (error of the order of 15%), only the central plasma $Z_{eff}(0)$ will be considered in the following.The edge electron temperature and density profiles are measured with thermal He and Li beams.

2. EXPERIMENTAL RESULTS

A significant fraction of all the values of the q.n.c., measured with the new Z_{eff} diagnostic, is plotted in Fig.1 as a function of the average electron density. The dashed line at q.n.c. = 3.6 [10^{-40} m ^{6} MW] corresponds to the Matthews scaling (see Sect. 3). Most of the data points pertain to the high confinement RI-mode discharges, while the few which refer to L-mode discharges are shown as reference points. Each point represents the q.n.c. measured during the flat top phase of a discharge. Different symbols refer to different days of operation; for each density different values of γ (= P_{rad} /P_{tot}) are considered.
For L-mode discharges the q.n.c. drops from 8 to about 4 when the input power, P_{tot}, is raised from 1.6 to 3.3 MW with related increase of the normalized beta β_N from 0.75 to about 1.1. Since the electron density profile and the confinement properties of the two series of discharges are very similar, the reduction of the q.n.c. by a factor of 2 at higher β_N depends only on the increase of the electron temperature profile and, more specifically, of the characteristic value of $T_e(a)$ which increases from about 30-35 to about 60-65 eV. (Since when γ is increased $T_e(a)$ decreases, we consider the value of $T_e(a)$ at γ about 0.6 as the characteristic edge temperature for the considered series).
Stricting speaking, for a neon seeded discharge to display RI-mode confinement properties γ should exceed 0.5, the electron density must rise only via limiter and wall desorption , $\bar{n}_{eo}$ has to be higher than 0.7 - 0.8 the Greenwald density and at least 20-25% of P_{tot} should be supplied by Neutral Beam co-injection: for the best conditions an enhancement factor with respect to the ITER-93 H mode scaling, f_{H93}, above 1 can be achieved. (The access to improved confinement in the RI-mode relies on the peaking of the density profile [4]). When one of these requirements is relaxed f_{H93} can slightly decrease, typically to about 0.8. The q.n.c. for the RI-mode does not show any trend when it is plotted versus density in spite of the fact that at higher density the characteristic $T_e(a)$ decreases typically from 65 to 50 eV. Indeed,

for most of the RI-mode discharges considered β_N is feedback controlled and set to 1.5 so that the temperature decreases with density. Only for very few of them β_N approaches 2, the beta limit of TEXTOR-94. The high level of scattering of the data points is due not only to the accuracy of P_{rad} and Z_{eff} measurements but also to different conditionings of the machine . However, the experimental data points show (see Fig.2) a dependence of the q.n.c. on the density peaking factor $n_e(0) / \bar{n}_{eo}$, f_p. At $f_p = 1.35$ the q.n.c. is 60 % higher than at $f_p = 1.6$. This dependence appears to be related to a change in transport since , on one hand f_p can be taken as a measure of particle confinement (the better f_p the higher the confinement), and on the other hand f_{H93} increases with f_p [4].

3. DISCUSSION

The quality of neon cooling (q.n.c. = $[P_{rad}/(Z_{eff}(0)-1)] / \bar{n}_{eo}^2$) measured on TEXTOR-94, ranges from about 8 to about 2.5 [10^{-40} m ^{6} MW] and its actual value depends on (and can be explained according to) the experimental conditions . When, for L-mode conditions, at a given $\bar{n}_{eo}$, β is increased, also the temperature - and specifically $T_e(a)$ - increases so that the q.n.c. suffers a drastic reduction: from 8 to about 4 (see ref. [2]). In contrast to the L-mode, for the RI-mode $T_e(a)$ appears to play only a marginal role, while the relevant parameter is seen to be the density peaking factor f_p. This is for two reasons: 1) for the RI-mode we have considered only discharges at relatively high beta with $T_e(a)$ generally in excess of 40 - 50 eV ; in this temperatute range the neon radiation function is relatively insensitive to changes in $T_e(a)$, and 2) the RI-mode can display, unlike the L-mode, quite a variety of particle confinement regimes: the density peaking factor f_p, indeed, in the RI-mode extends over a wide range (from 1.3 to 1.65) offering the possibility to scale the q.n.c. with f_p . The observed decrease of the q.n.c. versus f_p (and f_{H93}) suggests that optimization of the RI-mode neon seeded discharges on TEXTOR-94 and its scaling to reactor grade plasmas requires a balance between the benefits and disadvantages related to any f_p.

The multi-machine Matthews scaling [5] can be useful to predict Z_{eff} for a reactor grade plasma at a given level of P_{rad}. In its simplest form the scaling expresses the quality of impurity cooling as the product of a constant times the surface of the machine considered. We extrapolate the TEXTOR-94 data to an ITER-like reactor simply by considering the ratio between the surfaces of the two machines. Different measured q.n.c. would therefore give different values for Z_{eff} in an ITER-like reactor at given P_{rad} and $\bar{n}_{eo}$. The TEXTOR-94 data for the RI-mode discharges at $f_p = 1.35$ and at $f_p = 1.6$ would scale as $Z_{eff} = 1.5$ and $Z_{eff} = 1.8$ respectively for an ITER-like reactor at P_{rad} (edge) = 150 MW and $\bar{n}_{eo} = 1.2 \times 10^{20}$ m^{-3}. Assuming Z_{eff} to be determined by the neon concentration only, one would have $n_d/n_e = 95$ % and 92 % for the lower and for the higher f_p respectively. Since the value of f_{H93} at low f_p is 0.82 and at high f_p is 0.98 the product $n_d\tau_E$ would increase by about 15% at higher f_p. However, the bremsstrahlung radiation losses would increase by about 60% at higher f_p. The

behaviour of the helium ashes , which depends on the confinement regime [6], should also be taken into account.

[1] G. Telesca et al., Nucl. Fusion 36, 347 (1996)

[2] G. Telesca et al., presented at the 12th Int. Conf. P.S.I., J. Nucl. Mater. in press.

[3] A.M. Messiaen et al., Phys. Rev. Lett. 77, 2487 (1996)

[4] B. Unterberg et al., this Conference, invited paper.

[5] G. Matthews et al. presented at the 12th Int. Conf. P.S.I., J. Nucl. Mater. in press

[6] G. Mank et al., these Proceedings.

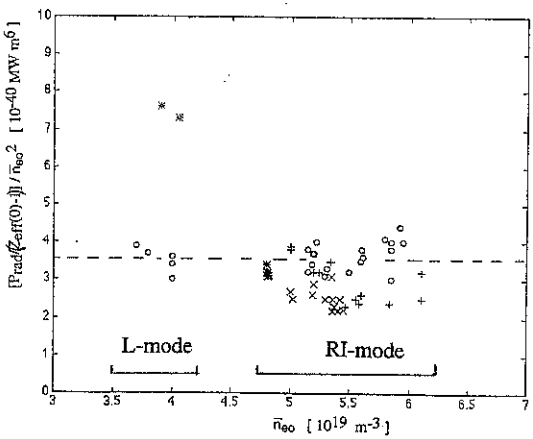

Fig.1 Quality of neon cooling vs. $\bar{n}_{eo}$ for L-mode and RI-mode discharges.

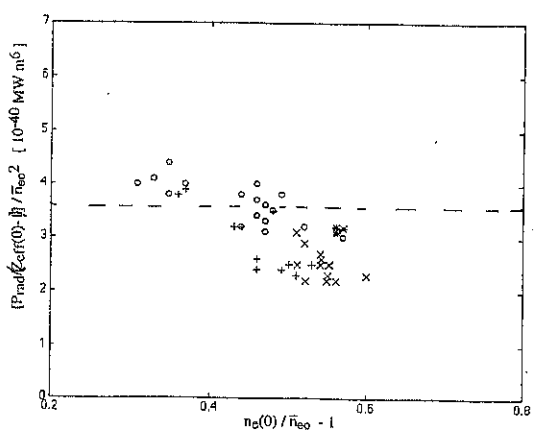

Fig.2 Quality of neon cooling vs. density peaking factor for RI-mode discharges.

Impurity production under radiative discharge conditions in TEXTOR-94

F.Weschenfelder, V.Philipps, A.Pospieszczyk, B.Schweer, B. Unterberg

Forschungszentrum Jülich GmbH, Institut für Plasmaphysik, EURATOM Association Trilateral Euregio Cluster, D-52425 Jülich

Introduction

One of the most urgent tasks for plasma research is the development of techniques which distribute the fusion power over large wall areas resulting in acceptable peak power fluxes to highly exposed limiter or divertor areas. One promising concept in this field is to seed suitable impurities into the plasma boundary and to radiate large parts of the fusion power in a radiative mantle [1]. A critical question of this concept is whether the content of the intrinsic and additionally seeded impurities in the plasma core can be kept at a tolerable level. An optimum for both, the amount of seeded and the level of intrinsic impurities released from the walls and limiters, has to be found. In this paper the impurity production at the limiters under radiative discharge conditions is investigated: How does the Ne-seeding and the resulting plasma edge cooling influence the impurity release from the graphite limiters in TEXTOR?

Experimental

Two experimental situations will be discussed in this paper. For line averaged densities around $4 \times 10^{13}cm^{-3}$ and around $6 \times 10^{13}cm^{-3}$ a γ-scan was performed, with γ defined as the fraction of the total power which is radiated due to the Ne-seeding (γ = total power / radiated power). The γ-level during all discharges was controlled by a feedback system which uses the Ne-VIII line emission as the feedback signal, a fast gas inlet system as neon source and the ALT-II pump limiter as sink [1]. For the low density case γ varied between 0.2 and 0.7, for the high density case between 0.5 and 0.9. All discharges were NBI and ICRH heated with constant NBI-power of ~1.2 MW for both conditions. For the density of $4 \times 10^{13}cm^{-3}$ the ICRH power was also kept constant to ~1.6 MW but for the high density case ICRH power had to be reduced for high γ-values (> 0.7) from 1.6 MW down to 0.6 MW to avoid β-limit instabilities or disruptions. The following diagnostics were used: To determine the deuterium and the carbon and oxygen fluxes the main ALT-II limiter (at r=46cm) emission spectroscopy of D_α, CI and OI was used across an ALT-II limiter plate in poloidal direction [2]. The ALT-II limiter is a graphite limiter. The neon and hydrogen fluxes in the SOL was measured by the Sniffer probe mass spectrometer [3] which was located for these discharges at a radius of 49cm. The He-beam diagnostic was used to determine the electron densities and temperatures in the plasma edge [4].

Results and Discussion

The most important observation is that the deuterium and the impurity fluxes in front of the ALT-II limiter decrease with increasing γ. Most significant is the strong decrease of the deuterium flux which is shown in fig.1 as dashed line. From the electron temperature T_e and

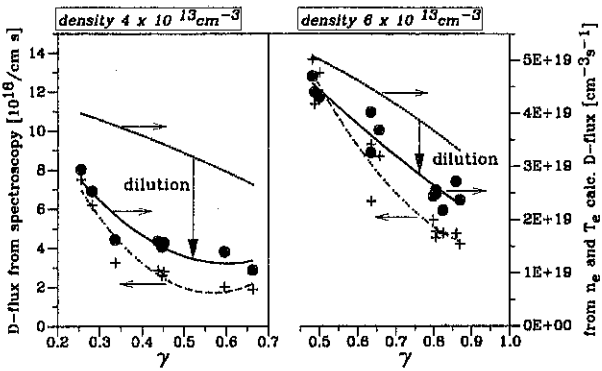

***Fig.1** Deuterium fluxes measured spectroscopically at the ALT-II limiter compared to the calculated fluxes from n_e and T_e. A better fit is achived if the dilution is taken into account.*

density n_e measured at a radius of 46cm the deuterium flux Γ_D parallel to the magnetic field lines can be calculated. Assuming at first a pure D-plasma (c_1 is a constant) [5]:

$$\Gamma_D = \frac{1}{2} \cdot n_e \cdot \sqrt{c_1 \cdot T_e}$$

The decrease of n_e and especially T_e results in a decrease of the calculated D-flux Γ_D. Fig.1 compares the calculated fluxes, shown as dotted lines, with the spectroscopically measured fluxes. A clear discrepancy can be seen which is more pronounced in the low density case. This suggests that the edge plasma is significantly diluted. To determine the amount of dilution the following relation was used:

$$n_e = n_D + \sum_i n_i \cdot Z_i$$

(n_D is the deuterium, n_i an impurity density, Z_i is the impurity charge state). Assuming that the measured relative impurity fluxes Γ_i / Γ_D are almost equal to the impurity concentrations n_i / n_D, the deuterium concentration n_D / n_e or the dilution $1\text{-}n_D / n_e$ can be calculated:

$$\frac{n_D}{n_e} = \frac{1}{1 + \frac{\Gamma_C}{\Gamma_D} \cdot 4 + \frac{\Gamma_O}{\Gamma_D} \cdot 4 + \frac{\Gamma_{Ne}}{\Gamma_D} \cdot 5}$$

A charge state of 4 is assumed for carbon and oxygen and a charge state of 5 for neon as expected for the plasma conditions at a radius of 46 cm. Using the measured flux ratios, shown in fig. 2, n_D/n_e can be calculated ranging between 0.7 at low γ and 0.45 at high γ in the low density case (4×10^{13}cm^{-3}) and between 0.9 (low γ) and 0.7 (high γ) in the high density case (6×10^{13}cm^{-3}). The strong dilution explains mainly the discrepancy between the measured D-fluxes and the fluxes calculated from n_e and T_e. With the relative deuterium concentration n_D/n_e and the calculated flux Γ_D the decrease of the hydrogen flux is calculated as shown in the solid points (•, and the solid line showing the general trend) in fig.1. They fit quite well to the measured deuterium fluxes shown as crosses (+, and the dashed line). The remaining difference may partly be caused by the coarse assumption that the relative fluxes are equal to the relative densities and that ion and electron temperatures are equal.

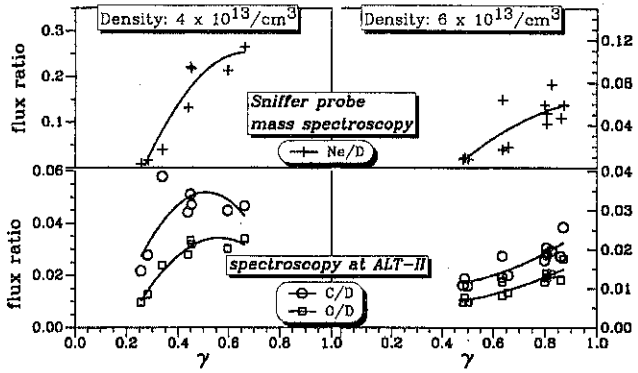

Fig.2 Flux ratios measured spectroscopically at the ALT-II limiter or with the Sniffer probe.

The strongly decreasing D-flux also lowers the impurity production at the limiter i.e. the sputtering is influenced. Spectroscopic measurements however show that the impurity fluxes of oxygen and carbon do not decrease as much as the D-flux. This behavior can be seen in the increase of the impurity production yields (relative fluxes) shown in fig. 2. The data show that sputtering of impurities is getting more important with higher γ. By using now the spectroscopically measured impurity fluxes from the ALT-II limiter, the electron temperature T_e at the limiter and the sputtering yields from the Bohdansky equations [6] the impurity fluxes from a graphite limiter due to D, O, C and Ne bombardment can be calculated. The result is shown in fig.3 for the high density case (6×10^{13}cm^{-3}). The decrease in the deuterium sputtering is caused by the decrease in the D-flux. The decrease of T_e has no influence since the deuterium sputtering yield of graphite is more or less constant for plasma temperatures $T_e >$ 40 eV. Sputtering fluxes due to the carbon and oxygen fluxes were also calculated and added in fig.3 to the D-sputtering flux. They raise the total sputtering flux almost independently of γ. The sputtering yield of neon is decreasing with increasing γ (decreasing T_e) but the neon flux at the limiter is increasing even more, so that the Ne-sputtering flux is roughly doubled with increasing γ. Adding this flux to the total sputtering flux results in the upper solid curve (with solid squares) in fig.3. The in-

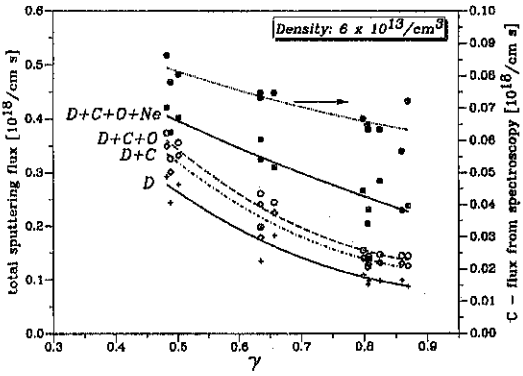

Fig. 3 Calculated sputtering fluxes of graphite bombarded with D^{4+}, C^{4+}, O^{4+} and Ne^{5+}. Additionally the measured C-flux from the limiter is shown. The fluxes are calculated with the Bodhansky equations.

creasing neon flux compensates somewhat the decrease in D-sputtering. The resulting total sputtering flux is compared with the carbon flux from the ALT-II limiter in fig.3. Both curves decrease less than the deuterium flux and are in good agreement.

Another process becomes important with increasing radiated power: photon induced release of impurities adsorbed at the walls. Fig.4 shows an indication for such a process. Shown is the neutral gas pressure of CO, CO_2 and of the hydrogen molecules measured at the TEXTOR wall during a series of discharges. As expected the hydrogen pressure is decreasing with increasing γ similar as the flux at the limiter. Opposite to that the CO pressure remains constant and the CO_2 pressure is even increasing. This demonstrates that the release of CO and CO_2 is not coupled to the deuterium flux to the walls but is due to photon induced release. The importance of this process has been shown earlier in TEXTOR [7]. Photons reaching the wall can produce free electrons in the surface which then enable the release of the ionized CO and CO_2 molecules attached at wall. This release mechanism may partly explain the oxygen flux measured at the limiter which remains constant with increasing γ.

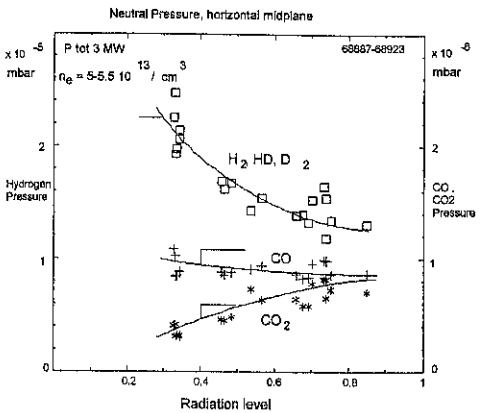

Fig.4 Neutral pressures of Hydrogen molecules, CO and CO_2 .

Summary

With an increasing fraction of radiated power due to Ne-seeding a decreasing D-flux at the main limiters of TEXTOR was observed. This decrease is partly due to a decrease in electron temperature but is also caused by the dilution of the edge plasma from neon. Sputtering of graphite from D-bombardment decreases with the decrease in D-flux. This effect is partly compensated by an increased sputtering from the seeded neon impurity. The oxygen fluxes at the limiters remain constant with increasing radiated power which is due to the enhanced photon induced release of carbon-oxides from the walls.

[1] A.M.X. Messiaen, J.X. Ongena, U. Samm et al. Phys. Review Letters 77, **12** (1996) 2487-2490
[2] A. Pospieszczyk, "Diagnostics of Edge Plasmas by Optical Methods", in "Atomic and Plasma-Material Processes in Controlled Thermonuclear Fusion", edt by R.K. Janev and H.W. Darwin, Elsevier, Amsterdam (1993) 213
[3] V. Philipps, E. Vietzke, M. Erdweg, Journal of Nucl. Matherials **162-164** (1989) 550
[4] E. Hintz and B. Schweer, Plasma Phy. Control. Fusion **37** (1995)
[5] P.C. Stangeby, "The plasma sheath in Physics of Plasma-Wall Interaction in Controlled Fusion", eds. D.E.Post and R.Behrisch, NATO ASI Series, Plenum Press, N.Y. (1986)
[6] W. Eckstein, C. Garcia-Rosales, J. Roth, W. Ottenberger, "Sputtering Data", Max-Planck-Institut für Plasmaphysik, Garching, Germany, Report IPP 9/82 (1993)
[7] V. Philipps, E. Vietzke, M. Erdweg and J. Winter, Journal of Nucl. Materials **200**, (1993) 355-359

Atomic and Molecular Hydrogen Reemission from heated TEXTOR-94 Carbon Limiters

A.Pospieszczyk, G.Sergienko*, D.Rusbüldt, V.Philipps, E.Vietzke
Institut für Plasmaphysik, Forschungszentrum Jülich GmbH,
EURATOM Association, Trilateral Euregio Cluster, D-52425 Jülich, Germany
*Inst. for High Temperatures, Association "IVTAN", Moscow, Russia

1. Introduction

The recycling of hydrogen at the walls and limiters of fusion devices determines particle and energy exhaust, wall erosion and several other processes. One key question is the proportion of hydrogen being recycled in form of atoms compared to hydrogen molecules at different wall and plasma conditions. In recent ion beam experiments it was found that above a temperature of 1000K the reemission of hydrogen molecules from graphite is decreasing with increasing temperature [1]. In that paper a relatively simple model had been developed, which explained the increasing hydrogen atom reemission with temperature by a thermal process for the release of hydrogen atoms from carbon. However, the model predicted also a flux dependence, which would shift the onset of atomic hydrogen emission to extraordinary high temperatures for fluxes, which are representative in the boundary layer of fusion devices. Therefore, similar experiments with hot limiters in a fusion plasma experiment were performed. Moreover, the change of the hydrogen source from molecules to atoms could elucidate the interpretation of the measured total hydrogen fluxes from the measurement of the atomic Balmer lines.

2. Experiment and methods

A graphite limiter (10 cm long, 6 cm wide and 5 cm high) with a toroidal and poloidal curvature of 8.5 and 6 cm, respectively, was introduced into TEXTOR-94 through a limiter lock from the bottom of the torus and had been positioned at the same plasma radius as the toroidal belt limiter ALT-II (r_{Lim}= 46 cm). This special limiter (surface 100 cm^2) was resistively heated up to a temperature of 1300 K in order to become independent of the heating by the plasma with varying loads. The TEXTOR vessel itself was at a temperature of 620 K and routinely boronized.

In order to determine the contribution of molecular hydrogen to the total hydrogen flux, high resolution emission spectroscopy of hydrogen molecules was performed. The emission spectra of a several bands ($3p^3\Pi_u \rightarrow 3s^3\Sigma_g$ (Fulcher) and $3d^1\Sigma^+_g \rightarrow 2p^1\Sigma^+_u$) were measured in the ranges 6000Å-6500Å and 4000Å-4400Å respectively. This was done both with a spectrometer with a resolution of about 0.2Å [2] and a spectrometer equipped with an intensified CCD camera as detector, which could be used for spatially (0.5mm) and spectroscopically resolved measurements. The latter wavelength region was particularly chosen for extraordinary high limiter temperatures in order to minimize the influence of the continuum radiation in the radially resolving spectrometer. The position of the observation volumes was set at a fixed toroidal position conventionally chosen near the location of largest power loading or a hole for gas blow experiments 15 mm from the center. More experimental details can be found in [3].

TEXTOR was operated under the following discharge conditions: I_p=350 kA, B_t=2.25 T, $\bar{n}_e(0)=3.6\times10^{13}$ cm^{-3}, $n_e(r=45.5\ cm)=6.5[7.5]\times10^{12}$ cm^{-3}, and $T_e(r=45.5\ cm)$=45[65] eV.

The numbers in brackets are valid for the NBI-heating of 1.3 MW, which was applied from 2.1s to 3.1 s during the discharge. Hydrogen has been used as working gas because the properties of its molecular emission spectrum is much better documented than for its isotopes.

3. Results

Fig.1 displays examples of the measured molecular hydrogen spectra for normal liner temperatures (about 600 K). In this wavelenth range, the lines of the R-,Q-, and P-branches of the (0-0), (1-1), (2-2), and (1-0) vibrational bands of the above mentioned transitions can be observed. The respective positions of the Q1-Q8 lines are marked at the bottom of the traces. One can notice that only the higher resolution instrument (Spek_H) is capable of detecting most of the molecular lines individually; however, for special purposes also a resolution of $\lambda/\Delta\lambda \approx 3\times10^4$ (Spek_L [with radial resolution]) may be sufficient. In the case of 1b) the spectrum contains also besides the molecular bands of H_2 and CH the atomic Balmer γ- and δ-lines; the latter was used as a measure for the atomic radiation - originating both from atoms by direct and molecules by dissociative excitation and because it fits into the same dynamic range as the molecular lines. There may be influences on this relatively highly excited level by the plasma electrons [4]; however, as the plasma conditions were not changed during the heating of the limiter they remain constant and can, therefore, be neglected.

Fig. 2 shows the time traces of CH, H_2 (Σ Q1-3), and H_δ from the spectral lines indicated in fig.1b. Also plotted is the temperature which has been derived from the continuum radiation appearing in the spectral range fig.1a. Before the discharge the limiter is uniformly heated to 670 K. During the ohmic part of the discharge, there is only a slight temperature increase of the surface. After starting the NBI heating the temperature increases to 2000 K within 1 s. In this latter phase one can already notice a drop in the H_2-, an even steeper one in the CH-, and an increase(!) in the H_δ-emission. After the NBI-heating the signals recover nearly to the same amount - except for CH, because the surface temperature is still too high for its maximum formation rate. The latter behaviour has, under stationary heating conditions, already been studied in [5]. However, quantitative results should not be derived from the NBI-heating phase as the temperature rise is normally confined to the highly loaded limiter parts, which may lead to interpretation difficulties in the optical (line integrated !) signals.

The different temperature of the surface is also reflected in the change of the rotational population of H_2, which can in our case be represented by the line ratio Q5/Q1 of the (0-0) band. Fig.3 shows this behaviour for the ohmic plasma phase between 1.4-1.9 s, when the limiter was gradually heated up to temperatures of 1400 K. However, this changing line intensity displays also the problems in the molecular spectroscopy of H_2. In order to avoid misinterpretations due to changing rotational temperatures it is often necessary to integrate a large number of lines within one band, which - in the case of H_2 - can be rather tedious.

In fig.4 the changes of the H_2-, CH-, and H_δ-emission as a function of the limiter temperature in the Ohmic part of the discharge is shown. Whereas for CH the well known drop occurs again at about 950 K, the intensity decrease of H_2 start first at about 1100 K. Simultaneously the atomic line emission from H_δ increases. One should note that when only a smaller number of individual Q_i-components is summed up (x), this would lead to an earlier drop of about 200 K; however, the general behaviour remains very similar for both cases of H_2-intensities.

In order to elucidate the nature of the hydrogen release, the radial line intensity distribution of

H_2 and H_δ is plotted in fig.5 for different surface temperatures.

4. Discussion

By comparing the results of fig.4 with the laboratory measurements of [1], one can notice that the drop in the H_2-production occurs at nearly the same surface temperatures. Therefore, a flux density dependence may be only marginally present and can certainly not be described by the model used there. However, the thermal origin of the majority of the released hydrogen is still valid and also proven by the penetration depths of H_δ for the two different temperatures of 670 K and 1370 K, which is very equal ($\approx$ 1.5 cm) and not very much different from the molecular one.

For a further interpretation of the intensity behaviour of the hydrogen lines in fig.4, one should have in mind that for constant plasma conditions also the total hydrogen flux (protons from molecules and atoms) from the limiter has to be constant for all limiter conditions. However, the atomic H_δ-intensity increases by 50% when the molecular H_2-intensity drops by 50% from 1100 K to 1370 K.

Analytically the ratio of atomic to total hydrogen flux can be expressed as follows (a full derivation cannot be given here): $\Gamma_H/\Gamma = \{2(k_1/k_2)(I_H/I_H^0) - 1\} / \{2(k_1/k_2) - 1\}$, where k_1 and k_2 are the factors for the conversion of atomic and molecular fluxes into Balmer line intensity I_H. I_H^0 is the value for high limiter temperatures, when the total flux contains only atoms and can be derived from $I_H = f(I_{H2})$ shown in fig.4 ($\approx$ 0.5). If $k_1/k_2 = 1$ (smaller values are not possible!) the release of hydrogen from the limiter surface below 1100 K would practically be only by molecules. However, for $k_1/k_2 \approx 2$, which may be a reasonable value [6], it is still 67%, but never less than 50% for all possible values of k_1/k_2. The remaining fraction of atomic flux may be represented by dotted parts in fig.5, which shows the difference between intensity from the thermal and the total H_δ-intensity. As these are the directly reflected hydrogen atoms, their penetration depth does not change for the two different limiter temperatures. However, the latter statements lead also to the conclusion that in the past the hydrogen flux may have been considerably underestimated by using the numbers for the conversion of H_α-photons into hydrogen flux from [7].

5. Summary and conclusions

- until 1100 K hydrogen is predominantly released as H_2
- above 1100 K: reduction of the H_2-flux (50% at 1370 K)
- no flux density dependence in comparison to ion beam experiments (only a slight shift to higher temperatures similar as for CH is found)
- the large fraction of molecular hydrogen may lead to different energy exhaust mechanisms in the boundary or divertor of a fusion plasma
- photon rates for hydrogen atoms and for the two atoms in the molecules are different; this may lead to an underestimation of the total hydrogen influx from Balmer line measurements

References

[1] P.Franzen and E.Vietzke, J.Vac.Sci.Technol. A12 (1994) 820.

[2] G.Sergienko, A.Pospieszczyk, D.Rusbüldt, 23rd EPS Plasma Phys.& Contr. Fusion (Kiev 1996), Vol.20C, p.751.

[3] V.Philipps, A.Pospieszczyk, B.Schweer et al., J. Nucl.Mater. 220-222 (1995) 467.

[4] K.Sawada, K.Eriguchi, T.Fujimoto, J.Appl.Phys. 73 (1993) 8122.

[5] A.Pospieszczyk, V.Philipps, E.Casarotto, U.Kögler, B.Schweer, B.Unterberg, F.Weschenfelder, to be published in J.Nucl.Mater. (1997), PSI 96, St.Raphael.

[6] U.Samm, H.L.Bay, P.Bogen, H.Hartwig, E.Hintz, K.Höthker, Y.T.Lie, A.Pospieszczyk, G.G.Ross, D.Rusbüldt, B.Schweer, Plasma Phys. and Contr. Fusion 29 (1987) 1321.

[7] L.C.Johnson and E.Hinnov, J Quant. Spectr. and Rad. Transf. 13 (1973) 33.

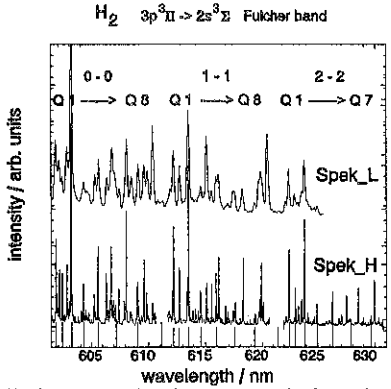

Fig.1a: H_2 - molecular spectrum in the red spectral range with two different resolutions

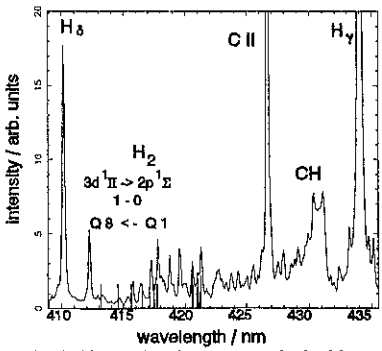

Fig.1b: H_2 - molecular spectrum in the blue spectral range with two different resolutions

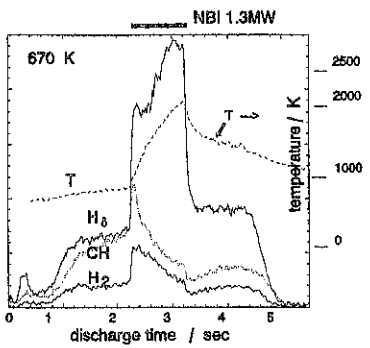

Fig.2: time traces of CH, H_2(Σ Q1-3), H_γ [fig.1b] for a limiter temperature of 670 K

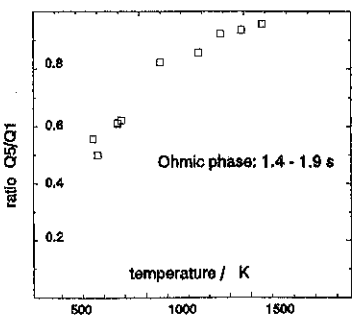

Fig.3: temperature change in the rotational temperature from the ratio Q5 / Q1

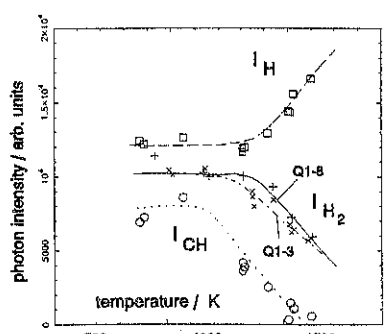

Fig.4: variation of the H_2, CH-, and H_γ intensities as a function of limiter temperature in the Ohmic part

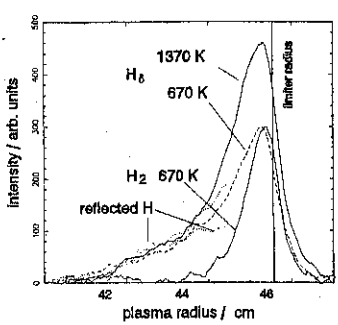

Fig.5: atomic and molecular intensity distributions for two different limiter temperatures

SPECTROSCOPIC STUDIES OF THE VELOCITY DISTRIBUTION AND PENETRATION DEPTH OF HELIUM AND NEON ATOMS RELEASED FROM CARBON AND TUNGSTEN TEST LIMITERS IN TEXTOR-94

P.Lindner[1], B. Unterberg[1], M. Brix[1], R. Jaspers[2],H. Knauf[1], A. Pospieszczyk[1], D. Rusbüldt[1], U. Samm[1], B.Schweer[1]

Partners in the Trilateral Euregio Cluster :
[1]Institut für Plasmaphysik, Forschungszentrum Jülich GmbH, EURATOM Association, D-52425 Jülich, Germany
[2]FOM-instituut voor Plasmafysica 'Rijnhuizen', Ass. EURATOM, Postbus 1207, 3420 BE Nieuwegein, The Netherlands

1 Introduction

Impurity transport is one of the key problems on the way to controlled nuclear fusion. In addition to particle transport in the plasma core, processes occurring at the plasma edge, namely the penetration of impurity neutrals released from the plasma facing components into the confined plasma, have a direct and significant influence on the central impurity density.
Helium and neon are impurities of special interest in this context: helium as the product of the DT- fusion process unavoidably present in a burning plasma and neon as a promising candidate within the concept of power exhaust from a radiating plasma mantel in a next step device like ITER. As a consequence, there is urgent need to investigate the plasma surface interaction of these species and their penetration into the confined plasma volume.
The velocity distribution of helium and neon atoms has been determined at TEXTOR-94 from the Doppler broadening of atomic line emission[1]. Two different release mechanisms, desorption and reflection have been identified. The influence of the plasma wall material (carbon and tungsten) on the velocity distribution of the neon atoms will be shown.
Finally, the influence of edge processes on the central impurity build-up is investigated by relating the particle confinement times of helium and neon to their penetration depth.

2 Experimental arrangement and principles of measurement

The experiments have been performed on the Tokamak TEXTOR-94 with a major radius R = 1.75 m and a minor radius a = 0.46 m, a toroidal magnetic field B_T= 2.25 T and a plasma current I_p = 350 kA. The plasma was heated by neutral beam co-injection (P_{NBI}=1.3MW) and the line average central electron density was varied between $2.5 \cdot 10^{13} cm^{-3}$ and $5 \cdot 10^{13}$ cm^{-3}. Neon feed-back was applied to vary the fraction γ_{rad} of the radiated power with respect to the total input power. The measurements shown below have been carried out using test limiters made of two different materials (carbon and tungsten) which are introduced into the vacuum vessel with the help of a limiter lock system at the bottom of the torus. The limiter is observed tangentially using a spectrometer equipped with an intensified CCD camera as detector which yields spectra of radially resolved line emission in the wavelength range (200 - 800) nm. The Doppler broadened intensity profile of line emission from neutral neon and helium has been measured from the top by guiding the emitted light with fibers to a high resolution ($\lambda/\Delta\lambda = 10^5$) spectrometer. In addition to the Doppler broadening the line shape is determined by the Zeeman- effect. For the NeI transition $3s'[1/2]_{J=1} \Rightarrow 3p'[1/2]_{J=0}$ at λ = 582.48 nm and the HeI transition $1s\,3s\,^1S \Rightarrow 1s2p\,^1P$ at λ = 728.13nm the Zeeman- splitting of the π- component with ΔM=0 is zero to a first order approximation. This component has been selected by a polarizer. A neon glow discharge through a Pluecker tube has been used for an exact in situ determination of the wavelength λ_0. The remaining Doppler shift $\Delta\lambda = \lambda_0 \upsilon / c$ of a line emitted by an atom moving with the velocity υ in the direction of the observer allows to deduce the velocity distribution f(υ) from the Doppler broadened profile.

The profiles of electron temperature (T_e) and density (n_e) , which are obtained by means of a thermal helium beam diagnostic, govern the excitation and ionisation processes of atoms in front of the limiter. The density of helium and neon in the core plasma is measured by charge exchange recombination spectroscopy (CXRS)[2].

3 Results and discussion

In fig.1 an intensity profile of NeI at a tungsten limiter is shown. Although a polarizer has been used, still small σ - components are visible, originating from diffuse light reflected at the rough surface of the limiter. The σ-components are cut away for the further calculations, as shown in fig.1.

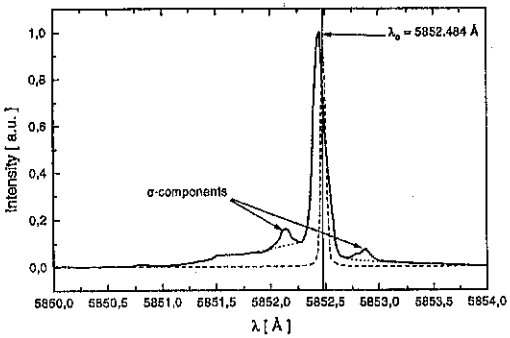

Figure 1: Profile of NeI 5852.484 Å line at the tungsten test limiter, with T_e=22eV and n_e=9.6 10^{12} cm^{-3} on LCFS (T_e,n_e is measured with helium beam diagnostic)

Fig. 2 shows the dependence of the velocity distribution of neon on edge temperature and density at the LCFS (r=46cm) and the limiter material.

The velocity distribution consists of a slow component, which can be attributed to desorbed particles (E_0=0.2eV), and a fast component. The fraction of fast particles is strongly increased at reduced T_e for both materials.

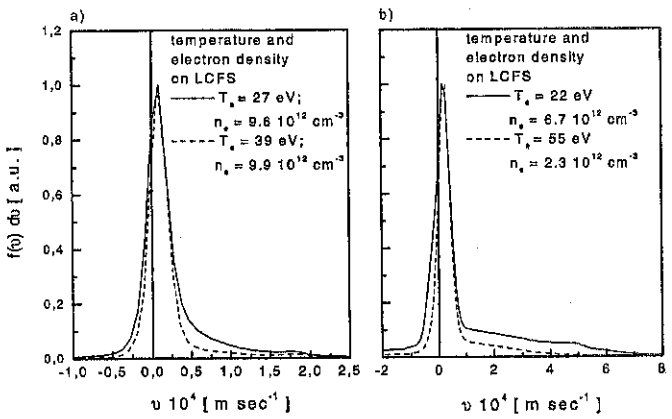

Figure 2: Velocity distribution of NeI at a carbon (a) and tungsten limiter(b)

Comparing carbon and tungsten limiters the latter shows a significantly higher velocity of the fast neon component. This finding can be explained by an increase of the particle- and energy- reflection coefficients (R_N, R_E) when going to low temperatures (= lower energies of ions hitting the limiter) and comparing low Z and high Z targets. We characterise the velocity distribution by their mean velocity. Fig. 3 shows its dependence on the electron temperature at the radius of the test limiter. The average velocity decreases with increasing T_e. Helium atoms are 1.7 times faster than neon atoms on the same target. $\langle\upsilon\rangle$ of neon on the tungsten limiter is a factor of 4 higher than $\langle\upsilon\rangle$ of neon on the carbon limiter.

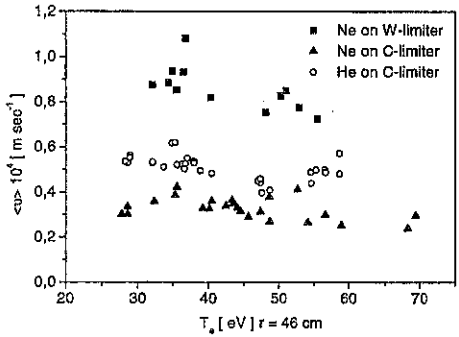

Figure 3: Mean velocity of neon on carbon and tungsten limiter and helium on carbon limiter

The measured f(υ) and n_e-, T_e -profiles are used to calculate the neutral density $n_A(r)$[3] in front of the limiter, the resulting ion source distribution Q(r) and the penetration depth λ_i according to

$$n_A(r) = n_A(0)\int_0^\infty f(\upsilon)\exp\left(-\frac{1}{\upsilon}\int_0^r n_e\langle\sigma\upsilon_e\rangle_{ion}\,dr'\right)d\upsilon \quad (1)$$

$$Q(r) = n_A n_e\langle\sigma\upsilon_e\rangle_{ion} \quad (2)$$

$$\lambda_i = \frac{\int Q(r)rdr}{\int Q(r)dr} \quad (3)$$

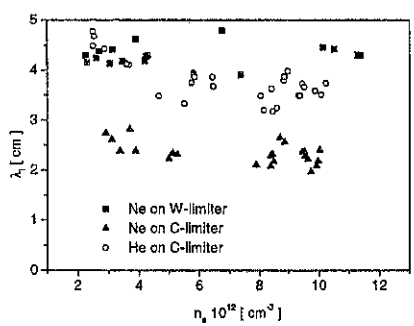

Figure 4: Penetration depth of helium and neon versus n_e on the LCFS

The weak dependence of the penetration depth on local plasma parameters has a reason in competing processes: with increasing density the temperature decreases and therefore the ionisation rate coefficient $\langle\sigma\upsilon_e\rangle_{ion}$ also decreases. On the other hand with a decreasing temperature the velocity of the particles increases. Both effects can compensate, as can be seen from a simplified expression for the penetration depth, valid for a homogenous plasma (in contrast to eq. 3, which applies to any plasma profile):

$$\lambda_i = \frac{\langle\upsilon\rangle}{n_e\langle\sigma\upsilon_e\rangle_{ion}} \quad (4).$$

The target material plays a role via different energy- and particle- reflection coefficients, which influence $\langle\upsilon\rangle$.

In a simple diffusion transport model [4] the particle confinement time of a species depends linearly on its penetration depth for a given diffusion coefficient and on the peaking factor f of the density impurity profile. The ratio of helium and neon particle confinement times is given by

$$\frac{\tau_p^{He}}{\tau_p^{Ne}} = \frac{n_p^{He}}{n_p^{Ne}} \frac{\Gamma_p^{Ne}}{\Gamma_p^{He}} \sim \frac{\lambda_i^{He}}{\lambda_i^{Ne}} \frac{f^{He}}{f^{Ne}}$$

The ratio n_{He}/n_{Ne} is measured by CXRS and the flux ratio $\Gamma_p^{Ne}/\Gamma_p^{He}$ is determined from measurements with a tangential spectrometer. The resulting data for a series of discharges with different line averaged central electron densities are given in the table below.

$\frac{\lambda_i^{He}}{\lambda_i^{Ne}}$	$\frac{\tau_p^{He}}{\tau_p^{Ne}}$	$\bar{n}_{e0}\ 10^{13} cm^{-3}$	$f_e = \bar{n}_{e0}/\bar{n}_e(r=40cm)$
1.56	2.85	4.8	1.7
1.61	3.86	4.6	1.9
1.65	4.29	3.2	2.1

Indeed, as expected qualitatively from the model, in all cases the larger penetration depth of helium causes a larger particle confinement time. But the quantitative difference in the ratios between penetration and confinement and the fact that in contrast to the penetration depth the ratio of confinement times varies with central density indicate that the transport of neon and helium ions is significantly different. A peaking of the helium profiles similar to the background plasma ($f^{He} = f_e = 1.7$ - 2.1 see table above)[5] and rather flat profiles for neon (f=1) can explain the measurements.

The measurements of neon and helium velocities at a limiter demonstrate clearly the influence of plasma-wall-interaction processes (particle reflection, desorption) and atomic physics (ionisation rates) on the global particle confinement times. This should be taken into account when considering the materials for plasma facing components in a fusion device.

4 References

[1] Bogen P. et al., J. Nucl. Mater. **162-164** 545-549 (1989)
[2] Jaspers R., poster at this conference, *Neon profiles and concentrations under radiative edge cooling conditions in TEXTOR-94*
[3] Pospieszczyk A., "Diagnostic of Edge Plasma by Optical Methods", in "Atomic Plasma- Material Processes in Controlled Thermonuclear Fusion", edt by R.K. Janev and H. W. Darwin (Elsevier, Amsterdam,1993)
[4] Stangeby P.C.; McCracken G.M, Nucl. Fus.,Vol 30, No.7 ,(1990)
[5] Hillis D.L. et al., J. Nucl. Mater. **196-198** 35 (1992)

Low Voltage Start-up Assisted by ICRF in TEXTOR-94

A.I.Lyssoivan[1], O.Neubauer[2], R.Koch[1], B.Giesen[2], P.Hüttemann[2], G.Van Oost[1], M.Vervier[1], F.Durodié[1], H.G.Esser[2], H.R.Koslowski[2], H.T.Lambertz[2], A.Messiaen[1], H.Reimer[2]

Partners in the Trilateral Euregio Cluster :

[1] - Laboratoire de Physique des Plasmas - Laboratorium voor Plasmafysica, Association "Euratom-Belgian State", Ecole Royale Militaire - Koninklijke Militaire School, B-1000 Brussels, Belgium

[2] - Institut für Plasmaphysik, Forschungszentrum Jülich, D-52425 Jülich, Germany

1. Introduction

Low voltage tokamak start-up will be required in reactor scale fusion devices. For the present ITER start-up scenario, the inductive electric field is limited to E≈0.3 V/m in the breakdown region to prevent the occurrence of a quench in the superconducting coils. To perform reliably start-up at such low electric field, non-inductive pre-ionisation, target plasma production and preheating are desirable.

Reduction of the breakdown loop voltage has been studied in many tokamaks using ECH [1-4] or LHH [5]. Pure inductive start-up at low voltage requires a careful control of prefill gas pressure and minimisation of stray (error) magnetic fields. Assistance by additional heating leads to improved reliability and extension of the range of prefill gas pressure and stray magnetic field, as shown with ECH on DIII-D [2].

An alternative to ECH assistance is the use of radio-frequency power in the ion cyclotron range of frequencies (ICRF). This technique was used for plasma production and "currentless" operation in stellarators [6-7] and has been recently successfully applied to tokamaks: in TEXTOR-94 for ICRF-wall conditioning / coating and start-up assistance [8-10] and in TORE SUPRA for ICRF-wall conditioning [11].

The initial attempts of ICRF assisted start-up in TEXTOR-94 [9] have been pursued and reliable tokamak start-up at low voltage (E_0=0.31 V/m at the vessel centre) assisted by ICRF power, has been achieved.

2. Experimental results and analysis

2.1 Experimental configuration

TEXTOR-94 is a medium size (R_0=1.75 m, a=0.46 m) circular cross-section tokamak. The vacuum vessel is a continuous resistive shell, with a total toroidal resistance of 1.55 mΩ. The OH system comprises an iron core and consists of magnetising (BM) and outer poloidal coils (Fig.1). The BV coils are used for equilibrium control whereas the KZ and KR coils allow fast position control. The BF system controls the plasma shape and is suited for stray field compensation during start-up.

In order to maximise the pulse length, the flux swing of TEXTOR-94 was increased, leading to operation with saturated iron core. This gives rise to stray fields in the plasma volume, which have to be properly compensated for successful start-up. Required values of the current in the BF coils were calculated for different values of the magnetising current (BM) by a 3-D code and confirmed by electron beam measurements at the centre of the plasma volume [12]. During the start-up phase, the voltage is produced by ramping down the BM current. This leads to a drastic variation in stray field which has to be compensated to allow successful start-up. This compensation is performed by the fast KZ system controlled by signals from vertical field pick-up coils located around the plasma volume.

However, even for the best possible compensation, a higher voltage is required for start-up as compared to the non-saturated iron core operation. For normal start-up, the required high voltage is produced by switching a resistor into the magnetising circuit. This operation is sensitive to faults and causes mechanical stresses to the machine. The idea is to avoid this high voltage phase by using ICRF assistance for start-up at lower voltages.

Studies of ICRF assisted start-up have been carried out with the existing ICRH system. This consists of two low field side (LFS) double loop antennas, one without (A1) and the other with Faraday screen (A2) [13]. A1 was fed in phase (*zero*-phasing) and A2 out of phase (π -

phasing). The power (P_{RFtot}=100-450 kW) was applied to both antennas from separate RF generators in overlapping pulses. The RF pulse lengths were varied from 0.6 s up to 1.0 s. RF starts at $t \leq -(0.2 - 0.4)$ s, producing an RF plasma before application of the loop voltage ($t = 0$ s) and providing afterwards preheating during the start-up and current ramp-up phases ($0 \leq t \leq 0.6$ s).

2.2. ICRF pre-ionisation and target plasma production

ICRF plasma production has been performed in various conditions in TEXTOR-94 [10]. Helium plasma with central line-averaged density up to $\bar{n}_{e0} \approx 3 \times 10^{12}$ cm^{-3} (in the high gas pressure case $p_{He} \approx 10^{-3}$ mbar) was reliably produced in a wide range of toroidal magnetic field $B_T \approx 0.36$-2.24 T ($2\omega_{CHe} \leq \omega \leq 12\omega_{CHe}$) with the same RF frequency (f=32.5 MHz).

The ICRF assisted start-up experiments were performed at the standard magnetic field $B_T = 2.24$ T and frequency (f=32.5 MHz), corresponding to 2nd harmonic heating with the $\omega=2\omega_{CHe}$ layer positioned at $r \approx +10$ cm (LFS). These experiments were usually performed in ^{4}He (continuous gas flow) because RF discharges are more reproducible with a high recycling gas than with deuterium [10, 14] or hydrogen [14]. After a fresh boronisation, an additional gas puff was needed during the pre-ionisation phase to compensate the strong wall pumping.

Low voltage start-up generally requires low gas pressure operation ($p_{He} \sim 10^{-5}$ mbar). The density achieved at different RF powers is shown in Fig.2, which also shows the coupling efficiency $\eta = R_{pl} / (R_{pl}+R_v) \leq 60\%$. (with R_{pl} the plasma and R_v the vacuum antenna resistance). The presence of residual inhomogeneous poloidal stray fields tends to destabilise the strongly interlinked RF power coupling and plasma production processes. Besides, antenna coupling is lower at lower gas pressure ($p_{He} \approx (4\text{-}9) \times 10^{-5}$ mbar). Both conditions result in a lower plasma density ($\bar{n}_{e0} \approx (0.2\text{-}7.0) \times 10^{11}$ cm^{-3}) in ICRF pre-ionisation experiments as compared with ICRF plasma production in pure toroidal magnetic field [8,10]. The RF plasma density increases with P_{RF}, while η is nearly independent of it. The efficiency of RF plasma production in deuterium was always lower than in helium (Fig.2, open crosses and triangles for η and $\bar{n}_{e0}$, respectively).

2.3 ICRF assisted low voltage start-up ($E_0 < 0.4$ V/m)

The present low voltage start-up experiments on TEXTOR-94 with ICRF pre-ionisation gave promising results. The production of an ICRF target plasma before applying the loop voltage allowed to initiate normal OH discharges at voltages as low as 3-5 V ($E_0 \leq 0.4$ V/m). Figure 3 shows the discharge with the lowest RF power (100 kW) (coupled by the screenless antenna only) for which low loop voltage start-up has been achieved up to now. There are two phases in the current ramp-up. During phase I, the loop voltage around the torus is determined by the maximum voltage of the BM power supply. During phase II, a pre-set current ramp rate is maintained until the final flat-top level of the current (300-500 kA) is reached ($t \approx 0.35$-0.40 s). Gas feed-back control (helium or deuterium) was usually applied during phase II to optimise plasma current ramp-up rate and to control plasma density.

Reliable and reproducible operation could be achieved not only with the usual RF power combination $P_{RF}(A1)$=250 kW + $P_{RF}(A2)$=150 kW [9] but also with the A1 antenna operated alone at 100 kW ($P_{RF}(A2)=0$), as shown above. However, with only 50 kW on A1, the current did not start. Neither did it with 150 kW on the A2 (shielded) antenna only. Figures 4 and 5 give the dependence of the plasma (+ vacuum vessel) resistance (V_{res}/I_p, here V_{res} is the resistive voltage [9]) and of the current ramp rate versus RF power during phase I and at the beginning of Phase II. Several features should be underlined. The plasma conductivity and current ramp rate increase with the RF power. The plasma conductivity reaches the maximum level at phase II, while the current ramp rate has the highest value (> 2 MA/s) already at the end of phase I. Below 100kW, the normal current ramp-up is not initiated, an RF plasma is formed that conducts a low plasma current in competition with the vacuum vessel. In that case the plasma is very resistive ($R_{pl} \sim 1$ mΩ) and after a modest rise ($dI_p/dt \sim 0.3$-0.6 MA/s) the small current becomes stationary and normal ramping-up does not take place. The existence of this RF power threshold confirms the importance of ICRF assistance not only for pre-ionisation and plasma build-up but also for target plasma preheating as well.

Figure 6 shows the influence of gas feed-back programming on plasma density and current ramp-up evolution. The early gas puff ($t \approx 10$ ms) results in a smooth and slow plasma density ramping and a reduction in plasma current ramp rate. The largest current ramp rate (for

the same loop voltage and RF power) was achieved with delayed gas puff (t≈200 ms). In this case the volt-second consumption was somewhat reduced during the start-up and current ramp-up phases as shown in Fig.7. For comparison, this figure also shows a former shot (see [9]) with delayed current ramp-up and a low current plateau (curve 5) leading to degradation of the volt-second performance. The plateau has been eliminated by careful compensation of the stray field (reducing the averaged vertical magnetic field $|\overline{B}_v|$ to about 10-15 G), early start of position control currents (at t ~ 20 ms), appropriate programming of the feedback control systems and proper first wall conditioning. The volt-second consumption is now similar to that of high voltage (12 V) start-up (curve 6) or even better by up to 0.2 Vs.

3. Conclusions

* Successful ICRF assisted low voltage start-up (E_0 ~ 0.3 V/m) was demonstrated for the first time on TEXTOR-94. Normal OH discharges in He and D, with He pre-filling, (I_p = 300-500 kA) were achieved with the help of a minimum of 100 kW ICRF pre-ionisation.
* ICRF plasma production and preheating have been performed in the standard 2nd harmonic ICRH scenario at P_{RF} = 100 - 450 kW using the existing RF system.
* Reproducible low voltage start-up was possible using, at minimum, only the screenless antenna at 100 kW (60% coupling efficiency), at gas pressure ~ (4-9)x10^{-5} mbar and in the presence of 10-15 G residual stray field. Operational limits are now under investigation.
* These experiments demonstrate the potential of the present ICRF antennas (especially those without Faraday screen) for plasma production and provide a strong indication of the usefulness of ICRF systems for low voltage start-up assistance.

References

[1] Alikaev V.V., et al., *Proc. 17th EPS Conf. on Controlled Fusion and Plasma Heating, Amsterdam 1990*, v.14B, part III, p.1084.
[2] Lloyd B., et al., *Nucl. Fusion* **31** 2031 (1991).
[3] Polman R.W., et al., *Proc. 18th EPS Conf. on Controlled Fusion and Plasma Heating, Berlin 1991*, v.15C, part III, p.317.
[4] Whaley D.R., et al., *Nucl. Fusion* **32** 757 (1992).
[5] Yoshino R. and Seki M., *Plasma Phys. Control. Fusion* **39** 205 (1997).
[6] Shvets O.M., et al., *Proc. 4th Int. Symp. on Heating in Toroidal Plasmas, Roma 1984*, v.1, p.513.
[7] Nishimura K., et al., *Proc. 7th Int. Workshop on Stellarators, Oak Ridge 1989*, IAEA, Vienna (1990), p.265.
[8] Esser H.G., et al., *12th Int. Con. on PSI, St.Raphael 1996*, to be published in Journal Nucl. Mater.
[9] Koch R., et al., *16th IAEA Fusion Energy Conf., Montreal 1996*, paper IAEA-CN-64/AP1-6.
[10] Koch R., et al., *12th Topical Conf. on Radio Frequency Power in Plasmas, Savannah 1997*, paper A01.
[11] Gauthier E., et al., *12th Int. Con. on PSI, St.Raphael 1996*, to be published in Journal Nucl. Mater.
[12] Neubauer O., et al., *Fusion Technology* **31** 154 (1997).
[13] Van Nieuvenhove R., et al., *Nucl. Fusion* **32** 1913 (1992).
[14] Lyssoivan A.I., et al., *Proc. 22nd EPS Conf. on Controlled Fusion and Plasma Physics, Bournemouth 1995*, v.19C, part III, p.341.

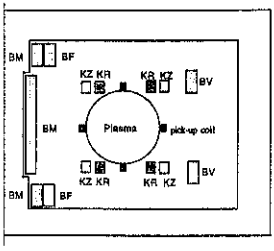

Fig.1. Configuration of OH system with compensated poloidal coils and magnetic diagnostic coils in TEXTOR-94.

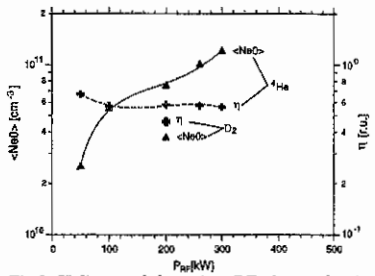

Fig.2 .Helium and deuterium RF plasma density and A1 antenna coupling efficiency vs P_{RF1}; P_{RF2}=0, B_T=2.24 T, $|B_v|$=10 G, p_{He}=7x10^{-5} mbar .

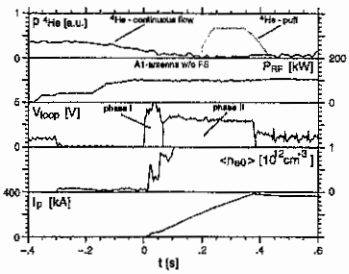

Fig.3 .Scenario of low voltage start-up assisted by ICRF power in the 2nd cyclotron harmonic regime.

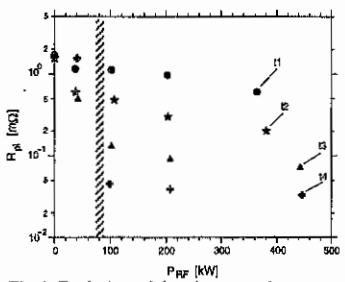

Fig.4. Evolution of the plasma resistance as a function of RF power during loop voltage phase I (t_1=10 ms, t_2=20 ms, t_3=30 ms) and phase II (t_4=60 ms), V_{loop}=4 V, $|B_v|$=10-15 G, p_{He}=4x10^{-5} mbar .

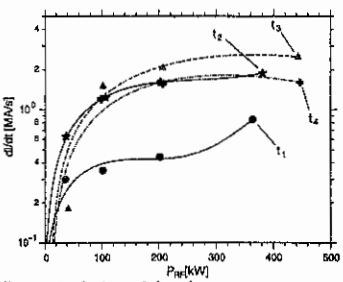

Fig.5. Evolution of the plasma current ramp rate during ICRF assisted low voltage start-up as a function of RF power (timing and parameters are mentioned in Fig.4).

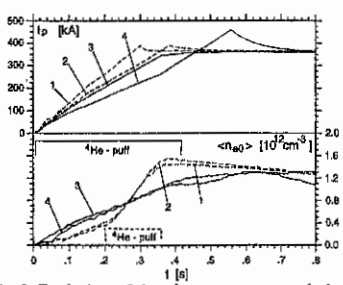

Fig.6. Evolution of the plasma current and plasma density ramp during ICRF assisted start-up at different loop voltages and gas puffing scenarios: curve 1 - V_{loop}=4.5 V, late gas puff; curve 2 - V_{loop}=3.4 V, late gas puff; curve 3 - V_{loop}=4.5 V, early gas puff; curve 4 - V_{loop}=3.4 V, early gas puff.

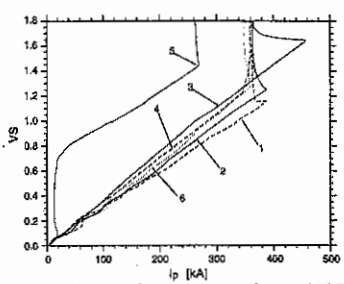

Fig.7. Volt-second consumption during ICRF assisted start-up and plasma current ramp-up phases vs plasma current: curves 1-4 - parameters are mentioned in Fig.6; curve 5 - V_{loop}= 5.0 V, late operation of position control system; curve 6 - V_{loop}=12 V, w/o ICRF.

Influence of high-Z limiter materials on the properties of the RI-mode in TEXTOR-94 with different heating schemes

J. Rapp, G. Van Oost†, G. Bertschinger*, L. Könen*, H.R. Koslowski*, A. Krämer-Flecken*, A. Messiaen†, J. Ongena†, V. Philipps*, A. Pospieszczyk*, U. Samm*, T. Tanabe‡, G. Telesca†, M.Z. Tokar* and B. Unterberg**

* Institut für Plasmaphysik Forschungszentrum Jülich GmbH, EURATOM Association, D–52425 Jülich Germany

†Laboratoire de Physique des Plasmas/Laboratorium voor Plasmafysica, ERM/KMS, EURATOM Association, B-1000 Brussels, Belgium

‡Center for Integrated Research, Nagoya University, Japan

1. Introduction

The Radiative Improved-(RI) mode is an operational regime, which features high energy confinement and strong edge radiation cooling due to line radiation of neon or argon [1]. The compatibility of this RI-mode with high-Z plasma facing materials as tungsten, which are intended to be used in future fusion reactors, is studied in this work. The key issue is the release and transport of tungsten and their effect on the plasma performance, which was already evaluated for L-mode discharges [2]. Furthermore, the influence of the heating scenario (NBI and/or ICRH) on those issues was investigated.

2. Experimental set-up

In the limiter tokamak TEXTOR-94 ($R_0 = 175cm$, $a = 46cm$ determined by the toroidal belt limiter ALT-II) a movable solid W test limiter was inserted through a limiter lock into the edge plasma. The impurity release from this limiter was evaluated from visible spectroscopy. The impurities in the core plasma were observed with VUV-spectroscopy and a 26-channel bolometric system. For a discharge with strong central radiation, we evaluated the tungsten concentration from the radial radiation profiles, assuming coronal equilibrium and using the data of Post [3]. This W-density was used to calibrate the spectroscopic W-quasicontinuum (W^{30+}) taking into account the background signal. Further we derive the W-density for pairs of discharges with the test limiter inserted and withdrawn.

3. General behaviour of tungsten in the RI-mode

To study the general behaviour of the tungsten source and the tungsten density in the core we varied the radial position of the test limiter, the total heating power and the radiated power fraction. In a RI-mode plasma ($P_{heat} = 2.95$MW, $\overline{n}_e = 5.0 \cdot 10^{13}$ cm^{-3}, $I_p = 350$kA) the position of the test limiter was varied from 48cm (withdrawn) to 45cm (1cm inside the last closed magnetic flux surface). The W-density in the plasma center increases up to $1.34 \cdot 10^9$ cm^{-3} for $r_L = 45$cm, but no influence on the energy confinement was seen. The enhancement factor was at a constant value of $f_{H93} = 0.91$, which is as good as ELMy H-mode. In figures 1 and 2 the evolution of the central W-density together with the W-flux at the test limiter is shown as a function of the total heating power with and without neon edge cooling. In this power-scan ($I_p = 350$kA, $\overline{n}_e = 5.0 \cdot 10^{13}$ cm^{-3}, $r_L = 45$cm) the

ICRH-power was varied at a constant level of neutral beam co-injection ($P_{NI} = 0.85$MW). Without neon edge radiation cooling the W-source is increasing slightly whereas the W-density is almost unchanged with enhanced heating powers (figure 1). In this range the edge temperature (r=45cm) rises from $T_e = 78$eV to 87eV, whereas the edge density remains constant ($n_e = 8.5 \cdot 10^{12}$ cm^{-3}). In the case of moderate neon cooling ($\gamma_{rad} \approx 65\%$) the evolution of the tungsten source is quite similar (as are the edge densities), but the W-density is clearly higher at lower ICRH heating power (figure 2). Under these conditions the edge temperature is constant as well.

The impact of the seeded neon on the W-release and its influence on the plasma core is shown in figure 3, where the W-flux, the W-density and the confinement enhancement factor f_{H93} is plotted versus the radiated power fraction (γ_{rad}). The edge density n_e(45cm) remains constant, whereas T_e(45cm) drops from 87eV to 55eV at the highest γ_{rad}. With increasing γ_{rad} the f_{H93} rises and above $\gamma_{rad} \approx 45\%$ the confinement is as good as ELMy H-mode. After a small increase the W-flux is monotonically decreasing. This shows up also in a decrease of the central W-density. To understand this behaviour, we calculated the W-sputtering using the sputter data of the Bohdansky formula [4] taking the measured values of the deuterium-, carbon-, oxygen- and neon-fluxes. In figure 4 the fractions of the sputtered W-flux caused by the different impinging species are displayed. The sum of all those different contributions results in the total W-flux, which is qualitatively in good agreement with the observed behaviour of the W-influx with increasing radiation level. Thus, the reduced W-flux is mostly a result of the reduction of the carbon- and oxygen-fluxes, which occurs under RI-mode conditions. The contribution of the deuterium sputtering to the total erosion is negligible and the W-flux released by neon is only slightly increased.

4. Difference in heating schemes

The experiments performed previously at TEXTOR-94 with high-Z elements were all carried out in ohmic and L-mode NBI ($H \rightarrow D$) discharges [2]. Under these conditions it was found, that for medium densities $\overline{n}_e \approx 3.0 \cdot 10^{13}$ cm^{-3} accumulation of tungsten occured in radiative cooled discharges with $\gamma_{rad} \geq 65\%$. No accumulation occured for higher densities $\overline{n}_e \geq 4.0 \cdot 10^{13}$ cm^{-3} at all radiation levels γ_{rad}, which was explained by a reduction of the tungsten source [2], and at sufficiently high ICRH power levels [5].

The RI-mode discharges described here are all carried out with NBI ($D \rightarrow D$) and ICRH. For this reason the difference of $D \rightarrow D$ to $H \rightarrow D$ NBI should be pointed out first. In comparable L-mode $D \rightarrow D$ NBI heated discharges at medium densities $\overline{n}_e \approx 3.0 \cdot 10^{13}$ cm^{-3} accumulation of tungsten was observed even in non-cooled discharges ($\gamma_{rad} \approx 35\%$, with the test limiter positioned at $r = 45.5$cm). The radiation profile was peaked with central values of $P_{rad} = 500$ mW/cm^{-3}. While the central value of the safety factor rose up to 1, the sawteeth disappeared, strong mode oscillations in the plasma core were observed. Adding neon in those discharges enhanced the central radiation up to $P_{rad} = 1100$ mW/cm^{-3}, which led to a stationary (for 2s) reversed magnetic shear ($q_0 = 2.2$, $q_{min} = 1.2$) [6]. For higher densities $\overline{n}_e \geq 4.5 \cdot 10^{13}$ cm^{-3} the threshold for the accumulation was at $\gamma_{rad} \approx 63\%$. Thus the critical neon concentration for the development of an accumulation instability is much less in $D \rightarrow D$ operation, than in comparable $H \rightarrow D$ heating scenarios.

Secondly a comparison of NBI heating and ICRH heating in RI-mode operation was carried out. We compare two different γ_{rad}-scans ($\overline{n}_e \approx 5.0 \cdot 10^{13}$ cm^{-3}, $I_p = 420$kA, test limiter position 45cm): (1.) dominated by NBI heating ($P_{NI} = 1.6$MW, $P_{ICRH} = 0.5$MW); (2.) dominated by ICRH heating ($P_{NI} = 0.5$MW, $P_{ICRH} = 1.3$MW). In figures 5 and 6 the evolution of the electron density profile for both heating schemes with increasing γ_{rad} is shown. In the case of NBI heating dominating the neon cooling leads to a strong peaking of the density profile and an enhancement factor $f_{H93} = 1.03$, which is as good as ELM-free H-mode for γ_{rad} values larger than $\approx 70\%$. In the ICRH dominated case the electron density profile steepens a little bit and f_{H93} saturates at 0.85. For both heating scenarios the W-density in the plasma core and the W-flux at the edge are displayed in figures 7 and 8. In the NBI heating dominated discharges the W-source and W-density do depend on the radiation level. In the case of dominating ICRH heating we found again a reduction of the W-source and W-density with increasing radiated power fraction. Accumulation of tungsten occured just for $\gamma_{rad} = 73\%$ in the NBI dominated case. To rule out a possible influence of the energy confinement, ICRH heating was compared with NBI heating by applying the energy feedback system [1]. With increasing NBI power the energy content of the plasma was feedback-controlled kept constant by acting on the level of ICRH power ($\tau_E = 50$ms). It was found that for $P_{NI}/P_{ICRH} = 1$ the electron density profile was significantly less peaked than in the case with $P_{NI}/P_{ICRH} = 2.5$, which led to W-accumulation. Thus the accumulation of tungsten is strongly correlated with the peaking of the electron density profile, which is significantly more pronounced in discharges with NBI heating dominating.

6. Summary and conclusion

We have showed that the improved confinement of the RI-mode does not necessarily lead to tungsten accumulation. RI-mode conditions led to a significant reduction of the fluxes of deuterium, carbon and oxygen, which reduces the tungsten source. We have found, that RI-mode discharges heated predominately with NBI lead to a significant peaking of the electron density profile in contrast to discharges which are dominated by ICRF heating. There is a strong indication that this peaking leads to the accumulation of tungsten in the plasma core. Compatibility of RI-mode and high-Z materials seems to be achieved, just if one finds a compromise between improved confinement and density peaking.

7. References

[1] A. Messiaen et al., Phys. Rev. Letters, **77**, 2487 (1996)
[2] J. Rapp et al., to be published in Plasma Phys. Control. Fusion
[3] D.E. Post et al., Atomic Data and Nuclear Data Tables, **20**, 397 (1977)
[4] J. Bohdansky et al., J. Nucl. Mater., **103-104**, 339 (1981)
[5] G. Van Oost et al., Europh.Conf.Abstr., Vol 19, Part III, 345 (1995)
[6] H.R. Koslowski et al., this conference

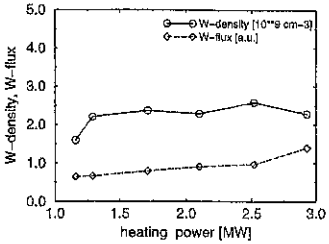

Fig.1: W-density and W-flux as function of heating power, NBI: 0.85MW, ICRH varied, without neon cooling Ip=350kA, ne=5.0 10**13cm-3, r(limiter)=45cm

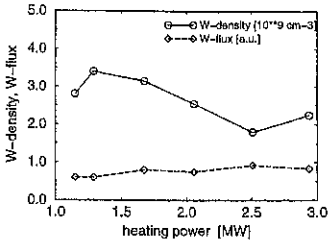

Fig.2: W-density and W-flux as function of heating power, NBI: 0.85MW, ICRH varied, with neon cooling (65%) Ip=350kA, ne=5.0 10**13cm-3, r(limiter)=45cm

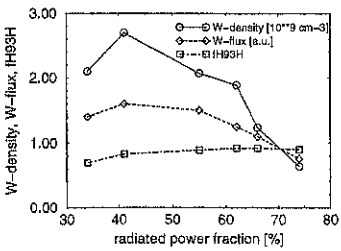

Fig.3: W-density, W-flux, fH93 as function of the radiated power fraction due to neon puffing, NBI: 0.85MW, ICRH: 1.85MW, Ip=350kA, ne=5.0 10**13cm-3, r(limiter)=45cm

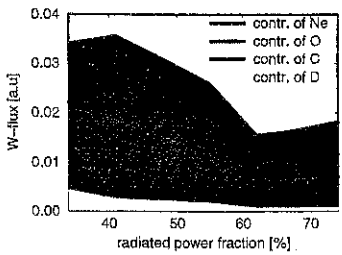

Fig.4: W-sputtering calculated as function of radiated power fraction using sputter data of Bohdansky formula with measured fluxes of D, C, O and Ne

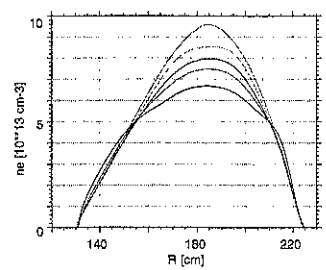

Fig.5: electron density profile evolution with neon puffing NBI: 1.6MW / ICRH: 0.5MW, Ip=420kA, ne=5.0 10**13cm-3, r(limiter)=46cm

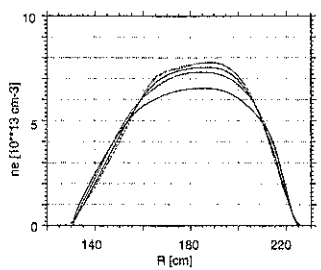

Fig.6: electron density profile evolution with neon puffing ICRH: 1.3MW / NBI: 0.5MW, Ip=420kA, ne=5.0 10**13cm-3, r(limiter)=46cm

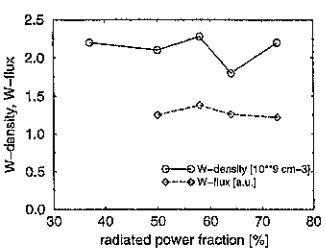

Fig.7: W-density, W-flux as function of radiated power fraction, NBI: 1.6MW / ICRH: 0.5MW, Ip=420kA, ne=5.0 10**13cm-3, r(limiter)=46cm

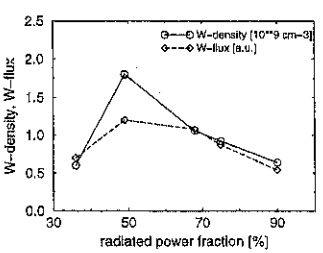

Fig.8: W-density, W-flux as function of radiated power fraction, ICRH: 1.3MW / NBI: 0.5MW, Ip=420kA, ne=5.0 10**13cm-3, r(limiter)=46cm

Infra-red high temporal resolution thermal measurements on TEXTOR-94

M. Ciotti[1], T. Denner[2], K. H. Finken[2], J. Hobirk[2], G. Mank[2], G. Maruccia[3], V. Vitale[1], R. Zanino[3].

[1]Associazione Euratom ENEA sulla fusione, C E Frascati, 00044 Frascati (Rome), Italy
[2]Institut für Plasmaphysik, Forschungszentrum Jülich, GMbH Association EURATOM-KFA*
[3]Dipartimento di Energetica, Politecnico, I-10129 Torino, Italy.

Introduction

Thermal load measurements are an essential supplement for discharges with high fractions of edge radiation. At TEXTOR-94 a new high confinement regime at high density with strong edge radiation impurity seeded (Radiative I-Mode) has been obtained; the RI mode is of particular interest since it combines features of global confinement with those of low convected power flux densities to material limiter. A large fraction of the power leaving the plasma is spread over the whole wall due to radiation.

TEXTOR-94 is equipped with a toroidal belt pump-limiter (ALT-II) positioned outboard at 45° below the mid plane; the major radius is 1.75 m and the minor is 0.46 m. The ALT II limiter consists of eight blades covered with graphite tiles in two rows. Tiles have a thickness of up to 0.02 m; the last closed flux surface is intersected in the central line of the blades.

Comparisons of the limiter thermal load between discharges at high beta with and without a radiative mantel are relevant issues. Aim of this contribution is to show the resulting reduced power flux to the ALT-II limiter.

Experimental apparatus

A new infra-red (I-R) system [4] has been installed on the TEXTOR-94 machine in the framework of a collaboration between Enea Frascati and KFA IPP Juelich. The system is based on a two dimensions Indium Antimonide (InSb) detector array with 128×128 pixels cooled at liquid nitrogen temperature that can be read up to 1000 frames/s. Up to 512 full frame images can be acquired, stored in a fast cache memory and than downloaded to a PC hard disk from where image analysis can be performed. The camera sensitivity can be changed in real time by using a custom algorithm [5], but since for TEXTOR-94 the limiter starting temperature is around 350 C and the maximum increase in the order of 500 C, this option is not needed. In order to successfully withstand the whole temperature increase without changing any parameter it was sufficient to equip the camera with an ad hoc filter (4.74-4.95 μm).

---

* Partner in the Trilateral Euregio Cluster (TEC)

One of the 8 ALT-2 blades is imaged to the I-R camera via an imaging and a field lens, both made of CaF_2. A clear full image of the limiter sector is thus obtained from which the plasma heating pattern is inferred also during fast events. The spatial resolution of the images is in the order of 0.007 m, considerably better than that from the I-R scanners previously used on the same location [6].

Experimental observations and discussion

Figure 1 shows the IR view in TEXTOR-94 including a full blade, a part of the wall (around 2 m^2) and a portion of the retracted bottom poloidal limiter. The image definition allows a clear sight of all the individual tiles and their holes, where the tightening screws are located. The tiles placed at the blade corners are considerably more heated because of the 0.12 m gap between two neighbouring blades. The power deposition inhomogeneity caused by the magnetic ripple is clearly resolved.

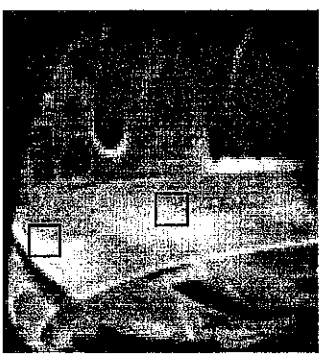

Fig 1 - The IR camera image of the TEXTOR-94 limiter. The temperature evolution averaged over the marked areas in this figure is reported in figure 3.

A comparison between the temperature increase for shots with the same plasma parameter (fig. 2) but with and without Ar injection has been performed. The diamagnetic energy is kept roughly constant after the transition into RI-mode by a feedback acting on the ion cyclotron (ICRH) input power. The temporal evolution of the surface temperature for the area marked on fig 1 is shown in fig. 2(E). At 1 s the tile surface starts to increase more steeply due to the onset of the neutral beam injection (NBI). From 1.5 s on, the temperature drops and increases later at a reduced slope. This decrease is caused by the Argon injection.

The heat flux averaged over the whole blade is calculated through a two dimensional finite elements program: it is enhanced to 500 kW/m^2 in the NBI phase and reduced to 250 kW/m^2 during the edge cooling phase as to be seen in fig 2 (F).

The image obtained at time =0 has been subtracted from the images obtained at time =3.5 s for both shots, to take into account the different starting temperature of the two shots. These images have been subtracted again from each other. The results are shown in fig 3. In the picture the differences between the heating pattern are evident. The surface temperature reduction is more marked in the more loaded areas, such as the short blade's side, the central area (due to the bump) and the leading edge.

The peaking factor for the two shots, defined as $\Delta T_{max}/\langle\Delta T\rangle$ is reduced from 7 to 4 , and the average surface temperature reduction on the whole limiter is of a factor of two.

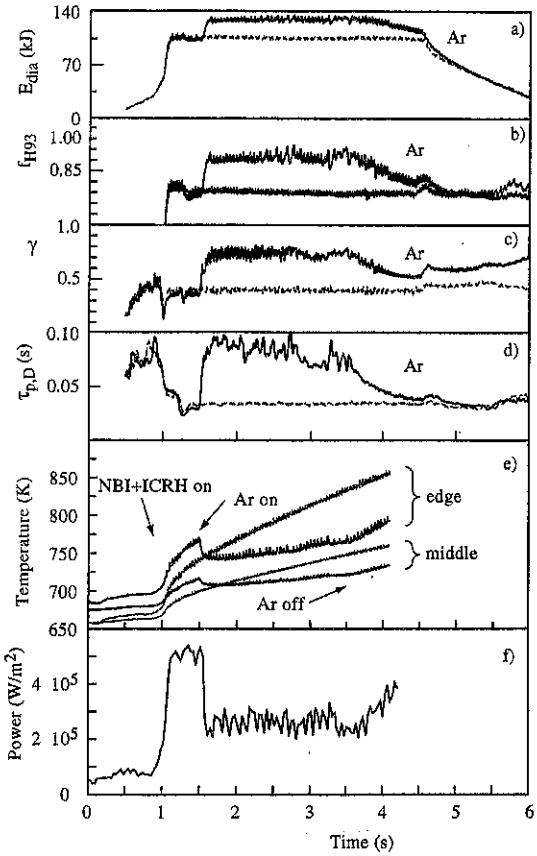

Fig. 2 - Comparison of shots 70288, (grey) w/o Argon injection, and 70289, with Argon (black). A) The plasma diamagnetic energy; B) the H-mode enhancement factor with respect to the ITER 93 scaling; C) The γ factor, defined as the ratio between the radiated and the input power; D) The particle confinement time; E) Temperature evolution for the areas marked in fig. 1. The temperature has been averaged over the square area (10×10 pixels) to have a more representative behavior; F) The impinging flux averaged over the blade as calculated by a two dimensions finite elements heat conduction code

The limiter shape has been planned to match a plasma with a power decay length of 0.007 m [3]. By calculating the flux along a poloidal section through a two-dimension heat conduction code it is possible to see a quite peaked profile during the NBI phase, that becomes nearly flat during the Ar injection. This leads us to the conclusion that the power decay length during the additional heating phase is shorter than 0.007 m and approaches this value during the Ar injection phase.

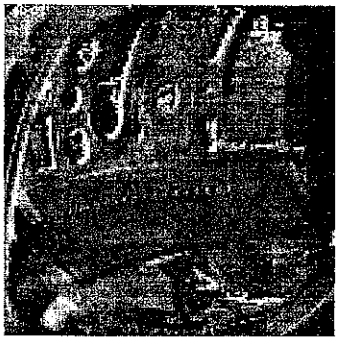

Fig. 3 - Differences in the heating patterns for shots with and w/o Ar injection at time 3.5 s. Black: zones where the surface temperature is strongly reduced (in between 20°C and 100 °C decrease). Dark grey: zones with a lower decrease (up to 20°C). An average small increase was found on the wall

By extrapolating to all the 8 blades the average flux inpinging onto one individual blade, it is possible to calculate that 50% of the input energy is collected by the limiter. The time integral of the radiated power signal as measured with the machine bolometric system was also taken; then it was corrected according to the ratio existing between the liner minus limiter surface and the liner surface to take into account that the radiation going onto the limiter has already been measured by the camera. In this way we obtain that 100% of the input power is detected.

Conclusion

Thermal loads during RI mode discharges are strongly reduced, surface temperature peaking factor decreases from 7 for shot w/o argon to 4 with Ar, power decay length is increased.

A full power balance is possible by detecting 100% of the input energy.

References

[1] G.H. Wolf et al; "Quasi-stationary elm-free high confinement with edge radiative cooling in Textor-94", XVI IAEA, Montreal, Canada.

[2] A. M. Messianen et al., Phys. Plasmas **4**, 1690-1698 (1997)

[3] B.L. Newberry et al. "ALT II armor tile design for upgraded Textor operation", ISFNT-3, 1994, Los Angeles

[4] M. Ciotti et al, Rev. Sci. Instrum., **68**, n. 1, part 1, 971-973 (1997)

[5[M. Ciotti et al., Elettro-ottica 96, Milano (May 1996), pp 251-255

[6] K.H. Finken et al., J. Nucl. Mater. **162-164** 655-660 (1989).

Triton burnup measurements at TEXTOR using activation techniques

F. Gadelmeier, G. Beikert, B. Wolle, St. Koch, St. Simenon,
K. Hübner, R. Bätzner, TEXTOR-team[1)]

Institut für Angewandte Physik, Ruprecht-Karls-Universität Heidelberg,
D-69120 Heidelberg, Germany
1) Institut für Plasmaphysik, Forschungszentrum Jülich GmbH, EURATOM Association,
D-52425 Jülich, Germany

1. Introduction

In deuterium plasma discharges 1.01 MeV tritons are produced by the reaction d(d,p)t with a nearly equal probability as that for the 2.45 MeV neutrons from the d(d,n)^{3}He reaction. A fraction of tritons will leave the plasma promptly. This fraction depends on the triton birth profile, the plasma current as well as on the toroidal magnetic field B_t [1,2]. The tritons which remain confined in the plasma (at TEXTOR about 3%, [3]) will slow down to thermal energies through Coulomb collisions on electrons. A fraction of confined tritons will undergo d(t,n)α reactions producing 14.1 MeV neutrons.

The d-t cross section has a maximum at a triton energy of 180 keV and is negligibly small at thermal energies. Since the confinement time of thermalized tritons is comparable to the slowing down time of 1.01 MeV tritons, the fusion reaction rate of thermalized tritons is negligible. The probability of a confined triton undergoing a fusion reaction is about 10^4 times larger than that of a triton which escapes from the plasma and encounters absorbed deuterium in the vessel walls [1]. Consequently, the triton burnup, defined as the ratio of the 14.1 MeV neutron rate ($R_{14.1}$) and the 2.45 MeV neutron rate ($R_{2.45}$), is a measure for the confinement of fast fusion products as well as for their slowing down in the plasma.

The 14.1 MeV neutron rate is proportional to the deuterium density n_d, the density of fast tritons $n_{t,fast}$, and the fusion reactivity $\langle\sigma_{dt}v\rangle$:

$$R_{14.1} = n_d n_{t,fast} \langle\sigma_{dt}v\rangle. \tag{1}$$

If f_c denotes the fraction of confined tritons and τ_s is their slowing down time, the density of fast tritons is $n_{t,fast}=f_c R_{2.45}\tau_s$. For electron temperatures of less than 2 keV and ion temperatures of less than 4 keV, which are typical for TEXTOR, the slowing down time is $\tau_s \propto T_e^{3/2}/n_e$ [4]. Thus, for classical slowing down of fast tritons the triton burnup is:

$$\frac{R_{14.1}}{R_{2.45}} \propto f_c \frac{n_d}{n_e} T_e^{3/2} \langle\sigma_{dt}v\rangle. \tag{2}$$

2. Neutron detection and detector calibration

At TEXTOR activation measurements are being used for calibrating and monitoring the 2.45 MeV neutron counters (^{3}He, BF_3 and scintillators) as well as for time integrated triton burnup measurements.

The calibration of the neutron counters is verified regularly using the $^{115}In(n,n')^{115}In^m$ reaction which has a threshold at about 0.5 keV. $^{115}In^m$ decays with a half-life of 4.49 hours emitting a 336 keV γ-quantum. In order to validate the calibration procedure by means of activation techniques, three activation reactions were employed, namely $^{115}In(n,n')^{115}In^m$, $^{58}Ni(n,p)^{58}Co^{m+g}$ and $^{47}Ti(n,p)^{47}Sc$. A comparison between the calibration factors, determined by means of activation measurements with indium, nickel and titanium samples, shows that the accuracy of the calibration is presently about 15%. This is mainly due to the uncertainties in the available activation cross section data. The 2.45 MeV neutron yield is measured with the calibrated neutron counters.

The 14.1 MeV neutron yield measurements are performed using the $^{28}Si(n,p)^{28}Al$ reaction, which has a threshold at 4.5 MeV. ^{28}Al decays with a half-life of 134.4 seconds emitting 1.778 MeV γ-rays. The short half-life of this reaction allows for measurements on a shot-to-shot basis. The statistical error of these measurements is less than 15%. The systematic error is mainly determined by the accuracy of the cross section at 14.1 MeV. Three main cross section data libraries are known from literature [5], which strongly differ from each other in the energy range around 14 MeV. Therefore, a direct estimation of the systematic error is as yet not possible and the following error estimations include only the statistical error.

The activation samples were irradiated near the plasma edge inside the vacuum vessel. The samples were transported between the irradiation position and the γ-counting station by a pneumatic transport system. The emitted γ-energy spectrum was measured by using a high purity germanium detector (HPGe). The detector efficiency has been measured with an accuracy of 1%, which includes the self absorption coefficient of the γ-rays in the sample. The fluence factor, which indicates the activation of the sample for a certain neutron yield, was calculated for a standard discharge using a Monte Carlo Code. Thus, the neutron yield of a discharge is given as the product of the measured activity and the fluence factor.

3. Measurements and Results

The triton burnup ratio was measured for about 60 deuterium discharges with neutral beam injection, partly combined with ICRH. The plasma parameters were as follows: B_t=2.25 T, I_p=350-500 kA, T_e=1-1.9 keV, n_e=2-7×10^{-13} cm^{-3}, and Z_{eff}=1.3-4.3, the main impurity being carbon. The neutron yield for these discharges varied between 3×10^{13} and 2×10^{14} neutrons.

The measured triton burnup ratios depend on the plasma parameters and range from 0.025% to 0.1%. The effective charge number Z_{eff} was determined from the electrical conductivity, hence the error is large. Nevertheless, we assume that for co-NBI as well as for counter-NBI heated discharges there exists a direct relation between the electrical conductivity and Z_{eff}.

A quantitative statement regarding the triton burnup behaviour is, due to an insufficient data base, not possible. Nevertheless, we can draw several qualitative conclusions. Figure 1 shows the triton burnup ratios for two types of discharges as a function of the plasma current I_p (discharges of each type have similar electron temperatures and effective charges). The measurements show an increase in triton burnup with increasing plasma current, i.e. increased triton confinement. A dependence of the triton burnup on the injected heating power (at TEXTOR '94 up to 5 MW) could not be observed. Figure 2 shows the measured triton burnup ratios as a function of the electron temperature for two types of discharges with I_p = 408 kA and Z_{eff} = 1.8-2.5 and Z_{eff} = 3.3-4.3, respectively. There is some scatter in the measured values. Nevertheless, an increase in triton burnup with increasing electron temperature can be observed. The dependence of the triton burnup on the effective charge number is shown in figure 3 for discharges with I_p = 408 kA and T_e = 1.4-1.6 keV. One can see that the triton burnup ratio is decreasing with increasing Z_{eff}. In conclusion, the experimental data are consistent with the classical slowing down theory.

Figures 1-3 show some scatter in the measured triton burnup ratios. Partly, the ratios lie outside the indicated error bars. Mainly, this is attributable to the shot-to-shot variation of the main plasma parameters. On the other hand, it can be also attributed to MHD-activities in the plasma or effects due to ICRH. In the future we intend to investigate these influences in more detail. A further objective will be a more precise estimation of the systematic error of the 14.1 MeV neutron yield measurement. This can be done by a comparison of the silicon measurements with other activation materials. Finally, we intend to improve the accuracy of the absolute neutron yield measurements.

References

[1] HEIDBRINK, W.W., CHRIEN, R.E., STRACHAN, J.D., Nucl. Fusion 23 (1983) 917.

[2] MIYAMOTO, K., Plasma Physics for Nuclear Fusion, MIT Press, Cambridge, MA (1989) 47.

[3] GROPPENBÄCHER, P., Universität Heidelberg, Diplomarbeit, (1995) 61

[4] STIX, T.H., Plasma Phys. 14 (1972) 367.

[5] BARNES, C.W. et al., Rev. Sci. Instrum. 66 (1), (1995) 888

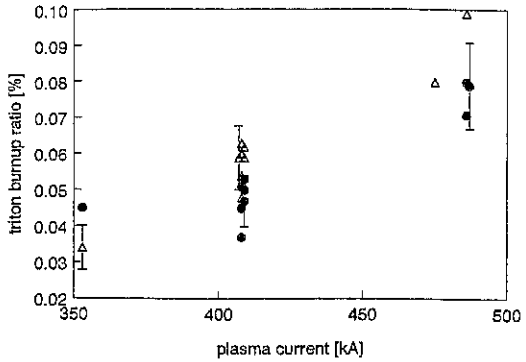

Figure 1: Triton burnup vs plasma current for discharges with T_e=1.2-1.35 keV and Z_{eff}=1.8-2.1 (circles), respectively T_e=1.45-1.6 keV and Z_{eff}=2.1-2.6 (triangles).

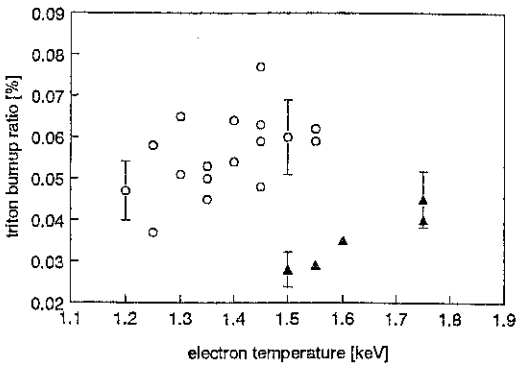

Figure 2: Triton burnup vs electron temperature for discharges with I_p=408 kA and Z_{eff}=1.8-2.5 (circles), respectively Z_{eff}=3.3-4.3 (triangles).

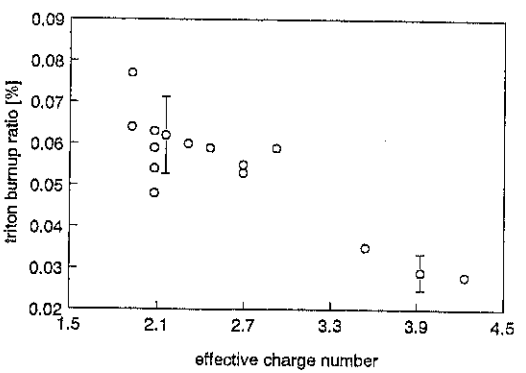

Figure 3: Triton burnup vs effective charge number for discharges with I_p=408 kA and T_e=1.4-1.6 keV

A new compact detector system for collimated D-D neutron flux measurements

T. Baloui, **B. Wolle**, K. Hübner
Institut für Angewandte Physik, Universität Heidelberg, D-69120 Heidelberg, Germany

1. Introduction

At a given measurement position on fusion experiments the neutron spectrum can considerably differ from the emitted 'virgin' neutron spectrum due to scattering processes in the vacuum vessel and structural components. Therefore, any measured neutron flux or spectrum consists of an unscattered 'direct' contribution and a scattered background which can be substantial and extends down to thermal velocities.

For the design of a comparably small detector system suitable for collimated neutron measurements close to the plasma an effective shielding material for the 2.45 MeV neutrons is required. Usually, materials containing a substantial amount of hydrogen are being used for building shielding and moderator components. However, due to the elastic scattering cross section which decreases by about one order in the energy range 0.01-2.5 MeV, the shielding of 2.5 MeV neutrons requires sufficiently large moderator volumes. Thus, for a compact detector and shielding design, the contribution to the detector signals from unshielded and unwanted high-energetic neutrons from outside the line-of-sight is quite large.

Our new concept is to detect moderated neutrons rather than the original 2.5 MeV neutrons. This offers the possibility to use a detector which is insensitive to the fraction of penetrating unwanted high-energetic neutrons. We are using Bonner spheres [1], which are comparatively cheap and commercially available neutron detectors with isotropic and in a wide energy range slowly varying response function [2]. Bonner spheres consist of an inner active detection volume sensitive only for thermal neutrons and a surrounding spherical moderator which determines the response function.

2. New conceptual detector design

Instead of using a 12 inch Bonner sphere sensitive for 2.5 MeV neutrons positioned behind a collimator opening for direct measurement of collimated 2.5 MeV neutrons we use a 3 inch Bonner sphere. As shown in figure 1, the 3 inch Bonner sphere is more sensitive to low-energetic neutrons than it is for high-energetic 2.5 MeV neutrons. Therefore, a different and novel detection concept can be applied. The conceptual design of our new detector has been developed and tested by MCNP simulations. The arrangement is shown in figure 2. It consists of Bonner sphere positioned outside the cone-of-sight, a compact shielding arrangement, dedicated moderator target placed directly behind the collimator opening, and a `high-pass' filter in the collimator opening, respectively. The collimator shielding consists of PE with a

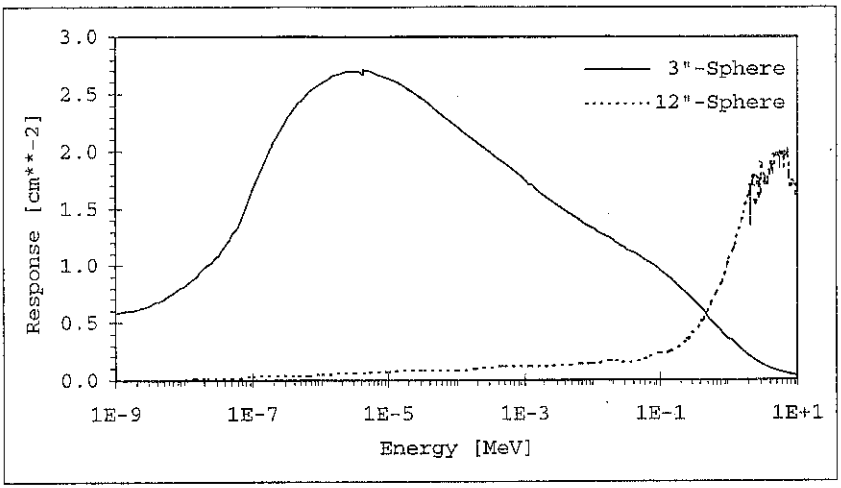

Figure 1. *Response functions of two Bonner spheres with different radii. The sphere with 12" radius is normally used for isotropic measurements of 2.5 MeV neutrons. The 3" sphere is used in our conceptual design.*

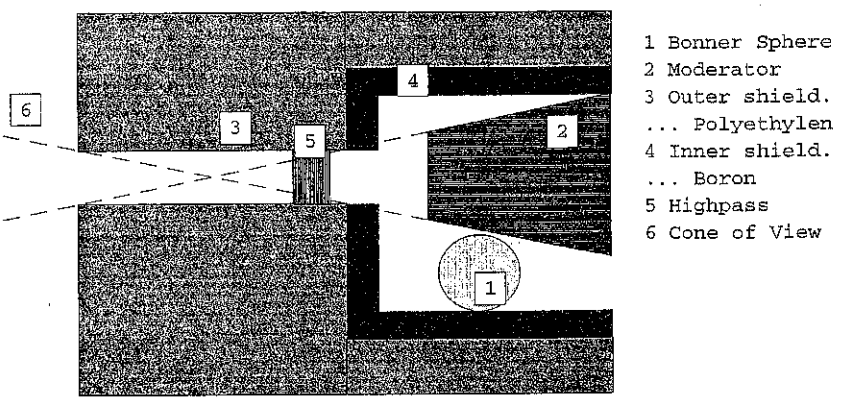

Figure 2. *Schematic sketch of the novel detector design. Incident neutrons are passing a PE plug serving as a high-energy filter. Detection occurs only for neutrons being scattered in the moderator target.*

thickness of several mean free-path-lengths (MFP), followed by a layer of 3 cm boron. As shown in figure 3 this is drastically reducing the background of deep penetrating initially high-energetic neutrons which are moderated near by the detector. By introducing a dedicated moderator target directly into the line-of-sight behind the collimator, the Bonner sphere measures only neutrons which are scattered in this moderator. The dimension of the moderator target in the direction of the line-of-sight is several MFPs, while its thickness is about one

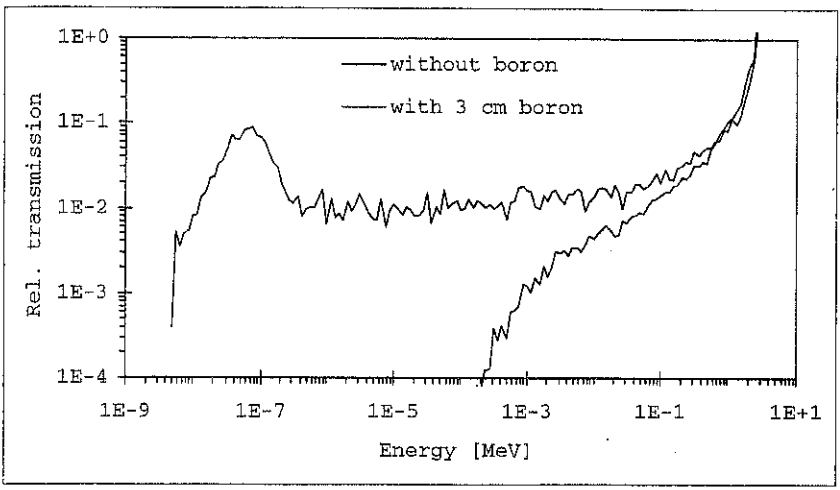

Figure 3. *The collimator shielding consists of PE with a thickness of several mean free-path-lengths followed by a layer of 3 cm boron. This is reducing the background of deep penetrating initially high-energetic neutrons which are moderated near by the detector. Plotted are the calculated fluences behind a 10 cm collimator shielding with and without boron for a 2.5 MeV point source.*

order less. Thus, the scattering probability for the small fraction of high-energetic neutrons penetrating the shielding from other directions is small, while the scattering probability for the incident neutrons coming through the collimator is close to 1. With increasing scattering angle the incident neutrons are being moderated to lower energies and, hence, the detection probability is increasing. In conclusion, the detection probability for neutrons passing through the collimator is large as compared to high-energetic neutrons penetrating the shielding from other directions.

By filling the rear end of the collimator opening with a PE plug of thickness l, a discrimination of high-energetic and low-energetic incident neutrons can be obtained. The reason is that the scattering probability for the incident neutrons increases with decreasing energy. As a result, less low-energetic neutrons hit the moderator target. The filter function relative to 2.5 MeV neutrons is approximately given by:

$$f(E) \approx \frac{W(E,l)}{W(2.5\,MeV,l)} = \left(\exp\left(1-\frac{\lambda(2.5\,MeV)}{\lambda(E)}\right)\right)^{\frac{1}{\lambda(2.5\,MeV)}},$$

where $W(E, l)$ and $W(2.5\ MeV, l)$ are the probabilities of unscattered penetration of neutrons with energy E and $E = 2.5$ MeV, respectively. Furthermore, λ denotes the MFPs. The effect of this filter can be seen in figure 4 where the detection efficiency for incident neutrons in the line-of-sight is plotted as a function of the neutron energy.

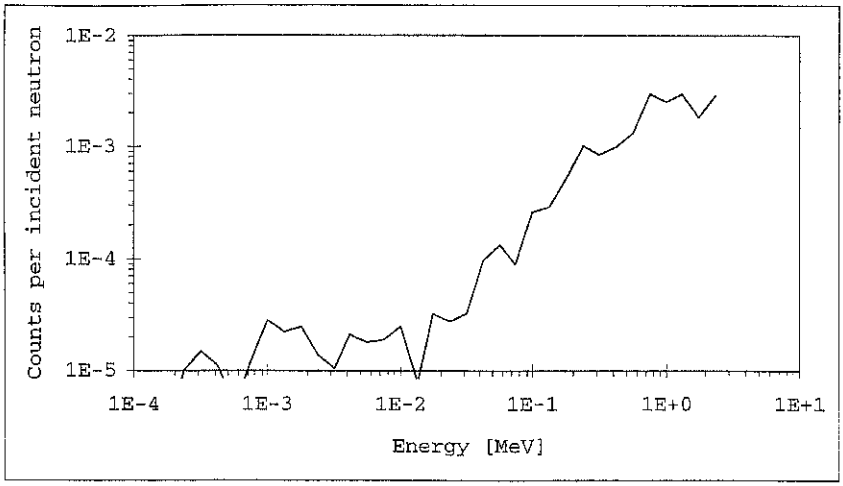

Figure 4. *Counts per incident neutron of the Bonner sphere as a function of the incident neutron energy for our detector design with a 3.5 cm PE high-pass filter.*

3. Conclusions

By means of numerical simulations a novel neutron detection concept based on Bonner spheres has been developed and tested. Our calculations show that collimators and shieldings with dimensions above 20 cm are required in order to obtain reasonable shielding and detection properties. We showed that a dedicated moderator can serve as an energetic high-pass which can effectively suppress the incident neutron scattering background below 0.1 MeV.

The numerical simulations show that the detection efficiency of our detector system is about 1/350 per incident 2.5 MeV neutron. Thus, the counts per fluence are 10^{-3} counts cm^2 at the center of the collimator opening. This value is nearly independent from the collimator geometry and the distance to the plasma neutron source. For a neutron production of 10^{11} neutrons per second within the cone-of-sight, the expected count rate is in the order of $5000s^{-1}$ can be expected. Therefore, our new detector will be mainly suited for larger fusion experiments with sufficient neutron production.

[1] Bramblett R L, Ewing R I and Bonner T W, *Nucl. Instrum. And Meth.* **9** (1960) 1

[2] Wiegel B, Alvera A V and Siebert B R L, Calculations of the Response Funktion of Bonner Spheres with Spherical ^{3}He Proportional Counter using a Realistic Detector Model, *Report* PTB-N-21, Physikalisch-Technische Bundesanstalt Braunschweig (1994)

Soft x-ray line spectroscopy with high time resolution at TEXTOR 94

O. Herzog*, G. Bertschinger, M. Bitter***, F.B. Rosmej*, H.-J. Kunze***

* Institut für Experimentalphysik V, Ruhr-Universität Bochum, Germany

** Institut für Plasmaphysik, IPP, Forschungszentrum-Jülich, Gemany

*** Princeton Plasma Physics Laboratories, PPPL, Princeton, USA

1. Introduction

At TEXTOR 94 a high resolution ($\lambda/\Delta\lambda$ = 6600) soft x-ray crystal spectrometer in „Johann-geometry" is used to measure [He]-like argon spectra. For this diagnostic a new CAMAC-system is developed permitting measurement and storage of 16000 spectra per discharge.

For the investigated discharges at TEXTOR 94 the profiles of the electron temperatures $T_e(r)$ and the central electron temperatures $T_e(0)$ were such that the emission of [He]-like argon is peaked at the centre of the plasma. Therefore, the measured spectra give information on the plasma centre despite the spectrometer collects the radiation along the line of sight. The central ion temperature is deduced from the width of a Doppler broadened line, the central toroidal plasma rotation is obtained from its shift taking into account the geometry of observation relative to the toroidal axis of the tokamak plasma. Relative intensities of the main transitions (resonance line, intercombination lines and forbidden line) of [He]-like ions and the so-called dielectronic satellites yield the central electron temperature of the plasma.

Till now we used a time resolution of 1 ms which allows the determination of the above plasma parameters even during sawtooth activity in TEXTOR 94.

We employed a multi-wire-proportional-counter as detector. In order not to exceed the limit of the counting rate ($3 \cdot 10^5$ counts/sec.) of this detector the amount of argon is controlled which is be puffed into the plasma. Unfortunately for a time resolution of 1 ms or lower the statistical errors in the spectra are not sufficient for single fits to deduce the above plasma parameters with sufficient precision and therefore the spectra are sampled, the respective time being synchronised to the sawtooth crash.

We present the experimental set-up and measurements with [He]-like argon. A modulation of the above plasma parameters in the sawtooth activity is shown.

2. The experimental set-up

Figure 1 shows the principle of a Johann type spectrometer. It is a curved crystal spectrometer with a bent crystal. The whole surface of the crystal collects the radiation at each wavelength

according to Bragg's law in a solid angle and focuses it at different positions on a Multi-Wire-Proportional Counter which is a one dimensional position sensitive detector. The position is determined by the running time of pulses generated by the photons which reached the detector volume. The pulses are divided in both directions of an internal delay line and the time between both is measured and registered by a time to digital conversion of a CAMAC LeCroy TDC 4204 module and read in a histogramming memory module STRUCK 621. The time resolution can be programmed by an external clock. The pulses of this clock switched the routing registers with the programmed frequency, the spectra respectively, from one time group to another. A scheme of the data acquisition system and the timing are shown in figure 2 . The technical details of the spectrometer are summarised in Table 1.

Figure 1:Principle of a Johann typed crystal spectrometer

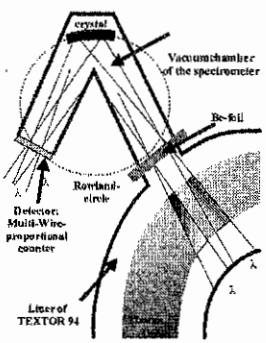

Figure 2: Data acquisition

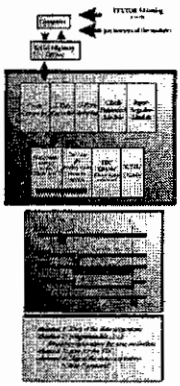

Table1: Parameter of the spectrometer

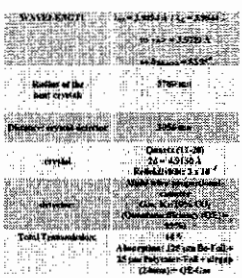

3. The measurement

A spectrum with all features obtained with an integration time of 100 ms is shown in figure 3. The main transitions (resonance line W, intercombination lines X and Y, and the forbidden line Z) and the dielectronic satellites and the innershell excited satellites are seen in this figure. Table 2 gives a listing of all transitions which can directly be identified. The higher n- satellites which are blended with the main lines are not examined in this work. Figure 4 indicates by a bar the times of 256 spectra taken in relation to the corresponding electron temperature from

ECE signals. The time resolution is 1 ms. The height of the bar corresponds to the intensity, and the modulation of the intensity relative to the sawtooth activity is directly seen.

If the time resolution is low (Δt = 1 ms) and the counting rate of the detector (200000 counts/s) is reached, a sampling procedure has to be used to obtain good statistics for the fitting procedure. For this purpose the times of the sawtooth crashes are determined and the duration of every sawtooth is divided into ten time groups. The spectra of corresponding times of several sawteeth are added. This procedure is shown in Figure 5.

Figure 3: Spectrum of [He]-like argon with integration time 100 ms

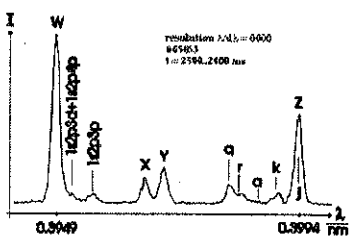

Table 2: Identified transitions and their wavelengths

W	3.9493	-
	3.9484	0.195
X	3.9481	-
	3.9478	0.300
	3.9447	0.320
Y	3.9391	-
	3.9384	0.420
	3.9360	0.162
	3.9301	1.30
	3.9293	3.40
Z	3.9243	-

Figure 4: Intensity Modulation of the spectra relative to the sawtooth

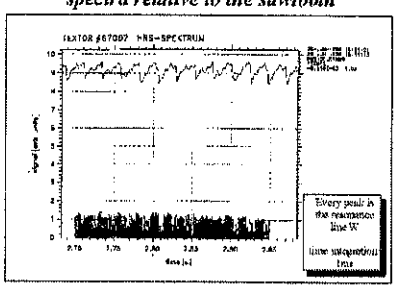

Figure 5: Sampling relative to the sawtooth crashes

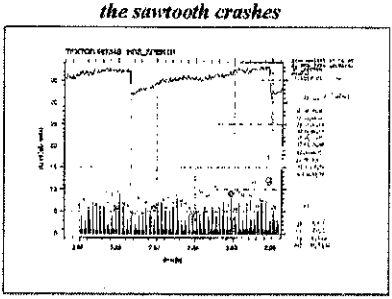

4. Results

The ion temperature is determined from the FWHM of the transition Z. When fitting with Voigt profiles the intensity of the j line is accounted for by comparison with the intensity of the k-line (also fitted). The position of the j line is taken from available atomic data. The detailed fitted region is shown in figure 6. Due to the geometrical situation of the spectrometer relative

to the toroidal axis of TEXTOR 94 ($\angle$ 10°) the toroidal rotation of the plasma can be determined from the line shift. This is shown in figure 7.

Figure 6: The spectral region around z with the k and j satellite. Experimental, fitted curves and the values of the dielectronic satellites

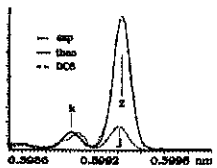

Figure 7: Toroidal plasma rotation in P

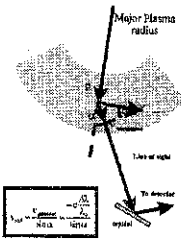

The plasma parameters derived relative to the sawtooth crashes are shown in figure 8 for the flat top phases of an ohmic discharge at TEXTOR 94 and for a neutral beam heated discharge at TEXTOR 94. It is seen that the direction of the toroidal rotation in the ohmic discharge is in a different direction than in the case of the neutral beam heated discharge which corresponds to the orientation of the normal plasma rotation and the direction of the neutral beam injector.

Figure 8: The results

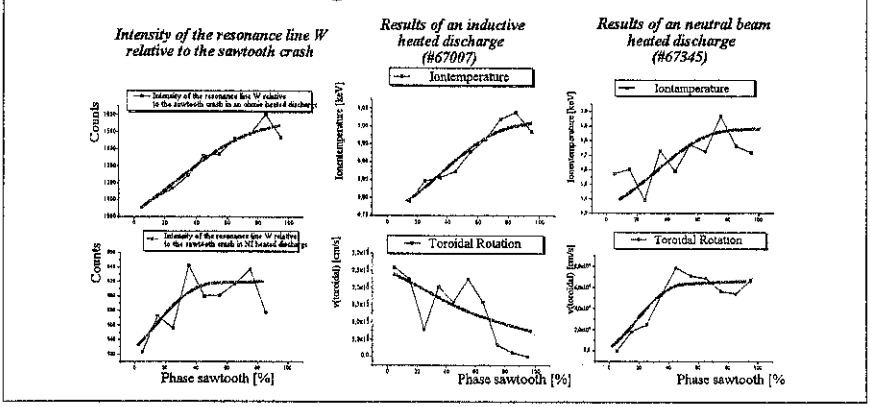

5. Conclusion

At TEXTOR 94 a high resolution soft x-ray spectrometer is installed having a high time resolution. The spectra allow the determination of central plasma parameters like the ion temperature and the toroidal plasma rotation even during the sawtooth.

LONG DURATION DISCHARGES OF THE TOKAMAK ISTTOK IN AN ALTERNATING PLASMA CURRENT REGIME

H. Fernandes, H. Figueiredo, C.A.F. Varandas, J.A.C. Cabral
Associação EURATOM/IST, Centro de Fusão Nuclear
Instituto Superior Técnico, 1096 Lisboa Codex, Portugal

1. INTRODUCTION

Alternating inductive plasma current (AC) operation has been referred to as a potential alternative conceptual scenario to that of a pure steady state fusion reactor [1-3]. In comparison with non-inductive current drive operation, AC discharges are technically simpler and have higher reliability and efficiency.

AC operation was firstly demonstrated on STOR-1M, with a smooth variation of the plasma current (I_p) from 4 to -4 kA [4]. Alternating discharges with sinusoidal or trapezoidal plasma current (I_p), one or more cycles and null or finite dwell time have been achieved on JET [5], CT-6B [6], CSTN-AC [7] and STOR-M [8].

This paper presents the results already obtained on ISTTOK aiming at the achievement of long duration, multi-cycle, square wave plasma current discharges without dwell time.

2. EXPERIMENTAL CONDITIONS

ISTTOK is a small size (R=46 cm, a=8.5 cm), circular cross section, iron core transformer ($\Delta\Phi$=0.22 Vs), limiter tokamak [9]. For the work described in this paper we used the following diagnostics: a Rogowski coil (I_p), a single chord microwave interferometer ($< n_e >$), a loop (V_L), a specially filtered fast photodiode (H_α) and a Langmuir probe ($n_{e(r=a)}$ and $T_{e(r=a)}$).

Forward discharges were done using the pre-discharge (1 mF, 5 kV, PRECO) and the electrolytic (3.8 F,350 V, ELCO) banks and the following external parameters: $p_B = 2\times10^{-4}$ Torr; $B_T = 0.45$ T; $V_{PRECO} \sim 1300$ V; $V_{ELCO} \sim 250$ V; transformer ratio N=40; B_v and B_h adjusted to maximum current flatness. These discharges are characterised by: $I_p \sim 4-5$ kA, duration $\tau_D \sim 40$ ms, $n_e \sim 7\times10^{18}$ m^{-3}, $T_e \sim 180$ eV, $T_i(C^{III}) \sim 150$ eV, energy confinement time,$\tau_E \sim 1.2$ ms, $\beta_{(r=0)} \sim 0.5\%$ and safety factor on axis $q_{(r=0)} \sim 1.2$ and on the edge $q_{(r=a)} \sim 5$.

The alternating discharges were performed using a specially designed power supply

based on an H-bridge of four fast IGBTs (Insulated Gate Bipolar Transistors), controlled by the central timing system [10]. The power supply half-period was limited to 35 ms ($\Delta\phi$=0.15 Vs) to avoid iron core saturation.

3. EXPERIMENTAL RESULTS

After a series of preliminary discharges with only a few half-cycles of current reversal, we have attained a maximum of six half-cycles at $I_p = \pm 4$ kA, lasting for about 180 ms. These long duration discharges presented in some cases (#5663) a significant dwell time (4 ms) in the positive-negative plasma current transition. On the inverse transitions there was no dwell time and the average plasma density around $I_p = 0$ remained at a high value ($1.7 \times 10^{18}\ m^{-3}$), when compared to its maximum ($4.8 \times 10^{18}\ m^{-3}$).

For optimisation of the AC operation it was proved necessary to install a new set of more symmetric windings for the vertical field (B_v) to minimise the error fields and to feed the horizontal windings by an independent DC power supply. In these conditions we have achieved a better current evolution, with almost a square wave shape and a plateau in the positive current direction (Fig. 1).

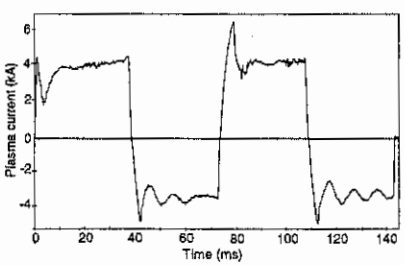

Fig. 1

Shot #5671 reveals, during two half-cycles: plasma current flat-tops in both directions at -4.5 and 5 kA (Fig. 2a); a plateau line average density increasing from 3.5×10^{18} to 4×10^{18} m^{-3} which drops to a minimum of $0.8 \times 10^{18}\ m^{-3}$ at current reversal (Fig. 2b); the continuous H_α emission with an intensity decreasing from 12 to 8 arbitrary units (Fig. 2c); the decrease of the plasma resistance along time from 1.2 to 0.9 mΩ (Fig. 2d), suggesting a temperature increase of about 20%, if we take in consideration the scaling of T_e (Thomson Scattering) with the plasma resistance (Spitzer resistivity). We note that the ratio between $< n_e >$ and the H_α intensity increases by about 70% suggesting that a better particle confinement in the third half-cycle was achieved.

Detailed analysis of the I_p transition (Fig. 3) reveals that the fastest reversal is that of the loop voltage (200 μs). I_p drops to zero also rather quickly (800 μs), while B_v decays in a longer time-scale due to its coil inductance, reaching zero in 2.4 ms, and $< n_e >$ remains, after loop voltage reversal, at a high value for about 400 μs and then drops

rapidly (200 μs) to its first minimum. A second n_e minimum is observed approximately at the mid-point between the instants at which $I_p = 0$ and $B_v = 0$. The inverse transition leads to similar results.

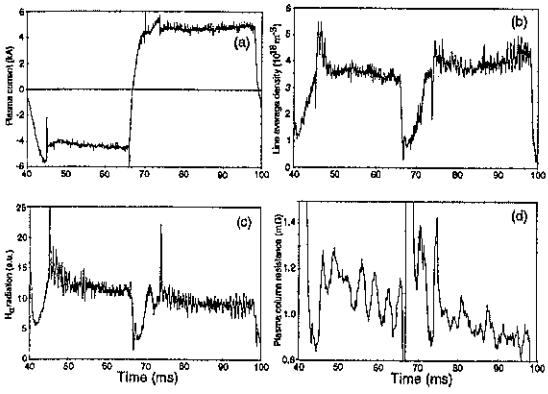

Fig. 2

We have seen that, while I_p is approaching zero, $< n_e >$ decreases rapidly towards its first minimum in some 200 μs. It is perhaps interesting to compare this time with that associated with the magnetic field gradient and curvature drifts, in the absence of any transverse B-fields. The global drift velocity is given, in tokamak geometry, $B_{(r)} = B_T R/(R+r)$, by $v_D = \pm m(v_\parallel^2 + v_\perp^2/2)/eRB_T$. For a Maxwellian distribution the average values of $v_\parallel^2/2$ are both equal to kT/m. Therefore, the average drift velocity can be written as $2kT/eRB_T$ where T is the plasma temperature. The maximum drift timeis attained at r=0, where the particles, in our tokamak, have to travel upwards 8.5 cm to the vertical limiter or 10 cm downwards to the vessel wall. For B_T=0.45 T the drift time is about 49 μs for kT=180 eV. Therefore at the first density minimum ($\Delta T \sim 200\ \mu s$) only a residual plasma with a temperature below 44 eV would still be partially confined.

With the Langmuir probe fed with a 50 Hz voltage (±100 V) we have seen (#5904) that, at current reversal, the edge temperature decayed to one half of its plateau value (11 eV) and that it rised afterwards to the same level while the edge density has dropped to 65% of its former value ($4.2 \times 10^{17}\ m^{-3}$) and becomes higher afterwards ($5.8 \times 10^{17}\ m^{-3}$).

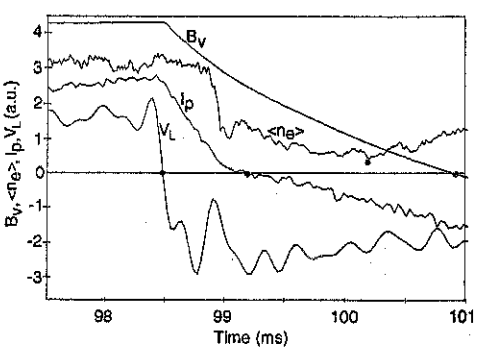

Fig. 3

Finally, by a fine adjustment of the gas puffing system, we have obtained in shot #6043 a discharge with seven half-cycles without any dwell time in a total time span of 220 ms (Fig. 4). The H_α radiation shows an increasing amplitude while I_p diminishes probably revealing an increase of n_e and (or) a slight decrease of T_e. However, the plasma current exhibits in some half cycles slow oscillations, probably related with edge biasing by the Langmuir probe.

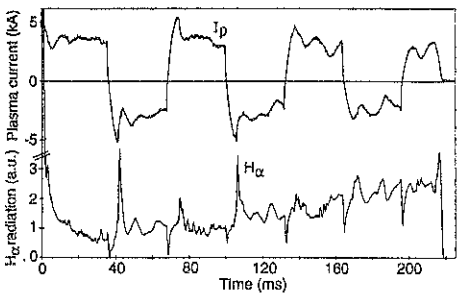

Fig. 4

4. CONCLUSIONS

Concluding we may state that multi-cycle alternating inductive discharge operation with flat-tops in the plasma current and without dwell time was achieved on ISTTOK. A maximum of seven half-cycles was obtained, enlarging the duration of the discharges from 40 to 220 ms. The plasma temporary increases of n_e and T_e were observed during a few half-cycles in some shots.

Acknowledgements -This work has been carried out in the frame of the Contract of Association between the European Atomic Energy Community and "Instituto Superior Técnico" and has also received financial support from "Junta Nacional de Investigação Científica e Tecnológica" (JNICT) and PRAXIS XXI.

REFERENCES

1. P.H. Rebut et al., (1993), Plasma Physics Controlled Fusion 35, A3.

2. Tubbing and JET Team (1993), Plasma Physics Controlled Fusion 35, B55.

3. O Mitarai et al., (1989), Fusion Technology 15, 204.

4. O. Mitarai et al., (1987), Nuclear Fusion 27, 604.

5. B.J.D. Tubbing et al., (1992), Nuclear Fusion, 32, 967.

6. X. Yang et al., (1996), Nuclear Fusion 36, 12, 1669.

7. K. Hayashi et al., 1996 Inter. Conf. on Plasma Physics, September, Nagoya, Japan.

8. O. Mitarai et al., (1997), Internal Report PPL-164, Plasma Physics Lab., Univ. of Saskatchewan.

9. C.A.F. Varandas et al., (1996), Fusion Technology 29, 105.

10. H. Fernandes et al., (1996) 19^{th} SOFT, Lisbon.

Avalanche Dynamics of Collapse and Non-local Model of Transport

T. Kubota[1], T. Iwasaki[1], S. -I. Itoh[2], M. Yagi[2], A. Fukuyama[3], K. Itoh[4], U. Stroth[5]
[1]Interdisciplinary Graduate School of Engineering Sciences,
Kyushu Univ.,Kasuga 816, Japan.
[2]Research Institute for Applied Mechanics, Kyushu Univ. 87, Kasuga 816, Japan.
[3]Faculty of Engineering, Okayama Univ., Okayama, 700, Japan.
[4]National Institute for Fusion Science, Nagoya 464-01, Japan.
[5]Max-Planck-Instutut für Plasmaphysik, 85748, Garching, Germany.

I. Introduction

The phenomena of the collapses and the transient responses in toroidal plasmas are the challenging issues in the physics of high temperature plasmas. In this article we study the nature of the energy transport of plasma from two points of view. At first we study the heat transport with the hysteresis characteristics of the heat conductivity and obtain the avalanche at the energy transport. Secondly we consider the non-local effect in the heat flux and obtain the hysteresis in gradient-flux relation.

II. Avalanche Dynamics

In magnetically confined plasmas, the rapid crash of the temperature profile has been observed in many experiments. The examples are the giant-ELM, the sawtooth crash, the internal collapse, and so on. Recently the model of the transport bifurcation between the H-mode and magnetic braiding mode (M-mode) was proposed to explain the giant-ELM[1].

We analyze the 1-dimensional dynamics of the heat transport of the edge plasma inside the separatrix with the hysteresis characteristics of the heat conductivity to study the energy burst of the giant-ELM. We introduce the hysteresis characteristics of the heat conductivities to the energy transport equations and obtain the avalanche at the energy flux and the rapid collapse of the temperature profile.

II-1. Model of Avalanche

We investigate the energy burst of the giant-ELM as the bifurcation of the transport coefficients with the hysteresis characteristics, which are mentioned as follows.

It is predicted that the heat conductivities bifurcate between the H-mode and the M-mode[1]. We assume, for the simplicity, that the heat conductivity at the H-mode, χ^H, is constant and independent of other parameters. The electron and ion heat conductivities in the M-mode are obtained in [1] as, $\chi_i^M = \sqrt{m_i / m_e} M \chi^H$ and $\chi_e^M = \sqrt{m_i / m_e} M \chi_i^M$, where M is constant parameter and j denote the particle species ($j = i,e$). The threshold value of the bifurcation are defined that when the pressure gradient α exceeds α_c, the transition from the H-mode to the M-mode occurs, and when the value of α reduces to α_l, the back-transition from the M-mode to the H-mode occurs, where α is defined as $\alpha \equiv -q^2 R d\beta/dr$ and q, R and β are the safety factor, the major radius and the beta value, respectively. The threshold

values, α_c and α_1, are the functions of magnetic well, R/a and s, where s is the shear parameter. Here, we assume that the threshold values, α_c and α_1, are given to be constant.

The hysteresis characteristics give rise to the collapse of the temperature profile accompanied with the avalanche process. The mechanism of the avalanche is as follows. When the pressure gradient, α, at any point exceeds the threshold value, α_c, the transition from the H-mode to the M-mode occurs and the heat flux in the M-mode region is enhanced due to the large heat conductivities, therefore α decreases. At the region adjacent to the M-mode region, α is forced to increase due to the enhanced heat flux from the M-mode region and if α exceeds the threshold value, α_c, a successive transition from the H-mode to the M-mode occurs. Therefore, this crash of the temperature profile propagates and the M-mode region spreads rapidly from the first transition point. It is the avalanche. α at the region which is subject to the M-mode is decreased due to the rapid outflow of enhanced heat flux. When the value of α is reduced to α_1, the back-transition from the M-mode to the H-mode occurs and the value of α starts to increase again.

II-2. Calculation of the 1-D Transport code

We include the hysteresis model of the heat conductivities among the energy transport equation. We solve the development of the profiles of plasma temperatures, T_e and T_i. The density profile and the magnetic field are fixed in time. The energy transport equation is ,

$$\frac{3}{2}\frac{\partial}{\partial t}\left(n(r)\,T_j(r,t)\right)=\frac{\partial}{\partial r}\left\{\chi_j\frac{\partial}{\partial r}\left(n(r)\,T_j(r,t)\right)\right\} \quad , \tag{1}$$

where n, T_j and χ_j are the density, the temperature and the heat conductivities, respectively, r is taken along the minor radius. χ_j obeys the hysteresis characteristics. The slab region near the plasma edge is the region of interest, $-L<r<0$. The boundary conditions are as follows. At the edge ($r=0$) we impose the constraint of the constant temperatures of the ion and the electron. The heat flux from the core plasma ($r=-L$) is constant as $Q=Q_{in}$. The background heat conductivity is assumed as $\chi^L=1.0\,m/s^2$. We choose the standard tokamak parameters as follows, the major and the minor radii are$R=1.3$ m, $a=0.35$ m, the toroidal magnetic field is $B_T=1.3$ T. We assume that $L=0.1$ m, the density is the linear function of r and $n(-L)=2.0\times10^{19}$ and $n(0)=5.0\times10^{18}$, the safety factor is also the linear function of r and $q(-L)=1.2$ and $q(0)=2$, the temperatures at the edge are $T_{e\,s}$=$T_{i\,s}$=$50eV$. The input heat flux Q_{in} is chosen so that Q_{in} preserves the temperature as $T_{e\,0}$=$0.34keV$, $T_{i\,0}$=$0.30keV$ at r=$-L$ under the background heat conductivity, that is, Q_{in}=$1.97\times10^4 Jm^{-2}s^{-1}$. The H-mode is imposed at the region from $r_1=-0.03m$ to $r_0=0m$. And χ^H is assumed as the parabolic function of r, whose minimum value is $\chi^H_{min}=0.1m^2/s$ at $r=r_1/2$. The threshold values is assumed as $\alpha_c=1.2$ and $\alpha_1=0.15$ and the numerical factor in the M-mode heat conductivities, M, is assumed as $M=0.5$. Each variable is normalized by a, $T_{e\,0}$ and τ_{Ap}, where τ_{Ap} is the poloidal Alfven time ($\tau_{Ap}=a\sqrt{\mu_0 n_i m_i}/B_p$).

At the H-mode region, if α exceeds the threshold value α_c, the transition from the

H-mode to the M-mode occurs and the avalanche process begins. The temperature is decreased by the enhanced heat transport. In Fig. 1, the time slice of the profile of the electron temperature, $\hat{T}_e$, is drawn, where the hat denotes the normalized value. The curve labeled (a) shows the profile of $\hat{T}_e$ just before the start of the avalanche process and the curves labeled (b) and (c) give the profile of $\hat{T}_e$ after $\hat{t} = 0.84$ and $\hat{t} = 5.87$ from the start of avalanche. We see from Fig. 1 of the curves (a) and (b), that the pivot point of the profile of $\hat{T}_e$ appears at the every early stage of avalanche, and that $\hat{T}_e$ is decreased inside of this point and $\hat{T}_e$ is increased outside by the enhanced heat flux from the inner region. By the passing of time, when the energy is exhausted enough by the enhanced transport, then the pivot point disappears, that is shown (a) and (c). After the back transition completes, the profile (a) is again realized.

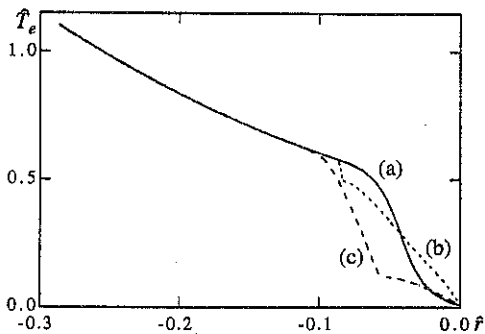

Fig. 1 The time slise of the electron temperature. (a) $\hat{t} = 0$, (b) $\hat{t} = 0.84$, (c) $\hat{t} = 5.87$.

III. Non-local Model Analysis of Heat Pulse Propagation

Recently, the experimental data for the transient transport of the heat pulse propagation has been accumulated. There reported an interesting observation that the heat flux changes faster than the change of the temperature profile in the experiment of the on-off of the central heating. The rapid change of the plasma state and its hysteresis nature were successfully modeled by a transport coefficient depending directly on the global heating power [2]. The purpose of this study is to propose another way, i.e., to consider the non-local effect in the heat flux and to investigate its dependence.

III-1 Non-local Model of The Heat Flux

To take the non-local effect in the heat flux into account, we propose the following model,

$$q(r) = -\int_0^a n_e \chi_e(T(r'), \nabla T(r')) K_f(r - r') \nabla T(r') dr' \quad , \tag{2}$$

where q is the electron heat flux, n_e is the electron density, χ_e is the electron diffusivity, $K_f(r - r') \equiv r / r' \left[C_{local} \delta(r - r') + C_{global} 1 / (\sqrt{\pi} l) \cdot \exp\{-(r - r')^2 / l^2\} \right]$ is the kernel which includes the non-local effects and T is the electron temperature. The weighting function r / r' is introduced to impose the boundary condition $q(0) = 0$. C_{local} and C_{global} are the numerical constants which represent the local effect and the non-local effect, and l is the half width of

the non-local effect. The kernel becomes the delta function when $l \to 0$. Then the heat flux reduces to that in the local transport model. By changing these parameters, we solve the energy transport equation numerically. We firstly assume $\chi_e = const$ to elucidate the non-local effect and the deposition profile is modeled as $P = P_0 \exp\{-100(r/a)^2\}$.

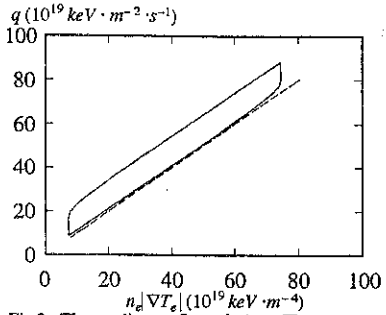

Fig.2 The gradient – flux relation. The parameters are $r/a = 0.5$, $l/a = 0.5$, $t_c = 0$, $C_{local} = 0.9$, $C_{global} = 0.1$. When $l/a = 0$, the hysteresis disappears (dashed line).

III-2. Simulation of Non-local Model

We use the following plasma parameters. Major and minor radii are $R = 2.0\ m$ and $a = 0.2\ m$. The constant electron density and diffusivity are $n_e = 4.0 \times 10^{19}\ m^{-3}$ and $\chi_e = 1.0\ m^2/\sec$ and $\tau_E \sim a^2/\chi_e = 0.04$ sec. The non-local effect little affects the stationary profile, $T_e(r)$, for the wide range of parameter l. The hysteresis is obtained in gradient-flux relation in the transient response, which is shown in Fig.2. A single linear line is obtained in the stationary case. When the central heating power changes from 0.1 to 1.0 MW (step function), the temperature gradient increases slowly but the heat flux increases rapidly because of the non-local effect which is included in our model. When the central heating power changes from 1.0 to 0.1 MW, the temperature gradient decreases slowly but the heat flux decreases rapidly. So the hysteresis is clockwise away from the region of heat deposition. On the other hand, the hysteresis is counter-clockwise at the region heated directly ($r/a \le 0.1$). The width of the hysteresis increases with l and has the peak where the value of r/a is nearly equal to l/a which is the case shown in Fig.2. If $l \to 0$, the width goes to zero because the heat flux is reduced to the local transport model. The width also depends on the time t_c, which is the switching time of the heating power. When $t_c = 0$ (the power is changed as the step function), the width takes the maximum value, and for the t_c larger than the energy confinement time, the width behaves as $1/t_c$. The hysteresis is prominent when $t_c << \tau_E$.

To investigate the model of diffusivity dependent on temperature or temperature gradient is left for our future work.

IV. Summary

In this article we study the characteristics of the heat transport including two model, i.e., the model of the hysteresis characteristics of the heat conductivities and that of the non-local effect in the heat flux. And we obtain the avalanche at the energy transport and the hysteresis in gradient-flux relation, respectively

References

[1] S.-I. Itoh, *et al.*, *PRL*, **76** (1996)920. *PPCF*, **38** (1996)527.

[2] U. Stroth et.al., *Plasma Physics and Controlled Fusion*, **38** (1996) 1087

Enhanced rotation velocities and electric fields, sub-neoclassical energy transport and density pinch from revisited neoclassical theory

André Rogister

Institut für Plasmaphysik, Forschungszentrum Jülich GmbH, EURATOM Association
Trilateral Euregio Cluster, , D-52425 Jülich, Germany

Abstract: The purpose of this paper is to show that the large negative radial electric fields which have by now been measured in front of the separatrix in H-mode discharges were predictable by a rigorous „revisited" neoclassical theory, including Finite Larmor Radius and Inertia effects. The same theory naturally leads to sub-neoclassical energy transport and new particle pinch terms. The calculation has so far been developed only in the high collisionality regime. To explain the observations therefore by no means requires assuming step sizes comparable to gradient-scale sizes!

I. Outline of the theory and improvement with respect to previous work.

The basic theory [1], from which the results presented here are derived, assumed the ordering

$$\Lambda_1 \equiv \left(q^2 R^2 N T_i\right) / \left(reB|L_T|\ \chi_{\|,i}\right) \sim 1 \qquad (1)$$

according to which

(i) gyro-viscous ($\alpha\eta_{3,i}\partial U_{\|,i} / \partial x$) and collision-viscous ($\alpha\eta_{0,i}\partial U_{\|,i} / \partial \ell$) frictions are allowed to be of the same order of magnitude if $L_{v\|,i} \sim L_T$, whereas the former is systematically neglected in conventional neoclassical theory (x is the radial variable; ℓ is the space-variable along field lines; the other notations are from Braginskii [2]); we note that – as is well-known from low frequency drift-wave theory – intertia and FLR terms bring about contributions of the same order of magnitude, but of opposite signs; as a consequence those codes which keep only one of the two effects into account are likely to give an incorrect answer;

(ii) energy convection and parallel diffusion rates on magnetic surfaces (respectively $T/reB|L_T|$ and $\chi_{\|,i} / Nq^2 R^2$) are considered on a par, whereas the former is again neglected in conventional neo-classical theory.

The parameter Λ_1 is typically of order 0.25 in the L (low) mode of confinement and outside the transport barrier of the H-mode; $\Lambda_1 \geq 1$ within the latter. We emphasize that con-

ventional neoclassical theory is incomplete also when $\Lambda_1 << 1$, as the ambipolarity constraint is degenerate (it provides no condition from which to obtain the radial electric field). The parameter Λ_1 factorizes out of the ambipolarity condition of the revisited theory in the limit $\Lambda_1 << 1$. The relevance of the high collisionality regime stems out from that ASDEX edge density profiles correspond to collisionality parameters of order 10 or more and DIII-D profiles to $\hat{\nu}_i \equiv qR\nu_i / \upsilon_{th,i}$ often larger than 1. Extension of the theory to the low collisionality regime is of course desirable — in spite of the tremendous difficulties of a *systematic* and *rigorous* analytical development — in view of both core and edge transport barriers.

II. Main results concerning energy and particle transport.

The results obtained in [1] hold for general axisymmetric configurations. Particularizing to circular cross-section tokamaks (and letting the parameter $\Lambda_2 \to o$, where Λ_2 is the ratio of the electron-ion temperature relaxation rate to the parallel ion energy diffusion rate on the magnetic surface), it can be shown that the flux surface average of the „radial" component of the revisited neoclassical heat flux is

$$q_{i,r} = -\left(1 + \frac{1.6q^2}{1+Q^2/S^2}\right)\chi_{\perp,i}\frac{\partial T_i}{\partial r} \qquad (2)$$

where

$$S = 2\left(\chi_{\parallel,i}/rN\right)B_\theta^2/B^2; \qquad Q \equiv 4\left(B_\varphi U_{\theta,i}/B\right) - 5\left(T/eB\right)\partial \ell n\, NT^{1/2}/\partial r \; ; \qquad (3)$$

$\chi_{\perp i}$ is defined in [2]; q is the safety factor; θ and φ are the poloidal and toroidal angles; we note that $Q/S \sim \Lambda_1$. The neoclassical contribution $1.6\, q^2\, \chi_{\perp,i}\partial T_i/\partial r$ to $q_{i,r}$ is reduced by the factor $1 + Q^2/S^2$ leading to the concept of sub-neoclassical energy transport. $q_{i,r}$ is moreover a multivalued function of $\lambda \propto |L_T| = |\partial \ell nT/\partial r|^{-1}$, as shown in Fig. 1 (condition to have three roots is $q > \sqrt{5}$ as may be shown by considering $\partial q_{i,r}/\partial \lambda^{-1}$). Such a property may obviously lead to bifurcation scenarios. The transition from L to H confinement will however be discussed here on the basis of the behaviour of the edge radial electric field and rotation velocity profiles.

The expression of the ambipolar particle flux is more complicated and will not be given in this short paper. It is nevertheless interesting to note that it contains, besides the standard expression given e.g. by Hinton and Hazeltine [3], a series of new terms proportional to

$q^2\partial\ell nT/\partial r$ and $Q^2/(Q^2 + S^2)$, $Q[(T/eB)\partial\ell nN/\partial r$; $E_r/B]/(Q^2 + S^2)$, etc. Those generally correspond to particle pinches, a characteristic velocity being a few cm s^{-1}.

III Edge radial electric field and rotation velocity profiles.

The non-trivial ambipolarity constraint and the parallel momentum equation of the revisited theory allow unambiguous determination of the radial electric field and of the parallel velocity profiles, or of any combination thereof, e.g. the polodial and the toroidal rotation velocities (the radial momentum equation still provides the well-known simple relation between U_φ, U_θ, $\partial P/\partial r$ and E_r). Assuming the density and temperature profiles to be frozen (e.g. proportional to a power of 1 + kx, with x measured from the separatrix inwards), we find that the general theory [1] leads to a nonlinear first order partial differential equation for either $U_{||,i}$ or E_r if (i) $\Lambda_1 << 1$ and (ii) the conventional orderings $E_r \sim (T/e)\partial\ell nP/\partial r$, $U_{||,i} \sim (T/eB_\theta)\ \partial\ell n\ P/\partial r$ and $L_{Er} \sim L_{u_{||}} \sim L_{T,N}$ are postulated. The solution of this equation may be expressed in terms of a certain function of a particular combination of space and time, function which is to be determined from the boundary condition, e.g. at x = o. It is found that the solution of the nonlinear equation diverges at some x < o (in the confined plasma) if certain criteria — involving the density of neutrals, the momentum injection rate per ion, their temperature and density profiles — are fulfilled. The postulated scaling assumptions must then be revised in the neighbourhood of the „singular" point, yielding eventually enhanced velocities and electric field and reduced variation scales thereof; the enhancement/reduction factor is $\sim \Lambda_1^{-2}$ (it should be noted that Λ_1, being defined with respect to N,T and L_T, is fixed). The above rescaling leads now to second order nonlinear equations, of which the solutions E_r and $U_{||,i}$ are well behaved, albeit large, near the former singular point. A schematic plot of E_r is shown in Fig. 2. The large radial electric field is always negative in front on the separatrix, as observed in experiments; a minimum value of some — 20 kV/m has been estimated from DIII-D and ASDEX density and temperature data [4, 5]. A corresponding maximum value $U_{\varphi,i} \sim 200$ km s^{-1} is found in the direction of the plasma current. Finally, the poloidal rotation velocity $(U_\theta B_\varphi/B)$ jumps to some 20 km s^{-1} inside the barrier, the width of which is $\sim \Lambda_1^2 L_T \sim$ 0.25 cm.

IV Concluding remarks

The question as to which boundary condition should be required at the separatrix is still open. The particular condition

$$U_{\|,i}^{-1}\,\partial U_{\|,i} / \partial x\big|_{x=o} = C$$

has been found to lead either to aperiodic or to periodic solutions of the differential equations depending on parameters already enumerated in Section III. Those solutions may correspond to L, H and dithering H modes. The above b.c. furthermore leads to a transition criterion of the form $P_{thres} \propto N^a B^b$ where P_{thres} is the power threshold, a > o and possibly b > o, as observed.

The physics contained in the equations leading to the results of this paper suggests that large electric field and rotation velocities develop locally when the plasma finds no other way of maintaining the ambipolarity of the fluxes. The resulting enhanced shear will ultimately suppress the turbulence and improve the confinement.

Acknowledgement: I am grateful to M.Z. Tokar for pointing out the bifurcation character of the revisited heat flux.

[1] Rogister, A., Phys. Plasmas 1 (1994) 619
[2] Braginskii, S., Transport Processes in a Plasma, in *Reviews of Plasma Physics*, (Consultant Bureau, New York 1965, M.A. Leontovich, editor) Vol 1, p. 205
[3] Hinton, F.L., Hazeltine, R.D., Rev. Mod. Physics 48 (1976) 239
[4] Kim, J. et al., Phys. Rev. Lett. 72 (1994) 2199
[5] Sutropp, W., et al., private communication (1997)

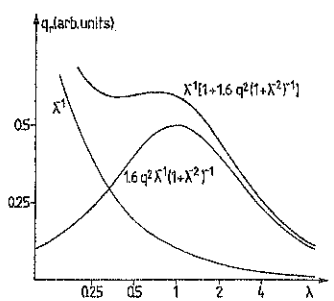

Fig. 1. Revisited heat flux for q=2.5

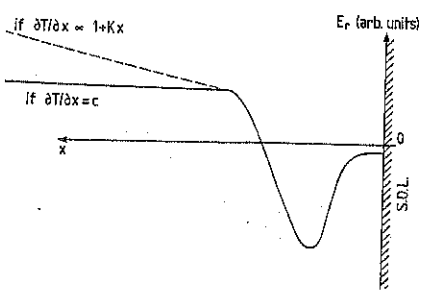

Fig. 2. Sketch of radial electric field in the case of the singular layer

DUST IN FUSION PLASMAS

J. Winter

Institute of Experimental Physics II, Ruhr-University Bochum, D-44780 Bochum, Germany

1. Introduction

Microparticles can play an important role in fusion devices. Their presence and their possible consequences for plasma operations and performance are only recently being addressed /1, 2/, although their existence is known since long. Dust and particulates are usually found in the bottoms areas of fusion devices after some operation period. Dust is an important safety issue or ITER and future fusion reactors due to T retention. The finely disperse particles are chemically reactive and may spontaneously react with oxygen or water vapour in the case of a vacuum- or coolant leak. This paper focuses on the discussion of mechanisms for dust formation in fusion devices with large area graphite wall armour and with surfaces treated by thin film wall conditioning (carbonization, boronization, siliconization). Since the considerations are very basic, however, they may apply to metal wall conditions, as well. Samples of dust collected from TEXTOR-94 are analysed visually, magnetically and by Scanning Electron Microscopy (SEM), including Energy Dispersive Analysis of X-rays (EDAX) for the determination of the composition. The impact of the findings on safety and plasma operation of fusion devices is discussed.

2. Dust Production Mechanisms

Important mechanism of dust formation are evaporation and sublimation of wall material which is thermally overloaded e.g. in the course of a disruption. Another generation mechanism is the spallation and flaking of thin films of redeposited material or of films which were grown intentionally for wall conditioning purposes /3/. Unipolar arcs can liberate fairly large particles and droplets of molten metal. In the case of future DT burning devices He embrittlement due to the decay of T and due to neutron induced spallation becomes probably important. In addition to these „passive" mechanisms dust particles may grow in situ during the fusion plasma itself from atomic or molecular precursors. This mechanism is particularly important in future long-pulse devices. The initiation of the growth mechanism may occur via sputtered atoms or from the seeding of the edge plasma with hydrocarbons from the chemical erosion of graphite wall components. Under the conditions of a detached limiter plasma, for

instance, with $n_e \approx 10^{18}$ m^{-3}, T_e < 5eV and a high fraction of neutral particles one obtains a concentration near the wall of about 5-10 % methane and higher hydrocarbons assuming an effective chemical erosion yield of ~ 1-2 % and taking into account that the hydrocarbons are released at a thermal velocity corresponding to about 100°C wall temperature. These conditions are close to those of a process plasma where dust formation has been observed by multiple ion-molecule reactions and agglomeration processes /4,5/. Once negatively charged particles are formed by electron attachment, they are well confined in the edge plasma. The sheath potential in front of the limiter surfaces repels them and prevents them from reaching the material surface. The magnetic field confines them in radial direction, the Larmor radii being small because of their low velocity. A friction force from the background plasma is acting on these particles, driving them away from the stagnation point. Thus probable locations of dust particles will be close to the limiter surface, where an effective trap from the superposition of these forces exists, see fig. 1. It is interesting to note that C_1, C_2, ..C_n clusters and several C_xH_y radicals exhibit a rather high electronegativity (CH_2 = 3.39 eV, C_2H = 2.94 eV) making their negative ions rather stable.

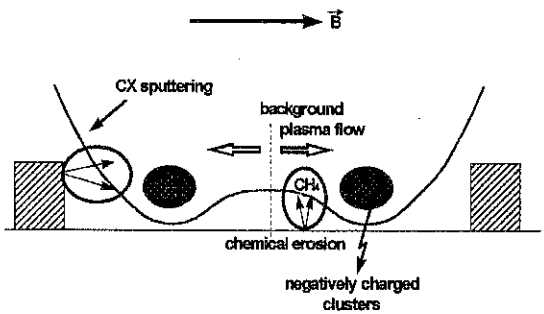

Fig. 1 Schematic representation of the effective potential for a negatively charged macromolecule or cluster in the scrape off layer of a limiter tokamak with indication of the sources of C atoms or hydrocarbon molecules.

3. Analysis of Dust from TEXTOR-94

Dust particles were collected from TEXTOR-94 during a recent opening. TEXTOR has large area graphite limiters. Wall conditioning by boronization /3/ is a standard procedure. Covering the wall surfaces by silicon (siliconization) was attempted by a novel technique using ICRF pulses in He-Silane mixtures /6/. The dust was collected by means of a vacuum cleaner

from the bottom porthole areas of TEXTOR-94. Coarse particles were removed from the sticky bag of the vacuum cleaner by shaking them off (coarse fraction); small particles were rinsed off the bag by 2-Propanole (suspension 1). The particles were investigated visually, by light microscopy and by SEM, including EDAX. For SEM investigations of the fine particles a drop of the suspension was put on a silicon wafer.

The main part of the coarse fraction consists of particles of typically 0.1 -0.5 mm size with irregular shape. A very important finding is the fact that about 15 % of the particles - including the smallest ones - are **ferromagnetic** as can be seen when using a permanent magnet. Fig. 2 shows a representative fraction of the magnetic coarse fraction, extracted from the whole ensemble by a magnet. Metal cuttings, spheres with diameters between 0.01 and 0.1 mm and irregular formed pieces can be distinguished. EDAX reveals the composition of Inconel for the metal cutting with a well noticeable low-Z-overlayer. Surprising is the existence of the large number of almost perfect spheres ranging in size between 0.01 mm and below and about 0.1 mm. Their composition is iron-rich with some Ni and Cr and only thin low-Z overlayers .

Fig. 2 Metal cutting and iron spheres in the magnetic coarse dust fraction

Their perfectly round shape suggests that, if created from a melt, they must have solidified before touching the wall surface. The third major constituent of the magnetic coarse fraction are redeposited low-Z-layers with significant metal incorporation. Their thickness is up to 0.05 mm, the metallic composition iron-rich with varying amounts of Ni and Cr, some Ca and Al. Many of them have a porous, blister-like surface texture.

Particles not attracted by a magnet have low contrast in SEM. Particles of almost pure Si have been observed which do not show the typical signatures of redeposited and flaked off

particles. They are probably produced by pyrolysis and growth in the plasma edge during Si injection experiments. Codeposited flaked-off films constitute another part of the coarse non magnetic fraction and resemble closely that of their magnetic counterparts with the exception of a lower metal content. The third group of non-magnetic big particles is graphite grains with sizes of ~ 0.1 mm, composed of well established graphite grains with typical diameters of 1μm - 10 μm. They originate from fatigued graphite armour tiles.

Many particles of sub-μm size exist (suspension 1), which themselves are agglomerates of individual particles of about 100-300 nm diameter. The size and structure of these small particles is consistent with what one would expect from plasma-induced growth SEM investigations of nanoparticles formed in process plasmas show similar sizes and a diffuse cauliflower-like structure with a tendency to form agglomerates /4,7/. The identification of these particles in the dust from TEXTOR-94 is taken as a strong indication for their growth in the edge of the fusion plasma or in boronization process plasmas.

4.Conclusions

Dust in fusion devices spans a wide size distribution from mm down to < 100 nm. The presence of particulates < 100 nm requires adequate measures to protect people working inside fusion devices. Part of the dust is **ferromagnetic**. These particles will be sucked into the main volume of the discharge chamber and accumulate at the inner wall around the midplane and cause problems during discharge initiation. The small particles identified in this study suggest plasma-induced growth as a likely mechanism. In long-pulse devices this may lead to the formation of significant quantities of dust. Particles are a sink for electrons and will alter the balance between electrons and protons in the edge plasmas and change the plasma dynamics.

References

/ 1/ J. Winter „Dust in Fusion Plasmas", 170 WE-Heraeus-Seminar, Bad Honnef, Jan. 15-17, 1997, abstracts

/ 2/ V. Tsytovich, G. Morfill, J. Winter et al. subm. for publication

/ 3/ J. Winter, Plasma Phys. Contr. Fusion 38 (1996), 1

/4/ A. Garscadden, B.N. Ganguly, P.D. Haaland and. J. Williams, Plasma Sources Sci. Technol. 3 (1994), 239

/5/ A. Leukens and J. Winter, Verhandl. DPG (VI) 32 (1997), 266

/6/ H.G. Esser, J. Winter, V. Philipps et al, Proc. 12 PSI,St. Raphael, France, 1996, J. Nucl. Materials, in press

/7/ H.M. Anderson, S. Rodovanov, J.G. Mock and P. Resnick, Plasma Sources Sci. Technol. 3 (1994), 302

Criterion and Destabilization of Tearing Mode in Reversed Magnetic Shear Tokamak Plasmas

D. Li

Institute of Plasma Physics, Chinese Academy of Sciences, Hefei 230031, P. R. China

Recently, off-axis sawteeth and double tearing reconnection were observed in reversed magnetic shear plasmas in TFTR[1] and TEXTOR. This paper presents analytical work on the criterion for the double-tearing instability and on the destabilization mechanism.

For single tearing mode, the ideal kink external equation

$$\frac{d^2\psi}{dr^2}+\frac{1}{r}\frac{d\psi}{dr}-\frac{m^2}{r^2}\psi-\frac{m}{B_\theta}\frac{dJ_0/dr}{m-nq}\psi=0, \tag{1}$$

can be transferred to the hypergeometric differential equation by proper transform and approximation. The flux perturbation function $\psi(r)$ is analytically obtained by inserting the boundary conditions at $r = 0$ and at conductive wall $r = r_w$, namely, $\psi(0)=\psi(r_w)=0$ and and the continuity condition at $r = r_s$.

Consequently, the analytical expression for criterion quantity $\Delta'^{(0)}$ is obtained as:[2]

$$\Delta'^{(0)} = -\frac{\pi\lambda}{r_s}\cot\left[\pi\left(\sqrt{m^2+\lambda}-m\right)\right] - \frac{\lambda}{r_s}\frac{\Gamma(b)\Gamma(-a)}{\Gamma(b-a+1)}\frac{(r_s/r_w)^{b-a}}{1-r_s/r_w}\frac{{}_2F_1(b,\ -a,\ b-a+1,\ r_s/r_w)}{{}_2F_1(1-b,\ 1+a,\ 2,\ 1-r_s/r_w)}. \tag{2}$$

where $a = m-\sqrt{m^2+\lambda}$, $b = m+\sqrt{m^2+\lambda}$, $c = 2m+1$, ${}_2F_1(\alpha,\beta,\gamma,x)$ is Gauss hypergeometric function, and $\lambda = -q^2(r_s)R_0J_0'(r_s)/B_0q'(r_s)$. In the right hand side of Eq. (2), the first term is an exact result which depends on poloidal mode number m, the resistive layer r_s, and the dimensionless parameter λ determined by the ratio of equilibrium current gradient and magnetic shear. The second term is an approximated result which is referred to the stabilization effect of a conducting wall and decays rapidly as r_s/r_w becomes small.

Without the conducting wall, one can naturally obtain a criterion from Eq. (2) for the instability threshold of a tearing mode

$$\left|(q_0 r_s / B_\theta) J_0' / q_0' - 1/4\right| > m. \tag{3}$$

In the large-m limit, equation (2) without the conducting wall is reduced to

$$\Delta^{\prime(0)} = -\pi(\lambda / r_s)\cot(\pi\lambda / 2m) \tag{4}$$

which was respectively obtained by Strauss using ballooning formalism,[3] and by Hegna and Callen solving Eq. (1) by 1/m expansion,[4] here $\lambda / 2m$ is equal to their parameter λ. Consequently, the large-m limit version of the criterion (3) has been obtained by several authors[3-6] as

$$\left|(q_0 r_s / B_\theta) J_0' / q_0'\right| > m. \tag{5}$$

In the limit case as $\lambda \to 0$, the well-known result $\Delta^{\prime(0)} = -2m / r_s$ is recovered.[7]

Obviously, λ is an essential parameter of tearing instability for both signs of magnetic shear. The values of $r_s\Delta^{\prime(0)}$ for the $m = 2$ mode as function of λ is given in Fig. 1 where the lower and higher curve is respectively plotted from Eq. (2) and (4). One would find that Strauss' formula is a good approximation only if $m >> 1$ and without the conducting wall.

For double tearing mode, it is even more difficult to calculate Δ' due to double singularities so that some authors used energy method to develop numerical code to avoid using $\Delta^{\prime(0)}$.[8] The problem can be solved if the solution could be analytically derived and satisfy both boundary conditions so that an analytic method could be developed to calculate Δ' for the double tearing mode. The dispersion relation is obtained based on the analytical solutions, the boundary conditions, and the continuity at both rational surfaces at r_1 and r_2 :

$$(\Delta_1' - \Delta_1'^{(0)} - A_{12})(\Delta_1' - \Delta_2'^{(0)} - A_{21}) - A_{12} = 0 \tag{6}$$

where $\Delta_i'^{(0)} = \dfrac{f'(r_i, r_w)}{f(r_i, r_w)} - \dfrac{f'(r_i, 0)}{f(r_i, 0)}$, $A_{12} = \left[\dfrac{f'(r_1, r_w)}{f(r_1, r_w)} - \dfrac{f'(r_1, r_2)}{f(r_1, r_2)}\right]$

$$A_{21} = \left[\frac{f'(r_2, r_1)}{f(r_2, r)} - \frac{f'(r_2, 0)}{f(r_2, 0)}\right],\quad A_{22} = \frac{f'(r_1, r_1) f'(r_2, r_2)}{[f(r_2, r_1)]^2}$$

$$f(x, z) = y_1(x)y_2(z) - y_1(z)y_2(x),\ f'(x, z) = y_1'(x)y_2(z) - y_1(z)y_2'(x)$$

in which $y_1(r)$ and $y_2(r)$ are linearly independent solutions of Eq. (1). Obviously, two branches of the double tearing mode interact intrinsically due to the structure of the mode and resulted islands. Δ'_1 (Δ'_2) is different from the uncoupled $\Delta_1'^{(0)}$ ($\Delta_2'^{(0)}$) even in sign.

One can observe from Eq. (2) that $\Delta'^{(0)} = f(m, \lambda) / r_s$ for all of r_s if without the conducting wall. This recovers the well-known result $\Delta'^{(0)} \to f(m) / r_s$ for $r_s \to 0$ as a special case.[9] Therefore, the inner branch of the double tearing mode has a large even explosive growth in linear phase. The value of $\Delta_1'^{(0)}$ increases dramatically as q_0 is approaching 2 for $m = 2$ mode in Figs. 2. Consequently, the new algebraic growth[9] like $\psi \propto t$ does become dominant in the nonlinear phase instead of Rutherford behavior[10] like $\psi \propto t^2$ because $\Delta_1'^{(0)}$ can be several tens even hundred times large comparing with the case in which the resistive layer is far from plasma core. Hence, the magnetic island width should be expressed as:[9]

$$w(t) \propto \left[\frac{\psi(0, t)}{\hat{s}_0 - (C_0 q_0 / \sqrt{2\pi}\eta)\partial\psi(0, t) / \partial t} \right]^{1/2}. \tag{7}$$

In the denominator, total magnetic shear consists of the equilibrium and quasilinear part. The magnetic island can rapidly become fatter and shorter as the total magnetic shear is near zero. When the islands of the inner branch rapidly expand and combine as a whole, the hot plasma in the core cannot be confined any more so that the "core crash" of the off-axis sawteeth occurs. This explanation is consistant with the experiment phenomena in TFTR.[1]. In this case, $\Delta_2'^{(0)}$ is much smaller than $\Delta_1'^{(0)}$ so that the coupling term A_{22} is negligible. However, when q_0 is not near $q_s = 2$, the magnitude of $\Delta_1'^{(0)}$ and $\Delta_2'^{(0)}$ can be of same order so that the coupling effect becomes strong. The interaction of two branches may cause the overlap of islands and the "annular crash" of the off-axis sawteeth.

In summary, the analytic expression of $\Delta'^{(0)}$ and instability criterion are obtained for arbitrary magnetic shear configuration. The dispersion relation of double tearing mode is derived by means of the structure of the external solution. The new algebraic growth does become dominant in the nonlinear phase instead of Rutherford behavior because $\Delta_1'^{(0)}$ can be very large even explosive. The explosive growth of the inner branch may result in the rapid

expansion and combination of islands which causes the "core crash". The interaction of two branches may cause the overlap of islands and the "annular crash".

Acknowledgments

It is my pleasure to thank Dr. A. Rogister (IPP/FZ) for constant encouragement and helpful discussions and Dr. Z. Chang (PPPL) for valuable discussions. This work was supported by a Fellowship of the Research Center Jülich, Germany and by the National Science Fund for Distinguished Young Scholars of China under Grant No. 19515513.

[1] Z. Chang et. al., Phys. Rev. Lett. 77, 3553 (1996).

[2] D. Li, Jül-Report No. 3377, Forschungszentrum Jülich (1997).

[3] H. R. Strauss, Phys. Fluids **24**, 2004 (1981).

[4] C. C. Hegna and J. D. Callen, Phys. Plasmas **1**, 2309 (1994).

[5] J. A. Wesson, Nucl. Fusion **18**, 87 (1978).

[6] P. H. Rutherford, in *From Particles to Plasmas*, edited by J. W. Van Dam (Addison-Wesley, New York, 1987), pp. 249-271.

[7] For example, W. Kerner, and H. Tasso, Phys. Rev. Lett. **49**, 654 (1982).

[8] R. B. White, in *Handbook of Plasma Physics*, edited by A. A. Galeev, and R. N. Sudan (North-Holland, Amsterdam, 1983), Vol. 1, pp. 611-676.

[9] D. Li, Phys. Plasmas **2**, 3275 (1995).

[10] P. H. Rutherford, Phys. Fluids **16**, 1903 (1973).

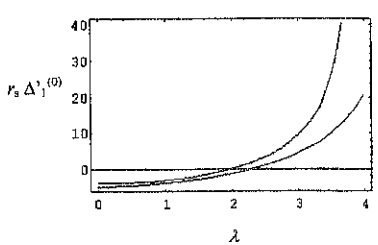

Fig 1. m=2 mode is destabilized as λ increases. The higher curve is plotted from Strauss' formula.

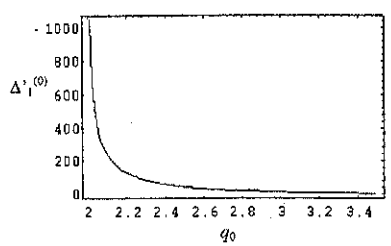

Fig 2. Value of $\Delta'_1{}^{(0)}$ increases dramatically as q_0 is near 2 for m=2 mode if r_w=2 and q_m=1.6.

A two–dimensional simulation of electrostatic drift wave turbulence in plasmas

G.J.J. Botha, M.G. Haines, R.J. Hastie
Blackett Laboratory, Imperial College, London SW7 2BZ, UK

Abstract

The generation of electrostatic drift wave turbulence is modelled by the Charney–Hasegawa–Mima equation. The unperturbed density gradient $n_0 = n_0(x)$ is chosen so that $dn_0/dx \neq 0$ and variable (i.e. v_{*e} is sheared). It is shown that this sheared flow leads to localised turbulence, maximising at the peak of ∇n_0. The dual cascade of the generalised energy and enstrophy is observed, with condensation of the generalised energy spectrum at the lower mode numbers. When the code is initialised with one mode, the dual cascade manifests only in the initial mode's harmonics.

The Hasegawa–Mima model of 2D electrostatic drift wave turbulence is well–known [1,2] and has been the subject of many numerical simulations which studied drift–wave turbulence in tokamaks [3]. The model consists of the Charney–Hasegawa–Mima (CHM) equation [4,5,6] which evolves the perturbed electrostatic potential ϕ_1 while the unperturbed density $n_0 = n_0(x)$ is fixed with characteristic length $L_n^{-1} = (1/n_0)(dn_0/dx)$. The results presented here [7] are an extension of the work by Prakash, Chu and Hasegawa [8] who considered short runs with a constant L_n^{-1}.

The CHM equation is given by

$$\frac{\partial}{\partial t}\left(\frac{e\phi_1}{T_e} - \frac{1}{\Omega_{ci}}\frac{c}{B}\nabla_\perp^2\phi_1\right) - \frac{c}{B}L_n^{-1}\frac{\partial\phi_1}{\partial y} - \frac{1}{\Omega_{ci}}\frac{c^2}{B^2}\left[\phi_1, \nabla_\perp^2\phi_1\right] = 0 \tag{1}$$

where Ω_{ci} is the ion cyclotron frequency, $\mathbf{B} = B\hat{z}$ is the magnetic field, T_e the constant electron temperature, c the speed of light, e the electron charge and $[\ ,\ ] = \partial/\partial x\partial/\partial y - \partial/\partial y\partial/\partial x$. This equation conserves the generalised energy

$$W = \int_V \frac{1}{n_0 T_e}\left[\frac{1}{2}\frac{n_1^2 T_e}{n_0} + \frac{1}{2}m_i n_0 v_E^2\right] dV \tag{2}$$

while the generalised enstrophy evolves according to

$$\frac{\partial U}{\partial t} - \frac{1}{\Omega_{ci}}\frac{c^2}{B^2}\int_x\int_y \frac{\partial\phi_1}{\partial y}\frac{\partial\phi_1}{\partial x}\frac{d}{dx}\left(L_n^{-1}\right)\frac{dxdy}{a_x a_y} + \frac{1}{\Omega_{ci}^2}\frac{c^3}{B^3}\frac{1}{2}\int_y\left(\frac{\partial^2\phi_1}{\partial x^2}\right)^2\frac{\partial\phi_1}{\partial x}\frac{dy}{a_y} = 0 \tag{3}$$

where a_x and a_y are the domain lengths along x and y respectively and where the generalised enstrophy is defined by

$$U = \int_V\left[\frac{1}{n_0 T_e}\left(\frac{1}{2}m_i n_0 v_E^2\right) + \frac{1}{2}\left(\frac{\nabla\times\mathbf{v}_E}{\Omega_{ci}}\right)^2\right] dV. \tag{4}$$

Equation 3 shows that the generalised enstrophy will only be conserved when L_n^{-1} is a constant and when either $\partial\phi_1/\partial x$ or $\partial^2\phi_1/\partial x^2$ is zero at the x boundaries.

The CHM equation is numerically implemented on a 2D regular Cartesian grid which is periodic in y and with $\phi_1 = 0$ at the x boundaries. When the ϕ_1 perturbations reach the x boundaries the simulation is terminated. The CHM equation is treated spectrally along y and is finite differenced along x. This results in a bi–tridiagonal system which is solved using the algorithm of Von Rosenberg [9]. Arakawa's finite difference scheme [10] is used to calculate the nonlinearity. The equation is advanced in time using a modified Euler predictor corrector method [11].

The accuracy of the numerical simulations is measured by the conservation of the generalised energy and enstrophy. During simulations the typical generalised energy loss is less than 0.75% and the generalised enstrophy loss less than 2.5%. The final time is 4.5×10^{-4}s which is $67.4|L_n|.c_s^{-1}$ or 14.5 $[2\pi/\max(\omega_{*e})]$.

$L_n^{-1} = L_n^{-1}(x)$ implies that the electron gradient drift v_{*e} is sheared (figure 1). This shear influences the ϕ_1 perturbations in that the larger dv_{*e}/dx is, the more localised the perturbations become. Figure 5 presents the time evolution of

$$\left(\frac{e\phi_1}{T_e}\right)_{rms} = \sqrt{\frac{1}{M}\sum_{j=1}^{M}\left[\frac{e\phi_1(x_i, y_j)}{T_e}\right]^2} \tag{5}$$

where M is the number of grid cells along y. The initial perturbation along x is a Gaussian and as time evolves, the ϕ_1 fluctuations move towards the x boundaries while the largest fluctuations develop where v_{*e} flows the fastest. By increasing $\max(v_{*e})$ the fluctuations become more localised near the centre of the x axis.

The gradient in v_{*e} also has an effect on the behaviour of large structures which form in the plasma. Figure 2 shows spatial trajectories of coherent structures by following local maxima as they move on the (x, y) plane. Figure 3 shows the change in their amplitudes during this time. As they move in the x direction, the value of the local v_{*e} change and this change is reflected in a change in their amplitudes. Figures 2, 3 and 5 were obtained by initialising with modes 7 and 11 in Fourier space.

Initialisation can be done with one mode or multiple modes along the y direction. In both cases the dual cascade of 2D turbulence [12] is observed. When one mode is used in the initialisation, only its harmonics are observed in the spectra of the generalised energy and enstrophy. Figure 4 was obtained with initial mode 9. Here equation 2 is written as

$$W = \int_V w dV = \sum_{m=-\infty}^{\infty} \mathcal{W}_m e^{i2\pi m y/a_y} \tag{6}$$

where the definition

$$\mathcal{W}_m = \frac{1}{a_x}\int_0^{a_x} w_m(x) dx \tag{7}$$

has been used. By doing the same with equation 4 the generalised enstrophy is written as $\mathcal{U}_m$ and presented in figure 4. When two or more modes are used during initialisation, all the modes in the spectra are present. In all cases the generalised energy condenses in the lower modes of its spectrum and this condensation is mirrored in the generalised enstrophy spectrum. A reflecting boundary was created at the highest mode in Fourier space and this reduced generalised enstrophy losses.

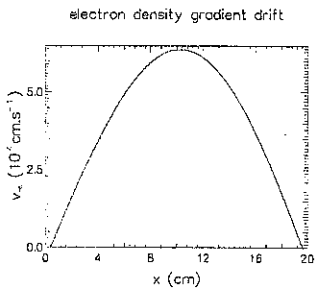

Figure 1: Profile of v_{*e}

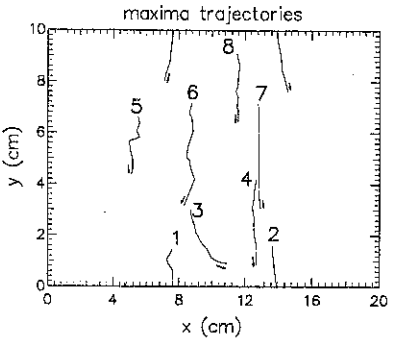

Figure 2: Spatial trajectories of maxima of $e\phi_1/T_e$ as they evolve in time. Each maximum is numbered and the numbers correspond to those in figure 3.

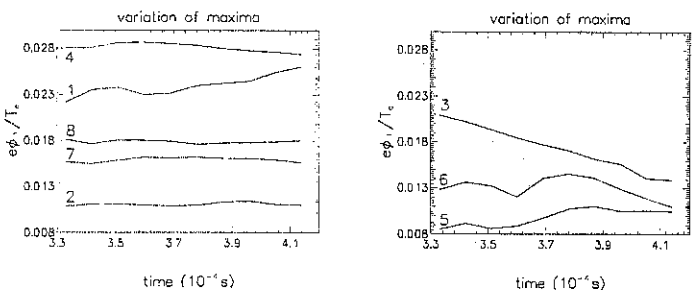

Figure 3: Time evolution of the amplitudes of the maxima of $e\phi_1/T_e$. Each maximum is numbered and the numbers correspond to those in figure 2.

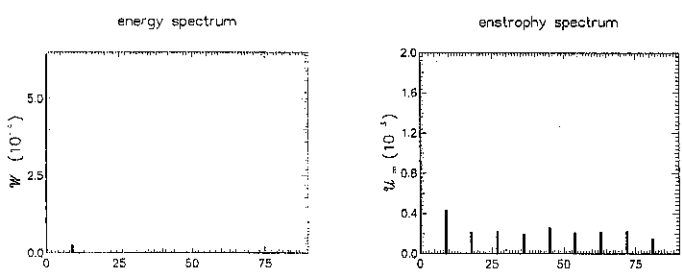

Figure 4: The generalised energy and enstrophy spectra at $t = 8.091 \times 10^{-5}s$

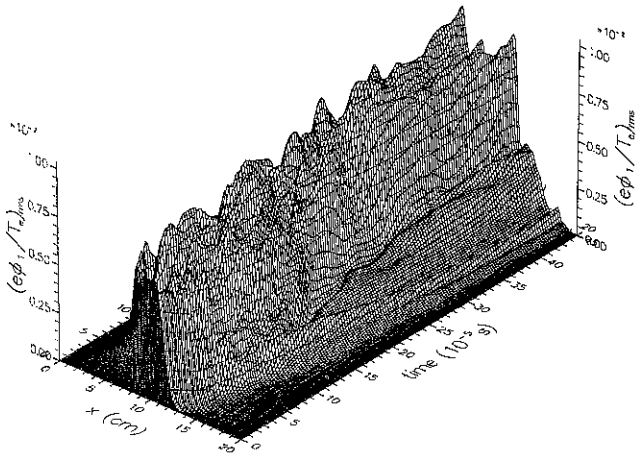

Figure 5: Time evolution of the x profile of $(e\phi_1/T_e)_{rms}$

These results show the influence of dv_{*e}/dx on the plasma perturbations. By increasing $\max(v_{*e})$ near the centre of the x axis with no flow along the x boundaries, the v_{*e} gradient is increased and the perturbations are more localised at the centre of the x axis. The coherent structures change amplitude when moving in the x direction.

The dual cascade of the generalised energy and enstrophy is observed. When the code is initialised with one mode, the cascade moves exclusively through the harmonics of this mode. The condensation in the lower generalised energy modes is mirrored in the generalised enstrophy spectrum.

References

[1] Horton W., Physics Reports **192** 1 (1990)
[2] Liewer P.C., Nuclear Fusion **25** 543 (1985)
[3] Arter W., Rep. Prog. Phys. **58** 1 (1995)
[4] Charney J.G., Geofys. Publ. Kosjones Norsk Videnskap. Akad. Oslo **17** 1 (1948)
[5] Hasegawa A., Mima K., Phys. Rev. Lett. **39** 205 (1977), Phys. Fluids **21** 87 (1978)
[6] Hasegawa A., Maclennan C.G., Kodama Y., Phys. Fluids **22** 2122 (1979)
[7] Botha G.J.J., Ph.D. thesis (Univ. of London, April 1997)
[8] Prakash M., Chu C.K., Hasegawa A., Phys. Fluids **29** 2426 (1986)
[9] Von Rosenberg D.U., *Methods for the Numerical Solution of Partial Differential Equations*, (Elsevier, New York 1969), Appendix C.
[10] Arakawa A., J. Comp. Physics **1** 119 (1966)
[11] Hoffman J.D., *Numerical Methods for Engineers and Scientists*, (McGraw-Hill, Inc., New York 1993), p. 265.
[12] Terry P.W., Newman D.E., Phys. Fluids B **5** 2080 (1993)

THE EFFECT OF LOCALLY ENHANCED RESISTIVITY ON RECONNECTION IN A PLASMA

J.P. Wainwright, J.Aparicio, **M.G. Haines** and R.J. Hastie
Blackett Laboratory, Imperial College of Science, Technology and Medicine,
Prince Consort Road, London SW7 2BZ, United Kingdom.

Abstract
A 3-D resistive MHD code has been employed to model reconnection at the m=1, n=1 surface of a tokamak, in periodic cylindrical geometry. Large current densities are expected at this reconnection layer. In these simulations when the current density exceeds a critical value, the local resistivity is increased by a numerical factor which is chosen to approximate the effects of turbulent transport. It is found that the reconnection times for this type of simulation are comparable to the reconnection times for a plasma where the resistivity is enhanced everywhere. It is found that it is only the average value of resistivity in the layer which determines the reconnection rate.

Introduction

It is found that many reconnection processes occur on faster time scales than those predicted using the simplest models. In Tokamaks the basic model of the assumed reconnection behaviour shown by sawteeth is non-linear and was developed by Kadomtsev[1] based on the Sweet-Parker[2,3] model. There is now some doubt as to the MHD nature of sawteeth but much can still be understood from this basic model and its extensions.

There is experimental evidence that the resistivity in the reconnection layer is higher than expected[4] and this anomalous resistivity was believed to be due to turbulent effects. Turbulent activity has been seen during Tokamak sawtooth activity[5] though whether it is cause or effect is not clear. We have constructed a model where localised turbulence may be triggered by large drift velocities in the plasma. Large currents are expected at the reconnection layer, so this would seem to be a reasonable triggering mechanism. We have investigated the consequences of such a model.

Simulation details

Simulations have been performed using a code written by Peter Kirby[6] which solves the equations of resistive MHD in periodic cylindrical geometry. It is non-linear, 3D, spectral in the periodic co-ordinates and called MERCURY. The code was modified to include the temporal evolution of the radial resistivity profile. This model assumes that the density is uniform and constant and that the resistivity is a function of radius and time only.

If the drift velocity exceeds the sound speed by a factor of about 5 or so then we locally increase the resistivity according to the formula $\eta = \eta_s(1 + \kappa(J - J_c)/J_c)$, where η_s is the Spitzer resistivity, J_c is the threshold condition and κ is the enhancement factor ($\sim$50-100).

The simulation is set up with an initial q profile which is flat on axis and equal to about 0.7, rising to about 2 at the edge. The axial magnetic field was set to 1.5T, the total current to 3MA and the (mean) deuterium ion number density to $2.5 \times 10^{19} m^{-3}$. The Lundquist number was set to the computationally comparatively high value of 2.7×10^7. Although this value is less than that found in experiments it was the highest practical value with which to run the code. The periodic length of the cylinder was L=2 π R =18.85m, the radius of the cylinder was a=1m. With these values the radial Alfvén transit time τ_A is $0.2\mu s$, and all times in our results are normalised to this value.

Reconnection was monitored in three ways. Firstly the energy associated with the m=1, n=1 component of the radial magnetic field is followed in time. This is representative of the slow destruction of the mode structure. Secondly the poloidal flux surfaces in the plane of the perturbed magnetic field are examined to follow the evolution of the magnetic island structure. Thirdly the evoution of the cylindrical q is monitored in order to see changes in the equilibrium. The relation of this term to the 'true' safety factor can only be made when the magnetic flux forms a symmetric configuration, (it does not apply if there are two magnetic axes) but it has some meaning in the final and initial states.

	Normalising value of resistivity	Mean enhancement factor
a	η_0	–
b	$60\eta_0$	–
c	η_0	60
d	$\eta_0/4$	240
e	$\eta_0/4$	60

Table 1: This table details the simulations used in this paper. The normalising value of resistivity was $2.8 \times 10^{-8} \Omega m$.

Computational Results

The reconnection problem was studied by examing the evolution of a perturbed radial magnetic field applied to the equilibrium described above. The chosen perturbation had a magnitude equal to 5% of the maximum axial field and Fourier components m=1, n=1, creating an initial configuration with $q_0 < 1$. The initial behaviour of this plasma is to achieve an unreconnected helical state in about 30 τ_A (see Rosenbluth[7]). The Lundquist number, defined by the on axis resistivity of 2.8 10^{-8} Ωm^{-1}, was 2 10^7 and Kadomstsev theory[1] predicts a reconnection time of 1.4 ms or about 9000 τ_A. This is computationally expensive to follow and it is used as a reference simulation. Deviations from this simulation can be considered to be new effects and it will be refered to as the basic case. A configuration is defined to have reconnected when the magnetic energy in the perturbed mode has vanished and the island structure is found to have disappeared.

Figure 1a shows the difference in the evolution of the basic case and a simulation where the resistivity has been multiplied everywhere by 60. With an $S^{-1/2}$ scaling law this situation should reconnect in about 1000 τ_A, and such behaviour is found. The basic case shows little decay in the energy stored in the perturbation while the more resistive case is evolving to remove the mode. Figure 2a and Figure 2b show

the flux plots based on $\mathbf{B}^*$ and the evolution of the new core is clearly seen in the more resistive case.

In Figure 1b the previous results are compared to a simulation where the resistivity is triggered locally. The condition for the onset of anomalous resistivity was implemented as a threshold on the current density. If the current density anywhere in the grid exceeds the average local current density by 40% then the resistivity at that radius is multiplied by a factor $(1 + \kappa(J - J_c)/J_c)$. The simulation shown has κ=60 but it was found that the maximum value of resistivity in the layer is of order 100 times the axial resistivity, though this settles down to about 60 times greater.It is found that the behaviour of this simulation is essentially the same as a simulation where the resistivity is multiplied by 60 everywhere and that it appears to be the resistivity in the layer which defines the evolution of the mode. This would imply that highly collisionless plasmas could have fast reconnection times if the reconnection in the layer was dominated by anomalous effects.

Figure 1c compares the basic case with the case where the resisitivity was enhanced everywhere by 60 and a case where the resistivity enhancement was applied locally with κ=240 but where the backround resistivity was reduced by a factor of 4. This has the effect of making the resistivity in the layer comparable to the previous cases. It is found that the reconnection behaviour is almost identical, implying that it is the absolute value of resistivity in the layer which is important and not the resistivity gradient nor the resistivity outside the reconnection layer. This is further illustrated in Figure 1d which shows that if the enhancement is reduced by a factor 4 a much slower reconnection is observed. The flux plots for the simulations based on an axial resistivity 4 times lower than the basic case are shown in Figures 2d and 2e (enhancement factors 240 and 60 respectively).

Conclusions

We have found that the reconnection of a small $m = 1$ instability in a cylindrical Tokamak is determined almost entirely by the value of the resistivity in the reconnection layer which can be anomalously triggered by a locally high drift velocity. The effect seems to be independent of the resistivity gradient.

References

[1] B.B. Kadomtsev, Sov.J.Plasma Phys., **1** 389 (1975)
[2] P.A. Sweet, Nuovo Cimento Suppl., **8** 188 (1958)
[3] E.N. Parker, Journal of Geophysical Research, **62(4)** 509 (1957)
[4] D.K. Baum et al., Phys.Fluids, **16** 226 (1972)
[5] J. Andreoletti et al., Plasma Phys. and Controlled Fusion, **31(4)** 643 (1989)
[6] P. Kirby, Computer Physics Communications, **47** 17 (1987)
[7] M.N. Rosenbluth et al., Phys.Fluids, **17** 1894 (1973)

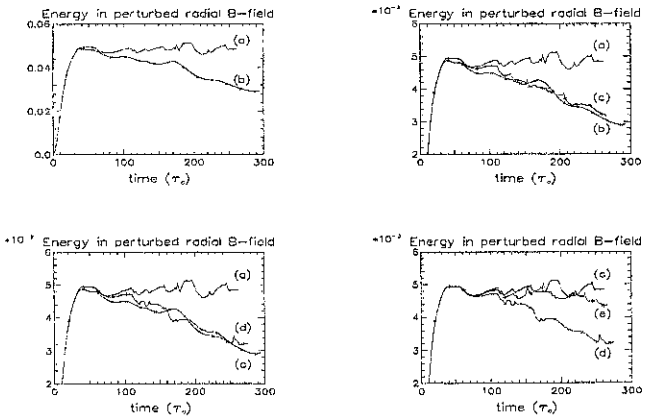

Figure 1: *These graphs show the evolution of the magnetic energy stored in the radial magnetic field of the instability. Simulation times are in Alfvén times and the simulations are detailed in Table 1.*

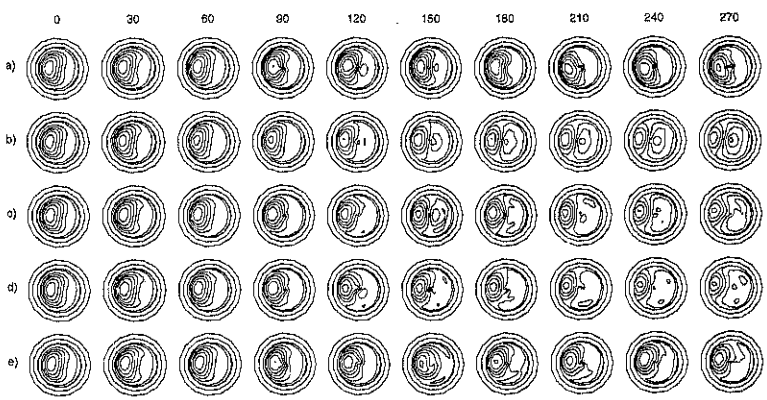

Figure 2: *These graphs show the flux surfaces defined by the field in the plane of the instability. Simulation times are in Alfvén times and the simulations are detailed in Table 1.*

Neoclassical Theory of Poloidal Rotation Damping

R. C. Morris, M. G. Haines, R. J. Hastie
Plasma Physics, Imperial College, London, SW7 2BZ, United Kingdom.

1. Introduction

The rate of decay of poloidal flow $U_\theta(t)$ in a tokamak in the banana regime has been a source of contention since 1972 when the first attempt was made to determine a characteristic damping time τ_p. Since then references [1]-[6] have calculated the value of τ_p such that $\tau_p \sim \epsilon^n \tau_{ii}$, where $n = 1, 1.5, -.5, 0, .5, 1$ respectively. The present work attempts to unify the result as much as possible by treating the damping calculation as an initial value problem.

The tokamak is modelled in the drift regime $\delta << 1$, where δ is the ratio between the ion Larmor radius ρ and the plasma scale length L, and also in the banana regime $\eta << 1$, where η is the ratio between the bounce time τ_b and the ion-ion collision time τ_{ii}. Flux coordinates (ψ, θ, ϕ) are used such that the magnetic field can be written $\mathbf{B} = \nabla\phi \times \nabla\psi + I(\psi)\nabla\phi$.

2. Background Theory

To first order in δ the flows in a tokamak plasma are within a flux surface. Since toroidal momentum is conserved a small change in the parallel flow $u_\parallel$ leads to a large readjustment in the radial electric field Φ' and it is this component of the poloidal flow which is seen to change.

The parallel flow evolves according to the surface averaged parallel component of the ion, momentum balance equation given by the expression

$$m_i n_i \frac{\partial}{\partial t}\langle \mathbf{B}\cdot\mathbf{u}_i\rangle = -\langle \mathbf{B}\cdot\nabla\cdot\mathbf{\Pi}_i\rangle, \tag{1}$$

where $\mathbf{\Pi}$. The parallel stress can be written as a velocity moment of the gyro-averaged, ion distribution function $\bar{f}_i$

$$\langle \mathbf{B}\cdot\nabla\cdot\mathbf{\Pi}\rangle = \langle Bm\int \mathbf{dv}\, v_\parallel^2\, \hat{\mathbf{n}}\cdot\nabla\bar{f}_i\rangle. \tag{2}$$

Now $\bar{f}_i$ is found by solving the *Drift Kinetic Equation*, which is written

$$\frac{\partial \bar{f}_i}{\partial t} + (\mathbf{v}_\parallel + \mathbf{v}_d)\cdot\nabla\bar{f}_i - e(\mathbf{v}_\parallel + \mathbf{v}_d)\cdot\mathbf{E}\frac{\partial \bar{f}_i}{\partial w} = C\{\bar{f}_i\}, \tag{3}$$

where w is the kinetic energy, $\mathbf{v}_d$ is the guiding-centre drift, $C\{f\}$ is the collision operator, and $\mathbf{E}$ is the electric field. The solution of equation (3) is achieved by expanding the distribution function in terms of the parameters δ and η such that

$$\begin{aligned} f &= f_0 + f_1 + \cdots \quad \text{where} \quad f_1 \sim \delta f_0 \\ f_1 &= f_1^{(0)} + f_1^{(1)} + \cdots \quad \text{where} \quad f_1^{(1)} \sim \eta f_1^{(0)}. \end{aligned} \tag{4}$$

It is well documented ([1]-[6]) that the use of these expansions leads to the first order distribution function $f_1^{(0)}$ being given by the solution to the *banana constraint equation*

$$\left\langle \frac{B}{v_\parallel}\left[C\{f_1^{(0)}\} - \frac{\partial f_1^{(0)}}{\partial t}\right]\right\rangle = 0. \tag{5}$$

3. Analytical Solution

The initial value nature of the problem can now be exploited by performing a Laplace transform of equation (5). On very short time scales ($\nu_{ii}/s << 1$), where s is the Lplace parameter, only those particles in a narrow layer of pitch-angle space adjacent to the trapped passing boundary can contribute to the damping process. Therefore the collision terms are neglected everywhere outside of this boundary layer. The distribution function $\bar{g}(s)$ at early times in the boundary layer can then be written

$$\bar{g}(s) = \left[1 - e^{-\sqrt{\frac{s}{\nu_{ii}}}(\lambda_c - \lambda)}\right]\left[\frac{Im}{TsD}(s\bar{\Phi}'(s) - \Phi'(t=0)) - \frac{g(t=0)}{s}\right], \tag{6}$$

where $\lambda = \mu/w$ is the pitchangle variable, $D = \langle B/\sqrt{1-\lambda B}\rangle$. Using this expression to calculate the stress in equation (2) and taking a Gaussian centred at $\lambda = \lambda_0$ for the initial distribution function, the resulting damping rate of the radial potential gradient is given by

$$\frac{\partial \Phi'(t)}{\partial t} \propto \sqrt{\frac{\epsilon\nu_{ii}}{t}}\, e^{-\alpha(\lambda_0 - \lambda_c)^2}, \tag{7}$$

where α is an arbitrary constant.

4. Numerical Solution

Equation (5) is now solved numerically for arbitrary time scales so that all collision terms are retained. Cranck-Nicholson differencing is used together with a *forward recursion, back solve* technique outlined in reference [7]. Internal boundary conditions express the continuity of the distribution function and conservation of flux (in λ) at the trapped passing boundary.

Figure 1 shows two contrasting initial distributions sketched in pitch-angle space. Here $\lambda_c = 1/B_{max}$ and marks the trapped-passing boundary and $\lambda_m = 1/B_{min}$ represents the far trapped region

Figure 1: *Initial distributions 1 and 2 in λ-space.*

In 1) the majority of the particles are situated deep in co-passing space whilst in 2) the bulk are close to the trapped-passing boundary. The decay of poloidal flow for each

of the initial conditions above is shown in figure 2. In each case an exponential fit has been attempted and the associated characteristic decay time τ_p is given with the figure.

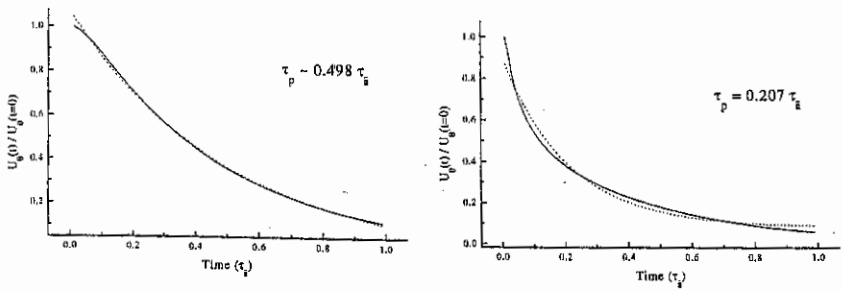

Figure 2: *The poloidal flow decay curves for initial conditions of figure 1*

For each of these runs the inverse aspect ratio ϵ was kept constant at a value of 0.3. However as ϵ was varied the decay curves altered and the variation for initial condition 1) is illustrated in figure 3.

Finally Figures 4 and 5 show the initial condition used by the previous authors and its numerical evolution.

5. Conclusions

The rate of decay of the poloidal flow in a tokamak has been found to have an analytic time dependence of $1/\sqrt{t}$. This singular behaviour arises from the collisional diffusion through pitch angle space of particles within a thin layer adjacent to the trapped-passing boundary. The result is confirmed numerically by comparison of the evolution curves in Figure 2. Here the decay of initial condition 1 is slow and virtually exponential whereas condition 2 decays rapidly at $t = 0$. Indeed as the localisation of the initial distribution to the boundary layer increases Figure 6 shows the increasing initial decay rate.

The analytic decay is proportional to $\sqrt{\epsilon}$ suggesting a relation to the fraction of trapped particles. However at later times when the decay is exponential Figure 3 shows a weak $\epsilon^{-0.12}$ dependence which gets weaker still at later times. That is, the asymptotic flow

Figure 3: *Variation of decay curves with* ϵ.

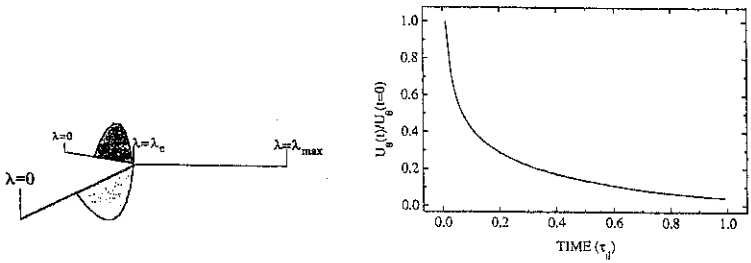

Figure 4: *Initial condition 3 and its poloidal flow decay curve*

tends to independence.

Initial condition number three is that used by the previous authors. However they consider a self-consistent decay reminiscent of the asymptotic decay of the present work. In fact the initial evolution of condition three exhibits almost singular decay predicted by the analytic theory.

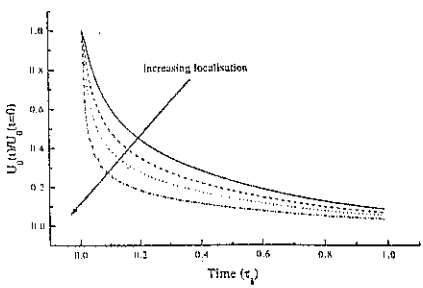

Figure 5: *Decay curves for increasing localisation*

References

[1] Stix T.H., *Phys.Fluids* **16** 1260 (1972)
[2] Hirshman S.P., *Nucl.Fusion* **18** 917 (1978)
[3] Callen J.D., *Culham Lab. Report* (1978)
[4] Shaing K.C. et al, *Phys.Fluids* **B1** 705 (1989)
[5] Taguchi M., *Plasma Phys.Controlled Fusion* **33** 859 (1991)
[6] Hsu C.T. et al, *Phys.Plasmas* **1** 132 (1994)

The Inward Heat Pinch

R. C. Morris, M. G. Haines, R. J. Hastie
Plasma Physics, Imperial College, London, SW7 2BZ, United Kingdom.

1. Introduction

This work is motivated by the experimental results on the DIII-D tokamak [1] in which electron cyclotron heating (ECH) is absorbed half way out from the minor axis and yet the electron temperature profile shows strong peaking on axis. That is, electron heat energy appears to flow up the temperature gradient.

Whilst linear, neoclassical theory [2,3] fails to predict such a large result it is shown here that a non-linear approach [4] can account for a substantial changes in the neoclassical transport coefficients.

First, the class of electrons responsible for the heat pinch is defined, and it is shown that the toroidal electric field E_ϕ can generate such a population. Subsequently the isotropic part of the electron distribution function is found to be driven to a non-Maxwellian form by the non-linear perturbation f_ϕ, and this is used to calculate the neoclassical transport coefficients.

2. Suprethermal Electron Population

The mechanism by which the electrons move in towards the minor axis of the tokamak vessel in the banana collisional regime is the neoclassical Ware pinch [5] of the trapped electrons. In order that the electrons arrive at the centre with sufficient energy to affect the temperature gradient they must have energies intermediate to the electron-electron downscatter and runaway conditions as illustrated in Figure 1 [4].

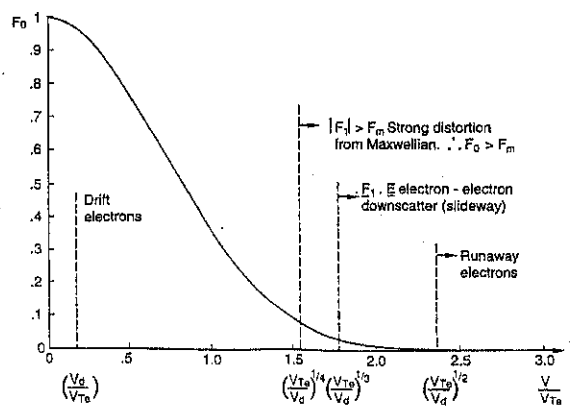

Figure 1: *Region of energy space occupied by pinch electrons [4].*

For a Maxwellian distribution the proportion of electrons at such energies would be insignificant, hence we require a mechanism to drive electrons out to these energies and sustain them. We consisder the effects of a toroidal electric field on the elelctron distribution function (f^e). When the latter is subject to a tensor expansion thus [6]

$$f_e = f_0(v) + \frac{\mathbf{f_1}(v)\cdot\mathbf{v}}{|v|} + \frac{\mathbf{f_2}(v):\mathbf{vv}}{|v|^2} + \cdots, \tag{1}$$

the Fokker-Planck equation to zeroth and first order is written

$$\frac{\partial f_0}{\partial t} - \frac{1}{3v^2}\frac{\partial}{\partial v}\left(\frac{eE_\phi}{m}v^2 f_\phi\right) = C\{f_\phi\}, \tag{2}$$

and

$$\frac{\partial f_\phi}{\partial t} = \left(\frac{eE_\phi}{m}\right)\frac{\partial f_0}{\partial v} + C\{f_\phi\}. \tag{3}$$

Here f_ϕ is the toroidal component of $\mathbf{f_1}(v)$, that is, the part of the distribution function driven directly by the electric field.

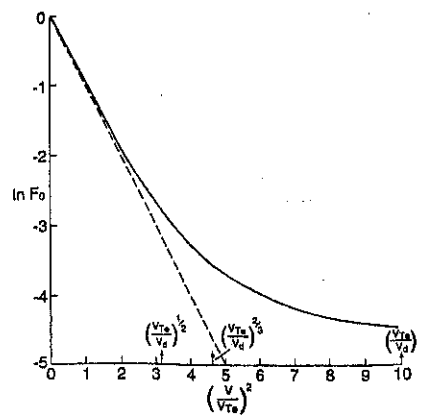

Figure 2: *Departure of f_ϕ from Maxwellian form [4].*

We neglect the time dependence of f_ϕ and the electron-electron collision term in equation (3) so that the first order perturbation takes the form

$$f_{1\phi} = \left(\frac{E_\phi}{E_D}\right)\frac{\partial f_0}{\partial v}. \tag{4}$$

This is now substituted into equation (2) to give

$$\frac{\partial f_0}{\partial t} - \frac{1}{3v^2}\frac{\partial}{\partial v}\left[\left(\frac{E_\phi}{E_D}\right)^2 v^5 \frac{\partial f_0}{\partial v}\right] = C^{ee}\{f_\phi\}. \tag{5}$$

By neglecting the electron-ion contribution to the collisonal energy diffusion and evaluating the Rosenbluth potentials with a Maxwellian distribution we find that the equation can be solved analytically [4] to give

$$\ln f_0 = -\int_0^\infty \frac{dx}{1+H(x)}, \tag{6}$$

where $H(x) = 4/3\,(E_\phi/E_D)/[(\sqrt{\pi}/2)\,\mathrm{erf}\{\sqrt{x}\} - \sqrt{x}\exp\{x\}]$. The departure of this function from a Maxwellian is illustrated in Figure 2. It shows a non-Maxwellian tail, a result of the perturbed distribution being non-linear at high energies.

This departure is confirmed by a numerical solution of equation (2), where the Rosenbluth potentials are calculated with the actual non-Maxwellian distribution

3. Transport Calculation

The perturbation f_ϕ is non-linear, that is $f_\phi \geq f_0$ only at high energies, hence any expansion of the distribution function must be velocity dependent.

This is in contrast to the parameter $\delta = \rho/L$ (ρ is the electron larmor radius and L is the plasma scale length) which is used to order the perturbation in neoclassical transport and is applied independent of energy. Under this ordering the problem is stricly linear and the electric field terms enter only as a linear peturbation.

In the present calculation we wish to include the non-linear effects of the electric field. However our chief interest is in the production of a non-Maxwellian tail in f_0. Any other electric field related effects are already included in the linear transport calculation at $O(\delta)$. Therefore as long as the high energy tail is established on a time scale which is short compared to the transport time scale we can use the form in equation (6) for the neoclassical ground state distribution function.

We note that the non-Maxwellian distribution function is established on a time scale defined by

$$\frac{\partial f_0}{\partial t} \sim \nu_{ee}, \tag{7}$$

where as the transport ordering implies

$$\frac{\partial f}{\partial t} \sim \delta^2 \nu_{ee}. \tag{8}$$

The neoclassical transport calculation is conducted in the thirteen moment approximation [3,7] and is analogous to its *Maxwellian* counterpart. The noteworthy differences between this and standard neoclassical transport fall into two categories.

(i) All friction and viscosity coefficients are altered. These modifications are in generally small(a few %) and affect all the transport coefficients similarly. The effects of these changes have not been qualitatively determined but do lead to the breaking of Onsager symmetry.

(ii) A new thermodynamic driving term appears in the heat flux equation, leading to the appearance of new components int the tranport coefficients.
The transport equations can be expressed thus:

$$\langle \Gamma_e^{\psi} \rangle = -\left[\alpha_{11}^e \left(\frac{n'}{n}\right) + \alpha_{13}^e \left(\frac{T_e'}{T_e}\right) + \alpha_{13}^i \left(\frac{T_i'}{T_i}\right) + \alpha_{14}^e \langle E_{\|} B \rangle + \alpha_1^e \left(\frac{P_e'}{P_e}\right)\right], \tag{9}$$

$$\langle q_e^{\psi} \rangle = -\left[\alpha_{31}^e \left(\frac{n'}{n}\right) + \alpha_{33}^e \left(\frac{T_e'}{T_e}\right) + \alpha_{33}^i \left(\frac{T_i'}{T_i}\right) + \alpha_{34}^e \langle E_{\|} B \rangle + \alpha_3^e \left(\frac{P_e'}{P_e}\right)\right], \tag{10}$$

Here the extra terms are given as gradients of the electron pressure tensor and the coefficients, α_1^e and α_3^e will formally be added to the density and electron temperature gradient terms. For a value of $E/E_D = 0.03$ the new coefficients are related to the ∇T_e thus coefficients $\alpha_1^e = -0.29\alpha_{13}^e$ and $\alpha_3^e = -0.29\alpha_{33}^e$

4. Conclusions It has been shown that a nonlinear treatment of the isotropic component of the electron distribution function can significantly alter the neoclassical transport coefficients, with new inward heat flux terms appearing in the final flux force equations. The new terms act to reduce the outward diffusive component of the heat flux and to increase the inward density gradient driven component. There is also a similar effect in the particle flux equation although the effect is smaller due to the smallness of the underlying non-diffusive coefficient.

The transport matrix no longer exhibits onsager symmetry. The symmetry breaking occurs between the friction and viscosity coefficients separately. Also the extra terms in the transport equations introduce asymmetry.

Whilst more work is required to find the electric field required to reverse the heat flow it is clear that the non-linear theory preented here makes a significant impact upon neoclassical transport.

References

[1] Luce T.C., Petty C.C., de Haas J.C.M., *Phys.Rev.Letts* **68** 52 (1991)
[3] Hinton F.L., Hazeltine R.D., *Rev.Mod.Phys***43** 239 (1976)
[2] Hirshman S.P., Sigmar D.J., *Nucl.Fusion* **21** 1079 (1981)
[4] Haines M.G., *Plasma Phys.Controlled Fusion* **38** 897 (1996)
[5] Ware A.A.,*Phys.Rev.Letts* **53** 262 (1970)
[6] Shkarovsky I.P.,*Can.J.Phys* 41 1753 (1963)
[7] Balescu R.,*Transport Proccesses in Plasmas*, Vol.2, North-Holland (1988)

Beam Tracing of Electromagnetic Waves in Inhomogeneous Plasmas

G.V. Pereverzev

Max-Planck-Institut für Plasmaphysik, EURATOM Association
Boltzmannstr. 2, D-85748 Garching, Germany

1. Introduction

A number of papers [1-8] have been published recently which are devoted to the role of diffraction effects in the propagation of RF waves in plasmas. Most of them [1-4] are based on the concept of the complex eikonal and are therefore restricted to a particular form of the wave packet. In [6] a general solution is found which is, however, restricted to the special case of electrostatic oscillations only. In [7] the consideration is quite general but the resulting equations are still rather complicated. In this report we present a method for describing electromagnetic waves in an arbitrary anisotropic inhomogeneous plasma. The relation of the method to other known techniques is also discussed.

2. Asymptotic solution

Consider the Maxwell equation

$$\left(\hat{\nabla} \times \left(\hat{\nabla} \times \mathbf{E}\right)\right) - \kappa^2 \hat{\varepsilon} \mathbf{E} = 0 \tag{1}$$

where $\hat{\varepsilon}$ is the dielectric tensor of a cold plasma, $\hat{\nabla} = L\nabla$, L is the characteristic length of the medium inhomogeneity and $\kappa = \omega L/c \gg 1$ is a large parameter. An asymptotic solution to Eq. (1) is sought in the form of the Gaussian beam of the n-th order

$$\mathbf{E}(\mathbf{r}) = e^{i\kappa s(\mathbf{r})} \left(\varphi_n \mathbf{a}(\mathbf{r}) - i\kappa^{-1/2} \varphi_n' \mathbf{b}(\mathbf{r}) - \tfrac{1}{2}\kappa^{-1} \varphi_n'' \mathbf{c}(\mathbf{r}) - i\kappa^{-1} \varphi_n \mathbf{d}(\mathbf{r}) + \mathcal{O}(\kappa^{-3/2})\right), \tag{2}$$

where $\varphi_n = \varphi_n(\sqrt{\kappa} w(\mathbf{r}))$ is the function of the parabolic cylinder. Expression (2) contains two unknown scalar functions $s(\mathbf{r})$, $w(\mathbf{r})$ and four vector functions $\mathbf{a}(\mathbf{r})$, $\mathbf{b}(\mathbf{r})$, $\mathbf{c}(\mathbf{r})$, $\mathbf{d}(\mathbf{r})$. It is assumed that all these functions together with their spatial derivatives are of order κ^0. However, $\hat{\nabla}[\varphi_n(\sqrt{\kappa} w)] = \sqrt{\kappa}\, \varphi_n' \hat{\nabla} w = \mathcal{O}(\sqrt{\kappa})$.

Expression (2) gives a particular solution to Eq. (1). In the 2D case, the general solution to the problem can be constructed as a linear combination of the beam modes (2). In some special cases, Eq. (2) can also yield a particular 3D solution. However, the general solution for the 3D case requires some additional terms in expression (2). This generalization will be considered in the extended version of this report. Here we restrict ourselves to the simplified expression (2) and investigate the existence of the solution in the form (2). A solvability condition is found which provides a set of equations for the unknown functions $s(\mathbf{r})$ and $w(\mathbf{r})$. Explicit expressions for the vectors $\mathbf{a}$ and $\mathbf{b}$ are also presented. With minor changes the derivation given here is valid also for a general 3D case. Moreover, the method can be easily extended to the case of hot plasmas.

On straightforward substitution Eq. (2) into Eq. (1), using the property of the functions of the parabolic cylinder $[\varphi_n'' + (2n+1-\kappa w^2)\varphi_n]N\mathbf{a} = 0$, with N being an arbitrary nonzero function, one obtains

$$\begin{aligned}\kappa^2\varphi_n\left(\hat{L}-\tfrac{1}{2}Nw^2\right)\mathbf{a} - i\kappa^{3/2}\varphi_n'\left(\hat{L}^{\perp}\mathbf{a}+\hat{L}\mathbf{b}\right) - \tfrac{1}{2}\kappa\varphi_n''\left(\hat{L}^{\perp\perp}\mathbf{a}+2\hat{L}^{\perp}\mathbf{b}+\hat{L}\mathbf{c}-N\mathbf{a}\right)\\ -i\kappa\varphi_n\left[\hat{L}\mathbf{d}+\hat{M}[\mathbf{a}]+iN\left(n+\tfrac{1}{2}\right)\mathbf{a}\right]+\mathcal{O}(\sqrt{\kappa})=0\end{aligned} \tag{3}$$

where the differential operator $\hat{M}[\mathbf{A}] = 2\left(\hat{\nabla}s\cdot\hat{\nabla}\right)\mathbf{A} - \hat{\nabla}s\left(\hat{\nabla}\cdot\mathbf{A}\right) - \hat{\nabla}\left(\hat{\nabla}s\cdot\mathbf{A}\right) + \mathbf{A}\hat{\nabla}^2 s$ and the algebraic operators

$$\hat{L}\mathbf{A} = \left(\hat{\nabla}s\times\left(\mathbf{A}\times\hat{\nabla}s\right)\right) - \hat{\varepsilon}\mathbf{A} = \left(\hat{\nabla}s\cdot\hat{\nabla}s\right)\mathbf{A} - \hat{\nabla}s\left(\hat{\nabla}s\cdot\mathbf{A}\right) - \hat{\varepsilon}\mathbf{A}, \tag{4}$$

$$\hat{L}^{\perp}\mathbf{A} = 2\left(\hat{\nabla}s\cdot\hat{\nabla}w\right)\mathbf{A} - \hat{\nabla}w\left(\hat{\nabla}s\cdot\mathbf{A}\right) - \hat{\nabla}s\left(\hat{\nabla}w\cdot\mathbf{A}\right), \tag{5}$$

$$\hat{L}^{\perp\perp}\mathbf{A} = 2\left(\hat{\nabla}w\cdot\hat{\nabla}w\right)\mathbf{A} - \hat{\nabla}w\left(\hat{\nabla}w\cdot\mathbf{A}\right) - \hat{\nabla}w\left(\hat{\nabla}w\cdot\mathbf{A}\right) \tag{6}$$

are introduced.

Equation (3) is fulfilled within the accuracy of $\mathcal{O}(\kappa^{-3/2})$ if the coefficients at higher powers of κ are equated to zero

$$\hat{L}\mathbf{a} = \tfrac{1}{2}Nw^2\mathbf{a}, \qquad \hat{L}\mathbf{b}+\hat{L}^{\perp}\mathbf{a}=0, \qquad \hat{L}\mathbf{c}+2\hat{L}^{\perp}\mathbf{b}+\hat{L}^{\perp\perp}\mathbf{a}=N\mathbf{a}, \tag{7}$$

$$\hat{L}\mathbf{d}+\hat{M}[\mathbf{a}]+iN\left(n+\tfrac{1}{2}\right)\mathbf{a} = \mathcal{O}(\kappa^{-1/2}). \tag{8}$$

We investigate now the solvability of the set of equations (7)-(8).

3. Solvability conditions

Consider first an auxiliary eigenvalue problem for the algebraic operator $\hat{L}$

$$\hat{L}\mathbf{e} = \left(\hat{\nabla}s\cdot\hat{\nabla}s\right)\mathbf{e} - \hat{\nabla}s\left(\hat{\nabla}s\cdot\mathbf{e}\right) - \hat{\varepsilon}\mathbf{e} = \lambda\mathbf{e}. \tag{9}$$

with $\mathbf{e}$ being a unit vector. The operator $\hat{L}$ is Hermitian and, therefore, it has three real eigenvalues $\lambda_0, \lambda_1, \lambda_2$. We assume that only one of them, e.g. λ_0, further denoted as H, can vanish. In general, H is not necessarily zero, and Eq. (9) represents an identity in some domain of a 6-dimensional phase space $\{\mathbf{r}/L,\ \hat{\nabla}s\} = \{x^\alpha,\ s_\beta\}$. It means that the identity can be differentiated in this phase space with respect to any of 6 variables x^α, s_β, while holding the other 5 fixed. Hereafter it is assumed that all Greek indices take values 1, 2, 3. The summation convention with respect to every repeated index over the range $\alpha = 1,2,3$ is implied. Let the Greek subscripts denote partial derivatives with respect to x^α, so that $s_\alpha = \partial s/\partial x^\alpha$, $w_\alpha = \partial w/\partial x^\alpha$, and so on. The Greek superscripts will denote partial derivatives with respect to s_α at x^α fixed: $H^\alpha = \partial H/\partial s_\alpha$, $H^{\alpha\beta} = \partial^2 H/\partial s_\alpha \partial s_\beta$, $\mathbf{e}^\alpha = \partial\mathbf{e}/\partial s_\alpha$, $\hat{L}^\alpha = \partial\hat{L}/\partial s_\alpha$, ... Making use of these notations, one can express the operators $\hat{L}^\perp$ and $\hat{L}^{\perp\perp}$ in Eqs. (5)-(6) as $\hat{L}^\perp = w_\alpha\hat{L}^\alpha$ and $\hat{L}^{\perp\perp} = w_\alpha w_\beta\hat{L}^{\alpha\beta}$, respectively, and also introduce the new quantities

$$H^\perp = w_\alpha H^\alpha, \qquad H^{\perp\perp} = w_\alpha w_\beta H^{\alpha\beta}, \qquad \mathbf{e}^\perp = w_\alpha\mathbf{e}^\alpha, \qquad \mathbf{e}^{\perp\perp} = w_\alpha w_\beta\mathbf{e}^{\alpha\beta}. \tag{10}$$

Sequential differentiation of Eq. (9) with respect to s_α, followed by inner multiplication with w_α, yields

$$\hat{L}^\perp \mathbf{e} + \hat{L}\mathbf{e}^\perp = H^\perp \mathbf{e} + H\mathbf{e}^\perp, \qquad \hat{L}^{\perp\perp}\mathbf{e} + 2\hat{L}^\perp \mathbf{e}^\perp + \hat{L}\mathbf{e}^{\perp\perp} = H^{\perp\perp}\mathbf{e} + 2H^\perp \mathbf{e}^\perp + H\mathbf{e}^{\perp\perp}. \quad (11)$$

Turn now to the solvability conditions for Eq. (7). Comparing the first of them with identity (9), one sees that a nontrivial solution given by $\mathbf{a}(\mathbf{r}) = A(\mathbf{r})\mathbf{e}(\mathbf{r})$ exists if

$$H = \tfrac{1}{2} N w^2. \quad (12)$$

It is seen that the right hand side of Eq. (12) vanishes if and only if $w(\mathbf{r}) = 0$. Consequently, $H|_{w=0} = 0$ and, conversely, $H = 0$ implies $w(\mathbf{r}) = 0$.

A solution $\mathbf{b}$ to the second equation in (7) obviously exists when $\det(\hat{L}) \neq 0$ (which, in our case, is equvivalent to $H \neq 0$ or $w \neq 0$). Otherwise, if $\det(\hat{L}) = 0$, the solvability condition reads $\mathbf{e}^* \hat{L}^\perp \mathbf{a} = A\mathbf{e}^* \hat{L}^\perp \mathbf{e} = 0$. Making use of Eq. (11) and $\mathbf{e}^* \cdot \mathbf{e} = 1$, one rewrites the condition as $\mathbf{e}^* \hat{L}^\perp \mathbf{e} = H^\perp + H\mathbf{e}^* \cdot \mathbf{e}^\perp = 0$. It follows that the sufficient condition of solvability is $H^\perp\big|_{w=0} = 0$. As long as $\mathbf{b}$ exists, it is natural to require in addition that $\mathbf{a}^* \cdot \mathbf{b} = 0$, thus ensuring that the first order correction in Eq. (2) is orthogonal to the main term. It is easy to show that the additional requirement results in the extension of the validity domain for the previously found solvability condition to the whole space

$$H^\perp = \frac{\partial H}{\partial s_\alpha}\frac{\partial w}{\partial x^\alpha} = 0. \quad (13)$$

If Eq. (13) is fulfilled then $\mathbf{b}$ is given by $\mathbf{b}(\mathbf{r}) = A(\mathbf{r})\mathbf{e}^\perp(\mathbf{r})$.

In a parallel fashion one finds that the solution to the third equation in (7) exists when $N = H^{\perp\perp}\big|_{w=0}$ which determines the function N and can be used in Eq. (12). Finally, one should consider the solvability condition for equation (8) with respect to the unknown vector function $\mathbf{d}$. This gives a differential equation to the scalar function $A(\mathbf{r})$ similar to that of the conventional geometric optics [9].

We conclude that the sufficient condition for the existence of the solution (2) to the Maxwell equation (1) reads

$$H = \frac{1}{2}\left(\frac{\partial^2 H}{\partial s_\alpha \partial s_\beta}\frac{\partial w}{\partial x^\alpha}\frac{\partial w}{\partial x^\beta}\right)\Bigg|_{w=0} w^2, \qquad \frac{\partial H}{\partial s_\alpha}\frac{\partial w}{\partial x^\alpha} = 0. \quad (14)$$

Equation (14) represents the main result of this report. The problem of solving the second order partial differential Maxwell equation (1) is now reduced to the much simpler set of two first order partial differential equations (14) with respect to the unknown functions $s(\mathbf{r}), w(\mathbf{r})$.

It is easy to check that, similar to the conventional geometric optics, Eq. (14) is invariant with respect to multiplying H with any nonzero function $f(x^\alpha, s_\beta) \neq 0$. In particular, taking into account that $D = \det(\hat{L}) = H\lambda_1\lambda_2$ and $\lambda_1\lambda_2 \neq 0$ one can replace H in Eq. (14) by D. We will show now that other known asymptotic methods are included in Eq. (14) as particular cases.

4. Relation to other asymptotic methods

Geometrical optics. The approach of the geometrical optics [9] can be obtained by noting that Eq. (14) admits the trivial particular solution $w(\mathbf{r}) \equiv 0$. Then Eq. (14) reads $H(\nabla s, \mathbf{r}) = 0$, or, which is the same $\det(\hat{L}) = 0$. The latter, in turn, is the well-known dispersion relation of the geometric optics for a cold plasma.

Parabolic equation. In the method of the parabolic equation [10,7] the full wave equation is reduced in such a way that the corpuscular description is adopted along the direction of the group velocity while across this direction the usual wave description is retained. In our approach, the reduction is equivalent to the transition from Eq. (1) to Eq. (3).

Complex eikonal. The well-known solution in the form of a complex eikonal [11] is a particular case of Eq. (2) for $n = 0$ so that $\mathbf{E}(\mathbf{r}) = \exp\{i\kappa s(\mathbf{r}) - \kappa I(\mathbf{r})\}\,\mathbf{a}(\mathbf{r})$ where $I \equiv \frac{1}{2}[w(\mathbf{r})]^2$. In this case, Eq. (14) can be easily reduced to

$$H = \frac{1}{2}\frac{\partial^2 H}{\partial s_\alpha \partial s_\beta}\frac{\partial I}{\partial x^\alpha}\frac{\partial I}{\partial x^\beta}, \qquad \frac{\partial H}{\partial s_\alpha}\frac{\partial I}{\partial x^\alpha} = 0 \tag{15}$$

which coincides with the solvability condition of the complex eikonal method. For the anisotropic medium this result was first obtained by Mazzucato [1] who used the expansion technique requiring that $|\nabla I| \ll |\nabla s|$. The derivation above shows that this additional requirement is not necessary.

Beam tracing. The first order partial differential set of equations (14) coincides in form and sense with that obtained in [6] for the electrostatic case. Therefore, the consideration of [6] is fully applicable for the more general case of electromagnetic waves treated here. It is shown in [6] that without loss of generality the problem (14) can be further reduced to a set of ordinary differential equations similar to those of the geometric optics.

References

[1] E. Mazzucato, *Phys. Fluids,* **B1**, 1855, (1989).

[2] S. Nowak and A. Orefice, *Phys. Fluids,* **B 5**, 1945, (1993).

[3] A. V. Timofeev, *Plasma Physics Reports,* **21**, 610, (1995).

[4] A. G. Peeters, *Phys. Plasmas,* **3**, 4386, (1996).

[5] G. V. Pereverzev, *Nucl. Fusion,* **32**, 1091, (1992).

[6] G. V. Pereverzev, in: *Reviews of Plasma Physics,* ed. by B. B. Kadomtsev, Consultants Bureau, New York, 1996, Vol. 19.

[7] R. E. Aamodt, *Phys. Plasmas,* **1**, 6, (1994).

[8] A. G. Peeters, G. V. Pereverzev, E. Westerhof, *The 10-th Workshop on EC Emission and ECRH,* Ameland, The Netherlands, 6–11 April, 1997.

[9] I. Bernstein and L. Friedland, in: *Handbook of Plasma Physics,* ed. by M. N. Rosenbluth and R. Z. Sagdeev, North-Holland Publishing Company, Amsterdam, Vol. 1, 1983.

[10] M. A. Leontovich and V. A. Fock, in: *Electromagnetic Diffraction and Propagation Problems,* by V. A. Fock, Pergamon Press, Oxford, 1965, page 213.

[11] S. Choudhary and L. B. Felsen, *Proceedings of the IEEE,* **62**, 1530, (1974).

Plasma Modelling for PSI-1

H. Kastelewicz[1], D. Reiter[2], R. Schneider[3], D. Coster[3], H. Meyer[3]

[1]Humboldt-Universität, Berlin, Germany
[2]IPP, Forschungszentrum Jülich GmbH, EURATOM Association, Germany
[3]Max-Planck-Institut für Plasmaphysik, EURATOM Association, Germany

Introduction

In the axisymmetric device PSI-1 an electric high-current arc is used to produce a magnetically confined plasma column of 1.8m length and about 5 to 10 cm diameter outside of the anode.

Because of the particular ring-shaped design of the anode-cathode system and the effect of the magnetic field the plasma is actually generated off-axis within a narrow shell near the inner anode surface. As a consequence, pronounced hollow radial profiles are built up for the plasma density and temperature which may essentially be modified downstream the plasma column due to radial diffusion, axial streaming and the interaction with the neutrals background (recycling).

Previous modelling of the plasma by the authors using the B2–Eirene code package / 1 / have been resrticted to the plasma column outside the anode since the actual version of the B2 code does not allow for electric fields and currents. In these calculations the radial plasma profiles at the anode exit (electron and ion densities, electron and ion temperatures, ion velocities) are boundary conditions of the code which must be prescribed in any way.

In order to avoid this large set of mostly unknown boundary parameters, the anode-cathode region has been included in the present model in a simplified manner by prescribing explicitely the electron energy source due to the discharge current. The latter is strongly localized (bound to the magnetic field) and may reasonably be estimated. The plasma state is thus directly related to external discharge parameters (input power, gas influx rate).

PSI-1 model

Fig. 1 shows an axial cross-section of the device and the geometrical assumptions of the model.
Like in the experiment, the neutral gas (atoms or molecules) flows in through a concentric hole in the cathode bottom and is pumped in the target chamber and the differential pumping stage according to given pumping efficiencies. Under steady-state conditions (which are considered here), both, the net influx and the pumping rates are equal.

The B2 calculational grid is defined by the magnetic flux surfaces and its orthogonals and incloses axially the whole plasma volume between the cathode bottom and the neutralizer plate. As boundary conditions in the radial direction the decay length ($\lambda = 1cm$) of the ion densities, the electron and ion temperatures and the parallel velocities are prescribed; in the parallel direction (neutralizer plate, outer anode surface, cathode bottom) Bohm conditions are used.
The anomalous radial transport is described by the transport coefficients: $D_i = 0.5m^2/s$ (ion diffusion), $\kappa_{e,i}/n_{e,i} = 1.0m^2/s$ (heat conduction), $\eta_i/m_i n_i = 0.2m^2/s$ (viscosity).

In order to simplify the boundary conditions, the inner anode surface is assumed to be identical with a magnetic flux surface (axial co-ordinate line) and the geometrical structure of the cathode is neglected. Both approximations should hardly influence the plasma results, particularly in the column outside the anode. On the other hand, the assumed electron energy source (see Fig. 1), in this approximation, excludes parallel components of the discharge current hitting the anode surface and is not representative, therefore, for the total discharge power.

In this paper the source will be characterized by a constant electron temperature $T_{e,source}$ in the specified region or by the corresponding energy $P_{e,source}$ transfered there to the plasma electrons. The electron temperature in the source region and the neutral gas influx rate are the only external parameters of the model.

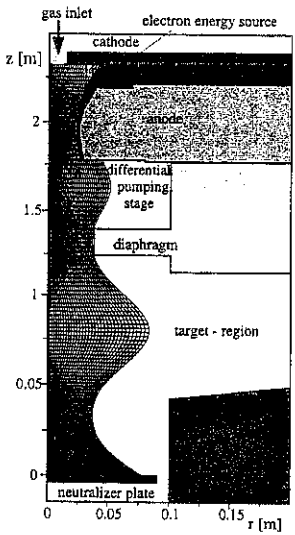

Fig. 1
Model system of the plasma generator PSI-1

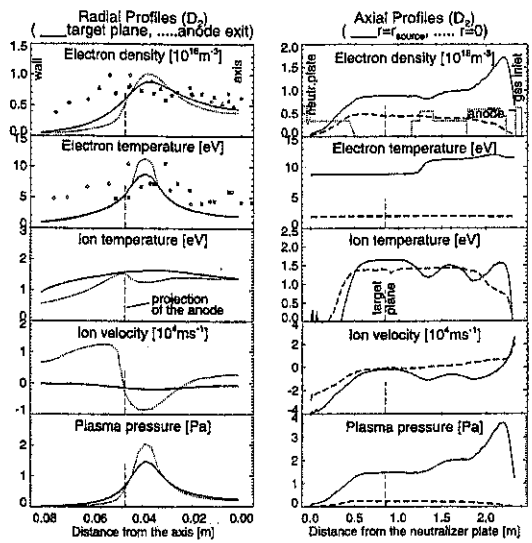

Fig. 2 Radial and axial plasma profiles for a D_2 plasma
The radial profiles at the anode exit (dotted lines) are projected along the magnetic field lines to the target plane. The axial profiles are along the magnetic flux surface just through the source region (full line) and at the column axis (dashed line).

Deuterium Plasma

We consider a steady state deuterium plasma for the following parameters:

Net gas influx rate: $F_{D_2} = 0.63 \times 10^{19} s^{-1}$

Electron source temperature: $T_{e,source} = 12eV \quad (P_{e,source} = 860W)$

The total ion and energy fluxes leaving the anode exit are in this case $F_{D^+} = 8 \times 10^{18} s^{-1}$

and $F_e = 250W$. The corresponding fluxes onto the neutralizer plate are $F_{D^+} = 1.7 \times 10^{19} s^{-1}$ and $F_e = 140W$ showing an enhanced ion flux due to local recycling. Some axial and radial profiles of essential plasma parameters are given in figs. 2.

In the target plane one gets radial plasma profiles which are in good agreement with experimental data (fig. 2). Comparing n_e in the target plane and at the anode exit one finds only a rather small flattening of the hollow profile. The relaxation effect of radial ion diffusion along the plasma column is largely compensated by two processes: (i) considerable ionization rates in the outer column layers with high electron temperature and (ii) near the symmetry axis, axial ion loss to the neutralizer plate but also – in the case of a deuterium plasma – to the anode side.

In this case an axial ion flow inversion back into the anode occurs near the column axis. The reason is a pressure gradient which is built up by "ion sources" due to radial inward diffusion and "sinks" at the neutralizer plate and the cathode bottom. If this flow reversal is artificially blocked or inverted by appropriate boundary conditions of the code (cf. / 1 /), a much steeper density profile at the anode exit ($n_{e,max}/n_{e,axis} \approx 5$) would be required to produce a profile like that of fig. 2 for the target plane.

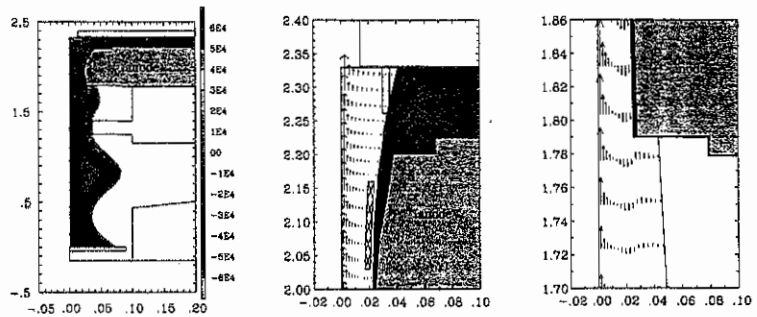

Fig. 3
Contour plot and arrow plot of the axial ion velocity showing flow reversal back to the anode.

Neutrals

The D and D_2 densities have steep gradients in the anode-cathode region but rather flat profiles in the column outside the anode due to the long mean free path of the neutrals. In the target chamber n_D increases radially in inward direction while n_{D_2} deceases due to the dissociation of molecules and the action of the wall (source for molecules and sink for atoms). The densities vary radially as $n_D \approx (1 \div 1.6) \times 10^{17} m^{-3}$ and $n_{D_2} \approx (2 \div 1.3) \times 10^{18} m^{-3}$, which roughly corresponds to an dissociation degree of 10% in the plasma column. The atom density agrees with mesurements with the two-photon spectroscopy but is smaller than results obtained by passive H_α spectroscopy. This discrepancy need still to be clarified. Uncertainties result in particular from the dissociation rates of vibrationally excited molecules.

The D_α radiation of the atoms has a clear hollow profile (as a consequence of the hollow T_e profile) with a maximum intensity of about $P_\alpha = 30 W/m^3$ in the target chamber.

Argon Plasma

The experimentally achieved densities for an argon plasma are usually higher than for deuterium. We consider here the following high-density case, but the principal results apply also for lower densities:

Net gas influx rate: $F_{Ar} = 7.8 \times 10^{19} s^{-1}$

Electron source temperature: $T_{e,source} = 12eV, \quad (P_{e,source} = 25kW)$

The total ion and energy fluxes out of the anode are $F_{Ar^+} = 1.3 \times 10^{19} s^{-1}$ and $F_e = 1.5kW$ and onto the neutralizer plate $F_{Ar^+} = 3.5 \times 10^{19} s^{-1}$ and $F_e = 250W$. The total radiated energy is $P_{rad} = 22kW$, the most part being radiated between anode and cathode.

In contrast to the deuterium plasma no hollow profiles for the electron density are found (even just outside the anode exit) and no ion flow inversion is built up. This is partly due to the more effective radial relaxation (smaller axial velocities) and the contribution of higher charge stages. Typical for the argon plasma is a very steep density decrease in the anode region.

In the target chamber the *neutral density* is nearly constant, $n_{Ar} \approx 1.0 \times 10^{19} m^{-3}$, and comparable with the ion density.

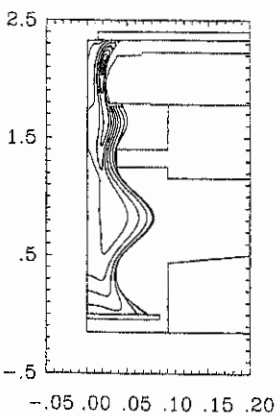

Fig. 4 Contourplot of the Ar line radiation (log. scale)

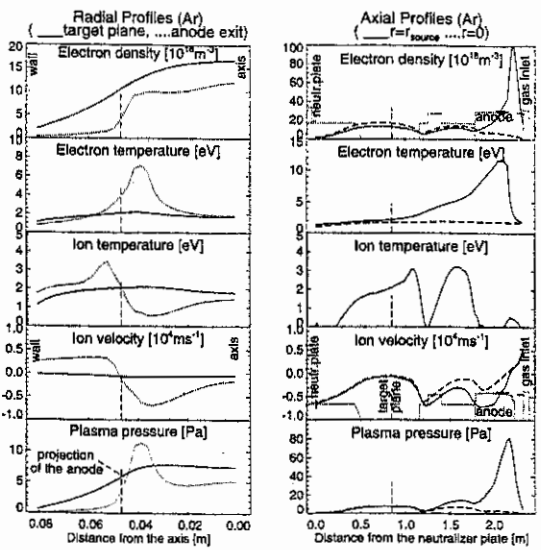

Fig. 5 Radial and axial plasma profiles for an Ar plasma

Reference

/ 1 / H. Kastelewicz, D. Reiter, R. Schneider et al., 23rd EPS Conf. on Fusion and Plasma Physics (Kiev,1996) p II-803

Sputtered Tungsten Atoms Investigated in a Linear Plasma Generator

J. Steinbrink, U. Wenzel, W. Bohmeyer, G.Fussmann and the PSI-Team
Max-Planck-Institut für Plasmaphysik, EURATOM Ass., D-10117 Berlin, Germany

Introduction

High Z materials are currently tested as an alternative to carbon as a plasma facing material [1]. Parts of the ITER divertor for instance are planned to be covered with tungsten. These activities call for reliable measurements of eroded fluxes. Most easily these fluxes can be determined by passive spectroscopy, provided the crucial atomic data, i.e. S/XB values, are available. In order to determine this important coefficient, that links the particle flux Γ to the photon flux I by

$$\Gamma = 4\pi \frac{S}{XB} I, \tag{1}$$

particular experiments have been performed in the plasma generator PSI-1.

The use of formula (1) is restricted to an experimental situation where the ionisation length λ_{ion} is small compared to the characteristic scale length of the plasma (for more details see [2]). In the experiment with $\lambda_{ion} = 2\,\mathrm{cm} - 4\,\mathrm{cm}$ this condition was only marginally met. For this reason it was necessary to model measured intensity profiles in front of a tungsten target to obtain the ionisation S and the excitation rate coefficient X separately. Since the branching ratio of the considered line is known ($B \approx 1$ taken from [3]), the S/XB-value can be calculated.

Experiment

A negatively biased tungsten target (1cm × 1cm) was exposed to the cylindrical plasma (radius ≈ 5cm) in the target chamber of the PSI-1 generator. The electron temperature T_e ranged from 2 eV to 20 eV and the electron densities n_e from $6 \cdot 10^{11}\mathrm{cm}^3$ to $7 \cdot 10^{12}\mathrm{cm}^3$, measured by a fast reciprocating Langmuir probe. The radial profile of the electron temperature tends to have a maximum at the plasma rim. By placing the target at this temperature peak of the plasma (see figure 1), we were able to measure the radiation of the eroded tungsten atoms up to electron temperatures of 17 eV. Different plasmas (D, He and Ar) were used to sputter the target. The target was biased negatively (U ranging from -35V to -330V) to give the plasma ions a kinetic energy (above threshold) to produce sufficiently high sputtering rates.

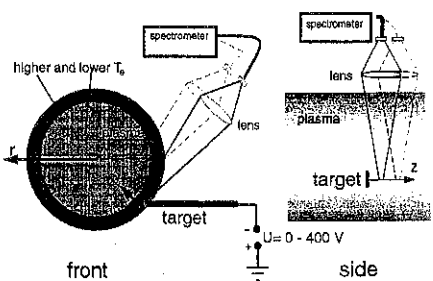

Figure 1: *A negatively biased tungsten target was exposed to the stationary plasma of the PSI-1 linear generator. To obtain intensity profiles spatial scans parallel to the y- and the z-axis with the line of sight were made.*

To determine the S/XB value, the tungsten flux Γ_W into the plasma has to be known. This flux was determined by the loss of weight of the target and dividing by the exposure time ($\approx$ 1h). The reduction of target mass was typically 0.5 to 2 % of the total target mass ($\approx 2\,g$) and could be weighed to an accuracy of $50\mu g$.

By measuring the ion flux Γ_{ion} to the target one can determine the sputtering yield $Y = \frac{\Gamma_W}{\Gamma_{ion}}$. For the different plasmas used the measured sputtering yields are compared to results obtained with ion beam experiments [4] in figure 2.

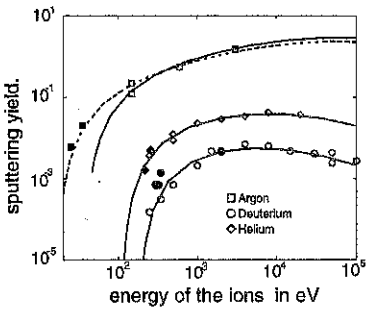

Figure 2: *The obtained sputtering yields (filled black) compared with results from ion beam experiments (open grey) [4]. All fits were obtained using the revised Bohdansky-formula [4].*

With a Czerny-Turner spectrometer and an attached multi-channel analyzer, spectra from 350 to 550nm were measured in front of the target. We observed 28 neutral tungsten lines including the most intense line at $\lambda = 400.9\,nm$. The lines of sight were scanned perpendicular (z-axis) and parallel (y-axis) to the target surface. The intensities were calibrated with an integrating sphere.

An example for an intensity profile perpendicular to the target surface (z-axis) is presented in figure 3. Most of the tungsten atoms leave the target in the ground state and are excited in the plasma. Within the electric sheath which can - depending on the bias voltage of the target - reach up to 2mm into the plasma, the electron density is very low. Consequently, the excitation is weak and the intensity rather small in front of the target. The decrease of intensity further away from the target is dominated by the ionisation of the neutral tungsten atoms and by the divergence of the neutral flux. Therefore, the decrease of the intensity includes information about the ionisation length λ_{ion} and the absolute intensity information about the excitation rate coefficient. The intensity profiles parallel to the target surface (y-axis) strongly depend on the angular distribution of the tungsten atoms. Due to the radial dependence of electron temperature, however, the determination of this distribution is not straight forward.

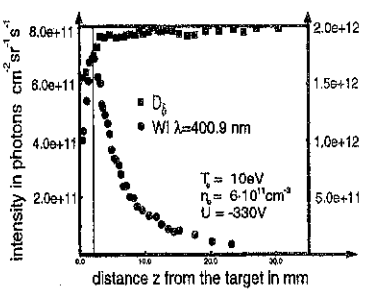

Figure 3: *Intensity profiles perpendicular to the target. The decrease close to the target ($z = 0$) is due to the poor excitation in the electric sheath. The reduction of the WI intensity away from the target is due to ionisation of neutrals and the divergence of the flux.*

Model

If we use a simple three-dimensional model to describe the intensity profiles, we can determine the ionisation rate coefficient S and the excitation rate coefficient X by fitting to the measured profiles. In the model the following assumptions are made:

- The atoms leave the target with an under-cosine (kidney-shaped) angular distribution f_θ. For such a distribution we achieved the best fit to the measured profiles. We choose a fitting function of the type $f_\theta = K \cos\theta \exp(\theta \tan(\theta_{max}))$, were K is the normalization factor and θ_{max} the angle under which the flux is maximal.

- Within the electric sheath ($z < z_0$) the electron density is taken to be zero, whereas $n_e = \text{const}$ is assumed within the observed plasma region ($z > z_0$).

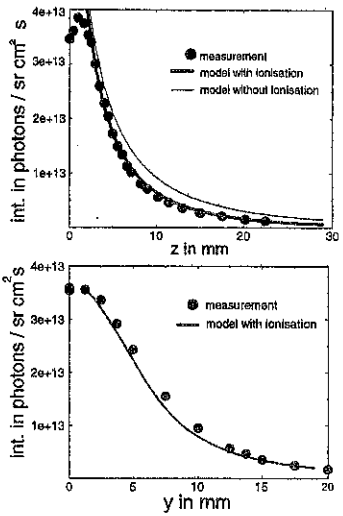

Figure 4: *The modeled intensity profile fits the measured values (here for an argon plasma $n_e = 3 \cdot 10^{12} cm^3$ and $T_e = 4eV$) very good.*

- The atoms leave the target with the average velocity v on a straight line (with coordinates r,θ). The reduction of the neutral density n along the line $\theta = \text{const}$ is described by the equation $\frac{\partial n}{\partial r} = \frac{n_e S}{v} n = \frac{n}{\lambda_{ion}}$ where v is calculated by averaging over the Thompson velocity distribution using the results from [5] to scale to the needed parameter for tungsten.

- After the atoms have entered the plasma, the density n_j of all excited levels is stationary.

The above assumptions lead to the following integral

$$I(z) = W_{ex} \int\int dF dl \frac{f_\theta}{r^2} \exp\left(-\frac{r - r_0}{\lambda_{ion}}\right) \tag{2}$$

for an intensity profile. The pathlength of the atoms in the electric sheath is $r_0 = \frac{z_0}{\cos(\theta)}$. The integration is carried out over the target surface (dF) and the line of sight (dl) considering the given geometric situation. The factor in front of the integral is given by

$$W_{ex} = \frac{1}{4\pi} X B n_e \frac{\Gamma}{v}; \tag{3}$$

it can be obtained by comparing the absolute values of the measurement with the calculated ones. The parameters θ_{max} and λ_{ion} are varied over a large range and the squared difference between model and measured profile is calculated . We find one single minimum for the squared difference as a function of the parameters for all results presented. An example for a fit is shown in figure 4. Using this method the coefficients of interest (S,X and $\frac{S}{XB}$) are given by

$$S = \frac{v}{n_e \lambda_{Ion}}, \quad XB = W_{ex} 4\pi \frac{v}{n_e \Gamma} \quad \text{and} \quad \frac{S}{XB} = \frac{\Gamma}{4\pi \lambda_{Ion} W_{ex}}. \tag{4}$$

The maximum error of these coefficients is dominated by the uncertainty in measuring the electron density $\pm 30\%$ and by the uncertainty with respect to the angular distribution of the neutral atoms. The latter case produces a maximum error for the ionisation length λ_{ion} of $\pm 20\%$.

Results

The experimental S/XB-values for the WI-line $\lambda = 400.9\,\mathrm{nm}$ and the ionisation rate coefficients S are presented in figures 5 and 6. S/XB has a maximum value of 24 ± 8 in the given range of the electron temperature. Note that the measured ionisation rate coefficient S, is substantially smaller (up to a factor of eight) than predicted by the Lotz-formula . Our values are about twice as large as the ionisation rates for WII measured by Montague et al. [6].

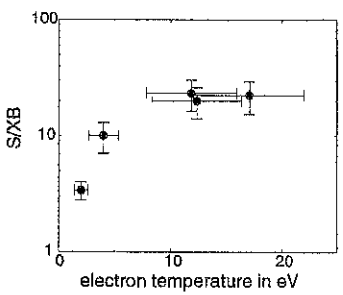

Figure 5: *S/XB is determined with a maximum value of* 24 ± 8.

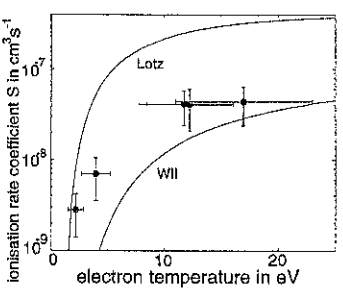

Figure 6: *The ionisation rate coefficient is substantially smaller than predicted by the Lotz-formula and a factor of two above the measured rate coefficient for WII (taken from [6]).*

References

[1] A. Thoma et. al., at this conference

[2] G. Fussmann et. al.,MPI für Plasmaphysik, IPP III/153, (Oct. 1989)

[3] E.A. Den Hartog et. al., J. Opt. Soc. Am. B,4(1),(January 1987)

[4] W. Eckstein et. al.,MPI für Plasmaphysik, **9/82**,(1993)

[5] H.L. Bay and B. Schweer, Jül-2032 Kernforschungsanlage Jülich GmbH;(1985)

[6] R.G. Montague and M.F.A. Harison,J. Phys. B: At. Mol. Phys.**17**, 2707-2771 ,(1984)

Cross-Field Diffusion by Charge Changing Collisions

G. Fussmann
Max-Planck-Institut für Plasmaphysik, Bereich Plasmadiagnostik
10117 Berlin, Mohrenstraße 41

Introduction

Transport of particles and energy across the magnetic field is still a poorly understood process in nuclear fusion research: The experimentally determined particle diffusion coefficients in such plasmas of typically D = 0.1 - 1 m^2/s are more than 100 times as large as those derived from classical theory which considers the random walk due to momentum exchanging collisions.
In this paper we consider a completely different type of transport which is caused by the sequence of ionization and recombination. For the multiple ionized ions the transport results from the fluttering of the gyro-radius. Most important, however, is the transport of protons initiated by recombination.
In the past the effect of recombination on transport has been investigated only with respect to charge transfer from impurity ions [1, 2], leading to very small effects. In contrast, the radiative recombination process considered here can produce substantial diffusion coefficients in hydrogen boundary density plasmas. In this paper we concentrate on the basic physics and demonstrate the importance of this particular transport mechanism by discussing the density build-up in the boundary region. A more extended description and the derivation of some of the expressions is given in [3].

Basic transport relations

In first order the particle flux densities are proportional to the gradient of the density n and the relation $\vec{\Gamma} = -D\nabla n$ defines the diffusion coefficient D. It is well known that the diffusion coefficient can be associated with a random walk process as follows:

$$D_x = \frac{1}{2} l^2 \nu \qquad (1)$$

where $l = (\langle \Delta x^2 \rangle_{av})^{1/2}$ is the average step size and ν is the characteristic frequency for the occurrence of the event causing the random walk. In a magnetized plasma the transport of the charged particles in the perpendicular direction is then associated with a change of their gyro-orbits and we obtain $D_\perp = 1/2\ (\Delta\rho)^2\ \nu$. The gyro-radius is connected with the perpendicular momentum $p_\perp$, the magnetic field B, and the charge q according to $\rho = p_\perp/qB$. Hence, there are two possibilities to produce diffusion: changing either the particle momentum (classical diffusion) or its charge.

Ion diffusion caused by fluttering of the charge state

Because the particles loose their identity (an atom may become an ion or vice versa) as a result of a charge changing collision, only the joint ambipolar transport of all particles according to

$$\vec{\Gamma} = -D\nabla n \quad \text{with} \quad n = \sum_{Z=1}^{Z_N} n_Z; \ \ and \ \ D = \sum_{Z=1}^{Z_N} D_Z \qquad (2)$$

is defined in general. The partial coefficients D_Z describe the diffusion due to the fluttering between two neighbouring charge states. With the fractional abundancies $f_Z = n_Z/\Sigma\ n_Z$ and the collision rates for ionization and recombination (ν^{ion}, ν^{rec}) they are obtained to

$$D_Z = \frac{1}{2}(\Delta\rho_{Z->Z-1})^2 f_Z \nu_Z^{rec} + \frac{1}{2}(\Delta\rho_{Z-1->Z})^2 f_{Z-1}\nu_{Z-1}^{ion} = \frac{\rho_1^2}{2Z^2(Z-1)^2}(f_Z\nu_Z^{rec} + f_{Z-1}\nu_{Z-1}^{ion}) \qquad (3)$$

These diffusion coefficients are generally very small [3]. Even for high energetic α-particles the typical values are as small as $D_2 \approx 10^{-3}$ m²/s. Clearly, the case Z = 1 needs a special treatment since $\rho_0 \to \infty$.

Recombinative induced diffusion in hydrogen

According to Eq. (3) this diffusion coefficient consists of two parts

$$D_1 = \frac{1}{2} l_0^2 f_0 \nu_0^{ion} + \frac{1}{2} l_1^2 f_1 \nu_1^{rec} \tag{4}$$

The first term describes the diffusion of the neutrals on account of ionization, i.e. shift by a gyro-radius ($l_0 = \rho_1$). It is negligible compared to the second term which describes the transport of the particles while they are in atomic state.

$$D_1 = \frac{1}{2} \left\langle v_i^2 \tau_{ion}^2 \right\rangle \nu_{rec} \tag{5}$$

With $\langle v_i^2 \rangle = T_i/m_i$, $\langle \tau_{ion}^2 \rangle = 2/(n_e S_{ion})^2$ and $\nu_{rec} = n_e S_{rec}$ we obtain

$$D_1 = \frac{T_i}{m_i} \frac{f_1}{n_e} \frac{S_{rec}}{S_{ion}^2} = \frac{T_i}{m_i n_e} F(T_e) \tag{6}$$

where $S_{ion} = \langle \sigma_{ion} v_e \rangle_e$ and $S_{rec} = \langle \sigma_{rec} v_e \rangle_e$ are the rate coefficients for ionization and recombination and the fractional abundancies are given by ionization equilibrium $f_0 = n_0/(n_0+n_1) = \nu_{rec}/(\nu_{rec} + \nu_{ion})$ and $f_1 = n_i/(n_0+n_1) = \nu_{ion}/(\nu_{rec} + \nu_{ion})$.

Inclusion of charge exchange collisions

CX-collisions will reduce the transport coefficients because they introduce additional changes of direction of the atoms. A more detailed analysis [3] shows that the average square length is to be replaced by $l_0^2 = (2\, T_i/m_i)/((\nu_{cx}+\nu_{ion})\, \nu_{ion})$ yielding

$$D_0^{cx} = \frac{T_i}{m_i} \frac{1}{(n_e S_{ion} + n_i S_{cx})}; \quad D_1^{cx} = \frac{T_i}{m_i} \frac{S_{rec}}{S_{ion}(n_e S_{ion} + n_i S_{cx})}, \tag{7}$$

where we have distinguished between the fully neutral ($f_0 = 1$) and fully ionized case ($f_i = 1$).

Results

The rate coefficients for hydrogen and the resulting diffusion coefficient D_1 are shown in the Figs. 1 and 2 as function of temperature ($T = T_e = T_i$).

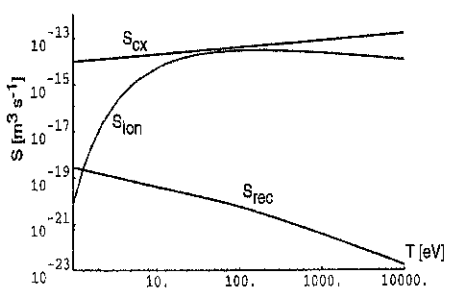

Fig. 1: The rate coefficients for hydrogen as a function of temperature.

The reduction due the charge exchange effect is seen to be important for the low and high temperature range. Note, however, that even with the cx-effect included the recombinative induced coefficient D_1^{cx} is much larger compared to the classical one.

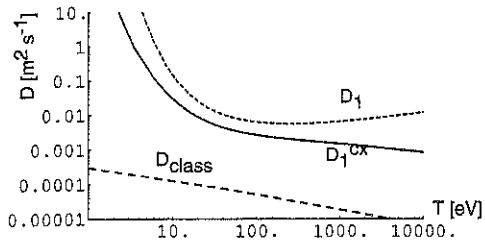

Fig. 2: The diffusion coefficients for hydrogen D_1 (without cx) and D_1^{cx} (with cx) in comparison with classical diffusion ($n_e = 10^{19}\ m^{-3}$, B = 3T).

Edge profiles and fluxes

To elucidate the diffusion process discussed before we analyze in the following the plasma build-up in the edge region by means of the continuity equations for electrons and neutrals

$$\frac{\partial n_e}{\partial t} = -\nabla \cdot \vec{\Gamma}_e + n_e n_0 S_{ion} - n_e^2 S_{rec};\ \frac{\partial n_0}{\partial t} = -\nabla \cdot \vec{\Gamma}_0 - n_e n_0 S_{ion} + n_e^2 S_{rec}. \tag{8}$$

Adding the two equations yields for the stationary state with 100% recycling

$$\vec{\Gamma}_e + \vec{\Gamma}_0 = 0. \tag{9}$$

Assuming anomalous transport for the electrons (with D_{an} = const.) and our previous result for the neutral fluxes (eq. (7)), the latter equation reads with $n_i = n_e$

$$-D_{an}\frac{\partial n_e}{\partial x} - D_0 \frac{\partial n_0}{\partial x} = 0, \tag{10}$$

where D_0 is proportional to n_e^{-1}. For T = const. this equation can be integrated and solved for the neutral density

$$n_0 = \frac{D_{an}}{2D_{0,\infty}} n_{e,\infty}\left[1 - \left(\frac{n_e}{n_{e,\infty}}\right)^2\right] + \frac{S_{rec}}{S_{ion}} n_{e,\infty}\ , \tag{11}$$

which is an extension of the expression given in [4]. By putting this into the first one of equations (8) we obtain

$$D_{an}\frac{d^2 n_e}{dx^2} = -n_e n_0 S_{ion} + n_e^2 S_{rec} = Q_0\ . \tag{12}$$

Here Q_0 is the effective source of the neutrals. With $y = n_e/n_{e,\infty} \le 1$ and $\gamma = 2\ S_{rec}/S_{ion}\ D_{0\infty}/D_{an} = 2\ D_{1\infty}/D_{an}$ and the scale length $\lambda = (4\ D_{0,\infty}/S_{ion}\ n_{e,\infty})^{1/2}$ this is written as

$$\lambda^2 \frac{1}{2}\frac{d^2 y}{dx^2} = -y\left[(1-y^2)+\gamma\right] + \gamma\, y^2 = -y(1-y^2) - \gamma\, y(1-y) \tag{13}$$

We notice that the term induced by recombination (γ) is also an effective sink for the neutrals (caused by a flux in the ion-electron channel) which is compensated by an enhanced recycling influx. Multiplying eq. (13) with $dy/d\xi$ where $\xi = x/\lambda$ allows a second integration

$$\frac{dy}{d\xi} = (1-y^2)\sqrt{1+\frac{2}{3}\gamma\frac{(1+2y)}{(1+y)^2}} \approx (1-y^2)+\frac{\gamma}{3}\frac{(1-y^2)(1+2y)}{(1+y)^2}, \qquad (14)$$

which tells as that the slope of the density and hence the net fluxes, and finally the density profile proper depend only weakly upon recombination. With $\gamma = 0$ we get the approximate profile $y = \tanh(\xi)$. There is, however, the problem that the net fluxes do not represent the directed ion and neutral fluxes which are of particular interest at the target boundary $x = 0$. We can determine these fluxes by integrating the recombinative part of the neutral source $Q_0^* = -2\lambda^2 D_{an}\gamma y(1-y) = 4 D_i/\lambda^2 y(1-y)$ over the edge region

$$\Gamma_0^* = -\int_x^\infty Q_o^* dx = \frac{4D_{i\infty}n_{e\infty}}{\lambda}\int_\xi^\infty y(1-y)d\xi \approx \frac{4D_{i\infty}n_{e\infty}}{\lambda}\int_y^1 \frac{y}{1+y}dy = \frac{4D_{i\infty}n_{e\infty}}{\lambda}\left[1-y+\log((1+y)/2)\right] \qquad (15)$$

yielding a flux at the target of $\Gamma_0^*(0) = 1.24\, D_{i\infty}n_{e\infty}/\lambda$. This flux is actually the opposite one that we estimated in the last section for the ions. According to eq. (2) we expect an ion flux of $\Gamma_i = -D_i\partial n_e/\partial x = -D_{i\infty}n_{e\infty}/\lambda\; y^{-1}dy/d\xi \approx -D_{i\infty}n_{e\infty}/\lambda\,(1-y^2)/y$ which diverges at $x = 0$ because the assumption $l_0 << \lambda$ breaks down, i.e. the produced neutrals reach the target before becoming ionized again. It is therefore reasonable to use the edge diffusion coefficient $D_i = D_{i\infty}$ yielding $\Gamma_i^* \approx -D_{i\infty}n_{e\infty}/\lambda\,(1-y^2)$. In Fig. 3 the three expressions for the fluxes are compared.

In conclusion, the anomalous plasma outflow $\Gamma_{an} = -D_{an}\,\partial n_e/\partial x$ is enhanced by recombination and additional fluxes of order $D_{i,edge}\,\partial n_e/\partial x$ are produced. Indications for the concomitant enhancement of the impurity influxes are found in detached ASDEX-Upgrade discharges (see D. Hildebrandt et al., this conference).

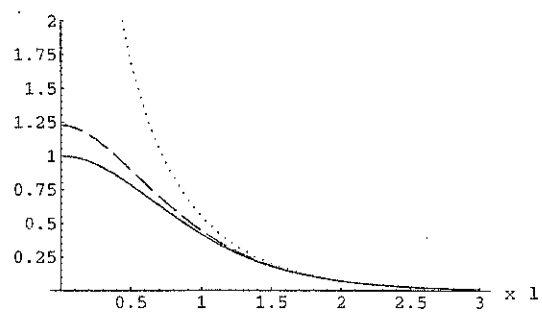

Fig. 3: Comparison of the recombinative induced flux relations Γ_0^* (dashed), $-\Gamma_i^*$(solid), and $-\Gamma_i$ (dotted).

Summary

The perpendicular diffusion coefficient associated with the recombination of ions into atomic state can be expressed as $D_i = F(T_e)T_i/m_i\, n_e$; it is thus independent of the magnetic field and inverse proportional to density and ion mass. Its temperature dependence is determined by the rate coefficients for ionization, recombination and charge exchange.

We find that the diffusion coefficient attributed to these processes is much larger than the classical one over the whole temperature range (1 eV < T < 10 keV) if the density is below 10^{20} m^{-3} and B > 2 T. This perhaps surprising result is a consequence of the large atomic step sizes compared to the small gyro-radii.

Of practical importance is this recombinative induced diffusion in the cooler edge regions of tokamaks and stellarators where in particular the chemical sputtering rates may be increased by the enhanced outflow. In general, this cross-field transport mechanism is assumed to prevail for many magnetized plasmas of sufficiently low density ($n_e < 10^{18}$ m^{-3}).

References:

[1] P. T. Greenland, J. Phys. B 21, L67-L71(1988)
[2] P. T. Greenland and M. F. Harrison, J. Phys. B 21, 4035-4048 (1988)
[3] G. Fussmann, Contrib. to Plasma Phys., 37, (1997), 101-115
[4] R. J. Goldston, P. H. Rutherford, *Introduction to Plasma Physics*, IOP Publishing Ltd (1995)

Time Evolution and Bifurcation of Temperature Profiles

P. Bachmann[1], **D. Sünder**[1], H. Wobig[2]

Max-Planck-Institut für Plasmaphysik, EURATOM Association
[1] Bereich Plasmadiagnostik, D-10117 Berlin, Germany
[2] Garching, Boltzmannstr. 2, D-85748 Garching, Germany

Introduction. Multiple stationary solutions of the one-dimensional heat conduction equation and bifurcation phenomena are known to be caused by the non-monotonic dependence of the impurity radiation function on the temperature [1], and the non-linearity of the heat flux in the high-recycling regime in front of the divertor target plates [2]. In this paper we report on bifurcation and time evolution of temperature profiles owing to localized heat sources and energy loss due to impurity radiation which are described by simple Gaussian model functions. The main result is that in dependence on the impurity density there may exist one, two or three stationary profiles. A linear stability analysis of stationary temperature profiles leads to a Schrödinger-type equation for the temperature perturbation. The solution of this equation shows that one of three temperature profiles is unstable. Finaly the fully time-dependent problem is solved.

Problem. Solutions to the following problem for the time dependent one-dimensional diffusion equation for the temperature $T(x,t)$ are considered:

$$\frac{\partial T}{\partial t} = \kappa \frac{\partial^2 T}{\partial x^2} + s(x) - q(T),\ x \in X := [0,1], t \in [0,\infty) \tag{1}$$

$$T(x,0) = T_1(x)\ (a);\quad T(0,t) = c_0,\ T(1,t) = c_1\ (b). \tag{2}$$

T_1 is a given function characterizing the initial condition (2a); (2b) represents a simple Dirichlet boundary (2) condition with the constants $c_{0,1}$. κ is the constant heat conductivity. The localized heat source function $s(x)$ and temperature dependent radiation loss function $q(T)$ are assumed to be given by the simple Gaussian model expressions:

$$s(x) := f_s \exp\left[-\frac{(x-x^*)^2}{\Delta_s}\right],\ q(T) := f_q \exp\left[-\frac{(T-T^*)^2}{\Delta_q}\right] \tag{3}$$

where the $f_{s,q}$ denote the strengths of the sources, x^*, T^* their localization and $\Delta_{s,q}$ their widths. Dimesionless quantities are used in what follows.

Stationary solution and bifurcation. Bifurcation of steady solutions $T_0(x)$ are considered. In order to elucidate its mechanism we analyse the simplified case $\Delta_s >> 1$ of a nearly constant source function ($s \simeq f_s$). Then the steady solution of (1) is implicitly given by

$$\left[\theta(x_{max}-x)\int_{\tau_0}^{\tau} + \theta(x-x_{max})\left(\int_{\tau_0}^{1}+\int_{\tau}^{1}\right)\right] \frac{d\tau'}{\sqrt{1-\tau'+g(\tau')-g(1)}} = ax, \tag{4}$$

$$g(\tau) := \frac{\pi}{2}\frac{f_q}{f_s}\frac{\sqrt{\Delta_q}}{T_{max}}\mathrm{erf}\left(\frac{\tau T_{max}-T^*}{\sqrt{\Delta_q}}\right),\ \tau := \frac{T_0}{T_{max}},\ \tau_{0,1} := \frac{c_{0,1}}{T_{max}}\ a := \sqrt{\frac{2f_s}{\kappa T_{max}}}.$$

$T_{max} \equiv T_0(x_{max})$ follows by inserting $\tau = \tau_1$, $x = 1$. ($\theta(x)$ - step function, erf(x) - error function). Its dependence on the parameters κ, $f_{q,s}$, T^*, x^*, $\Delta_{q,s}$ shows that the solution is *not unique*, in the sense that 1, 2 or 3 values may exist. Assuming $\kappa = 0.5, \Delta_q = 0.1, T^* = 1$, this multiple valuedness is demonstrated in Fig. 1 for different parameters, where the high- and low-temperature bifurcation points $(T^{(h)}_{max}, f^{(h)}_q), (T^{(l)}_{max}, f^{(l)}_q)$ are determined by the relation $dT_{max}/df_q|_{f^{(h)}_q, f^{(l)}_q} = \infty$ appearing above a threshold value $f_{s,thr}$ (Fig 1a). Stationary temperature and radiation profiles are displayed in Fig. 2. The larger the maximum temperature the more the radiation is shifted to the boundary.

Stability analysis. Suppose that the boundary value problem (2b) to eq. (1) has the *steady solution* $T = T_0(x)$; its *stability* will now be investigated. Expressing $T = T_0(x) + \delta T(x,t)$, and linearizing eq. (1) with respect to the small perturbation δT, leads to the Schrödinger-like equation

$$\frac{\partial}{\partial t}\delta T = \kappa \frac{\partial^2}{\partial x^2}\delta T - q'(T_0)\delta T,\ q'(T) := \frac{d}{dT}q(T),\ \delta T = 0 \text{ at } x = 0, 1. \tag{5}$$

where $q'(T_0)$ plays the role of the effective potential. Taking normal modes of the form $\delta T = \tilde{T}(x)e^{-\lambda t}$, the *eigenvalue problem*

$$\kappa \frac{d^2\tilde{T}}{dx^2} + [\lambda - q'(T_0)]\,\tilde{T} = 0,\ \tilde{T}(0) = 0, \tilde{T}(1) = 0 \tag{6}$$

results. Since the operators are Hermitian, the eigenvalue is real and can be found by a minimisation procedure

$$\lambda := \text{Min}\ \frac{\kappa \int_0^1 dx\ \tilde{T}'^2 + \int_0^1 dx\ q'(T_0)\tilde{T}^2}{\int_0^1 dx\ \tilde{T}^2}, \tag{7}$$

where $q' = -2(T_0 - T^*)q(T_0)/\Delta_q$ can change its sign and depends nonlinearly on the radiation factor f_q ($T_0 = T_0(x, f_q)$). Expanding $\tilde{T}$ in harmonics of $\sin \pi x$, $\tilde{T} = \sum_n a_n \sin(n\pi x)$, the dependence of λ on f_q shows that the low- and high-temperature profiles are stable but the middle-temperature branch is unstable. This is demonstrated in Fig. 3 where the effective potential and the eigenvalues λ as a function of f_q are displayed.

Time evolution. Solutions of the fully time-dependent problem (1), (2) with the initial temperature profile

$$T_1(x) = 4x(1-x)[u_0 + u_1 \sin(u_2 \pi x)] \tag{8}$$

show that in dependence of the parameters u_n (n=0,1,2) either the low- or the high-temperature state can be attained. This is demonstrated in Fig. 4.

Summary. In the frame of a simple time dependent one-dimensional model we have shown that (i) bifurcation phenomena strongly depend on the parameters of the system, especially on the impurity radiation factor f_q, (ii) multiple stationary temperature and radiation profiles may exist, (iii) in the case of three stationary states the middle-temperature branch is unstable, (iv) solutions of the fully time-dependent problem in dependence of the initial temperature profiles attain either the stationary low- or the high-temperature state.

References.
[1] H. Capes, Ph. Ghendrih, A. Samain, Phys. Fluids B4 (1992) 1287
[2] D. Sünder, H. Wobig, 20th EPS, Lisboa 1993, Contrib. Papers II-819

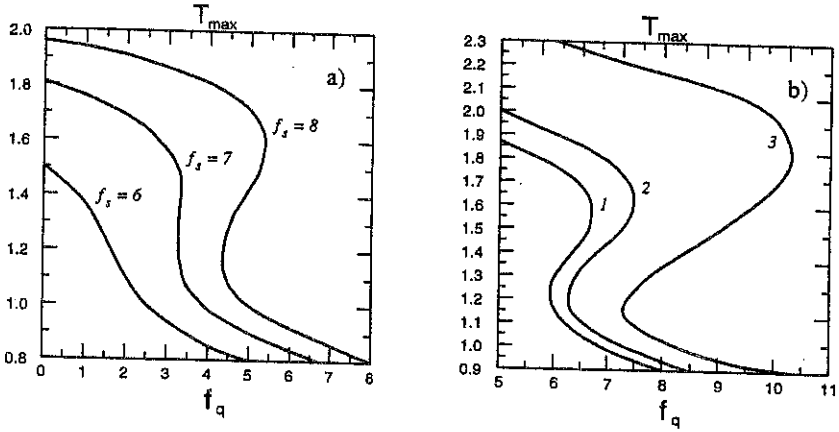

Fig. 1. T_{max} as a function of f_q for (a) $c_{0,1} = 0, x^* = 0.5, \Delta_s = 5$ and (b) 1 - $c_{0,1} = 0, f_s = 15, x^* = 0.4, \Delta_s = 0.05$, 2 - $c_{0,1} = 0, f_s = 15, x^* = 0.5, \Delta_s = 0.05$, 3 - $c_0 = 0, c_1 = 0.5, f_s = 15, x^* = 0.5, \Delta_s = 0.05$.

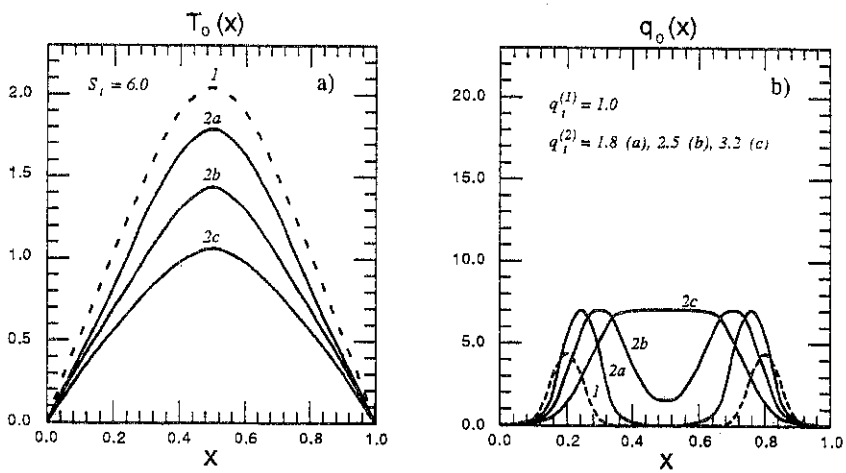

Fig. 2. Stationary temperature (a) and radiation (b) profiles for $f_s = 15, x^* = 0.5, \Delta_s = 0.05$ and $f_q = 4.3$ (1) and $f_q = 7$ (2a, b, c) where s_t and q_t are the total energy input and radiation power.

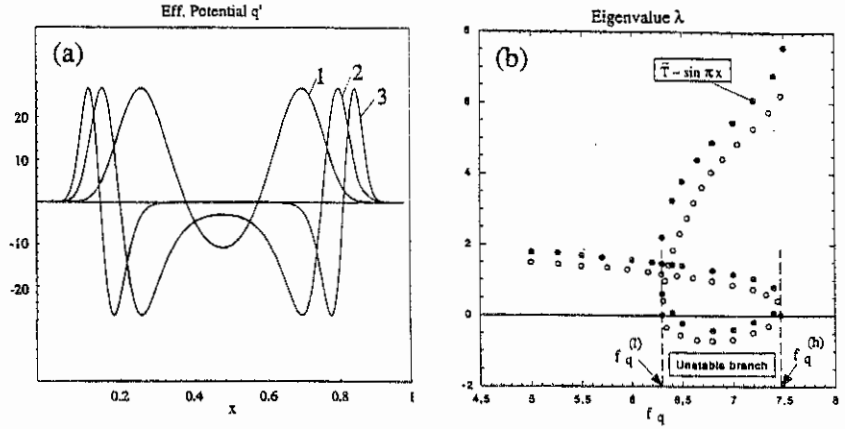

Fig. 3. Effective potentials (a) for (1) low-, (2) middle- and (3) high-temperature profiles and the eigenvalue (b) vs f_q for $f_s = 15, x^* = 0.5, \Delta_s = 0.05$.

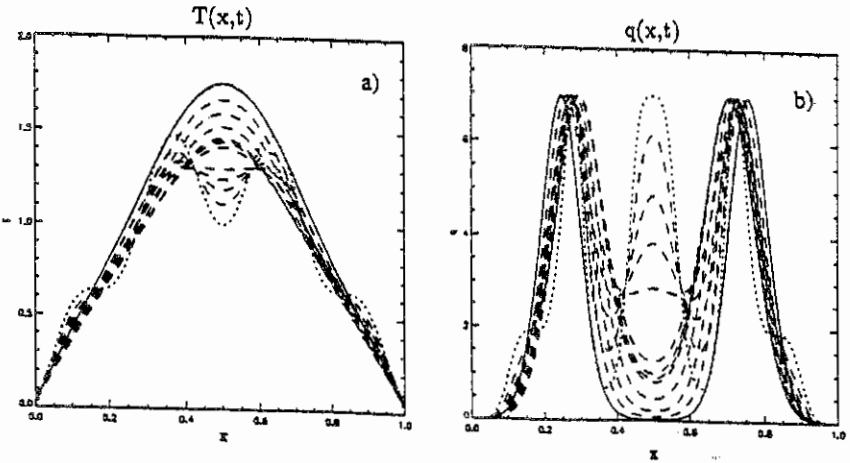

Fig. 4. Time evolution of temperature (a) and radiation (b) profiles for $c_{0,1} = 0, f_s = 15, x^* = 0.5, \Delta_s = 0.05, f_q = 7, u_0 = 1.30, u_1 = 0.2$ and $u_2 = 7$ ($\cdots$ $t = 0$, — - $t = \infty$).

Electric stopping in hot plasma wall interactions

I.S.Landman[1], H.Würz[2]

1 Troitsk Institute for Innovation and Fusion Research, 142092 Troitsk, Russia
2 Forschungszentrum Karlsruhe, INR, Postfach 3640, D/76021 Karlsruhe

1. Introduction

Results from numerical modelling of ITER typical hot plasma divertor target interactions [1,2] and from disruption simulation experiments [3] have shown that evaporated divertor material forms a dense rather cold plasma shield which protects the target from further excessive evaporation. For the energy deposition of the hot plasma onto the initially unshielded solid target and later on into the plasma shield and the target behind, the energy flux carried by the hot plasma has to be known. An electric potential formed in the cold and hot plasma region influences the energy deposition profile, deflects the hot plasma by **E×B** drift and results additionally in self compression of the plasma shield edge.

Recently an analysis of electrostatic shielding was reported for perpendicular impact of a hot plasma onto a cold plasma shield [4]. However to prevent unlimited propagation of cold electrons from the plasma shield into the hot plasma a reversed potential drop had to be postulated at the cold-hot plasma interface.

A realistic estimation on electric shielding in hot plasma wall interactions has to include the inclined impact of the magnetized hot plasma. The analysis to be reported here was performed for perpendicular and inclined impact of the magnetized hot plasma into the cold dense plasma shield.

2. The problem

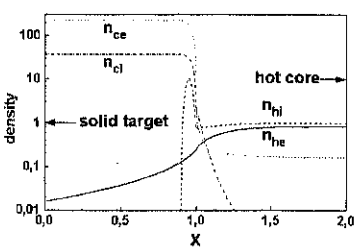

Fig.1 Density distributions of hot and cold particles. For x<1 the length is given in units of λ_{he}, for x>1 in units of 10 r_D.

Perpendicular impact of the hot plasma schematically is shown in Fig.1. The spatial coordinate x is directed from the target to the core (poloidal direction). The dense and rather cold plasma shield consists of ionized target material of density n_{ci} and temperature T_c and cold electrons of the same temperature and density $n_{ce}=Zn_{ci}$ with Z the average charge. The cold plasma is described by the hydrodynamics equations. The energy transfer in the plasma shield by radiation, hot plasma energy deposition and electron heat conduction establishes rather constant values of T_c and Z in most part of the plasma shield. The hot collisionless plasma consists of electrons of temperature T_h and density n_{he} and of hydrogen like ions of density n_{hi} which are assumed to be mono-energetic, their energy is given as $W_{hi}=GT_h$, G~1. The process of hot plasma interaction with the plasma shield is both electrical (for hot electrons) and collisional stopping of the hot particles in the plasma shield. The stopping length λ_{hi} of the hot ions is assumed to be much shorter than the electrical λ_E and the hot electron stopping length λ_{he}. Moreover it is valid $r_D \ll \lambda_{hi} \ll \lambda_E \ll \lambda_{he}$ with r_D the Debye length and λ_{he} comparable to the thickness of the plasma shield.

A part of the hot electrons is reflected at the sheath. Those who overcome the sheath potential continuously loose their energy till they finally approach the temperature T_c of the cold plasma and then they join the subsystem of the collisional cold electrons.

In case of inclined impact of the hot plasma along the guiding magnetic field line the cold electrons of the plasma shield only compensate the x-component of the electric current of the hot electrons, its z-component (toroidal direction) is not compensated because there is no electric charge accumulation in this direction. This arises because electrons undergoing Coulomb collisions with ions may jump between magnetic field lines within the distance of the electron Larmor radius. In the transverse (lateral) direction (y-direction) the plasma shield is limited in size, thus the current in this direction is zero for cold and hot electrons separately. The net electron flux is given as:

$$\mathbf{j}_e = \mathbf{j}_{he} - \mathbf{j}_{ce}. \tag{1}$$

Outside of the collisional region the electric current is zero. The ion current and current loops initiated in the core region of the hot plasma are neglected.

3. Mathematical description

For perpendicular impact in addition to the zero current condition (1) the Poisson equation for $E=-d\varphi/dx$ is used:

$$dE/dx = 4\pi e\delta n, \qquad \delta n = n_{hi} + Zn_{ci} - n_{he} - n_{ce} \tag{2}$$

together with the boundary conditions of quasi-neutrality $E\to 0$ at $x\to L,+\infty$. The indexes L and ∞ denote the inner ($x=L$) and outer ($x\to+\infty$) side of the sheath. The necessary requirement for joining together the collisional region and the sheath is the isothermal sound speed of cold electrons at the sheath entrance: $v_{ce}(L)=((Z+1)T_c/m_e)^{1/2}$. The hot electrons Maxwellian distributed at $x=+\infty$ because of their uncollisionality keep their Boltzmann distribution at arbitrary x. Thus it is obtained for $n_{he}(x)$ and $j_{he}(x)$:

$$n_{he}(x) = e^{-u}\int_{-\infty}^{v_m} f_M(v)dv = \theta n_{he}^{\infty} e^{-u} k(u_L - u), \quad k(t) = 1 - \tfrac{1}{2}\mathrm{erfc}\sqrt{\max(0,t)}, \tag{3}$$

$$j_{he} = e^{-u}\int_{-\infty}^{v_m} v f_M(v)dv = -\left(\theta/2\sqrt{\pi}\right)\, v_{The} n_{he}^{\infty} \exp\left(\max(u_L,u)\right) \tag{4}$$

with $u=-e\varphi/T_h$, $\theta=\exp(\min(0,(x-L)/\lambda_{he}))$ the 'attenuation factor' of collisional stopping, $v_{The}=(2T_h/m_e)^{1/2}$ the thermal velocity of the hot electrons, and $v_m=(2e(\varphi-\varphi_L)/m_e)^{1/2}$, v_m guaranties that no hot electrons are coming back from the slowing down region $x<L$. Density $n_{hi}(x)$ and flux j_{hi} of the mono-energetic hot ions in the sheath are obtained from the flux and energy conservation equations as

$$n_{hi} = n_{hi}^{\infty}(1 + u/G)^{-1/2}, \quad j_{hi} = n_{hi}^{\infty}\sqrt{2w_{hi}/m_i}. \tag{5}$$

Cold electrons are described by the following hydrodynamics equation:

$$m_e v_{ce}\, dv_{ce}/dx = -\left(T_c/n_{ce}\right) dn_{ce}/dx - eE - m_e v_{ce}/\tau_{ce} \tag{6}$$

with τ_{ce} the momentum relaxation time of cold electron-ion collisions. In the collisional region eq (6) results in Ohm's law $-ej_{ce}=\sigma E$ with σ the electric conductivity. In the sheath the pressure gradient and the collisional terms are neglected. For n_{ce} and j_{ce} it is obtained:

$$n_{ce} = n_{ce}^{\infty}(1 - u/u_L)^{-1/2}, \; j_{ce} = n_{ce}^{\infty} v_{ce}^{\infty}, \quad v_{ce}^{\infty} = \left(-2e\varphi_L/m_e\right)^{1/2}. \tag{7}$$

Cold ions are described with an equation similar to (6) in the rest frame, resulting in the Boltzmann distribution: $n_{ci}=n^{\infty}_{ci}\exp(Ze(\varphi_L-\varphi)/T_c)$.

For inclined impact a Vlasov-Poisson model is used. The Hamilton function is used for solution of the Vlasov equation. H is given according to

$$H(t,x,z,p) = (1/2m)\left(p_x^2 + \left(p_y - B_0(e/c)X\right)^2 + \left(p_z - (e/c)A_z(t,x)\right)^2\right) + e\phi(x). \tag{8}$$

with **p** the canonical momentum, X the coordinate directed perpendicularly to the vacuum magnetic field B_0, and A_z and ϕ the magnetic and the usual electric potential.
The Maxwell equations for the y-component of the magnetic field and for the z-component of the vortex electric field generated by the net current j_e have been used additionally:

$$\partial B_y/\partial x = -4\pi(e/c)j_e, \qquad \partial B_y/\partial t = c\,\partial E_z/\partial x. \tag{9}$$

The distribution function of hot particles depends on the motion integral p_y and the adiabatic invariants I and H'. I and H' are given as:

$$I = (\omega/\pi)\int_{X_{min}}^{X_{max}} p_X dX, \qquad H' = H - e\int_{-\infty}^{t} E_z v_z dt' \tag{10}$$

with $\omega=eB_0/mc$ the gyration frequency. The integration over X is carried out between the turning points X_{min}, X_{max} of the particle's gyration projection onto the X-axis. The integration over t is carried out along the particle's trajectory. The time integral in eq (10) is mainly a function of x, what allows to introduce the effective potential Φ according to

$$\Phi = \phi - \int_{-\infty}^{t} E_z v_z dt' \tag{11}$$

In terms of the effective potential the expressions for the density and the flux of the hot and the cold electrons and for accelerated at the sheath entrance remain the same as in eqs (3), (4) and (7). Only the expression for the density of the hot ions is too lengthy to be given here.

4. Main results

The whole set of equations was solved consistently for both cases. For pependicular impact the obtained characteristic behavior of the densities is given in Fig.1. The behavior of the potential in the collisional region is described by the simple formula:

$$u = u_L + \ln\left(1 + K\left(1 - e^{-\xi}\right)\right) \tag{12}$$

with the dimensionless parameters ξ and K where $\xi=(L-x)/\lambda_{ie}$ and K is given as

$$K \approx \sqrt{T_h/T_c}\,(z+1)e^{-u_L}\Big/\left(2\sqrt{\pi}\sqrt{G+u_L}\right) >> 1 \tag{13}$$

Values of u_L as function of the parameter G are given in Table 1. The range of validity of the parameter G was checked by applying the Bohm criterion at $u\to\infty$. As a result of this analysis it was obtained that for G<0.55 the electric potential will be non-monotonic.

Table 1. $u_L(G)$

G	0.55	1	2	5
u_L	0.90	0.69	0.58	0.52

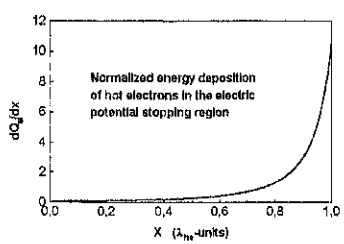

Fig.2

The normalized distribution of the energy deposition of hot electrons into the shielding layer is shown in Fig.2. The energy fractions deposited separately by electrical and collisional stopping are 11% for collisional stopping, 80% for electrical stopping and 9% for the stopping of hot ions (for the case G=1, Z=6, $T_h/T_c=10^2$, $(m_i/m_e)^{1/2}=70$).

For inclined impact the analysis was performed for the sheath and the ion subsheath region. The calculated distributions of electron and ion densities and of effective potential are sown in Fig.3 for the sheath and in Fig. 4 for the ion sub-sheath. The behavior of the effective potential is rather close to that one for perpendicular impact if the spatial coordinate is shortened by the factor $\sin\alpha$ with α the inclination angle. The potential in the ion subsheath changes only slightly in contrast to the traditional subsheath problem [5] where the main potential drop occurs in the

subsheath. For inclined impact hot ions cannot be absorbed immedately by the cold plasma because their stopping range λ_{hi} is much larger than their full path of immersion into the cold plasma. Thus their density doesn't decrease significantly in the ion subsheath region. The Bohm criterion is valid if $G_{\perp}=G\sin\eta>1.75$ with η the pitch-angle of the monoenergetic hot ions at $x=\infty$. To fulfill this condition acceleration of the hot ions in the magnetic presheath is required [6].

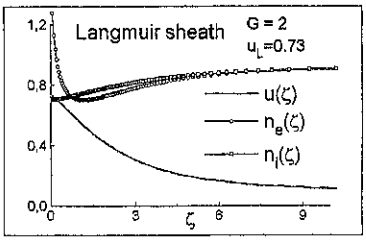

Fig.3

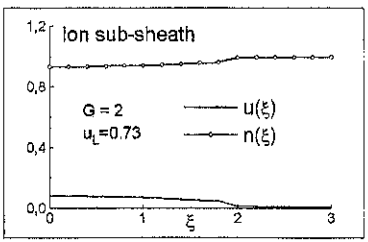

Fig.4

5. Discussion and conclusions

From the quasineutrality equation $\delta n=0$ it follows that the effective potential Φ is constant in the transition region between the sheath and the hot core. Hence it follows from eq (11) that the potential $\phi(x)$ changes significantly in this region, i.e. a strong electric field $E_x=\partial\phi/\partial x$ arises which causes an $\mathbf{E}\times\mathbf{B}$ drift of the incoming hot plasma in the y-direction. The drift velocity v_d given as cE_x/B_0 is about 1.5×10^5 cm/s.

The increase of the magnetic pressure gradient caused by B_y could result in a self-compression of the plasma shield edge. After the time $t[\mu s]\sim 30(T_e/100eV)^2$ B_y reaches a value which is comparable to the cold plasma pressure. thus becoming a substantial feature of the cold plasma expansion. If the temperature of the cold plasma is less than $\sim 10^2$ eV this time becomes much smaller than the characteristic disruption time. Therefore the dynamics of the cold plasma shield is influenced by the time evolution of B_y. A substantial part of the incoming energy is spent for the generation of B_y.

A more detailed description of electrical stopping should analyse the Knudsen layer between the collisional region and the sheath with the aim to describe the escaping of the cold'run-away' electrons. Additionally reflection of hot electrons from the electrical barrier in the collisional region should be considered. In this case the inclined motion of hot electrons with respect to the guiding magnetic field has to be taken into account. The Coulomb stopping of hot electrons should be described by using the Boltzmann kinetic equation. Moreover the shock wave dynamics of the self-compression of the edge of the shielding layer by the magnetic field B_y and the dynamics of the $\mathbf{E}\times\mathbf{B}$ drift of the hot plasma should be studied in detail.

References

1. B.Bazylev at al. EPS-22, Bournemouth, v.19C, part II, p.277, 3-7 July 1995.
2. H.Wuerz at al. J.Nucl.Mat. 212-215, p. 1349, 1994.
3. N.I.Arkhipov at al. 18th SOFT Karlsruhe, 1994.
4. L.L.Lengyel at al. Nuclear Fusion, v.36, n.12, 1679, 1996.
5. D.D. Ryutov, Contrib. Plasma Phys. 36, (1996) 213, p. 207.
6. R. Chodura, in Phys. Plasma Wall Inter. Contr. Fus. ed. by D.E. Post, R. Behrisch (Plenum, New York, 1986).

Matching of a non-Gaussian gyrotron output beam to an ECRH transmission line using thermographic measurements

L. Empacher, G. Gantenbein, W. Kasparek
Institut für Plasmaforschung, Universität Stuttgart, Pfaffenwaldring 31, 70569 Stuttgart, F.R.G.
V. Erckmann, H. Laqua,
Max-Planck-Institut für Plasmaphysik, EURATOM-Association, 85748 Garching, F.R.G.

Abstract

Measurements of the power distribution of a 140 GHz gyrotron beam have been performed by recording the temperature profiles on a target plate by an infrared camera. On the basis of these measurements, a reconstruction of the phase distribution of the beam has been performed using an iterative technique. From the knowledge of the complete electric field distribution, phase-correcting mirrors have been designed in order to couple the beam to an HE_{11} mode in an oversized corrugated waveguide.

Introduction

At the stellarator experiment W7-AS of IPP Garching new gyrotrons operating at 140 GHz with an output power of 0.5 MW and a pulse length of up to 2 s have been installed. In these tubes the output power is coupled through a laterally mounted single disc boron nitride window which is circumferentially cooled. In order to reduce the thermal stress of this window during long pulse operation these gyrotrons have special mirrors inside the tube to produce a flattened power profile instead of a profile peaked in the centre of the window. This means that the emitted beam contains not only the fundamental free-space mode (Gaussian beam, TEM_{00}) but also higher order free-space modes. These modes are not useful for further transmission of the millimetre wave power in a corrugated waveguide system. To get optimum coupling to the HE_{11} mode of a corrugated waveguide, a transformation of the gyrotron output with two phase-correcting mirrors to a single-mode beam (fundamental Gaussian beam) is necessary. To calculate the surface of these mirrors, the amplitude and phase profiles of the output beams of the gyrotrons are required.

Experimental set-up

Figure 1 shows the experimental set-up for the measurement. A PVC-plate has been used as microwave target for the temperature measurement. This PVC-plate has a corrugated surface in order to minimise reflections back to the gyrotron. Four light emitting diodes serve as markers for the alignment of the pictures to each other and to be able to rectify the pictures from the

oblique view of the camera. Since the microwave absorption of PVC depends on temperature, a calibration is required. The measurements of the beam profiles have been performed with a PtSi focal plane array camera with a thermal resolution of 0.1 °C and a spatial resolution of the order of 0.5 mm. The images have been recorded digitally (244 x 320 pixels, 12 bit). A typical gyrotron pulse with a reduced power of 200 kW and a length of 9 ms heats the target plate up to a maximum temperature of 70 °C. Thermal convection and cooling down of the target can be neglected during the frame time of the camera of 40 ms. The transmitted power of the gyrotron beam has been absorbed in a dummy load. At the end of the measurement procedure a series of 8 thermal images taken at different distances z from the gyrotron window were available for reconstruction of the phase and amplitude distribution of the beam (see Fig. 2).

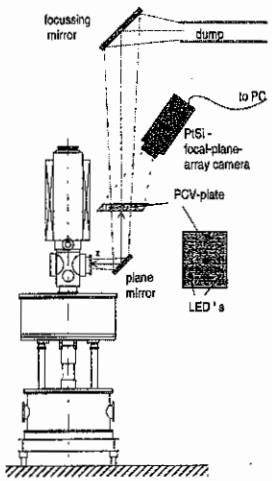

Fig. 1: Experimental set-up

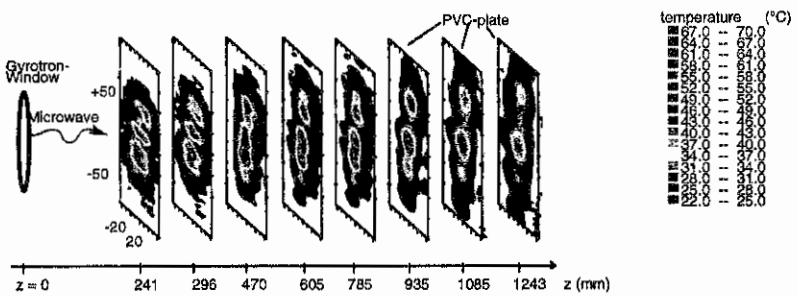

Fig. 2: Temperature profiles of the PVC-target, measured at different distances from the gyrotron window

Phase reconstruction

The reconstruction of the phase on the basis of the amplitude distribution at two different cross sections is possible with an iteration algorithm [1,2]. This algorithm is schematically shown in Fig. 3.

The amplitude distributions $|E_1(x,y)|^2$ at z_1 and $|E_2(x,y)|^2$ at z_2 are given by measurements. E_1 is multiplied with a complex phasor, $u_1 = E_1 e^{i\varphi_1}$, which is arbitrary in the first step, and the free

space propagation of this field to $z = z_2$ is calculated, resulting in $\tilde{u}_2 = \tilde{E}_2 e^{i\varphi_2}$. Replacing $\tilde{E}_2$ by the measured amplitude E_2 ($u_2 = E_2 e^{i\varphi_2}$) and calculating the free-space propagation back to z_1 yields $\tilde{u}_1 = \tilde{E}_1 e^{i\varphi_1}$. This procedure is repeated several times. In each step one combines the phase factor with the measured amplitude pattern and neglects the calculated amplitude pattern. The convergence is defined by means of a matching coefficient $\eta_k = \dfrac{\left[\int \tilde{E}_k \cdot E_k \, dx dy\right]^2}{\int |\tilde{E}_k|^2 \, dx \, dy \cdot \int |E_k|^2 \, dx \, dy}$.

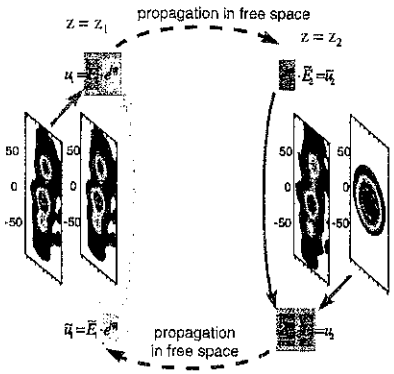

Fig. 3: Phase Reconstruction algorithm

A typical value for η_k of 97-98 % is achieved.

Figure 4 shows the comparison of two measured amplitude distributions with the corresponding patterns resulting from the reconstruction.

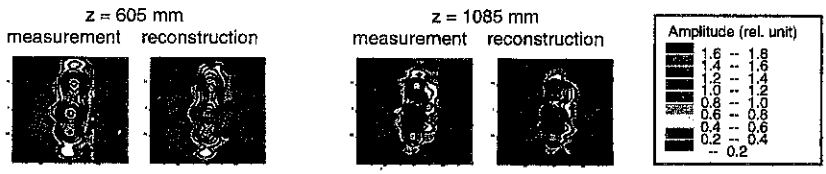

Fig. 4: Comparison of two measured amplitude distributions with the corresponding patterns resulting from the beam reconstruction

Design of the matching mirrors

The reconstruction algorithm has been also used to find the distribution of phase shift for the two matching mirrors with given field at the position of the first mirror and the wanted field (TEM_{00}) at the position of the waveguide input after the second mirror. From the phase $\varphi(x,y)$ the mirror surface $z(x,y)$ is given by

$$z_{\text{mirror}}(x,y) = \frac{\lambda}{4\pi} \cdot \frac{1}{\cos(\alpha)} \cdot \varphi\left(x, \frac{y}{\cos(\alpha)}\right)$$

where α is the angle of incident. To get a smooth surface without steps it is possible to add multiples of 2π. Since the amplitude measurement is not perfect and since we work in two dimensions it can happen that the reconstruction leads to a continuous complex phase factor that can not be transformed to a real continuous phase shift. This may lead to steps which cannot be

smoothed afterwards. However, by filtering of high Fourier components during the free space propagation it is possible to avoid these steps.

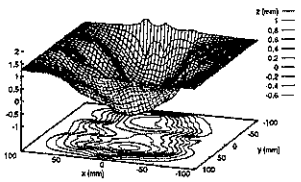

Fig. 5a: Surface of phase correcting mirror M1

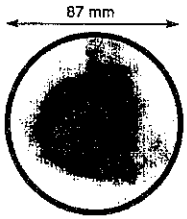

Fig. 5b: Burn pattern at the waveguide entrance

Results

Since the measured temperature pattern is changing its structure with increasing distance z from the output window due to enhanced divergence of the higher order modes it is most advantageous to evaluate pictures taken as close as possible to the window flange. The calculations showed that the Gaussian content of the gyrotron output beam is 78 %, this value has been theoretically increased up to 96 % with the technique described above. Figure 5a shows the contour of the first phase correcting mirror installed in the system. The burn pattern at the entrance of the corrugated waveguide is given and in Fig. 5b. Up to now the system has been tested with a power of up to 680 kW and a pulse length of up to 2 s with 500 kW using mirrors designed on the basis of these measurements by the Institute of Applied Physics, Nizhny Novgorod.

Summary

Thermographic measurements with high dynamic range allow a precise reconstruction of the complex field of a gyrotron beam. Based on this field, mirrors have been designed to convert the multi-mode output beam to a nearly Gaussian mode.

References

[1] B.Z. Katsenelenbaum, V.V. Semenov, Radiotechnika i Elektronika **12** (1967)

[2] A.V. Chirkov, G.G. Denisov and N.L. Aleksandrov, Optics comm. **115** (1995), p. 449-452

[3] A.A. Bogdashov et al., Int. J. Infrared and Millimetre Waves, **10** (1995), p. 735

RESPONSE OF THE ELECTRON DISTRIBUTION TO MODULATED HEATING

V. Krivenski
Asociación EURATOM/CIEMAT para Fusión, CIEMAT, Madrid

The reaction of the plasma to a variation in the strength, or nature, of the external forces acting upon it, is a major source of insight into the microscopic plasma dynamics. As such, it has been the object of a good deal of measurements and calculations. Focusing on the electron component, and on regimes where the electrons are weakly coupled to the ions, both the macroscopic response to the modulation of the RF power, and the microscopic transient response to an abrupt modification in the RF power level have been measured and analyzed (see, e.g., Refs. 1-4).

This paper reports on the establishment of periodic-in-time, non-thermal distribution functions, when the RF modulation frequency is of the order of the collision frequency of the resonant electrons.

In this regime one may assume radial transport to be negligible, and can focus on the dynamics of the electron distribution function resulting from quasilinear and collisional effects. We find that, for finite power-levels ECRH, non-thermal features appear in the tail of the electron distribution, the amplitude of which is periodic, but, in general, out of phase with the RF modulation, the phase-delay being a function of the electrons energy.

The paper considers only the dynamics of the tail of the distribution. One can argue, however, that under certain conditions similar features can also appear in the bulk of distribution function, when ECRH is modulated to perform transport studies.

1. Kinetic Equation

In order to get a qualitative understanding of the problem, it is useful to consider a simplified kinetic equation, which just describes the quasilinear diffusion, and the collisional drag and energy diffusion of the electrons in the tail of the distribution. Of course, the effect of pitch-angle scattering is not negligible, and should be included when making quantitative comparisons with experimental results, together with an accurate description of bulk collisions.

We consider the following kinetic equation: $\partial f/\partial t = (\partial f/\partial t)_{\mathrm{EC}} + (\partial f/\partial t)_{\mathrm{coll}}$, with $\left(\gamma = \sqrt{1+u^2/\mu}\,,\ \mu = m_e c^2/T_e,\ u = p/p_{\mathrm{th}}\right)$:

$$\left(\frac{\partial f}{\partial t}\right)_{\mathrm{EC}} = \frac{u_{\parallel}}{\gamma}\frac{\partial}{\partial \gamma}\frac{\gamma}{u_{\parallel}}u_{\perp}^2\, D\,\frac{\partial f}{\partial \gamma}\bigg|_{\gamma-(\omega/2\omega_c)u_{\perp}^2/2=\mathrm{const.}}$$

$$\approx \frac{1}{u}\frac{\partial}{\partial u}\gamma^2 u D\,\frac{\partial f}{\partial \gamma}\bigg|_{u_{\parallel}^2\approx\mathrm{const.}} \qquad (\text{for } \omega \approx 2\omega_c),$$

and $\left(\nu_{\mathrm{coll}} = \dfrac{2\pi\Lambda e^4}{m_e^{1/2}}\dfrac{n_e}{T_e^{3/2}}\right)$:

$$\left(\frac{\partial f}{\partial t}\right)_{\text{coll}} = \nu_{\text{coll}} \frac{2}{u^2}\frac{\partial}{\partial u}\left(\frac{\gamma^3}{u}\frac{\partial f}{\partial u}+\gamma^2 f\right) \approx \nu_{\text{coll}} \frac{u}{u_{\text{res}}}\frac{2}{u^2}\frac{\partial}{\partial u}\left(\frac{\gamma^3}{u}\frac{\partial f}{\partial u}+\gamma^2 f\right).$$

The distribution function is normalized according to: $\int_0^\infty du\, u\, f = 1$. The model diffusion coefficient is written for 2nd harmonic, X-mode heating:

$$D = \frac{d}{\gamma} u^2 \exp\left[-(u-u_{\text{res}})^2/\Delta u^2\right].$$

The spirit of the previous approximations is to keep, as much as possible, the 1D equation identical to the 2D kinetic equation near the resonance, $u \approx u_{\text{res}}$, where the quasilinear effects are strongest, and to modify it near $u \approx 0$, where the distribution function is practically Maxwellian.

In order to visualize the distribution function, we also make use of the following "emission coefficient": $\beta = u^4/\gamma^2 f$.

The numerical results discussed in the next section are computed using the following parameters (temperature and density are those of Ref. 5):

$$T_e = 220\ \text{eV}, n_e = 3.2\times10^{12}\ \text{cm}^{-3}, u_{\text{res}} = 3.9, \Delta u = 0.5, d \Rightarrow d\left[1+0.1\sin(2\pi t/t_{\text{mod}})\right].$$

2. Sinusoidal Heating

Figure 1(a) shows the time evolution of the non-Maxwellian component of β, for energies below, at, and above the maximum of the diffusion coefficient. The average power absorbed by the tail, for $t \to \infty$, is 0.2 W/cm^3, compared to 0.3 W/cm^3 for the initial Maxwellian distribution, i.e., we are in a weakly quasilinear regime. At higher modulation frequencies [see Fig. 1(b)] it is apparent the decrease of the modulation amplitudes. This is shown in more detail in Figs. 2 and 3.

Figures 1(a) and (b) show clearly the existence of phase-delays between the oscillation of the distribution function at different energies and the modulation of the power. These delays are computed by using the cross-correlation with the input power, and are presented in Fig. 4 as a function of the modulation frequency. Figure 5 shows their surprisingly weak dependence on the average input power, which is caused by strong quasilinear saturation of the absorption. This effect is shown in detail in Figs. 6 and 7: the ramp-up of the power decreases, via quasilinear flattening, the absorption coefficient of the tail, decreasing as a result the amplitude of the perturbation on the tail for increasing power inputs (see Fig. 8), which is quite the opposite one may have at first expected.

The numerical results suggest that the characteristic time evolution of the gradient of the distribution function at resonant energies triggers the delays in the oscillation of the distribution function observed at higher and lower energies, these delays being propagated by collisional drag and diffusion mechanisms, and amplified at lower energies by stronger collisionality.

3. Conclusions

We have shown that modulated heating – even when considered in the absence of transport, as a simple local kinetic process – modifies the distribution function and bestows an amazing time and energy structure upon it. Recently, modulation experiments performed on TJ-IU[5] have shown the existence of phase-delays in the electron cyclotron emission spectra, increasing with the modulation frequency, that can be considered a signature of that structure.

References

1 L. Giannone, *et al.*, Nucl. Fusion **32**, 1985 (1992).
2 G. Gorini, P. Mantica, *et al.*, Phys. Rev. Lett. **71**, 2038 (1993).
3 U. Stroth, L. Giannone, H-J Hartfuss, *et al.*, Plasma Phys. Control. Fusion **38**, 611 (1996).
4 G. Giruzzi, J. L. Ségui, *et al.*, Phys. Rev. Lett. **74**, 550 (1995).
5 E. de la Luna, *et al.*, *10th Joint Workshop on ECE and ECRH* (1997).

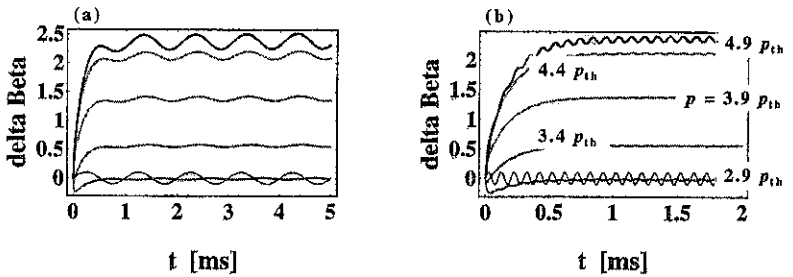

Fig. 1 Time evolution of the non-Maxwellian part of β for $d = 5$ ms^{-1} at different, regularly spaced momenta: (a) fmod = 1 kHz, (b) fmod = 10 kHz. The maximum of the diffusion coefficient is at p = 3.9 p_{th} (at the maximum, the energy relaxation frequency is 0.7 kHz). The 10% modulation of the power is also shown at the bottom of the figures for reference.

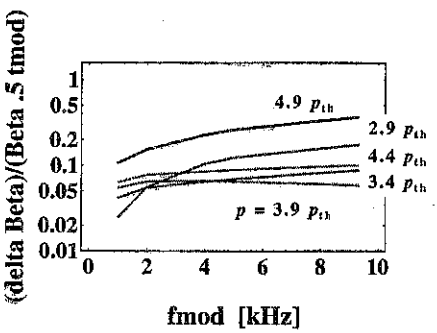

Fig. 2 Normalized modulation amplitude of β for $d = 5$ ms^{-1}. The behaviour is almost linear with the modulation frequency near the maximum of the diffusion coefficient.

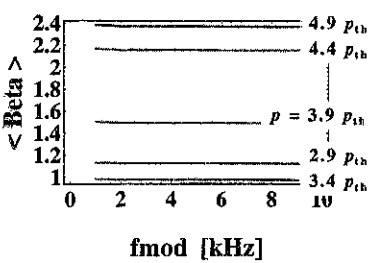

Fig. 3 Average value of β for the conditions of Fig. 2.

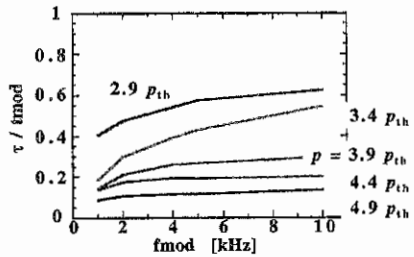

Fig. 4 Normalized phase-delay of β with respect to the input power, for the conditions of Fig. 2. For comparison, the phase-delay at thermodynamical equilibrium is $\tau / t_{mod} = 1/4 = 0.25$.

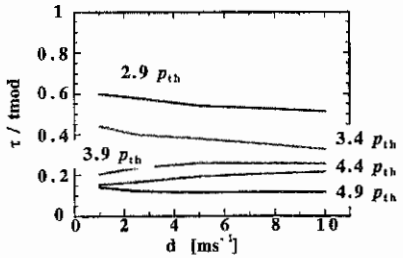

Fig. 5 Normalized phase-delay of β with respect to the input power, for several diffusion coefficients: d = 1, 2.5, 5, 10 ms^{-1}, and fmod = 4 kHz.

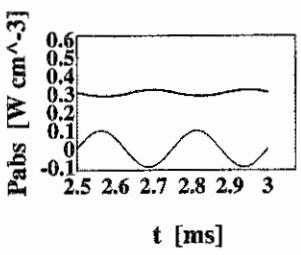

Fig. 6 Time evolution of the power absorption computed taking into account only the oscillation of the distribution function (i.e., d = const.), for fmod = 4 kHz, and d = 10 ms^{-1}. At the bottom the modulation factor of the power is shown. The relative amplitude of the absorption modulation is 6.7%, and its phase-delay is nearly π.

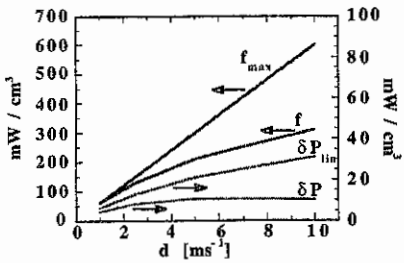

Fig. 7 Maxwellian, and $t \to \infty$ average absorption rates for the conditions of Fig. 5 (left-hand scale): it is apparent the quasilinear saturation of the power absorption. Amplitude of the modulated power absorption (righ-hand scale), the linear rate (10% of the average absorption), and the actual rate resulting from the antimodulation of the damping described in Fig. 6.

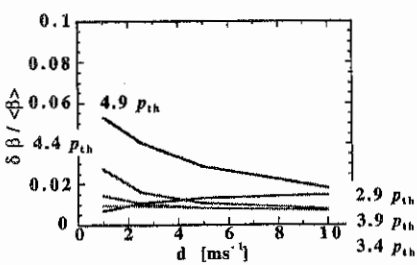

Fig. 8 Relative amplitude modulation of of β for the conditions of Fig. 5.

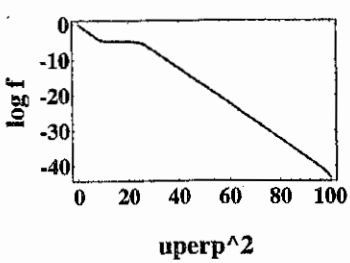

Fig. 9 Average distribution functions for $t \to \infty$ and the conditions of Fig. 6.

Comparison of reflectometry techniques for density profile measurements in turbulent plasmas

T. Estrada, V. Zhuravlev, J. Sánchez, E. de la Luna and M. Francés
Asociación Euratom-CIEMAT, 28040 Madrid. Spain.

Abstract

A two dimensional code based on the WKB approximation is used to simulate the ability of the different reflectometry techniques to reproduce the average density profile in a turbulent ITER size plasma. Analysis is performed for Pulse Radar, Amplitude Modulation (AM) and Frequency Modulation (FM swept frequency) systems. The effects of turbulence with non-perpendicular reflection and plasma rotation are analyzed.

The code has also been used to analyze the feasibility of correlation measurements. In addition to the use of these studies for turbulence analysis, these measurements can be used as a robust method for the determination of the signal time delay and therefore of the density profile.

Introduction

It is well known that the reflecting layer for microwave frequencies in fusion plasmas shows a complex corrugated structure which can lead to strong interference in the reflectometer beam. This interference causes strong amplitude oscillations and random-like phase behaviour which difficult the density measurement. Previous work [1], simulating the reflectometer signals with a 2-dim WKB code, has shown that the three reflectometry methods are able to produce acceptable profiles in turbulent conditions ("frozen" turbulence with perpendicular launching). One of the major points of concern when comparing reflectometry techniques is trying to evaluate the limitations that a given choice for the ITER reflectometry front end would impose. In principle, AM and Pulse Radar systems are less affected by turbulence (time delay measurement corresponds to a frozen plasma) but are more demanding on the waveguide performance. FM systems can tolerate some parasitic reflections and dispersion in the transmission line, but the measurement of the time delay is done in a (short but finite) time interval while turbulence is evolving. In this context, it would be very useful to simulate the operation of FM systems in conditions of non-perpendicular launching and rotating turbulent structures (identified as a possible cause for the "phase runaway" which can introduce systematic errors in the profile measurement).

The knowledge of the turbulence structure is critical for modelling reflectometry measurements because of the strong dependence of the results on the parameters of turbulence. The spatial correlation of the reflectometry signals may be used to obtain information about these parameters, but there are still some difficulties in the interpretation of these measurements.

Simulation results for non-perpendicular reflection and plasma rotation

Using the 2-dim WKB code [1], the phase delay and amplitude of the reflected signal are computed as a function of the carrier frequency for a 2-dim turbulent density distribution, and from these data the measurement of different types of reflectometers are simulated. Two

elements are considered in order to simulate the ITER conditions which could cause phase runaway: oblique reflection and rotating turbulent structures. These calculations are performed for the gradient zone of the ITER plasma (R=8.14 m, a=2.8 m): with $n_e(0)=10^{14}$ cm^{-3} and B_0= 5 T (frequency sweep: 105-165 GHz for the X-mode), the average poloidal wavelength of the turbulent structure, λ_θ, is 6 cm and its amplitude, $\tilde{n}$, is constant along the radius ($\tilde{n}/n$ raises to the periphery).

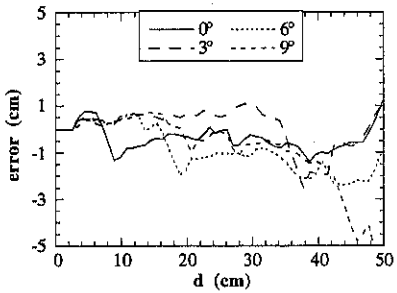

Fig. 1.- Error in the position of the reflecting layer for different angles of horn axis

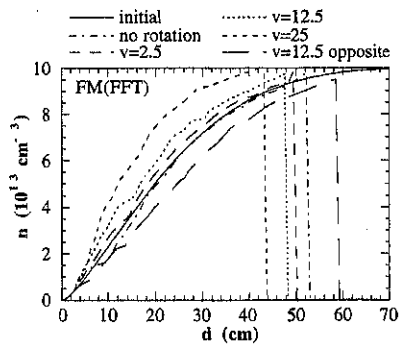

Fig. 2.- Density profiles for the FM reflectometer for a case of a rotating turbulent structure with different v

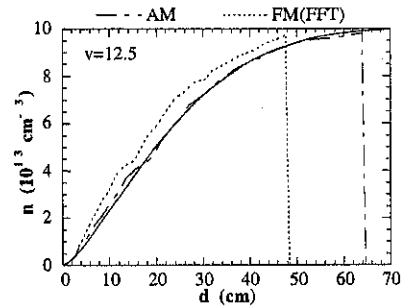

Fig. 3.- Density profile for AM and FM systems for a rotating turbulent structure with v=12.5. Solid line: original average density profile

As a first study, oblique reflection on a static plasma has been considered with a moderate turbulence level (1.5 % (rms) of the central density). In addition to the possible higher level of interference in oblique reflection, the effect of refraction could be also a source of error when using 1-dim reconstruction algorithms. Angles of horn axes are tilted from the position of normal reflection to 3°, 6° and 9°. Fig. 1 shows the error in the reconstructed density profile for the case of the Pulse Radar reflectometer. Errors of the order of 1.5 cm are found for all the analyzed reflectometry techniques with no significant dependence on the angle of tilting.

In order to perform simulations with rotating plasmas we have chosen the parameter "v" as relative speed, being the number of turbulence wavelengths passing in front of the antenna during the (linear) sweep time. For example, v=2.5 corresponds to a sweep rate of 4 GHz/μs and 200 kHz turbulence. The results of the simulations with an antenna tilt of 5° for FM technique with FFT analysis are shown on Fig. 2. For small values of the parameter v the effect of the rotation is small in the reconstructed density profile. With increasing v the systematic error increases reaching unacceptable levels. Opposite direction of rotation leads to the inversion of the error. The same calculations for the AM reflectometer do not show such errors (see Fig. 3). This result could be

expected being the AM an instantaneous measurement of the time delay (with the three spectral components reflecting simultaneously in the plasma).

Simulation of correlation measurements

Simulated rotating plasma reflection layers, separated in radial direction, are used to generate reflectometer signals for each incident frequency. Simulation results compare cases with different perturbation parameters: λ_θ = 1-6 cm and $\tilde{n}/n$ = 2-16 %, with a radial correlation length of the order of 1 cm. The beam size at the reflecting layer is about 2-3 cm and the frequencies are 75-77 GHz with O-mode propagation and perpendicular launching.

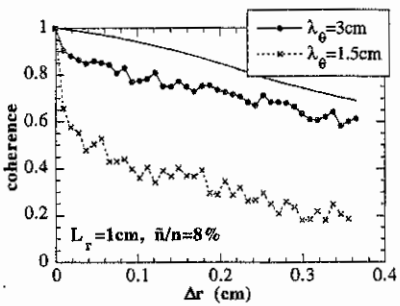

Fig. 4.- Radial correlation of the phase fluctuations for two cases with λ=3 and 1.5 cm (ñ/n=8 %.). Solid line: radial correlation of the density

In the cases of long λ_θ (longer than the beam size) and low $\tilde{n}/n$, 2-dim effects are very weak and the phase fluctuations are similar to the density fluctuations. For shorter λ_θ and higher $\tilde{n}/n$, destructive interference effects become stronger: simultaneous reflection from different poloidal points takes place and the phase variations do not follow the density fluctuations. Fig. 4 displays the comparison between weak and strong 2-dim effects: in the first case the radial correlation of the phase is comparable to the radial correlation of the density but it drops faster as the interference effects become stronger. As a consequence, using the phase signals, big errors should appear in the determination of the radial correlation length. The radial correlation of the amplitude of the reflected signals is very close to the correlation of the density only when λ_θ and the beam size at the reflecting layer are of the same order. Under these conditions the poloidal structure of the cut-off layer acts like a lens: focusing the reflected beam when the layer has a concave shape and vice versa. As a result the amplitude presents maxima associated with the minima in the density fluctuations. The behaviour of the amplitude is different when λ_θ is shorter or longer than the beam size. For longer λ_θ the amplitude in average is higher and is almost independent of the density fluctuations and for shorter λ_θ the amplitude falls due to destructive interference effects (except for very low density fluctuation levels: $\tilde{n}/n \leq 2\%$). In both cases the radial correlation of the amplitude drops faster than the radial correlation of the density. In Fig. 5 the radial correlation of the amplitude for $\tilde{n}/n$=8 % and different λ_θ (5, 3 and 1.5 cm) is displayed.

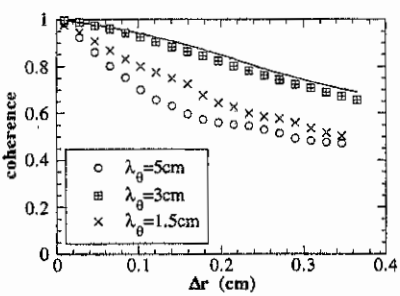

Fig. 5.- Correlation of the amplitude of reflected signal for different perturbation wavelengths. Solid line: radial correlation of the density

To properly measure the radial correlation with a two channel homodyne reflectometer one of the frequencies must be swept around the other one which is fixed. In this way a maxima-minima structure in the correlation is obtained as the incident frequency is swept [2]. The simulation results show that in case of high destructive interference the radial correlation between the homodyne signals is closer to the correlation of the density than the one between the phases. This effect could be explained considering that during the time period in which the correlation is evaluated the intervals with destructive interference have lower amplitude than those with weak 2-dim effects and consequently their contribution to the correlation is smaller. In this structure the distance between consecutive maxima corresponds to increments of π in the phase offset of the reflectometer as the incident frequency is swept, thus, the time delay can be derived. Even in the cases of strong 2-dim effects, in which the maxima in the correlation of the homodyne signal are lower than the density correlation, this time delay is in very good agreement with the time delay obtained from the unperturbed density profile. As an example two cases with different $\tilde{n}/n$ and the same λ_θ are displayed in Fig. 6 together with the cos of the phase delay of the unperturbed density profile.

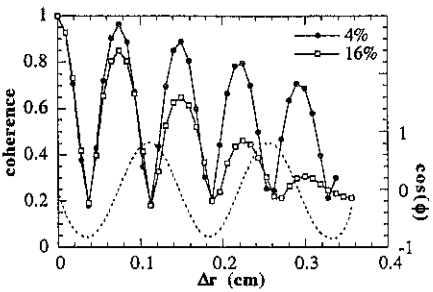

Fig. 6.- Correlation of the homodyne signals for $\tilde{n}/n$=4 and 16 % (λ=3 cm) and phase delay from the unperturbed density profile (broken line)

Conclusions

The 2-dim WKB code, able to compute interference effects, was used for qualitative investigation of the perturbations in reflectometry measurements induced by turbulence. The different reflectometry techniques (AM, Pulse Radar and FM) are able to measure the density profile in a turbulent ITER size plasma with acceptable accuracy. Plasma rotation together with non-perpendicular reflection lead to systematic errors for the FM reflectometer. These errors could be eliminated by extremely fast frequency sweep.

Correlation measurements using the reflectometry phase signal may provide a useful tool to obtain information on radial correlation lengths of the turbulence only in cases in which the 2-dim effects are weak. The time delay deduced from the radial correlation of the homodyne signals is in very good agreement with the time delay obtained from the unperturbed density profile. This kind of measurements can be used to obtain the density profile in turbulent plasmas with parasitic reflections due to poor access and complicated waveguides.

References

[1] V. Zhuravlev, J. Sánchez and E. de la Luna. Plasma Phys Control Fusion **38** (1996) p 2231

[2] J. Sánchez, B. Brañas, E. de la Luna and T. Estrada. Rev. Sci. Instrum. **64** (1993) p 487

Helium beam diagnostic: a discussion of line intensity ratios

M.Brix and B.Schweer

Institut für Plasmaphysik, Forschungszentrum Jülich GmbH, EURATOM Association,

Trilateral Euregio Cluster, D-52425 Jülich, Germany

Introduction

In the boundary plasma of TEXTOR-94, thermal helium beams are used to measure routinely profiles of electron temperature and density with high radial and temporal resolution ($\Delta t \leq 1$ms, Δr=1.2mm, examples are presented in [1]). Three helium lines are detected simultaneously: the singlet lines λ_1 =728.1nm, λ_2 =667.8nm and the triplet line λ_3 =706.5nm. The line intensity ratio $I(\lambda_1)/I(\lambda_3)$ is a strong function of T_e whereas $I(\lambda_2)/I(\lambda_1)$ depends mainly on n_e (fig.1). A comparison of the line intensity ratios with the results of a collisional radiative model (cr-model) allows to determine T_e and n_e [2]. The temperature measurement is only possible for sufficiently large electron densities $n_e > 10^{18}m^{-3}$. The electron temperatures are overestimated for smaller densities, because the triplet states have not yet reached their equilibrium population density. The penetration of the beam is limited by the ionisation of the helium atoms. Figure 2 shows the ionisation length of a monoenergetic helium beam penetrating into a uniform plasma with a velocity v=1.7 km/s. The radial extent of the helium line emissions in an edge plasma depends also on the gradients of T_e and n_e (see Fig. 3 for the TEXTOR-94 boundary plasma).

The quality of the derived T_e and n_e values depends essentially on the accuracy of the cr-model. The aim of this report is the discussion of the cr-model and of the atomic data.

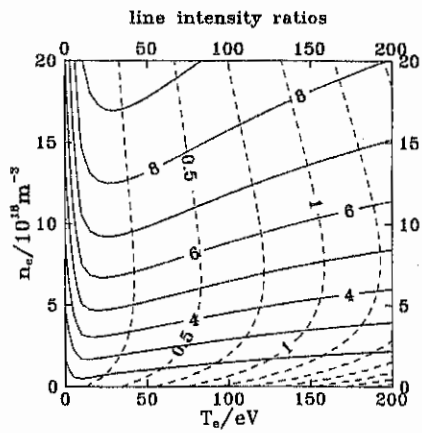

fig. 1 line intensity ratios
dashed line T_e ratio $I(\lambda_1) / I(\lambda_3)$
solid line n_e ratio $I(\lambda_2) / I(\lambda_1)$

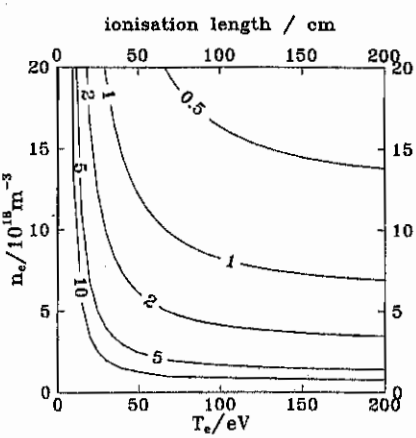

fig. 2 ionisation length of a helium beam penetrating into a uniform plasma with v_{beam}= 1.7 km/s

Analysis of the collisional radiative model

The rate coefficients for electron impact excitation from the ground state to the singlet states have a different energy dependence than those for excitation to the triplet states. Therefore, all singlet to triplet line intensity ratios depend mainly on T_e [3].

Only a few line intensity ratios are a strong function of n_e, e.g. $I(\lambda_2) / I(\lambda_1)$, I(501nm)/ I(505nm). A detailed analysis of the cr-model in the T_e-n_e-range shows, that some states are depopulated mainly by electron impact (depopulation proportional to n_e), others are emptied only by spontaneous emissions (depopulation independent of n_e).

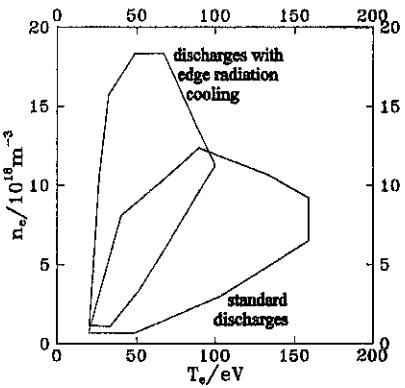

fig. 3 range of T_e and n_e, where the helium beam diagnostic has been successfully used for the measurement of T_e and n_e profiles in the boundary plasma of TEXTOR-94

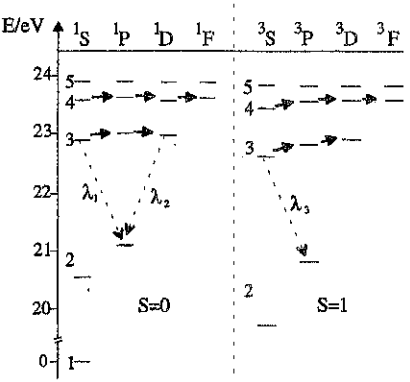

fig. 4 level diagram of helium **dashed arrows** indicate the helium lines used for the measurement of T_e and n_e **solid arrows** indicate important rate coefficients between the highly excited states

The cr-model calculates the population densities of the states with principal quantum number $n \leq 4$ regarding spontaneous emissions, electron impact excitation and electron impact ionisation [4]. The accuracy of the rate coefficients influences the population densities significantly. First calculations have been carried out on the basis of the electron impact rate coefficients calculated (with the computer code ATOM) by Abramov et al. [5]. These calculations made reasonable predictions for the line intensity ratios mentioned above. Nevertheless, deviations occurred in some T_e-n_e-ranges and the predictions of other HeI line intensity ratios disagreed with measurements .

Meanwhile, the accuracy of the rate coefficients for electron impact excitation from the ground state [6] and from the metastable states [7] improved significantly . Among others,

these rate coefficients are provided in ADAS [8]. However, the situation for the electron impact excitation rate coefficient between the highly excited states is not yet satisfying. In particular, the rate coefficients for dipole allowed excitation between two states with the same principal quantum number play an important role for the excitation and depopulation (horizontal arrows in fig.4). Figure 5 compares the calculated values for the rate coefficient 3^1S -3^1P given by two different groups: Abramov and Vainshtein (code ATOM [9]) and H.Summers (ADAS). Large deviations are typically found for T_e<10eV because the fitting formula used in ATOM is not adequate in this range [9]. Above 10eV, the deviations are smaller than 30%. A comparison of other rate coefficients shows deviations up to 100%.

The influence of the states with n>4 has been estimated by extending the cr-model for the n=5 states. The necessary data for electron impact excitation from the ground and metastable states were found in the literature whereas some dipole allowed excitation rates had to be calculated with ATOM [9]. The influence on the relative population densities (population density of the excited state normalised to the ground state) of the s and p states is negligible, the influence on the d states is less than 10%. Therefore, the states with n>4 can be neglected for the calculation of line intensity ratios.

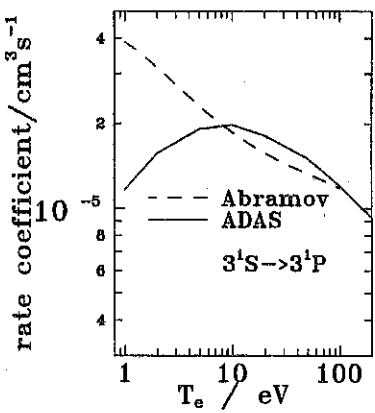

fig. 5 comparison of the electron impact rate coefficient 3^1S -3^1P

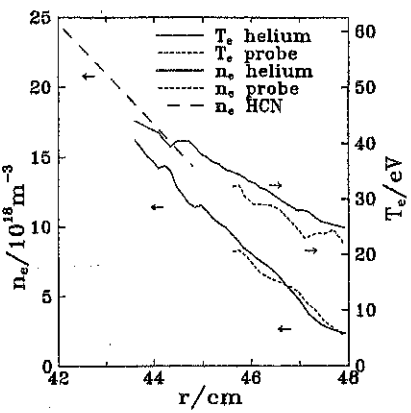

fig. 6 comparison of profiles
T_e and n_e helium beam diagnostic
T_e and n_e fast scanning probe [10]
n_e HCN interferometer

Measurement and Discussion

The helium lines chosen for the diagnostic at TEXTOR-94 are a good choice, because they are sufficiently intense to measure electron temperatures and densities with high temporal resolution. Usually, background line radiation does not significantly influence the

measurement. Nevertheless, in some cases (e.g. experiments with additional helium injection, edge radiation cooling with argon) the background light has to be measured separately.

The results determined with the helium beam diagnostic were compared in a wide T_e-n_e-range (fig.3) with a) T_e and n_e profiles measured with a fast scanning probe [10], b) profiles and time traces of n_e measured with a thermal lithium beam and c) n_e profiles and time traces measured with the HCN-interferometer (fig. 6). The results obtained with the helium beam diagnostic are in good agreement (deviations less than 30%), if the line intensity ratios are calculated on the basis of the rate coefficients provided by ADAS.

Additional HeI line intensities in the visible spectral range were measured and compared with the predictions of the cr-model (based on the ADAS data). The singlet lines λ=501.5nm and λ=504.7nm agree within the experimental errors, the measured values for the singlet line λ=492.2nm and for the triplet line λ=447.1nm are 10...30% smaller than expected. The weak triplet line λ=471.3nm was superimposed by an impurity line. However, the consistence comparisons do not yet cover the whole T_e-n_e-range mentioned in fig. 3.

Conclusion

The accuracy of the method has been improved significantly by using a more accurate set of rate coefficients.

References

[1] B.Unterberg et al., invited talk at this conference, *The influence of plasma edge properties on high confinement discharges with a radiating plasma mantle at the tokamak TEXTOR-94*

[2] E.Hintz and B.Schweer, Plasma Phys. Control. Fusion 37 (1995) A87-A101

[3] N.Brenning, J.Quant.Spectrosc.Radiat.Transfer 24 (1980) 293

[4] B.Brosda, PhD thesis, Ruhr-Universität Bochum, Germany, 1993

[5] V. A. Abramov, L. A. Vainstein, *Recommended cross-sections and rates for electron inelastic collisions with Helium atoms, I.V.* Kurchatov Institute, Moskau, 1987

[6] F.J. de Heer et al., Atomic and plasma-material interaction data for fusion, (supplement to J. of Nucl.Fusion) Vol. 3 (1993) 19-32

[7] F.J. de Heer et al., Atomic and plasma-material interaction data for fusion, (supplement to J. of Nucl.Fusion) Vol. 8 to be published

[8] ADAS, a collection of computer codes and atomic data for the modelling of line radiation of atoms and ions developed by a group of scientists and institutes working in plasma- and astrophysics, adf04-file helike_kvil97he, H.P.Summers, University of Strathclyde, UK, 1997

[9] L.Vainshtein, Lebedev Physical Institute, Moskau, private communication,1996

[10] J.Boedo, *Scanning probes in tokamaks*, Rev. Sci. Ins., to be published

CURRENT FLOWS IN THE DIVERTOR PLASMA OF HELIOTRON E

V.V.Chechkin, V.S.Voitsenya, **T.Mizuuchi**[A], E.L.Sorokovoj, M. Nakasuga[B], K. Nagasaki[A], H.Zushi[B], H.Okada[A], S.Bessho[B], A.Hayakawa[A], H.Funaba[A], T.Hamada[A], K.Kondo[B], F.Sano[A], T.Obiki[A], S.Masuzaki[C], O.Motojima[C]

Institute of Plasma Physics, National Science Center "Khar'kov Institute of Physics and Technology", 310108 Khar'kov, Ukraine
[A] *Institute of Advanced Energy, Kyoto University, Gokasho Uji 611, Japan*
[B] *Graduate School of Energy Science Kyoto University, Gokasho, Uji 611 Japan*
[C] *National Institute for Fusion Science, Nagoya 464-01, Japan*

1. Introduction

For the first time, non-ambipolar particle flows in the SOL plasma of a closed magnetic trap drew attention in the single-null divertor experiment on the JET tokamak [1]. Similar electric currents were also observed in the diverted SOL plasma of the DIII-D tokamak [2]. A possible explanation of these currents is based on thermoelectric effect [3,4]. Among other driving mechanisms mentioned are loop voltage, outward magnetic helicity transport, and the bootstrap effect (see [2] and the references therein).

The study of electric currents in the SOL plasma is of interest for many reasons. In particular, these currents correlate with the boundary plasma stability and L-H transitions [1,2]. The associated potentials should be taken into account, when controlling boundary plasma stability and divertor flow distribution by applying a bias voltage to special electrodes or divertor plates. As an intrinsic element of the mechanism of particle and heat loss from the bulk plasma, these currents can create an appreciable energy load on the grounded divertor plates.

In the Heliotron E heliotron/torsatron, with "currentless" plasma production and heating (ECH), an evidence of electric current generation in the SOL plasma (divertor plasma) has been also obtained [5,6]. The object of this work is the search of some links (mainly qualitative) between floating potential and electric current in the divertor plasma, on the one hand, and characteristics of the divertor field lines and plasma heating (NBI, NBI+ECH), on the other hand.

2. Experimental conditions

An ECH produced target plasma is supported and heated by NBI with $P_{inj} \leq 3$ MW and pulse length up to 200 ms. An ECH pulse (typically 30 ms) with frequencies of 53 GHz (fundamental EC frequency, generated power ≤0.4 MW) and of 106 GHz (2nd EC harmonic, 0.3 MW) can be imposed on NBI. Typical plasma parameters are: $\bar{n}_e \sim (1.5\text{-}2.5)\times10^{13}$ cm^{-3}, $T_e \sim 0.5\text{-}1$ keV, $T_i \sim 0.35\text{-}0.5$ keV.

To study the divertor plasma, 50 collecting plates (CPs) 5×0.8 cm^2 [5] working as electric probes are used. 8 arrays of these plates, 6 or 7 plates in each array, are arranged poloidally on rounded parts of the vacuum chamber (i.e., in the clearance between the helical windings) at the distance of 1.5 cm from the wall in 4 poloidal cross-sections with the 1/8 field period interval. The position of an array is determined by the poloidal angle Θ of its center: 90° (top), 45°, 0°, 315° (outboard side of the torus), 270° (bottom), 225°, 180°, 135° (inboard side). Thus, using all CP arrays, it is possible to examine plasma flows, which hit the wall in 8 segments of one field period. In the course of measurements, the floating potential of the isolated plates, V_f, the ion saturation current to the plates (with the -120 V bias), j_s, and the current to the grounded plates, j_p, are recorded.

3. Experimental results and their discussion

Earlier [5,6] it has been already observed (in ECH conditions) that the potential V_f has different polarity, depending on Θ and position (number) of plate for a given Θ. In accord with the sign of V_f, an ion or electron current j_p comes to the grounded CP. As an example, in Fig. 1 shown are j_p and V_f distributions over CPs (in fact, poloidal distributions) at Θ=0° during NBI (shaded rectangles, $P_{inj} \approx 3$ MW). The CP positions are indicated by numbers 1,2,...,6 and by fat segments on the horizontal axis (θ-axis). Also, the calculated dependence on θ of the connection length L for open field lines, with the starting points of calculation (0,5° is the step) laying on the line of CP disposition, is drawn in Fig.1. The families of field line sections starting from CPs in the toroidal magnetic field $\boldsymbol{B}$ direction and oppositely are indicated as A and B, respectively. The locations of measured maxima of the divertor flows (current j_s) correspond to the calculated locations of L maxima. It follows from Fig. 1 that the positions of the $|j_p|$ maxima also are close to those of the L maxima. The maximum values of the current j_p (tens mA/cm^2) are comparable with j_s.

In relatively simple conditions (NBI, a low injection power $P_{inj} \approx 0.7$ MW, the injection angle is 62°, a single inlet is positioned nearly toroidally symmetric about CPs), a periodicity is observed in behaviour of the j_p and V_f maxima variations with Θ on the top, bottom and outboard sides of the torus (Fig. 2). With this, the $V_f(\Theta)$ and $j_p(\Theta)$ variations along the field lines belonging to different families (A or B) are in antiphase.

To set a link between the Fig. 2 dependencies and the characteristics of the longest divertor field lines ($L \geq 2$ m), some calculated parameters of these field lines are presented in Fig. 3: the azimutal positions of starting points (P2, P3, P5, P6) and ends (●,✚), the numbers M and N of field periods and poloidal turns, respectively, passed by the field lines (M,N for ●, $\overline{M},\overline{N}$ for ✚, $M<0$ for the $\boldsymbol{B}$ direction, $N>0$ for counterclockwise rotation). The signs ± indicate the V_f and j_p polarity, according to Fig.2. It follows from Fig. 2 and Fig. 3 juxtaposition that under conditions considered the observed periodicity of $V_f(\Theta)$ and $j_p(\Theta)$ variations results from the combination of 3 factors: (1) a specific symmetry of divertor field line trajectories in a heliotron (symmetry of poloidal positions of starting points and ends about the midplane for field line bundles traversing in A and B directions); (2) the location of the heating source almost toroidally symmetric about CPs; (3) a constancy in the character of poloidal distribution of SOL plasma potential along the torus (the potential of the upper part is everywhere higher than the potential of the lower part). Basing on thermoelectric effect and the formulae (12,17) in [4], an 1.2-1.5 excess of the SOL plasma temperature in the higher part over that of the lower part might be a possible reason for the deduced non-uniformity in poloidal distribution of SOL plasma potential.

When going from the NBI source with the inlet being almost toroidally symmetric about CPs, to an NBI source of comparable injection power (0.5 MW) but located nearer to CPs on the side B, then those $V_f(\Theta)$ (and $j_p(\Theta)$) variations undergo larger changes, which are measured along the field lines coming from the side B (Fig. 4).

Comparing the changes, which $V_f(\Theta)$ variations undergo with transition from the oblique NBI (62°, ○) to (1) pure perpendicular NBI (90°, perpendicular ion energy increase, ●, Fig.4) or to (2) oblique NBI + ECH combination (perpendicular electron energy increase, ●, Fig. 5), we see that these changes occur in opposite directions. This could be considered as an evidence of trapped particle species effect on potential and electric current distributions in the SOL plasma. In contrast to the oblique NBI only case (Fig. 2), in the Fig. 4 and Fig. 5 cases a trend can be observed to formation of SOL plasma regions with alternating directions of the poloidal electric field E_θ within one field period.

Qualitatively, the effect of heating power on $V_f(\Theta)$ (and $j_p(\Theta)$) variations is made clear by Fig. 6, where the $V_f(\Theta)$ dependencies are compared, as measured in the cases of (1) low power NBI ($P_{inj} \approx 0.7$ MW), (2) low power NBI + ECH (0.56 MW generated power), and (3) high power NBI ($P_{inj} \approx 2$ MW). Contrary to the low power NBI cases (Figs 2,4), with transition to the high power NBI, the changes in $V_f(\Theta)$ variations occur in the same directions as in the case of ECH imposed on NBI (Fig. 5). The addition of 0.56 MW ECH results in stronger changes of V_f and j_p than the NBI power rise to 2 MW. Presumably, this can be associated with an essentially collisional character of thermoelectric effect and a stronger influence of ECH on the electron temperature in SOL.

[1] HARBOUR, P.J., et al., J. Nucl. Mater. **162-164** (1989) 236.
[2] SHAFFER, M.J., LEIKIND, B.J., Nucl. Fusion **31** (1991) 1750.
[3] HARBOUR, P.J., Contrib. Plasma Phys. **28** (1988) 417.
[4] STAEBLER, J.M., HINTON, F.L., Nucl. Fusion **29** (1989) 1820.
[5] MIZUUCHI, T., et al., in Controlled Fusion and Plasma Physics (Proc. 18th EPS Conf. Berlin, 1991), Vol. 15B, P. III, EPS, Geneva (1995) III-65.
[6] ZUSHI, H., et al., Paper presented at IAEA TCM on H-Mode Physics - 5th Workshop on H-Mode Physics, Princeton(1995).

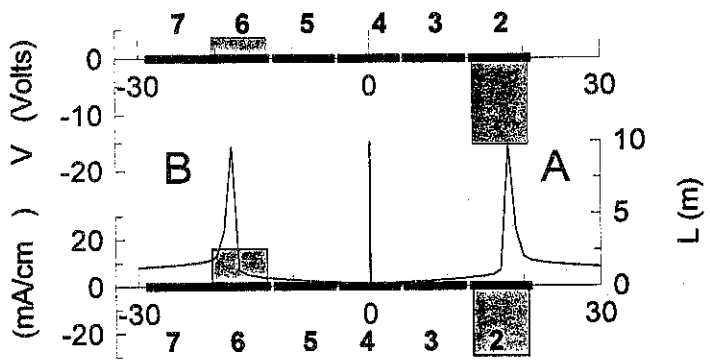

Fig.1. V_f and j_p distributions over collecting plates at $\Theta=0^o$; NBI, 3 MW (#73435). Solid lines A and B: calculated connection length L vs θ.

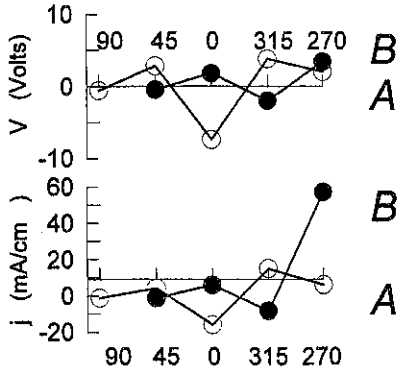

Fig.2. Maximum values of V_f and j_p vs Θ (NBI, 0.7 MW, 62°, #74263-74271)

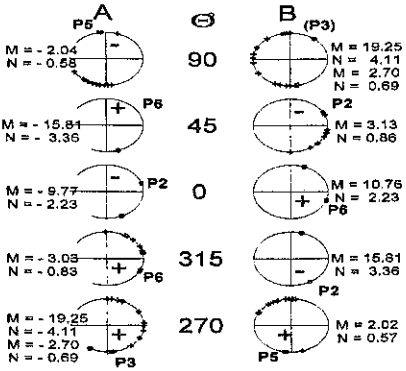

Fig.3. Calculated characteristics of the divertor field lines on the top, bottom, and outboard sides of the torus

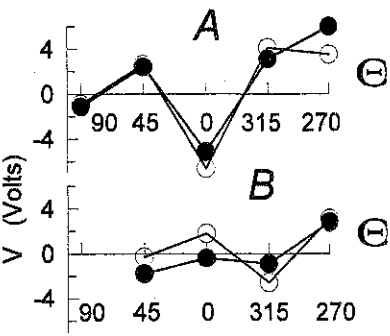

Fig.4. The effect on $V_f(\Theta)$ of NBI inlet position: ○, 9 field periods from array; ●, 6 field periods; #74073-74080.73892-73902

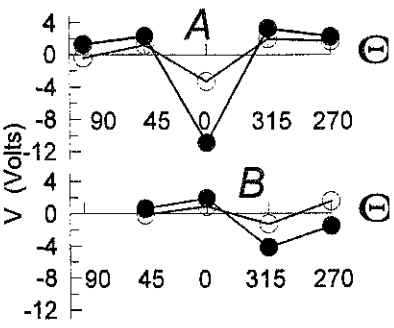

Fig.5. The effect of ECH on $V_f(\Theta)$: ○, NBI, (0.7 MW, 62°); ●,NBI+ECH(106 GHz); Θ= 0° CP #74248-74255

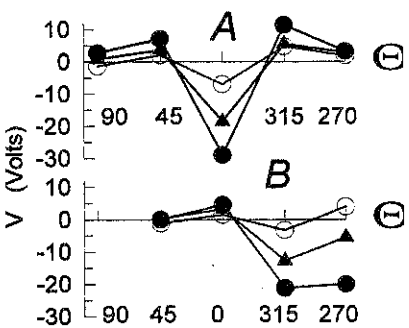

Fig.6 The effect of heating power on Vf(Θ) variations: ○, NBI (0.7 MW); ●, NBI + ECH (0.55 MW); ▲, NBI (2 MW). #74073-74080

DOMINANT ION HEATING SCENARIOS AND TWO ION HYBRID RESONANCE SCENARIOS IN ITER

V.Vdovin, RNC Kurchatov Institute, Moscow
A.Fukuyama, Okayama university, Japan
T.Watari, National Institute of Fusion Studies, Nagoya, Japan

Abstract. In the work we propose and validate with full wave code [1] scenario for a reactor grade plasma: "heavy" minority Tritium fundamental harmonic RF heating with outside of magnetic axis displaced IC resonance. With that IC resonance displacement the D-T ion hybrid resonance is out of plasma. Transport calculations have shown new operational scenario for the ITER with Hot Ion mode, possessing a reliable burn control, easy satisfaction to Greenwald density limit and more 100 MW of Alphas power help for L-H transition in ITER plasma. Usual second tritium harmonic can also deposit up to 80% of RF power to ions again with outside displaced IC resonance. In another regimes with some higher frequency the D-T hybrid resonance provides possibility off axis well localized driven current drive density control.

In present ITER design [2] it is expected to have in burning plasma 9-14% of He ash and 2% of Be^9 (surface material of the first wall), so amount of tritium and deuterium content f_T (=f_D) is 33-37 %. And interesting to evaluate in driven burn conditions the "heavy" minority heating scenario with $\omega = \omega_{cT}$ resonance ($\omega = \omega_{cD}$ is not appropriate to strong Alphas absorption competition) displaced in some extent outside of magnetic axis to eliminate from
plasma D-T hybrid resonance. Very important that Fast Waves (FW) absorption by electrons is strongly decreased in this scenario due to small FW parallel phase velocity $\omega / k_{//} < V_{Te}$, the decreased size plasma boundary - IC resonance layer $\Delta a \approx \frac{2}{3} a$ with its significantly lower off axis averaged electron beta, as it is seen from optical thickness for electron absorption:

$$\tau_e \equiv \frac{\sqrt{\pi}}{4} \Delta a < \beta_e \xi e^{-\xi^2} > \ << 1, \quad \left(\frac{\omega}{k_{//}} = V_{Te} \right)$$

Here<...> means space averaging over boundary - resonance distance.

In Fig.1 we show power deposition of FW to the tritons at ion temperature T_{io}= 27 keV ($T_{eo} = T_{io}$, $\alpha_T = 1.0$), plasma density n_{eo}=8.5 $10^{19} m^{-3}$, $<n_e>$= 7 10^{19} m^{-3}, impurity content 9% He, 2% Be and Argon seed to keep Z_{eff}=1.7 for a divertor operation needs. Also shown are quasi poloidal FW electric field contour plots (Abs(ReE_N)). The full wave calculations have been done at ITER DDR [2] high beta equilibrium plasma with parabolic pressure profile (R_o= 814 cm, B_o=5.7 T,
f = 25 Mhz, N_{tor}=42) and real antenna configuration. In this run up to 98% of RF power was absorbed by tritons. The code self consistently treats parallel electric field, kinetic plasma response is described by usual "reduced order" scheme.

The transport calculations with a dominant ion RF heating reveal new HOT ION operational ITER regime, one example of that is given in the Table 1, showing high Q = 20 driven burn with P_{alpha} =300 MW in sawteething He ash and Be deluted plasma, with a density below Greenwald's limit. The ion temperature twicely exceeds the electron one, even without internal transport barier creation. Decrease of RF power from 70 MW to 35 MW leads to about 200 MW of Alphas power, providing reliable burn control.

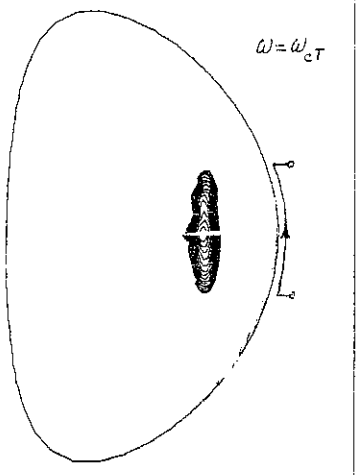

Fig.1a Power deposition to tritons

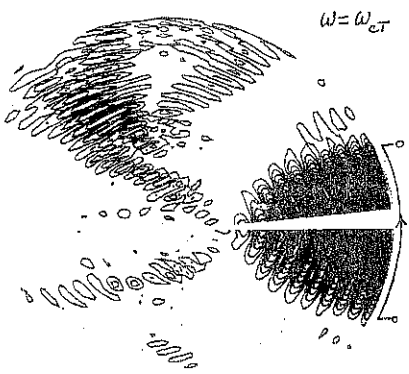

Fig.1b Poloidal electric field

Usual second Tritium harmonic can also provide up to 80% of RF power to tritium and deuterium deposition at conditions of displacement resonance off axis outside to the same position as in previos fundamental harmonic scenario. Power depositions to the tritons are given in Figs.2 at frequency 50 MHz, plasma density $<n_e>=1\ 10^{20} m^{-3}$ tritons temperature 40.5 keV (due to tail formation), deuterium one 27 keV, N=42.

It was shown that in L mode at lower plasma density $4\ 10^{19}\ m^{-3}$ the dominant ion heating provides 100 - 160 MW of Alpha power help for L - H transition, depending on transport conductivity assumptions. It has occured that this help at lower density only possible to realize with a broad RF power deposition to ions (several frequencies, k// shaping, etc.).

The D-T hybrid resonance appears in ITER plasma at some higher frequencies (26 - 30 MHz) and provides very localized RF driven current density control (for example, near q = 1 and q = 2 surfaces) as shown in Figs.3,4. Contour plots of poloidal electric field reveal fine structure at two ion hybrid resonance region, manifesting slow electrostatic wave excitation due to FW convertion. We stress that in this case at $\omega / k_{//} < V_{Te}$ the first converted wave is not Ion Bernstein Wave, but kinetic electrotastatic wave with its more larger perpendicular wave lengths. Typically about 50% of RF power is absorbed by electrons, remaining part of RF power goes to ions. Control runs have shown that if parallel electric field was enforced to be zero (code permits such an option) - then RF power going to electrons approaches ~ 100% and fine structure near D-T hybrid resonance disappears. We conclude that selfconsistent treatment of parallel electric field of waves is a crucial element in large scale high beta reactor plasma where electron absorption dominates in usual high frequencies ICR ITER scenarios [2] and must be especially correctly treated at low frequencies.

Table 1.

representative ITER in driven Hot Ion mode (case $\chi_i = 0.6\chi_*$)

Volume averaged ion temperature,	$< T_i >$	23 keV
Volume averaged electron temperature	$< T_e >$	12.9 keV
Volume averaged density	$< n_e >$	0.7×10^{20} m^{-3}
Impurity fractions	f_{He}, f_{Be9}	0.09, 0.02
Effective Z	Z_{eff}	1.70
Radiated power	P_{rad}	82 MW
Transport confinement time in the run	τ_{run}	4.29 sec
Transport confinement time, τ_E	$0.85\tau_{E,th}^{ELM\text{-}free}$	4.27 sec
Central ion temperature	T_{i0}	50 keV
Central electron temperature	T_{e0}	27.5 keV
Alpha particles power	P_α	299 MW
RF power to tritons	P_{RF}	70 MW
Q factor	Q	21
DT triple product	$<n_{DT}>(<T_e> + <T_i>)\tau_E/2$	3.2×10^{21}m^{-3}keV s

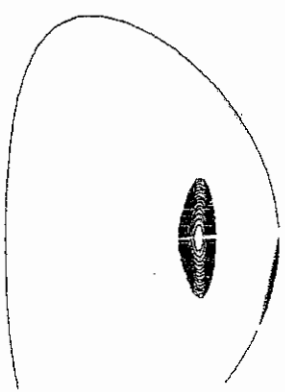

Fig.2 Left: power to tritons at $W=2W_{CT}$

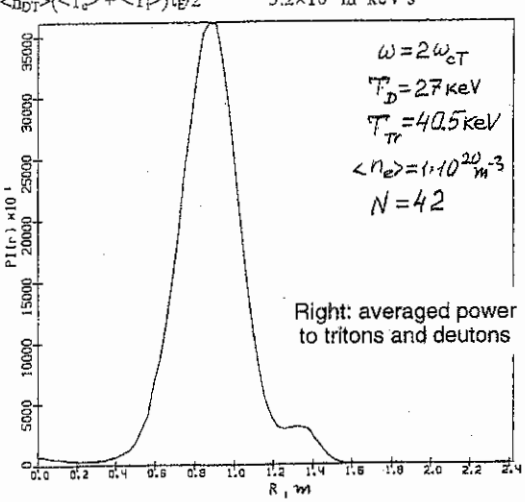

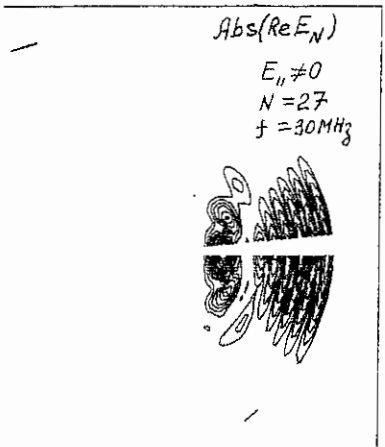

Fig.3a SW exitation at DT HR

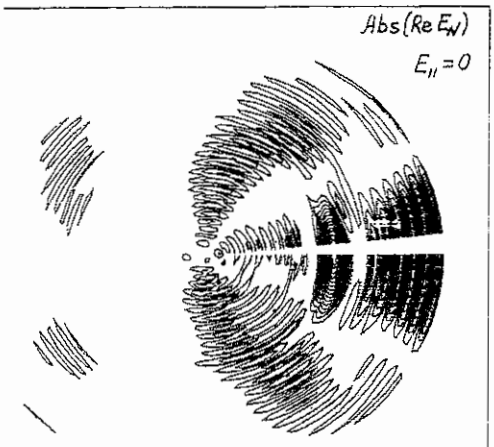

Fig.3b HR at E//=0

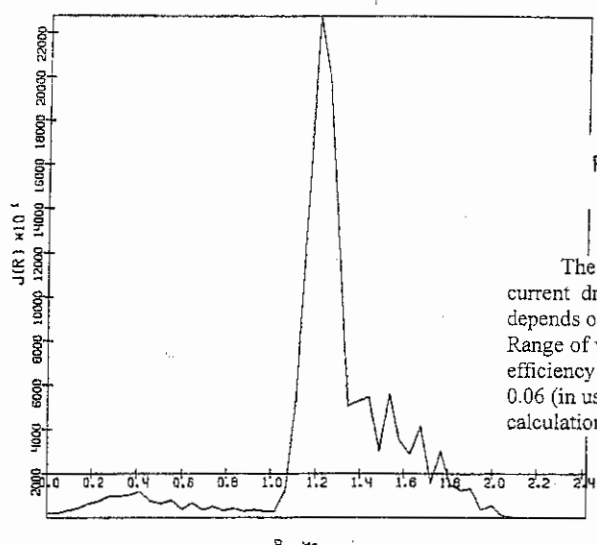

Fig.4 CD profile at DT hybrid resonance

The computations have shown that current drive efficiency gamma strongly depends on equilibrium magnetic structure. Range of values Mode Converted CD efficiency gamma varied from 0.16 to 0.06 (in usual SI units) and more extensive calculations must be done.

Toroidal broadening of IC resonance [3], not treated by us, will increase ion absorption rate further. From other hand finite Larmor radius effects can decrease this rate in fundamental harmonic scenario in some extent. We plan to investigate these effects.

References. 1. V.Vdovin, T.Watari,A.Fukuyama, NIFS 469, 1996
2. ITER Document Design Report, San Diego, ITER JCT, 1996
3. M.Brambilla, Physics Letters 188A, 1994

Observation of Improved Ohmic Confinement in Highly Elongated TCV Discharges

C.Nieswand, F.Hofmann, R.Behn, I.Furno, J.-M.Moret, Z.A.Pietrzyk, A.Pochelon, H.Reimerdes, H.Weisen

Centre de Recherches en Physique des Plasmas
Ecole Polytechnique Fédérale de Lausanne
Association EURATOM-Confédération Suisse
CH-1015 Lausanne, Switzerland

1 Introduction

The primary goals of the TCV tokamak are to produce plasmas with high elongation and to investigate confinement behaviour for a variety of plasma shapes [1]. A spontaneous transition to an improved ohmic confinement regime has recently been observed in moderately and highly elongated discharges limited by the central column. The observed features are similar to those observed in ASDEX (IOC regime).

2 General Observations during Improved Confinement

The transition to improved confinement is characterized by a spontaneous increase of plasma density, by about 10%, even when the external gas fuelling is reduced and a simultaneous increase of the electron temperature by more than 15%. Thus the total stored energy grows and the loop voltage and consequently the ohmic heating power drop. Both effects yield an improvement in β and the global energy confinement deduced from the equilibrium reconstruction code and confirmed by Thomson scattering measurements. The neutron rate and the Soft X-ray emissivity grow substantially and Z_{eff} is only moderately increased from 1.8 to 2.2.

Unlike ohmic ELM-free H-modes, where in general the density rises uncontrollable, this confinement mode can be maintained for the entire current flat top of more than one second. The plasma density saturates after the transition since the density feedback reduces the gas fuelling. Changes in the D_α emission can be attributed to this reduction of fuelling rather than to a change in particle transport or recycling near the edge. A slight change of the internal plasma inductance l_i, modifications of density and temperature profiles and changes of the sawtooth behaviour indicate that particle and energy transport are affected in the whole plasma volume.

2.1 Low Plasma Current

The transition was first observed in discharges at low current and moderate elongation (240-300kA, $q_{95} \approx 5$, κ=1.6-1.9, $\delta \approx 0.25$, $B_t = 1.43$T). In these plasmas the transition occurres

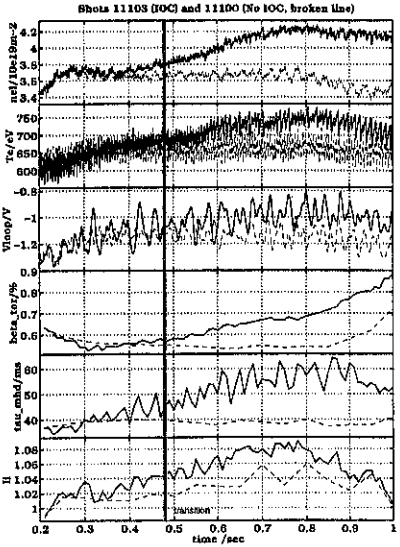

Figure 1: Comparison of an IOC plasma (solid lines) and a non IOC plasma (broken lines). (255kA, $q_{95} \approx 5$, κ=1.8, $\delta = 0.28$, $B_t \approx 1.43T$)

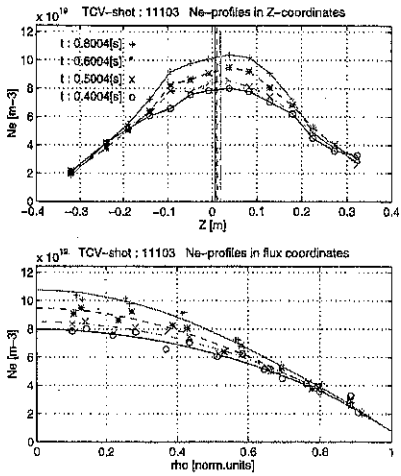

Figure 2: Electron density profile peaking during improved confinement at low current

during the current flat top when the plasma configuration is fully established (see figure 1). The electron energy confinement time deduced from Thomson scattering data increased from 16ms to 30ms after the transition. The equilibrium reconstruction reveals higher values. For "normal" confinement the energy confinement time saturates at high density, while plasmas with improved confinement do not show this behaviour.

The sawtooth period grows after the transition and in a few cases the sawtooth activity disappears completely. Soft X-ray tomography does not indicate a significant change in the q=1 surface position.

The electron density profile clearly peaks after the transition, caused by an increase of the central density whereas the edge density remains constant (figure 2). The central electron temperature increases slightly. This indicates a small change of the current density profile also suggested by an increase in the plasma inductance.

2.2 High Plasma Current

In highly elongated plasmas at high current (500-800kA, $q_{95} \approx$ 2-3, κ =2-2.5, $\delta \approx 0.25$) the transition occurs during the shaping phase of the scenario and sometimes even before the current flat top is reached (figure 3). Changes due to modifications of the configuration and due to a transition are therefore difficult to distinguish. An improvement of the electron energy confinement time from 12ms up to 20ms was observed. The highest value of β_{tor} of

2.9% ever achieved in TCV (as obtained from purely magnetic equilibrium reconstruction) was obtained under these conditions.

In contrast to the low current case the sawtooth period usually shortens and strong MHD activity often leads to minor or even major disruptions. Analysis of the signals of poloidal and toroidal magnetic probes suggest an (n=2,m=3) structure for the dominant mode, which grows during a few milliseconds and disappears shortly before the disruption (figure 4). Presently the operational domain of TCV at high elongation is limited on the low current side by the vertical instability and on the high current side by non-axisymmetric MHD activity [2].

The electron temperature profiles are essentially flat near the centre with indications of

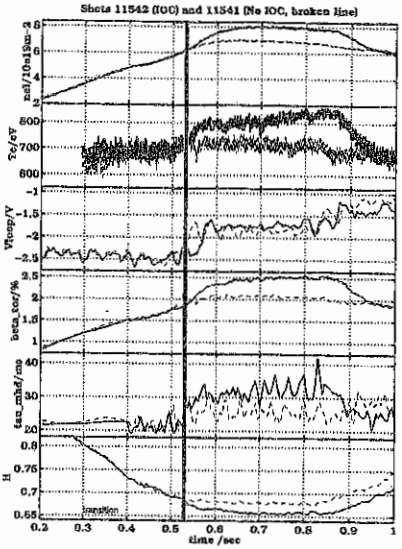

Figure 3: Comparison of an IOC plasma (solid lines) and a non IOC plasma (broken lines). (710kA, $q_{95} \approx 3$, κ=2.3, δ = 0.35, B_t = 1T)

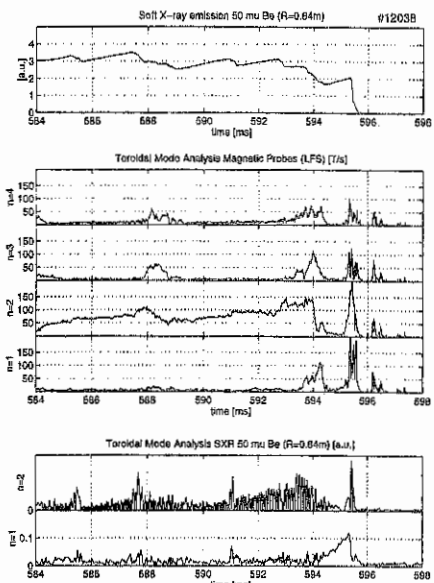

Figure 4: Mode n=2,m=3 observed in a high current discharge with improved confinement

"shoulders" near the q=1 surface and steep gradients towards the outside.

In contrast to the low current case, the plasma inductance decreases slightly.

3.Conditions for IOC

Up to now improved confinement was only observed with plasmas at elongations above 1.35. Low triangularity seems to be favourable as well as a slight tilt of the plasma. Both of these modifications reduce the extent of the plasma-wall interaction zone. This is consistent with the observation that wall conditions have a large effect on accessibility and quality of the improved confinement mode. Better improvement in confinement and faster transitions can be obtained whith low recycling walls. These conditions are

also favourable for H-modes in diverted TCV plasmas. A few discharges in a series of improved confinement shots switched to H-mode!

4.Conclusions

Transitions to an improved confinement regime for limited ohmically heated plasmas have been observed. Some of the observed features are very similar to those of the IOC regime observed in ASDEX in diverted discharges [3].

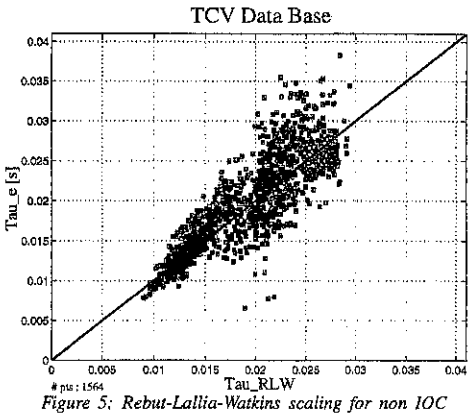

Figure 5: Rebut-Lallia-Watkins scaling for non IOC discharges (grey) and IOC dicharges (black)

The Rebut-Lallia-Watkins scaling was found to be appropriate for ohmic TCV discharges [4,5]. Plasmas with improved confinement do not deviate from RLW-scaling more than plasmas with "normal" confinement (figure 5). The RLW-scaling predicts the confinement time in the improved confinement mode reasonably well because of its strong power dependence (P^{-1}) and because of the reduced ohmic heating power in improved ohmic confinement.

High elongation and wall conditions with low recycling are favourable for reaching this regime. Profile changes, changes in internal inductance and changes in the sawtooth behaviour suggest a global change in the current density profile.

Acknowledgements

The authors acknowledge the support of the entire TCV team. This work was partly supported by the Swiss National Science Foundation.

References

[1] Hofmann, F. et al., Plasma Phys. Control. Fusion **36** (1994) B277

[2] Hofmann, F. et al., Poster P2.010, this conference

[3] Söldner, F.X. et al., Phys.Rev.Let. **61** (1988) 1105

[4] Nieswand, C. et al., 38th APS Meeting DPP. (1996) 6P38

[5] Weisen,H. et al., LRP571/97 (1997), submitted to Nuclear Fusion

Non-local plasma response induced by peripheral perturbations in the RTP tokamak

P.Mantica[1], M.R. de Baar, J. de Kloe, F. De Luca[2,1], P. Galli[2,1], G. Gorini[2,1], G.M.D. Hogeweij, A. Jacchia[1], N.J. Lopes Cardozo, A.A.M. Oomens and the RTP-team

FOM Instituut voor Plasmafysica 'Rijnhuizen', Associatie Euratom-FOM, P.O.Box 1207, 3430 BE Nieuwegein, The Netherlands
[1] Istituto di Fisica del Plasma, Ass. Euratom-ENEA-CNR, Milano, Italy
[2] INFM and Dipartimento di Fisica, Università degli Studi di Milano, Milano, Italy

Evidence from transient transport experiments in tokamaks suggests that the electron heat transport cannot be adequately described in terms of a diffusivity coefficient depending only on local plasma parameters. The non-local character of electron heat transport appears more clearly when fast electron temperature (T_e) perturbations are induced at the plasma periphery. Experiments of this kind have been performed in the RTP tokamak. The new findings confirm and extend the evidence from other tokamaks, particularly TEXT and TFTR [1,2,3,4].
In these experiments in RTP, different types of peripheral perturbations have been used : 1) Oblique injection of frozen H_2 pellets to induce a rapid and localised cooling of the plasma periphery ("cold pulse"); 2) Either modulated ECH with very external resonance location or fast I_p ramps to induce positive T_e pulses in the outermost plasma region. In both cases a distinct non-local behaviour in transport is observed, namely a fast reaction of the temperature in the plasma core opposite in sign with respect to the induced edge perturbation (Figs.1,2). This kind of response is inconsistent with purely local transport models.

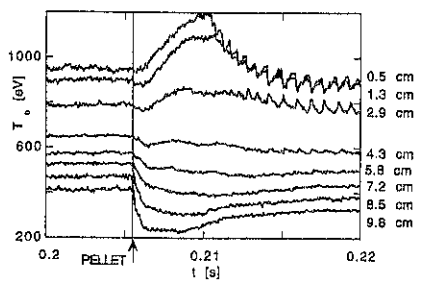

Fig.1: T_e time traces during an oblique pellet injection at low density.

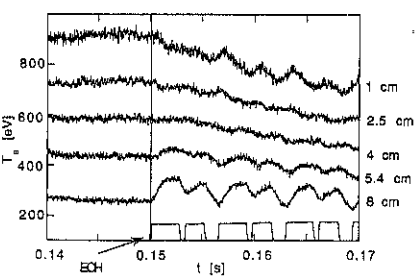

Fig.2: T_e time traces with peripheral MECH. The power was deposited at r=12.5 cm.

In the case of Fig.1, the pellet impact parameter is r=11.2 cm (r/a=0.7). The region of direct particle deposition is limited to ±0.5 cm around the pellet trajectory. However, as discussed in [5], a fast anomalous density increase is observed in a larger region. In the present case these effects should be limited to r=11.2±1.5 cm. The density increase in the peripheral region induces a rapid cooling of the plasma periphery (Fig.3). The central T_e rise is delayed with respect to the edge T_e drop by about 600 μs. It is very interesting that, apart from this delay, the time evolution of the central T_e mimics well the time evolution of the edge T_e. In fact, in cases where the pellet is vaporized before reaching the plasma (i.e. only a cold gas puff is injected) the observations are similar to those in Fig.1, but on a slower time scale. A scan of the pellet deposition radius has shown that the central T_e rise is present for deposition radii $\geq$ 7 cm (r/a=0.4). The time evolution of the T_e and p_e (pressure) radial profiles (from ECE

measurements) for the case of Fig.1 is shown in Figs.3,4 and has been confirmed by high resolution Thomson scattering measurements. One can see that the T_e profile shows a fixed point which identifies the region of the rise. The positive T_e variation (ΔT_e) is maximum in the centre. Δp_e vanishes near the edge (adiabatic pellet cooling). This suggests that it is the edge ΔT_e, rather than Δp_e, that triggers the non-local T_e rise.

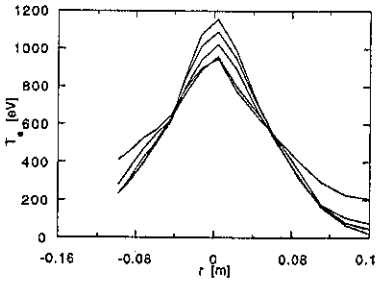

Fig.3: T_e profile evolution for the shot of Fig.1 from t=205 ms to t=209 ms.

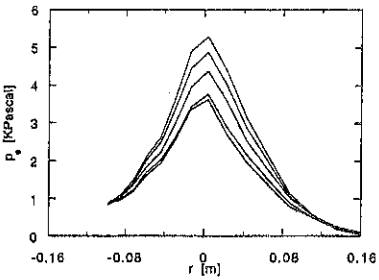

Fig.4: p_e profile evolution for the shot of Fig.1 from t=205 ms to t=209 ms.

Scans of various plasma parameters (n_e, I_p, B_T, P_{ECH}, T_e) have been performed, showing a crucial role of the plasma density in controlling the non-local rise. Figs.5,6 show that the region of the rise shrinks and the relative change in central temperature decreases with increasing density. The region of the rise is definitely larger than the q=1 surface. At a given density, it increases with increasing plasma current. Application of EC power does not reduce the non-local effect. EC heated discharges, allowing to decouple n_e, and T_e, show that the parameter controlling the non-local rise is n_e rather than n_e/T_e as suggested in [4].

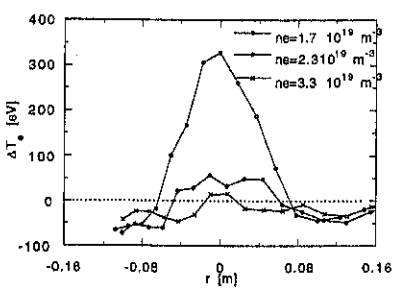

Fig.5: Behaviour of T_e perturbation with increasing density. Ip was kept constant (q_a=5.2).

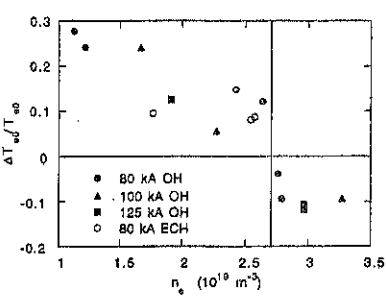

Fig.6: Dependence of relative central T_e variation on line averaged density.

Above a line average critical density value n_e=2.7 $10^{19}m^{-3}$, the central T_e rise disappears and a rapid T_e drop is observed instead. In Fig.7 one can see that the negative perturbation in the central channels is too fast to be due to the propagation of the cold front from the edge. Therefore the central T_e drop also has a non-local character. This is similar to what has been observed in JET [6,7,8], where always negative but instantaneous reactions of the plasma core to edge cooling induced by laser ablation have been observed. Evidence from RTP suggests that such negative non-local reaction may always be present, but below the critical density it is masked by the huge non-local rise. Actually, the positive reaction is slightly delayed with

respect to the negative one, so that signs of the presence of both a positive and a negative central reactions can be seen already in low density cases (Fig.1), but more clearly in cases near the density critical value, such as shown in Fig.8.

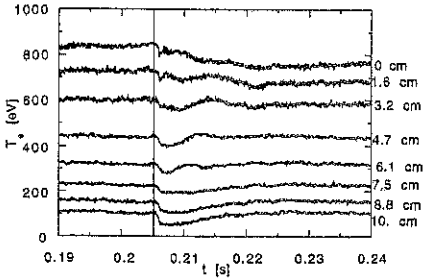

Fig.7: T_e time traces during an oblique pellet injection at high density.

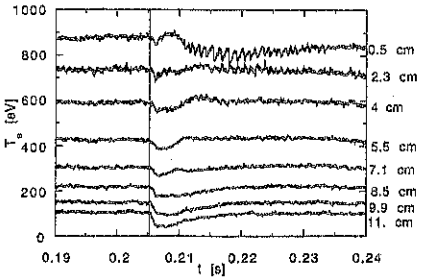

Fig.8: T_e time traces during an oblique pellet injection at a density near the critical value.

In sawtoothing discharges an immediate (also non-local) increase in the sawtooth period and amplitude is observed (Fig.9). The reheat rate remains unchanged. As suggested in [3,4], such changes may be important clues to understanding the non-local mechanisms. However, evidence from RTP suggests that they may rather be related to the non-local drop than to the non-local rise, since they are observed also in high density discharges where the non-local rise is damped and only the non-local drop is present (Fig.10).

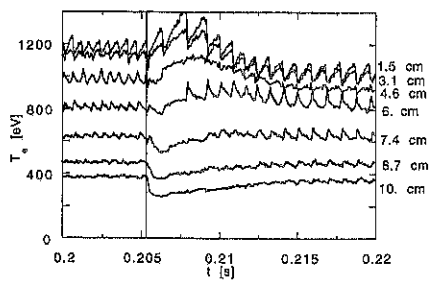

Fig.9:T_e time traces during an oblique pellet injection in a sawtoothing discharge at low density.

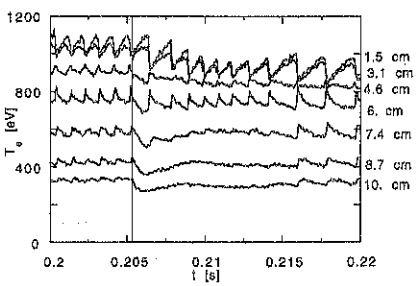

Fig.10:T_e time traces during an oblique pellet injection in a sawtoothing discharge at high density.

Within this picture of two phenomena of different nature simultaneously present, one would argue that addressing the question whether the T_e rise is due to a decrease in the electron heat diffusivity χ_e in the central region is probably too simplistic. In fact the central non-local T_e drop observed in JET was attributed to a fast increase of χ_e across most of the plasma [7,8]. To help clarifying this point, oblique pellet injection into on- and off-axis modulated ECH (MECH) discharges has been performed on RTP, with the expectation that a change in χ_e would be reflected by a change in the modulated wave. One can see that in the on-axis case (Fig.11) no increase in the modulation amplitude is observed, even in the channels that exhibit the non-local T_e rise. If anything, a small decrease is observed. On the other hand, in off-axis MECH discharges (Fig.12) a pronounced decrease is observed in peripheral channels. This cannot be due to the density, whose time behaviour is different. The MECH wave in the central channels

still remains unchanged. Detailed analysis of these experiments is in progress, however the data seem to indicate that the cause of the non-local central T_e rise should not be sought in a change of diffusive transport, but rather of other transport components, to which the fast modulation is less sensitive. Convection is a possible candidate, as suggested in [2].

Finally, oblique pellet injection has been applied to negative central shear (NCS) plasmas with hollow T_e profiles, obtained in RTP by strong off-axis EC heating [9]. The non-local rise is present in these plasmas, too, but the reaction in the centre is much slower than in the case of peaked T_e profiles, while the reaction at the radial positions of the (off-axis) maxima of the T_e profile remains fast (Fig.13). Therefore, the T_e profile evolution shows that in the first milliseconds the rise is concentrated around the T_e maxima, leaving the centre almost unaffected (Fig.13). Fig.14 shows the T_e profile evolution for a pellet in NCS plasmas.

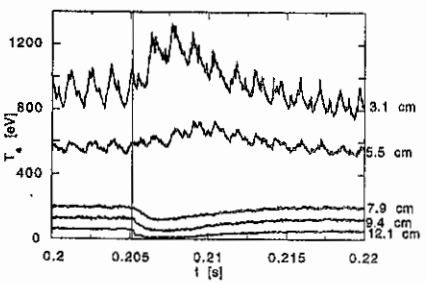

Fig.11: T_e time traces during an oblique pellet injection in a on-axis MECH discharge.

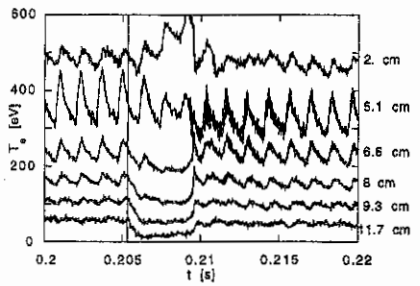

Fig.12: T_e time traces during an oblique pellet injection in a off-axis (r=6 cm) MECH discharge.

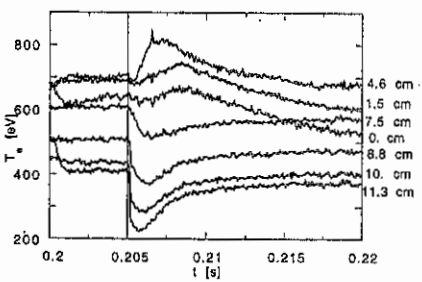

Fig.13: T_e time traces during an oblique pellet injection in a NCS discharge .

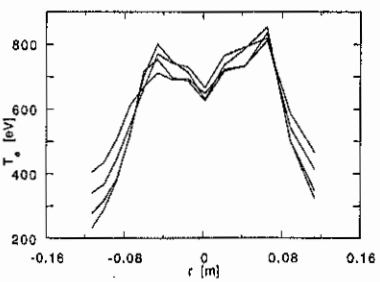

Fig.14: T_e profile evolution for the shot of Fig.13 from t=205 ms to t=209 ms.

This work was performed under the Euratom-FOM and the Euratom-ENEA-CNR association agreements, with financial support from NWO, CNR and Euratom.

[1] K.W.Gentle et al., Phys.Rev.Lett. **74** (1995) 3620.
[2] K.W.Gentle et al., submitted for publication to Phys. Plasmas.
[3] M.W.Kissick et al., Nucl.Fusion **36** (1996) 1691.
[4] M.W.Kissick et al., Univ. of Wisconsin Report, UW-CPTC 96-6 (1996).
[5] J.De Kloe et al., this conference.
[6] P.Galli et al., Proc. 23rd EPS Conf. Kiev (1996), Vol. 20C, Part 1, 135.
[7] P.Galli et al., submitted for publication to Nucl. Fusion.
[8] P.Mantica et al., this conference.
[9] G.M.D.Hogeweij et al., Phys.Rev.Lett. **76** (1996) 632.

ν* DEPENDENCE OF THE BETA LIMIT IN JET

G.T.A. Huysmans, G. Cordey, C. Gormezano, A.C.C. Sips, B.J.D. Tubbing
JET Joint Undertaking, Abingdon, OX14 3EA, UK.

Introduction

From the ITER multi machine database containing data on beta limits from DIII-D, COMPASS, TFTR, JT60-U and ASDEX-U, it appears that the beta limit decreases with decreasing collisionality [1]. At high values of the collisionality, ν*, the maximum value for β_N (= β a[m] B[T]/I[MA]) is close to 4, a value typical for the ideal MHD stability limit. At lower values of ν* (typical for ITER) the maximum β_N is limited by low m/n magnetic islands which have been interpreted as neo-classical tearing modes.

Previously in JET, the beta limit has been studied mostly in 1MA/1T discharges. In an ITER like configuration (q_{95}=3.1, $\langle n_e \rangle \sim 2.2\ 10^{19}$ cm^{-3}) β_N values of 3.8 for about 1 second were achieved [2]. Neo-classical tearing modes have not been observed in these discharges. The beta limit in these discharges appears to be set by an increased ELM activity and fishbones.

JET high beta discharges

Recently, in JET, long pulse high beta discharges have been established at the ITER parameters for the shaping (ellipticity =1.75, triangularity = 0.25), q_{95} (= 3.5), and the collisionality, at toroidal fields 1.0 to 1.7 T. Normalised beta values above 3 have been sustained for several seconds, limited by the length of the heating pulse. Fig.1 shows an example of a 1.7 T/1.7MA high beta discharge. With the available additional heating power of ~24 MW, the beta limit has been reached in 1 Tesla and 1.4 Tesla discharges. The maximum normalised beta in this case is just below 4. At 1.7 Tesla the maximum normalised beta is just above 3 and is limited by the total heating power (see Fig.2).

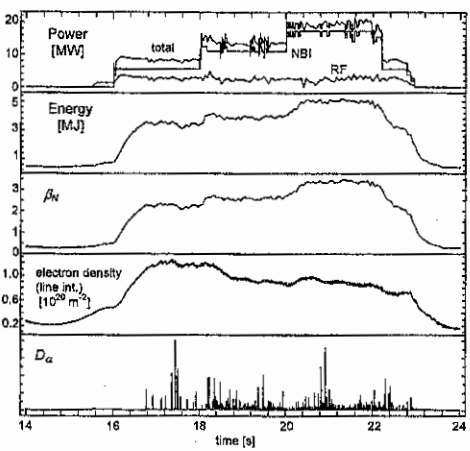

Fig.1 Overview of JET high beta discharge #40562 with B_0=1.7T, I_p=1.7MA, $\langle n_e \rangle$=2.8 $10^{19} m^{-3}$ (at t = 21s).

The confinement in these elmy H-mode discharges is relatively good. Figure 3 shows the confinement enhancement factor $H_{89\text{-}P}$ as a function of the normalised beta at the time of the maximum beta. Even at a normalised beta as high a 3.7 the confinement factor is larger than 2. The confinement does degrade when the heating power exceeds the power needed to reach the beta limit.

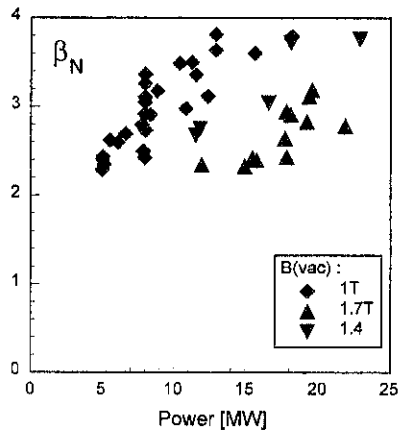

Fig.2 The maximum normalised β_N as a function of the total heating power in the 1996/97 JET high β discharges. β_N = 80 W_{dia} ε / (3 B_0 I_p A), (W_{dia} diamagnetic energy, ε inverse aspect ratio, A area poloidal cross section, B_0 toroidal field, I_p plasma current).

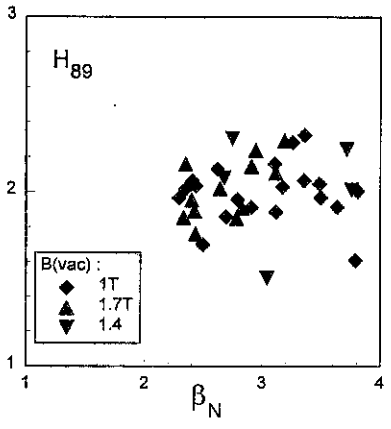

Fig.3 The confinement factor H_{89} as a function of the normalised beta (β_N)

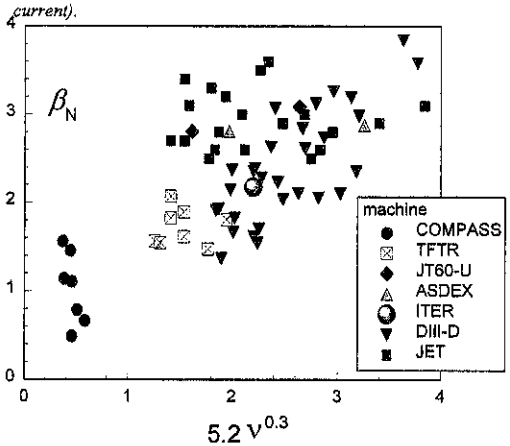

Fig. 4 ν^* dependence of the normalised beta (based on diamagnetic energy) sustained for at least one second. Included are points from the ITER multi-machine database [1] (Collisionality parameter defined as: $\nu^* = 0.012\ n_e\ (10^{20})\ q\ R\ /\ (\varepsilon^{3/2}\ T_e^2$ (keV)) at q=2 radius).

ν^* dependence

A database with 55 recent JET high beta discharges ($\beta_N > 2.5$) has been compiled. Figure 4 shows the points in the database as a function of the collisionality and the normalised beta sustained for at least one second. It appears that the normalised beta reached does not depend on the collisionality, i.e. the JET data does not agree with the linear scaling of β_N with $5.2\ \nu^{*0.3}$ as used in the ITER physics assessment [1]. There is also no obvious sign of low m/n magnetic islands, i.e. neo-classical tearing modes. The points in Fig.4 are based on the total diamagnetic energy, using an estimate of the thermal energy reduces the normalized beta by 20 - 35 %. However, also the thermal β_N does not show any dependence on the collisionality.

Observed MHD

The predominant MHD activity observed during the high beta phase is due to MHD modes localised in the plasma centre and ELMs. Islands (i.e. neo-classical tearing modes) have, so far, not been observed.

ELMs

The steady state high beta discharges are elmy H-modes with regular type 1 ELMs. With increasing input power and therefore increasing β_N the ELM frequency increases (see Fig. 1). The amplitude of each ELM (as measured from the amplitude of the D_α signal) varies considerably but does not appear to increase with increasing input power (or β_N).

Central modes

The character of the central MHD modes varies considerably. Fishbones are very common, but also continuous n=1 modes are observed, central n=2 modes are less frequently seen.

Sawteeth are observed in the low power phase of these discharges. At high β_N there are, generally, no sawteeth. This is either due to a sawtooth stabilisation by the large fraction of fast particles or by the changes in the current profile due to the increased bootstrap current which causes q on axis to increase.

Ideal MHD Stability limits

The ideal MHD ballooning and kink stability limits for discharge #40565 at the time of maximum beta (β_N=3.8) have been calculated with the HELENA equilibrium code [3] and the MISHKA-1 stability code [4]. Figure 5 show the normalised pressure gradient as a function of the minor radius and the ideal MHD ballooning limit. The n=1 external kink mode is stable up to $\beta_N = 5.2$. Thus, the observed beta limit with β_N just below 4 is consistent with the limit set by ideal MHD ballooning modes.

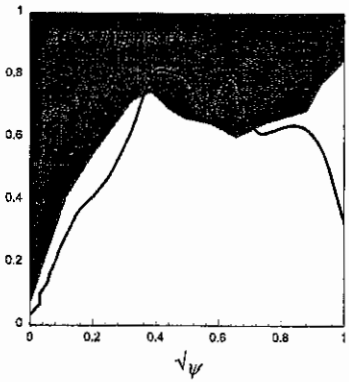

Fig. 5 The ballooning stability limit (marginally stable α/q^2) as a function of radius and the experimental pressure gradient (α/q^2) for discharge 40565, at β_N=3.8.

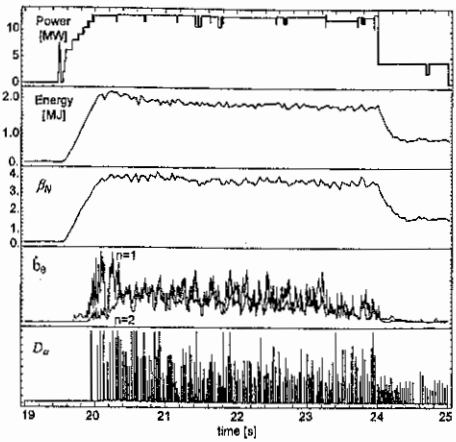

Fig.6 The time traces of a 4 second high beta discharge, #38564, B_0=1.0T, I_p=1.0 MA, $<n_e> \sim 1.8\ 10^{19}\ m^{-3}$.

Summary

Long pulse high beta discharges with the ITER values for the shaping, q_{95} and collisionality and a normalised beta larger than 3 have been sustained in JET for up to 4 seconds. Fig.6 shows the time traces of a 4 second high beta discharge (#38564) at B_0=1.0T, I_p=1.0 MA.

A database of 55 high beta discharges shows no dependence of the sustained normalised beta with collisionality as suggested in the ITER physics assessment [1].

The MHD activity at high beta is due to ELMs, fishbones and continuous n=1 and n=2 modes in the plasma centre. Sawteeth are, in general, absent in the high beta phase. So far, no neo-classical tearing modes observed in the JET high beta discharges. This may be due to the absence of sawteeth (or long sawtooth free period), i.e no seed island is created. Even though there are ELMs and fishbones which can in principle create seed islands.

The observed limit to the normalised beta just below 4 is consistent with the ideal MHD ballooning limit.

References

[1] O. Sauter et al., *Beta limits in long pulse tokamak discharges*, Phys. Plasmas 4, (5) 1997, p1654.

[2] C.D. Challis et al., *Quasi Steady State Advanced Tokamak Scenarios in JET*, 22nd EPS Conf. Controlled Fusion and Plasma Physics, Bournemouth 1995, Volume 19c, part II, p. 69.

[3] G.T.A. Huysmans, J.P. Goedbloed, and W.O.K. Kerner, CP90 Conf. on Comp. Physics Proc., World Scientific Publ. Co.,(Ed. A. Tenner) 1991, p.371

[4] A.B. Mikhailovskii, G.T.A. Huysmans, W.O.K. Kerner, S.E. Sharapov, *Optimisation of Computational MHD Normal Mode Analysis in Tokamaks*, JET Report, JET-P(96)25 (1996), accepted for publication in Reports Plasma Physics.

Quasi-stationary high confinement by pellet injection in TEXTOR-94

J. Hobirk[1], A. Messiaen[2], K. H. Finken[1],
M. Brix[1], R. Jaspers[3], H. R. Koslowski[1], A. Krämer-Flecken[1], G. Mank[1],
J. Ongena[2], G. Van Oost[2], J. Rapp[1], G. Telesca[1], B. Unterberg[1]

Trilateral Euregio Cluster:
[1] Institut für Plasmaphysik, Forschungszentrum Jülich GmbH, EURATOM Association, D-52425 Jülich, Germany
[2] Laboratoire de Physique des Plasmas / Laboratorium voor Plasmafysica, Ecole Royale Militaire - Koninklijke Militaire School, Association "EURATOM-Belgian State", B-1000 Brussels, Belgium
[3] FOM-Instituut voor Plasmafysica Rijnhuizen, EURATOM Association, Neuwegein, The Netherlands

1 Introduction

It is well known that the confinement properties of a high temperature plasma change after injection of a deuterium pellet. In most of the experiments with ohmic heating, it is seen that the improvement of the energy confinement time is transient and holds for some 10 or 100 milliseconds [1].

In auxiliary heated discharges the situation is different, sometimes is the confinement improved after injection and in other cases even it deteriorates the confinement. These enhancements are always transient. A special case is the PEP-mode discharge where the initial condition prior to neutral beam injection is modified by pellet injection resulting in a transient enhanced confinement [2].

In TEXTOR-94 one or more pellets were injected into radiative cooled auxiliary heated discharges with improved confinement [3]. This results in quasi-stationary high confinement with peaked density profiles.

2 Quasi-stationary confinement after pellet injection

The discharges are performed at a current of 420kA. At t=0.8s the ICRH power rises to a value of 1.23MW. The neutral beam injection starts at 1s with a power of 1.1MW. Between 1s and 1.3s the discharge is in L-mode confinement. From t=1.3s to the end of the experiment the neon injection is feedback controlled by the Ne-VIII radiation. Shortly after 1.3s a transition to a RI-mode type confinement occurs. The energy in the plasma and with this also the energy confinement rises to a stationary value. It coincides with a strong rise in gamma (P_{rad}/P_{tot}) and density. This can be seen from picture 1.

At t=2.05s a pellet is injected with a velocity of 960m/s and penetrates 27cm into the plasma. The pellet with a particle content of $7 \cdot 10^{19}$ atoms yields in a strong increase

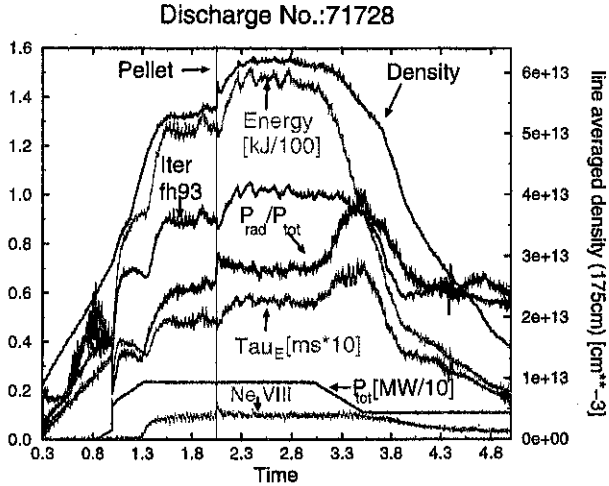

Figure 1: Transition to quasi-stationary high confinement

in density. Thereafter, the total number of electrons immediately decays, such that after 22ms the total number of electrons is reduced by half of the pellet particle content (Figure 2). This reduction is typical for strongly heated discharges. In contrast to L-mode

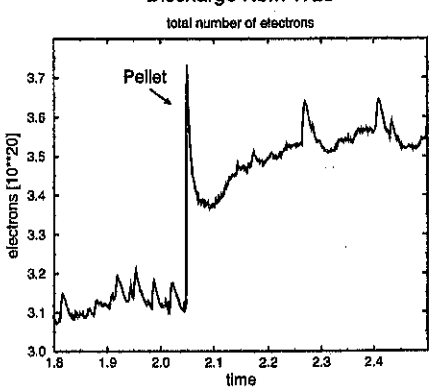

Figure 2: Total number of electrons

conditions, however, the density starts to increase again. This suggest that the pellet has mainly an indirect effect, i.e. it triggers a state of further improved confinement. Synchronously with the density rise also the energy and the energy confinement time increase, confirming the RI-mode scaling proportional to the density [3]. The radiation level is slightly higher in the high confinement phase due to the higher density. In figure 1 the f_H93 scaling factor with respect to the Elm-free H mode scaling ITERH93P is also

shown. This factor is rising due to the pellet injection from 0.9 to 1.0 in the example discharge. Sequential injection of 2 pellets appears to lead to even better confinement resulting in a f_H93 scaling factor of 1.08; with the normal RI-mode yielded only 0.88 in the same discharge. The results of some discharges can be seen in figure 3

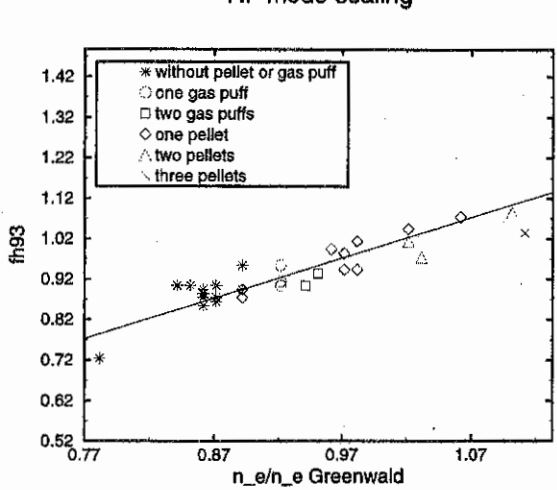

Figure 3: RI-mode scaling with short gas puffs or pellet fuelled discharges

From 3s on the heating power and the density are reduced to permit a safe landing of the discharge.

The high confinement phase following the pellet injection shows the following additional positive effects: 1) Z_{eff} is reduced by 15%. 2) τ_P is not enhanced as in high confinement H-mode discharges but remains nearly constant 3) τ_E increases by 18%.

3 Quasi-stationary high confinement after a short gas puff

It is also possible to establish a quasi-stationary higher confinement in RI-mode discharges with a **short** and **not** too strong gas puff. The discharges are similar to the pellet fuelled ones and the particle confinement time stays also nearly constant. One example of a discharge is plotted in figure 4. It is important, however, that the preceding gas puff is sufficiently short so that the density profiles do not broaden too much. Otherwise we obtain even a reduction of the energy confinement.

Since the gas fuelled discharges lead to density profiles which are slightly less steepened than those obtained with pellet fuelling, however, the overall confinement is less improved as compared to the pellet case. The number of particles (gas puff) injected in the discharge

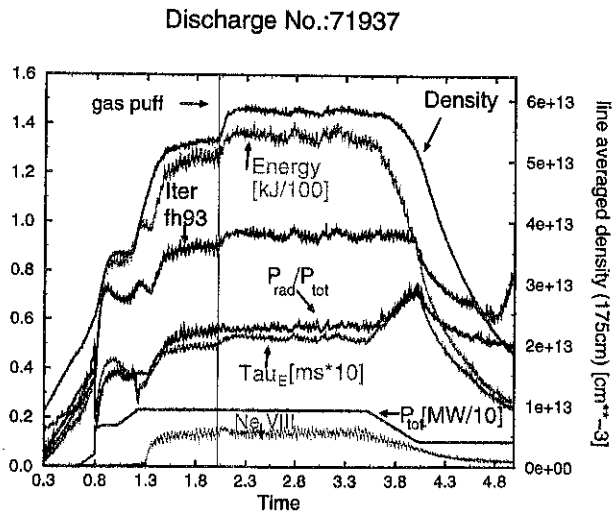

Figure 4: Transition to quasi-stationary high confinement with a gas puff

as shown in figure 4 was 5 times larger than thar injected by a pellet as shown in figure 1.

4 Summary

RI-mode discharges in TEXTOR-94 could be further improved by either injection a pellet or a short gas puff. The discharge comes again into a quasi-stationary high confinement phase with increased energy confinement but nearly unchanged particle confinement. In the pellet fuelled discharges enhancement factor of f_H=1.08 was reached using two sequential pellets.

References

[1] M. Kaufmann et al. Pellet injection with improved confinement in asdex. *Nuclear Fusion*, 28(5):827–848, May 1988.

[2] P Smeulders et al. Survy of pellet enhanced performance in jet discharges. *Nuclear Fusion*, 35(2):225–242, Feb 1995.

[3] A Messiaen et al. High confinement and high density with stationary plasma energy and strong edge radiation in the textor-94 tokamak. *Physical Review Letters*, 77(12):2487–2490, September 1996.

ITER Physics Experiments in JET D/T Plasmas

The JET Team
(presented by J Jacquinot)

JET Joint Undertaking, Abingdon, Oxon, OX14 3EA, UK

Introduction

Experiments performed with Hydrogen and Deuterium plasmas in several tokamaks have shown that the behaviour of the plasma edge and transport phenomena in the core could depend on the isotopic composition. TFTR results showed that D/T mixtures could have more favourable thermal confinement properties than pure Deuterium plasmas in certain conditions. The effect was more pronounced in high power supershots than in L-mode plasmas[1]. TFTR also reported more pronounced edge relaxations in H-mode produced in high β_p plasmas.

JET has started a phase of operation with Tritium. Emphasis is placed in obtaining data in conditions similar to those required in ITER. Care was taken to operate with similar q, ν^* and plasma shape. Data was taken with heat and particle exhaust controlled with a pumped divertor as necessary in ITER. We report here the results obtained during the first 2 weeks of operation of a campaign planned to last three months.

Experimental Set-up

Tritium can be introduced in JET with the operation of a gas valve located near the vessel wall or with Tritium neutral beams ($\leq$ 11MW, $\leq$ 160keV). This article will concentrate on data obtained with the gas valve which is representative of ITER edge fuelling conditions. The gas valve was under density feedback control and could supply up to 500bl s^{-1}.

The reported experiments required the injection of 11g in the JET vessel and 71 D/T discharges were produced. In addition, about 8.5g were used for NBI conditioning. A full Tritium recovery cycle from the exhaust gas of the tokamak and the NBI systems has been performed in a very successful way. The reprocessing cycle required four days[2].

Vessel Conditions, Wall Change-over to D/T and Tritium Inventory

The vacuum vessel is maintained at 320°C while the divertor structure is water-cooled at 30°C. The divertor target tiles are at an intermediate temperature between 150°C and 170°C. The vessel is pumped by four turbo pumps and by a Helium-cooled cryo pump located along the side of the outer divertor leg giving a pumping speed of 200,000l/s (for D_2).

Before the first Tritium injection the tokamak had been conditioned and operated with Deuterium plasmas exclusively. Gas recycling at the edge was therefore dominated by

Deuterium. For instance, Hydrogen density was measured to be less than 2% of the Deuterium density. The change in the plasma isotopic composition was monitored during a series of identical discharges fuelled only with Tritium gas puffing. During this experiment the cryo pump was only cooled at liquid nitrogen temperature to limit Tritium consumption. Fig 1 shows the change of $\gamma_T = n_T/(n_T + n_D)$ ratio during the succession of discharges. During the first discharge fuelled with Tritium, γ_T reached 60% before ICRH heating and reduced to 35% after heating due to heat induced desorption of Deuterium from vessel components. After only five discharges, γ_T reached a value of 0.6 both before and after heating. Measurements taken by a Neutral Particle analyser, spectroscopic observation of the T_α/D_α line intensities and data interpretation of the 14MeV neutron flux indicate that the isotopic composition is nearly constant throughout the plasma radius. This data is similar to that obtained previously with Hydrogen[3]. It also agrees with a multi-reservoir model involving two quite different time constants and indicates that the wall Tritium inventory was about 1g after 20 Tritium discharges.

H-mode Power Threshold, ELM Behaviour and Confinement

Data on H-mode threshold has been obtained with ICRH (several frequencies) and with NBI (80keV Deuterium) at magnetic fields between 1 and 3.4T. Power is ramped slowly over 3s for accurate determination of the threshold power. In the case of NBI, an equivalent power ramp is obtained by pulse width modulation of the eight beam sources. Fig 2 compares a pure Deuterium RF-heated discharge with a D/T (50/50) discharge with otherwise identical parameters. Clearly the H-mode is triggered earlier, eg with about 20% lower input power. Also apparent is the larger size and the lower frequency of the edge relaxations (ELMs) in Tritium discharges. Fig 2 also shows that, with Tritium, long ELM-free periods appear at lower power and that, as in Deuterium, RF-heated discharges have lower edge relaxations than NBI-heated discharges. The H-mode power threshold is identical with NBI or ICRH. Fig 3 shows threshold data obtained in DD discharges and compares it with that obtained in D/T for two ranges of tritium concentrations as indicated in the figure. The 45°-line represents the scaling given by the H-mode Database Group at Montreal[4] for DD discharges. For illustration, a line with a slope reduced by a factor 2/3 is also drawn. Lower power threshold for H-mode in D/T discharges is observed in a variety of conditions. The reduction is commensurate with a A^{-1} scaling. Work is in progress to determine more precisely a new scaling which includes atomic mass.

A comparison of the behaviour of two discharges where D°-beam is injected into a Deuterium or a Tritium discharge is shown in Fig 4. D/T concentrations are given in the figure. NBI power trace was very similar in the two discharges. Again, from the power ramp-up phase, it is noted that H-mode threshold (appearance of ELMs) is lower in the case of Tritium discharge. Also, the Tritium discharge has several long ELM-free periods. This leads to higher density and higher stored energy as compared to the Deuterium discharge. Confinement enhancement factor H93 is also higher in the Tritium case. Further analysis is required to separate the changes due to the different ELMing conditions from changes in bulk confinement. In ICRF heated discharges with high frequency ELMs, the global energy confinement is about 8% larger in

Tritium discharges than in Deuterium during the flat top of the heating pulse. The gas fuelling efficiency is also larger by about 10%.

A fusion power of 3MW was produced with 11MW of NBI and 4MW of ICRH at 3.2MA and 3.4T during a scan of ITER-similar conditions.

ICRH Heating Regimes

The JET ICRH system couples power via four antennas each made of four current straps which can be phased independently. Experiments have been performed in D/T plasmas with up to 95% Tritium. Second harmonic heating ($2\omega_{CT}$ resonance on-axis with 34MHz at 3.4T) and D-minority heating (ω_{CD} resonance slightly off-axis with 28MHz at 3.4T) were used. The $2\omega_{CT}$ experiments were also carried out with 1% He^3 injected to increase the damping with minority He^3 heating. In Fig 5, we show a comparison of $2\omega_{CT}$ heating with and without 1% He^3 where the input power trace was very similar in the two cases. The ITERH93 thermal confinement factor H93TH (fast ion energy subtracted) is found to be significantly higher with He^3 added. Note that the H93TH factor is practically the same in the L-mode and separates when the power is significantly above the H-mode threshold. The ELM behaviour in the two cases is also different. With He^3 added, some discrete ELMs with higher amplitude are found in addition to the high frequency ELMs. The neutron rate, line-averaged plasma density and ion temperature (at r/a=0.4) in the two cases are shown in Fig 6. Analysis of the observed neutron reaction rate is being made in order to compare the code prediction of the supra-thermal tail formation.

Conclusions and Summary

About 11g of Tritium has been injected in JET during 71 Tritium edge fuelled experiments. It was easy to establish and control 50/50 D/T mixtures. The experiments produced a total of $2\ 10^{19}$ neutrons (60MJ of fusion power) and a fusion power of 3MW. The Active Gas Handling System can reprocess efficiently the tokamak exhaust gas and recover the Tritium in high purity form.

The observation of a reduction of the H-mode power threshold by more than 20% in D/T plasmas compared to pure D is a highly favourable result for ITER. There is also some increase in global confinement (~ 10%) which requires further investigation. However, ELMs are somewhat larger but still quite moderate in ICRH heated discharges. The ITER ICRH reference scenario ($2\omega_{CT}$) heats as well as or better than the usual $2\omega_{CD}$ scenario.

References

[1] K. M. McGuire et al, 16th IAEA Fus. Energy Conf., Montreal, 1996.

[2] A. Bell et al, Active Gas Handling System, to be published.

[3] L. Horton et al, Journal of Nucl. Mat. (1992), p 139.

[4] T. Takizijka and H-mode database Group, 16th IAEA Fus. Energy Conf., Montreal 1996, Paper S-5.

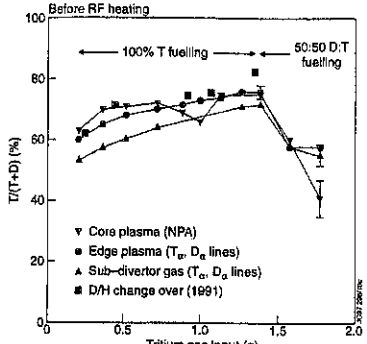

Fig 1. Evolution of $n\tau/(n\tau + nD)$ during the first series of plasma discharges fuelled by a Tritium gas valve. H-modes were produced with RF, NBI and ohmic.

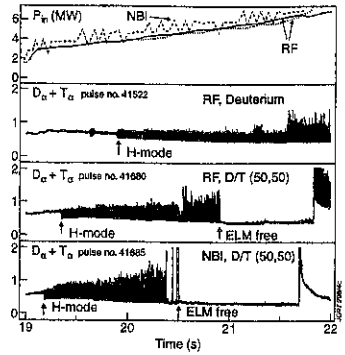

Fig 2. Traces of the input power and line intensity of the $D\alpha + T\alpha$ lines during 3 discharges differing only in isotopic composition and heating methods.

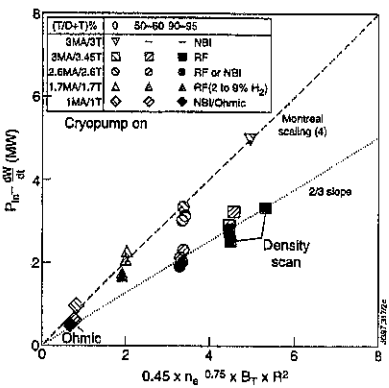

Fig 3. Scaling of the power required for an L to H dithering transition.

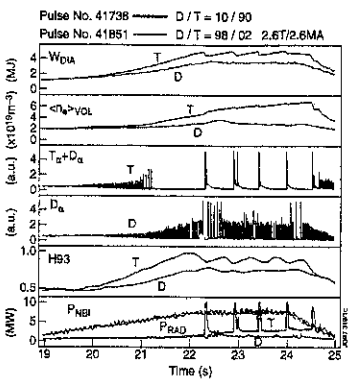

Fig 4. A comparison of discharges with D^0-beam injected into deuterium or tritium plasmas. Fast ion energy has not been removed.

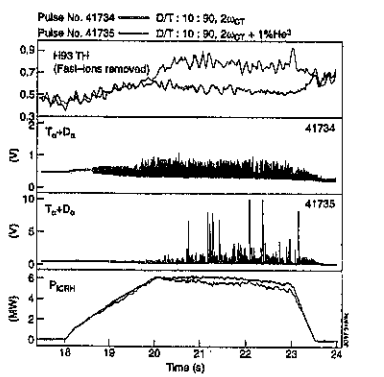

Fig 5. Confinement and ELM behaviour in ICRF heating at $2\omega_{CT}$ with and without He^3.

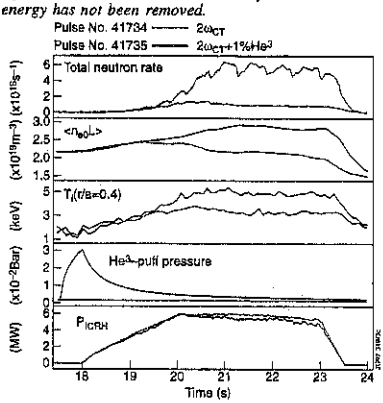

Fig 6. Neutron rate and ion temperature with ICRF heating at $2\omega_{CT}$ with and without He^3.

On the light emission of aluminum micro–pellet cloud

G. Veres, J.S. Bakos, B. Kardon, S. Kálvin, G. Kocsis, S. Zoletnik

KFKI Research Institute for Particle and Nuclear Physics,
P.O.B. 49, H–1525 Budapest, Hungary

In the pellet-plasma interaction experiments the answers to the questions on how much power impurities radiate away in a hot plasma and how the line radiation of a given ion is related to its concentration are very important and still unknown in detail. The total emitted radiation affects through the energy balance equation almost any quantity that characterizes the plasma: the temperature, the pressure and density, just to name a few of them. On the other hand in plasma diagnostics the direct measurement of impurity concentrations is rather difficult and usually the line radiation of the different impurity ions is accessible. To correctly interpret the measurements the knowledge of the relationship between the line emission and total impurity concentration is important.

Micro-pellets are well suited for both theoretical and experimental studies of processes that appears in the interaction. Due to their couple-of-tens-of-micrometers size they do not alter the global plasma parameters and represent a well defined impurity source in time and space. Attempts were done to describe the main characteristics of the pellet cloud (energy balance, ionization of species, cloud acceleration).

During the past years intensive research has been done on the MT-1M tokamak (R=0.4 m, $a_{max} = 0.12$ m, $B_T = 1$ T, $\langle n_e \rangle = 2 \cdot 10^{19}$ m^{-3}) in the micro-pellet–plasma interaction field. Series of experiments were done with pellets of different size and velocity. The details of the experiments have been reported elsewhere and will not be repeated here [2]. During the experiments aluminum micro–pellets with total atom content varied between 10^{14}–10^{15} were injected radially into the plasma of the MT–1M tokamak; and the extensions of the Al I, Al II and Al III line radiation were measured along the magnetic field lines.

In order to estimate the intensity of the line radiation emitted by pellet cloud ions a single cell hydrodynamic model [1] was combined with an atomic physics model. The single cell model was originally developed to explain the expansion – measured in the experiments – of an aluminum micro–pellet cloud along the magnetic field lines ($B_\parallel$) [2]. Due to the rapid change of plasma parameters of cloud ions, no equilibrium condition can be applied in computation of the excited level populations. Neither the conditions of the corona, nor the local thermodinamical equilibrium are fulfilled. So the atomic physics part of the updated model calculates the populations of selected excited states of the aluminum ions (Al^+ and Al^{++}) via finite-rate computations . In this scope electron impact excitation/deexcitation, spontaneous emission and electron impact ionization (from the excited levels as well) are incorporated assuming Maxwellian electron velocity distribution for both the background plasma and cold cloud electrons stemming from the ionization of the cloud ions.

The model calculations showed that most of the energy deposited in the pellet cloud by the background electrons is radiated away via line radiation originated in a

couple of resonant transitions. In this case the calculated $B_{\|}$ size of the cloud differs significantly from that of the measured one. In order to adjust the calculated $B_{\|}$ cloud size towards the measured values, the total light emission power has somehow to be reduced, depending on the pellet size in some cases even by at least two orders of magnitude. This substantial reduction of the radiation power can only be explained by inclusion of new physical phenomena into the model. Two possible explanations have emerged and probably both of them play role in the process.

In a recent paper [3] the authors have reported the formulation of non-Maxwellian electron velocity distributions in a rapidly ionizing laser plasma. The electron velocity distribution of the cloud electrons – they dominate the ionization/excitation processes due to their high density – might also deviate from the Maxwellian, namely the high energy tail can relatively be depleted, since the cloud electron temperature is much less than the ionization/excitation energies. This non-Maxwellian distribution drops the excitation rates, which on the other hand drops the total light emission power. Following the analysis in [3], the excitation/ionization rates were cut-off at low electron temperatures with a $1 - \exp(-(kT_e/\chi)^m)$ factor, where T_e is the electron temperature, χ is the excitation/ionization energy and m varied between 2 and 5, but mostly 4 was used.

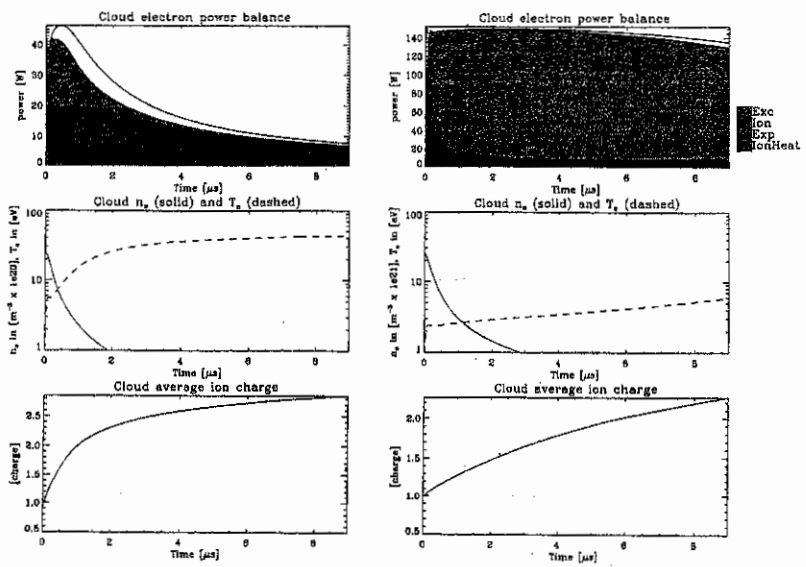

Figures 1. and 2. The electron power balance, density, temperature and average ion charge of the cloud for $2 \cdot 10^{12}$ *(Fig.1.) and* $2 \cdot 10^{13}$ *(Fig.2.) total ion numbers. The excitation/ionization rates and transition probabilities were not reduced.*

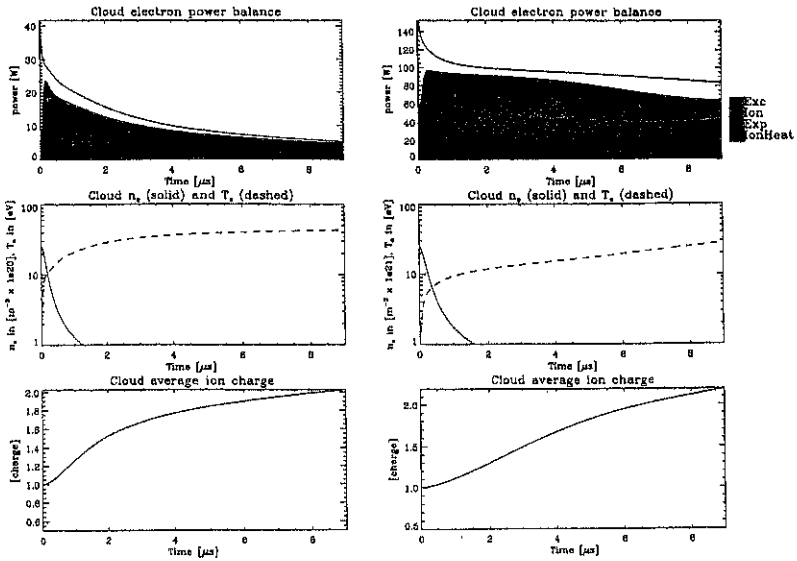

Figures 3. and 4. Like in Figures 1. and 2. but with reduced excitation/ionization rates and transition probabilities.

Conditions close to divertors in tokamaks are alike to those existing close to a pellet. As in the case of divertors, due to high ion densities involved optical re-absorption might be substantial [4]. Once a photon has re-absorbed and caused an excitation, the excitation can decay via electron impact deexcitation, what also drops the total light emission power. Optical re-absorption might be treated via formally reduced transition probabilities, as described in [5]. For the resonant transitions the transition probabilities were reduced arbitrarily by a factor of two.

The data in Figures 1. and 2. were obtained with the original rates and transition probabilities. In Figure 1. the total ion content was $2 \cdot 10^{12}$, whereas in Figure 2. it was $2 \cdot 10^{13}$. In the power balance *Exc*, *Ion*, *Exp* and *IonHeat* stands for powers that go to excitation of ionic levels, ionization of species, expansion of the cloud and heating the cloud ions, respectively; and the dashed line shows the emitted radiative power. It can instantly be seen, that the greater a pellet, the more dominant is the excitation/radiation power and the slower the increase of the cloud electron temperature and average ion charge is. The slow increase of the cloud electron temperature means slow diffusion, that results in small pellet cloud sizes what is in contradiction with the experiments.

Figures 3. and 4. were obtained at similar conditions as Fig. 1. and 2. but with reduced excitation/ionization rates and transition probabilities. The emitted radiation

power is reduced substantially. Despite the reduced ionization rates, the average ion charge is barely decreased and the cloud electron temperature is increased by more than 100 percents!

One can conclude, that if the model calculations would like to reproduce the experimental results, reduced total radiative emission power is necessary, and that two possible solutions to this problem might be the existence of non-Maxwellian electron velocity distributions and optical re-absorption.

The results of these calculations can only show the trends, and for more precise comparison multidimensional models and refined evaluation of the rates and transition probabilities are necessary. These ongoing improved calculations take into account the above mentioned considerations.

References:

[1] S. Zoletnik, J. S. Bakos, B. Kardon, S. Kálvin, G. Kocsis, G. Mank, G. Petravich, A. Pospieszczyk, G. Veres, I. Veres, *23rd EPS Conf. on Contr. Fusion and Plasma Phys.*, Kiev, 1996, p. III–1307.

[2] S. Zoletnik, G. Kocsis, G. Bürger, P.N. Ignácz, B. Kardon, S. Kálvin, J.S. Bakos, *Rev. Sci. Instrum.* **66** (1995) 2904.

[3] Y.T.Lee and M.Lamoureux, *Phys. Fluids B* **5** (1993) 2235.

[4] R.C.Isler, R.W.Wood, C.C.Klepper, N.H.Brooks, M.E.Fenstermacher and A.W.Leonard, *Phys. Plasmas* **4** (1997) 355.

[5] M.H.Key and R.J.Hutcheon *Adv. At. Mol. Phys* **16** (1980) 201.

Author Index

Author Index

Author Index

Author Index

Author Index

Author Index

Author Index

Author Index

Author Index

Author Index

Author Index

Author Index

Author Index

Author Index

Author Index

Author Index

Author Index

Author Index

Author Index

Author Index